J. Keith Nelson
Editor

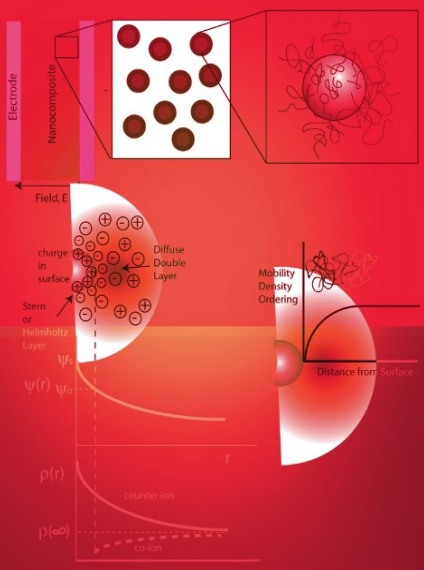

Dielectric Polymer Nanocomposites

Springer

Dielectric Polymer Nanocomposites

J. Keith Nelson
Editor

Dielectric Polymer Nanocomposites

Springer

Editor
J. Keith Nelson
Rensselaer Polytechnic Institut
Dept. Electrical, Computer & Systems Engineering
110 8th Street
Troy NY 12180
USA
k.nelson@ieee.org

ISBN 978-1-4419-1590-0 e-ISBN 978-1-4419-1591-7
DOI 10.1007/978-1-4419-1591-7
Springer New York Dordrecht Heidelberg London

Library of Congress Control Number: 2009936797

Cover graphics courtesy Dr. L.S. Schadler

Printed on acid-free paper

Springer is part of Springer Science+Business Media (www.springer.com)

Preface

The age old discipline of electrical insulation has seen something of a revival in the twenty-first century due to the finding that anomalous, and often advantageous, properties of polymers can be obtained by the appropriate incorporation of a variety of materials of nanometric dimensions. However, it will be clear to readers of this book that this is a fast moving technology which is in its infancy. There are still many unknowns, and, indeed, even as the book it being assembled, new aspects are being uncovered which may cause us to reconsider our thinking. It must consequently be said that the nature of the field is such that the text does contain some speculation and informed guesswork. This is in the interests of providing a basis for a healthy debate on the emerging thinking. The book has been prepared to provide a springboard for both industrialists and academic researchers by providing both practical information such as the compounding and formulation of this class of material, and also the properties and underlying mechanisms attributable to nanodielectrics.

This is a highly multidisciplinary field. As an electrical engineer, I quickly get out of my depth with schoolboy chemistry. Consequently, it has been found necessary to assemble teams of people with the broad range of disciplines needed. It is thus perhaps not surprising that the corresponding mix of chemists, engineers, materials scientists and physicists are represented in the authorship which has been drawn from many of the organizations who have played a leading role in the establishment of this technology from all over the world. For this reason, the reader will also find the book to be interleaved with "tutorial" material designed to provide the technical background for the understanding of the physics and chemistry being discussed. While much of the development work is going on in Universities, the end user will be industry, and so some attempt has been made to map the developments onto the commercial landscape. This has been done by documenting properties that can be enhanced and by providing some indication of the present and possible future applications which may be facilitated.

The book is laid out to permit the reader to get an overview by reading Chap. 1 which then leads in to the subsequent chapters which provide more detail of the aspects important to nanomaterials as electrical insulation. It is not the function of this book to try to examine the large number of other applications for solid nanomaterials, although thermal and mechanical properties important to their use as electrical insulation are featured. It is firmly believed that the future for the use of this class

of materials as electrical insulation relies on our ability to "tailor" properties to the desired application. This requires a mechanistic understanding which is not yet complete, but an attempt is made to provide a window on the emerging picture and also to provide some basis for modeling which ultimately may find application in the process of creating nanodielectrics with the properties needed (within limits). The reader will find that, although each chapter has been configured to highlight a different aspect of nanodielectrics, duplication of some topics is present. This is particularly so with respect to the nature and part played by the internal interfaces which are widely regarded as the key to the way in which this class of materials behaves. This duplication is deliberate since the way in which the interface is viewed varies according to the discipline of each author, and the different insights offer important complimentary contributions to our understanding.

Dielectric Nanocomposites started for me through a joint project with the University of Leicester, UK at the turn of the century, and has become a large part of my effort at Rensselaer in the last few years. However, it has truly been a team effort. It really is a great pleasure to acknowledge the numerous contributions made by Drs. Fothergill, MacCrone, Reed, Roy, Schadler and Smith and Mss. Hu, Hui and Travelpiece whose work has colored this book in substantial ways. The midnight oil burned by my wife, Christine, in undertaking proof reading is also lovingly recognized.

J. Keith Nelson Rensselaer Polytechnic Institute
Troy, NY

Contents

Preface v

1 Background, Principles and Promise of Nanodielectrics 1
J. Keith Nelson

2 The Processing of Nanocomposites 31
F. Bellucci, D. Fabiani, G.C. Montanari, and L. Testa

3 Special Considerations for Clay-Based Materials 65
Takahiro Imai

4 The Chemistry and Physics of the Interface Region and Functionalization 95
C.W. Reed

5 Modeling the Physics and Chemistry of Interfaces in Nanodielectrics 133
R. Ramprasad, N. Shi, and C. Tang

6 Mechanical and Thermal Properties 163
Patricia Irwin, Wei Zhang, Yang Cao, Xiaomei Fang, and Daniel Qi Tan

7 Electrical Properties 197
J.C. Fothergill

8 Interface Properties and Surface Erosion Resistance 229
Toshikatsu Tanaka

9 Non-linear Field Grading Materials and Carbon Nanotube Nanocomposites with Controlled Conductivity 259
L.S. Schadler, X. Wang, J.K. Nelson, and H. Hillborg

10 The Emerging Mechanistic Picture 285
R.J. Fleming

11 Industrial Applications Perspective of Nanodielectrics 321
Enis Tuncer and Isidor Sauers

A Diagnostic Methods for Mechanistic Studies in Polymer Nanocomposites 339

Index 363

Contributors

F. Bellucci Politecnico di Torino, Torino, Italy

Yang Cao GE Global Research Center, Niskayuna, NY, USA

D. Fabiani Università di Bologna, Bologna, Italy

Xiaomei Fang GE Global Research Center, Niskayuna, NY, USA

R.J. Fleming Monash University, Melbourne, VIC, Australia

J.C. Fothergill University of Leicester, Leicester, UK

H. Hillborg ABB AB, Corporate Research, Västerås, Sweden

Takahiro Imai Toshiba Corporation, Japan

Patricia Irwin GE Global Research Center, Niskayuna, NY, USA

G.C. Montanari Università di Bologna, Bologna, Italy

J. Keith Nelson Rensselaer Polytechnic Institute, Troy, NY, USA

R. Ramprasad Chemical, Materials and Biomolecular Engineering, Institute of Materials Science, University of Connecticut, Storrs, CT, USA

C.W. Reed Consultant, Scotia, NY, USA

Isidor Sauers Oak Ridge National Laboratory, Oak Ridge, TN, USA

L.S. Schadler Rensselaer Polytechnic Institute, Troy, NY, USA

N. Shi Shocking Technologies, Inc., San Jose, CA, USA

Daniel Qi Tan GE Global Research Center, Niskayuna, NY, USA

Toshikatsu Tanaka Waseda University, Japan

C. Tang Chemical, Materials and Biomolecular Engineering, Institute of Materials Science, University of Connecticut, Storrs, CT, USA

L. Testa Techimp Systems Srl, Zola Predosa (BO), Italy

Enis Tuncer Oak Ridge National Laboratory, Oak Ridge, TN, USA

X. Wang Rensselaer Polytechnic Institute, Troy, NY, USA

Wei Zhang GE Global Research Center, Niskayuna, NY, USA

Chapter 1
Background, Principles and Promise of Nanodielectrics

J. Keith Nelson

1.1 An Introductory Perspective of Electrical Insulation

Electrical insulation is pervasive. Every piece of electrical equipment relies on it in one form or another, and thus it is a huge market segment. Nevertheless, many forms of insulation today have changed only marginally in half a century, and the whole discipline has long been regarded as "mature science." As such, industry has been reluctant to invest much in insulation research since other areas have been seen to have more promise. However, the quantity of electrical insulation in use means that even incremental gains in properties can have substantial commercial significance. This is particularly so in the electric power field where, for some equipment such as cables, the insulation cost is a substantial portion of the whole.

The major electrical properties usually considered in selecting an insulation system may be categorized as:

(a) The electric strength
(b) The relative permittivity
(c) The dielectric loss (as typified by the loss tangent, tan δ)

The relative importance of these properties clearly depends on the application, but the electric strength is universally regarded as a dominant parameter. Since it is a quantity that is stochastically distributed, it is not only the mean value, but its statistical distribution which is important. Indeed, in the design context, very large factors of safety have to be built into the design of all insulation systems to allow for the substantial variability exhibited in the electric strength of solid and liquid insulants, particularly when large areas/volumes of insulation are involved. This results from a weak link concept of dielectric failure which associates a larger size with an increased probability of having some sort of imperfection (void, particle, processing defect, etc.) which might precipitate failure. Consequentially, any reduction in that variability is also a valuable attribute. It must also not be assumed that the performance of *electrical* insulation relies only on *electrical* properties. In that

J.K. Nelson (✉)
Rensselaer Polytechnic Institute, Troy, NY, USA
e-mail: k.nelson@ieee.org

J.K. Nelson (ed.), *Dielectric Polymer Nanocomposites*,
DOI 10.1007/978-1-4419-1591-7_1,

context, mechanical and thermal properties may play the dominant role in some applications. For example, most electrical failures of the composite insulation in large electrical machines usually have a mechanical or thermal precursor. Specialist applications may also require the consideration of other properties such as arc resistance or thermal expansion coefficient. When the total picture is accounted for, there is, in fact, a considerable scope for making improvements in insulation systems, and there is sometimes a compelling economic incentive.

Study of the history of electrical insulation would suggest that the introduction of a truly new insulating polymer is quite a rare event. The majority of "new" systems have often involved the use of additives to existing materials, blends and copolymers, etc. In this context, the use of fillers in polymeric systems has been widely employed. The practice of using fillers is often to impart a specific property to the insulating structure such as enhanced permittivity, corona resistance, thermal or mechanical performance, etc. However, the practice has also often been widely employed to reduce the cost of an expensive polymer by substituting some of the bulk by inexpensive fillers such as clay. Conventionally these fillers have been solid particles in the micron size range.

1.1.1 The Emergence of Nanocomposites

Although there were some early trials in which the size of the filler particles in a polymer was reduced, it seems that the true significance of the results was not recognized in the wider context. Notably, a US patent (Johnston and Markovitz 1988) issued in 1988 showed that some advantages could be gained for micaeous systems used for the groundwall insulation of form-wound generators. Similarly work with silica nanoparticles (Henk et al. 1999) found that voltage endurance of polymer insulation could be enhanced if the filler particle size was reduced. Surprisingly, such early initiatives went largely unnoticed, as did a landmark theoretical paper by Lewis (1994) which is now much quoted as being the start of the nanodielectrics initiative. However, it was not until the possibilities were highlighted by new experimental work published by a UK/US team in 2002 (Nelson et al. 2002) that interest in the area became worldwide. This may be gauged from Fig. 1.1 which depicts a timeline of publication activity compiled from a Compendex™ database search based on the terms "nanodielectrics" and "dielectric nanocomposite." It is very clear from Fig. 1.1 that nanodielectrics are a twenty-first century phenomena. While nanotechnology has been utilized in the semiconductor, biological and sensor arenas for substantially longer, utilization of the technology in insulation systems has been slow to be developed. This does mean, however, that this is now a very fast evolving field which this book is designed to address, and it is expected that significant developments, particularly with regard to the tailoring of properties, will be forthcoming in the next decade. Professional Societies have reacted to the burgeoning interest by producing special issues of their archival Journals dedicated to nanodielectrics. Examples may be found from the Institute of Physics (Stevens 2005), the Institute

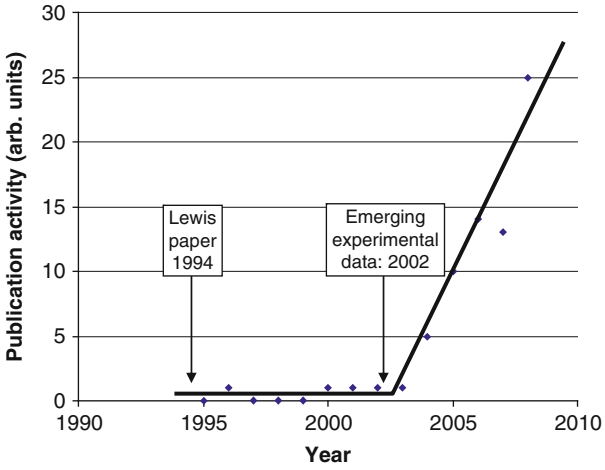

Fig. 1.1 Publication activity in the field of nanodielectrics

of Electrical and Electronics Engineers (Dissado and Fothergill 2004; Nelson and Schadler 2008) and the Institute of Electrical Engineers of Japan (Tanaka 2006). In the same way, technical conferences are emerging with special sessions devoted to this technology. An early review (Tanaka et al. 2004) also provides a useful global perspective.

For electrical insulation, a *nanocomposite* may be defined as a conventional dielectric material (usually, but not necessarily, a polymer) into which filler particles, of a few to a few tens of nanometers in size, have been introduced, to form a well dispersed homogeneous blend. Although the term *nanodielectric* can mean any dielectric system considered on a nanoscale, for this book the terms *nanocomposite* and *nanodielectric* are used interchangeably to refer to polymer/nanoparticle mixtures. The dispersion and distribution of the nanoparticle filler will be a recurring theme since, only when the processing is done correctly, can the full advantages be realized. A recent text on polymeric nanocomposites (Bhattacharya et al. 2008) although not concerned with these materials as dielectrics, does nevertheless contain valuable insight into the preparation and characterization specifically of silicate nanocomposites. Similarly, the Polymer Nanocomposites Handbook (Gupta, Kennel and Kim 2010) is a useful resource for many of the allied issues, but is more focused on carbon-based composites.

1.1.2 Multifunctionality

Although this book is predominantly involved with the electrical properties of these materials since their use as electrical insulation systems is the thrust, nevertheless some of the other properties outlined in Sect. 1.1. become important for practical applications. Furthermore, in many cases, the electrical failure of insulation will

have a mechanical, thermal or environmental origin. Indeed some electrical failure mechanisms such as electromechanical and thermal breakdown (Nelson 1983) require the involvement of non-electrical properties. Although the use of conventional (μm-sized) fillers inevitably means that one property is being augmented usually at the expense of another, the indications are that once the filler size is reduced to a few nanometers, this is not necessarily so. For example, the use of conventional fillers to affect the thermal or mechanical properties, flammability, etc. almost always involves a significant reduction in the electric strength of the resulting composite (Ueki and Zanin 1999). As a result, there is the promise that materials can be engineered to be multifunctional as has been demonstrated by the introduction of nanoscopic high-order structures into epoxy to suppress phonon scattering and enhance thermal conductivity (Fukushima et al. 2006). Another good example of this is the development of capacitor dielectrics introduced in Chap. 11. Past attempts to improve the energy density of capacitors through enhancement of relative permittivity have often been unsuccessful since the addition of fillers to achieve this is accompanied by a reduction in the electric strength. Since the energy storage is dependent on the *square* of the electric field and only linearly with permittivity, the failure of such attempts is obvious, particularly when it is recognized that, at modest loadings, most of the stress is carried by the base polymer and not by a high permittivity inclusion. However, this may not be the case with nanocomposites which explains the widespread interest in this technology for capacitor applications.

It is, of course, the industrial applications which will drive the development of the technology. A recent report (Tanaka et al. 2008) of an investigation conducted by a committee of the Institute of Electrical Engineers of Japan has highlighted the areas of electrical insulation most likely to be able to capitalize on the advantages of nanodielectrics. These may be summarized as: outdoor insulation, switchgear, DC cable applications, magnet wire development, electrochemical capacitors, and insulation for inverter-fed motors. Although these applications are clearly centered on the power industry, parallel initiatives for the electronics arena are obviously likely to follow. Some of the applications cited by this committee report are discussed in Chap. 11, but they all seek to capitalize on the known favorable property enhancements in thermal properties (Chap. 6), voltage endurance and space charge distribution (Chap. 7), and erosion resistance (Chap. 8).

1.1.3 A Philosophical Perspective

While the physical and chemical understanding of this new class of materials is far from complete, an attempt is made in Chap. 10 to provide some insight into the underlying mechanistic picture. This is very important since only when this knowledge is developed will it be possible to tailor the properties, and engineer insulation systems in an informed way.

In the most simplistic case, we can consider composites to be particulate materials (here assumed monodisperse and spherical) embodied in a polymer matrix.

However, in reality the important interface between the particle and the polymer will be complex and spatially extensive. The emerging picture suggests that this interface is, in fact, a zone of interaction with a radial build of very approximately 10–20 nm and models are being developed along these lines to try to predict nanocomposite behavior (Tanaka et al. 2005) and to obtain insight into the structure (Raetzke and Kindersberger 2006). The true nature of these zones is the subject of much interest, and Lewis (2004) has suggested that they may contain diffuse charges similar to the Gouy-Chapman-Stern electrochemical regions well known in liquid dielectrics (Walmsley and Woodford 1981). Without being concerned with the exact nature of these layers, Fig. 1.2 shows how they might look for (a) a conventional micron-sized filler and (b) for a nanofilled material. Although clearly not to scale, Fig. 1.2 shows that the interfacial region surrounding the particles is *dominant* for the nanocomposite, whereas it is insignificant for the conventional material.

It will also be evident from Fig. 1.3 that, as the particle size is reduced, the proportion of the total material, which appears at the interface, starts to become

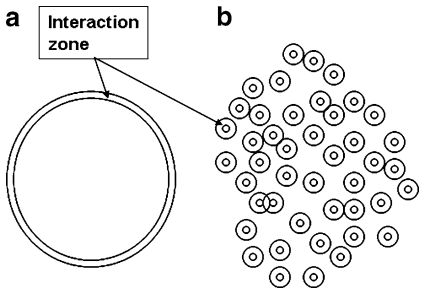

Fig. 1.2 Representation of interactions zones for (**a**) a microparticle and (**b**) an assembly of nanoparticles (*not to scale*)

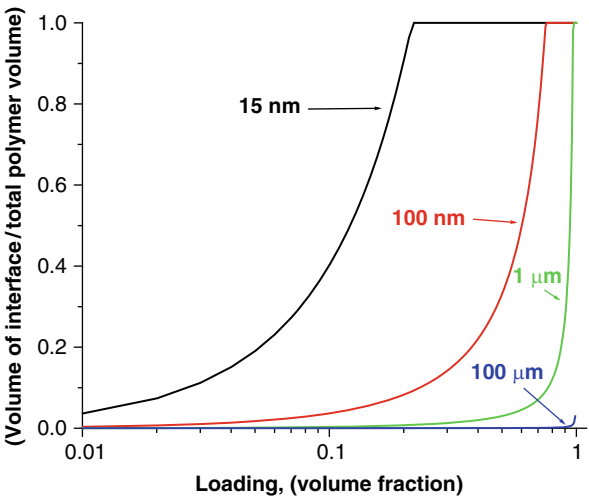

Fig. 1.3 Surface-to-volume ratios of nanocomposites as a function of nanoparticle loading

very significant. When Figs. 1.2 and 1.3 are considered together, it becomes clear that, for a nanocomposite, most of the bulk material is, in fact, composed of interface. Consequently, although the composite may have been compounded from a base polymer and a nanometric inclusion, the properties of the resulting composite may be more likely to resemble those of the interface zones rather than those of the original constituents. It that sense, a truly new material has been formed, which may not behave in the same way as the base polymer from which it was derived. It is thus evident that the challenge is to engineer the interaction zone in a way that provides the desired properties. This may sometimes be accomplished by physical means (e.g. tethered entanglement (Zhu and Sternstein 2003)) or by chemical functionalization of the particulate surface (Reed 2007). Such chemical treatments are often coupling agents which are designed to improve or alter the bonding at the surface and have become an important part of the compounding of dielectric nanomaterials. These methods are detailed in Chap. 4 and offer the opportunity for a measure of self-assembly. Understandably, the physics that underlies the interfacial region is the subject of an increasing interest. If one imagines a solid phase, such as an oxide particle with a diameter of a few tens of nanometers, is composed of several thousand molecular units, immersed in a host phase, the distribution of forces in the particle interior, away from the interface, may be considered constant (except for spatial fluctuations on an atomic scale). As the interfacial region is approached, however, considerable modification of those forces might be expected due to the presence of the host (Smith 2009). In this way, the interfacial region of a nanocomposite might be better described as the region where these forces, and thus the intensity of any material property that depends on them, are in transition from the interior values of the particle to the bulk values of the host.

As Lewis points out, the exact size of this interfacial zone, or transition region, depends on the attribute being studied. For example, the nature and extent of the interface would likely be different for the energy barrier to electron emission, from one phase to the other, than it would be for the distribution of mechanical stresses (Lewis 2004a). Quantum-mechanical effects and the influence of particle shape on the local electric field distribution, both likely to be relatively insignificant in the area around conventional fillers, more strongly assert themselves as the filler particle size is reduced to nanometric dimensions (Fréchette and Reed 2007). Additionally, the reordering of species into interfacial polarization layers (Maxwell-Wagner effect) can have important consequences for local electrical conductivity (Lewis 2004a), which in turn can play a major role in macroscopic electrical properties, due to the large volume of the bulk that is dominated by the polymer-particle interfaces. In this way, for a situation in which interparticle distances never exceeded the radial build of the interaction zones ($\sim$20 nm), the bulk is perturbed by the nanofiller as depicted diagrammatically in Fig. 1.2. For nanoparticles this can be achieved with modest ($<$10%) loadings due to the modified percolation threshold provided by the interaction zone.

1.2 The Compounding of Dielectric Nanocomposites

Study of the literature indicates that a wide range of polymers, both thermosets and thermoplastics, have been used as the base materials for nanodielectrics. This means that the processing takes many different forms such as in situ polymerization, solution dispersion or melt mixing. For electrical insulation, melt compounding is widely used since it does not involve solvents which can sometimes adversely affect the dielectric loss. The nature of the included particle is also very varied being determined by the properties desired in the composite. However, the three major classifications which have emerged are further discussed in Chap. 2 and may be summarized as:

1. Inorganic oxides
2. Clays (layered silicates)
3. Specialist materials such as carbon nanotubes and non-linear particles

The third category is addressed in Chap. 9 of this book and is often the basis for the emerging field of "smart" materials whose properties may be altered in response to circumstances. A good example of this is the very practical case of stress-grading formulations capable of exhibiting conductivities which are dependent on the prevailing electric field.

In all these cases, for both in situ polymerization and mechanical blending, the importance of the proper dispersion and distribution of the nanophase elements within the host polymer cannot be overemphasized enough. It is the key to the appearance of the desired, and sometimes anomalous, properties, particularly for dielectric strength (Vaughan et al. 2006). Indeed, it is likely that some of the very early reported results (Nelson et al. 2002) were for less than optimal compounding conditions. Furthermore, it is likely that much of the inconsistency of properties reported in the literature results from variations in the processing applied. At the heart of the issue is the tendency of the finely divided materials to form aggregates in the mix. At the internal interfaces present in composites, the local chemical environment changes and the net internal forces are not zero. The resulting surface energy creates an interfacial tension which must be overcome in order to maintain particle separation and overcome agglomeration. The theory of these surface free energy mechanisms in composites may be found elsewhere (Bhattacharya et al. 2008). A number of measures need to be adopted to counteract this tendency depending on the system under consideration. However, in general, great care needs to be taken during melt mixing to control moisture conditions, and considerable amounts of shear force need to be applied during compounding to break up agglomerates. Ultrasonic methods have also been found effective in this regard. This topic is sufficiently important that two chapters have been devoted to the issue. Chapter 2 deals with the general cases involving nanoparticles derived from inorganic oxides such as SiO_2, TiO_2 and Al_2O_3 and for clays. Chapter 3 covers in much more detail the methods required to combat the special problems associated with clay fillers, such as montmorillonite. The polar nature of these materials makes them insufficiently organophilic to be compatible with non-polar polymers. Hence, layered silicates

need to be organically modified before being dispersed within the host polymer. This is done by expanding the galleries between the layers using cationic surfactants to lower the surface energy and allow entry of the polymer to form an intercalated structure. Further disaggregation may ideally also be applied to form a completely exfoliated morphology with random orientation of the layers. It is, however, considerably more difficult to achieve fully exfoliated structures than intercalated ones (Green and Vaughan 2008) because of shear force delamination and thermal instabilities. Chapter 3 also provides an industrial manufacturing perspective on the compounding of clay-based nanodielectrics.

1.2.1 The Importance and Assessment of Dispersion

The dispersion can conveniently be assessed using electron microscopy. Although the scanning electron microscope (SEM) is routinely used on a cryocracked sample for this purpose, as nanoparticles have become smaller, the resolution provided by even a field emission SEM is somewhat marginal. Improvements can be obtained by milling a hole in the material using a focused ion beam, and then using SEM to image the side of the hole. However, the more difficult transmission electron microscopy (TEM) sometimes becomes necessary with the attendant complication of sectioning the material. The skilled practitioner can make a reasonable assessment of any aggregation that has taken place from a casual study of the photomicrographs, but a more formalized estimate of the compounding quality is often needed.

For this purpose, a Quadrat-based method is often used (Kim et al. 2007) in which a micrograph is divided into areas, which are usually continuous rectangles of the same size, called quadrats. The number of particles in each quadrat is tallied, and an index is generated accordingly. For example, the third moment of the central deviation which is known as skewness can be used as the index (Hui et al. 2008). Skewness measures the asymmetry of the distribution of variables. If there are large aggregates, it means that some particles are gathered in a small number of quadrats, while many quadrats are left empty; this asymmetry results in non-zero skewness. Higher skewness indicates a poorer dispersion. Skewness can be calculated from (1.1).

$$\frac{N}{(N-1)(N-2)} \sum_{i=1}^{N} \left(\frac{x_i - \overline{x}}{\sigma} \right)^3 \tag{1.1}$$

where x_i denotes the number of particles in the ith quadrat; $\bar{x}$ is the mean of x_i ($i = 1, 2, \ldots, N$), and σ is the standard deviation of x_i.

As an alternative approach, a nearest-neighborhood distance method can be employed where the distance between the gravity centers of each particle is measured. For an arbitrary particle i, the distances between i and other particles are sorted from smallest to largest. Consider the distance W_k from an arbitrary particle to the kth nearest particle, under complete spatial randomness the expectation is:

$$E(W_k) = k(2k)!/\left\{(2^k k!)^2 \lambda^{1/2}\right\}, \quad k = 1, 2, \ldots \tag{1.2}$$

where λ is the particle density (Cressie 1991). For a study region with an area of S, and with n particles within this region, the particle density is

$$\lambda = \frac{n}{S} \tag{1.3}$$

For a sample of n particles, the kth nearest neighbor distances can be measured and symbolized as:

$$\{W_{ki} : i = 1, 2, \cdots, n\}, k = 1, 2, \cdots, K \tag{1.4}$$

The ratio of the nearest mean distance to the expected kth nearest neighbor is the kth nearest neighborhood distance series:

$$R_k = \left\{ \sum_{i=1}^{n} W_{ki}/n \right\} \left\{ (2^k k!)^2 \lambda^{1/2} \right\} / k(2k)!, \quad k = 1, 2, \ldots \tag{1.5}$$

The ratios R_k versus k are then plotted to inspect for departures from 1: $R_k > 1$ indicates regularity and $R_k < 1$ indicates clustering, for small k. If points are randomly spaced within clusters, R_k should be less than 1 and approximately constant for small k and should increase as k approaches and exceeds the cluster size. The larger the departure is from unity, the more significant the regularity or clustering (Tewari and Gokhale 2005).

More recently a combined method has been proposed (Hui et al. 2008) in which both dispersion and distribution can be defined as two independent aspects of mixing. The degree of dispersion is only related to the particle count variation of aggregates and particles, and the degree of distribution is related to the distance between each aggregate/particle. These two aspects may be combined. Dispersion is evaluated through equivalent radius deviation over the primary particle size. The equivalent radius means the radius of an equivalent circle within which the area is the same as the aggregate.

$$\sigma = \frac{\sqrt{\frac{1}{N} \sum_{i=1}^{N} (x_i - x_o)^2}}{x_o} \tag{1.6}$$

where, x_i is the equivalent radius for the ith aggregate/particle, x_o is the primary particle radius and N is the number of aggregates/particles. Distribution is evaluated through the first nearest-neighborhood distance between the gravity centers of aggregates or particles.

By way of illustration, TEM images of vinyl-silane treated and untreated 12.5 wt% nano-silica/XLPE are shown in Figs. 1.4 and 1.5. Public domain software ImageJ® may be employed to carry out the required image processing and measurement. After the TEM images are digitized, ImageJ® is then able to measure

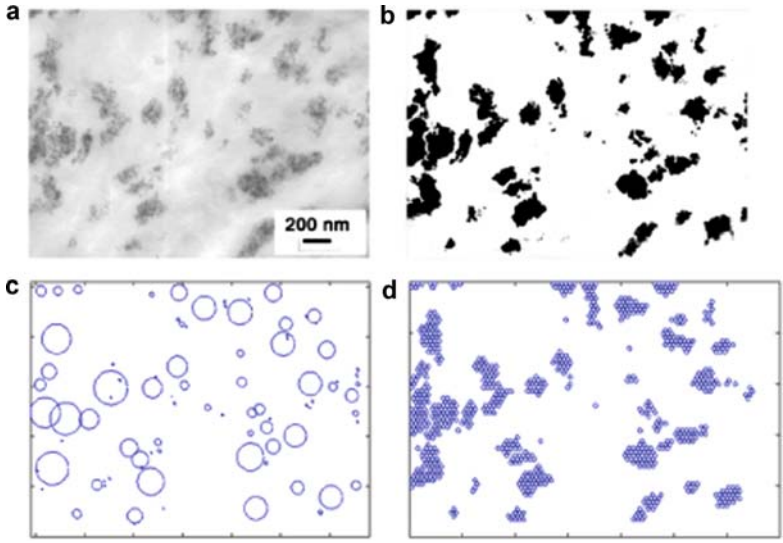

Fig. 1.4 TEM image of vinyl-silane treated 12.5 wt% nano-silica/XLPE (Hui et al. 2008), (**a**) Original TEM image, (**b**) binary image, (**c**) equivalent circle image, (**d**) discrete particle image

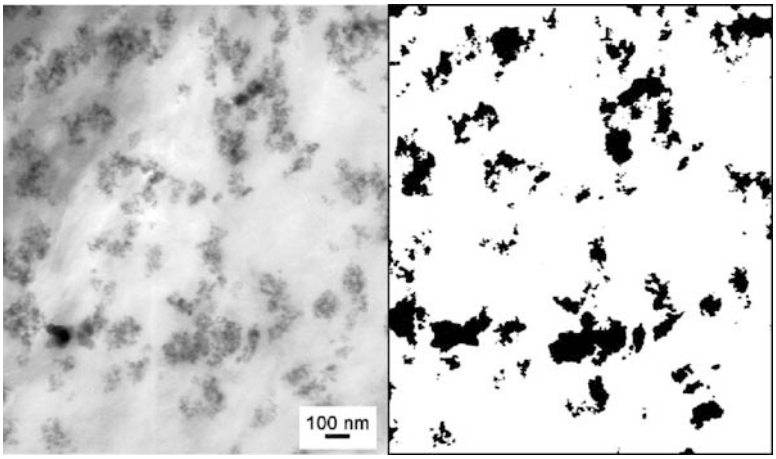

Fig. 1.5 Original (left) and binary TEM image of untreated 12.5 wt% nano-silica/XLPE (Hui et al. 2008)

the area as well as the coordinates of the gravity center of every aggregate/particle. Considering that the thickness of a TEM sample is around 50 nm, it is reasonable to assume a non-overlap arrangement of the particles in an aggregate. According to the measured area of an aggregate, it is possible to calculate the number of particles assembled. Further, making use of the pixel value of the binary image, the coordinates of every single particle can be obtained.

Table 1.1 Quantification comparison

		Treated silica/XLPE	Untreated silica/XLPE
Skewness		2.43	2.67
1st nearest neighborhood distance		0.60	0.75
Combined method	Equivalent radius deviation	1.48	1.32
	1st nearest neighborhood distance	0.43	0.59

Figure 1.4a is the original TEM image, and Fig. 1.4b is the binary image processed by ImageJ®. Figure 1.4c is the equivalent circle image regenerated from the area and gravity center of aggregates/particles measured by ImageJ®, and Fig. 1.4d is the discrete particle image generated by placing a full plate of particles and checking the binary value of Fig. 1.4b to determine whether there is a particle or not. Figure 1.5 shows a TEM image of untreated 12.5 wt% nano-silica/XLPE. Similar analysis procedures may be applied.

For comparison, Quadrat-based skewness, the first nearest distance method, extended nearest neighborhood distance method, k-function, and finally the combined method have been applied to these two images. The indices results are listed in Table 1.1 where the skewness and the first nearest distance serve as overall indices. For skewness, a quadrat size of 200 nm^2 was chosen. A higher value indicates poor dispersion and distribution. For the first nearest distance, the larger the departure from unit value, the poorer the dispersion and distribution. Subjectively, Fig. 1.4 has larger aggregates compared to Fig. 1.5. The first nearest distance confirms this subjective judgment. However, the skewness measure gives a contrary indication, but is sometimes reduced due to aggregates of similar size.

The combined method evaluates separately the two aspects. Equivalent radius deviation indicates the degree of dispersion. Higher values indicate poor dispersion. Fig. 1.4 has a larger value of deviation, which means there are more aggregates compared to Fig. 1.5. The first nearest distance shows a departure from unity which means that, even for the parental points, there is still a tendency of clustering in both images. Consequently, Fig. 1.4 has a poorer degree of distribution. For multi-scale information, the untreated material shown in Fig. 1.5 has higher nearest distance values, therefore, the distribution is better.

By means such as these, the particle dispersion and distribution can be characterized numerically, and assessment of the composites made without any arbitrary subjective judgments playing a role which is currently often the practice. Further assessment by X-ray methods is outlined in Sect. 2.4.

1.2.2 Functionalization

One of the most effective ways to engineer the interface regions is to chemically adjust the particulate surface so as to modify the bonding with the matrix and/or generate chemical species that can play a role in the charge storage and transport

in the nanocomposite. In this context, it has recently been shown (MacCrone et al. 2008) using Electron Paramagnetic Resonance (EPR) techniques that the application of such methods can generate surface states that provide trap sites which, in turn, can modify several of the electrical characteristics. An outline of the EPR method can be found in Sect. A.4. To use semiconductor parlance, donors and acceptors, in a polymer/SiO_2 interface region have been identified as electron states associated with oxygen. Based on an electronic structure and spatial arrangement of donor and acceptor sites, charge transport can be expected to occur essentially by thermally activated electron hopping from an occupied oxygen donor site to a near neighbor vacant oxygen acceptor site. The energies of these sites are modified by the applied and local electric fields in such a way as to induce hopping motion in the appropriate direction.

The chemical aspects of functionalization are covered in detail in Chap. 4, but Fig. 1.6 shows the principle applied to a polyethylene – silica nanocomposite where the silica nanoparticles have been treated with triethoxyvinylsilane.

Figure 1.7 shows the associated FTIR spectra of vinylsilane-treated particles and vinylsilane-treated nanofillers in cross-linked polyethylene indicating that the surface treatment resulted in covalent bonding between the nanoparticles and the XLPE.

There are two significant differences between these spectra:

1. Many of the features of the particles (such as free silanol groups at 3,747 cm^{-1} and a broad peak centered around 3,500 cm^{-1}) are gone, and
2. Some new features are added. A peak at 1,580–1,680 cm^{-1} representing the carbon-carbon double bond (-C = C-), which was present in the vinylsilane-treated particles (from the vinyl group), is replaced by the peak at 2,860 –2,970 cm^{-1} representing the single bond of carbon (-CH_2-CH_2-).

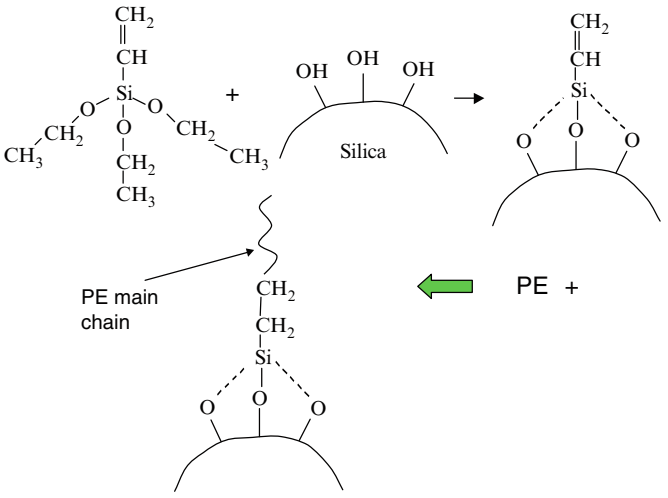

Fig. 1.6 The use of a vinylsilane functionalizing agent with a polyolefin-silica nanocomposite (Roy et al. 2005)

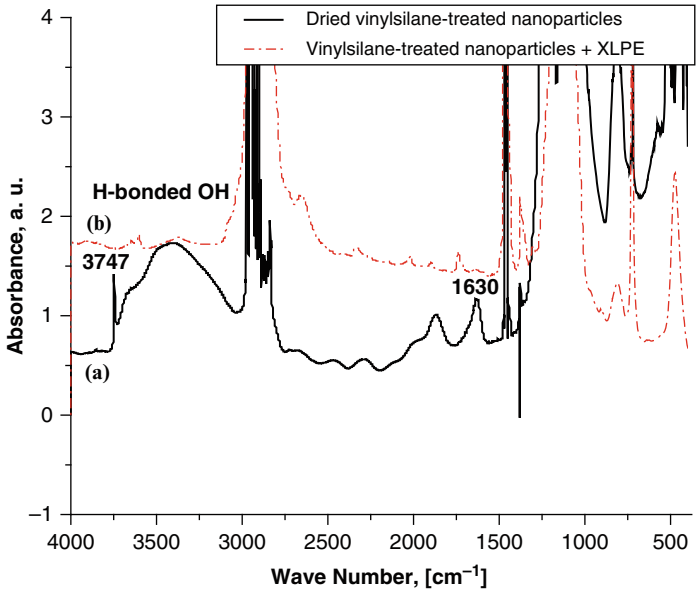

Fig. 1.7 A comparison of the FTIR spectra of treated SiO_2 nanoparticles before and after incorporation into a polyethylene matrix (Roy et al. 2005)

This leads one to conclude that vinyltriethoxysilane is chemically bonded to a silica particle on one end, and to polyethylene on the other as shown in the schematic of Fig. 1.6. The behavior of the resulting composite is also somewhat dependent on whether the functionalizing compound is polar or non-polar. The differences appear in the trapping of charges in the interface region as revealed by thermally stimulated current methods and by dielectric spectroscopy applied to nanocomposites prepared in this way.

Functionalization can also be efficacious in the processing of nanocomposites. Agglomeration is very dependent on the chemistry of the nanoparticle surfaces. In the above example, the termination of the amorphous silica (SiO_2) chains or rings at the particle surface tends to generate silanol groups ($\equiv$ Si-OH), some of which, according to proton Nuclear Magnetic Resonance (NMR) spectroscopic studies, display properties of hydrogen bonding (Liu and Maciel 1996), which can interfere with particle mixing in the composite melt. Additionally, silica is hydrophilic, and this attraction to atmospheric water can cause considerable difficulties in the initial mixing of the composite material. Zou et al. performed a hydration study on silica in epoxy systems, and, using a percolation model, were able to show that several monolayers of water surrounding nanoparticles were responsible for observable changes in electrical properties, and that even a heavy loading of microparticles in epoxy did not result in the same degradation (Zou et al. 2008). A layer of water several molecules deep can easily be supported by the hydrogen bonding at the particle surface (Iler 1979), and this provides an explanation for the sensitivity of compound-

ing to residual moisture. However, functionalizing the surface of nanosilica, in the manner depicted in Fig. 1.6, reduces the number of reactive silanol-terminated surface groups. Additionally, the presence of the vinylsilane links adds steric hindrance to the ingress of water towards the particle surfaces. In the silica-epoxy work cited here, the creation of a hydrophobic nanosilica surface through functionalization resulted in nanocomposites that absorbed the same amount or even less atmospheric water than the base epoxy resin (Zou et al. 2008). This is another example of the multifunctionality introduced in Sect. 1.1.2.

1.3 Property Modifications

This text is concerned with nanocomposite properties of two types:

- Those that generate useful enhancements to polymers for practical applications, and
- Those that produce clues to unraveling the underlying physics and chemistry which dictates the behavior exhibited.

It is the first category which is currently driving the thrust and giving rise to the remarkable rise in interest depicted in Fig. 1.1. However, it is becoming clear that it is the second class of property changes that will provide the ability to "engineer" the next generation of nanodielectrics. It is the documentation of this type of property change and/or diagnostic response which is fueling efforts to provide mechanistic understanding such as introduced in Chap. 10 and elsewhere in this book. Both of these groups of properties are covered in detail in later chapters, but it is appropriate to outline here those that are driving the technology; in many cases because they offer significant improvements in a science which has long been regarded as mature technology. It will also be evident in reading this book, that there are numerous instances where there is no agreement in establishing some of the properties and trends. Not only is this because the chemistry of the interface is very variable, but also because there are large differences in the rigor and care applied to the processing of this new class of material. Not until processing methods and assessment are properly specified and quantified will this technology reach a proper level of maturity.

1.3.1 Property Augmentation of Practical Significance

From a design perspective, perhaps the most important attribute of a dielectric is its breakdown strength and Fig. 1.8 provides a comparison on the basis of Weibull statistics between the DC uniform-field electric strength of a cross-linked polyolefin-SiO_2 nanodielectric in comparison with its microcomposite counterpart and the base polymer from which it is formulated. The reduction of electric strength

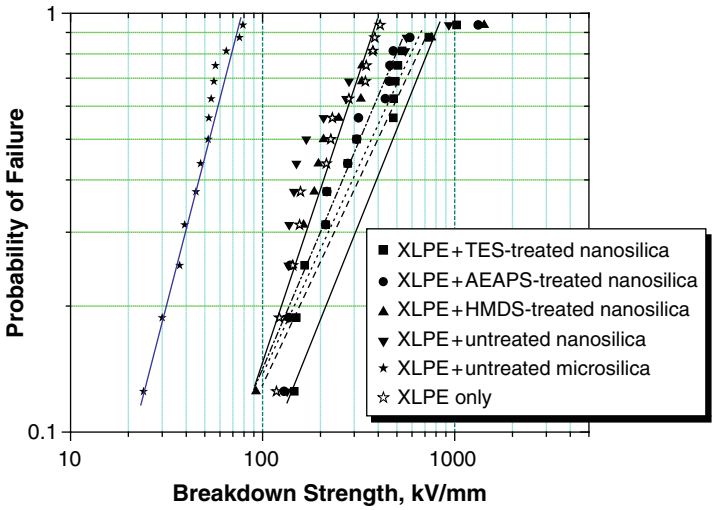

Fig. 1.8 Weibull plots of the breakdown probability of XLPE together with a variety of composites. *TES* Triethoxyvinylsilane; *AEAPS* aminopropyl-trimethoxysilane; *HMDS* hexamethyldisilazane (Roy et al. 2007)

Table 1.2 Characteristic breakdown voltage (kV/mm) of XLPE and several nanocomposites at a range of temperatures (Weibull shape parameter in parenthesis)

Temperature / Materials	25 °C	60 °C	70 °C	80 °C
XLPE	269 (2.49)	183 (2.65)	129 (3.66)	79 (3.84)
XLPE + Untreated Nanosilica	314 (2.07)	260 (2.27)	213 (2.49)	83 (3.09)
XLPE + AEAPS Treated Nanosilic	400 (1.69)	266 (2.20)	263 (1.79)	134 (2.11)
XLPE + HMDS Treated Nanosilic	336 (1.69)	225 (1.97)	208 (2.14)	128 (2.09)
XLPE + TES Treated Nanosilica	446 (1.73)	422 (2.22)	344 (2.17)	220 (2.87)

occasioned by the use of conventional fillers is clearly seen as is the augmentation provided by nanotechnology embodying a variety of functionalizating agents. Table 1.2 provides data for the same system (polyethylene (XLPE) cross linked with dicumyl peroxide) as a function of temperature from which the enhancement in characteristic value is evident and accentuated at high temperature (Roy et al. 2007). Comparison of the top and bottom rows of Table 1.2 indicates a 65% improvement at room temperature, but an enhancement of 185% at 80 °C. The lower shape parameter for the nanocomposite also indicates a smaller spread in the statistical scatter which is a bonus from the design perspective.

In assessing the results of Table 1.2, several caveats must be made. Firstly, this kind of improvement can only be obtained with very careful formulation, compounding and processing. It is also very dependent on optimizing the loading of the

nanocomposite (here 5% by weight). Unfortunately, the optimum loading is very system specific and can vary widely in the range 1–20%. Currently, the paucity of understanding on the breakdown process dictates that the optimum is determined by test. Additionally, the results given in Table 1.2 are for direct voltages. Although improvements can be demonstrated for power frequency alternating voltage, and for impulse, they are not so large. This may be seen, for example, in the comparison given for epoxy/clay system (Sarathi et al. 2006), but is quite general and seen for many nanocomposites. This is likely connected to a fundamental difference in the way that nanocomposites behave with regard to internal charge storage and transport outlined in Sect. 1.3.2.

Of perhaps greater significance is the change that can be brought about in the voltage endurance of insulating polymers through the incorporation of nanoparticles. This characteristic is universally seen in most systems, but is illustrated in Fig. 1.9 for an epoxy-TiO_2 formulation where a nanocomposite is being compared with the conventional counterpart. When comparisons are made with the base resin it is not unusual to see a two orders of magnitude improvement in endurance for a divergent electric field (7.5 μm radius point-plane sample with a 2 mm gap) test such as this. This is a very substantial improvement and cannot readily be explained by space charge shielding, but is more likely to be due to the scattering effects of the nanophase inclusions which act as a plurality of barriers to inhibit the propagation of electrical treeing discharges.

The electrical properties are covered in detail in Chap. 7, but it is perhaps appropriate to record here that several groups have documented (Smith et al. 2008; Singha and Thomas 2008) that the conventional mixing rules which have traditionally been applied to polymer composites do not necessarily provide meaningful

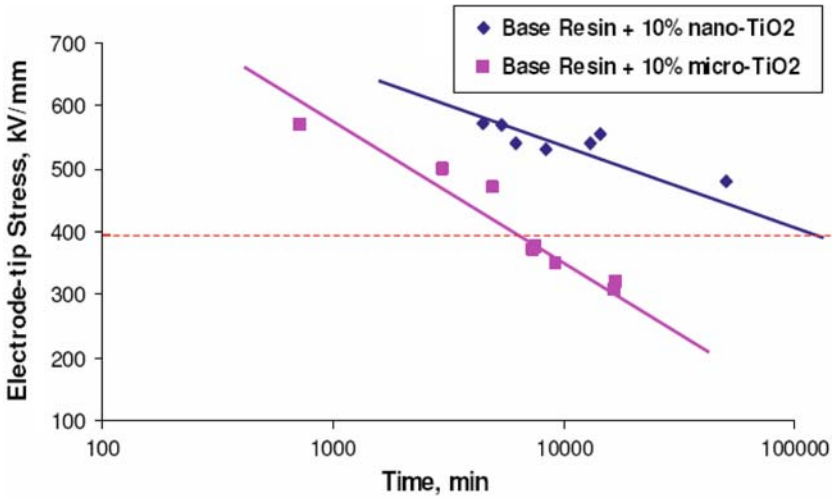

Fig. 1.9 Voltage endurance comparison between 10% loaded microcomposite and nanocomposite (Nelson and Hu 2005)

results when used for nanocomposites. To take the polymer nanocomposite system used in Fig. 1.9 at 1 kHz as an example, it has been found that the incorporation of nanophase TiO_2 (with a relative permittivity $\approx$100) in an epoxy (with a relative permittivity $\approx$5), can yield a composite which has a relative permittivity which is *less* than the base epoxy at frequencies high enough to avoid the region where interfacial processes come into play. Such a phenomena cannot readily be described by the Lichtenecker-Rother formula or, indeed, any other conventional mixing model (Tareev 1975). This anomaly again points to the unique role played by the physics and chemistry of the interface in these materials and the importance of functionalization in providing coupling at the interface region. This is further discussed in Sect. 7.2.2 in relation to the electrical response of nanodielectrics. Attempts to model this at the particle level (Tanaka et al. 2005; Smith 2009) suggest that constriction of dipole movement in the interface region is the likely cause of the reduction of polarization encountered particularly as it is known that nanometric inclusions tend to restrict the relaxation and freedom of chain molecules (Bhattacharya et al. 2008).

Chapter 6 covers the mechanical and thermal properties of composites where improvements can be made through the use of nanodielectrics. For example, in polyimide-based nanocomposites (Irwin et al. 2003), improvements have been obtained in mechanical strength to failure, scratch hardness and thermal conductivity (relative to equivalent micron-sized composites), although the latter is only linearly related to the loading. Similarly, a doubling of Young's modulus and an increase in yield stress (Montanari et al. 2004) have been demonstrated through the use of 10% organophilic silicates in polypropylene. Changes such as these come about for a variety of reasons such as the nucleation of crystallinity, changes in glass-transition (Takala 2008) and morphology, tethered entanglement (Zhu and Sternstein 2003), etc. In particular, modest increases in polymer operating temperature can be obtained which is critical in many applications.

However, it is the influence on polymer degradation and surface erosion in dielectrics under discharge conditions which has attracted considerable attention, and is the subject of Chap. 8. This property is clearly allied to the voltage endurance enhancements documented in Fig. 1.9. An example is shown in Fig. 1.10 taken from work on mass produced epoxy-clay nanocomposites (Tanaka et al. 2008) with a 5 wt% loading subjected to alternating voltage surface discharges in a rod-plane configuration (see *insert* in Fig. 1.10). In this case the erosion depth is used as an indicator of degradation resistance, but other work (Maity et al. 2008) on epoxy-metal oxide has shown the same effect by monitoring the surface roughness or the volume of the material eroded in similar circumstances. The functionalization of the alumina particles using 3-glycidoxypropyltrimethoxysilane is also shown to be effective at enhancing the resistance to degradation. Although the significant improvement in degradation resistance afforded by this technology is clear from Fig. 1.10, it also suggests that there may be advantages to be gained through the use of well-chosen micro/nano particulate combinations.

Consideration of the combined results of Figs. 1.9 and 1.10 makes it clear that nanodielectrics offer a substantial improvement in partial discharge (PD) resistance.

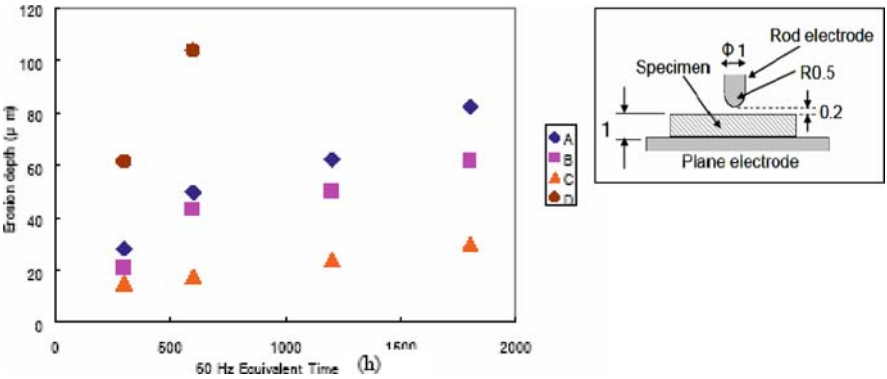

Fig. 1.10 Erosion depth data for epoxy-clay composites in relation to the base resin (Tanaka et al. 2008). A & B: Nanocomposites with different preparation methods, C: Micro-nano mixed composite, D: Base Epoxy (Tanaka et al. 2008)

This is brought about not only by an increased resistance to channeling, but also by the restriction of PD-caused erosion as may be seen, for example, in epoxy/alumina materials (Kozako et al. 2006) which extended previous similar work on polyamide nanocomposites using a synthetic mica filler (Kozako et al. 2004). It has been shown that both enhancements in PD inception voltage and also reduction in discharge magnitudes can be achieved by quite small loadings of nanomaterial. The commercial implications of these results are obvious since high-voltage electrical insulation is a pervasive commodity.

1.3.2 Property Characterization for Diagnostic Purposes

The Appendix provides an outline of some of the diagnostic methods which can be used with dielectrics to aid the understanding of the underlying charge storage and transport which often give rise to the useful property improvements. Unfortunately, recent research has indicated that nanodielectrics do not always behave in the same way. This is perhaps not surprising in view of the model outlined in Sect. 1.1.3 where the properties will be largely determined by the physics and chemistry of the pervasive interface zone which will be different depending on the constituents and chemical coupling (if employed). This section should be read in combination with that Appendix if necessary. The electrical characterization of dielectrics in this way is particularly important for composites where much occurs at the internal interfaces which cannot be accessed. The information obtained from characterization of this sort is extremely important in establishing the emerging mechanistic picture covered in Chap. 10.

1.3.2.1 Dielectric Spectroscopy

Power frequency determinations of relative permittivity and dielectric loss (tan δ) are important in defining a material and measurement can be made under high voltage conditions. However, the ability to make real and imaginary permittivity measurements over a large frequency range and at temperatures which encompass the range from below glass transition to melting/decomposition can provide considerable mechanistic insight and sometimes identify moisture and other contaminants. This is particularly useful for composites because the internal interfaces can contribute to interfacial polarization (the Maxwell-Wagner effect) which usually manifests itself at low frequencies (Bartnikas 1983).

The example shown in Fig. 1.11 is taken from a study aimed at examining the effects of water on 3.37% epoxy-SiO_2 nanocomposites (Zou et al. 2008). It is immediately obvious that most of the changes in the structure of the spectrum occur in the frequency range below 10^{-1} Hz and so conventional power frequency measurements cannot be used for this purpose. Figure 1.11a shows the real (C') and imaginary (C'') capacitance for the dry material. C' is constant at low frequencies

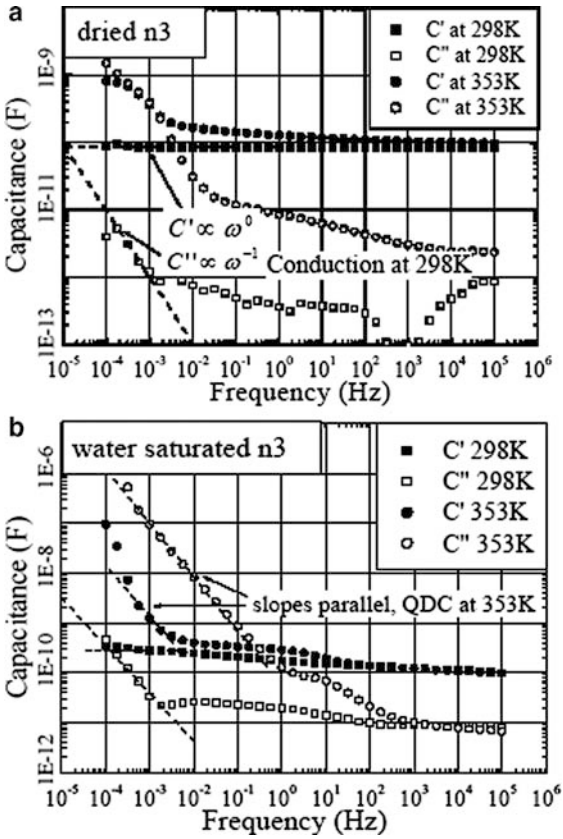

Fig. 1.11 Dielectric spectroscopy of an epoxy-SiO_2 nanocomposite at 298 and 353 °K. (**a**) dried, (**b**) water saturated (Zou et al. 2008)

and $C'' \propto \omega^{-1}$ (where ω is the angular frequency) as would be expected from a classical frequency independent conduction mechanism. In contrast, Fig 1.11b shows the situation for the same material at high humidity and temperature. Now C′ is no longer independent of frequency and the slopes of C′ and C″ are parallel suggesting that there is a low frequency dispersion (Jonscher 1983) or quasi-DC (QDC) behavior (Dissado and Hill 1984). By consideration of the temperature dependence, an activation energy can be established for this process. Since it is lower than that for the base epoxy (Vantico CY255/HY227), it is concluded that the unfunctionalized nanocomposite provides pathways for moisture ingress. It has also been found (Zhang and Stevens 2008) that this results from an interplay between the interfacial water mobility and the interface bonding which is critically dependent on functionalization. As a result, while such moisture migration would certainly not be desirable in a material operating in a high humidity environment, the characteristic may be modified. The same water ingress has been seen for polyolefin nanocomposites, but, for a polyolefin-SiO_2 nanocomposite which has been formulated with a trioxyvinylsilane coupling agent at an optimized 12.5% loading, electrochemical treeing studies using Ashcraft-type samples (Ashcraft 1977) have shown substantially improved aqueous performance when compared with conventional cable-grade X-linked polyethylene. This is illustrated by the tree growth data of Fig. 1.12 (Hui 2009) and suggests that the presence of the interfacial regions is effective in arresting tree growth even in the presence of water, presumably in a similar fashion to the methodology in play for electrical trees, as discussed in Sect. 1.3.1.

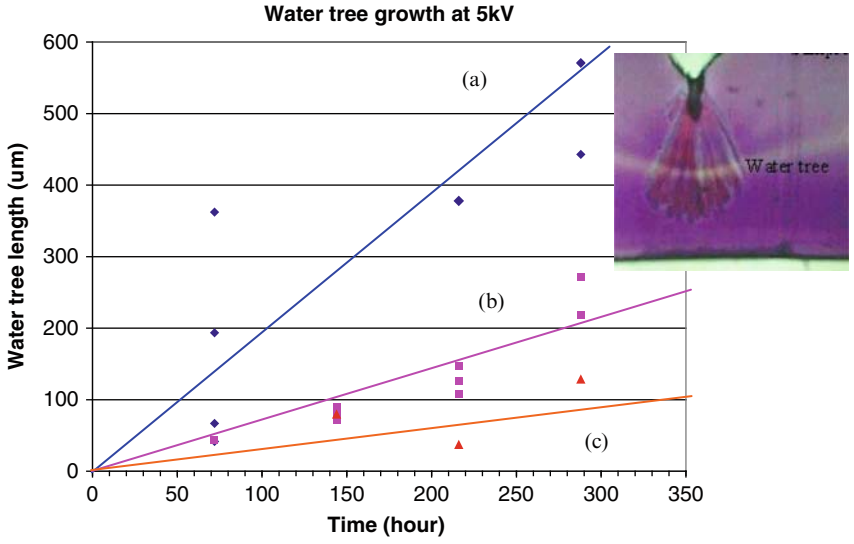

Fig. 1.12 Electrochemical tree growth for a polyethylene-SiO_2 vinylsilane functionalized nanocomposite in comparison with base X-linked polyethylene. (**a**) XLPE, (**b**) 5% SiO_2 loading, (**c**) 12.5% SiO_2 loading (Hui et al. 2009) (*Insert*: Water tree propagation)

1.3.2.2 Internal Space Charge Characteristics

A number of methods are now available for estimating the magnitude and distribution of space charges within a stressed dielectric. The pulsed electroacoustic (PEA) technique is one of those which is described in Sect. A.2, and has become a widely applied tool for this purpose. Many research groups have found that nanocomposites yield very different magnitude, distribution and behavior when compared with either the base resin from which they are derived or an equivalent microcomposite. Unfortunately, however, once again, one cannot generalize except to say that, typically, nanodielectrics exhibit smaller internal space charge density and are characterized by a shorter time constant for charge decay, which is probably due to the nature of the interfacial layer introduced in Sect. 1.1.3. Clearly, since the field generated by any internal charge will augment that due to an applied voltage, the space charge in a dielectric has an influence on the perceived applied field required for failure. The internal charge behavior will also be different for a direct voltage than for a time-variable voltage application which can have a bearing on the relative dielectric integrity exhibited. Clearly the impact is often greatest when heterocharge accumulates close to an electrode which can enhance the surface field and facilitate charge carrier injection. Such behavior is illustrated in Fig. 1.13 in which a low density polyethylene 70 μm film is compared with a nanocomposite formed using 1% nanometric magnesium oxide (MgO) with a nominal electric field of 200 kV mm^{-1}. Such an applied field would be substantially higher than the threshold required for charge injection (≈20 kV mm^{-1}). The overriding feature of Fig. 1.13 is the lack of internal charge accumulation for the LDPE/MgO nanocomposite even after 20 min with an electric field as high as 200 kV mm^{-1} (Takada et al. 2008). In contrast, the base polymer at the same field has accumulated substantial positive (hetero)charge in front of the cathode which has resulted in a doubling of the field in front of the cathode (compare Fig. 1.13b and d). Such fundamental changes in the internal charge are common, and in some materials (Nelson and Hu 2006) have even shown a change of sign of the internal charge providing evidence for mechanistic differences brought about by even modest loadings of nanoparticulates.

There are also many instances when the introduction of nanoscale fillers results in an improvement (reduction) in the bulk electrical conductivity in dielectrics. The work of Kikuma et al. (2006) is a good example of this and has been attributed to the formation of homocharge adjacent to the electrodes which can be expected, in turn, to reduce electrode emission into the bulk. In polyethylene/MgO nanodielectrics this can be achieved with as little as 0.5% of magnesium oxide (Hayase et al. 2006).

1.3.2.3 Dielectric Absorption

The response of a linear system in the frequency domain (Sect. 1.3.2.1) may be transformed into a time-dependent response. In particular, the decay of the current

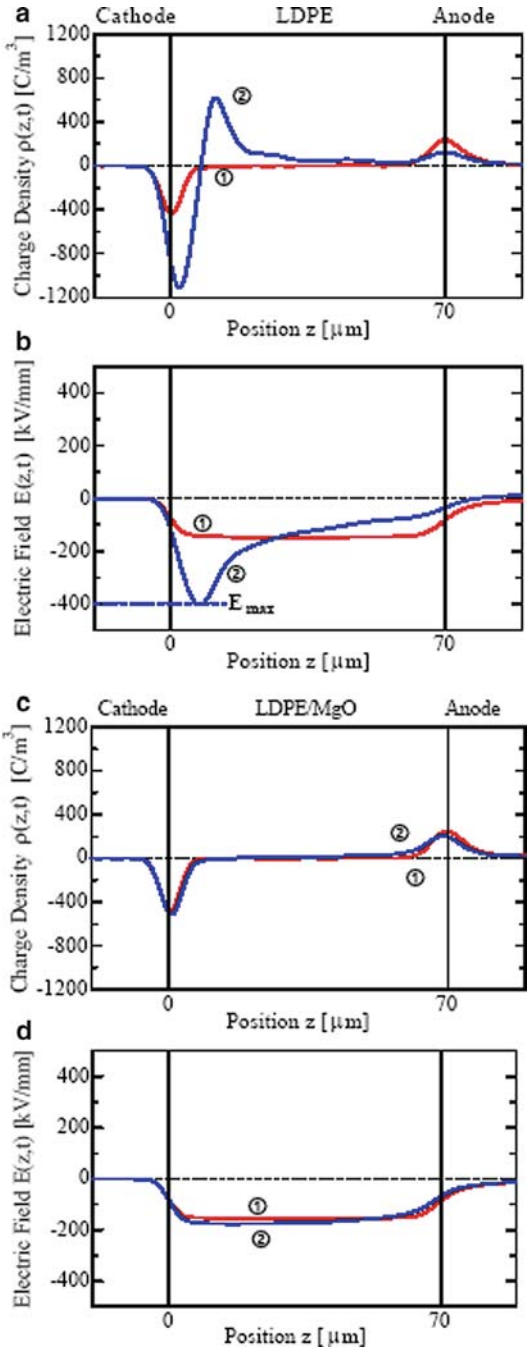

Fig. 1.13 Space charge accumulation and associated internal field for LDPE and LDPE/MgO nanodielectric. (**a**) and (**b**) charge density and field for LDPE. (**c**) and (**d**) charge density and field for LDPE/MgO. ① Instantaneous; ② 20 min after stress application (Takada et al. 2008)

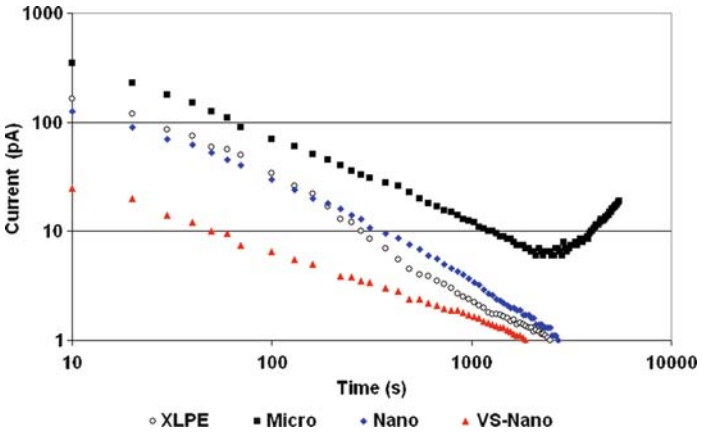

Fig. 1.14 Dielectric absorption characteristics for X-linked polyethylene and both functionalized and unfunctionalized SiO_2 nanocomposites (*lower three curves*) and an equivalent microcomposite (*upper curve*). Applied field: 20 kV mm^{-1} (Smith 2009)

through a dielectric after a direct voltage has been applied can yield valuable insight when the method is applied to composites. Figure 1.14 shows a case where polyethylene and its nanocomposites exhibit a power law relationship (approximate linear plot on a log-log scale), but there is a marked difference in the case of a conventional (micro) composite which shows a behavior typical of interfacial polarization (Raju 2003). It would appear that the build up of internal charge at the internal interfaces is mitigated in the case of nanomaterials which is consistent with the space charge studies highlighted in Sect. 1.3.2.2. It is also possible to use transit time methods to estimate the carrier mobility (Many and Rakavy 1962) as discussed in Sect. A.5. Such estimates have been made for polyethylene-SiO_2 and are shown in Fig. 1.15 which suggests that nanodielectrics exhibit a decreasing mobility with electric field in contrast to the opposite effect seen both for the host polymer and for a micromaterial (Roy et al. 2007). However, it is also not certain that the form of the SiO_2 is the same for the micro- and nanoparticles. Once again, it would appear that nanodielectrics were behaving in a fundamentally different way. In this instance the behavior would appear to be only dependent on the particle size since a decreasing mobility is found which is independent of the nature of the chemical coupling used. The electric fields at the low end of Fig. 1.15 are not particularly high, and are below the threshold required for copious injection. Such threshold fields are dependent on the functionalization. Although these results are for 5% (by weight) composites, the carrier mobility is further reduced for nanodielectrics as the loading is increased.

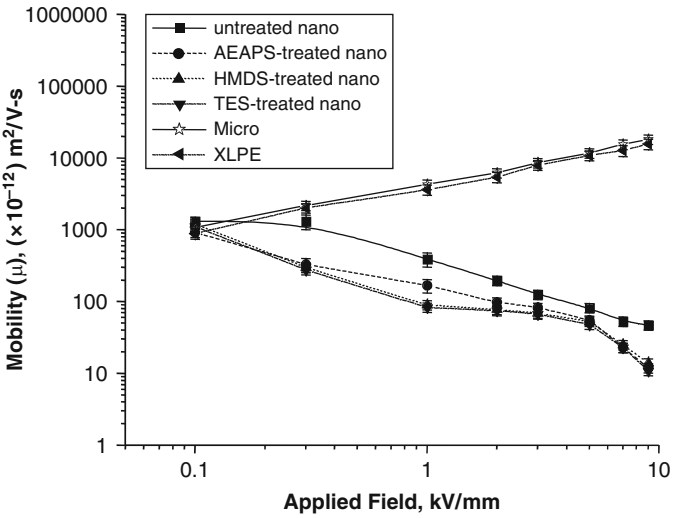

Fig. 1.15 Carrier mobilities in X-linked polyethylene and 5% composites as a function of electric field Functionalizing agents: *AEAPS* n-(2-aminoethyl) 3-aminopropyltrimethoxysilane; *HMDS* hexamethyldisilazane; *TES* triethoxyvinylsilane (Roy et al. 2007)

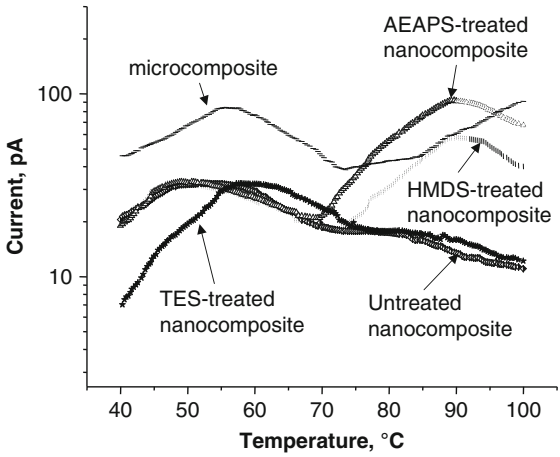

Fig. 1.16 Thermally stimulated depolarization spectra for a range of polyethylene-SiO_2 composites with coupling agents corresponding to those designated in Fig. 1.15 (Roy et al. 2007)

1.3.2.4 Thermally Stimulated Currents

As discussed in Sect. A.3, obtaining thermally stimulated current characteristics from an insulating material provides information both about relaxations occurring as a result of molecular motions (such as that occurring at glass transition), and also reveals the presence of charges trapped at sites in the structure which are released by thermal activation.

Several features seen in Fig. 1.16 provide important evidence for the behavior of nanodielectrics. Firstly, the peaks seen in the temperature range 50–60 °C can be identified with traps associated with the amorphous-crystalline interface in polyethylene (Ieda et al. 1980; Suzuoki et al. 1977). The upward shift for the triethoxyvinylsilane-treated material is expected since end-chain and segmental motion will be restricted due to the resulting chemical linkages and the higher level of crystallinity associated with this material. The peaks occurring at about 90 °C are due to trapped charges associated with the surface modifier groups. In this context, it should be recognized that the n-(2-aminoethyl) 3-aminopropyl-trimethoxysilane and hexamethyldisilazane are polar in contrast to the triethoxyvinylsilane which is essentially non-polar, suppressing this peak and making the nanomaterial behave like the untreated SiO_2. It is possible to extract trap depths from these curves as cited in Sect. A.3 and the polar surface modifier groups produce traps that are in excess of 2 eV which is similar to traps introduced by amine groups (Ieda et al. 1977).

1.3.2.5 Electroluminescence

The detection of light emission from stressed polymers is not a straightforward technique. Since electric fields are usually close to breakdown, the magnitude of the emission is very small demanding high sensitivity, and additionally many polymers of interest are not transparent. Since electroluminescence can originate from either

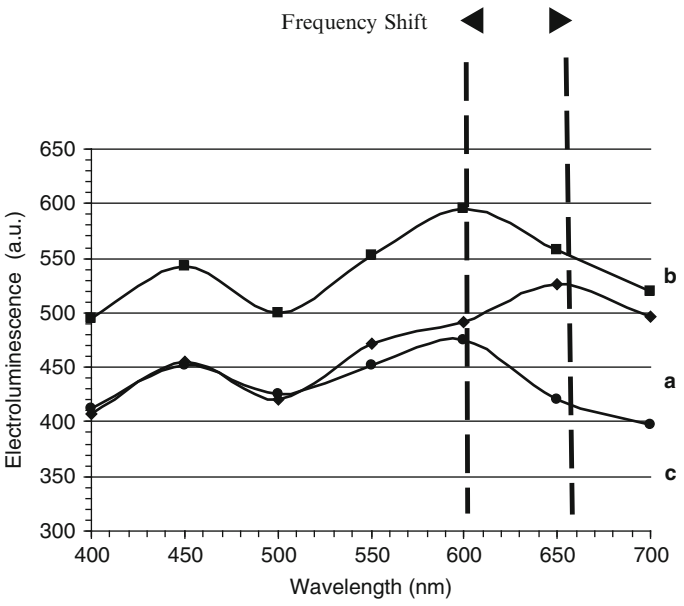

Fig. 1.17 Frequency resolved electroluminescence spectra for 10% TiO_2/epoxy composites (nano (**a**), and micro (**b**)) in comparison with the cured base resin (**c**) (Nelson and Hu 2006)

charge recombination or from "hot" electron processes (Teyssedre et al. 1999), the interpretation is also not always straightforward. Nevertheless, the method does provide valuable insight into the behavior of nanocomposites when they are compared both with the base resin and also with an equivalent microcomposite of the same loading. Using an epoxy-TiO_2 system as an example, Fig. 1.17 would indicate that the use of a filler of nanometric dimensions creates a "red shift" to longer wavelengths of the emitted radiation (when corrected for the photomultiplier response). Since the emission centers in the material are not known, one has to interpret this with care, but if the technique is used in conjunction with an assessment of the propagation of charge fronts into the material in the manner discussed in Sect. 1.3.2.2, it does suggest that the carrier energy is reduced by the introduction of the nanophase material. In turn, this suggests that scattering may have a dominating influence which would be consistent with the enhanced voltage endurance universally observed.

The allied technique of photoluminescence, in which the energy to bring about luminescence is supplied, not from the applied field, but from outside photon irradiation, has also been successfully applied to nanocomposites (Fuse et al. 2008). Like the electroluminescence technique, it permits the nature of electronic states to be investigated by examining the optical absorption and photoluminescence using vacuum ultraviolet photons.

1.4 Other Issues

The consideration of property modifications brought about by the incorporation of nanofillers must also take into account changes that will be brought about in addition to the assumed interface effects which are thought to dominate. Examples already introduced would include the glass transition temperature, the crystallinity and other morphological phenomena which are known to affect the electrical properties; particularly the electric strength. Not only are the crystallization kinetics and morphology of polymers dependent on conditions (pressure, cooling rate, residence time, etc.) established during molding or extrusion, but, in nanocomposites, there is also an influence of the additional phase, particularly when admixed particulates act as nucleating agents (Vaughan et al. 2006). This usually results in a larger number of smaller crystallites. While often overlooked in research laboratories, such issues of rheology (expressed in terms of shear viscosity and shear modulus) and morphology can become pivotal when a material is transitioned from a development stage to scaled-up production.

Percolation effects must also be considered, and these are covered in Sect. 7.1.7 with regard to the electrical properties, and again in Sect. 9.4 in the context of conductivity modification. The "classical" picture of a percolation limit brought about at the particulate loading when the particles start to be in contact usually occurs for loadings which are higher than have commonly been used for nanodielectrics. Although this may not be true in the case where a linear, or non-linear, conductivity is

being sought such as described in Chap. 9, it may also not be true more generally if the picture of the structure characterized by Fig. 1.2b is correct. If the radial build of a spherical interaction zone is of the order of 10 nm, then some overlap can be expected at the modest loadings currently in use. Emerging models which attempt to describe this process (Smith 2009; Tanaka et al. 2005; Youngs et al. 2005; Bowler 2004)) are being adapted to allow for this effect and to try to predict bulk properties and relaxation frequencies on the basis of geometry, permittivity and the dielectric loss of the constituents. In particular, the description of the region surrounding a nanoparticle in terms of a Gouy-Chapman layer (Lewis 2004) would imply the presence of a *local* diffuse charge region which may have conductivity that will not necessarily be totally reflected in the bulk properties measured externally. However, such physical macroscopic models do little to account for the interface chemistry on which much of the future development will hinge. For that purpose atomic level modeling techniques are needed such as are introduced in Chap. 5. Such descriptions have now matured to the point where they can offer the possibility of taking into account the interfacial electronic structure (Shi and Ramprasad 2008).

Another phenomenon in polymers which is often overlooked is that of free volume. The concept provides a measure of occupancy and is often related to microvoid content (Dissado and Fothergill 1992). However, the free volume will also be affected by defects, chain interruptions, etc. and the introduction of nanoparticles will certainly affect the free volume. There is, however, a paucity of reliable data for dielectric nanocomposites, but the issue is important since there is a school of thought which couples breakdown strength to the free volume exhibited. Artbauer (1996) has expanded on earlier derivations to account for mean free path issues, and demonstrated a free volume theory which is in agreement with observations. Indeed, the change in electric strength occurring as a result of the glass transition in a polymer is certainly mirrored by the concomitant increase in free volume attributable to the transition from the glassy state (Sabuni and Nelson 1979). It is thus very plausible that changes in free volume brought about through the formation of nanocomposites will also be reflected in the breakdown strength exhibited; particularly as it is known that the free volume decreases with increasing crystallinity which can be affected, in turn, by nanoparticles (Dlubek et al. 2002). Section 4.3 addresses the issue of free volume from the chemical perspective.

References

Artbauer J (1996) Electric strength of polymers. J Phys D 29:446–456

Ashcraft AC (1977) Water treeing in polyethylene dielectrics. World Electrochemical Conf. Paper 3A–13 Moscow, USSR

Bartnikas R (1983) Dielectric loss in solids. In: Bartnikas R, Eichhorn RM (eds) Engineering dielectrics IIA. ASTM, Philadelphia

Bhattacharya SN, Gupta RK, Kamal MR (2008) Polymeric nanocomposites. Hanser, Munich

Bowler N (2004) Effects of lossy layered filler particles on the bulk permittivity of composite material. J Phys D 37:326–333

Cressie NAC (1991) Statistics for spatial Data. Wiley, New York
Dissado LA, Fothergill JC (1992) Electrical degradation and breakdown of polymers. Peregrinus, London
Dissado LA, Fothergill JC (2004) Dielectrics and nanotechnology. Trans IEEE DEI-11:737–738
Dissado LA, Hill RM (1984) Anomalous low-frequency dispersion: near direct current conductivity in disordered low-dimensional materials. J Chem Soc Faraday Trans II 80:291–319
Dlubek G, Stejny J, Lüpke T et al (2002) Free-volume variation in polyethylene of different crystallinities: positron lifetime, density and X-ray studies. J Polym Sci B 40:65–81
Fréchette MF, Reed CW (2007) The role of molecular dielectrics in shaping the interface of polymer nanodielectrics. Annu Rep IEEE Conf Electr Insul Dielectr Phen: 279–285
Fukushima K, Takahashi H, Takezawa Y et al (2006) High thermal conductivity resin composites with controlled nanostructures for electric devices. IEEJ Trans Fundam Mater 126:1167–1172
Fuse N, Okada M, Ohki Y et al (2008) Photoluminescence in polyamide/mica and polyethylene/MgO nanocomposites induced by ultraviolet photons. Trans IEEE DEI-15:1215–1223
Green C, Vaughan A (2008) Nanodielectrics – how much do we really understand? IEEE Electr Insul Mag 24:6–16
Gupta RK, Kennel E, Kim K-J (2010) Polymer nanocomposites handbook. CRC, Boca Raton
Hayase Y, Aoyama H, Matsui K et al (2006) Space charge formation in LDPE/MgO nanocomposite film under ultra-high DC electric stress. IEEJ Trans Fundam Mater 126:1084–1089
Henk PO, Kortsen TW, Kvarts T (1999) Increasing the electrical discharge endurance of acid anhydride cured DGEBA epoxy resin by dispersion of nanoparticle silica. High Perform Polym 11:281–296
Hui L, Smith RC, Wang X et al (2008) Quantification of particulate mixing in nanocomposites. Annu Rep IEEE Conf Electr Insul Dielectr Phen: 317–320
Hui L, Nelson JK, Schadler LS et al (2009) Electrochemical treeing in nanodielectrics. Annu Rep IEEE Conf Electr Insul Dielectr Phen (to be published)
Ieda M, Mizutani T, Suzuoki Y (1980) TSC and TL studies of carrier trapping in insulating polymers, vol 32. Memoirs of the Faculty of Engineering, Nagoya University, Nagoya, pp 173–219
Iler RK (1979) The chemistry of silica. Wiley, New York
Irwin PC, Cao Y, Bansal A et al (2003) Thermal and mechanical properties of polyimide nanocomposites. Annu Rep IEEE Conf Electr Insul Dielectr Phen: 120–123
Johnston DR, Markovitz M (1988) Corona resistant insulation. US Patent # 4760296
Jonscher AK (1983) Dielectric relaxation in solids. Chelsea Dielectric Press, London
Kikuma T, Fuse N, Tanaka et al (2006) Filler content dependence of dielectric properties of low-density polyethylene/MgO nanocomposites. IEEJ Trans Fundam Mater 126:1072–1077
Kim D, Lee JS, Barry CMF et al (2007) Microscopic measurement of the degree of mixing for nanoparticles in polymer nanocomposites by TEM Images. Microsc Res Tech 70:539–546
Kozako M, Fuse N, Ohki Y et al (2004) Surface degradation of polyamide nanocomposites caused by partial discharges using IEC(b) electrodes. Trans IEEE DEI-11:833–839
Kozako M, Ohki Y, Kohtoh M et al (2006) Preparation and various characteristics of epoxy/alumina nanocomposites. IEEJ Trans Fundam Mater 126:1121–1127
Lewis TJ (1994) Nanometric dielectrics. Trans IEEE DEI-1:812–825
Lewis TJ (2004) Interfaces are the dominant feature of dielectrics at the nanometric level. Trans IEEE DEI-11:739–753
Lewis TJ (2004a) Interfaces and nanodielectrics are synonymous. IEEE Int Conf Solid Dielectr 2:792–795
Liu CC, Maciel GE (1996) The fumed silica surface: a study by NMR. J Am Chem Soc 118:5103–5119
MacCrone RK, Nelson JK, Smith RC et al (2008) The use of electron paramagnetic resonance in the probing of the nanodielectric interface. Trans IEEE DEI-15:197–204
Maity P, Kasisomayajula SV, Parameswaran P et al (2008) Improvement in surface degradation properties of polymer composites due to pre-processed nanometric alumina fillers. Trans IEEE DEI-15:63–72

Many A, Rakavy G (1972) Theory of transient space-charge-limited currents in solids in the presence of trapping. Phys Rev 126:1980–1988

Montanari GC, Fabiani D, Palmieri F et al (2004) Modification of electrical properties and performance of EVA and PP insulation through nanostructure by organophilic silicates. Trans IEEE DEI-11:754–762

Nelson JK (1983) Breakdown strength of solids. In: Bartnikas R, Eichhorn RM (eds) Engineering dielectrics IIA. ASTM, Philadelphia

Nelson JK, Schadler LS (2008) Nanodielectrics. Trans IEEE DEI-15:1–1

Nelson JK, Fothergill JC, Dissado LA et al (2002) Towards an understanding of nanometric dielectrics. Annu Rep IEEE Conf Electr Insul Dielectr Phen: 295–298

Nelson JK, Hu Y (2005) Nanocomposite dielectrics – properties and implications. J Phys D 38:213–222

Nelson JK, Hu Y (2006) Candidate mechanisms responsible for property changes in dielectric nanocomposites. Proc Int Conf on Prop & Appl of Dielectr Mater, Bali, Indonesia, pp 150–153

Raetzke S, Kindersberger J (2006) The effect of interface structures in nanodielectrics. IEEJ Trans Fundam Mater 126:1044–1049

Raju GG (2003) Dielectrics in electric fields. Marcel Dekker, New York

Reed CW (2007) Self-assembly of polymer nanocomposites for dielectrics and HV insulation. Proc IEEE Int Conf Solid Dielectr, Winchester, UK, pp 317–320

Roy M, Nelson JK, MacCrone RK et al (2005) Polymer nanocomposite dielectrics – the role of the interface. Trans IEEE DEI-12:629–643, 1273

Roy M, Nelson JK, MacCrone RK et al (2007) Candidate mechanisms controlling the electrical characteristics of silica/XLPE nanodielectrics. J Mater Sci 42:3789–3799

Sabuni H, Nelson JK (1979) The effects of plasticizer on the electric strength of polystyrene. J Mater Sci 14:2791–2796

Sarathi R, Sahu RK, Kumar PR et al (2006) Understanding the performance of epoxy nanocomposites – a physico-chemical approach. IEEJ Trans Fundam Mater 126:1112–1120

Shi N, Ramprasad R (2008) Local properties at interfaces in nanodielectrics: An ab initio computational study. Trans IEEE DEI-15:170–177

Singha S, Thomas MJ (2008) Permittivity and tan delta characteristics of epoxy nanocomposites in the frequency range 1 MHz-1GHz. Trans IEEE DEI-15:2–11

Smith RC (2009) Mechanistic electrical behavior of crosslinked polyethylene/silica nanocomposites. Ph.D. Thesis, Rensselaer Polytechnic Institute

Smith RC, Liang C, Landry M et al (2008) The mechanisms leading to the useful electrical properties of polymer nanodielectrics. Trans IEEE DEI-15:187–196

Stevens GC (2005) Dielectrics at meso and nano scales. J Phys D 38:174

Suzuoki Y, Yasuda M, Mizutani T et al (1977) Investigation of carrier traps in polyethylene by PSDC and TSC. Jpn J Appl Phys 16:1929–1931

Takada T, Hayase Y, Tanaka Y et al (2008) Space charge trapping on electrical potential well caused by permanent and induced dipoles for LDPE/MgO nanocomposite. Trans IEEE DEI-15:152–160

Tanaka T, Montanari GC, Mülhaupt R (2004) Polymer nanocomposites as dielectrics and electrical insulation – perspectives for processing technologies, material characterization and future applications. Trans IEEE DEI-11:763–784

Tanaka T (2006) Nanocomposite dielectrics – manufacture, characterization and applications. IEEJ Trans Fundam Mater 126:1019

Tanaka T, Kozako N, Fuse N et al (2005) Proposal of a multi-core model for polymer nanocomposite dielectrics. Trans IEEE DEI-12:669–681

Tanaka T, Mizutani Y, Imai T, Fuse N (2008) Digest report of investigation committee on polymer nanocomposites and their applications as dielectrics and electrical insulation. Proc Int Symp Electr Insul IEEJ DR-1

Tanaka T, Ohki Y, Ochi M et al (2008) Enhanced partial discharge resistance of epoxy/clay nanocomposite prepared by newly developed organic modification and solubilization methods. Trans IEEE DEI-15:81–89

Takala M, Karttunen M, Pelto J et al (2008) Thermal, mechanical and dielectric properties of nanostructured epoxy-polyhedral oligomeric silsesquioxane composites. Trans IEEE DEI-15:1224–1235

Tareev B (1975) Physics of dielectric materials. Mir Publishers, Moscow

Tewari A, Gokhale AM (2005) Nearest neighbor distances in uniform – random poly-dispersed microstructures. Mater Sci Eng A 396:22–27

Teyssedre G, Cissé L, Mary D et al (1999) Identification of the components of the electroluminescence spectrum of PE excited in uniform fields. Trans IEEE DEI-6:11–19

Ueki MM, Zanin M (1999) Influence of additives on the dielectric strength of high-density polyethylene. Trans IEEE DEI-6:876–881

Vaughan AS, Swingler SG, Zhang Y (2006) Polyethylene nanodielectrics: the influence of nanoclays on structure formation and dielectric breakdown. IEEJ Trans Fundam Mater 126:1057–1063

Walmsley HL, Woodford G (1981) The generation of electric currents by the laminar flow of dielectric liquids. J Phys D 14:1761–1782

Youngs IJ, Bowler N, Lymer KP, Hussain S (2005) Dielectric relaxation in metal-coated particles: the dramatic role of nano-scale coatings. J Phys D 38:188–201

Zhang C, Stevens GC (2008) The dielectric response of polar and non-polar nanodielectrics. Trans IEEE. DEI-15:606–617

Zhu A-J, Sternstein SS (2003) Nonlinear viscoelasticity of nanofilled polymers: interfaces, chain statistics and properties recovery kinetics. Compos Sci Technol 63:1113–1126

Zou C, Fothergill JC, Rowe SW (2008) The effect of water absorption on the dielectric properties of epoxy nanocomposites. Trans IEEE DEI-15:106–117

Chapter 2
The Processing of Nanocomposites

F. Bellucci, D. Fabiani, G.C. Montanari, and L. Testa

2.1 Introduction to Nanofillers

Different types of commercially available nanoparticles (or nanofillers) can be used inside polymeric materials to improve their electric properties. Depending on the property to be modified, the most suitable nanofiller dispersed in a proper density has to be chosen to obtain the desired effect.

2.1.1 Classification of the Fillers

First of all it has to be recalled that shape is one of the most important characteristics of a nanofiller, as it may influence significantly the interaction between nanoparticles and the polymer matrix. A quantification of the interaction surface can be provided by the *aspect ratio* of the nanoparticle, i.e., the ratio of its longest dimension to its shortest dimension. On the basis of the shape, nanoparticles can be distinguished in:

- (Quasi)-spherical particles
- Whiskers and rod particles
- Platelet (lamellar) particles

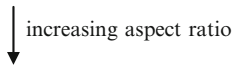

F. Bellucci
Politecnico di Torino, Torino, Italy

D. Fabiani and G.C. Montanari (✉)
Università di Bologna, Bologna, Italy
e-mail: giancario.montanari@mail.ing.unibo.it

L. Testa
Techimp Systems Srl, Zola Predosa (BO), Italy

J.K. Nelson (ed.), *Dielectric Polymer Nanocomposites*,
DOI 10.1007/978-1-4419-1591-7_2,

In the following a synthetic description of the most common nanoparticles used for electrical insulating nanocomposites (NC) is reported. As a first classification, they can be clustered in four main groups, such as:

1. Silicon oxides (silica)
2. Metallic oxides and hydroxides (alumina, titanium oxide, magnesium oxide, zinc oxide, boehmite, hydrotalcites, etc.)
3. Nanoclays (montmorillonite, hectorite, etc.)
4. Carbon nanotubes

Silicon dioxide (chemical formula of SiO_2) is also known as silica and has been known for its hardness for a long time. Silica alone or in combination with metallic oxides forming silicates, in fact, is the most abundant element in the earth's crust. It can be commonly found in nature as sand or quartz mineral and is the main constituent of glass. As a nanofiller it appears like a quasi-spherical shape (aspect ratio close to 1) with diameter ranging from a few nanometers to 100 nm (see Fig. 2.1).

Nanosilica synthesis has improved significantly during the last decade. The first techniques involved the thermal hydrolysis of silane, resulting in hardly dispersible nanoparticles which tended to form aggregates very easily. Nowadays, well-defined nanoparticles which are highly compatible with the target matrix can be obtained through the sol–gel process. Through this technique, in fact, it is possible also to functionalize the surface of the nanoparticle, e.g., resulting in superhydrophobic/hydrophilic behavior.

This nanofiller is commonly used in both thermoplastic and thermosetting insulating materials with a density in the range 1–20% wt. According to the type of polymer matrix (hydrophilic/hydrophobic), a compatibilization process could be needed to disperse the nanofiller uniformly.

Metal oxides are often used as nanofillers to build dielectric nanostructured materials. Indeed, they have generally an electrically insulating behavior and can be dispersed quite easily due to their hygroscopic nature, especially in polar polymers, e.g., epoxy resin, rubber, ethylene-vinylacetate copolymer (EVA). A surface

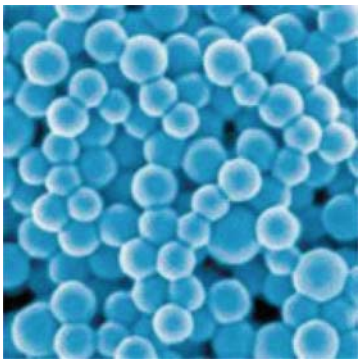

Fig. 2.1 Electron microscopy of silica nanoparticles

functionalization (or compatibilization treatment) is needed to disperse them in non-polar polymers, such as polypropylene (PP) or polyethylene (PE). The most important oxides are:

- Titanium dioxide, also known as titanium(IV) oxide or titania, is the naturally occurring oxide of titanium (chemical formula TiO_2). As a nanofiller it can be produced both in whiskers and quasi-spherical particles. It is used as a nanoadditive for some polyolefins and, particularly, epoxy resins.
- Magnesium oxide, or magnesia, has the empirical formula MgO and is formed by an ionic bond between one magnesium and one oxygen atom. Due to its highly hygroscopic nature, care must be taken to protect it from moisture. A few applications have been shown recently as a nanofiller for low-density polyethylene (LDPE) (Murakami et al. 2008).
- Aluminum oxide (chemical formula Al_2O_3) is often referred to as alumina. It is produced by the Bayer process from bauxite and it is used widely in electrical insulation, e.g., to improve thermal conductivity of epoxy resin components.
- Zinc oxide is an inorganic compound (with the formula ZnO). The powder is widely used as an additive inside numerous materials and products including plastics, ceramics, glass, rubber (e.g., car tyres), batteries, fire retardants, etc. It has a semiconductor behavior. In electrical insulating materials some recent work has showed interesting properties if coupled with LDPE (Fleming et al. 2008).

Nanoclays belong to the family of phyllosilicates, also called layered silicates. A silicate is a compound containing prevailingly Si and O (base formula SiO_4) forming a tetrahedral structure. Since each tetrahedral has an excess of negative net electrical charge, the silicate must have that charge balanced by some metal cations to achieve an electrically neutral compound. These metals, usually Fe, Mg, K, Na and Ca, have also the fundamental purpose to bind together the different silicate tetrahedral structures. Phyllosilicates consist of two-dimensional layers where a central octahedral sheet of alumina is fused to two external silica tetrahedrons by the tip, so that the oxygen ions of the octahedral sheet shares also the tetrahedral sheets, as shown in Fig. 2.2 (Pavlidou and Papaspyridesb 2008; Beyer 2002).

The layered structure of montmorillonite (MMT) is obtained by partially substituting the three-valent Al-cation in the octahedral sheet by the divalent Mg-cation, The excess of negative charge is balanced by hydrated Na^+ and Ca^+ ions in the interlayer (Manias et al. 2001). It is noteworthy that since the layers are kept together by relatively weak forces, polar molecules (e.g., water) can penetrate in the interlayer gap, thus swelling the whole structure (Chin et al. 2001) (for dehydrated MMT the interlayer distance is about 1 nm) (Solomon et al. 2001).

Besides MMT, hectorite and saponite are the most common layered silicates used in NC insulating materials. Their chemical formula is given in Table 2.1 (Alexandre and Dubois 2000). These materials have a great interest in the field of electrical insulating material manufacturing owing to their high aspect ratio (up to 1,000) and peculiar intercalation/exfoliation capability which can be exploited to improve polymer electrical, thermal and mechanical properties.

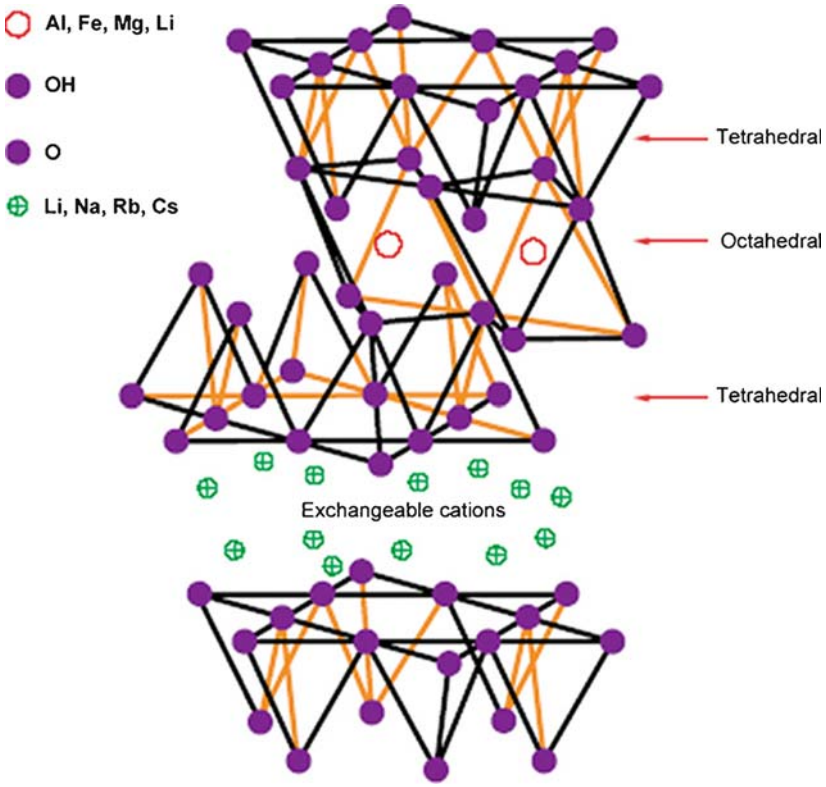

Fig. 2.2 The structure of a 2:1 layered silicate (Beyer 2002). Reproduced from Beyer by permission of Elsevier Science Ltd., UK

Table 2.1 Chemical structure of commonly used 2:1 phyllosilicates (Alexandre and Dubois 2000). Reproduced from Alexandre and Dubois by permission of Elsevier Science Ltd., UK

2:1 Phyllosilicates	General formula
Montmorillonite	Mx(Al4–xMgx)Si8O20(OH)4
Hectorite	Mx(Mg6–xLix)Si8O20(OH)4
Saponite	MxMg6(Si8–xAlx)O20(OH)4

M monovalent cation; *x* degree of isomorphous substitution (between 0.5 and 1.3)

It is well known that original layered silicates can be dispersed only in hydrophilic polymers, e.g., polyvinyl-alcohol (PVA) and polyethylene-oxide (PEO). A modification of the nanoclay is needed to render the clay hydrophobic, thus miscible with other polymers, as will be explained in the next Section.

Two different types of polymer/layered silicate NC are obtainable, namely intercalated and exfoliated nanocomposites (Pavlidou and Papaspyridesb 2008; Ray and Bousima 2005), see Fig. 2.3.

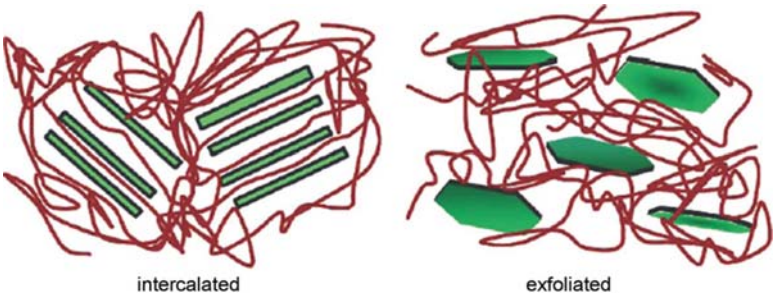

Fig. 2.3 Schematic illustration of two different types of achievable polymer/layered silicate NC, i.e., intercalated and exfoliated (Pavlidou and Papaspyridesb 2008; Ray and Bousima 2005). Reproduced from Ray and Bousima by permission of Elsevier Science Ltd., UK

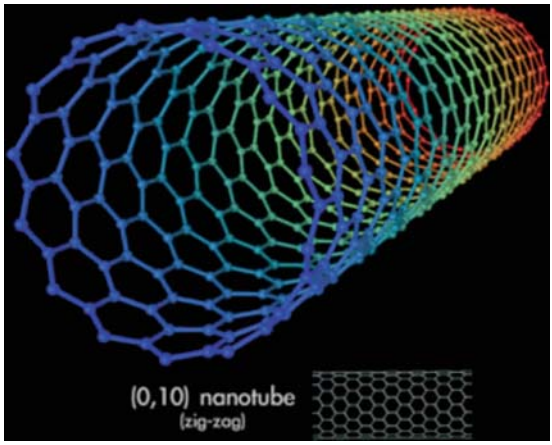

Fig. 2.4 An example of a carbon nanotube

Intercalated NC are generated by the insertion of the polymer chains into the interlayer silicate galleries, maintaining the pilled structure with an increased interlayer distance between each lamella couple. The result is a well-ordered multilayer structure of alternating polymeric and inorganic layers.

Exfoliated NC are characterized by a complete separation of the individual clay lamellae in a continuous polymer matrix by an average distance that depends on clay loading. Usually the exfoliated structure is achieved with a clay amount lower than 3 wt%.

Layered silicates are among the preferred materials for dielectric NC manufacturing. They are used to improve electrical properties, particularly minimizing space charge accumulation, increasing electric strength and endurance, resistance to partial discharge erosion and thermal/mechanical properties. For these reasons they will be treated in detail in Chap. 3 which is devoted to this important class of material.

Carbon nanotubes (CNT) are allotropes of carbon and are constituted by hexagonal networks of carbon atoms (see Fig. 2.4), forming cylinders having a diameter of about 1 nm and a length in the range 100–10,000 nm, thus very high aspect ratio.

CNT present exceptional mechanical and thermal properties. Moreover, they can be electrically conductors, semiconductors or insulators depending on their chirality. In polymers for electrical applications, they can be used to obtain semiconductive nanostructured materials having tuned electrical conductivity (Lee et al. 2008). However, CNT easily aggregate together, which leads to poor dispersion of CNT in the polymer matrix. The composites become conductive (not dielectric) if CNT are in contact each other. Therefore, surface modification of CNT is usually required. In addition, the modification of the CNT surface can also improve compatibility between the CNT and polymer matrix. Several methods have been developed to prepare the functionalized-CNT materials, e.g., organic modification and in situ polymerization of CNT with specific organic molecules. The use of CNT and other fillers to control the conductivity of polymers will be treated in depth in Chap. 9.

2.1.2 Surface Filler Treatment

Nanoparticles are generally agglomerated as a result of their high surface energy, therefore the disaggregation of nanoparticle agglomerates before or during composites manufacturing proves to be a key issue in obtaining a good filler dispersion and to bring the nanoparticles into full play (Rong et al. 2006). Additionally, switching the surface feature of nanoparticles from hydrophilic to increase the filler/polymer matrix compatibility (i.e., the compatibilization process) is also critical.

Silica nanoparticles are a promising nanofiller for polymeric materials. Because of the enormous surface area of silica nanoparticles, both fumed and precipitated, the surface silanol functional groups play a key role in determining the particle physical properties. Indeed, in the unmodified state, the silanol groups impart a hydrophilic character to the material. Moreover the surface hydroxyls increase the tendency to create hydrogen bonds between nanoparticles, thus directly resulting in the formation of aggregates. These bonds are powerful enough so that they can maintain the particles agglomerated even during the compounding process where powerful shear stresses are applied on the surface of the agglomerates. Therefore, the modification of the filler surface by coupling agents like trialkoxysilanes improves their dispersibility in organic media. Silanization of the silica surface provides a basis for the transformation of the greater part of silanol groups into hydrophobic alkyl groups through self-assembly with silane-like molecules. Mica, glass and metal oxide surfaces can all be silanized, because they contain hydroxyl groups which attack and displace the alkoxy groups on the silane thus forming a covalent-Si-O-Si-bond. Trialkoxysilanes, alkylchlorosilanes and alkylsilazanes can be used to modify the filler surface due to their ability to readily undergo hydrolysis and condensation reactions (Beari et al. 2001), as represented in the scheme shown in Fig. 2.5. The detailed chemistry of this process is covered in Chap. 4.

The silica surface functionalization plays an important role in lowering the cohesion forces among the inorganic particles and in enhancing the compatibility with

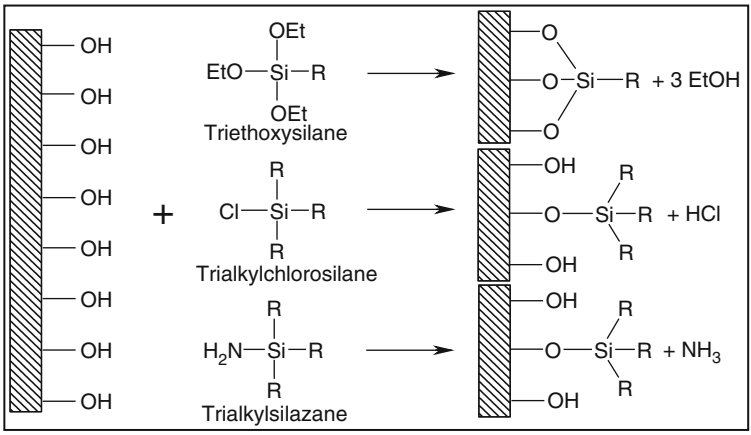

Fig. 2.5 Schematic representation of silanization reactions

polymer and, consequently, their dispersibility in the organic matrices (Bula et al. 2007). Moreover, the organic groups (represented in Fig. 2.5 by R) can contain functionalities able to react with monomers or prepolymers and they are useful to prepare NC in which part of the polymer chains are covalently bonded to the silica surface (Bauer et al. 2003). The formation of chemical bonds between the inorganic and organic components is of great importance to guarantee the proper dispersion degree of the filler in polymeric matrices.

The surface modification through silanization can be applied whenever free and reactive hydroxyl groups are present on the nanoparticles surface. Indeed this process is widely used to modify the surface tension of all metal oxides, such as titania (Ma et al. 2005), zinc oxide (Hong et al. 2006), iron oxide nanoparticles (Guo et al. 2008; Kortaberria et al. 2008), silicates such as sepiolites (Frost and Mendelovici 2006; Tartaglione et al. 2008; Zhang et al. 2005), montmorillonites, hectorites, and hydroxides such as boehmites, hydrotalcites, etc.

Organic modification of clays is applied routinely, in order to obtain the desired degree of delamination of the individual silicate layers in the matrix (intercalation or exfoliation). The most commonly employed surfactants are alkylammonium or alkylphosphonium ions, which contain one or more long alkyl tails. In the organoclays, they lower the surface energy of the inorganic host and improve the wetting characteristic of the polymer matrix, thus resulting in a larger interlayer spacing, see Fig. 2.6. This is sufficiently important that it is covered in detail in Chap. 3.

Another type of silicate modification aiming at improving polymer compatibility involves silane treatment of exposed hydroxyl groups, located at the platelets edges (see Fig. 2.7), in order to produce covalently bound organic functionalities (Rong et al. 2006; Di Gianni et al. 2008). However, the reactions which involve edge −OH groups do not increase the interlayer distance. Therefore, they are not useful for intercalation, but they can be used to enhance platelet miscibility with the polymeric matrix.

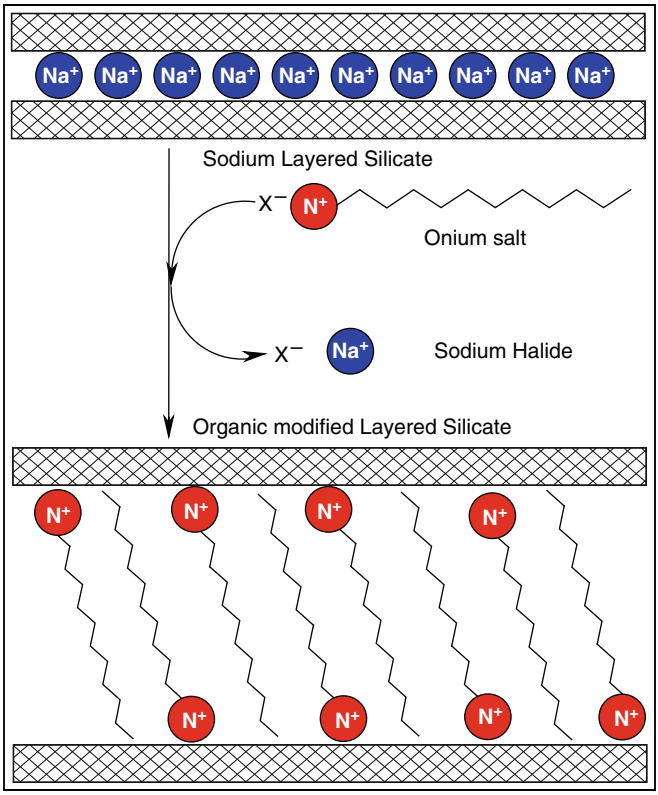

Fig. 2.6 Scheme of the cationic exchange process

Fig. 2.7 Structure of the phyllosilicate layer

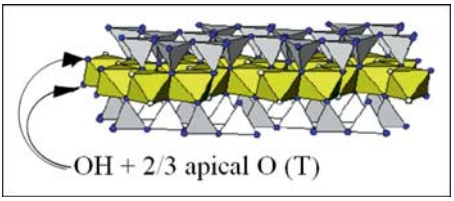

Additionally, hydrotalcite-like compounds, also known as "anionic clays" or "layered double hydroxides" (LDH) constitute a large family of materials with general formula $[M(II)_{1-x}M(III)_x(OH)_2]\left(A^{n-}{}_{x/n}\right)\cdot mH_2O$ where M(II) is a divalent cation such as Mg, Ni, Zn, Cu or Co and M(III) is a trivalent cation such as Al, Cr, Fe or Ga with A^{n-} an anion of charge n such as $CO_3{}^{2-}$, Cl^-, NO^{3-} or organic anion (Cavani et al. 1991). The x value generally ranges between 0.2 and 0.4 and determines the layer charge density and the anion exchange capacity. In these compounds, the trivalent metal isomorphically substitutes a metal in the divalent state of oxidation of the hydroxide structure, generating charges that are compensated by the

intercalation of hydrated anions. These hydrated anions are free to move, as they are located in the interlayer spacings. They are exchangeable, the characteristic anionic exchange capacity (AEC) being attributed to these compounds. LDHs containing various metal cations and carbonate anions are formed in many natural minerals and can be easily synthesized under laboratory conditions (Cavani et al. 1991).

For the synthesis of polymer NC, pristine LDH is not suitable as it has a very small interlayer spacing which makes intercalation of polymeric chains/segments practically impossible. Therefore, pre-treatment of LDH is necessary. The intrinsic hydrophilic surface property of LDHs can be modified through exchanging the interlayer anions with anionic surfactants (Pavan et al. 1999). When large surfactant anions are incorporated into LDHs, the interlayer spacing of LDHs increases and yields modified LDHs with hydrophobic surface properties.

There are several ways reported in literature for the modification of LDH (Carlino 1997; Bergaya et al. 2006), for example:

- Ion exchange method (Latterini et al. 2007; Costantino et al. 2007);
- Co-precipitation in the presence of organic species (Prevot et al. 2001; Wang et al. 2005);
- Regeneration method, based on a unique property of these materials, which can regenerate their original structure from their oxide form, when the latter is dispersed in an aqueous solution containing the proper anion (You et al. 2002; Costa et al. 2008).

As in the case of most inorganic fillers, another type of LDH modification, aimed at improving polymer compatibility, involves silane treatment of exposed hydroxyl groups (Zhu et al. 2008).

Carbon nanotube-based NC can be achieved only by solving two main problems: the large contact area of CNT and the relatively strong inter-tube attraction via Van der Waals's forces. These forces make the CNT spontaneously bundle together, which cause poor interfacial adhesion between the raw CNT and the matrix. Thus, chemical and physical modification of the CNT surface is necessary to realize many of their potential applications (Bahr and Tour 2002; Niyogi et al. 2002).

Two of the key challenges that detract from realizing composites made out of carbon nanotubes are securing a reliable control over their surface chemistry through either covalent or non-covalent modification, and achieving dispersion. Recently the development of CNT-based NC has been achieved thanks to approaches that have been used to exfoliate bundles of CNT through the wrapping of the tubular surface by various species of polymers (Thostenson et al. 2001), aromatic compounds (Nakashima et al. 2002) and surfactants (Islam et al. 2003).

Different chemical functionalization techniques have been devised for enhancing the interfacial adhesion between the nanotubes and the matrix (Tasis et al. 2006). One of these is the oxidative process utilizing strong acids such as HNO_3 or H_2SO_4 in which carboxylic acid moieties are created on nanotubes. The silanization of functionalized nanotubes is another preferred method used to enhance the interfacial adhesion between nanotubes and the matrix. The silane coupling agents most commonly used are organosilanes (Kathi and Rhee 2008).

The direct fluorination of Single Wall Carbon Nanotube (SWNT) and their subsequent derivation provide a versatile tool for the preparation and manipulation of nanotubes with variable sidewall functionalities (Khabashesku et al. 2002). Recent studies have shown that fluorine in SWNTs can be efficiently displaced by alkylamino functionalities.

The plasma treatment for the functionalization of carbon nanotubes represents a novel approach easy to scale up to industrial application. More recently there were a lot of attempts to fluorinate carbon nanotube sidewalls in a similar manner (Valentini et al. 2008).

2.2 Classification of the Processing of Nanocomposites

Four different techniques for production of polymer NC are available:

1. In situ polymerization
2. Melt blending
3. Solvent method
4. Sol–gel method

The in situ polymerization and the melt blending methods are the most commonly used techniques for manufacturing thermosetting and thermoplastic NC, respectively. In the following Sections the above mentioned techniques are discussed, and further details regarding the in situ polymerization are provided in Chap. 3, in the context of clay-based NC and the underlying chemistry may be found in Chap. 4.

2.2.1 In Situ Polymerization Process

In situ polymerization was the first technique used to synthesize NC materials based on polyamide/nanoclay (Okada and Usuki 2006). In principle, it is a very simple technique and is schematized in Fig. 2.8. The organic-modified layered silicate is swollen within a liquid monomer or a monomer solution so that the monomer can penetrate into the interlayer space between lamellae (Pavlidou and Papaspyridesb

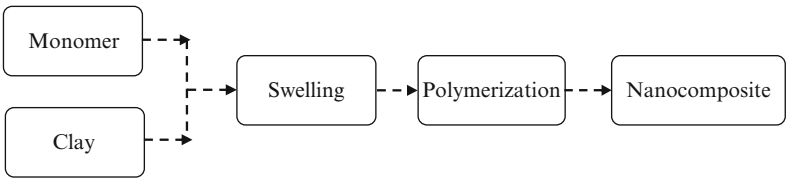

Fig. 2.8 Schematic diagram showing the in situ polymerization process

2008). Then a polymerization reaction is initiated between the intercalated sheets by heat, radiation, diffusion of a proper initiator or by a catalyst fixed through cationic exchange inside the interlayer before the swelling. Polymerization produces long-chain polymers within the clay galleries resulting in an intercalated NC. Balancing intra- and extra-gallery polymerization rates, the clay layers can delaminate and the resulting material can be characterized by an exfoliated structure.

This method can be used both on thermoplastic and thermosetting polymers with different nanofillers, e.g., layered silicate or metallic oxides, and can be combined with shear compounding to optimize nanofiller dispersion. Recently, this method has been applied directly to polymer extrusion, obtaining the NC in a single step by means of a highly productive industrial technique (Koo 2006). These particular aspects of in situ polymerization will be discussed in detail for thermoplastic and thermosetting materials in the following.

2.2.1.1 Thermoplastic Materials

The first successful attempts to obtain thermoplastic NC were made by Toyota researchers modifying montmorillonite (MMT) by means of an amino-acid compatibilizer ($COOH - (CH2)n - 1 - NH2+$, with $n = 2, 3, 4, 5, 6, 8, 11, 12, 18$). The ε-caprolactam monomer was swollen at 100°C by the modified MMT and then polymerized to obtain a polyamide/MMT nanocomposite (Usuki et al. 1993). Comparing different nanofillers and compatibilizers, two main results were found. (a) Clays having larger cation exchange capacity (CEC) achieve a good exfoliation of the silicate lamellae (Fornes et al. 2002). (b) The length of the atom carbon chain of the compatibilizer affects significantly the swelling capability of the nanoclay as shown in Fig. 2.9: the longer the chain length, the larger the extent of intercalation of the polymer (Usuki et al. 1993).

Depending on the amount of MMT introduced, exfoliated (for less than 15 wt%) or intercalated structures (from 15 to 70 wt%) could be obtained. Further work

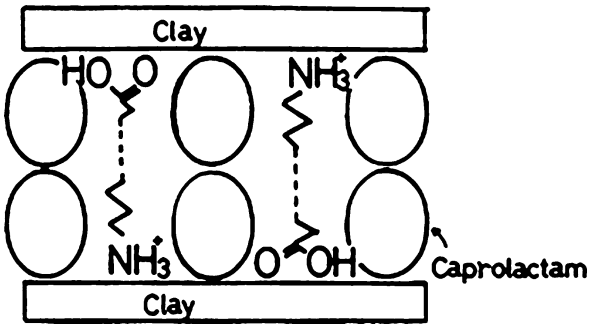

Fig. 2.9 Swelling behavior of organo-modified montmorillonite (MMT) by caprolactam (Usuki et al. 1993). Reproduced from Usuki et al. by permission of Journal of Materials Research, USA

demonstrated that intercalative polymerization of ε-caprolactam could be realized without modifying the MMT surface. Indeed, this monomer was able to directly intercalate the MMT in water in the presence of hydrochloric acid. At high temperature (200°C), with excess of ε-caprolactam, the clay so modified can be swollen again and the polymerization occurs as soon as the temperature is raised to 260°C.

The in situ polymerization method has also been used for NC manufactured with different kinds of thermoplastic polymer matrices, such as polyolefins (PP, PE, EVA) (Sun and Garces 2002; Bergman et al. 1999; Tudor et al. 1996; Jin et al. 2002), polyethylene terephthalate (PET) (Ke et al. 1999), polymethylmethacrylate (PMMA) (Okamoto et al. 2001), polystyrene (PS) (Akelah and Moet 1996), etc. For example PET/MMT intercalated NC were obtained by using the in situ-polymerization between the organoclay and PET monomers (ethylene glycol and terephthalic acid) (Ke et al. 1999).

Nanomaterials based on PE (Jin et al. 2002) have been realized by means of the polymerization-filling technique (PFT). This method is based on the in situ-polymerization of ethylene directly from the nanofillers treated on the surface through a Ziegler-Natta (ZN) catalyst. It should be observed that this technique can be applied only after a drying pretreatment of the nanofillers that makes it less hydrophilic. The dry nanoclay can then easily be dispersed in non-polar solvents (e.g., toluene) and surface-treated at 150°C with a pre-catalyst (e.g., a metallocene compound) to form the active ZN catalyst species. Finally, the polymer formation occurs by adding the ethylene monomer.

It has to be observed that, even if in situ polymerization has been used in the past to produce several thermoplastic NC, nowadays this technique has lost its importance for thermoplastics owing to some disadvantages. In fact, a very long time is needed to prepare the polymerization reaction. Moreover, exfoliation cannot always be thermodynamically stable, and the lamellae can aggregate during the further processing steps (Sepehr et al. 2005).

2.2.1.2 Thermosetting Materials

In spite of the aforementioned disadvantages, in situ polymerization is the only feasible technique for the preparation of thermosetting NC which cannot be synthesized by melt blending, which is the most important technique for NC preparation (Lan and Pinnavaia 1994; Becker et al. 2002).

In the case of organoclays used as nanofillers, both exfoliated and intercalated NC can be obtained. Exfoliation is affected significantly by several features of organoclays, e.g., their nature, the catalytic effect to accelerate the curing reaction, and the miscibility with the curing agent. For instance, as long as the intralayer and extralayer polymerization reactions occur at a comparable rate, the curing heat produced is enough to overcome the attractive forces between the silicate lamellae, resulting in an exfoliated NC structure. On the contrary, if the extralayer polymerization is faster, such resin will cure before the intralayer resin produces enough curing heat to drive the clay to exfoliate, consequently exfoliation will not be reached.

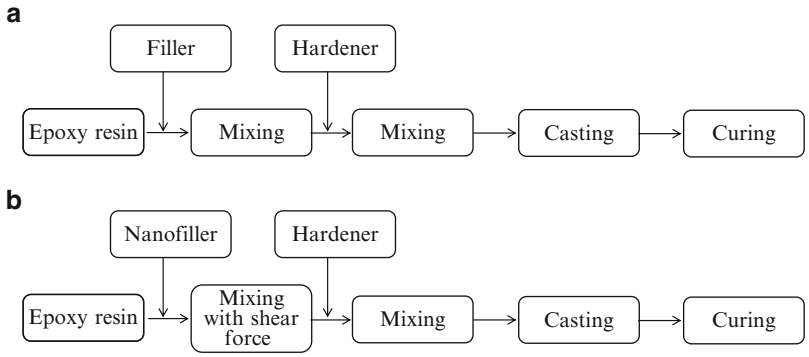

Fig. 2.10 Preparation scheme for (**a**) conventional filled epoxy and (**b**) nano-filled composites. Reproduced from Imai et al. by permission of IEEE, USA

Therefore, it can be concluded that factors supporting polymerization of intragallery resin can make the exfoliation of the clay feasible. Such factors include, e.g., the catalytic effect of organoclay on the curing reaction, the good attraction of the curing agent to the clay, the long alkyl-chain of the compatibilizer, resulting in more effective penetration of the monomer in the galleries and weaker attractive forces between the silicate lamellae (Jiankun et al. 2001).

Another important factor influencing the dispersion and the distribution of the nanofillers in the resin matrix is the mixing procedure applied during the incorporation of nanofillers to the prepolymers. The direct mixing method to obtain nanocomposite materials is similar to the traditional methods used to obtain microcomposites. It consists of the dispersion of an organically modified nanofiller in the epoxy resin before the addition of the hardener and the curing procedure. The preparation scheme for the direct mixing method, used to obtain microcomposites and nanocomposites, is depicted in Fig. 2.10.

As can be seen, in order to disaggregate the nanofiller clusters and to obtain a good dispersion and distribution in the polymer matrix an elevated shear force must be applied in the mixing process. It has been reported in the literature that this preparation method provides nanocomposites with improved electrical performance and with a thermal expansion coefficient very close to that of the conventional filled epoxy (Imai et al. 2006).

Some recent work (Koerner et al. 2006) showed that shear has a large impact on NC final morphology. Indeed, by using proper mechanical processing conditions and stirring rate, uniform dispersion and an excellent exfoliation is reachable also in NC which typically provide only intercalated structures after curing. This can be obtained, for instance, by maximizing the epoxy viscosity through stopping the curing progress before gelation and compounding at low temperatures close to resin glass transition. High viscosity, and thus large shear forces, make the NC more homogeneous.

Different curing techniques can be used to polymerize the NC. Even if the most common procedures involve thermal-curing agents, photo-reticulation by

ultraviolet (UV) light is another interesting technique that has been used very recently, especially to produce thin electrical insulating coatings. An example of NC cycloaliphatic epoxy resin filled by a nanoclay (in the range 1–7 wt%) prepared by photo-curing has been reported (Davidson 1998; Sangermano et al. 2006). The mixture has been ultrasonificated for 30 min and the cationic photoinitiator (triphenylsulfonium hexafluoroantimonate) added at 2 wt%. The obtained mixture has been photocured by means of a UV lamp with an intensity on the surface of the sample of 200 mW/cm^2 for 1 min.

The UV curing technique is becoming increasingly important due to its unique characteristics. First, the polymer formation is realized by a fast transformation of the liquid monomer into the solid film with tailored physical, chemical and mechanical properties. Moreover, it can be considered an environmentally friendly technique, due to the solvent free process and is usually carried out at room temperature, thus allowing energy saving. Furthermore, the cationic photopolymerization process of epoxy systems present some advantages compared to the radical one: lack of inhibition by oxygen, low shrinkage, good adhesion and mechanical properties of cured films (Sangermano et al. 2006). The only disadvantage is that this technique does not allow thick insulators to be fabricated. In fact, for complete photo-polymerization to occur in the whole insulation, epoxy NC thickness cannot exceed some hundred micrometers.

2.2.2 Solvent Method

This method is also known as intercalation of polymer or pre-polymer from solution when applied to prepare NC with layered silicates. It is based on a solvent system in which the polymer or pre-polymer is soluble and silicate layers are swellable (Sinha Ray and Okamoto 2003; Hussain et al. 2006). The layered silicate is first swollen in a solvent, such as water, chloroform, toluene or other organic solvent able to swell the clay and dissolve the polymer. When the polymer and layered silicate solutions are mixed, the polymer chains intercalate and displace the solvent within the interlayer of the silicate. Upon solvent removal (done by means of solvent evaporation (Koh et al. 2008)) or precipitation in non-solvent media (Pourbas and Raeesi 2005), the intercalated structure remains, resulting in polymer/layered silicate NC as schematically represented in Fig. 2.11. This method is good for the intercalation of polymers with little or no polarity into layered structures and facilitates production of thin films with polymer-oriented clay intercalated layers.

In the case of carbon nanotube-based NC preparation, the solution method has been largely employed for thermoplastic matrices: it involves the preparation of a polymer solution and the mixing with a dispersion of CNTs in the same solvent. For example, the dispersion of CNTs in aqueous polyvinylalcohol solutions has been reported (Shaffer and Windle 1999): stirring was required to prevent CNT aggregation and the polymer sterically stabilized the system. Unpurified SWNTs produced by the arc discharge method were used in another study (Stéphan et al. 2000): they

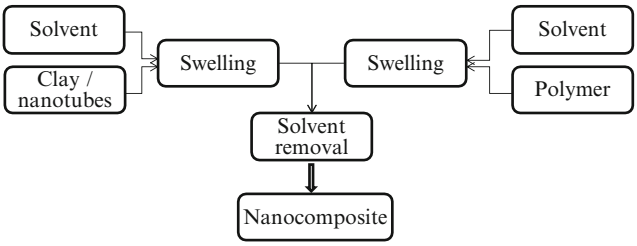

Fig. 2.11 Schematic diagram showing the solvent method. Reproduced from Montanari et al. by permission of IEEE, USA

were mixed with polymethylmethacrylate in toluene by sonication. A 200 nm thick film was obtained by spin casting and the Raman spectra suggested that polymethylmethacrylate intercalated into CNT bundles. At low concentration, the quantity of intercalated polymethylmethacrylate may lead to a destruction of bundles, causing a uniform dispersion of CNTs in the solution. These films were prepared for use in multilayer diodes. Polystyrene has also been dissolved in toluene and MWNTs were dispersed in the same solvent by high energy sonication (Qian et al. 2000). Next, the mixture of the polystyrene solution and the MWNT suspension was cast producing a uniform 0.4 mm thick film. A homogeneous dispersion was obtained without CNT attrition.

From the commercial point of view, this method involves the copious use of organic solvents, which is usually environmentally unfriendly and often economically prohibitive.

2.2.3 Melt Blending

Extrusion melt compounding of dispersive nanofillers with polymeric materials is considered the most effective way for producing NC. From the practical point of view, if technologically possible, this process is more economical and more profitable than in situ polymerization, solvent casting techniques and sol–gel methods. This procedure allows NC to be formulated using ordinary compounding devices: extruders or special mixers, without the necessity of using advanced polymer technology.

The melt blending technology does not represent any limitation, provided that the best mixing condition and formulation are defined for each polymer. Indeed mixing parameters strongly affect the polymeric NC morphology (Paul and Robeson 2008). In this context, the morphology describes the *dispersion*, *particle size* and *distribution* of the nanofiller in the polymer matrix. The means to quantify some of these characteristics have been discussed in Chap. 1.

Major variables to take into account are: proper balance of distributive and dispersing mixing and, in turn, length of the different zones, design of blocks, design of screw, specifically length and position of mixing zone, screw length, melt

temperature, residence time of melt, and shear (Wang et al. 2004). The nature of the extruder and the screw configuration are important to achieve good nanofiller dispersion (Sinha Ray and Okamoto 2003). Longer residence times in the extruder favour better dispersion. In some cases, having a higher melt viscosity is helpful in achieving dispersion, apparently because of the higher stresses that can be imposed on the nanofiller particles (Fornes et al. 2001).

The key to a fundamental understanding of the mixing process and its optimization is the clear distinction between "dispersive" and "distributive" mixing mechanisms, and identification of the important process characteristics enhancing realization of these mechanisms. In a multiphase system, such as polymer and nanoparticles, dispersive mixing involves the reduction of the cohesive minor components, such as clusters of solid nanoparticles. Distributive mixing is the process of spreading the minor component throughout the matrix in order to obtain a good spatial distribution. In any mixing device, these two mechanisms may occur simultaneously or stepwise.

The conditions under which dispersive mixing occurs are determined by the balance between the cohesive force holding nanoparticle agglomerates together and the disruptive hydrodynamic forces. The magnitude of the applied stresses plays a decisive role in determining the particle size distribution (Cho and Paul 2001).

In mixing equipment, the complex flow geometry generates field patterns which represent a superposition of flow ranging from pure rotation to pure elongation. The main steps for the liquid-solid dispersive mixing are:

- The incorporation of the filler into the liquid matrix.
- The wetting of the solid phase by the liquid one.
- The fragmentation of the solid agglomerates, which can be divided into two different processes: the erosion and the break up. The first is a low energy fracture and it prevails in the low shear regions, whereas the second is the high energy fracture and it prevails in the big shear regions of the mixer.
- The agglomeration of the dispersed particles due to the cohesive forces between the particles and provoked by the particle-particle collisions (Sinha Ray and Okamoto 2003).

Simple shear flow is not very efficient in achieving dispersive mixing, because particles in the fluid are not only sheared, but are also rotated, whereas elongational flow is much more efficient than shear flow in achieving effective dispersion. Indeed, in elongational flow particles undergo a stretching type of deformation without any rotation.

NC preparation has been reported by using new mixing devices imparting elongational flow rather than shear flow (Nassar et al. 2005). Utracki carried out melt compounding using an extensional flow mixer (EFM) attached to a single screw extruder or a twin screw extruder (Utracki 2008). The preparation of PA6 (Nylon-6) and PP composites was accomplished by using the above extruders with or without EFM. By comparing the NC final features, the most effective method turned out to be the one based on a single screw extruder with EFM. More recently it

was demonstrated that the elongational deformation, which the material undergoes during an injection molding process, might favor the clay dispersion in the polymer matrix (Frache et al. 2008).

However, no matter how well these process considerations are optimized, it is clear that complete dispersion of nanoparticles, or nearly so, cannot be achieved unless there is a good thermodynamic affinity between the nanofiller surfaces and the polymer matrix.

2.2.4 Sol–Gel Process

The sol–gel method is widely used in the preparation processes for inorganic/organic NC (Tanaka et al. 2004). The advantages of the sol–gel method are (1) the synthesis process is done at room temperature and (2) organic polymers can be introduced at the initial stage, in which the nanoparticle of sol can remain homogeneously dispersed at a nanometric scale.

The sol–gel method consists of hydrolysis of the constituent molecular precursors and subsequent polycondensation to glass-like form. It allows incorporation of organic and inorganic additives during the process of formation of the glassy network at room temperature. This method has been used traditionally to fabricate glasses and ceramics. Recently, at the same time, it has been used for polycrystals, porous composites, and organic-inorganic composites. Sol–gel reaction is started from metal alkoxide, M(OR)n. It should be melted, e.g., in water, alcohol, acid, ammonia, in order to be homogeneously dispersed. Metal alkoxide is hydrolyzed through reaction with water and turns out to be metal hydroxide and alcohol. There are many kinds of metals used, such as Na, Ba, Cu, Al, Si, Ti, Zr, Ge, V, W and Y. Silicon alkoxides such as tetraethoxysilane (TEOS) and tetramethoxysilane (TMOS), are also often used. In the case of TEOS, for example, an amorphous polymer with three dimensional network structures of silica is formed by polymerization reaction followed by hydrolysis (Chujo 2001).

$$\begin{gathered}
\mathrm{Si(OC_2H_5)_4 + H_2O \rightarrow (OC_2H_5)_3Si - OH + C_2H_5OH} \\
\equiv \mathrm{Si - OH + HO - Si \equiv \rightarrow \equiv Si - O - Si \equiv + H_2O} \\
\equiv \mathrm{Si - OH + (OC_2H_5)_2Si - \rightarrow \equiv Si - O - Si \equiv + C_2H_5OH}
\end{gathered}$$

The sol–gel method is now expected to become a key technology in the near future, as new modified methods, such as a continuous sol–gel, have been developed recently. Various companies have introduced highly-functional organosols of silicic acid, produced either by sol–gel condensation of tetraethoxysilane, or acidification of sodium silicates, followed by functionalization with various trialkoxysilanes. Another very versatile sol–gel route leads to the industrial preparation of dispersible boehmite nanofillers. In the Sasol process aluminum or magnesium metal is activated by etching off the surface oxide layer. Reaction with alcohol produces alkoxides and hydrogen. Upon hydrolysis, the aluminumalcoxides form boehmite

mineral that is obtained as a nanoparticle dispersion. The boehmite minerals can be rendered organophilic by reaction with carboxylic or benzenesulfonic acids. The by-product alcohol is recycled in this process. In contrast to natural organophilic boehmite, the sol–gel reaction product is much easier to redisperse and does not possess other metal ions as impurities.

2.3 Effects of Contaminants

2.3.1 Effect of By-Products of a Compatibilization Process

As described in the Sect. 2.1.2, a surface treatment of the inorganic filler is generally required in order to obtain a good dispersion in the polymer matrix and, therefore, to maximize the filler/polymer interface area and improve the dielectric properties of the composite. For example, in the case of thermoplastic insulating materials filled with layered silicates, the cation exchange of the interlayer sodium cations by protonated octadecylamine (ODA) is necessary to make an organophillic silicate and to obtain intercalated or exfoliated NC, by direct dispersion of organoclay in the molten state with an extruder (Zanetti et al. 2001; Montanari, Cavallini et al. 2004).

The byproducts of the cation exchange, i.e., sodium chloride and alkylammonium chloride, can significantly worsen the dielectric properties of the composite and thus have to be removed by a washing treatment before the manufacturing of the composite. A non-accurate washing treatment leaves a large amount of ionic charge in the dielectric bulk, particularly at the interface between the filler particles and the polymer, giving rise to various phenomena which may compromise the performance of the composite as an electrical insulator.

In the following, some examples of the effects on the properties of a NC are shown. The NC are obtained by polyethylene-vinylacetate (EVA) containing 12% wt of vinylacetate, as polymeric matrix, and synthetic fluorohectorite (MEE), organically modified by means of exchange of interlayer sodium cations for protonated octadecylamine (ODA), NH3+, as filler. The filler was subjected to a two-step purification procedure after the compatibilization process (Montanari, Cavallini et al. 2004; Montanari et al. 2005). In the first step, the nanoclay powder was suspended in demineralized water ($<10\,\mu S$) and stirred at 60°C for 24 h in order to remove sodium chloride. The suspension was filtered under vacuum; this procedure was repeated for three times. The second step consisted of Soxhlet extraction with ethanol for 72 h, which provided the elimination of alkylammonium chloride.

In order to obtain evidence of the reduction of the ionic charge within the dielectric bulk (as a consequence of the above described washing treatment), the maximum accumulated space charge, measured by means of the Pulsed Electro Acoustic technique (PEA) on NC specimens obtained from unwashed (EVA + MEE) and washed (EVA + MEE-w) are reported in Fig. 2.12. The principle of this technique is described in Sect. A.2. As can be seen, the amount of accumulated

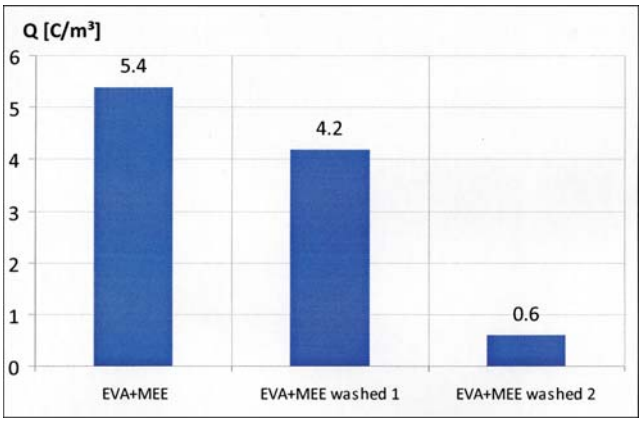

Fig. 2.12 Maximum accumulated charge density after 1 h of polarization under 60 kV/mm, EVA + MEE is the NC obtained from unwashed filler, EVA + MEE washed 1 is the NC obtained from filler subjected to the first step of the purification treatment, EVA + MEE washed 2 is the NC obtained from filler subjected to both steps of the purification treatment (Montanari, Cavallini et al. 2004)

space charge, evaluated as the integral of the absolute value of the space charge density along the axis parallel to the applied electric field, is reduced to 1/10 as an effect of the two washing treatments described above.

The space charge accumulation in the dielectric bulk can significantly impact the dielectric properties of the final NC. In fact, the presence of ionic species in the dielectric bulk can lead to a considerable distortion of the electric field distribution with respect to the Laplacian field (i.e., the electric field distribution in absence of free charges) and give rise to local enhancements of the electric field.

Figure 2.13 reports the space charge patterns, obtained by PEA measurements performed on pure EVA specimens, on EVA + MEE and on EVA + MEE-washed (Luque and Ayuso 1998), polarized under a Laplacian electric field of 60 kV/mm for 10^4 s. The electric field distributions along the axis parallel to the applied electric field at two instants of the polarization stage (10 and 10^3 s), calculated from the space charge density profiles, are also reported in Fig. 2.13. The accumulation of homocharge in the unwashed specimen gives rise to a significant enhancement of the local electric field in the central part of the specimen.

It is noteworthy that the electric field calculated from the charge profile can be an underestimation of the real distortion of the electric field, since the resolution of the PEA measurement, about a few microns, can be larger than the distance between positive and negative charge packets. Therefore while the dipolar charge distribution cannot be detected by the PEA method, it can give rise to very high electric field peak values and the actual distortion of the electric field from the Laplacian distribution can be much higher than that calculated. The high value of the local electric field may locally exceed the dielectric strength of the composite and give rise to an electric avalanche in the dielectric bulk and to insulation breakdown after a few minutes of voltage application.

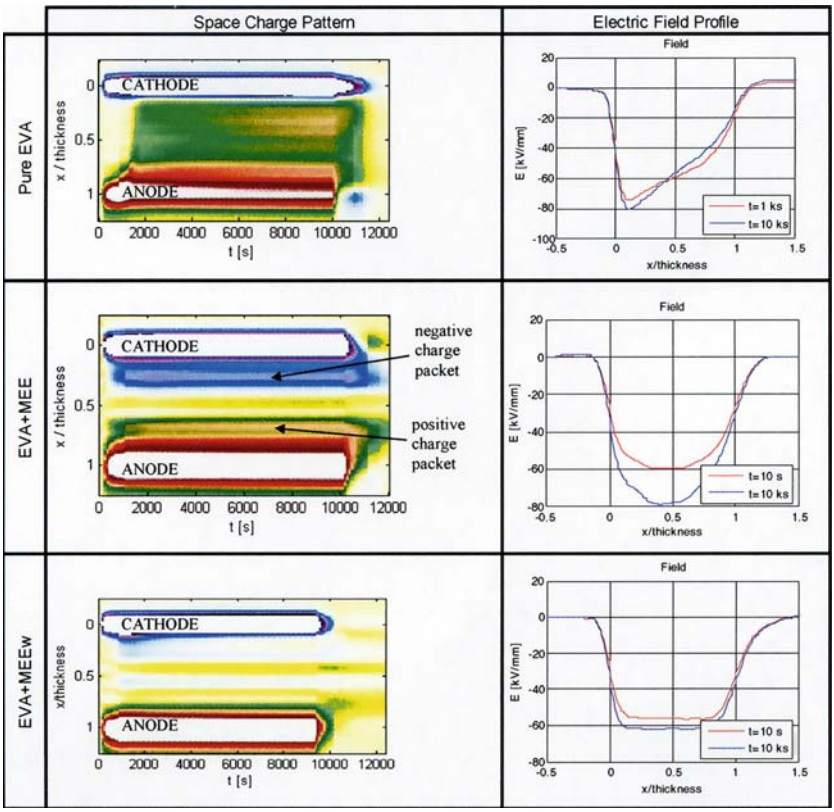

Fig. 2.13 Space charge patterns for base EVA, EVA + MEE and EVA + MEE-washed specimens, and relevant electric field profiles under geometric 60 kV/mm poling field. The cold and warm colors in the patterns represent negative and positive charge, respectively; x-axis = polarization + depolarization time, y-axis = electrodes + insulation thickness

The ionic charge introduced in the NC from the inadequate washing treatment also causes a reduction of the threshold for space charge accumulation as reported elsewhere (Montanari, Cavallini et al. 2004) due to the high availability of free charge in the NC bulk.

In addition, the presence of such charge, which is mainly localized at the interface between the filler particles and the polymer, can enhance the dielectric losses of the NC and give rise to interfacial polarization. As an example, Fig. 2.14 reports the comparison of the imaginary permittivity of the NC specimen obtained from washed and unwashed filler (Montanari et al. 2005). The imaginary permittivity of the washed specimen is five times lower than that of the unwashed specimen at low frequency (100 Hz) and in the typical operating temperature range of a polymeric electrical insulation apparatus (70–90°C).

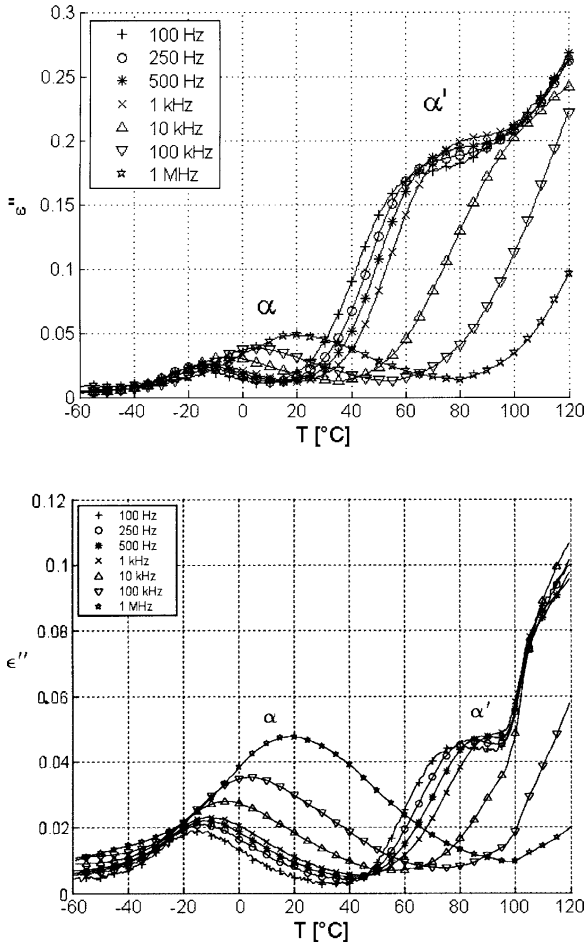

Fig. 2.14 Imaginary permittivity of EVA + MEE (*top*) and of EVA + MEE-washed (*bottom*), the relaxation process typical of base EVA (α) and that introduced by the nanofiller (α′) are also evident (Montanari et al. 2005). Reproduced from Montanari et al. by permission of IEEE, USA

The presence of ionic charge localized at the interface between the filler particles and the polymer, may give rise also to interfacial polarization phenomena. This can be observed from Fig. 2.15, where the real and imaginary permittivity of the washed and unwashed NC specimens are reported. The dielectric spectroscopy technique is outlined in Sect. A.1. The washed specimen has an imaginary permittivity at room temperature in the low frequency region about one order of magnitude lower than that of the unwashed specimen.

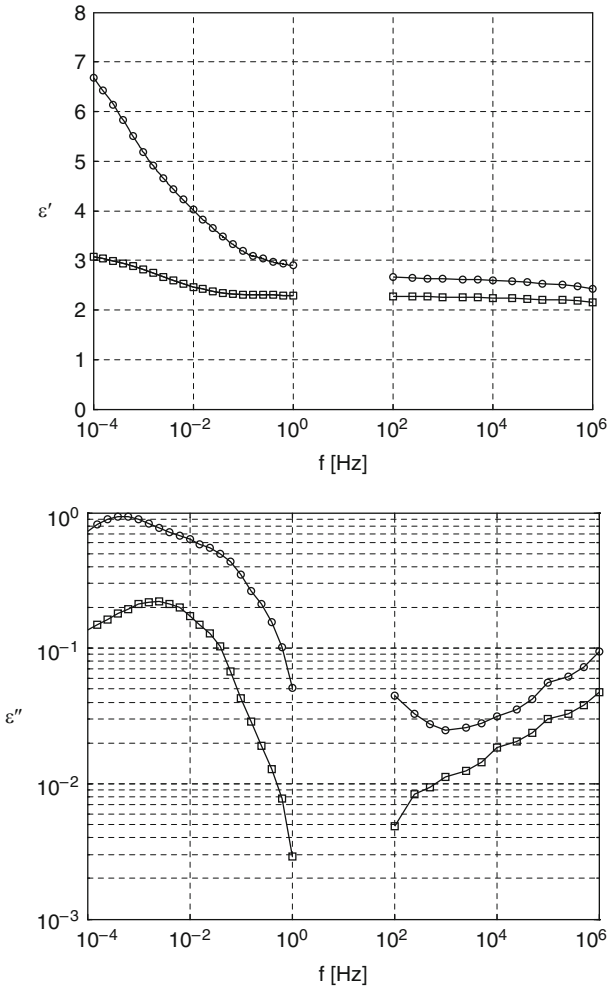

Fig. 2.15 Real (*top*) and imaginary (*bottom*) permittivity of EVA + MEE (*dots*) and EVA + MEE-washed (*squares*) (Montanari et al. 2005). Reproduced from Montanari et al. by permission of IEEE, USA

2.3.2 Effect of Moisture

The importance of proper washing aimed to remove the by-products of the compatibilization treatment, was shown in Sect. 2.3.1. It is noteworthy, however, that the washing treatment, if not properly carried out, may also give rise to undesired effects in the properties of the final NC. The particles of the inorganic filler can absorb water, in the washing treatment or as an effect of exposure to a humid environment.

The water molecules, which are characterized by high dipolar moment, are attracted from the filler particles which generally have high charge concentration

localized at the interfacial surfaces (e.g., montmorillonite). Therefore, the water adsorbed by the filler particles before the manufacturing process is introduced in the NC, localizes in proximity of the interface between the filler particles and the polymer matrix, and surrounding each filler particle as a thin shell (Montanari et al. 2006; Zou et al. 2008). It is also clear that the exposure to a humid environment after the manufacturing process may cause the adsorption of water in the NC, due to the above discussed hydrophilic properties of the compatibilized nanofiller. Also in this case, the water molecules are localized near the interfaces between the filler particles and the polymer.

If the concentration of water introduced in the NC is high enough, percolation or sub-percolation paths, depending on filler concentration and water content, are formed within the dielectric bulk from one water shell to the other. Such percolation paths enhance charge transport processes in the dielectric bulk increasing conductivity and losses of the NC and lowering its electric strength.

The charge transport between adjacent water shells is provided by a charge hopping process between localized conductive states. As a result, the closer the water shells the higher is the hopping probability (Fabiani et al. 2009). Since the probability of having two adjacent lamellae at a distance of a few nanometers, and thus of triggering local percolation processes, depends on the aspect ratio of the particles, the higher the aspect ratio of the filler particles, the higher the percolation probability and, consequently, the increase of conductivity and losses of the final NC.

The strong dependence of the steady-state conduction current as a function of the aspect ratio of the filler in an aqueous environment may be judged from the experimental results shown in Fig. 2.16. Two different fillers were used to prepare NC specimens, i.e., fluorohectorite (filler with particle maximum size of 500 nm along the lamella surface, thickness of 1 nm and aspect ratio >100 (Zanetti et al. 2001)) and boehmite (having particle shape close to spherical, with average particle size of 200 nm and aspect ratio $\cong$ 1). The fillers were stored in a non-dry environment (RH 50%) for 1 week before specimen manufacturing, in order to allow them to absorb some water. All the fillers were then subjected to a common drying process (1 h at 80°C under vacuum) needed to disaggregate the nanoparticles and disperse them properly in the matrix. This treatment, however, is not able to completely remove all the water associated with the particles. A further drying treatment (at 80°C under vacuum) was applied to a part of the fillers for a time ranging from 1 to 16 h. The composite obtained from the fillers subjected to the first drying process are designated "wet" in Fig. 2.16, those obtained from the filler subjected to the further drying process are termed "dry." The water content of the obtained specimens with 5% wt of the above mentioned fillers (for detailed manufacturing technique see (Fabiani et al. 2008, 2009)) was measured through the Karl-Fisher technique. The detected values are reported in the Table 2.2.

Figure 2.16 reports the steady state conduction current density, measured under a poling electric field of 10 kV/mm, on the wet and dry NC obtained from the fillers with different aspect ratios. The NC based on fluorohectorite, in spite of the lower content with respect to the specimen obtained from boehmite, shows a larger increase of the conductivity with increasing water content.

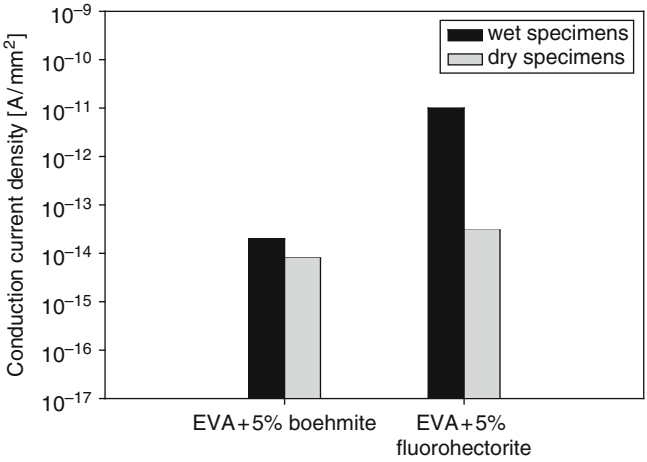

Fig. 2.16 Steady state conduction current for wet and dry NC specimens. Two types of nanofillers at 5%wt: boehmite (aspect ratio ≅ 1) and fluorohectorite(aspect ratio ≅ 100). Electric field = 10 kV/mm (Fabiani et al. 2009). Reproduced from Fabiani et al. by permission of IEEE, USA

Table 2.2 Water content of both dry and wet nanocomposites

	1 h (ppm)	8 h (ppm)
EVA + Boehmite	850 ± 5%	770 ± 5%
EVA + Fluorohectorite	400 ± 5%	200 ± 5%

The formation of percolation paths, caused by the presence of water at the interface between the filler particles and the polymer matrix, affects other dielectric properties, such as the electric strength. The scale parameter values of the Weibull distribution of DC electric strength (values corresponding to failure probability of 63.2%), relevant to wet and dry boehmite and fluorohectorite specimens, are reported in Fig. 2.17. As can be observed, wet specimens show a smaller electric strength with respect to dry specimens, particularly in fluorohectorite-based materials which display a reduction of about 40%

Figure 2.18 shows the effect of water content on space charge accumulation at electric fields of 40 kV/mm for EVA specimens filled with 5–10% of fluorohectorite (dry and wet). As can be seen, the maximum amount of accumulated charge (measured by the PEA method at the beginning of depolarization period) decreases with the drying treatment of the nanofiller. The amount of accumulated charge depends also on nanofiller content, increasing significantly when nanofiller rises to 10% wt.

Figure 2.19 reports similar results on fluorohectorite and boehmite specimens at 10 kV/mm (Fig. 2.19a) and 60 kV/mm (Fig. 2.19b). In particular, the specimens containing fluorohectorite show a large reduction of space charge build-up as a consequence of the drying process (note that at 60 kV/mm the wet specimen failed before the test was completed due to massive space charge accumulation). A smaller reduction, in contrast, is detected on boehmite specimens. The increase of the accumulated space charge associated with the increase of water content can be explained

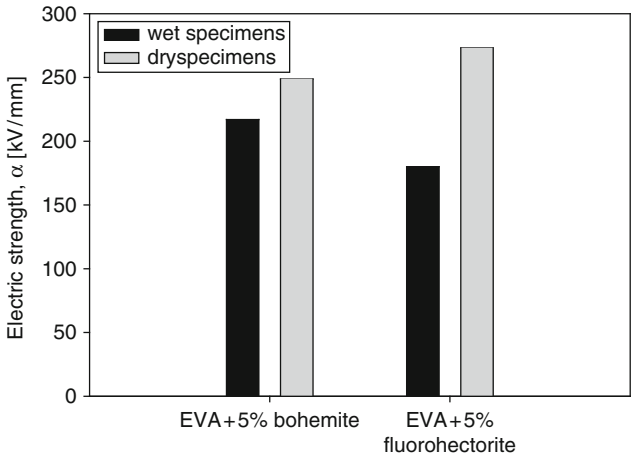

Fig. 2.17 Electric strength (Weibull scale parameter) for wet and dry NC specimens. Nanofillers: boehmite (5%wt) and fluorohectorite (5%wt) (Fabiani et al. 2009). Reproduced from Fabiani et al. by permission of IEEE, USA

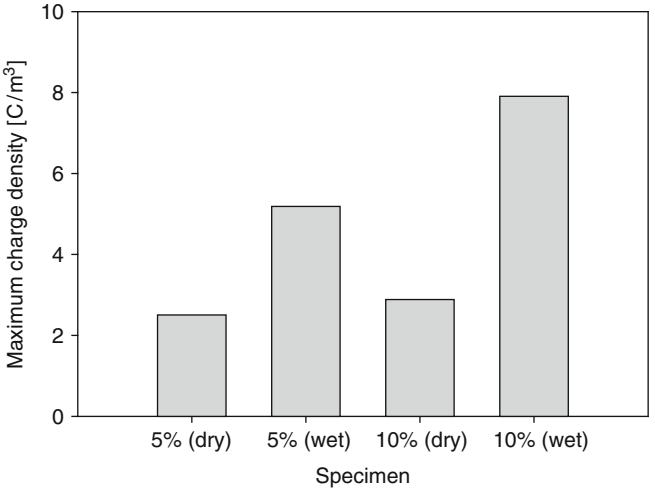

Fig. 2.18 Maximum stored charge density for dry and wet nanostructured specimens. Nanofiller: fluorohectorite at 5% and 10% wt. Test field: 40 kV/mm (Fabiani et al. 2009). Reproduced from Fabiani et al. by permission of IEEE, USA

considering that the water is able to modify the charge injection/extraction processes from the electrodes, as well as charge transport in the bulk. On one hand, the injection barrier at the electrode/insulation interface can be reduced in the presence of water molecules, thus allowing much more charge to be injected in the insulation. On the other hand, charge dynamics in the bulk can increase significantly due to quasi-percolation paths. In addition, ionic conduction can be brought

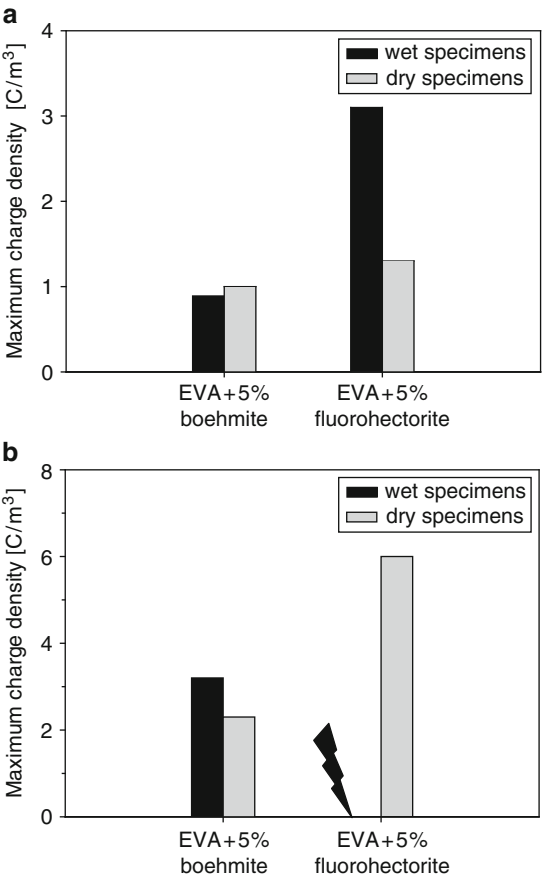

Fig. 2.19 Maximum stored charge density for wet and dry NC specimens. Nanofillers: boehmite (5%wt) and fluorohectorite. Electric field = 10 kV/mm (**a**) and 60 kV/mm (**b**). The *arrow* indicates that the test was not completed due to specimen breakdown (Fabiani et al. 2009). Reproduced from Fabiani et al. by permission of IEEE, USA

about by the presence of water. Therefore, depending on the prevailing mechanism (injection/transport) and the presence of ionic charge, an increase/decrease of space charge accumulation can be detected in the wet specimens. The increase of space charge accumulation in wet specimens observed in Figs. 2.19 and 2.18 (particularly in those having higher aspect ratio), indicates that injection enhancement and/or ionic charge formation prevail in this case. This explains also why increasing the layered silicate content from 5 to 10% wt, a larger amount of charge is measured in the wet specimens (Fig. 2.18).

From these examples cited, it can be observed that the electrical properties of the final NC can be strongly affected by the presence of moisture coming from wet filler or absorbed by the composite from a humid environment. In particular, the space charge measurement and the dielectric spectroscopy techniques can provide quantitative indications of the effects of the presence of such contaminants. Further evidence of this phenomenon can be obtained from Fig. 2.20 in which the imaginary permittivity of dry and wet NC specimens based on fluorohectorite and

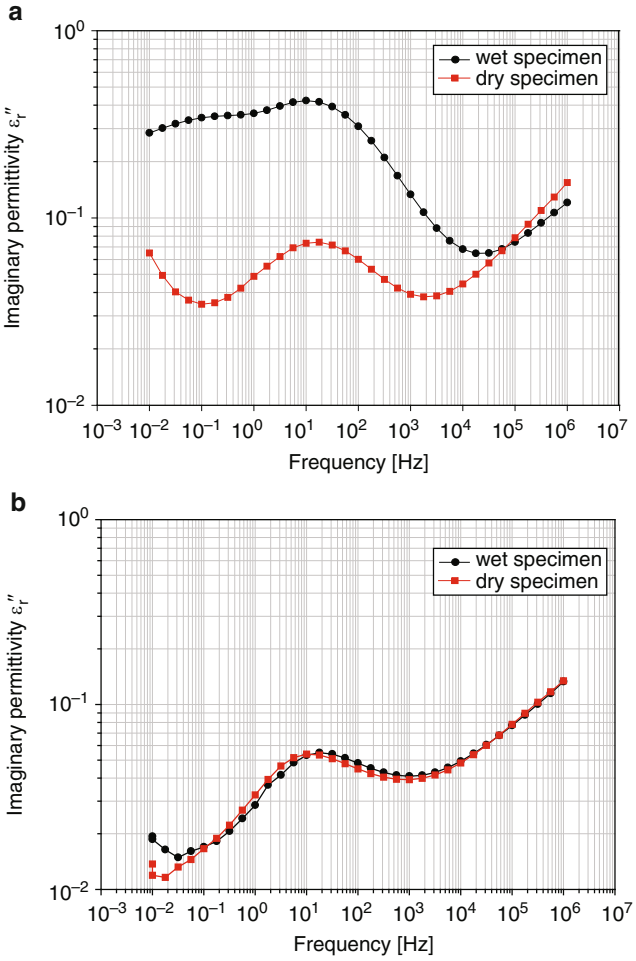

Fig. 2.20 Imaginary permittivity of NC obtained by (**a**) wet and dry fluorohectorite filler; (**b**) wet and dry boehmite filler (Fabiani et al. 2009). Reproduced from Fabiani et al. by permission of IEEE, USA

boehmite is reported. As can be seen, the NC based on the fluorohectorite shows the most significant variation of the imaginary permittivity spectrum between the dry and wet specimens, with respect to the boehmite based specimen. This can be explained considering the effect of the percolation paths, which are present in the fluorohectorite-based specimen and are practically absent in the boehmite-based specimen, due to the low aspect ratio of the boehmite nanoparticles and the consequent relatively high distance between the particles (Fabiani et al. 2009).

The dielectric spectroscopy technique can thus provide information regarding both the polarization processes of the NC and the possible presence of contaminants deriving from the manufacturing process. This information can be used to improve and optimize the steps of the manufacturing process and to perform quality control.

2.4 The Assessment of Dispersion and Morphological Characterization

Assessing the degree of nanofiller dispersion and distribution is crucial to deliver consistent properties of NC materials. Two difficulties appear at the NC preparation stage: the control of processing conditions in order to reach nanodispersion and how to characterize accurately the dispersion state achieved.

Most of the studies reported in the literature concern polymer layered silicate NC. For clay based NC X-ray diffraction (XRD) and TEM are the most widely used techniques to characterize clay dispersion (Alexandre and Dubois 2000; Giannelis 1996; Okamoto et al. 2001).

X-ray diffraction allows the measure of the interplatelet distance (d) in intercalated structures using the Bragg's law

$$\sin(\Theta) = \frac{n\lambda}{2d} \tag{2.1}$$

where Θ is the incident angle, n the integer and λ the wavelength of the incident X-ray beam. The observation of the changes in the diffraction angle corresponding to the plane $d(001)$ of the clay enables the dispersion to be characterized. The more polymer chains are intercalated between the platelets, the more the layer distance d increases and so the more the diffraction angle Θ decreases. For exfoliated samples, there is no more layer structure, causing no more observation of diffraction for the $d001$, as schematically shown in Fig. 2.21.

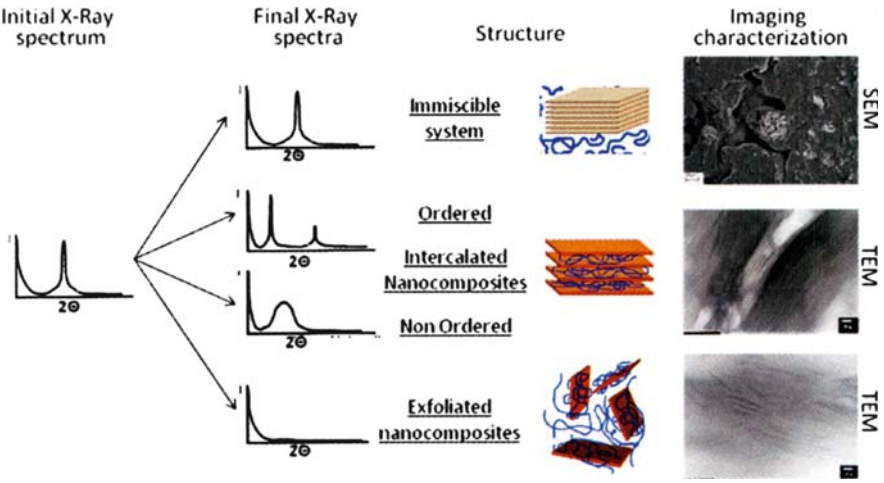

Fig. 2.21 XRD spectrum analysis of layered silicates: behavior of the diffraction angle for the intercalated/exfoliated structures

XRD is capable of detecting exfoliation and intercalation, but is limited because of clay dilution, preferred orientation, mixed-layering and other peak broadening factors. Moreover, the disappearance of the clay basal peaks from the wide angle X-ray diffraction (WAXD) pattern cannot be considered a sufficient sign that exfoliation has occurred unless the angular range is explored beyond the low angle limit of WAXD. To overcome this problem, analyses with the small angle X-ray scattering (SAXS) have been introduced recently in the NC morphology assessment (Causin et al. 2005). Many authors (Gelfer et al. 2006; Vaia et al. 2003; Yoonessi et al. 2005) have reported SAXS investigations on hybrid organic-inorganic materials to describe the morphology of hybrid materials over a broad scale in the nanosize range.

However XRD (WAXD or SAXS) analysis is not used alone in studies to deduce the NC morphology. Direct imaging methods, such as scanning electron microscopy SEM or transmission electron microscopy TEM and XRD, are often combined to strengthen the conclusion derived from the separated analysis (see Fig. 2.20).

TEM is based upon electron density and diffraction contrast differences between the clay structures and the polymer matrix. Unlike XRD, TEM permits the direct observation of the clay structures. The organo-clay structures, as well as the other silicon-based nanofillers in a polymer NC, naturally appear as dark features in the TEM micrographs. If the structures are sufficiently thick (that is, thicker than the microtomed sections) they can be observed easily independently of the orientation of the silicate layers.

Image analysis procedures can be used to quantify the dispersion from TEM pictures. The average thicknesses, lengths, and aspect ratios of each class of tactoids could be measured, as well as their relative proportions and the average distances between two adjacent tactoids (Vermogen et al. 2005). Examples of this were introduced in Chap. 1. The main disadvantage of these imaging methods is that a large number of pictures are necessary to obtain a statistical representative view of the whole sample.

Dynamic melt rheometry is a powerful method to inspect the effect of inorganic filler on the motion and relaxation of polymer chains. Indeed, the use of melt rheology to characterize polymer-clay NC has been used widely and different models have been employed to quantify the degree of exfoliation/intercalation of the clay in the polymeric matrix (Krishnamoorti and Giannelis 1997; Zhao et al. 2005). Intercalation and/or exfoliation processes induce the appearance of shear-thinning effects which are more apparent as the dispersion of the nanoparticles in the polymer matrix improves. Viscosity curves shift towards higher values, at low shear rates, as well.

The rheological behavior of polyamide-based NC was studied and the results were related to TEM observations (Incarnato et al. 2004). Their results indicate that the flow curve shape of the NC is associated with the exfoliation and intercalation level of the silicate platelets in the polymer matrix. Hybrids having complex viscosity curves with moderate deviations from pseudo-Newtonian trend show microscale morphology comprised of intercalated aggregates. Wagener and Reisinger (2003) developed a method to quantify shear thinning of polymer–clay NC and used the shear thinning exponent n to compare the extent of platelet delamination. This

parameter is obtained from the flow curves by fitting to a power law. They concluded that the shear thinning exponent n is a semi-quantitative measure of the degree of exfoliation and delamination. However, there is no obvious relation between the shear thinning exponent n and the degree of delamination. The average number of nanoplatelets per tactoid for a given NC cannot be calculated from n.

The methods described for the clay-based polymer NC are used widely for all nanostructured polymeric materials. For example, Becker et al. (1998) used SAXS analysis coupled with TEM observation to assess the degree of dispersion of silica nanoparticles in a thermoplastic polymer. On the other hand, several studies on the employment of rheological testing as a powerful method to determine the dispersion of carbon nanotubes based polymer NC have been developed in the last years (Shi et al. 2005; Valentino et al. 2008; Nobile et al. 2007).

References

Akelah A, Moet M (1996) Polymer-clay nanocomposites: free radical grafting of polystyrene on to organophilic montmorillonite interlayers. J Mater Sci 31:3589–3596

Alexandre M, Dubois P (2000) Polymer-layered silicate nanocomposites: preparation, properties and uses of a new class of materials. Mater Sci Eng R 28:1–63

Bahr JL, Tour JM (2002) Covalent chemistry of single-wall carbon nanotubes, a review. J Mater Chem 12:1952–1958

Bauer F, Glasel HJ et al (2003) Trialkoxysilane grafting onto nanoparticles for the preparation of clear coat polyacrylate systems with excellent scratch performance. Prog Org Coatings 47:147–153

Beari F, Brand M et al (2001) Organofunctional alkoxysilanes in dilute aqueous solution: new accounts on the dynamic structural mutability. J Organomet Chem 625:208

Becker C, Kutsch B et al (1998) SAXS and TEM investigations on thermoplastic nanocomposites containing functionalized silica nanoparticles. J Sol–Gel Sci Tech 13:499–502

Becker O, Varley R, Simon G (2002) Morphology, thermal relaxations and mechanical properties of layered silicate nanocomposites based upon high-functionality epoxy resins. Polymer 43:4365–4373

Bergaya F, Theng BKG, Lagaly G (2006) Handbook of clay science. Development in clay science, vol 1. Elsevier, UK

Bergman JS, Chen H, Giannelis EP et al (1999) Synthesis and characterization of polyolefin-silicate nanocomposites: a catalyst intercalation and in situ polymerization approach. J Chem Soc Chem Commun 21:2179–2180

Beyer G (2002) Nanocomposites: a new class of flame retardants for polymers. Plast Addit Compound 4(10):22–27

Bula K, Jesionowski T et al (2007) The effect of filler surface modification and processing conditions on distribution behaviour of silica nanofillers in polyesters. Colloid Polym Sci 285:1267–1273

Carlino S (1997) The intercalation of carboxylic acids into layered double hydroxides: a critical evaluation and review of the different methods. Solid State Ionics 98:73–81

Causin V, Marega C et al (2005) Assessing organo-clay dispersion in polymer layered silicate nanocomposites: a SAXS approach. Polymer 46:9533–9537

Cavani F, Trifiro F, Vaccari V (1991) Hydrotalcite-type anionic clays: preparation, properties and applications. Catal Today 11:173–179

Chin I-J, Thurn-Albrecht T, Kim H-C et al (2001) On exfoliation of montmorillonite in epoxy. Polymer 42:5947–5952

Cho JW, Paul DR (2001) Nylon 6 nanocomposites by melt compounding. Polymer 42:1083–1090
Chujo K (2001) Advanced technology and application of polymer nanocomposite. CMC Press, Japan, pp 1–240
Costa FR, Leuteritz A et al (2008) Intercalation of Mg-Al layered double hydroxide by anionic surfactants: preparation and characterization. Appl Clay Sci 38:153–158
Costantino U, Montanari F et al (2007) Preparation and characterisation of hydrotalcite/carboxyadamantane intercalation compounds as fillers of polymeric nanocomposites. J Mater Chem 17:1079–1086
Davidson RS (1998) Exploring the science, technology and applications of U.V and E.B. curing. SITA Technology Ltd., London, UK
Di Gianni A, Amerio E et al (2008) Preparation of polymer/clay mineral nanocomposites via dispersion of silanated montmorillonite in a UV curable epoxy matrix. Appl Clay Sci 42:116–124
Fabiani D, Montanari GC et al (2008) Effect of water adsorption on the dielectric properties of polymer nanocomposites. Proc. IEEE ISEIM 1:510–513
Fabiani D, Montanari GC, Testa L (2009) Effect of water contamination on the electric properties of nanostructured insulating materials. IEEE T Diel Elec Ins 17
Fleming RJ, Ammala A, Lang SB et al (2008) Conductivity and space charge in LDPE containing nano- and micro-sized ZnO particles. Trans IEEE DEI-15:118–126
Fornes TD, Yoon PJ et al (2001) Nylon 6 nanocomposites: the effect of matrix molecular weight. Polymer 42:9929–9940
Fornes TD, Yoon PJ, Hunter DL et al (2002) Effect of organoclay structure on nylon 6 nanocomposite morphology and properties. Polymer 43:5915–5933
Frache A, Monticelli O et al (2008) Preparation of nanocomposites based on PP and PA6 by direct injection molding. Polym Eng Sci 48:2373–2238
Frost RL, Mendelovici E (2006) Modification of fibrous silicates surfaces with organic derivatives: an infrared spectroscopic study. J Colloid Interface Sci 294:47–52
Gelfer MY, Song HH et al (2003) Effects of organoclays on morphology and thermal and rheological properties of polystyrene and poly(methyl methacrylate) blends. J Polym Sci Polym Phys 41:44–54
Giannelis E (1996) Polymer layered silicate nanocomposites. Adv Mater 8:29–35
Guo Z, Lei K et al (2008) Fabrication and characterization of iron oxide nanoparticles reinforced vinyl-ester resin nanocomposites. Compos Sci Tech 68:1513–1520
Hong RY, Qian JZ, Cao JX (2006) Synthesis and characterization of PMMA grafted ZnO nanoparticles. Powder Technol 163:160–168
Hussain F, Hojjati M et al (2006) Review article: polymer-matrix nanocomposites, processing, manufacturing, and application: an overview. J Compos Mater 40:1511–1575
Imai T, Sawa F, Nakano et al (2006) Effects of nano- and micro-filler mixture on electrical insulation properties of epoxy based composites. Trans IEEE DEI-13: 319–326
Incarnato L, Scarfato P et al (2004) Rheological behavior of new melt compounded copolyamide nanocomposites. Polymer 45:3487–3496
Islam MF, Rojas E et al (2003) High weight fraction surfactant solubilization of single-wall carbon nanotubes in water. Nano Lett 3:269–273
Jiankun L, Yucai K, Zongneng Q, Xiao-Su Y (2001) Study on intercalation and exfoliation behavior of organoclays in epoxy resin. J Polym Sci Polym Phys 39:115–120
Jin Y-H, Park H-J, Im S-S et al (2002) Polyethylene/clay nanocomposite by in situ exfoliation of montmorillonite during Ziegler-Natta polymerization of ethylene. Macromol Rapid Commun 23:135–140
Kathi J, Rhee KY (2008) Surface modification of multi-walled carbon nanotubes using 3-aminopropyltriethoxysilane. J Mater Sci 43:33–37
Ke YC, Long CF, Qi ZN (1999) Crystallization, properties, and crystal and nanoscale morphology of PET-clay nanocomposites. J Appl Polym Sci 71:1139–1146
Khabashesku VN, Billups WE, Margrave JL (2002) Fluorination of single-wall carbon nanotubes and subsequent derivatization reactions. Acc Chem Res 35:1087–1095

Koerner H, Misra D, Tan A et al (2006) Montmorillonite-thermoset nanocomposites via cryocompounding. Polymer 47:3426–3435
Koh HC, Park JS et al (2008) Preparation and gas permeation properties of biodegradable polymer/layered silicate nanocomposite membranes. Desalination 233:201–209
Koo JH (2006) Polymer nanocomposites: processing, characterization, and applications. McGraw-Hill, New York, NY
Kortaberria G, Arruti P et al (2008) Local dynamics in epoxy coatings containing iron oxide nanoparticles by dielectric relaxation spectroscopy. J Appl Polymer Sci 109:3224–3229
Krishnamoorti R, Giannelis EP (1997) Rheology of end-tethered polymer layered silicate nanocomposites. Macromolecules 30:4097–4102
Lan T, Pinnavaia TJ (1994) Clay-reinforced epoxy nanocomposites. Chem Mater 6:2216–2219
Latterini L, Nocchetti M et al (2007) Structural, photophysical, and photochemical characterization of 9-anthracenecarboxylate – Hydrotalcite nanocomposites: evidence of a reversible light-driven reaction. Langmuir 23:12337–12343
Lee KY, Kim KY, Han WY, Park DH (2008) Thermal, electrical characteristics and morphology of poly(ethylene-co-ethyl acrylate)/CNT nanocomposites. Trans IEEE DEI-15:205–213
Luque de Castro MD, Garcõa-Ayuso LE (1998) Soxhlet extraction of solid materials: an outdated technique with a promising innovative future. Anal Chim Acta 369:1–10
Ma D, Akpalu Y et al (2005) Effect of titania nanoparticles on the morphology of low density polyethylene. J Polym Sci B Polym Phys 43:488–497
Manias E, Touny A, Wu L et al (2001) Polypropylene/montmorillonite nanocomposites. Review of the synthetic routes and materials properties. Chem Mater 13:3516–3523
Montanari GC, Cavallini A et al (2004) Microscopic and nanoscopic EVA composite investigation: electrical properties and effect of purification treatment. Proc IEEE CEIDP 1:318–321
Montanari GC, Fabiani D et al (2004) Modification of electrical properties and performance of EVA and PP insulation through nanostructuration by organophilic silicates. Trans IEEE DEI-11:754–762
Montanari GC, Motori A et al (2005) Dielectric spectroscopy analysis of EVA-silicate nanocomposite insulating materials. Proc. of IEEE ISEIM 1:245–250
Montanari GC, Palmieri F et al (2006) Polarization processes of nanocomposite silicate-EVA and PP materials. Trans IEEJ 126:1090–1096
Murakami Y, Nemoto M, Okuzumi S et al (2008) DC conduction and electrical breakdown of MgO/LDPE nanocomposite. Trans IEEE DEI-15:33–39
Nakashima N, Tomonari Y, Murakami H (2002) Water-soluble single-walled carbon nanotubes via noncovalent sidewall-functionalization with a pyrene-carrying ammonium ion. Chem Lett 31:638–639
Nassar N, Utracki LA, Kamal MR (2005) Melt intercalation in montmorillonite/polystyrene nanocomposites. Int Polym Process 20(4):423–431
Niyogi S, Hamon MA et al (2002) Chemistry of single-walled carbon nanotubes. Acc Chem Res 35:1105–1111
Nobile MR, Simon GP et al (2007) Rheological and structure investigation of melt mixed multi-walled carbon nanotube/PE composites. Macromol Symp 247:78–87
Okada A, Usuki A (2006) Twenty years of polymer-clay nanocomposites. Macromol Mater Eng 291:1449–1476
Okamoto M, Morita S, Kotaka T (2001) Dispersed structure and ionic conductivity of smectic clay/polymer nanocomposites. Polymer 42:2685–2688
Paul DR, Robeson LM (2008) Polymer nanotechnology: nanocomposites. Polymer 49:3187–3204
Pavan PC, Crepaldi EL et al (1999) Adsorption of sodium dodecylsulfate on a hydrotalcite-like compound. Effect of temperature, pH and ionic strength. Colloids Surf A154:399–411
Pourabas B, Raeesi V (2005) Preparation of ABS/montmorillonite nanocomposite using a solvent/non-solvent method. Polymer 46:5533–5540
Pavlidou S, Papaspyridesb CD (2008) A review on polymer-layered silicate nanocomposites. Prog Polym Sci 33:1119–1198

Prevot V, Forano C, Besse JP (2001) Hybrid derivatives of layered double hydroxides. Appl Clay Sci 18:3–15

Qian D, Dickey EC, Andrews R, Rantell T (2000) Load transfer and deformation mechanisms in carbon nanotube-polystyrene composites. Appl Phys Lett 76:2868–2680

Ray SS, Bousima M (2005) Biodegradable polymers and their layered silicate nanocomposites: in greening the 21st century materials world. Prog Mater Sci 50:962–1079

Rong MZ, Zhang MQ, Ruan WH (2006) Surface modification of nanoscale fillers for improving properties of polymer nanocomposites: a review. Mater Sci Technol 22:787–796

Sangermano M, Bongiovanni R, Malucelli G, Priola A (2006) New developments in cationic photopolymerization: process and properties. In: Bregg RK (ed) Horizons in polymer research. Nova Science Publisher Inc., New York

Sepehr M, Utracki LA, Zheng X, Wilkie CA (2005) Polystyrenes with macro-intercalated organoclay. Part I. Compounding and characterization. Polymer 46:11557–11568

Shaffer MSP, Windle AH (1999) Fabrication and characterization of carbon nanotube/poly(vinyl alcohol) composites. Adv Mater 11:937–947

Shi X, Hudson JL et al (2005) Rheological behaviour and mechanical characterization of injectable poly(propylene fumarate)/single-walled carbon nanotube composites for bone tissue engineering. Nanotechnology 16:S531–S538

Sinha Ray S, Okamoto M (2003) Polymer/layered silicate nanocomposites: a review from preparation to processing. Prog Polym Sci 28:1539–1641

Solomon MJ, Almusallam AS, Seefeldt KF et al (2001) Rheology of polypropylene/clay hybrid materials. Macromolecules 34:1864–1872

Stéphan C, Nguyen TP et al (2000) Characterization of singlewalled carbon nanotubes-PMMA composites. Synth Met 108:139–149

Sun T, Garces JM (2002) High-performance polypropylene-clay nanocomposites by in situ polymerization with metallocene/clay catalysts. Adv Mater 14:128–130

Tanaka T, Montanari GC, Mulhaupt R (2004) Polymer nanocomposites as dielectrics and electrical insulation-perspectives for processing technologies, material characterization and future applications. Trans IEEE DEI-11:763–784

Tartaglione G, Tabuani D, Camino G (2008) Thermal and morphological characterisation of organically modified sepiolite. Microporous Mesoporous Mater 107:161–168

Tasis D, Tagmatarchis N et al (2006) Chemistry of carbon nanotube. Chem Rev 106:1105–1115

Thostenson ET, Ren Z, Chou TW (2001) Advances in the science and technology of carbon nanotubes and their composites: a review. Compos Sci Technol 61:1899–1912

Tudor J, Willington L, O'Hare D, Royan B (1996) Intercalation of catalytically active metal complexes in phyllosilicates and their application as propene polymerization catalyst. Chem Commun 17:2031–2032

Usuki A, Kawasumi M, Kojima Y et al (1993) Swelling behavior of montmorillonite cation exchanged for ω-amino acid by ε-caprolactam. J Mater Res 8:1174–1178

Utracki LA (2008) Polymeric nanocomposites: compounding and performance. J Nanosci Nanotechnol 8:1582–1596

Vaia RA, Liu W, Koerner H (2003) Analysis of small-angle scattering of suspensions of organically modified montmorillonite: implications to phase behavior of polymer. J Polym Sci Polym Phys 41:3214–3236

Valentini L, Puglia D et al (2008) Use of plasma fluorinated single-walled carbon nanotubes for the preparation of nanocomposites with epoxy matrix. Compos Sci Tech 68:1008–1014

Valentino O, Sarno M et al (2008) Influence of the polymer structure and nanotube concentration on the conductivity and rheological properties of polyethylene/CNT composites. Phys E: Low-Dim Sys Nanostruct 40:2440–2445

Vermogen A, Masenelli-Varlot K et al (2005) Evaluation of the structure and dispersion in polymer-layered silicate nanocomposites. Macromolecules 38:9661–9669

Wagener R, Reisinger TJG (2003) A rheological method to compare the degree of exfoliation of nanocomposites. Polymer 44:7513–7518

Wang B, Zhang H et al (2005) Surface modification of layered double hydroxides and incorporation of hydrophobic organic compounds. Mater Chem Phys 92:190–196

Wang K, Liang S et al (2004) The interplay of thermodynamics and shear on the dispersion of polymer nanocomposites. Polymer 45:7953–7960

Yoonessi M, Toghiani H et al (2005) Clay delamination in clay/poly(dicyclopentadiene) nanocomposites quantified by small angle neutron scattering and high-resolution transmission electron microscopy. Macromolecules 38:818–831

You Y, Zhao H, Vance GF (2002) Hybrid organic-inorganic derivatives of layered double hydroxides and dodecylbenzenesulfonate: preparation and adsorption characteristics. J Mater Chem 12:907–912

Zanetti M, Camino G et al (2001) Synthesis and thermal behaviour of layered silicate – EVA nanocomposites. Polymer 42:4501–4507

Zhang F, Fuqiang Z et al (2005) Synthesis and properties of sepiolite/poly (acrylic acid-co-acrylamide) nanocomposites. Polym Bull 55:419–428

Zhao J, Morgan AB, Harris JD (2005) Rheological characterization of polystyrene-clay nanocomposites to compare the degree of exfoliation and dispersion. Polymer 46:8641–8660

Zhu J, Yuan P et al (2008) In situ synthesis of surfactant/silane-modified hydrotalcites. J Colloid Interface Sci 319:498–504

Zou C, Fothergill JC, Rowe SW (2008) The effect of water absorption on the dielectric properties of epoxy nanocomposites. Trans IEEE DEI-15:106–117

Chapter 3
Special Considerations for Clay-Based Materials

Takahiro Imai

3.1 The Nature of Clay Composites

Polymer composites, which are composed of polymer and inorganic materials to achieve their necessary properties, have a very long history. For example, fiber-reinforced plastics (FRP), which are composed of epoxy resin and glass/carbon fiber, are widely used in various industries and in our immediate surroundings.

However, recent rapid progress in nanotechnology has stimulated research and development on new high performance materials. Clay nanocomposites have attracted a lot of interest since the Toyota research group developed the nylon-6/clay nanocomposite in 1987. Figure 3.1 compares the dimensions of glass fiber and clay (Usuki 2003), and shows that clay has much smaller size than glass fiber. The clay nanocomposites comprise clays of nano-scale dimension dispersed in polymer materials. The addition of small amounts of clays in polymers can work as reinforcement in the same way as glass fiber or micro-scale inorganic filler, and, thus, clay nanocomposites are anticipated as the next high performance industrial materials. This chapter describes typical structures and properties of clay and clay nanocomposites, and further details on the underlying chemical aspects may be found in Chap. 4.

3.1.1 Structure and Properties of Clay

Clays. which have the general formula of $(Ca, Na, H)(Al, Mg, Fe, Zn)_2(Si, Al)_4O_{10}(OH)_2 - xH_2O$, are hydrous aluminum phyllosilicates. They are classified into four typical groups: Smectite, Kaolin, Chlorite and Illite. In particular, the smectite group, including montmorillonite, nontronite and saponite, is suitable for reinforcement in clay nanocomposites. The structure of this clay (smectite) is shown in Fig. 3.2 (Coop Chemical Corp 2000; Imai et al. 2004). It has a laminated

T. Imai (✉)
Toshiba Corporation, Japan
e-mail: takahiro2.imai@toshiba.co.jp

J.K. Nelson (ed.), *Dielectric Polymer Nanocomposites*,
DOI 10.1007/978-1-4419-1591-7_3,

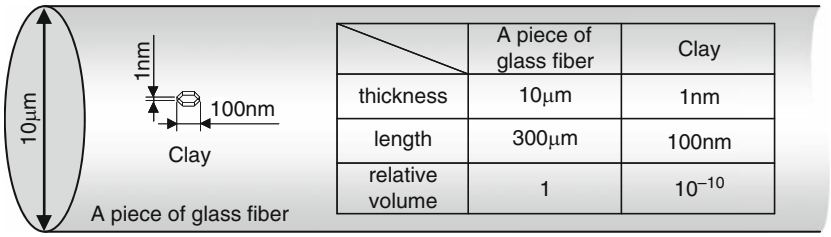

	A piece of glass fiber	Clay
thickness	10μm	1nm
length	300μm	100nm
relative volume	1	10^{-10}

Fig. 3.1 Comparison of a piece of glass fiber and a clay (Usuki 2003)

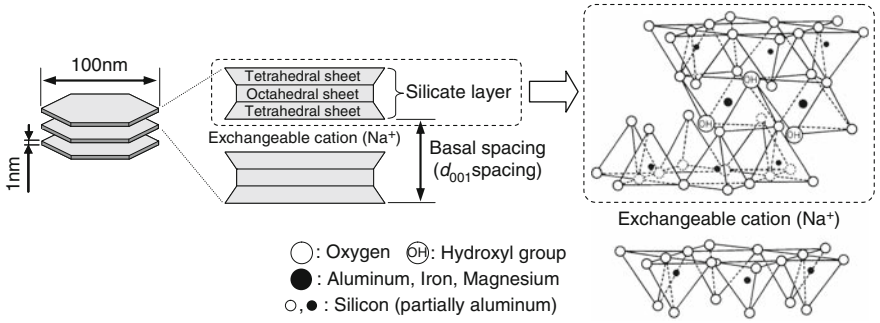

Fig. 3.2 Structure of clay (smectite) (Coop Chemical Corp 2000; Imai et al. 2004)

structure composed of a base unit (silicate layer) 100 nm long, 100 nm wide and 1 nm thick. This layer comprises Si-O tetrahedral sheets and Al-O, Mg-O octahedral sheets stacked in the order of tetrahedral sheet/octahedral sheet/tetrahedral sheet.

Moreover, the substitution of Al atoms for Si atoms in the tetrahedral sheet, or the substitution of divalent metal ion for trivalent metal ion in the octahedral sheet, generates a negative charge in the smectite. Cations such as sodium ions exist between the silicate layers to compensate for this negative charge. This structure imparts cation exchange ability to the smectite, and the cation exchange reaction enables the smectite to have an organic modifier (e.g., alkyl-onium ion) between the silicate layers. The properties of the smectite (montmorillonite) are summarized in Table 3.1 (Chujo 2003).

3.1.2 Characteristics of Clay Nanocomposites

Extensive research has been conducted on clay nanocomposites since the nylon-6/clay nanocomposite was developed in 1987, although much of the earlier work has been concerned with thermal and mechanical properties. In addition to nylon-6 (polyamide) nanocomposites, many kinds of clay nanocomposites based on epoxy resin (Lan and Pinnavaia 1994; Kornmann et al. 1999), polystyrene (Vaia et al.

Table 3.1 Properties of smectite (montmorillonite) (Chujo 2003)

Properties			
Swelling		ml/2 g	65
pH (2% aqueous dispersion)		–	10.2
Electric conductivity		μS/cm	675
Viscosity (4% aqueous dispersion)		mPa s	280
Visible light transmittance (1% aqueous dispersion)		%	1
Particle diameter		nm	100–2,000
Specific surface (N_2, BET)		m^2/g	20
MB (methylene blue) absorbed amount		mmol/100 g	130
Cation exchange ability		meq/100 g	108.6
Precipitation cation amount	Na^+	meq/100 g	114.1
	K^+	meq/100 g	2.8
	Mg^{2+}	meq/100 g	3.4
	Ca^{2+}	meq/100 g	18.2
Chemical composition	SiO_2	%	64.4
	Al_2O_3	%	25.9
	Fe_2O_3	%	3.5
	MgO	%	2.4
	CaO	%	0.7
	Na_2O	%	2.3
	K_2O	%	0.1

1993; Zhu et al. 2001), acrylate resin (polymethylmethacrylate) (Yeh et al. 2002), polypropylene (Okamoto et al. 2001) and polylactate (Ray et al. 2003; Krikorian and Pochan 2003) have been reported. Moreover, some clay nanocomposites such as "NANOCON™" by Unitika Ltd. have already been commercialized.

The properties of clay nanocomposites are broadly divided into fundamental properties and functional properties, as shown in Table 3.2. Clay dispersion in polymer materials can improve the fundamental properties that the polymers innately possess. Enhancements of electrical insulation properties (Imai 2006), mechanical properties (Lan and Pinnavaia 1994) and thermal properties (Messersmith and Giannelis 1994) in clay nanocomposites have been reported. Moreover, clay dispersion in polymer materials can impart new functional properties that the base polymers do not inherently possess. Polymer materials with new functions such as gas barrier (Yano et al. 1993) and flame resistance (Zhu et al. 2001) due to the effects of clay dispersion have also been reported.

3.1.3 Effects of Clay Dispersion on Polymer Properties

Prior to describing the important issues relating to the processing of clay-based nanodielectrics, it is appropriate to document some examples in which clay dispersion improves polymer properties.

Table 3.2 Properties of clay nanocomposites

Properties		
Fundamental properties	Mechanical properties	Flexural strength (higher)
		Tensile strength (higher)
		Elastic modulus (higher)
	Thermal properties	Heat distortion temperature (higher)
		Glass transition temperature (higher)
		Weight loss (lower)
		Thermal expansion (lower)
	Electrical insulation properties	Partial discharge resistance (higher)
		Insulation breakdown strength (higher)
		Insulation breakdown time (longer)
		Space charge (lower accumulation)
	Dimensional stability	
	Transparency	
Functional properties	Gas barrier	
	Flame resistance	
	Biodegradability	
	Foaming	

3.1.3.1 Mechanical Properties

Some mechanical properties of clay nanocomposites are shown in Fig. 3.3 (Lan and Pinnavaia 1994; Manias et al. 2001). Epoxy-based nanocomposites, which are cured with amine hardener, contain clays modified by octadecylammonium ions. Both (a) tensile strength and (b) tensile modulus increase with increase in clay loading. Moreover, for polypropylene-based nanocomposites, the nanocomposites have higher Young's modulus and yield stress than those of the equivalent microcomposite. Clay reinforcement of polymer improves mechanical properties.

3.1.3.2 Thermal Properties

Clay dispersion improves the thermal resistance of the polymer. Dynamic mechanical analysis (DMA) results for epoxy/clay nanocomposite are shown in Fig. 3.4 (Messersmith and Giannelis 1994). This epoxy-based nanocomposite, which is cured with poly-ether-diamine, has 4 wt% clay modified by bis(2-hydroxyethyl) methyl tallow alkyl-ammonium ions. It has a higher storage modulus than the base epoxy resin in both the glassy and rubbery state.

Moreover, a broad $\tan\delta$ peak appears and shifts to a higher temperature in the nanocomposite. The improvement of thermal resistance is attributed to the restriction of the cross-link network at the epoxy/clay interface.

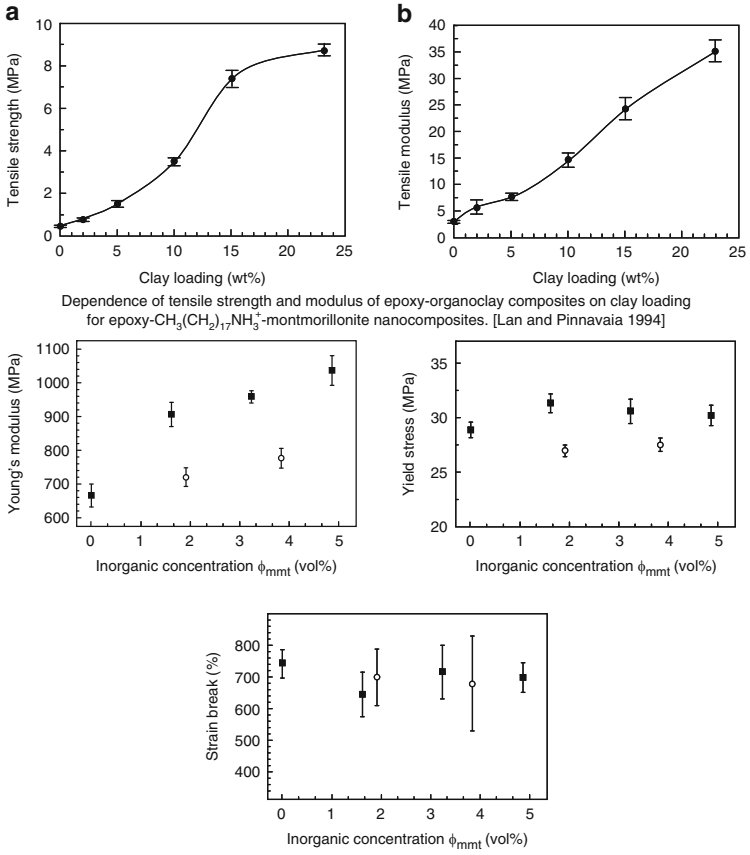

Fig. 3.3 Improvement of mechanical properties in clay nanocomposites (Lan and Pinnavaia 1994; Manias et al. 2001)

3.1.3.3 Electrical Insulation (Partial Discharge Resistance)

The partial discharge resistance of polyamide-based clay nanocomposites was evaluated (Kozako et al. 2004). The base polyamide and the clay nanocomposites were eroded by partial discharge (PD) using the IEC (b) electrode system, as shown in Fig. 3.5a. Figure 3.5b compares the average surface roughness of each specimen after PD erosion. The surface roughness decreases with increase in clay content.

The base polyamide is gradually eroded by the PD. However, when the surface of the clay nanocomposite is eroded, PD-resistant clays appear at the surface. These clays protect the polyamide from PD erosion. Therefore, clay nanocomposites have higher resistance to PD erosion than the base polyamide.

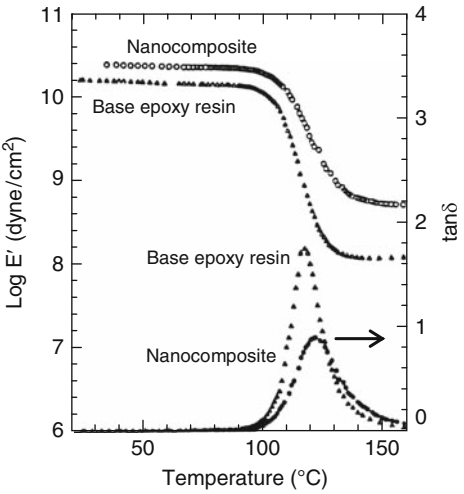

Temperature dependence of E' (open symbols) and tand (shaded symbols) for base epoxy resin and anocomposite containing 4wt% organoclay.

Fig. 3.4 Improvement of thermal resistance in clay nanocomposite (Messersmith and Giannelis 1994)

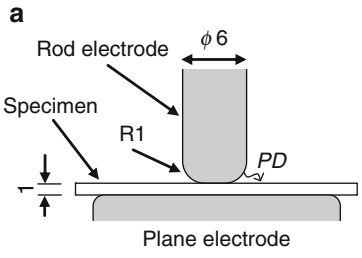

IEC (b) electrode configuration for partial discharge degradation test

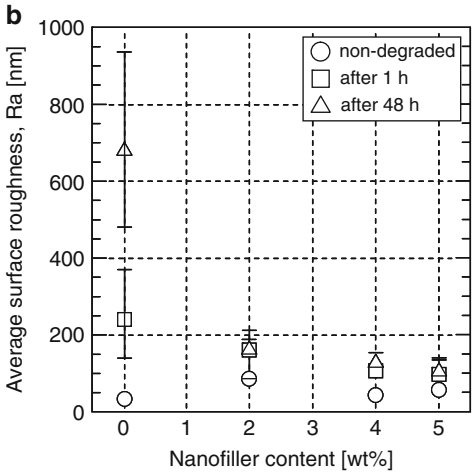

Relation between average surface roughness at an ac voltage of 6 kV_{rms} and nanofiller content

Fig. 3.5 Improvement of partial discharge resistance in clay nanocomposite (Kozako et al. 2004)

3.1.3.4 Electrical Insulation (Insulation Breakdown Time)

Insulation breakdown time is improved by the effects of clay dispersion. Figure 3.6a compares the insulation breakdown time of the base epoxy resin and the epoxy/clay nanocomposite in needle-plate electrode configuration (Imai 2006). The

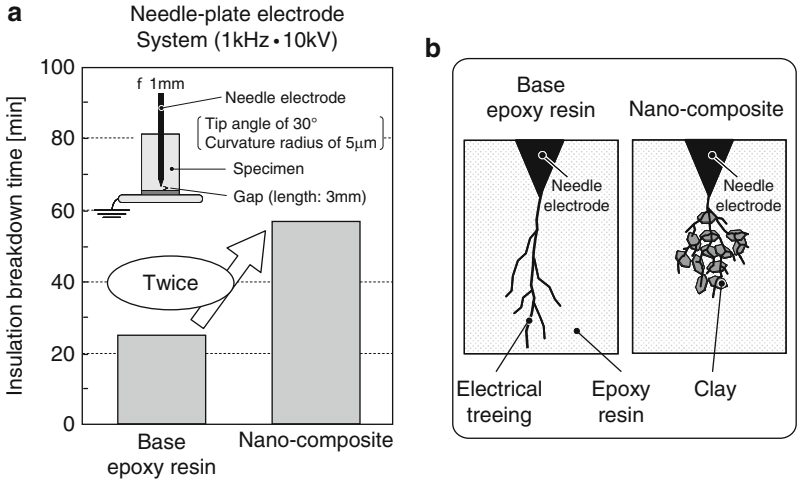

Fig. 3.6 Improvement of insulation breakdown time in clay nanocomposite (Imai 2006), (**a**) Comparison of time to insulation breakdown, (**b**) Estimate models of tree propagation

epoxy-based nanocomposite, which is cured with acid anhydride, has 5 wt% clay modified by alkyl-ammonium ions. The nanocomposite has twice the breakdown time of the base epoxy resin.

Electrical treeing propagates with many branches in the nanocomposite, whereas tree propagation is relatively straight in the base epoxy resin, as shown in Fig. 3.6b. The difference in tree behavior seems to affect the breakdown properties (Imai et al. 2004). In the nanocomposite, the trees propagate slowly because the electrical field around the tips of the branched trees is decreased, leading to longer breakdown time.

3.1.3.5 Gas Barrier

Clay dispersion imparts a new function to the polymer. Gas barrier properties due to clay dispersion in polyimide-based nanocomposites have been reported. Figure 3.7 shows the permeability coefficient of water vapor, He and O_2 (Yano et al. 1993). The permeability coefficient of each gas decreases with increasing clay content. The total path of the gas diffusion becomes longer due to the clay dispersion. Thus, clay nanocomposites have excellent gas barrier properties.

3.1.3.6 Flame Resistance

Polystyrene-based clay nanocomposites exhibit significant flame resistance properties. Figure 3.8 compares the peak heat release rate in base polystyrene and three kinds of polystyrene-based clay nanocomposites. The three nanocomposites have

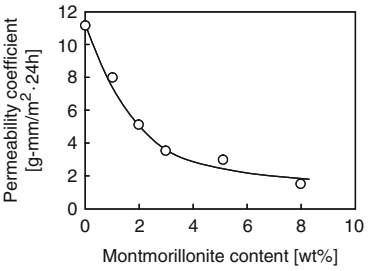

Montmorillonite content dependence of permeability coefficient of water vapor in polyimide-clay hybrid.

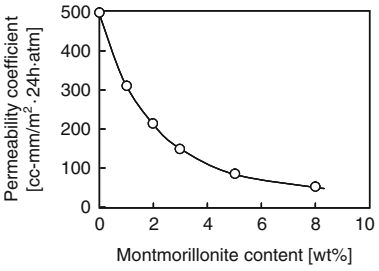

Montmorillonite content dependence of permeability coefficient of He in polyimide-clay hybrid.

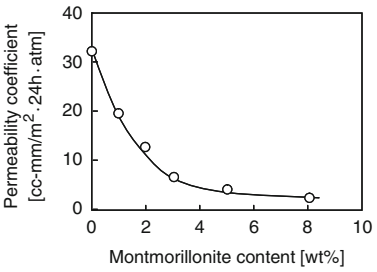

Montmorillonite content dependence of permeability coefficient of O_2 in polyimide-clay hybrid.

Fig. 3.7 Gas barrier properties in clay nanocomposites (Yano et al. 1993)

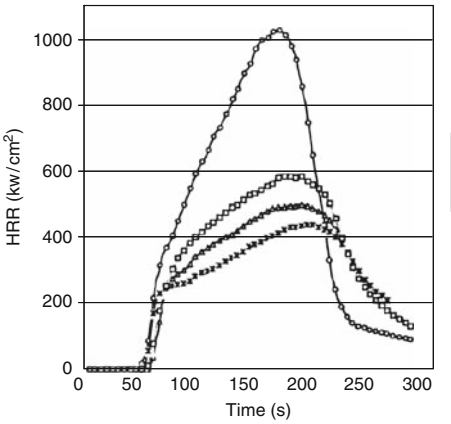

Peak of heat release rates (HRR) for polystyrene and vthe three nanocomposites. The ps-vb16-3 means that the nanocomposite is formed using 3wt% of the N, N-dimethyl-n-hexadecyl (4vinylbenzyl) ammonium ions (vb16) modified clays with polystyrene. The ps-oh16-3 means that the nanocomposite is formed using 3wt% of the N,N-dimethyl -n-hexadecyl-(4-hydroxymethylbenzyl) ammonium ions (oh16) modified clays with polystyrene. The ps-p16-3 means that the nanocomposite is formed using 3wt% of the n-hexadecyl triphenylphosphonium ions (p16) modified clays with polystyrene.

Fig. 3.8 Flame resistance in clay nanocomposites (Zhu et al. 2001)

different kinds of organic modifiers. The peak heat release rates of all the clay nanocomposites are lower than that of the polystyrene. A mechanism has been suggested by which the formation of clay serves as a barrier to both mass and energy transport (Zhu et al. 2001). Clay layers form a ceramic skin on the burning polymer surface. Meanwhile the catalytic sites residing in the clay sheets promote the formation of a char phase which is in competition with the formation of volatiles.

3.2 Intercalation and Exfoliation

The structures of clay nanocomposites are classified into three main categories based on the nature of clay dispersion in the polymers as shown in Fig. 3.9. Ordered-intercalation-type clay nanocomposites have a structure formed by the insertion of polymer chains into the galley between clay layers (Ray et al. 2003). In ordered-flocculation-type clay nanocomposites, the hydroxyl groups at the edge face of clays combine with another clay edge face. The clays oriented by edge face binding have a stronger effect on the reinforcement of the polymer than the ordered-intercalation-type. Exfoliation-type clay nanocomposites have a structure in which fully exfoliated clay layers are dispersed in the polymer. Moreover, the fully exfoliated clay layers generally impart superior properties to the nanocomposites.

These structures of clay nanocomposites are attributed to many factors in the manufacturing method such as organic modification of clays and the compounding of the materials. This section describes the method of manufacturing clay nanocomposites and the influence of different manufacturing methods on their properties.

3.2.1 Preparation Methods of Clay Nanocomposites

Clay nanocomposites are made by an intercalation and exfoliation process, as shown in Fig. 3.10. In the intercalation process, the cation exchange reaction between

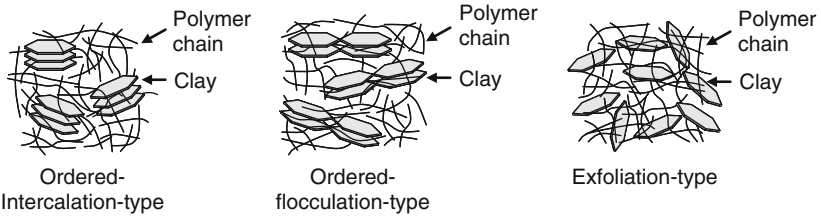

Fig. 3.9 Structure of clay nanocomposites

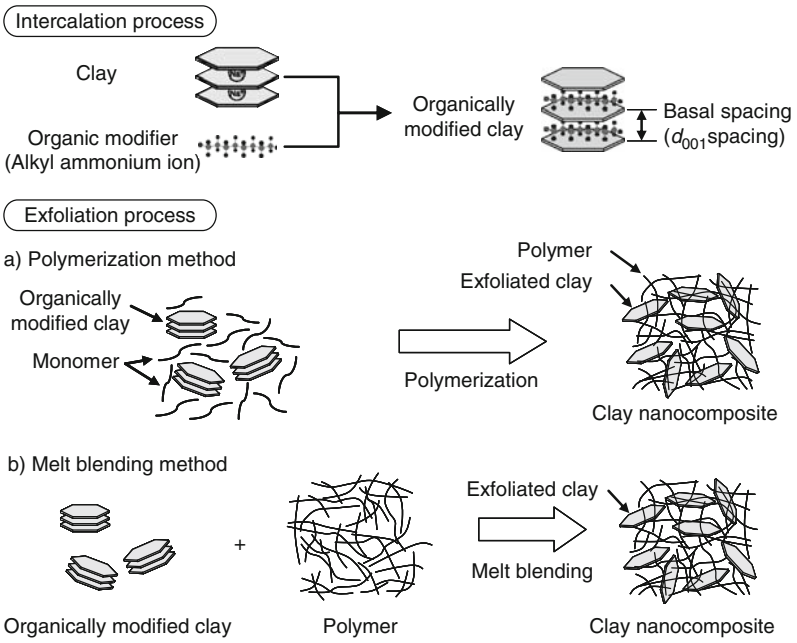

Fig. 3.10 Methods of forming clay nanocomposites

the original clays with sodium ions and modifier (alkyl-ammonium ions) forms organically modified clays. The basal spacing (d_{001} spacing) of organically modified clays expands compared to that of the original clays, due to the insertion of alkyl-ammonium ions instead of sodium ions between the clay layers. There are two exfoliation methods: the polymerization method and the melt blending method. In the polymerization method, the organically modified clays are dispersed in the monomer. After that, the clay nanocomposites are obtained by polymerization. The polymerization reaction becomes a driving force for the exfoliation of the clays (Kato and Usuki 2001; Lan et al. 1995). In the melt blending method, the clay nanocomposites are obtained by blending of organically modified clays and the polymer in the melt. The dispersion or exfoliation of the clays is promoted by blending with mechanical shear.

The polymerization method requires a chemical plant to polymerize the monomer dispersed with organically modified clays, while the melt blending method has the advantage that the clay nanocomposites can be made relatively easily using thermoplastic resins. However, it is more difficult to make fully exfoliation-type clay nanocomposites with the melt blending method (Kato and Usuki 2001). The mechanical properties and thermal resistance of polyamide (PA6)-based clay nanocomposites made by these methods are summarized in Table 3.3 (Chujo 2003). This table demonstrates that PA6-based clay nanocomposite made by the polymerization method has superior flexural strength, flexural modulus and heat distortion temperature (HDT) to those made by the melt blending method.

Table 3.3 Comparison of melt blending method and polymerization method in polyamide/clay nanocomposites (Chujo 2003)

		Polyamide[a] (PA6)	PA6/clay nanocomposites by melt blending method	PA6/clay nanocomposites by polymerization method
Amounts of clays (Nanomer 1.24TC[b])	wt%	0	5.5	5.5
Flexural strength	MPa	97.5	124.3	143.3
Flexural modulus	MPa	2,420	3,740	4,247
Heat distortion temperature (HDT, 264psi)	°C	59.8	116.4	131.9

[a]Capron 8202 35FAV manufactured by Allied Sigma company
[b]Organically modified clay manufactured by Nanocor company

3.2.2 Improved Methods for Manufacturing Epoxy-Based Clay Nanocomposites

Methods for manufacturing clay nanocomposites are continually being improved. Examples of these improvements are highlighted based on the example of epoxy-based clay nanocomposites. Epoxy resin has been widely utilized in various applications such as adhesives, coatings and electronic encapsulates. In particular, such resins are widely used as insulation materials in the electric power industry.

Typical methods for manufacturing epoxy-based clay nanocomposites are shown in Fig. 3.11. Organically modified clays and epoxy resin are mixed with considerable shear force. A hardener is then added to the mixture, and the clay nanocomposite is obtained by curing in the presence of the hardener. Electron microscope pictures of epoxy-based clay nanocomposite are shown in Fig. 3.12 (Imai et al. 2004). The shear force mixing disperses the clays homogeneously. This clay nanocomposite is of the ordered-intercalation type. Moreover, small-angle X-ray scattering (SAXS) spectra also demonstrate that the clay nanocomposite has an ordered-intercalation-type structure, as shown in Fig. 3.13 (Imai et al. 2006). Broad peaks appear at 1.44 and 2.56°, although the base epoxy resin shows no peaks. The broad peaks in the clay nanocomposite are attributed to the laminated structure of the clays dispersed in the epoxy resin.

Exfoliation-type epoxy-based clay nanocomposites have also been reported (Chen and Tolle 2004). Organically modified clays have swelling characteristics. Organic solvent (polar solvent) is inserted into the galley between the clay layers, and expands the basal spacing of the clay, as shown in Fig. 3.14. Ultrasonification is used in the presence of acetone to swell the organically modified clay. The resulting suspension and the epoxy resin are then mixed with shear force and ultrasonification. The clay nanocomposite is obtained by curing in the presence of amine hardener after acetone evaporation. The electron microscope pictures shown in Fig. 3.15 demonstrate that this clay nanocomposite is of the exfoliation type.

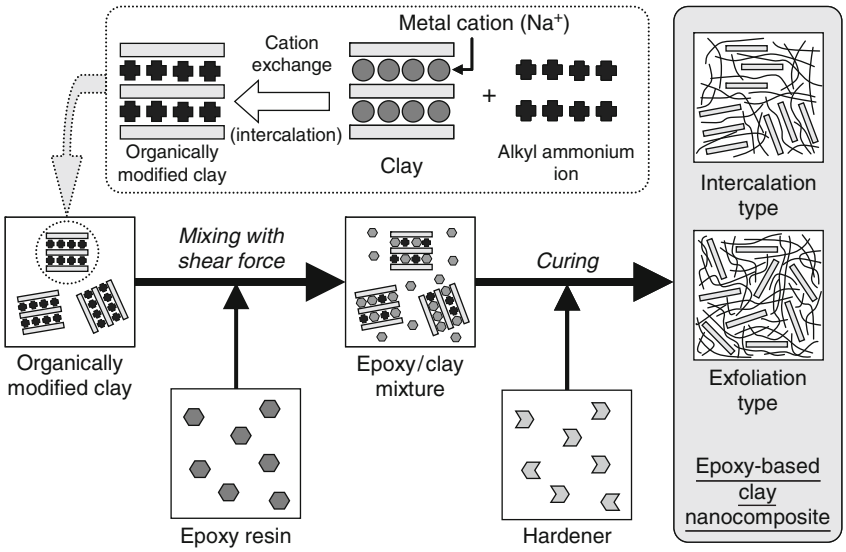

Fig. 3.11 Method for making epoxy-based clay nanocomposites

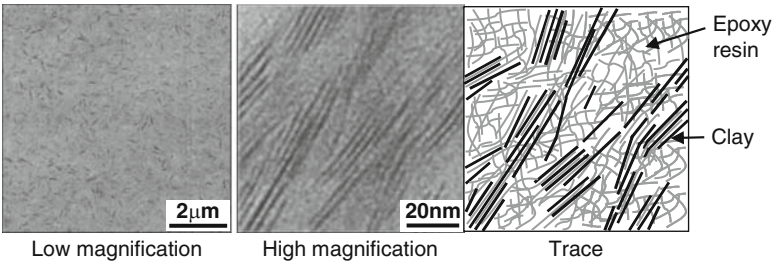

Fig. 3.12 Electron microscope pictures of intercalation-type epoxy-based clay nanocomposite (Imai et al. 2004)

3.3 Chemical Treatments and Organic Modification

Chemical treatments and organic modification (functionalization) play an important role in the manufacture of clay nanocomposites. Original clays with metal ion between clay layers have a hydrophilic property and lack affinity to the polymer. Therefore, chemical treatments and organic modification are required for homogeneous dispersion in the polymer. Generally, clays are organically modified by ion exchange between metal ions and alkyl-onium ions in the intercalation process. In particular, the clays with alkyl-ammonium ions between layers have a hydrophobic property, and have good affinity to the polymer. Moreover, chemical treatments using a silane coupling agent are less commonly considered to form chemical bonds between the hydroxyl groups of smectite clays and the polymer.

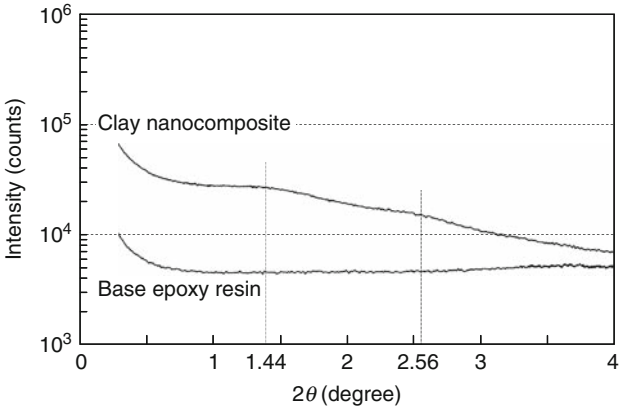

Fig. 3.13 Small-angle X-ray scattering (SAXS) spectra of base epoxy resin and clay nanocomposite (Imai et al. 2006)

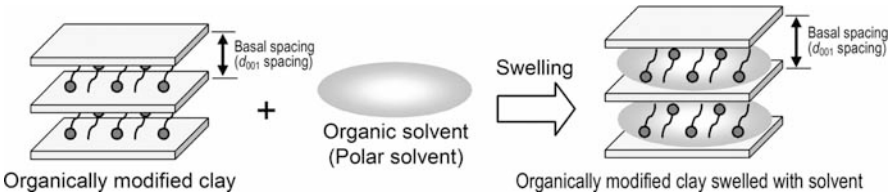

Fig. 3.14 Swelling of organically modified clay

A modifier such as alkyl-ammonium ion is a dominant factor in deciding the structure and properties of clay nanocomposites.

3.3.1 Organic Modifier of Clays and Modification Method

Typical alkyl-ammonium ions are summarized in Table 3.4. In particular, quaternary alkyl-ammonium ions are suitable as modifiers of clays for nanocomposites, and some kinds of clays modified with the quaternary alkyl-ammonium ions have been commercialized (Chujo 2003). Selection of an organic modifier of clays is very important for homogeneous dispersion in the polymer. Therefore, it is necessary to find a modifier that is compatible with the polarity of the polymer. Organic modifiers with hydroxyl groups are generally suited to polymers with large polarity such as polyamide and polylactic acid, and organic modifiers with long alkyl chains are suited to polymers with small polarity such as polyolefins.

Figure 3.16 shows a typical detailed scheme for the organic modification of clay. Alkyl-ammonium ions are dissolved in an acidic solution. The original (unmodified) clays are then dispersed and mixed in this solution. The cation exchange

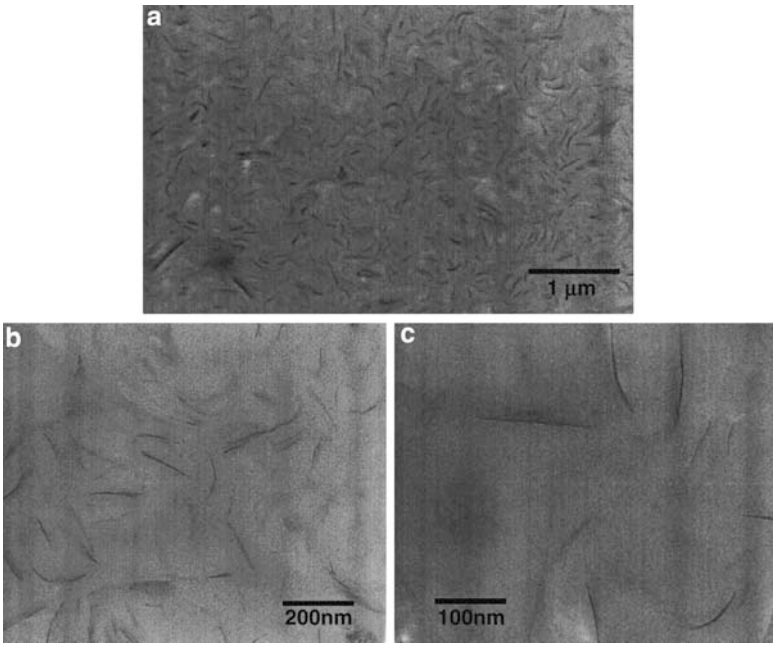

Fig. 3.15 Electron microscope pictures of exfoliation-type epoxy-based clay nanocomposite. Organically modified clay content is 3 wt%. (**a**) low magnification, (**b**) medium magnification, (**c**) high magnification (Chen and Tolle 2004)

reaction causes the alkyl-ammonium ions to be inserted between the clay layers during mixing. After that, the clays are filtrated and washed to remove sodium ions derived from the original clays. Organically modified clays are obtained by drying in a vacuum.

The alkyl-chain length of the organic modifier has an impact on the basal spacing of the modified clay. The influence of "n" in the primary alkyl-ammonium ions (H_2N^+-$(CH_2)_{n-1}$-CH_3) on the basal spacing and formation of the alkyl-ammonium ions is shown in Table 3.5 (Lan et al. 1995). The basal spacing of the modified clays slightly increase with increasing "n" in the air-dried condition. The arrangement of the modifier at the gallery between the layers changes from monolayer to bilayer on "n" reaching 11. Moreover, comparison of basal spacing in the air-dried condition and the calculated value of alkyl-ammonium ion length indicates that the formation of alkyl-ammonium ions is not perpendicular to the surface of the clay layers but is diagonal or parallel to the surface, as shown in Fig. 3.17. However, the formation of alkyl-ammonium ions in the epoxy solvated clays is close to perpendicular to the surface.

Table 3.4 Organic modifier of clays

Organic modifier (Alkyl-ammonium ion)		Example
Primary alkyl-ammonium ion	$H_2N^+–R$	H_2N^+-$(CH_2)_{n-1}$-CH_3
	(R: alkyl group)	(n=8,1 1, 12,18 etc)
		H_2N^+-$(CH_2)_{n-1}$-COOH
		(n=8,1 1, 12,18 etc)
Tertiary alkyl-ammonium ion	R_1 HN^+–R_2 R_3	CH_3 HN^+–$(CH_2)_{11}$-CH_3 CH_3
	(R: alkyl group)	CH_3 HN^+–$(CH_2)_{17}$-CH_3 CH_3
Quaternary alkyl-ammonium ion	R_1 R_4–N^+–R_2 R_3	CH_3 CH_3–N^+–$(CH_2)_{17}$-CH_3 $(CH_2)_{15}$-CH_3
	(R: alkyl group)	$(CH_2)_7$-CH_3 CH_3–N^+–$(CH_2)_7$-CH_3 $(CH_2)_7$-CH_3
		T CH_3–N^+–T (T: tallow) CH_3
		$(CH_2)_2$-OH CH_3–N^+–T (T: tallow) $(CH_2)_2$-OH
		CH_3 CH_3–N^+–CH_2–⬡ (T: tallow hydride) HT

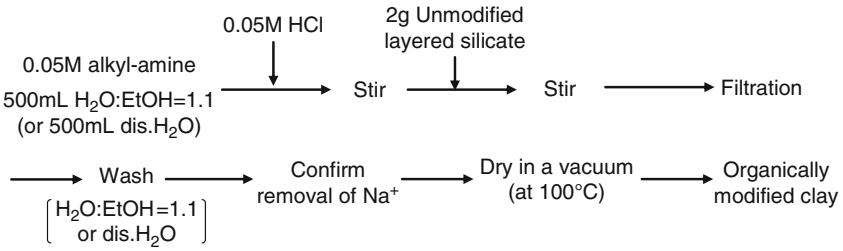

Fig. 3.16 Scheme for organic modification of clay

Table 3.5 Basal spacing (d_{001}, Å) of alkyl-ammonium exchanged montmorillonites (Lan et al. 1995)

Gallery cation	Initial cation orientation[a]	Air-dried	Epoxy solvated	Calculated value[b]
$CH_3(CH_2)_3NH_3^+$	monolayer	13.5	16.5	19.6
$CH_3(CH_2)_7NH_3^+$	monolayer	13.8	27.2	24.7
$CH_3(CH_2)_9NH_3^+$	monolayer	13.8	30.0	27.2
$CH_3(CH_2)_{11}NH_3^+$	bilayer	15.6	31.9	29.8
$CH_3(CH_2)_{15}NH_3^+$	bilayer	17.6	34.1	34.9
$CH_3(CH_2)_{17}NH_3^+$	bilayer	18.0	36.7	37.4

[a]Orientation of alkyl-ammonium ion under air-dried conditions
[b]Basal spacing are calculated assuming the galley cation adopts a vertical orientation relative to the layer and an all trans configuration such that $d_{001} = 12.8 + 3.0 + 1.27(n - 1)$(Å), where 12.8 Å is the d_{001} of NH_4^+-montmorillonite, 3.0 Å is the size of $-CH_3$ end group, 1.27 Å is the distance increase upon adding one $-CH_2-$ group to the alkyl chain

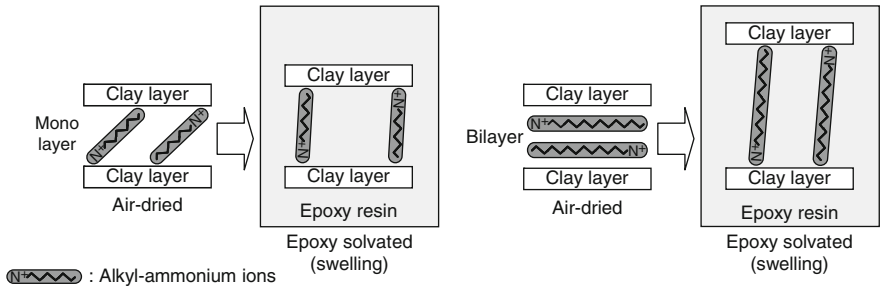

Fig. 3.17 Arrangement of the modifier in the gallery between layers

3.3.2 Confirming Organic Modification of Clays

Several kinds of chemical analysis confirm the organic modification of clays. Here, chemical analysis methods are explained by comparing the original (unmodified) clay to the organically modified clay. Alkyl-ammonium ions, which have C17 methylene chains $(CH_2)_{17}$, exist between clay layers in the organically modified clay.

First, the FT-IR (Fourier transform infrared) spectra are shown in Fig. 3.18. Three peaks attributed to the methylene chains appear, at 2,925, 2,850, and 1,465 cm^{-1}. However, the original clay has no peaks. This is evidence that the organically modified clay has alkyl-ammonium ions between its layers.

Next, the thermogravimetric curves are shown in Fig. 3.19. The weight loss of the organically modified clay is larger than that of the original clay. Heating decreases the number of alkyl-ammonium ions in the organically modified clay. Moreover, this is calculated from the weight loss when the weight loss becomes

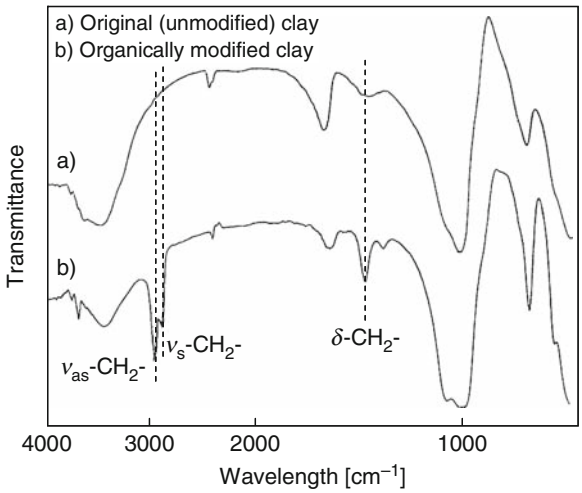

Fig. 3.18 FT-IR spectra of original (unmodified) clay and organically modified clay

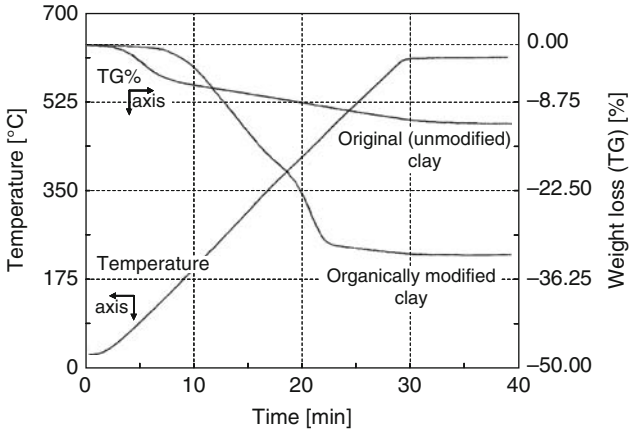

Fig. 3.19 Thermogravimetric curves of original (unmodified) clay and organically modified clay

constant. For example, the number of alkyl-ammonium ions in the organically modified clay (25.7%) is obtained by subtracting the weight loss of the original clay (6.7%) from the weight loss of the organically modified clay (32.4%) at 600 °C. In this modified clay, the cation exchange reaction occurs so that alkyl-ammonium ions of 100 meq/100 g are inserted between the clay layers. The weight loss calculation shows that the number of the alkyl-ammonium ions in the modified clay is in fact 94 meq/100 g.

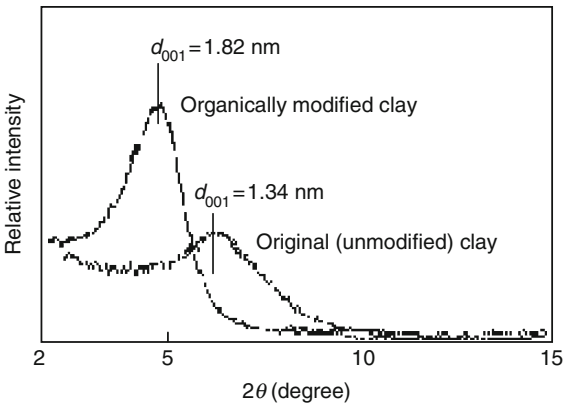

Fig. 3.20 X-ray diffraction (XRD) spectra of original (unmodified) clay and organically modified clay

Finally, the X-ray diffraction spectra are shown in Fig. 3.20. A peak appears at $2\theta = 4.8°$ in the organically modified clay. This peak is attributed to the diffraction at the basal spacing (d_{001} spacing), and the calculation based on Bragg's law estimates the basal spacing at 1.82 nm. However, a peak appears at $2\theta = 6.6°$ in the original clay, and its basal spacing is estimated at 1.34 nm. Therefore, this X-ray diffraction demonstrates that the basal spacing expands due to the organic modification of the clay.

3.3.3 Factors in the Intercalation Process

Factors in the intercalation process are summarized in Table 3.6 (Chujo 2003). Although these factors apply to epoxy/clay nanocomposites, they seem to be helpful in explaining clay nanomaterials based on other polymers. For example, Fig. 3.21 shows the influence of the carbon number of alkyl-ammonium ions on the tensile strength and the tensile modulus in the epoxy/clay nanocomposites (Lan and Pinnavaia 1994). 10 wt% clay modified with $CH_3\text{-}(CH_2)_{n-1}\text{-}NH_3^+$ (n = 8, 12, 18) are dispersed in the epoxy resin. Each clay nanocomposite is obtained by curing of the poly-ether-diamine hardener (Jeffamine D2000). Clays modified with alkyl-ammonium ions having more than 12 carbon number significantly improve the mechanical properties of the epoxy/clay nanocomposites.

3.4 Compounding of Layered Silicate Nanocomposites

Compounding of clays (layered silicates) and polymer is an important process that directly affects the structure and properties of the resulting nanocomposites. Insufficient compounding tends to degrade the properties due to aggregation of clays. Clay has huge surface energy because of its nano-scale diameter. For example, talc,

Table 3.6 Factors in intercalation process for epoxy/clay nanocomposites (Chujo 2003)

Factors of intercalation process	Appropriate condition
Quantity of organic cation exchanged in clay	Lower quantity is better (Approximately 90 meq/100 g)
Carbon number of alkyl-ammonium ion	Large carbon number is better (Longer than C12)
Number of methyl group in alkyl-ammonium ion	Lower number is better (0 or 1 methyl group is better)
Degree of cation exchange (Residue concentration of Na^+ ions)	Complete cation exchange is required

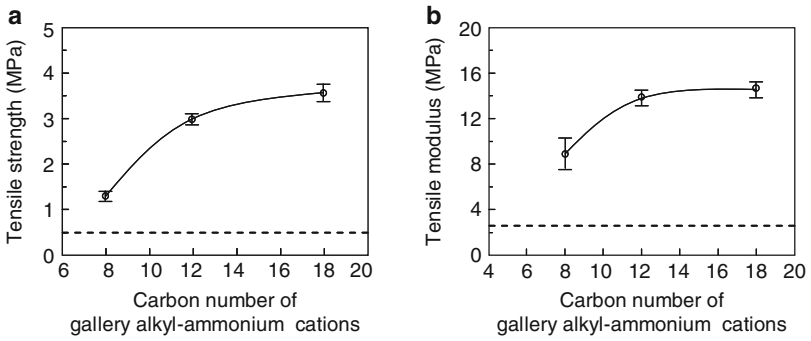

Fig. 3.21 Effects of alkyl-ammonium organic modification on epoxy nanocomposite properties. (**a**) Tensile strength, (**b**) Tensile modulus (Lan and Pinnavaia 1994)

which has a similar structure to clay and a larger diameter than clay, shows a relationship between diameter and apparent cohesion as shown in Fig. 3.22 (Tatsumi 2008). The apparent cohesion increases sharply when the diameter becomes smaller than 2–3 μm. Therefore, one can easily imagine the very large apparent cohesion of clay with nano-scale diameter. In compounding of clays and polymers, it is necessary to reduce the aggregation of clays to nano-scale and to exfoliate in order to enable the nanocomposites to exhibit enhanced properties in comparison with conventional composites.

This section describes factors influencing the exfoliation process and the rheological characteristics of clay-based composites.

3.4.1 Factors in the Exfoliation Process

Factors in the exfoliation process concerning epoxy/clay nanocomposites are summarized in Table 3.7 (Chujo 2003). Figure 3.23a shows the influence of the

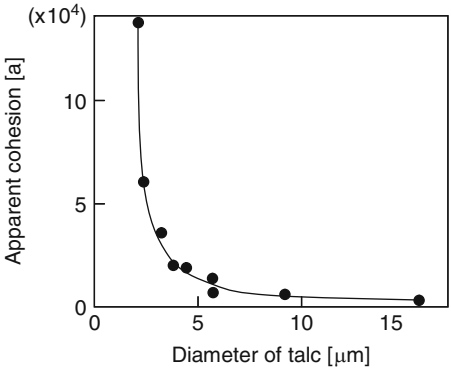

Fig. 3.22 Influence of diameter of talc on apparent cohesion (Tatsumi 2008)

Table 3.7 Factors in exfoliation process for epoxy/clay nanocomposites (Chujo 2003)

Factors of exfoliation process	Appropriate condition
Reactivity of hardener (Molecular structure, Steric hindrance)	Lower reactivity is better
Mixing time of epoxy resin and clays	Longer mixing time is better (Longer than 12 h)
Mixing method of epoxy resin and clays	Mixing with shear force is required (Melt mixer, Screw extruder, etc.)

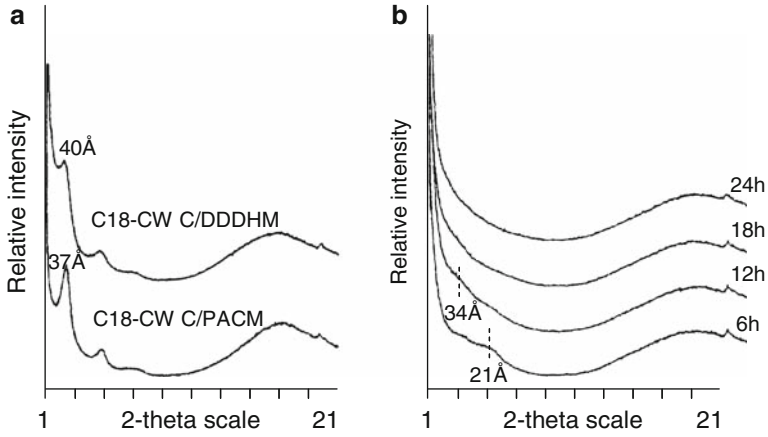

X-ray diffractograms showing the influence of the nature of the curing agent on the delamination of the C18-CWC organoclay (5wt%).

X-ray diffractograms showing the influence of the swelling duration at 75oC on the delamination of the organophilic clay (5wt%) after polymerization for the C18-CWC Jeffamine D230 system.

Fig. 3.23 Influence of amine hardener or mixing time in exfoliation process on structure of nanocomposite, (**a**) Nature of the amine hardener, (**b**) Mixing time of epoxy resin and clays (Kornmann et al. 1999)

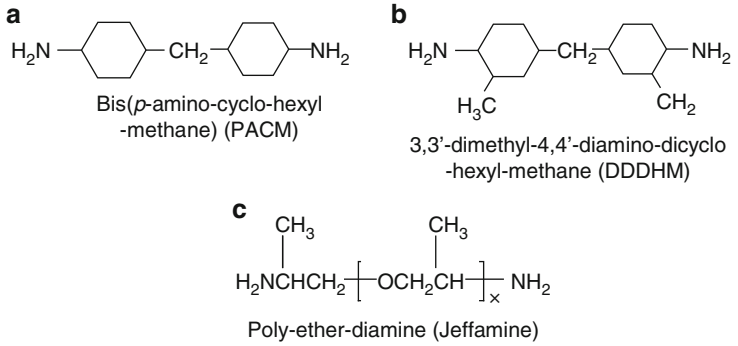

Fig. 3.24 Amine hardener for epoxy resin, (**a**) Bis(*p*-amino-cyclo-hexyl-methane (PACM), (**b**) 3, 3′-dimethyl-4, 4′-diamino-dicyclo-hexyl-methane (DDDHM), (**c**) Poly-ether-diamine

hardener's reactivity on the structure of the nanocomposites (Kornmann et al. 1999). In nanocomposites, including organically modified clays with octadecylammonium ion (H_2N^+-$(CH_2)_{17}$-CH_3, C18-CWC), each basal spacing (d_{001} spacing) is dependant on the kind of hardener. The clay nanocomposite, which is cured with the bis(*p*-amino-cyclo-hexyl-methane) (PACM) shown in Fig. 3.24a, has a diffraction peak attributed to 37 Å (0.37 nm) of basal spacing. However, the basal spacing of clay nanocomposite cured with 3, 3′-dimethyl-4, 4′-diamino-dicyclo-hexyl-methane (DDDHM) shown in Fig. 3.24b expands to 40 Å (0.40 nm). Moreover, the peak is lower than that of the nanocomposite cured with PACM. This indicates that the clays are more exfoliated in the nanocomposite cured with DDDHM than in the nanocomposite cured with PACM.

The DDDHM hardener has methyl groups as side-chains. The steric hindrance of the methyl groups slows down the kinetics of the curing reaction in the DDDHM/epoxy system, enabling the curing reaction to progress completely around the clays as well as inside then. The curing reaction inside the clay promotes its exfoliation and dispersion. However, the PACM hardener without methyl groups has higher reactivity than the DDDHM hardener. In the PACM/epoxy system, the curing reaction around the clays precedes the reaction inside them. Consequently, the clay nanocomposite in the PACM/epoxy system has an order-intercalation-type structure (not an exfoliation-type structure).

Next, Fig. 3.23b shows the influence of the mixing time of the epoxy resin and the clays on the structure of the nanocomposites. The epoxy resin and the clays modified with octadecylammonium ions are mixed for 6, 12, 18, and 24 h. Each mixture is then cured with poly-ether-diamine (Jeffamine D230), as shown in Fig. 3.24c. The X-ray diffraction (XRD) spectra of the nanocomposites show that the basal spacing of the clay expands from 21 Å (0.21 nm) to 34 Å (0.34 nm) with increase in mixing time. The diffraction peak, which is attributed to the laminated structure of the clay, disappears from the nanocomposite after 24 h of mixing. This nanocomposite has an exfoliation-type structure.

As stated above, a detailed investigation was conducted on the epoxy/clay nanocomposite, and appropriate conditions were shown for both intercalation and exfoliation processes. Consequently, a manufacturing method based on these guidelines needs to be determined for exfoliation-type epoxy/clay nanocomposites.

3.4.2 Rheological Characteristics of Polymer Containing Clays

Simple rheograms of fluids are shown in Fig. 3.25. Newtonian flow has rheological properties in which viscosity is constant irrespective of shear rate. In shear thickening (dilatancy) flow, viscosity increases with increasing shear rate. However, in shear thinning, viscosity decreases with increasing shear rate. (Thixotropic flow means shear thinning with time dependence. Figure 3.25 does not show time dependence).

Addition of small amounts of clays provides fluid with shear thinning behavior for well-dispersed clays. For example, rheograms of base epoxy resin (without clays) and epoxy resins including 5 wt% clays (montmorillonite, MMT) are shown in Fig. 3.26 (Matheson and Vaughan 2008). Both the base epoxy resin and the epoxy resin including clays without ultrasonification-assisted dispersion show Newtonian behavior. However, epoxy resin including clays with ultrasonification-assisted dispersion shows non-Newtonian behavior. Ultrasonification promotes clay dispersion in epoxy resin, so non-Newtonian behavior appears to be due to interaction at the interface between the clays and the epoxy resin.

The influence of shear rate on exfoliation of clays in a polymer was investigated using a simulation technique based on coarse-grained molecular dynamics (Sawa et al. 2004). Simulation results for various shear rates are shown in Fig. 3.27a–d. When the shear rate is low (0.0, 0.1), the clays keep the shape of aggregations, as shown in Fig. 3.27a, b. However, when the shear rate is high (0.25, 0.5), the clays are dispersed without aggregation, as shown in Fig. 3.27c, d.

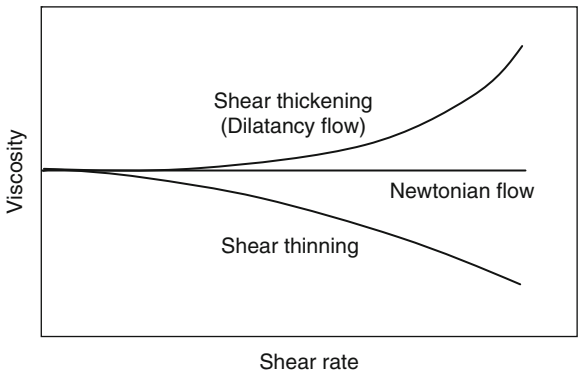

Fig. 3.25 Rheogram of fluids

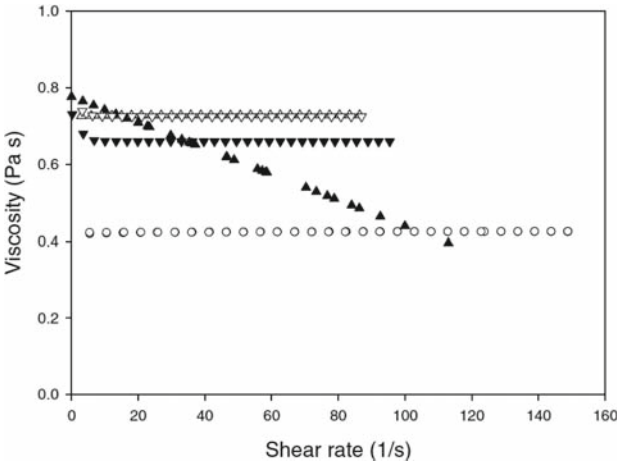

Fig. 3.26 Rheogram of base epoxy resin and epoxy resins including clays (Matheson and Vaughan 2008)

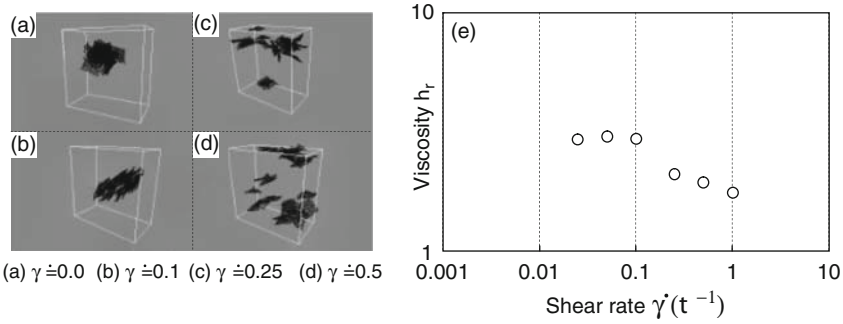

Fig. 3.27 Coarse-grained molecular dynamics simulation of clay dispersion in polymer (Sawa et al. 2004)

The relationship between shear rate and viscosity is shown in Fig. 3.27e. The polymer's viscosity is constant at shear rates in the range from 0.025 to 0.1, thus confirming Newtonian behavior. However, the viscosity decreases with increasing shear rate in the range from 0.25 to 1. These results are attributed to the dispersion of the clays. The high dispersion of clays at high shear rate enables the polymer to exhibit shear thinning behavior. Moreover, another simulation indicates the possibility that the clays are dispersed at a low shear rate when the viscosity of the polymer is high.

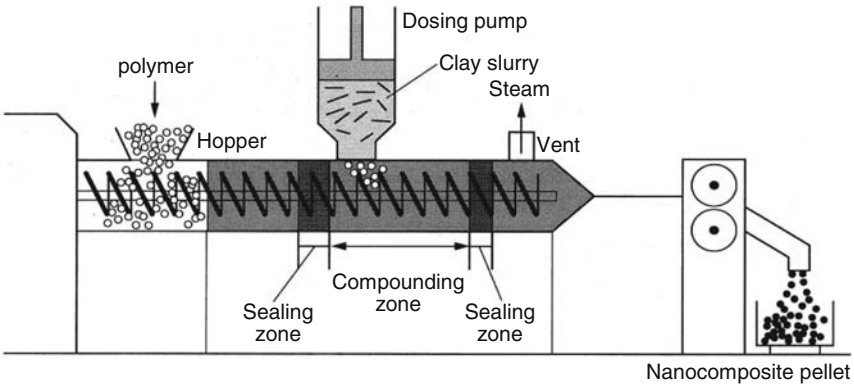

Fig. 3.28 Preparation of nanocomposite by injection of clay slurry (Hasegawa and Usuki 2001)

As stated above, clay dispersion has an impact on polymer rheology. The compounding of polymer and clays to form exfoliation type nanocomposite needs to be considered in terms of rheology.

3.4.3 Manufacture of Nanocomposite Using Unmodified Clays

Organic modification of clays (intercalation process) has been considered an essential process in the manufacture of nanocomposites. However, a low-cost manufacturing method using unmodified clays has recently been developed.

A Toyota research group has succeeded in dispersing unmodified clays in polyamide using a water slurry technique (Hasegawa and Usuki 2001). Polyamide resin is supplied from the hopper of an extruder, and the clay slurry is injected from a dosing pump, as shown in Fig. 3.28. The clays exfoliate during the compounding process, and the steam is exhausted from the vent at the end of the extruder. The polyamide/clay nanocomposite is finally processed into pellets.

The properties of the polyamide-based nanocomposite using unmodified clays is inferior to that using organically modified clays. However, this manufacturing method without organic modification of clays seems to be an innovative method from the viewpoint of industrial manufacturing.

3.5 In Situ Polymerization

In situ polymerization is an effective method for manufacturing exfoliation-type clay nanocomposites. The beginning of polymerization in the gallery between clay layers promotes exfoliation. Exfoliation and high dispersion of clays give the poly-

mer excellent properties. This section describes the manufacturing method and representative properties of polyamide-based and epoxy-based clay nanocomposites using in situ polymerization.

3.5.1 Manufacture and Properties of Polyamide-Based Clay Nanocomposite

The first clay nanocomposite made by the Toyota research group takes advantage of in situ polymerization. The method of manufacturing polyamide-based clay nanocomposite is shown in Fig. 3.29 (Kato and Usuki 2001). In the first step, the original clays are organically modified by 12-amino-dodecanoic acid (H_2N-(CH_{11})-COOH) by a cation exchange reaction in an acidic solution. In the second step, melt mixing of the modified clay and ε-caprolactam (melting point 70 °C) causes the ε-caprolactam to be inserted in the gallery between the clay layers. In the third step, the ε-caprolactam is polymerized by a ring-opening reaction at 250 °C. The basal spacing of the clays increases as polymerization progresses. Finally, the clay nanocomposite (Nylon-6/clay hybrid, NCH), which is an exfoliation-type nanocomposite with homogeneously dispersed clay, is obtained.

The mechanical and thermal properties of polyamide (nylon-6)-based clay nanocomposites using in situ polymerization are shown in Table 3.8 (Usuki et al. 1995). The four kinds of nanocomposites have mechanical and thermal properties superior to those of the base polyamide (nylon-6). Different kinds of clays, such as montmorillonite, mica, saponite and hectorite, are used in the nanocomposites.

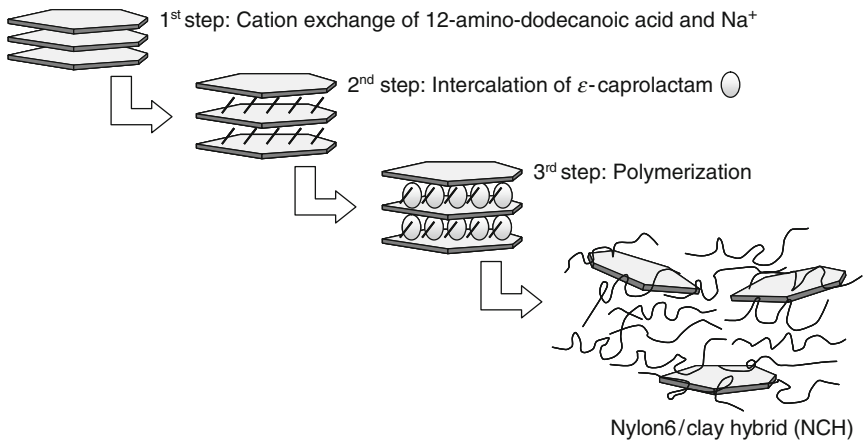

Fig. 3.29 Method for manufacturing polyamide/clay nanocomposite using in situ polymerization (Kato and Usuki 2001)

Table 3.8 Mechanical and thermal properties of nylon-6/clay hybrid and nylon-6 (Usuki et al. 1995)

	Clays				
Properties	NCH Montmorillonite	NCHM Mica	NCHP Saponite	NCHH Hectorite	Nylon-6 No
Tensile strength (MPa)					
23 °C	97.2	93.1	84.7	89.5	68.6
120 °C	32.3	30.2	29.0	26.4	26.6
Elongation (%)					
23 °C	7.3	7.2	>100	>100	>100
Tensile modulus (GPa)					
23 °C	1.87	2.02	1.59	1.65	1.11
120 °C	0.61	0.52	0.29	0.29	0.19
Heat distortion temperature (°C)	152	145	107	93	65
Heat of fusion (J/g)	61.1	57.2	51.5	48.4	70.9
Heat of fusion (J/nylon-6 1g)	63.6	59.6	53.4	50.4	70.9

Hectorite is the smallest size clay, with hectorite < saponite < montmorillonite < mica in increasing order of size. However, the nanocomposite using montmorillonite shows the best properties of the four. Much smaller size clays seem to be unnecessary for polyamide reinforcement.

3.5.2 Manufacture and Properties of Epoxy-Based Clay Nanocomposite

Clay nanocomposites using in situ polymerization in the epoxy resin have also been reported (Harada et al. 2007). This nanocomposite is manufactured by the swelling method described in Sect. 3.2.2. Generally, the curing reaction between the epoxy resin and the acid anhydride hardener is slow, and an accelerator is sometimes used to speed it up. Tertiary ammonium ions (one of the accelerators) are inserted between the clay layers. The clays modified by tertiary ammonium ions are dispersed in the epoxy resin. The clay nanocomposite is then obtained by curing in the presence of an acid anhydride hardener. In this system, the curing reaction starts between the clay layers in which the accelerators exist, as shown in Fig. 3.30. Therefore, the cross-linking network of the epoxy resin starts to form from inside the clay layer. The beginning of the curing reaction between the clay layers promotes exfoliation of the clay.

The fracture energy of each clay nanocomposite is shown in Table 3.9 (Harada et al. 2007). The nanocomposite using the solubilization method with shear stress is manufactured according to the scheme shown in Fig. 3.30. In the nanocomposite using the solubilization method, the modified clay and the epoxy resin are mixed without shear force. Moreover, in the nanocomposite using the organo method, the swelling is abbreviated, and the modified clay and the epoxy resin are mixed

Table 3.9 Fracture energy of epoxy/clay nanocomposites (5 wt% clay loading) (Harada et al. 2007)

Curing system	Fracture energy (kN/m)
Unmodified epoxy (base epoxy resin without clays)	49.2 ± 8.1
Nanocomposite using organo method (without swelling and shear stress)	16.1 ± 1.6
Nanocomposite using solubilization method (without shear stress)	42.5 ± 3.1
Nanocomposite using solubilization method with shear stress	62.7 ± 9.0

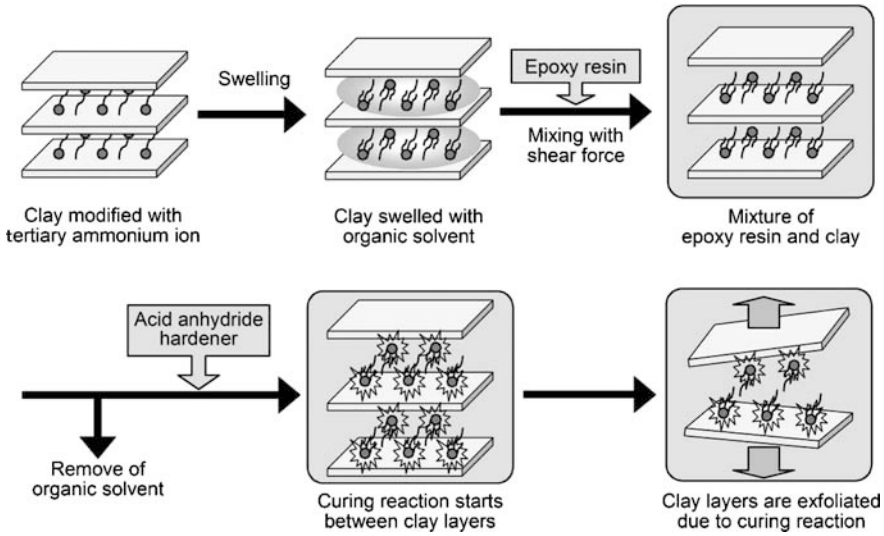

Fig. 3.30 Manufacturing method (solubilization method) for epoxy/clay nanocomposite using in situ polymerization

without shear force. The nanocomposite using the solubilization method with shear stress has the largest fracture energy of all. The clays in this nanocomposite have the largest basal spacing, and are exfoliated in the epoxy resin. The homogeneously dispersed clays reduce the concentration of fracture stress at the interface between the clays and the epoxy resin. Therefore, the fracture energy is enhanced in the nanocomposite using the solubilization method with shear stress.

3.6 Summary

This chapter has shown that development of clay nanocomposites is a rapidly-advancing field. A lot of research and development of clay nanocomposites has been conducted in the chemical and electrical fields. Improvements in manufacturing methods and the fundamental/functional properties of clay nanocomposites continue to this day.

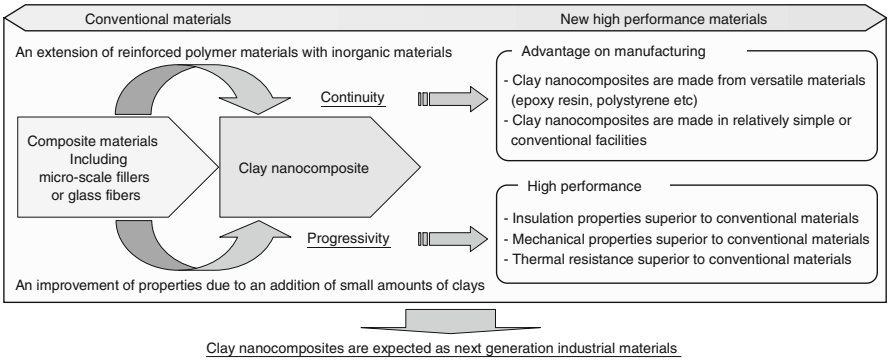

Fig. 3.31 Clay nanocomposites with "continuity" and "progressivity" (IEEJ 2008)

Many researchers and engineers have paid attention to clay nanocomposites because of their "continuity" and the "progressivity" as shown in Fig. 3.31 (IEEJ 2008). As an extension of reinforced polymer materials with inorganic materials, clay nanocomposites have continuity with conventional composites including micro-scale fillers or glass fibers. This has advantages in manufacturing. Clay nanocomposites do not need new materials, but they are made from existing components in relatively simple or conventional facilities. They have many advantages in terms of improved properties due to the addition of small amounts of clay, which produce enhanced performance materials. Clay nanocomposites have insulation properties, mechanical properties and thermal resistance properties that are superior to those of conventional materials.

References

Coop Chemical Corporation (2000) Technical brochure. 2–5 (in Japanese)

Chen C, Tolle TB (2004) Fully exfoliated layered silicate epoxy nanocomposites. J Polym Sci B Polym Phys 42:3981–3986

Chujo K (2003) Polymer nanocomposites. Kogyo Chosakai Publishing Inc, Tokyo (in Japanese)

Harada M, Aoki M, Ochi M et al (2007) Proceedings of the Thermosetting Plastics Symposium Japan, pp 193–196 (in Japanese)

Harada M, Miyamoto T, Ochi M (2007) Dispersibility and mechanical properties of epoxy/clay nanocomposites prepared by different clay treatment methods. Proceedings of the 10th Pacific Polymer Conference (PPC10), pp 240

Hasegawa N, Usuki A (2001) Development of polyamide-clay nanocomposites. Proceedings of Annual Meeting of the Japan Society of Polymer Processing (JSPP), Seikei-kakou, pp 01153–01154 (in Japanese)

IEEJ (The Institute of Electrical Engineers of Japan) Investigating R&D Committee on Polymer Nanocomposites and their Applications as Dielectrics and Electrical Insulation (2008) Characteristics evaluation and potential applications of polymer nanocomposites as evolutional electrical insulating materials. IEEJ Technical Report No. 1148 72 (in Japanese)

Imai T, Sawa F, Ozaki T et al (2004) Preparation and insulation properties of epoxy-layered silicate nanocomposite. The Institute of Electrical Engineers of Japan (IEEJ) Trans FM 124:1065–1072 (in Japanese)

Imai T, Sawa F, Ozaki T et al (2004) Partial discharge resistance enhancement of organic insulating materials by nano-size particle dispersion technique. The paper of Technical Meeting on Dielectrics and Electrical Insulation, IEE Japan, DEI-04-78, pp 35–38 (in Japanese)

Imai T, Sawa F, Yoshimitsu T et al (2004) Preparation and insulation properties of epoxy-layered silicate nanocomposite. Proceedings of IEEE Conference on Electrical Insulation and Dielectric Phenomena (CEIDP), pp 402–405

Imai T (2006) Nanocomposite insulating materials for environmental-conscious heavy electric apparatuses. Toshiba Rev 61:60–61

Imai T, Komiya G, Murayama K et al (2008) Improving epoxy-based insulating materials with nano-fillers toward practical application. Proceedings of IEEE International Symposium on Electrical Insulation (ISEI), pp 201–204

Kato M, Usuki A (2001) Intercalation method. Kogyo Zairyo 49:22–27(in Japanese)

Kornmann X, Lindberg H, Berglund L (1999) Synthesis of epoxy-clay nanocomposites. Society of Plastics Engineers (SPE), Proceedings of ANTEC '99, pp 1623–1627

Kozako M, Fuse N, Ohki Y et al (2004) Surface degradation of polyamide nanocomposites caused by partial discharge using IEC (b) electrodes. Trans IEEE DEI-11:833–839

Krikorian V, Pochan D (2003) Poly (L-lactic acid)/layered silicate nanocomposite: fabrication, characterization, and properties. Chem Mater 15:4317–4324

Lan T, Pinnavaia T (1994) Clay-reinforced epoxy nanocomposites. Chem Mater 6:2216–2219

Lan T, Kaviratna P D, Pinnavaia T J (1995) Mechanism of clay tactoid exfoliation in epoxy-clay nanocomposites. Chem Mater 7:2144–2150

Manias E, Touny A, Wu L et al (2001) Polypropylene/montmorillonite nanocomposites. Review of the synthetic routes and materials properties. Chem Mater 13:3516–3523

Matheson TN, Vaughan AS (2008) Impact of sonication on the electrical properties of epoxy-clay composites. Proceedings of IEEE International Symposium on Electrical Insulation (ISEI), pp 219–222

Messersmith P, Giannelis E (1994) Synthesis and characterization of layered silicate-epoxy nanocomposites. Chem Mater 6:1719–1725

Okamoto M, Nam P, Maiti P et al (2001) Biaxial flow-Induced alignment of silicate layers in polypropylene/clay nanocomposite foam. Nano Lett 1:503–505

Ray S S, Okamoto K, Okamoto M (2003) Structure-properties relationship in biodegradable poly(butylenes succinate)/layered silicate nanocomposites. Macromolecules 36:2355–2367

Ray S S, Yamada K, Okamoto M et al (2003) New polylactide/layered silicate nanocomposites. 3. High-performance biodegradable materials. Chem Mater 15:1456–1465

Sawa F, Imai T, Yoshimitsu T et al (2004) Rheology of epoxy/clay based layered silicate under shear flow. Proceedings of The XIVth International Congress on Rheology (ICR), pp 459–460

Tatsumi M (2008) Plastics 59:24–28 (in Japanese)

Usuki A, Koiwai A, Kojima Y et al (1995) Interaction of nylon6-clay surface and mechanical properties of nylon6-clay hybrid. J Polym Sci 55:119–123

Usuki A (2003) Inorganic/polymer Nano-interface control, NTS lic, Tokyo (in Japanese)

Vaia R, Ishii H, Giannelis E (1993) Synthesis and properties of two-dimensional nanostructure by direct intercalation of polymer melts in layered silicates. Chem Mater 5:1694–1696

Yano K, Usuki A, Okada A et al (1993) Synthesis and properties of polyimide-clay hybrid. J Polym Sci A Polym Chem 31:2493–2498

Yeh J, Liou S, Lin C et al (2002) Anticorrosively enhanced PMMA-clay nanocomposite materials with quaternary alkylphosphonium salt as an intercalating agent. Chem Mater 14:154–161

Zhu J, Morgan A, Lamelas F et al (2001) Fire properties of polystyrene-clay nanocomposites. Chem Mater 13:3774–3780

Zhu J, Uhi F, Morgan A et al (2001) Studies on the mechanism by which the formation of nanocomposites enhances thermal stability. Chem Mater 13:4649–4654

Chapter 4
The Chemistry and Physics of the Interface Region and Functionalization

C.W. Reed

4.1 Introduction

Two cases of dielectric polymer nanocomposites are discussed in which inorganic nanoparticles are dispersed in a wide variety of polymers to give the polymeric nanocomposite:

1. Spherical inorganic particles
2. Intercalated or exfoliated, layered natural or synthetic clays or micas

A major distinction is made in describing the chemistry of these two classes of polymer nanocomposites. In the case of spherical inorganic particles of known, fixed stoichiometry, there generally is a wish to eliminate the affects of water and prevent it from compromising bonding and performance (Unfortunately, the drying process is not always successful (if attempted at all) and, consequently, different results can arise). In the case of intercalated or exfoliated layered clays and micas, one utilizes water or other polar solvents to assist in separating the layers, before functionalization takes place, with or without the assistance of compatibilizer molecules. In the latter case, a strong effort is needed to remove the water (or other solvent) as the polymer is added.

The interface region of interest is considered to extend from the surface of the particle, via functionalization (if present) and, often, a coupling agent or compatibilizer, through a region of modified polymer, until the polymer properties resume those of the host polymer. Thus, the inorganic particle surface is included in the interface region. The chemistry of these features will be addressed here. It is assumed that the spherical nanoparticles are suitably dispersed in the polymer, by some mixing procedure, or that full exfoliation has been achieved (in the case of a layered silicate). The practical aspects of the compounding strategies have been addressed in Chaps. 2 and 3.

For nanocomposites formed with spherical nanoparticles, chemical bonding between the functionalized surface, to a coupling agent and to the polymer matrix

C.W. Reed (✉)
Consultant, Scotia, NY, USA
e-mail: reedcw@nycap.rr.com.

J.K. Nelson (ed.), *Dielectric Polymer Nanocomposites*,
DOI 10.1007/978-1-4419-1591-7_4,

is via covalent bonding. For intercalated or exfoliated layered nanocomposites, the bonding is via a mixture of strong ionic bonds to the opened/separated galleries and covalent bonding or coordinate bonding or simple van der Waals forces, sometimes via compatibilizer chemicals, to a polymer matrix. Polymer nanocomposites are characterized by low concentrations of nanoparticles with size in the nanometric range, and very large specific surface area. All are either organo-philic or organophobic. While the chemistry of the particle surface and the coupling to the polymer matrix can be controlled and described, the interaction on the adjacent interface region is still poorly understood and often not well controlled. The affect upon the glass transition temperature of the nanocomposite is a good example of this lack of understanding (Sect. 4.8); as also is the nature of electrical conduction in the region, responsible for the significant suppression of electrical space charge and electroluminescence noted by researchers.

As has been noted previously, Lewis (1994, 2004, 2005) recognized the interface as the dominant factor of dielectrics at the nanometric level. He described the region outside of the nanoparticle surface in terms of an extended Helmholtz double layer or Gouy-Chapman layer. The chemical and physical basis for such an interface layer will be considered in Sect. 4.9.

4.1.1 Characterization

Techniques are available to provide the chemical and physical information and analysis of the nanoparticle, surface functionality, coupling agent chemistry and surface coverage, structure of the interface region, and overall nanocomposite macroscopic information. Such methods are listed in Table 4.1 and form the basis for this chapter. Some of the techniques listed are further described in the Appendix.

4.2 The Physical and Chemical Structure of Polymers

4.2.1 Key Physical and Chemical Properties of Polymers Used for Polymer Nanocomposites

Consideration of a wide range of polymers for use in dielectric polymer nanocomposites has attracted both academia and industry over the past decade, seeking to achieve some unique performance benefit and challenge an understanding of the new science. A brief summary is provided of the range of polymers and their chemical and physical differences. Typically, they are long chains of covalently connected atoms, frequently carbon, but sometimes S or N, sometimes 5 or 6 membered ring structures, such as phenylene or imide rings. Attached to the chains can be simple hydrogen or halogen atoms or methyl groups, but also a variety of aromatic

Table 4.1 Chemical characterization methods used for polymer nanocomposite identification

Method	Inference
Elemental analysis	Information on particle stoichiometry
Transmission and ATR infra red	Chemical structure, functional groups
Polarized and non-polarized light Fourier Transform infra red (FTIR)	Chemical structure, functional groups, morphology
Chemical assay	Gravimetric and titrometric analysis to determine nanoparticle functionality, coverage and coupling agent coverage
X-ray photoelectron spectroscopy (XPS)	Surface chemistry and bonding
Electron paramagnetic resonance (EPR)	Free radical and charged oxygen information
Transmission electron microscopy (TEM)	Dispersion of particles
Small angle x-ray	Crystallinity
Wide angle scattering (WAXS)	Intercalated clay interlayer distances
Differential scanning calorimetry (DSC)	Glass transition temperature (T_g), melting point
Modulated temperature differential scanning calorimetry (MTDSC)	Reduced chain segment mobility
Dielectric spectroscopy	Maxwell-Wagner-Sillars polarization, and conduction
P-V-T equation of state measurements	Free volume
Thermally-stimulated current (TSC)	Energy levels of charge traps

or non-aromatic ester or other polar side groups. As noted, atom-to-atom bonding along the chains is by strong covalent bonding, as is also the bonding to any attached side groups and within the side groups. Only synthetic polymers are considered, each made with a range of molecular weights and with different amounts of linearity and branching, to provide resins (powders or pellets) that can be melted and turned into shapes . . .molded or film. . .for the desired application.

Polymers are categorized as either polar, if there are polarizable (i.e., orientable) dipoles either along the chains or on side groups, or non-polar if the chains and side groups exhibit only electronic and atomic polarizability and there are no dipoles. The major categories of polymer are:

Thermoplastics (Amorphous or polycrystalline)

Possess a melting point and can be melted, cooled to a solid and then remelted, cooled to solidify; can be repeated multiple times.

Thermosets (Crosslinked)

Extended 3-D structures which cannot be melted and reused. They are either one part or two part liquid chemicals which upon heating, with or without aid (e.g., a chemical crosslinking agent or radiation) are transformed into rigid 3-D structures.

Rubbers

Polymers with unsaturation or rigid block structures which allows the material to be extensively deformed but the material can completely or significantly recover up to some maximum load level.

Within each of these categories lies a range of polymer materials, with different chemical structures and different thermal capabilities. They may offer useful properties from room temperature to 400°C . . .a few can even exceed this. . .; while some are especially good at temperatures as low at 77 K.

Within the class of thermoplastics lie totally amorphous polymers such as Polyphenylene oxide (PPO), Polycarbonate (PC), Polymethylmethacrylate (PMMA), Polysulfone (PS) and Polyetherimide (PEI). These have glass transition temperatures (T_g) ranging from 160 to 220°C and are only useful up to about 15°C below their glass temperatures. They have permittivities ranging from 2.55 to 3.2 and although they have polar groups along their chains, these are largely hindered from orientation.

Within the class of thermoplastics lie polycrystalline (or semicrystalline) polymers including: Polyethylene (PE), Polypropylene (PP), Polystyrene (PSy), Polymethylmethacrylate (PMMA), Polyvinyl chloride (PVC), Polyvinyl fluoride (PVF), Polyvinyl alcohol (PVOH), Polyethylene terephthalate (PET), Polyethylene naphthalate (PEN), Polyetherketone (PEEK), Polyamides (PA), Polyimide (PI), Polyvinylidene fluoride (PVDF), and Polyvinylidene chloride (PVDC). These may have fairly low glass temperatures but crystalline melting points that are much higher (e.g., PE with a T_g of around 0°C and melting point starting about 80°C; isotactic PSy with a T_g of 100°C and melting point in the range 240–250°C; PET with a T_g of around 80°C and melting point around 140°C). Since melting of the crystallites occurs over a temperature range, its crystallinity enables a polymer to be used up to a temperature somewhat higher than the start of melting.

A distinction between the fully amorphous polymers and the semi-crystalline polymers, is that the former typically have polar side groups (which can only partially orient in an applied electric field and therefore do not have the high permittivity one might expect), and lower molecular weights, since the polar side groups can contribute a relatively stronger van der Waals force. Whereas, the semi-crystalline polymers often have high molecular weights (tens or hundreds of thousands, or even in excess of a million), and are often very linear molecules, which enhances their capability for crystallization. Many of the amorphous and polycrystalline polymers listed have both atactic and isotactic forms, each of which usually has different glass transition temperatures and quite different crystalline melting point ranges and forms. For example, isotactic polypropylene (iPP) is particularly suitable for extrusion and biaxial orientation and lamellar crystal formation, to form films in the 2–10 μm thickness range suitable for HV capacitor application.

Polymethylmethacrylate is an example, shared by many polymers, of being available in either a fully amorphous or semicrystalline form. When made by a conventional free radical method, the alkyl methacrylate polymers are invariably amorphous. By varying the polymerization temperature, however, or by the use of specific catalysts, many have been made in crystallizable forms with a high degree of either syndiotactic or isotactic stereoregularity. Most dielectric studies have been made using the amorphous polymer.

Within the class of thermosets lie epoxies plus a number of chemicals that can be cross-linked and fit this category of polymers. Examples that can be cited include: Bisphenol-A epoxies, Cycloaliphatic epoxies, Polyesters, Polyester imides, and Polyamide imides. The starting point for such thermosets are single or two part, low molecular weight resins; sometimes a linear molecule, or a fairly branched structure. Cross-linking is carried out chemically via functional groups, such as

epoxides, present on the resins, which are positioned in regular intervals along the resin backbone or on side groups. The level of crosslinking determines the ductility or lack thereof of the resulting 3-D polymer, which might have a quite high molecular weight. The typical bisphenol-A epoxy resin used in many of the epoxy nanocomposites described below, is shown with two reactive 3-membered-ring epoxide groups which provide the cross-linking function:

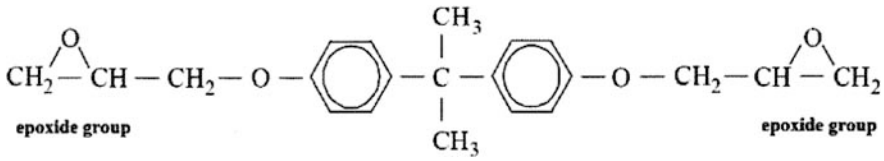

Thermosets exhibit high mechanical strength (good tensile strength, small elongation, and high modulus), but can exhibit brittleness, so they are often modified in a variety of ways to provide some ductility, if needed. They do not melt, but decompose chemically when overheated. Within the cross-linked chemical structure, however, the non-cross-linked resin usually exhibits glass-rubber behavior; therefore, a glass transition temperature, T_g, can usually be measured. For an epoxy, a wide range of glass transition temperatures can be achieved, ranging typically from around 50°C to around 120°C or even higher.

Within the class of rubbers lie materials with wide ranging mechanical performance such as: Polybutylenes, Polyisobutylenes, Polyurethanes, Silicone rubbers, Fluorosilicone rubbers, Fluorocarbons, and Perfluorocarbons. The latter four are characterized by high temperature performance (200–400°C) and outstanding mechanical properties and/or excellent low (<0°C) temperature qualities.

There are also polymers such as cross-linked polyethylene (XLPE), ethylene propylene rubber (EPR), and ethylene propylene rubber/ethylene propylene dimer (EPR/EPDM), with intermediate properties. They are mildly chemically cross-linked, usually via a chemical cross-linking agent such as dicumyl peroxide, though sometimes by radiation. Because of the mild cross-linking, they still have rubber qualities.

Other categories of polymers are those of polymer blends and copolymers. With polymer blends, two or more polymers are blended together to promote a superior quality material or simply offset a weakness that one of them might have. Furthermore, both miscible and immiscible polymer blend structures can be made using compatibilizers

4.2.2 Comparison of Polymers and Rubbers for Use in Nanocomposites and Their Role in the Interface Region

The above polymer classes (all thought to be amenable to the formation of nanocomposites) represent a wide variety of properties, thermal capability, and cost; so that

nanocomposites can be tailored to a given application where unique qualities are needed, for example, in the medical, space or power industries. There has been notable success in commercially applying some polymer nanocomposites, but most of the studies to date have focused on characterizing, evaluating and understanding this class of material. Hence, to the extent that a thermoplastic or thermoset or rubber is suitable for a given application, enhancement of its properties via the addition of nanoparticles can potentially lead to a superior product. It is believed that each of these classes of polymer has an advantage as a nanocomposite material.

Creating a superior product from these base polymers relies on having a capability to modify the structure in a controlled manner to produce predicted changes that will affect the interface. This might be done for each of the three classes, choosing simple, highly controlled materials for testing (e.g., molecular weight, selected functional end groups, linearity and branching, hindered side groups, highly orientable side groups, high purity levels, deliberate introduction of polar and non-polar guest molecules with selective compatibilizer qualities for the host nanoparticle and polymer, addition of free radical tagging groups, such as nitric oxide, suitable for electron paramagnetic resonance measurements). These are factors which can affect the bonding at the particle surface, the configuration of the polymer chains at the surface, the polarizability at the surface, and the attraction and contribution of polar impurities.

4.3 Morphology, Glass Transition and Free Volume of Polymers

Morphology refers to different forms of crystallization and other polymer growth features, such as orientation and columnar growth that characterize many polycrystalline polymers. It is well known that a variety of molecular inorganic-organic salts, such as sodium benzoate, are nucleating agents for crystal growth in several of the above polycrystalline polymers, such as PP, and therefore, we might expect that nanoparticles will perform similarly. Different crystalline forms occur, even for a polymer such as PE, PP, or PET. These forms depend upon molecular weight, level of linearity or branching, the potential presence of nucleating agents, thermal history, and orientation (if the polymer is mono- or biaxially-oriented) (Tobolsky 1960). The book by McCrum (1967) provides an excellent picture of the involvement of crystallinity in the dielectric and mechanical relaxation properties of many of the major polycrystalline polymers. Hill (1969) addresses the molecular aspects of the role of crystallinity.

Many polymers exhibit glassy properties at low temperatures but at some characteristic temperature, the so-called "glass transition temperature" or simply the "glass temperature" (T_g), their properties change to those of a rubber (Tobolsky 1960). Many macroscopic properties of the polymer, such as dielectric loss, dc conduction, and mechanical properties exhibit relatively sharp changes at this temperature. Linearity, branching, crystallinity, and the ratio of cis-to trans-chain configurations, affect the specific value of the glass temperature, so it is expected to provide a sensitive tool for the polymer within the interface region. Sometimes the change

to a rubber is gradual, over a broader temperature range. In Sect. 4.8, the glass transition temperature of polymer nanocomposites is examined.

For an amorphous polymer, the glass-rubber transition marks a change from a rigid to a soft solid, and then, as temperature is further increased, to a highly viscous liquid. For a semicrystalline polymer, there is a margin from the glass temperature up to the temperature where crystal melting takes place, when the polymer can still exhibit useful properties and performance. As noted above, with PE and PP, this margin has enabled the significant usage of these polymers as insulating materials and in a multitude of non electrical applications at temperatures significantly above their glass transition temperature.

Polymer free volume controls gas and small molecule diffusion (Crank 1968), as well as the mobility of polar side groups and segmental (crankshaft) motion of the chains and of ions involved in charge transport (McCrum 1967). There are also adherents of a free volume model for the electronic breakdown mechanism in polymers (Artbauer 1996): thus, the early interest in whether nanoparticles would lower free volume, and therefore improve breakdown performance (Nelson 2005).

The model for free volume in polymers has evolved from the lattice-hole theory for polymers and oligomer melts due to Simha and Somcynsky (1969), later refined by Nies and Stroekes (1990), and Nies and Xie (1993). Rogers (1993a, b) showed the general validity of the theory for more than 50 polymers. In 2001, Utracki and Simha presented an analytical representation of solutions to the lattice-hole theory, with good results for polystyrene and polyphenylene ether blends. In 2003, Utracki demonstrated a procedure for extracting the free volume and reducing parameters from the experimental P-V-T data. The modeling of free volume in polymer structures remains an important research topic (Utracki 2001; Bendler 2003, 2005).

Generally, free volume is measured by the P-V-T equation of state method, utilizing the Simha-Somcynsky equation of state (Simha 1969). However, because of the time consuming nature of obtaining free volume in polymers using this method, alternative methods have been developed, such as positron annihilation (Consolati 2007). When correlated against the usual equation of state method, positron annihilation provides a faithful estimate with much less time. However, it is limited in its availability to a few locations with a positron source.

The impact, upon morphology, glass transition, and free volume, of the incorporation of nano fillers, both spherical oxides and layered clays, into different polymers is described in Sect. 4.8.

4.4 Nanoparticles

4.4.1 Spherical Inorganic Particles

Unless stated otherwise, the nanoparticles made by a fuming or colloidal process, are spherical, or roughly spherical, as a result of the symmetrical growth process that each method can achieve. It is possible to obtain fairly well mono-dispersed

spherical particles with each of these methods; however, a typical fuming process from several suppliers provides a distribution of particle sizes. Many researchers report that they have used a range of particle sizes. It is suggested that polydispersed particles allow better overlap of the interface regions and that this may be desirable for properties such as electrical conduction and thermal conductivity (Lewis 2004).

A wide range of inorganic spherical nanoparticles have been made and investigated in polymer matrices. Silicon dioxide (SiO_2), silicon nitride (Si_3N_4), silicon oxynitride (SiON), aluminum oxide (Al_2O_3), titanium dioxide (TiO_2), zinc oxide (ZnO), boron nitride (BN), and aluminum nitride (AlN) are among the more popular structures, made with either a fuming process or a sol–gel process. Permittivities (at 1 kHz) of these materials range from relatively low (2.3–3.8) for SiO_2, Si_3N_4, BN, and AlN, up to ~9 for Al_2O_3, to around 100 for TiO_2. Barium titanate ($BaTiO_3$), on the other hand, is an example of a nanoparticle with high permittivity (~4,000 at 25°C, dropping to ~2,000 at 120°C), investigated for potential high-energy-density capacitor application (Tuncer 2008).

Usually, volatile chemical precursors are used in making these inorganic nanoparticles, in conjunction with an oxidant gas (e.g., O_2 or N_2O) or, if a nitride is to be made, with a source of readily dissociable nitrogen (e.g., NH_3). For SiO_2, gases such as SiH_4 or SiH_2Cl_2 are used, and reacted (fumed) at some desired temperature in a contained, flowing gas stream, allowing time for growth of the particles to take place. For a premium material, the reactant gases would have high purity (99.99%) and flow would be controlled in a suitable, inert carrier gas. Oxidant and thermal conditions allow for the production of a highly stoichiometric chemical structure (e.g., SiO_2) and for the controlled introduction of hydroxyl functionality at the particle surface, to a desired surface density. The latter can be checked via a simple chemical assay.

A similar process exists for TiO_2, using titanium isopropoxide or titanium pentachloride, and for other, widely used, fumed inorganics. For high thermal conductivity nanoparticles, such as BN and AlN, the chemistry can become more complex and, very often, its details kept proprietary. However, data sheets, as well as MSDS information, are required by law, so one can get information on final composition and on potential less desirable impurities.

Different crystalline structures for such spherical nanoparticles can be achieved depending on the fuming process. Nano SiO_2 often has a quartz structure, with linked SiO_2 tetrahedra, resulting in its low permittivity and UV transparency, while nano TiO_2 typically has the rutile structure (Wells 1950). If the preparation conditions are not well controlled, the shape of such inorganic nanoparticles may not be spherical, and the surface functionality they possess may vary considerably.

The nanoparticles made by such a "fuming" process should be hermetically sealed to prevent rapid water absorption, with potential subsequent complications. A better solution, however, is to introduce a coupling agent, as a vapor downstream, that is both hydrophobic and designed to bond covalently with the desired polymer matrix. The temperature/time behavior in the downstream section of the fuming reactor can be controlled to complete the covalent attachment of a monolayer of the

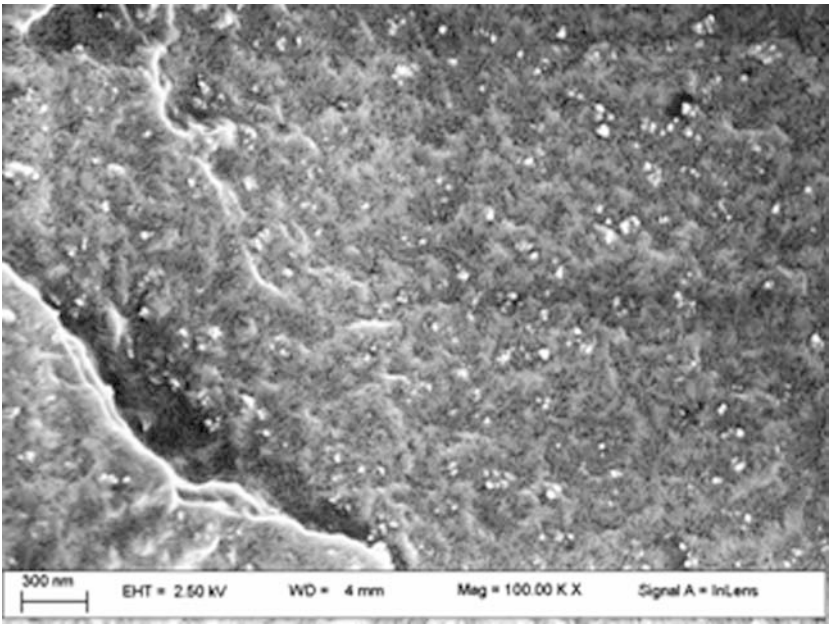

Fig. 4.1 Micrograph showing the SiO_2 dispersion in cross-linked polyethylene (Smith 2008)

coupling agent to the nanoparticle, while avoiding undesired excess coverage. The chemical selection of a coupling agent is discussed in Sect. 4.6. Formation of the nanocomposite from spherical nanoparticles, such as SiO_2, is carried out in a high-shear process to insure the uniform dispersion depicted in Fig. 4.1.

When inorganic spherical nanoparticles are not treated immediately, the work of Yang (2005) on the room temperature handling of silica nanoparticles will be of interest. The room temperature oxidation kinetics were studied by X-ray photoelectron spectroscopy (XPS).

4.4.2 Colloidal Spherical Particles

This technique can provide spherical particles of inorganics such as SiO_2 and TiO_2 with excellent stoichiometric structure, reproducible nanometric size, and desirable surface functionality (e.g., hydroxyl groups or amino groups) using a sol–gel process (Brinker 1990; Tabatabaei 2006). It is, however, generally a time consuming process, and the steps must be followed rigorously. Using ammonium hydroxide (NH_4OH), or other ammonium solutions, Si_3N_4 can be made with well-defined insulating or semiconducting properties.

Both inorganic or composite organic-inorganic nanometric-size colloidal particles can be made, at relatively low temperature, by hydrolysis of molecular

precursors followed by polycondensation to a glass-like form. A metal alkoxide (e.g., $Si(OC_2H_5)_4$) is first hydolyzed, then converted into a 3-D network by polymerization (Yun 2005). Besides Si, metals such as Na, Ba, Cu, Al, Ti, Zr, Ge, V, W, and Y can be converted into sol–gel "glasses" with nanometric-sized particles. The area of sol–gel technology appears to be growing rapidly, with interest in the introduction of highly functionalized organosols and in the development of a continuous sol–gel process. To-date, however, there has been limited interest in dielectric applications.

An example of nanocomposites made with sol–gel silica and flexible ether and large planar naphthalene polyetherimides (PEI) is given in the work by Chen (2008).

4.4.3 Intercalated and Exfoliated Nanoparticles

The major categories of such particles are the natural and synthetic (layered) inorganic clays and the micas. Useful nanocomposite materials from each of these categories can be made with either an intercalated structure, or, with additional processing, a completely exfoliated structure as was discussed in Chap. 3. Historically, as interest in nanotechnology began to flourish, around 1990, it was found that nanodispersed particles of layered silicates (clays) could improve mechanical properties, gas barrier behavior, thermal resistance, and flame retardancy of polymers, even if added in amounts as small as 2%. Even today, the reasons for these improvements are not fully understood. Depending on the polymer, such nanocomposites can be made in different ways: by in situ polymerization in the presence of the clay; by intercalation from the melt; or by intercalation from solution as discussed in Sect. 2.2.1. However, it cannot be reliably predicted which of these methods will work for a given polymer, and lead to preferred material properties. The situation is particularly complicated for hydrophobic polymers that require organically modified clays. The specific modification of the clay is designed to facilitate, via the organic ligand, the intercalation and exfoliation processes. The interface layer of surfactant molecules, located between the inorganic clay particles and the polymer, governs the entropy and enthalpy of intercalation of the polymer between the silicate layers and mechanical coupling between the particles and polymer chains responsible for improved material properties.

Such layered silicates belong to the family of 2:1 phyllosilicates (Ray 2003) shown in Chap. 2 (Fig. 2.2), whose crystal structure consists of layers of two tetrahedrally-coordinated silicon atoms covalently connected to an edge-shared octahedral sheet of either aluminum or magnesium hydroxide. The layer thickness (tetrahedral-octahedral-tetrahedral) is only around 1 nm; the lateral dimensions from around 3 nm, to as much as several μm or larger, depending on the silicate. Stacking of the layers leads to a gap between the layers, referred to as the interlayer or "gallery." Substitution within the layers (e.g., Al^{3+} replaced by Mg^{2+} or Fe^{2+}, or Mg^{2+} replaced by Li^{1+}) produces negative charges, which are counterbalanced by alkali and alkaline earth cations within the galleries. This type of silicate is

categorized by a moderate surface charge known as the "cation exchange capacity" (CEC). This charge varies from layer to layer; hence CEC implies an average for the whole crystal.

A schematic of the alternative melt and in situ polymerization methods for making intercalated and exfoliated polymer/layered silicate nanocomposite was shown previously in Fig. 3.10. A schematic close-up of the resulting composites is shown in Fig. 3.9.

Montmorrilonite (MMT), hectorite, and saponite are among the most commonly used and evaluated of the layered silicates. SEM photographs of the structure and dispersion of MMT in polyethylene nanocomposites are shown in Figs. 4.2 and 4.3.

While much of the early work on such nanocomposites used natural clays and micas, with water as the solvent for separating the galleries, synthetic clays have found

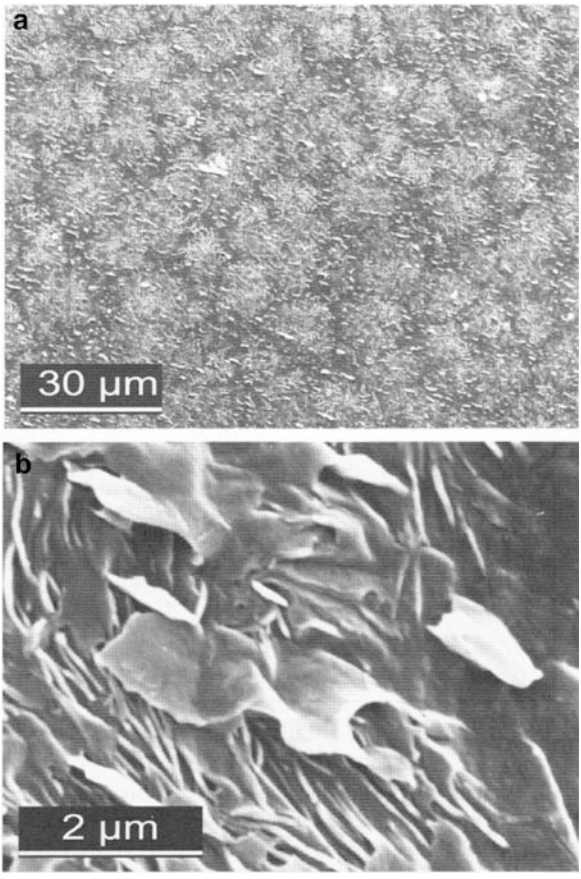

Fig. 4.2 Two SEM micrographs showing the structure of BLP 120/10/20: (**a**) shows the MMT is well dispersed; (**b**) contains high magnification detail showing isolated MMT tactoids (Green 2008)

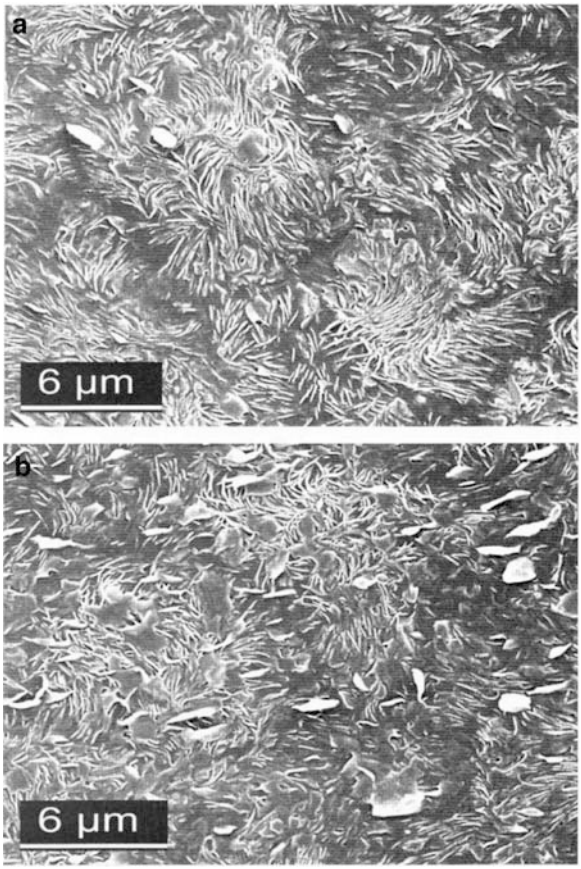

Fig. 4.3 SEM photographs showing the effect of increasing the MMT loading on samples crystallized at 117C: (**a**) 5 parts MMT; (**b**) 20 parts MMT (Green 2008)

increased interest because they offer more versatility due to their greater purity, ease of characterization and reproducibility, and therefore suitability for research; albeit at somewhat higher cost. Work by Montanari (2004) illustrates a good example of such a synthetic layered material. The nanofiller was a synthetic fluorohectorite, modified with protonated octodecylamine NH_3 + ODA. Its exfoliation and performance in both ethylene vinyl acetate (EVA) and polypropylene (PP) were found to be quite different, as one might expect from the fact that one polymer (PP) is non-polar (and hydrophobic) while the other (EVA) is polar (and hydrophilic). With EVA, exfoliation was achieved up to a vinyl acetate content of roughly 12%. However, with PP, exfoliation required a compatibilizer (20%), consisting of isotactic PP + 3.5% maleic anhydride grafted to the backbone of the polymer. Exfoliation was confirmed with TEM and wide angle x-ray measurements.

A further example, which illustrates the varied chemistry that pertains to intercalated and exfoliated nanocomposites comes from the work of Jeschke (2005). It is described here and will be covered again in Sect. 4.9, where results from the insertion of a nitric oxide tagging chemical into the dynamics of ion exchange surfactants are described. The nanoparticles were three synthetic fluoromicas (Laponite RD, Laponite RDS, and Somasif ME 100), from which nanocomposites were formed with PSy. After dispersing the clays in water, nanoclays were then made by ion exchanging with a 100:1 mixture of hexadecyltrimethyl ammonium chloride and 4-(N,N-dimethyl-N-hexadecyl)ammonium-2,2,6,6-tetramethylpiperidene-1-oxyl-iodide in a 50:50 mixture of deionized water and ethanol. After mixing, washing was performed until a $AgNO_3$ test for chloride ions was negative. Similar organoclays were made using nitric oxide tagging of the same ion exchange resins. Nanocomposites of the resulting tagged and non-tagged organoclays were then made using different molecular weights of PSy. Responding to the nitric oxide free radicals, electron paramagnetic resonance (EPR) experiments were then conducted to study the structure and dynamics of the surfactant layer at the particle-PSy interface, as described in Sect. 4.9.

It is generally found that the synthesis of dielectric polymer composites using synthetic or natural layered materials (clays, micas, etc.) requires the use of a compatibilizer. Several PE and PP suppliers now offer grafted (maleic anhydride) compatibilizer products for molding and extrusion purposes. Otherwise, a wide assortment of compatibilizer chemicals are available through the commercial polymer industry (Datta 1996), which are potentially of benefit for achieving stable polymer nanocomposites based on natural and synthetic clays and other layered inorganics.

While water has been extensively used in the development of solution intercalated and exfoliated polymer nanocomposites, interest in the use of other polar solvents and combinations of solvents (e.g., toluene, chloroform, ethanol and other alcohols, and even nitrobenzene) has increased during the past 6 years. This trend is highlighted in the papers presented at the second (2003), third (2005) and fourth (2007) International Symposium on Polymer Nanocomposite Science and Technology organized by the National Research Council of Canada, Boucherville, Quebec.

In situ polymerization, as depicted in Fig. 3.10, was used in the work by Fuse (2008) using synthetic mica nanofillers ($Na\ Mg_{2.5}\ Si_4\ O_{10}\ F_2$) (Katahira 1999).

An extensive list of the polymers used in layered silicate nanocomposites is given by Tanaka et al. (2004).

4.4.4 Other Nanoparticle Structures

Other polymeric nanocomposites that are somewhat different to the solid spherical inorganics and layered clays described above are (1) the epoxy-polyhedral oligomeric silsesquioxane composites (Takala 2008, 2008), (2) polyurethanes,

made with a range of "hard" block organics in the nanometric size range, which have outstanding mechanical properties and find dielectric use in space applications, and (3) other organic-organic structures.

4.4.5 Bonding in Nanoparticles

Bonding in the spherical, fumed or colloidal particles described above and in the tetrahedral or octahedral layers of the 2:1 phyllosilicates (Fig. 2.2) is by chemically and thermally strong, covalent bonds. These are bonds formed when two unpaired electrons ("valence electrons") with equal or similar valence-orbital energy, one from each of two adjacent atoms, share a common orbital, typically an s or p orbital. For example, spherical SiO_2 particles made by fuming, are made up of Si-O and O-O covalent bonds, principally with covalent O-H and Si-H bonds located on the particle exterior, as confirmed by FTIR, XPS, and titrometric determination.

Bonding of the intercalated or exfoliated clay layers, with the ion exchange resin used to prepare the layer for compatibility with the polymer to be used for intercalation or exfoliation (Fig. 3.10), is by ionic bonding, in which one or more valence electrons from one atom, in a two atom pair, are transferred from one atom to the other, "electronegative" atom. For example, in diatomic NaCl, an ionic bond is formed when a 3s Na valence electron is transferred to the single vacancy in the 3p Cl orbital. Typically, the clay layer is negatively charged and the ion exchange chemical (often a surfactant) is positively charged. This ionic bond is basically strong, but is vulnerable to solvation problems if the process is not carried out carefully.

If a coupling agent is used, first it is chemically reacted, from the vapor or liquid, to the nanoparticle, forming a stable covalent bond to the surface; then, after dispersal in the polymer melt, further reaction is undertaken in which the polymer is covalently bonded to the coupling agent and thus to the nanoparticle.

If the polymer is not deliberately bonded to the nanoparticle, as in many of the investigations on polymer nanocomposites, it will be bonded to the particle by weak van der Waals forces, after first being attracted to the particle surface by dielectrophoretic forces. If the polymer has polar side groups, the van der Waals forces will increase, but they are always substantially less than those for covalent bonding. Water, present in many experiments, can be attached by weak hydrogen bonding (Sects. 4.9.1 and 4.9.2). The bond strengths of different bonds of interest are given in Table 4.2.

Concentrations of nanoparticles are typically given in weight percent, though sometimes in volume percent, requiring information on the particle density. The typical concentration of either spherical inorganic or layered clay particle is from 1 to 5% by weight but concentrations as low as 0.1% and as high as 10, or even 20%, are sometimes used in investigative studies.

Table 4.2 Bond strengths of covalent bonds involved in typical polymer nanocomposites

Bond	Bond strength (kJ/mole)
C-H	413
C-C	346
C = C	610
C-F	495
O-O	146
O = O	497
N-H	390
O-H	463
H-F	565
C-O	360
C = O	740
Si-O	464
Si-Si	226
Hydrogen bond in water	22
Typical van der Waals bond	18

Note: when attached to other atoms or groups of atoms, the bond strength will be different

4.5 The Surface Chemistry of Nanoparticles and Its Role in Charge Injection and Trapping

The surface chemistry of nanoparticles has been covered in general terms, with some detail in the case of spherical particles and how they are made and the functionality they have. However, charge injection was not mentioned. This area is of great interest, but as yet, its potential role has not been established. On the other hand, effects such as charge trapping and polarization are generally acknowledged to take place.

Pioneering work at Rensselaer Polytechnic Institute (Nelson 2004; MacCrone 2007, 2008) has examined the technique of electron paramagnetic resonance (EPR) at high electric fields as one avenue for probing the nanodielectric interface, in order to explain their results on space charge (Nelson and Fothergill 2004) and electroluminescence behavior (Details of this technique may be found in Sect. A.4 in the Appendix). Their most recent results were carried out on SiO_2 nanoparticles in XLPE, with and without an applied electric field of up to 25 kV/mm. EPR spectra indicate that the acceptor/donors were oxygen radicals in the polymer, probably originating during cross-linking. When the field was applied, additional oxygen radicals resulted. The role of these results in conduction mechanisms and the future potential for the technique were then discussed.

The possibility of charge injection from nanoparticles has been considered as investigators have sought to understand space charge and other high electric field phenomena. However, there has been no direct evidence for such injection, nor has there been verification, via SEM or XPS methods for example, that nanoparticles with semiconducting qualities have been used. The work of Schamm (2004) on nanofilms of SIPOS indicates the viability of changing the electronic states in

inorganic nanoparticles such as SiO_2 to achieve controlled functional qualities from polymer nanocomposites, such as charge injection. Charge trapping is covered both experimentally and theoretically by Takada (2008) and the interface chemistry and physics, covering the layers exterior to the surface, are treated in Sect. 4.9.

4.5.1 Functionalization

A preferred nanoparticle comes already functionalized as a result of the method of particle synthesis. For example, spherical SiO_2 particles made by a controlled fuming process, using a silane gas with an oxidant gas, can be obtained with a variable concentration of surface hydroxyl groups. A chemical assay performed by the supplier can readily confirm the surface concentration, and help to establish a reproducible process.

Sometimes investigators have preferred to functionalize their nanoparticles separately. This was the case in work by Kochetov (2009) with BN and AlN nanoparticles, where a treatment with the coupling agent γ-glycidoxypropyltrimethoxy silane was performed to functionalize the particles being incorporated into a bisphenol-A epoxy with anhydride hardener.

4.6 The Choice and Basis for Coupling Agents

Coupling agents are mainly applied in the preparation of spherical nanoparticles and the formation of the associated polymer nanocomposites. Coupling agents are sometimes used with the intercalated or exfoliated nanocomposites, although compatibilizer chemicals normally used with such materials provide a similar function. Coupling agents are typically fairly low molecular weight chemicals with chemical end groups (functionality) for chemical reaction to both an inorganic particle surface (typically a particle, of nanometric (or micron) size, or a fibre) with one of the end groups and to a polymer molecule with the other end. (They are also used to bond polymers onto metallic surfaces). They have been widely used in the chemical and polymer industries for over 50 years. Typically, they have boiling points between 50 and 300°C, and are used in either the liquid or vapor phase. A wide range of coupling agent chemicals are available with different thermal, physical, and functional properties, and different levels of purity.

As described in Sect. 4.4, a preferred application of a coupling agent in the case of spherical inorganic oxide particles is from a vapor, as a final, in situ step of the fuming process. It can result in a precise amount of coupling, via covalent bonding to the virgin particle surface, so that there is no contamination possible and a clean hydrophobic surface is ready for the formation of the polymer nanocomposite. Alternatively, after preparation of the nanoparticle, it may be given a liquid treatment with coupling agent (instead of a vapor treatment). In this case, after the coupling

agent is bonded to the particle surface at an optimum temperature, any unreacted, surplus liquid can be removed by heat and vacuum. For such a liquid application process, the level and quality of the coupling agent on the nanoparticle surface may not be as well controlled, potentially accounting for different results by different investigators.

The importance of a coupling agent applied to the surface of a nanoparticle is that it sets the stage for the quality and properties of the interface region involving the polymer matrix before the matrix resumes its normal properties. The inappropriate choice or method of application of this coupling agent can detrimentally affect properties. However, even the best coupling agent for a given nanocomposite may perform poorly if applied inappropriately; conversely, an optimum choice can enhance the overall polymer nanocomposite properties.

A second, though not-always-stated function of the coupling agent is to prevent interactions with, and interference from, the presence of water. Even very short exposure to water during handling of the nanoparticle can add difficulty to achieving a reproducible nanocomposite. Long term, the surface of the nanoparticle is vulnerable to the presence of water, since water can hydrolyse any conceivable bond between the inorganic and organic phases.

The work by Roy et al. (2005) illustrates the significant role of a coupling agent in affecting nanocomposite morphology and resulting electrical properties. Separate groups of spherical SiO_2 nanoparticles were untreated or treated with an amine-silane coupling agent or with vinyltriethoxysilane oligomer, compounded into the polyethylene, then chemically cross-linked with dicumyl peroxide at a higher temperature than used for compounding, to give a cross-linked polyethylene (XLPE) nanocomposite. With the vinyltriethoxysilane coupling agent, the triethoxy groups were first covalently bonded to hydroxyl groups on the SiO_2 particle surface, then the vinyl group reacted chemically with the PE at the crosslinking temperature, thereby covalently bonding particles to the polymer matrix.

The base XLPE material, the XLPE with no coupling agent, and XLPE with an amine coupling agent, each had approximately the same (44–45%) crystallinity, whereas XLPE with nano SiO_2 particles covalently bonded via a triethoxy coupling agent, had a crystallinity of 60%, or roughly 35% higher. (The 60 Hz voltage endurance performance with this coupling agent was also significantly better). The work did not investigate how the additional crystallization arises, and whether it extends radially from spherical particles and, if so, how far it extends.

Another interesting example of orientation extending beyond oxide particle surfaces with silane coupling agents, is from the work of Kahn (1973), using liquid crystals. A methylamino-propyl silane resulted in parallel alignment of the liquid crystals, whereas octadecyl-amino-propylsilane caused perpendicular alignment.

In older work on coupling agents, covering not only micro fillers, but also fumed and colloidal fillers in the nanometric size range, significant attention was given to the affect of coupling agents on the local morphology. Plueddemann (1982) summarizes some of these. “Deformable Layer Theories” examine flexible, thermoplastic, deformable layers, in order to minimize local mechanical stresses. Broutman (1973) estimates that a modulus of about 80 MPa can do this. A “Restrained Layer Theory”

(Gaehde 1975) proposes that the local polymer resin should have a modulus between that of the particle and the polymer matrix. The theory suggests that the silane coupling agent functions by "tightening up" the local polymer structure.

These examples show that, for a given nanoparticle and polymer matrix, the selection of the coupling agent is important, in leading to a final structure with enhanced qualities and long term performance. Multiple considerations need to be made in selecting a preferred coupling agent chemical. Thermal stability and other physical properties must be suitable for all subsequent processing. Vinyltriethoxysilane, vinyltrimethoxy silane, 3-glcidoxypropyltrimethoxy silane ("Glymo"), and N-(2-aminoethyl) 3 aminopropyl-trimethoxy silane ("AEAPS") are some of the more commonly used coupling agents in the nanocomposites field.

In addition to having the desired functionality, boiling point and thermal stability, another important quality that the coupling agent should possess is a high surface tension for the nanoparticle surface. It needs to allow the fluid vapor to readily "wet" the surface, and provide the optimum steric arrangement for reaction and bonding to occur. Table 4.3 illustrates how variable, and sometimes less desirable, are the surface tensions of different commercial silane coupling agents.

Other classes of viable, commercial coupling agent are used widely for bonding polymers to inorganic fillers and fibres, such as chromium, allylorthosilicates and other organofunctional orthosilicates, orthoesters, and others. Generally, however, these do not contribute the same degree of water resistance as the organofunctional silanes. While they may not be preferred from the application standpoint, they can be useful in the design of experiments, since they contain atoms such as the halogens which can serve as tagging chemicals in FTIR, XPS, EPR and other analysis techniques.

Table 4.3 Critical surface tensions, γ, of silane coupling agents on glass (Plueddemann 1982)

Coupling agent	γ (dynes/cm)
$CF_3(CF_2)(CH_2O(CH)_3Si(OC_2H_5)_3$	14
$(CF_3)_2CFO(CH_2)Si(OCH_3)_3$	14
$CH_3Si(OCH_3)$	22.5
$C_2H_5Si(OC_2H_5)_3$	26–33
$CH_2 = CHSi(OC_2H_5)_3$	30
$CH_2 = CHSi(OCH_3)_3$	25
$CH_2 = C(CH_3)COO(CH_2)_3Si(OCH_3)_3$	28
$H_2NCH_2CH_2NH(CH_2)_3Si(OCH_3)_3$	33.5
$CH_3C_6H_4Si(OCH_3)_3$	34
$H_2N(CH_2)_3Si(OC_2H_5)_3$	35
$BrCH_2C_6H_4Si(OCH_3)_3$	39.5
$O\text{-}CH_2\text{-}CH\text{-}CH_2O(CH_2)_3Si(OCH_3)_3$	38.5–42.5
$C_6H_5Si(OCH_3)_3$	40
$Cl(CH_2)_3Si(OCH_3)_3$	40.5
$HS(CH_2)_3Si(OCH)_3$	41
$p\text{-}ClC_6H_4CH_2CH_2Si(OCH_3)_3$	40–45
$BrC_6H_4Si(OCH_3)_3$	43.5

4.7 Use of Compatibilizers for Intercalated and Exfoliated Nanocomposites

The use of specific ion exchange resins (Katahira 1999), surfactants, and precompatibilization of non-polar polymers such as PP (Montanari 2004) in preparing intercalated and exfoliated nanocomposites has been noted previously. However, the recipes being used could feasibly be improved by a different choice of compatibilizer. These might be grafted onto the polymer backbone or onto side groups, added as a molecular material during processing (or during final dispersion in the polymer melt), or during in situ polymerization. Many such molecular nucleophilic and electrophilic compatibilizers have been developed for the polymer blends field of commercial polymers (Datta 1996) in making successful miscible and immiscible blends. The thermodynamics and kinetics of these compatibilizer materials and their use in reactive compatibilization, could assist in many of the current investigations.

4.8 Morphology, Glass Transition and Free Volume in Polymer Nanocomposites

While there may not be direct evidence for the radial range of the Gouy-Chapman layer or of the extent of entanglement in the interface region, measurements of crystallization, glass transition temperature, and free volume are quantitative and provide important indirect information on the nanocomposite interface.

The results of Roy (2005) in finding a significant increase in crystallinity with spherical SiO_2 nanoparticles in XLPE was assigned to the specific use of the coupling agent vinyltriethoxysilane and it was theorized that each ethoxy group of a coupling agent molecule covalently bonds to three adjacent surface hydroxyl groups on the SiO_2 particles, so that its vinyl group is directed perpendicularly from the surface. As a result, when bonding to the PE occurs, directionality is effected in the surrounding PE before cross-linking with dicumyl peroxide occurs. Thus, the nanoparticle, with its pre-applied coupling agent, performs as a nucleating agent. (Presumably, the kinetics of these steps can be measured, to optimize the process).

No equivalent information on other spherical/fumed nanoparticle-polymer systems has been found to confirm that "nucleation enhancement" can be repeated with other polymer nanocomposites. It is notable that, in the work by Roy, another coupling agent applied to the same grade of SiO_2 particles from the same supplier, did not produce such an effect.

However, with clay and mica intercalated and exfoliated polymer nanocomposites, a wide variety of results have been reported, ranging from very little, if any, effect upon polymer morphology (especially crystallization), to major effects. The work of Green and Vaughan (2008), and Green et al. (2008) illustrates these differences. A description is given of the issues involved in achieving reproducible qualities such as structure, dispersion and morphology in intercalated and exfoliated

nanocomposites. In their 2006 work on MMT nanoclays in PE, Vaughan et al. (2006), noted a significant role of the clay on matrix morphology. However, in their 2008 work on MMT functionalized with dimethyl-di(hydrogenated tallow) quaternary amine in a matrix of 10% high density PE+ 90% low density PE, where good exfoliation and dispersion were confirmed, very little affect on polymer crystallization was observed. Analysis of the crystallization kinetics of the matrix polymer suggested only a weak interaction with the MMT. Photomicrographs of the MMT tactoids observed by these authors were shown in Figs. 4.2 and 4.3.

Further discussion of the wide range of morphological changes observed in different layered nanocomposites is given in the work of Frechette (2007, 2008). An illustration of as yet unexplained anomalies, which can occur with layered inorganics in polymer nanocomposites, is with the crystallization of PA spherulites in synthetic mica, where "stair-like" structures were formed in the amorphous regions (Kozako 2004). The writer sees an analogy between the importance of the role of the coupling agent in controlling the matrix polymer structure around spherical inorganic nanoparticles and that of the role of the ion exchange chemistry in the coupling of exfoliated clay particles with a matrix polymer.

In examining the literature on the effect of nanoparticles on melting point and glass transition temperature, a "topical review" performed by Alcoutlabi and McKenna (2005) involving over 400 publications is pertinent. These involved both theoretical and experimental work on a wide range of polymer nanocomposite materials, and detail the effects of size and confinement at the nanometric size on both the melting temperature, T_m, and the glass transition temperature T_g. It seems that the existing theories are unable to explain the range of behaviors seen.

However, Bendler (2009) takes a more optimistic view and presents a quantitative analysis that shows that most, if not all, experimental results on the nanoconfinement of the glass transition temperature can be explained by a defect diffusion model. The model incorporates defect-defect interaction enthalpy, defect concentrations, defect lattice geometry, correlation length, and percolation fraction to determine T_g; it provides a quantitative relationship between the percolation fraction of rigid to mobile regions and T_g. The results clearly explain confinement effects that had been difficult to understand previously.

An illustration of the sensitivity of T_g to filler concentration of spherical nanoparticles of ZnO, Al_2O_3, and TiO_2, (i.e., three oxides with widely different permittivities) in epoxy nanocomposites, is shown in Figs. 4.4 and 4.5.

From the data shown in Figs. 4.4 and 4.5 and the review cited above, it is the writer's view that there is no *a priori* basis, at this time, to say how the incorporation of nanoparticles into a polymer matrix will affect either melting point or the glass transition temperature. The writer's experience suggests that it is related to the level of bonding at the particle surface (with/without a coupling agent) to the molecules of the polymer. If the bonding permits the individual adjacent polymer molecules to rearrange, to a reasonable extent, as thermodynamics dictates, the melting point and glass transition may be unaffected. If rearrangement is significantly restricted, to an extended distance radially from the particle surface, such properties are likely to change.

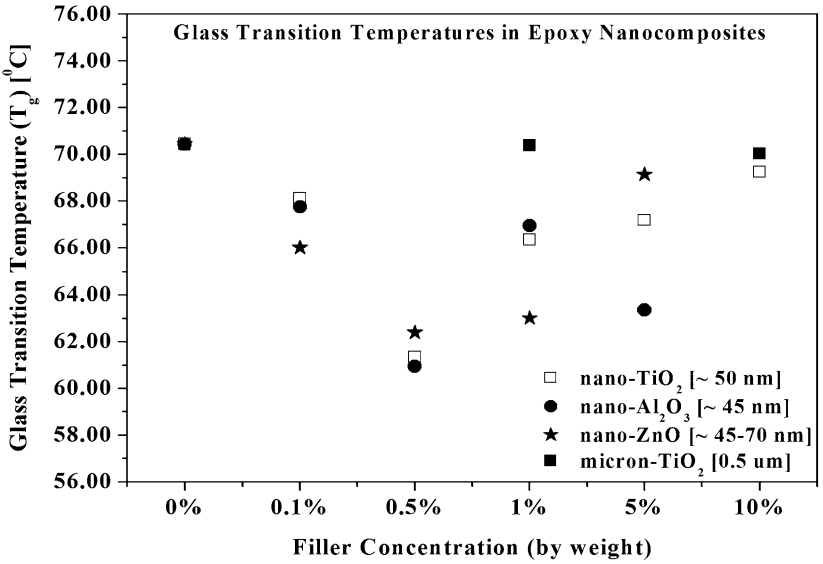

Fig. 4.4 Variation of glass transition temperatures in epoxy nanocomposites with respect to filler concentration (Singha 2008)

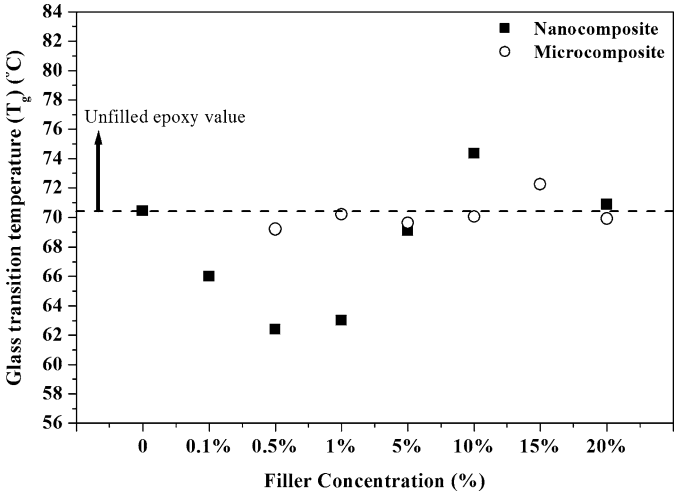

Fig. 4.5 T_g variations in epoxy-ZnO nanocomposites (Singha 2008)

Information on the impact of nanoparticles on free volume is limited. The work of Nelson (2005) using P-V-T measurements on TiO_2 spherical nanoparticles in a bisphenol-A epoxy, then fitted to Simha-Somcynsky's equation of state (Simha 1969), finds an increase in the relative free volume of 2–3% over the temperature range from 370 to 500 K. The results are explained by the presence of a highly mobile interlayer between the filler and the matrix.

With exfoliated clays, however, Utracki (2003) found contrary results, namely a marked decrease in free volume for three different clay-polymer systems. With polyamide-6(PA6) in a nanocomposite of MMT clay, the free volume is reduced by 15–17% over the temperature range from 227 to 327°C. The author's lattice-hole theory enables him to deduce (1) that the PA is end-tethered to the MMT, (2) the number of polymer molecules attached to each clay platelet, and (3) that the first 60 Å of polymer are "solidly" adsorbed and that further away bulk mobility is recovered. It was concluded that the reduction in segmental mobility of the author's "hairy clay platelet" model is responsible for the observed reduction in free volume. In work on the clay Cloisite 10A in polystyrene, the same author (Utracki 2003) finds a minimum in the decrease in free volume at an organoclay content of around 3–4% in the temperature range 87–287°C. At 287°C the decrease was around 4%; at 87°C it was around 6%. With Cloisite 15A (MMT intercalated with 145% 2M2HT) in a PP nanocomposite at concentrations of 1, 2, 3, and 4 wt%, decreases in free volume of as much as 13% showed a good fit with the "hairy clay platelet" model. A plot of the reduction of polymer free volume reduction in the 2% nanocomposites in PA-6, PP, and PSy against interlayer spacing, d_{001}, showed a good linear relationship.

Further measurements of free volume are needed to investigate the reproducibility of the above results, and it will also be of interest to look for potential correlations with permittivity and glass transition temperature measurements.

4.9 Interface Chemistry and Physics, Bonding, and Entanglement

In Sect. 4.6, the role of the coupling agent in affecting the local (interface) polymer morphology was briefly discussed. This related to the polymer immediately exterior to the coupling agent. However, the interface region is considered to extend beyond this, up to where the polymer properties are unaffected by the nanoparticles. As noted previously, from an electrical standpoint, Lewis has described this region in terms of a modified Helmholtz Double Layer or a Gouy-Chapman layer where positive and negative charged layers reside. Others describe this, potentially, as a region of entanglement or tethered entanglement (Sternstein and Zhu 2002).

4.9.1 Chemistry

Chemical bonding between the nanoparticle and the polymer matrix, often involving a coupling agent or compatibilizer chemical, can usually be confirmed by FTIR, as reported by many investigators. FTIR catalog data on polymers and many commercial coupling agents (Hummel 1966) provides reference information on key vibration-rotational peaks in the wavelength range from 830 to 4,000 cm^{-1}, so it

is convenient to first make measurements on the treated nanoparticles, then on the polymer nanocomposite after mixing. Subtraction of the spectra is used to identify changes in the chemistry and the functional groups and chemical bonding involved. FTIR measurements by Nelson (2004) shows (Fig. A.8 in the Appendix) how the surface hydroxyls on spherical TiO_2 particles react with epoxide (-CH_2(-O-)CH_2–) groups, in competition with the amine (-NH_2-) groups of the hardener. Singha (2009) finds a different situation for FTIR measurements in epoxies with and without ZnO nanoparticles, where surface hydroxyl groups do not bond to the epoxy but rather appear to hydrogen bond with free water (Fig. 4.6). (The separate work of Nelson and Singha was carried out independently with the same bisphenol-A resin (CY1300) and tri-ethylene tetramine hardener (HY 956) but different nanoparticles, TiO_2 and uncoated ZnO. The pretreatment of TiO_2, if any, was not reported; the ZnO was untreated. Thus, there is uncertainty about particle functionalization differences and the potential role of water, or possible combinations thereof, that might account for the different results).

However, the interface region outside of the particle surface appears to produce a range of properties and considerable speculation on the part of investigators on the underlying physics and chemistry for its cause. A range of experimental approaches has been used to obtain an improved picture, both chemical and physical, of the interface region that can explain the unique or outstanding properties exhibited by polymer nanocomposites, which have been described in other chapters of this book. These include measurements of morphology, glass transition temperature, and free volume, as described in Sect. 4.9. However, three other measurements which enable specific conclusions to be made about the physics of the interface region immediately exterior to the nanoparticle surface are:

1. Dielectric relaxation measurements from low frequencies (10^{-4} Hz) up to frequencies of around 1 MHz
2. Electron paramagnetic resonance (EPR) measurements, especially those using chemical tagging with agents such as nitric oxide
3. Temperature modulated differential scanning calorimeter (MTDSC) measurements

The selected studies below are not exclusive but they are relatively comprehensive, supported by FTIR and other characterization techniques, and appear to provide reasonably clear conclusions while identifying some of the complexities that are present.

4.9.2 Dielectric Relaxation Measurements

Broadband (10^{-2} Hz to 1 GHz) dielectric measurements of the real and imaginary components of permittivity (see Sect. A.1) allow the simultaneous assessment of interfacial polarization at the nanoparticle surface, exterior to the surface, or electronic or (impurity) ionic conduction processes, at low frequency, and a broad range

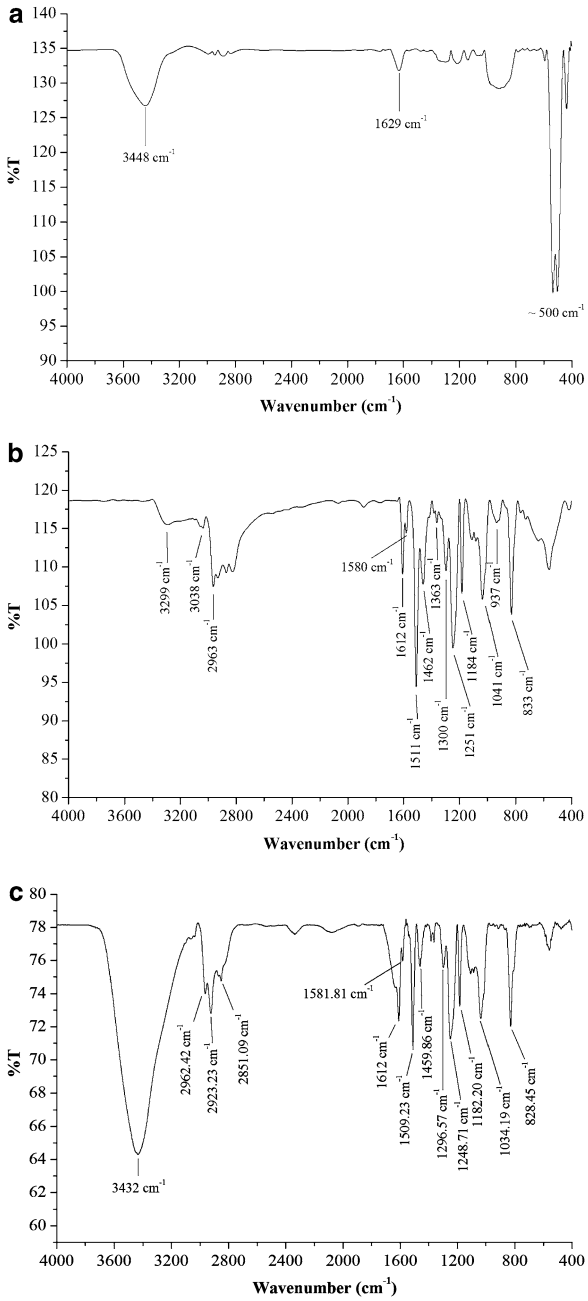

Fig. 4.6 FTIR spectra of filler and epoxy systems (**a**) ZnO nanocomposite, (**b**) unfilled epoxy system, (**c**) epoxy nanocomposite system (Singha 2009)

of relaxation processes due to dipoles, at higher frequencies. The high frequency relaxation measurements provide a reflection of the (conformational and dipolar) organization of the polymer chains, and of the influence of the nanoparticles. Hence, such measurements provide complementary information on the role of the interface in the properties of the nanocomposite and evidence for the influence on the matrix polymer structure.

Singha and colleagues (2008a, b, 2009) have examined vacuum-dried Al_2O_3, TiO_2, and ZnO at concentrations of 0.1, 0.5, 1.0 and 5% in a bisphenol-A epoxy with a triethylene tetramine hardener, primarily focusing on the real part of the permittivity (ε'), but somewhat on the imaginary part (ε'' or $\tan\delta = \varepsilon''/\varepsilon'$); with all measurements at room temperature. In measurements from 10^{-2} to 1 MHz or 1 GHz, for each of these spherical inorganic oxide nanofillers, it was found that the real permittivity had decreased at 0.1% loading, but then progressively increased again up to the 5% loading. The data for ZnO only is shown in Fig. 4.7. With $\tan\delta$ measurements, there was very little difference. The authors suggest that the lowering of permittivity is caused by the restrictions imposed on the mobility of dipolar groups (in the epoxy) by the interaction of the nanoparticle. They compare this result on lowering of the permittivity with similar results by other investigations on TiO_2 in epoxy (Nelson 2004) and on organically-modified layered silicates (Imai 2002). The authors also perform a Lichteneker-Rother mixing rule analysis (Vo 2002) on their permittivity measurements with Al_2O_3 and TiO_2, from which they conclude that the lowering of permittivity is the result of a minimum influence of filler permittivity and a strong polymer-nanoparticle interaction.

With $\tan\delta$ measurements, there was very little difference between the Al_2O_3-epoxy nanocomposites and the untreated epoxy, over the full frequency range, indicating to the writer that the nanoparticle-polymer interaction extended very little

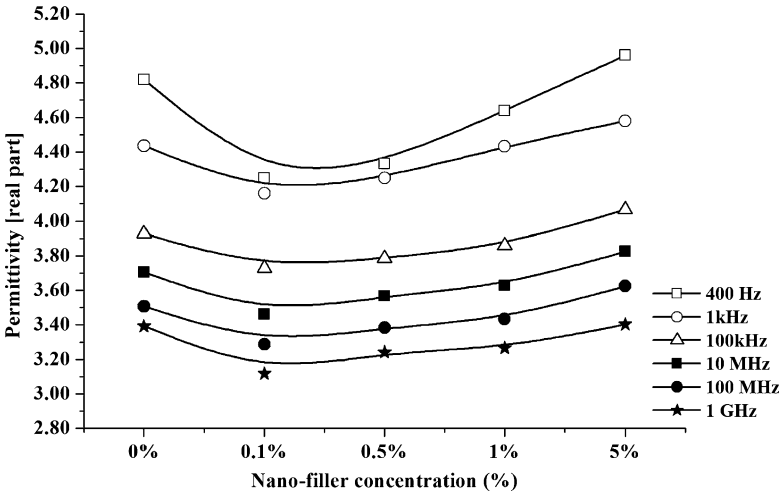

Fig. 4.7 Permittivity variations in epoxy-ZnO nanocomposites with respect to filler loadings (Singha 2009)

from the particle surface, or, in other words, that the interface region was very thin. On the other hand, with TiO_2-epoxy nanocomposites, there were some deviations at certain frequencies, suggesting that there is some alteration of the epoxy structure.

As noted, Singha's results on permittivity (2008a, 2009) were complemented by T_g and FTIR measurements. It is interesting that T_g also dropped relatively significantly (~10°C) at loadings of 0.1–0.5%, then increased back to the value for the unfilled epoxy at higher loadings (Figs. 4.4 and 4.5). The FTIR results, shown only for the ZnO nanocomposites, were also of particular interest, since they show that there was no bonding of epoxy to the nanoparticles. Instead, there was a strong bonding (3,500 cm^{-1}) of water to surface hydroxyl groups. Another strong peak, at 1,630 cm^{-1}, was considered to be due to bending vibrations in absorbed water molecules. (Evidently, their samples had not been dried completely).

Whereas Singha used nanoparticles of widely varying permittivity with the same epoxy resin in investigating of the role of the interface, Zhang and Stevens (2003, 2008) had a different approach. They examined the influence of two polymers with different polarities, one polar and one non-polar, in nanocomposites with (nearly) spherical Al_2O_3. Among their more striking results was that, for dry samples, broad band dielectric measurements showed no differences between unfilled resin and the nanocomposite, i.e., the characteristic conformational (α) and secondary relaxation (β and γ) processes due to dipoles in the epoxy phase of the nanocomposite are unaffected by the presence of the nanoparticles.

The polar polymer used by Zhang was an epoxy: diglycidyl ether of bisphenol-A (DGEBA) resin cured with methyl hexahydro-phthallic anhydride. The non-polar polymer was a low density PE (LLDPE). The Al_2O_3 nanoparticles were extensively dried before use. However, a major variable of the experiments was the effect of water, and measurements were made first at equilibrium levels of water of, for the epoxy ~0.4% and for LLDPE ~0.06%, then after rigorous drying of the samples. Dielectric measurements were made over the frequency range from 10^{-2} to 10^6 Hz, i.e., over a range suitable to identify low frequency interfacial losses plus higher frequency relaxation behavior characteristic of the polymers and of the nanofiller. Concentrations of filler were: 1 and 5% Al_2O_3 in the epoxy nanocomposites and 1, 5, and 10% Al_2O_3 in the LLDPE. To emphasize polymer motions and therefore any restriction of motion at the nanoparticle surfaces, measurements were conducted from −50 to +70°C. Measurements were limited to the imaginary permittivity, ε'', i.e., no real permittivity data are shown.

For the dried Al_2O_3-epoxy nanocomposites, there was no difference in tan δ between the dried, unfilled resin and the dried nanocomposite over the full frequency range; while at low frequency, there was very little dispersion. (Both epoxy and Al_2O_3 nanocomposite show β and γ relaxations characteristic of the epoxy, which can be deconvolved into individual peaks (using Havriliac-Negami fitting). These findings lead the writer to conclude: (1) that the cross-linked epoxy chemical structure (with its large array of dipoles) is largely unaffected by the Al_2O_3 nanoparticles (i.e., there is only a very thin interface layer) and (2) that, despite the permittivity differences, there is no significant interfacial polarization between the nanoparticles and the epoxy matrix.

For the undried Al_2O_3-epoxy nanocomposites, the dielectric response was very different for the undried, unfilled epoxy and the nano-filled epoxy. In addition to the β and γ relaxations of the epoxy for both the unfilled epoxy and the nanocomposite, there is a ω peak due to water which is different in the two cases. For the unfilled epoxy it has an activation energy of 52.7 kJ/mole, but for the nanocomposite it has a slightly lower activation energy (48.9 kJ/mole), which is shifted by two orders of magnitude in frequency, up to −10°C; above −10°C, and it shows no activation energy up to 70°C.

The authors concluded that the water is in a locally bonded state at the lower temperature; however, at the higher temperatures, it has increased interfacial mobility with reduced local binding.

With Al_2O_3-LLDPE nanocomposites, there were some different, unusual results. The dried samples showed a dielectric loss peak at low frequencies which had the same unusual dielectric behavior as found with undried epoxy, and hence was considered to be related to residual water in the nanocomposite. It was also found that the low frequency losses of undried Al_2O_3-LLDPE nanocomposites were lower than those of undried LLDPE. The authors believe that this is related to the trapping of ionic impurities from residual catalyst at nanoparticle surfaces. Some work by Frubing (2001) on the use of fillers in PE as dielectric probes, provides complementary information in analyzing Zhang's work.

Cole-Cole (ε′ vs. ε″) plots are used by Fuse (2008, 2009) and Singha et al. (2010) to separate interfacial/conduction processes from relaxation processes, as shown in Figs. 4.8 and 4.9. Singha has also used the alternative plots of electric modulus versus frequency plots which appear to make the separation clearer. On the same samples, he also makes AC conductivity measurements; from these and the modulus-frequency plots, he argues that the interfacial behavior reflects a decrease in carrier mobility. The lowering of permittivity he relates to a reduction in the concentration of charge carriers and then concludes that the observed lowering of conductivity is due to a combination of the two effects.

Different curing agents and clay dispersion also cause differences in the low frequency (interfacial polarization) and high frequency (dipolar relaxation) behavior of epoxy-clay nanocomposites (Tagami 2008).

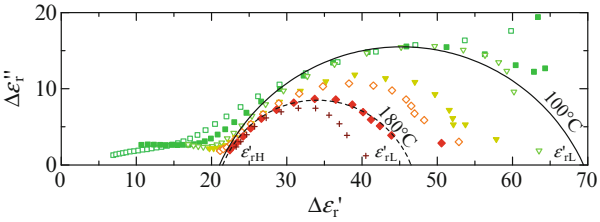

Fig. 4.8 Cole-Cole plot for polyamide-6 used in nanocomposites with mica showing the characteristic semicircular dipole relaxation plots and deviations due to conduction processes (Fuse 2009)

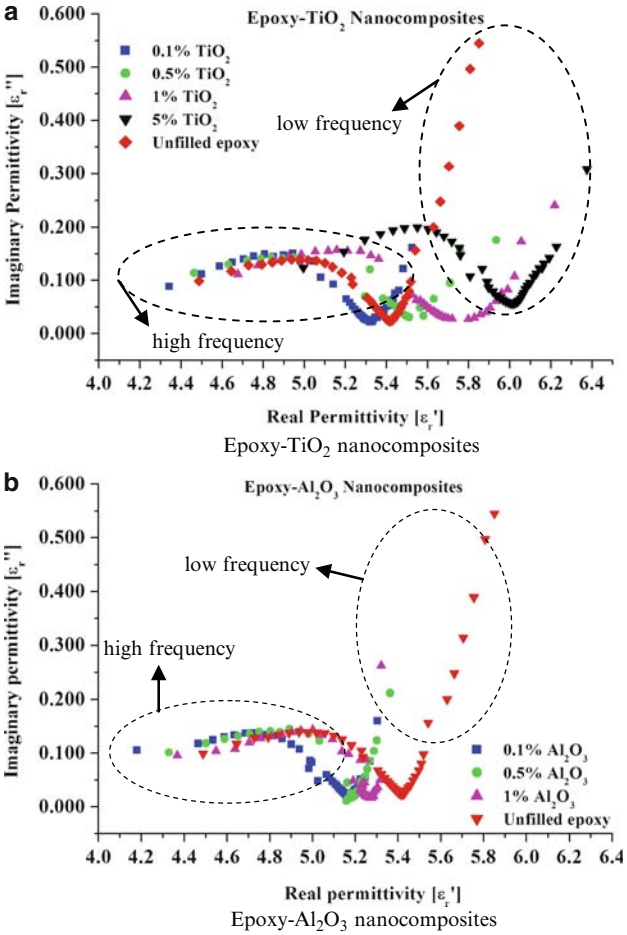

Fig. 4.9 Cole-Cole plots for TiO_2- and Al_2O_3-epoxy nanocomposites showing the low frequency deviations due to interfacial polarization or conduction (**a**) Epoxy-TiO_2 nanocomposite, (**b**) Epoxy-Al_2O_3 nanocomposite (Singha et al. 2010)

The differences cited above for several investigations and the conclusions drawn by the authors, supported by additional analysis methods, appear to be very reasonable. They do, however, confirm the complex, and sometimes unusual, nature of the underlying interface phenomena; mirroring to some degree the measurements of glass temperature and free volume.

4.9.3 Electron Paramagnetic Resonance Measurements

EPR has been successfully used to study the structure and dynamics of the surfactant layer in organoclays. In his experiments, Jeschke (2003) used tagging with nitric oxide (Fig. 4.10) of different ion exchange surfactants to probe positionally

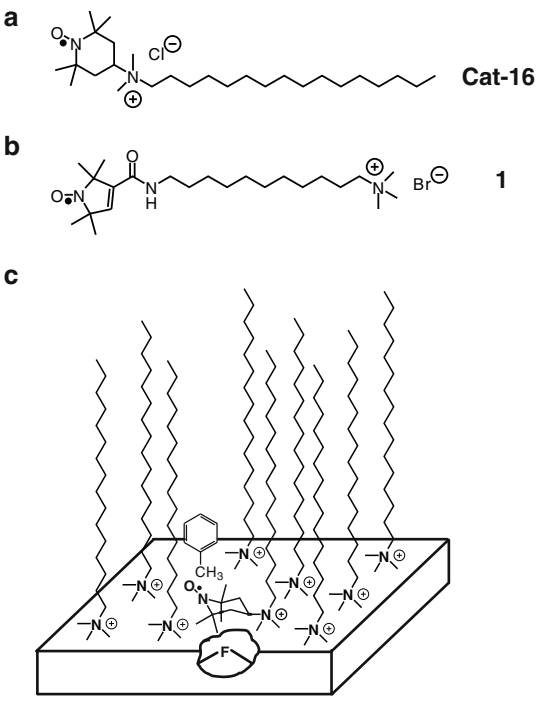

Fig. 4.10 Structure of the anchor group-labeled surfactant spin probe Cat-16 (**a**), the tail-labeled surfactant spin probe 1 (**b**). and a sketch of the surfactant layer on the clay particle and interactions probed by local elemental analysis (**c**) (Jeschke 2003)

and dynamically, the interface of the different synthetic organoclays described in Sect. 4.4. Both conventional continuous wave (CW) EPR and modern pulsed EPR measurements were conducted on organoclay particles made with two synthetic Laponite fluoromicas and in polymer-Laponite nanocomposites in PSy. One Laponite had a lateral particle size of 25 nm; the other was much larger, 1.5 μm. The PSy had molecular weights of 10,000, 30,000, and 1,000,000. Measurements were made from 20 to 160°C. The nitric oxide tags were stable up to 160°C, enabling the dynamics to be studied at temperatures relevant to melt intercalation. EPR has both high selectivity and sensitivity, and such spin probe techniques can provide information on dynamics with time scales of 10 ns to 1 μs and on structures with length scales between 0.5 and 10 nm.

It was found that the anchor groups of a major fraction of the surfactant molecules are only weakly mobile up to temperatures well above the glass transition temperature for PSy (= 100°C). Intercalation with PSy immobilizes, rather than mobilizing the anchor group region. Different mobilities were observed for surfactant fractions at different anchor group locations, with only a small fraction observed for the large expandable fluoromica particles (1.5 μm) and comparable numbers with similar mobilities for the smaller (20 nm) Laponite particles. This indicated that the mobile fraction was associated with the edges of the particles.

The different molecular weights of PSy produce quite different mobility behavior. At 40°C, the fraction became more mobile by intercalation with PSy 1,000,000, but more immobile with PSy 10,000. However, the trend reversed at higher

temperature. Above T_g, intercalation consistently led to decreased mobility of the major surfactant fraction; a stronger effect was observed with PSy 10,000. An interpretation by the authors was that, for their preparation conditions, complete intercalation occurred with PSy 10,000 but not for the higher molecular weight. Modification of the fluoromica particles by phosphonate groups, helped to confirm these results.

The EPR technique also provided local elemental information on the localization of the tagged surfactant to ^{19}F nuclei of the fluoromica, as a result of significant hyperfine coupling. Certainly, the technique offers distinct promise for understanding the dynamics of the interface in layered nanocomposites and, probably, spherical inorganic nanocomposites.

4.9.4 Temperature-Modulated DSC Measurements

This technique has been described by Reading (1994) and by Wunderlich (1994). Miltner and Van Mele (2005) have used it to quantify the reduction in polymer segment mobility and in polymer-filler interactions using several organically-modified clays in PA6, EVA, PVAc matrices, and one non-polar polymer, high-density polyethylene, HDPE. WAXS and TEM measurements were used to corroborate some of the findings.

The clays and their modifiers used were: Cloisite 30B MMT modified with bis(2-hydroxyethyl)methyl tallowalkyl ammonium; Cloisite 20A and Nanofil 5, two MMTs modified with di(hydrogenated tallowalkyl) dimethyl ammonium; Nanofil 784 and Nanofil 948, modified with w-aminolauric acid and dimethyldistearylamine, respectively; and for comparison, an unmodified bentonite clay, Majorbenton B. Nanocomposite samples were made by melt blending.

Both quasi-isothermal crystallization and glass transition behavior were measured (except for the HDPE nanocomposites which have too high a degree of crystallinity). For the semicrystalline matrices, an excess heat capacity is found which correlates with the polymer-modifier-filler structures. A similar correlation was found with the glass transition region. The results, supported by WAXS and TEM, are interpreted as a reflection of a restriction of polymer segment mobility in the vicinity of the nanofiller. The HDPE-clay nanocomposites exhibited much weaker effects, i.e., much less reduction of polymer segment mobility. The reduced interaction of the non-polar polymer structure with the polar nanoparticles is viewed as a notable feature to be addressed in future modeling work.

4.9.5 The Gouy-Chapman Layer: Interface Impurity Chemistry

From the chemical standpoint of the polymer, the writer does not view there to be any difference between this region and the region beyond, reserved for the polymer

matrix. However, in this region, (immediately exterior to the monolayer of coupling agent), any impurity, polar or non-polar, ionic or non-ionic, will aggregate, drawn toward the polar particle surface. Once an electric field is applied, polar impurities, especially ionic materials, will be drawn into the region by electrophoretic forces, each species with some characteristic mobility. (If the polymer is polar (e.g., PVOH, PET, PVDF) all dipoles will try to orient (polarize) as an electric field is applied, to the extent possible due to the surrounding polymer structure. Dissociation of impurities will also be enhanced by the higher permittivity polymers. If it is present, water will be one of these impurities (Sect. 4.11), and its high permittivity ($\sim$80) will locally enhance the dissociation of all other dissociable impurities. Another contribution to enhanced dissociation when a high electric field is applied (e.g., when performing breakdown, space charge or electroluminescence measurements), arises from high permittivity nanoparticles such as TiO_2 and $BaTiO_3$, which increase the local electric field in the polymer matrix immediately outside the particle surface through the Second Wien Effect (Devins 1972). This scenario of possibilities for charge and polarization effects is likely responsible for a "so-called" Gouy-Chapman layer described by Lewis (2005). One may wish to retain these "impurities" in order to engineer electrical stress grading around the nanoparticles, but otherwise, they do not represent a chemical change in the polymer matrix.

With relatively low permittivities (2–6), if water is largely absent, the dissociation constants are probably low ($\sim 10^{-6}$) (Reed 1971). Whether or not tethered entanglement is present is difficult to say. If present, it is not significant in many cases. In the work of Nelson (2005), the level of crystallization in XLPE with SiO_2 spherical nanofiller was unchanged for no coupling agent or a hydrophilic amine coupling agent, in comparison with unfilled XLPE. It is difficult to explain such results if significant entanglement was present.

Outside of the sphere of the coupling agent, the interface region will become the repository for "impurity" chemicals. How quickly this happens depends on the electrostatic and electrophoretic forces, on the size of the dissociable or polar species, and on electrical forces, if an electric field is applied. In this region, water can dominate the physics of polarization, charge relaxation (the relaxation time, $\tau \propto \rho.\varepsilon$, where ρ = resistivity and ε = permittivity) as well as space charge behavior and electroluminescence.

4.9.6 Entanglement

Many of the studies described above conclude that restricted movement of the polymer matrix occurs close to the particle interface. However, it is of interest whether restricted movement, or entanglement, occurs within the bulk of the polymer, outside this region.

There is a paucity of information that can meaningfully advance our understanding of entanglement. On the basis of non-linear visco-elastic measurements on nanocomposite melts (Sternstein and Zhu 2002), the possibility has been considered, but controlled investigations to verify and quantify the effect in molded

nanocomposite samples have not been done. It is likely to be most evident very near to the nanoparticle surface and to be influenced by the functionality of the particle and the polymer to which bonding will occur. An examination of the (high frequency) dielectric relaxation literature, especially that for the secondary relaxations of side groups and of the main chain (i.e., crankshaft) movement, suggests that entanglement is not present in many of the studies with epoxies and at least in some of the studies with non-polar polymers. The lack of any difference in crystallinity between SiO_2-XLPE and the base XLPE, except with a particular coupling agent, was another example cited above.

4.10 Nucleation Effects

From the results of Nelson reported in Sect. 4.8, for a system of SiO_2 nanoparticles in XLPE, there is good evidence for a valuable role of nanoparticles as nucleating agents for crystallization. However, seemingly, this does not occur automatically and no other reports on the enhancement of crystallization have been noted. The authors relate the effect to the use of a specific coupling agent, vinyltriethoxysilane, and the way in which it has bonded to the SiO_2 particle surface, with the reactive vinyl group directed perpendicular to the spherical surface. This would favor radial crystal growth from the particle surface. As noted, a second coupling agent used by the authors, plus samples without coupling agent, had unchanged levels of crystallization.

4.11 The Role of Water in Nanocomposites

Precautions to eliminate the presence of water at a spherical particle surface and prevent its impact on the addition of a silane coupling agent are identified above. Once the polymer is bonded to the nanoparticle surface via the covalent silane coupling agent, the interface should exhibit good (long term) hydrophobic qualities. This is likely to be important for the long term stability of the polymer nanocomposite as a viable dielectric material.

However, water can readily diffuse through most polymers (PVDF, PVDCl, and PET have some, though limited, barrier qualities to water) and hence water can quickly access the interface region immediately exterior to the coupling region. If the polymer is polar, or if impurities (polar molecules or ionic impurities) have diffused to this region, drawn by electrophoretic forces, the water can exhibit undesirable effects, especially long term. The water will enhance the local permittivity, and thereby lead to enhanced ionic dissociation if dissociable species are present (e.g., residual catalyst salts, alcohols, organic acids). This may lead to a reduction of space charge development (DC) or electric stress relaxation (AC), which are beneficial short term effects.

The papers by Singha (2008) and Zhang (2008) above illustrate the role of water in dielectric relaxation measurements. Other investigators have focused on clarifying this role.

Papers by Zou (2008) and Fontanella (2009) illustrate the behavior due to water when hydrophobicity has not been provided at the nanoparticle surface and it is concluded by both sets of authors that significant accumulation of water at this location is responsible for water uptake results and dielectric loss measurements and capacitance or permittivity results. The work by Zou is with silica in epoxy, while that by Fontanella is with mesoporous silica and with γ alumina in PSy. At 100% RH, Zou estimates that water surrounds the silica particles to five monolayers of free water, exterior to which a further layer of "dispersed" water is present. He concludes that if the surfaces had been "functionalized to be hydrophobic," considerable reduction of water would occur. Fontanella found a loss peak around 250 K and 1,000 Hz, with a relatively high enthalpy and unusually low pre-exponential; this was attributed to water attached to hydroxyl groups. (Neither author looked around 1 MHz, where the relaxation due to free (i.e., not bound to hydroxyl or carbonyl groups) water might be).

Fabiani et al. (2010) examined the influence of water on the electrical properties of organically-modified nanoclays (Fluorohectorite and Bohemite) in the thermoplastic polymer, ethylene vinyl acetate (EVA). After thorough drying, the uptake of relatively large amounts of water was investigated. It was found that the aspect ratio of the nanoclays plays a major role in water uptake and in dielectric loss behavior. A percolation model was used to account for the uptake of water.

4.12 Final Remarks

Measurements over a broad range with spherical inorganic particles and intercalated and exfoliated natural and synthetic clays and micas, in polar and non-polar polymers, have significantly improved our data base on dielectric polymer nanocomposites. FTIR, glass transition temperature, free volume, electron paramagnetic resonance, and broadband dielectric spectroscopy, among others, are pointing to the major macroscopic effects of the interface region, involving both chemical and physical effects. Measurements by different investigators sometimes show quite different results, but these can often be related to experimental differences, sometimes rather subtle. In terms of the future, much of the work currently underway in this field looks likely to continue, in order to improve our understanding of the interface. For an improved understanding, more controlled experiments are suggested: for example using tagging agents with the EPR technique and broadband spectroscopy; the use of engineered coupling agents; improved characterization; and modeling.

Acknowledgements The writer acknowledges many pleasant and productive interactions with J.K Nelson, R.A MacCrone, L.S Schadler, and several students, at the Rensselaer Polytechnic Institute, during their work on SiO_2-XLPE nanocomposites, in triggering his involvement in this field; and with M.F. Frechette of IREQ in collaboration on the fundamentals of nanodielectric science.

References

Alcoutlabi M, McKenna GB (2005) Effects of confinement on material behavior at the nanometric size scale. J Phys Condens Matter 17:R461–R524

Artbauer J (1996) The electric strength of polymers. J Phys D 29:446–456

Bendler JT, Fontanella JJ, Ahlesinger MF et al (2003) The need to reconsider traditional free volume theory for polymer electrolytes. Electrochim Acta 48:2267–2272

Bendler JT, Fontanella JJ, Shlesinger MF et al(2005) Free-volume dynamics in glasses and supercooled liquids. Phys Rev E71:1–10

Bendler JT, Fontanella JJ, Shlesinger MF et al(2009) The defect diffusion model and the glass transition in nanoscale and bulk films. J Comput Theor Nanosci 6:1–5

Brinker CJ, Scherer GW (1990) sol–gel science. Academic, Boston

Broutman LJ, Agarwal BD (1973) SPI 28th Annu Tech Conf Reinf Plast 5-B

Chen BK, Du JU, Hou CW (2008) The effects of chemical structure on the dielectric properties of polyetherimide and nanocomposites. Trans IEEE DEI-15:127–133

Consolati G, Quasso F (2007) Estimation of free volume holes in amorphous polymers by means of positron annihilation spectroscopy. Simha Symposium on Polymer Physics, October 17–18

Crank J, Park GS (1968) Diffusion in polymers. Academic, London

Datta S, Lohse DJ (1996) Polymeric compatabilizers: uses and benefits in polymer blends. Hanser Gardner, New York. ISBN 9781569901946

Devins JC, Rzad SJ (1977) A new class of additives to inhibit tree growth in solid extruded cable insulation. EPRI Project RP 7851-1, Final Report: August 1977

Fabiani D, Montanari GC, Testa L (2010) Effect of aspect ratio and water contamination on the electrical properties of nanostructured insulating materials. Trans IEEE DEI-17 In press

Fontanella JJ, Wintersgill MC, Edmondson CA et al (2009) Water-associated dielectric relaxation in oxide nanoparticles. J Phys D Appl Phys 42:1–6

Frechette MF, Larocque RY, Trudeau M et al (2008) Nanostructured polymer microcomposites: a distinct class of insulating materials. Trans IEEE DEI-15:90–105

Frubing P, Blischke D, Gerhard-Mulhaupt G et al (2001) Complete relaxation map of polyethylene: filler-induced chemical modifications as dielectric probes. J Phys D Appl Phys 34:3051–3057

Fuse N, Okada M, Ohki Y et al (2009) Photoluminescence in polyamide/mica and polyethylene/MgO nanocomposites induced by ultraviolet photons. Trans IEEE DEI-15:1215–1223

Fuse N, Sato H, Tanaka T et al (2008) Effects of mica nanofillers on the complex permittivity of polyamide nanofillers. IEEE DEIS Conf Electr Insul Dielectr Phen 6–5

Fuse N, Sato H, Ohki Y et al (2009) Effects of nanofiller loading on the molecular motion and carrier transport in polyamide. Trans IEEE DEI-16:524–530

Gaehde J (1975) Effect of silane-modified Kaolin filler on the orientation of high density polyethylene in the interface region. Plaste Kautschuk 22:626

Green CD, Vaughan AS, Mitchell GR et al (2008) Structure property relationships in polyethylene/montmorillonite nanodielectrics. Trans IEEE DEI-15:134–143

Green CD, Vaughan A (2008) Nanodielectrics – how much do we really understand, IEEE Electr Insul Mag 24:6–16

Hill NE, Vaughan WE, Price AH et al (1969) Dielectric properties and molecular behavior. Van Nostrand Reinhold Company, London

Hummel DO (1966) Infrared spectra of polymer in the medium and long wavelength range. Polymer Reviews 14: Interscience Publishers, Wiley, New York

Imai T, Hirano Y, Hirai H et al (2002) Preparation and properties of epoxy-organically modified layered silicate nanocomposites. Proc, IEEE Int Symp Electr Insul: 379–383

Jeschke G, Panek G, Schleidt S et al (2003) Addressing the interface in polymer clay nanocomposites by electron paramagnetic resonance spectroscopy on surfactant probes. Polymer Nanocomposites 2003, International Symposium on Polymer Nanocomposites Science and Technology Paper 49

Kahn FJ (1973) The orientation of liquid crystals on mineral surfaces treated with silane coupling agents. Appl Phys Lett 22:386

Katahira S, Yasue K, Inagaki M (1999) Intercalation of *E*-caprolactam ions into organic hosts. J Mater Res 14:1178–1180

Kochetov R, Andritsch T, Lafont U et al (2009) Preparation and dielectric properties of epoxy-BN and epoxy AlN nanocomposites. IEEE Electr Insul Conf: 397–400

Kozako M, Fuse N, Ohki Y et al (2004) Surface degradation of polyamide nanocomposites caused by partial discharges using IEC(b) electrodes. Trans IEEE DEI-11:833–839

Lewis TJ (1994) Nanometric dielectrics. Trans IEEE DEI-1:812–815

Lewis TJ (2004) Interfaces are the dominant feature of dielectrics at the nanometric level. Trans IEEE DEI-11:739–753

Lewis TJ (2005) Interfaces: nanometric dielectrics. J Phys D Appl Phys 38:202–212

MacCrone RK, Nelson JK, Schadler LS et al (2007) The use of electron paramagnetic resonance (EPR) in the probing of the dielectric interface. IEEE 9th Int Conf Solid Dielectr: 428–431

MacCrone RK, Nelson JK, Smith RC et al (2008) The use of electron paramagnetic resonance in the probing of the nano-dielectric interface. Trans IEEE DEI-15:197–204

McCrum NG, Read BA, Williams G (1967) Anelastic and dielectric effects in polymeric solids. Wiley, London. Chapters 2, 5, 8–14

Miltner HE, Van Mele B (2005) Experimental evidence for reduced chain segment mobility in polymeric nanocomposites. International Symposium on Polymer Nanocomposites Science and Technology: Paper 7.02

Mohapatra SR, Thakur AK, Choudhary RNP (2008) Vibrational spectroscopy analysis of ion conduction mechanism in dispersed phase polymer nanocomposites. J Polym Sci B Polym Phys 47(1):60–71

Montanari GC, Fabiani D, Palmieri F et al (2004) Modification of electrical properties and performance of EVA and PP insulation through nanostructure by organophilic silicates. Trans IEEE DEI-11:754–762

Nelson JK, Fothergill JC (2004) Internal charge behavior of nanocomposites. Nanotechnology 15:1–10

Nelson JK, Utracki LA, MacCrone RK et al (2004) Role of the interface in determining the dielectric properties of nanocomposites. IEEE DEIS Conf Electr Insul Dielectr Phen: 314–317

Nies E, Stroeks A (1990) A modified hole theory of polymeric fluids. 1. Equation of state of pure components. Macromolecules 23:4008

Nies E, Xie H (1993) Quasi-chemical approximation for nonrandomness in the hole theory of polymeric fluids. 1. Equation of state behavior of pure components. Macromolecules 26:1683

Plueddemann EP (1982) Silane coupling agents. Plenum, New York. pp 1–235

Ray SS, Okamoto M (2003) Polymer/layered silicate nanocomposites: a review from preparation to processing. Prog Polym Sci 28:1539–1641

Reading M, Luget A, Wilson R (1994) Modulated differential calorimetry. Thermochimica Acta 238:295–307

Reed CW (1971) The influence of impurities on the dielectric losses of poly(2,6-dimethyl-1,4-phenylene ether). The dielectric properties of polymers. Plenum, New York. pp 191–199

Reed, CW (1972) The influence of residual solvent and crystallinity on the dielectric relaxation of solvent-cast polymer films. 1971 Annual report, conference on electrical insulation and dielectrics phenomena, National Academy of Sciences Pub ISBN 0-309-02032-8, p 89

Rogers PA (1993a) Pressure-volume-temperature relationships for polymeric liquids: a review of equations of state and their characteristic parameters of 56 polymers. J Appl Polym Sci 48:1061–1080

Rogers PA (1993b) Pressure-volume-temperature relationships for poly(vinylidene fluoride) and polyamide-11. J Appl Polym Sci 50:2075–2083

Roy M, Nelson JK, Reed CW (2005) Polymer nanocomposite dielectrics – the role of the interface. Trans IEEE DEI-12:629–643

Schamm S, Berjoan R, Barathieu P (2004) Study of the chemical and structural organization of SIPOS films at the nanometer scale by TEM-EELS and ZPS. Mater Sci Eng B107:58–65

Simha R, Somcynsky T (1969) On the statistical thermodynamics of spherical and chain molecule fluids. Macromolecules 2:342–350

Smith RC, Liang C, Landry M, et al (2008) The mechanisms leading to the useful electrical properties of polymer nanodielectrics. Trans IEEE DEI-15:187–196
Singha S, Thomas MJ (2008a) Permittivity and tan δ characteristics of epoxy nanocomposites in the frequency range of 1 MHz–1 GHz. Trans IEEE DEI-15:2–11
Singha S, Thomas MJ (2008b) Dielectric properties of epoxy nanocomposites. Trans IEEE DEI-15:12–23
Singha S, Thomas MJ (2008c) Reduction of permittivity in epoxy nanocomposites at low nanofiller loadings. IEEE DEIS Conf Electr Insul Dielectr Phen: 8–6
Singha S, Thomas MJ (2009) Influence of filler loading on dielectric properties of epoxy-ZnO nanocomposites. Trans IEEE DEI-16:531–542
Singha S, Thomas MJ, Kulkarni A (2009) Complex permittivity of epoxy nanocomposites at low frequency. Trans IEEE DEI-17 In press
Sternstein SS, Zhu A-J (2002) Reinforcement mechanism of nanofilled polymer melts as elucidated by nonlinear viscoelastic behavior. Macromolecules 35:7262–7273
Sun Y, Zhang Z, Wong CP (2005) Influence of interphase and moisture on the dielectric spectroscopy of epoxy/silica composites. Polymer 46:2297–2305
Tabatabaei S, Shukohfar A, Aghababazadeh R et al (2006) Experimental study of the synthesis and characterization of silica nanoparticles via the sol–gel method. J Phys Conf Ser 26:371–374
Tagami N, Okada M, Hirai N et al (2008) Dielectric properties of epoxy-clay nanocomposites – effects of curing agent and clay dispersion method. Trans IEEE DEI-15:24–32
Takada T, Hayase Y, Tanaka Y et al (2008) Space charge trapping in electrical potential well caused by permanent and induced dipoles for LDPE/MgO nanocomposites. Trans IEEE DEI-15:152–160
Takala M, Kartunnen M, Salovaara P et al (2008) Dielectric properties of nanostructured polypropylene – polyhedral oligomeric silsesquioxane. Trans IEEE DEI-15:40–51
Takala M, Karttunen K, Peltro J et al (2008) Thermal, mechanical, and dielectric properties of nanostructured epoxy-polyhedral oligomeric silsesquioxane composites. Trans IEEE DEI-15:1224–1235
Tanaka T, Montanari GC, Mulhaupt R (2004) Polymer nanocomposites as dielectrics and electrical insulation: perspectives for processing technologies, material characterization, and future applications. Trans IEEE DEI-11:763–784
Tobolsky AV (1960) Properties and structure of polymers. Wiley, New York. pp 43–71
Tuncer E, Sauers I, James DR et al (2008) Nanodielectric system for cryogenic applications: barium titanate filled polyvinyl alcohol. Trans IEEE DEI-15:236–242
Utracki LA, Simha R (2001) Analytical representation of solutions to lattice-hole theory. Macromol Theor Simul 10:17–23
Utracki LA, Simha R, Garcia-Rejon A (2003) Pressure-volume-temperature dependence of poly-*E*-caprolactam/clay nanocomposites. Macromolecules 36:2114–2121
Vaughan AS, Swingler SG, Zhang Y (2006) Polyethylene nanodielectrics: the influence of nanoclays on structure formation and dielectric breakdown. Trans IEE Jpn 126:1057–1063
Vo HT, Shi FG (2002) Towards model based engineering of optoelectronic packaging materials: dielectric constant modeling. Microelectr J 33:409–415
Wells AF (1950) Structural inorganic chemistry. Oxford University Press, Oxford. pp 76–78, 358–371, 567–569
Wunderlich B, Jin YY, Boller A (1994) Mathematical-description of differential scanning calorimetry based on periodic temperature modulation. Thermochim Acta 238:277–293
Yang DQ, Meunier M, Sacher E (2005) The surface modification of nanoporous SiO_x thin films with a monofunctional organosiloxane. Appl Surf Sci 252(5):1197–1201
Yang DQ, Gillet JN, Meunier M et al (2005) Room temperature oxidation kinetics of Si nanoparticles in air, determined by x-ray photoelectron spectroscopy. J Appl Phys 97:024303
Yun DS, Kim HJ, Yoo JW (2005) Preparation of silica nanospheres: effect of silicon alkoxide and alcohol on silica nanospheres. Bull Korean Chem Soc 26:1927–1928
Zhang C, Mason R, Stevens GC (2006) Preparation, characterization, and dielectric properties of epoxy and polyethylene nanocomposites. IEEJ Trans Fundam Mater 126:1105–1111

Zhang C, Stevens GC (2008) The dielectric response of polar and non-polar nanodielectrics. Trans IEEE DEI-15:606–617

Zou C, Fothergill JC, Rowe SW (2008) The effect of water absorption on the dielectric properties of epoxy nanocomposites. Trans IEEE DEI-15:106–117

Chapter 5
Modeling the Physics and Chemistry of Interfaces in Nanodielectrics

R. Ramprasad, N. Shi, and C. Tang

5.1 Introduction

Phenomena such as charge conduction, dielectric response, and dielectric degradation or breakdown are the result of complex processes operating at multiple temporal and spatial scales. Charge injection into the dielectric in the presence of an electric field is determined by the electronic structure at the electrode-dielectric interface, e.g., through Schottky barriers (Robertson et al. 2007), interfacial defects or traps (Teyssedre and Laurent 2005), etc. Subsequent conduction of charge carriers through the dielectric may be caused by band conduction or defect states in the dielectric (Teyssedre and Laurent 2005; Arnold et al. 1994; O'Dwyer 1973). The dielectric response of the insulator to an external electric field is determined by the polarization contributions from ions and electrons of the system (Resta 1994; King-Smith and Vanderbilt 1993), as well as microscopic and macroscopic imperfections (Boggs 2005, 2004). Degradation and eventual breakdown of the dielectric are complex phenomena, with origins at the electronic, atomic, and macroscopic levels, and influenced strongly by both the conduction and dielectric response (Lombardo et al. 2005; Zheng and Boggs 2005; Boggs 2004, 2005; McPherson et al. 2003; Arnold et al. 1994). An adequate understanding of dielectric breakdown requires statistical treatment (Lombardo et al. 2005). Many of these phenomena are discussed in detail in Chaps. 4, 7, and 10 of this book.

To compound matters further, in multiple-component dielectric systems, as component sizes shrink to the atomic or nanoscale, the structure and chemistry at interfaces within the dielectric become important and can sometimes dominate the overall properties. For instance, while atomic level interfacial features such as dangling bonds, under- or over-coordination, multiple-oxidation states, impurities, etc., may be less important in larger scale systems owing to the smaller volume fraction

R. Ramprasad (✉) and C. Tang
Chemical, Materials and Biomolecular Engineering, Institute of Materials Science, University of Connecticut, Storrs, CT, USA
e-mail: rampi@ims.uconn.edu

N. Shi
Shocking Technologies, Inc., San Jose, CA, USA

J.K. Nelson (ed.), *Dielectric Polymer Nanocomposites*,
DOI 10.1007/978-1-4419-1591-7_5,

occupied by the interfacial region, the consequences of such effects, especially on electrical properties, can reach unanticipated magnitudes in nanoscale systems (Green et al. 2001; Lewis 1994, 2004) as is clear from the depiction in Fig. 1.2.

In this chapter, recent developments in the atomic-level computational modeling of interfacial phenomena are described using density functional theory (DFT) techniques (Martin 2004; Kohn and Sham 1965; Hohenberg and Kohn 1964). Fortunately, such computational methods, also referred to as ab initio methods, have reached a level of maturity, sophistication, and practicability that materials and device design through these methods is becoming a reality (Hafner et al. 2006). Quantities such as band offsets at insulator-insulator and metal-insulator interfaces, position-dependent dielectric constants in multi-component systems across interfaces, electron-phonon interactions, diffusion, migration and segregation of atomic level point defects, etc., can be computed reliably for a wide range of systems, as described in this chapter.

An overview of ab initio DFT methods and their ability to predict a variety of diverse material properties is provided, followed by applications of these techniques to study several phenomena relevant to nanoscale dielectrics. Discussion of these phenomena is "materials-neutral," i.e., polymeric as well as non-polymeric systems appropriate for advanced capacitor and transistor technologies are considered in an attempt to highlight the utility of DFT computational methods to the phenomena under study.

5.2 Ab Initio Modeling Techniques

Many physical properties are determined by the total energy. For instance, the equilibrium structure of a molecule or a crystal is the one that has the lowest total energy; surfaces, interfaces, defects and other (meta)stable structures correspond to local minima in the total energy hypersurface in phase-space;[1] the curvatures of the total energy hypersurface at energy minima are related to the vibrational and phonon frequencies, force constants and elastic moduli; activation energies of chemical reactions, diffusion and phase transitions are "passes" in the total energy hypersurface between local minima ("valleys") corresponding to the reactants and products; and so on.

Quantum mechanics provides a prescription for the computational determination of the total energy hypersurface mentioned above, as well as the electronic energies and the associated electronic wave functions which can be used to quantify properties particularly relevant to the subject of this book. Although philosophical questions remain concerning the interpretations and completeness of this theory, those quantities that modern quantum theory address are predicted with incredible

[1] The dimensionality of the hypersurface is $3n$-6 ($3n$-5 for systems with linear geometry), if n is the number of particles (atoms) in the system.

accuracy. Quantum mechanics-based calculations have an additional appeal because they are *inherently parameter-free* and do not rely on any experimental input other than the values of the electronic and ionic charges and masses, and so are referred to as "first principles" or "ab initio" methods.

Of all the quantum mechanics-based methods currently in use, density functional theory (DFT) offers the best trade-off between accuracy and computational cost. Through several time-tested approximations for efficient treatment of the electronic wave functions, nuclear-electron and electron-electron interactions (Martin 2004), DFT has become a powerful tool and has become complimentary to experiments. DFT calculations involving a few to several hundred atoms per repeating unit cell have become routine, and those involving a few thousand atoms are possible given the increasing processor speeds, improved algorithms and decreasing processor prices (Bottin et al. 2008).

Within DFT, the following eigenvalue equation (in atomic units) is solved:

$$[-\nabla^2 + V_{eff}(r)]\psi_i(r) = \varepsilon_i \psi_i(r) \tag{5.1}$$

where the first term in brackets represents the electronic kinetic energy (with ∇ being the gradient operator), and the second term, $V_{eff}(r)$, represents the effective potential energy seen by an electron. $V_{eff}(r)$ contains all the electron-electron and electron-nuclear interactions, as well as the potential caused by an external electric field. ψ_i and ε_i represent the spectrum of electronic wave functions and energies, respectively, indexed by i.

The first step in this computational approach is to construct a reasonable atomic level model of the system of interest, in part guided by experiments and in part guided by chemical intuition. Next, the atomic coordinates are optimized by requiring that the total energy of the system (which is a function of the spectrum of occupied eigenenergies ε_i, and wave functions ψ_i) is a minimum, and the forces on each atom are close to zero, where the force on each atom is related to the first derivative of the total energy with respect to the position of that atom. The electronic eigenenergies, ε, provide an estimate of the band gap and, when appropriate, the energetic locations of defect or trap states. $V_{eff}(r)$ for the optimized system provides information concerning the potential seen by each electron within the system and is used to compute band offsets, ionization potentials, electron affinities, and work functions. Dielectric response and coupling of electron states with phonons can be determined using many techniques and will be discussed separately in subsequent sections.

Some comments concerning the expected accuracy of DFT predictions are in order. The greatest strength of DFT is its ability to predict structural details of materials, typically to within 1% of experimental values. Figure 5.1 shows the correlation between DFT predictions of structural properties and experimental data for several classes of systems. Vibrational frequencies of molecules, phonon frequencies of solids, elastic constants of solids, and relative energies are predicted to within 2% of experiments by DFT. Figure 5.2a compares DFT predictions of vibrational frequencies of diatomic molecules with experiments, and Fig. 5.2b shows a similar comparison for bulk and shear moduli for various solids. Dielectric constants

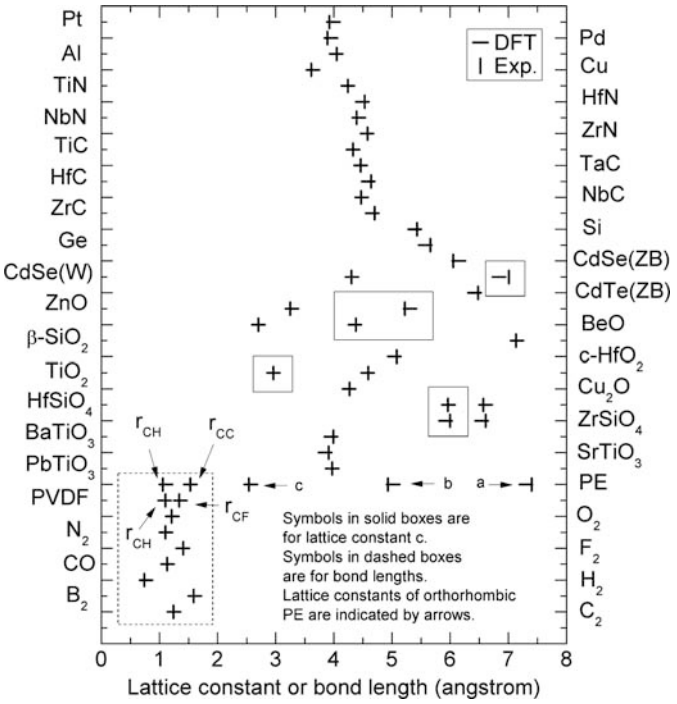

Fig. 5.1 Comparison of DFT-computed structural parameters with experiments for a variety of metals, semiconductors, insulators, polymers, and molecules. ZB and W represent the zinc blend and wurtzite crystal structures, respectively. Data are from various sources including (Kobayashi 2001; Kamran et al. 2009; Sun et al. 2003)

of insulators are typically predicted to within 5% of experiments, as portrayed in Fig. 5.2c for both static and optical dielectric constants. The larger discrepancy in this case is primarily caused by the lack of sufficiently accurate single crystal experimental data.

The greatest deficiency of DFT is its inability to predict band gaps in semiconductors and insulators to the same level of accuracy achievable in the case of the other properties; DFT band gaps are underestimated relative to experimental determinations by up to 50%, as shown in Fig. 5.2d. However, the shape and the width of the bands, and trends in changes in the band gap (e.g., due to external pressure) are predicted accurately (Ramprasad et al. 1996; Smelyansky and Tse 1996). This "band gap problem" is a consequence of the approximations made within DFT. Techniques to handle such deficiencies are currently available (Shishkin et al. 2007; Mitáš and Martin 1994; Williamson et al. 1998; Paulus 2006) and result in satisfactory agreement of the computed band gaps with experiments as shown in Fig. 5.2d for the case of the GW approximation, in which quasi-particle corrections to the DFT single-particle energies are included. Such beyond-DFT approaches are far too demanding computationally at the present time to treat systems composed of more than ten atoms per unit cell.

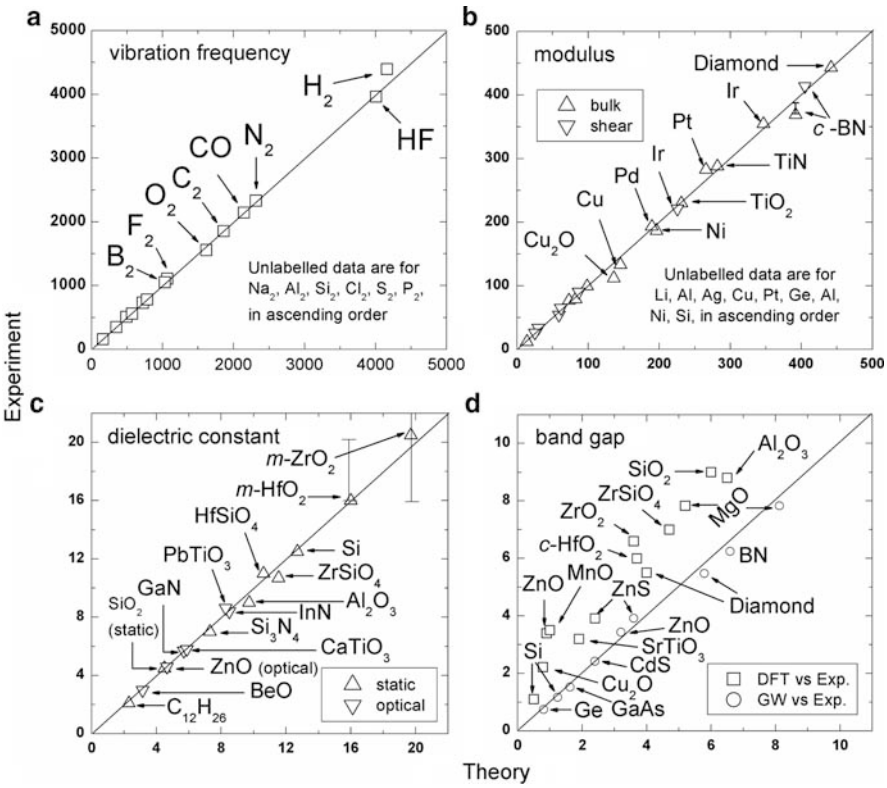

Fig. 5.2 Comparison between DFT predictions (horizontal axes) and experimental values (vertical axes) for (**a**) vibrational frequencies of diatomic molecules, (**b**) bulk and shear moduli of solids, (**c**) static and optical dielectric constants of insulators, and (**d**) band gaps of insulators. Frequencies are in cm^{-1}, elastic moduli in GPa, and band gaps in eV. Data are from various sources including (Sun et al. 2003; Kamran et al. 2009; Bernardini and Fiorentini 1998; Becke 1986; Robertson et al. 2006). Data for GW method in (**d**) are from (Shishkin et al. 2007)

5.3 DFT Modeling of Polymers

Before discussing interfacial phenomena, progress will be reviewed in using DFT computations to understand important electrical properties of bulk polymeric systems relevant to this book. In this brief survey, attention is directed mainly to polyethylene (PE) and polyvinylidene fluoride (PVDF), both of which have been studied from the perspective of their potential applications in high voltage and capacitor-based energy storage systems.

The electronic structure of PE has been studied by several researchers (Serra et al. 2000; Montanari and Jones 1997; Miao et al. 1996; Springborg and Lev 1989). In particular, these efforts indicate that the PE valence band states are dominated by C-C and C-H bonding interactions. These states are localized mainly in the chain

region and referred to as intrachain states. In contrast to the valence band states, the conduction band states are interchain in nature, i.e., they are located primarily *between* chains. This implies that a conduction electron in its lowest energy state occupies the region between chains, and, when provided with the opportunity, can easily be channeled out of the crystal. This behavior is consistent with the notion that the system has a zero or negative electron affinity, i.e., the conduction band minimum (CBM) is at or above the vacuum level.

Experimentally, it has been shown that PE does indeed have a negative electron affinity (Ueno et al. 1986; Dudde and Reihl 1992; Bloor 1976). Electron affinity is essentially a surface property. In an attempt to characterize it computationally, Righi et al. (2001) studied the electronic structure of PE surfaces by considering an orthorhombic crystalline PE slab. For the (001) surface, they found a surface state -1.2 ± 0.5 eV below the CBM. These surface states penetrate very little into the bulk PE and decay exponentially about 3 Å into the vacuum. For the (110) surface they found, in addition to the surface state below the CBM which was similar to the case of the (001) surface, extra surface states slightly above the CBM, corresponding to the propagation of free electrons in the plane of the surface. The electron affinity was calculated to be -0.10 and -0.17 eV for the (001) and (110) surface, respectively, comparing favorably with the experimental values -0.5 ± 0.5 eV (Ueno et al. 1986; Dudde and Reihl 1992; Bloor 1976). The surface states that occur within the band gap of PE could act as traps for injected electrons; hence, such unoccupied states below the CBM are referred to as "electron traps." The agreement of the trap depth with the activation energies (0.7–1.1 eV) obtained from the measurement of electron conductivity in PE (Ieda 1984) indicates that surface states constitute an important factor controlling the mobility of electrons.

In addition to the surface states that may trap charge carriers, energy levels within the band gap may be created due to physical or chemical defects in the polymer (Meunier et al. 2001; Meunier and Quirke 2000). Physical defects are conformational disorders and could occur in the amorphous regions within PE, while chemical defects include impurities, additives, and broken bonds. Physical defects could result in unoccupied energy levels 0.15–0.3 eV below the CBM, while chemical defects (depending on the type of defect) may result in much deeper trap levels, greater than 1 eV, similar to the surface states discussed above.

PVDF and its copolymers have excellent electromechanical properties and are promising candidates for high-performance, high-energy-density capacitors discussed in Chap. 11. Recently a very high energy density capacitor with fast discharge speed and low loss was obtained using a copolymer of vinyledene fluoride-chlorotrifluoroethylene, P(VDF-CTFE), exploiting the reversible nonpolar (α) to polar (β) phase transition (Chu et al. 2006). First principles calculations have been used to investigate their phase equilibria as a function of applied electric field and the concentration of CTFE (Ranjan et al. 2007). The calculations reveal that both PVDF and dilute P(VDF-CTFE) prefer the α phase at zero field but transform to the β phase at some critical field below the breakdown field, resulting in an abrupt change in the displacement field from nearly zero in the α phase to 0.2 C/m^2 in the β phase. The critical field required for the transition decreases with increasing CTFE

content, and reaches zero for concentration higher than 17%. In disordered P(VDF-CTFE), a distribution of concentrations leads to a range of transition fields, which results in a smooth increase in the displacement field with the applied field and a large energy density, as observed experimentally in P(VDF-CTFE) 91/9% polymer (Chu et al. 2006).

5.4 Interfacial Electronic Structure

5.4.1 Background

The presence of an interface between dissimilar materials causes a disruption in the properties across the interface. For instance, the electronic structure, characterized, for example, in terms of the locations of the CBM, the valence band maximum (VBM), and the Fermi energy (in the case of metals) is discontinuous across the interface. These discontinuities, and their modifications due to charge transfer across the interface and point defects at the interface, control conduction across *and* along the interface. In this section, basic interface electronic structure concepts are introduced briefly and then recent progress in this field based on computational studies is reported.

Figure 5.3 (left) shows a schematic of the electronic structure across a metal-insulator interface. The metal is characterized by the Fermi energy (E_F), whose location below the vacuum level defines the metal work function (Φ_M). The insulator, on the other hand, is characterized by its CBM and VBM, whose positions relative to the vacuum level define the electron affinity (discussed in Sect. 5.3) and ionization potentials, respectively, of the insulator. Thermal or electric field induced injection of electrons from the metal to the conduction band of the insulator is controlled by the offset between E_F and the CBM, also called the Schottky barrier height (SBH) for electrons. Likewise, an interface between two different insulators is characterized by offsets between the conduction bands or the valence bands of the two

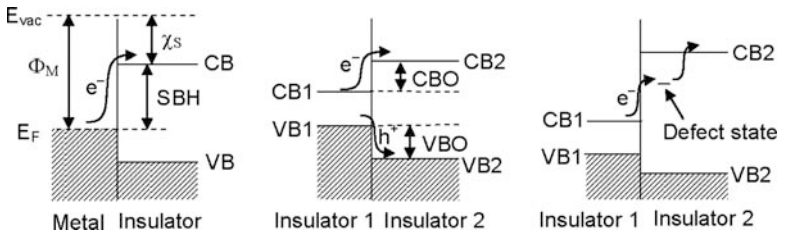

Fig. 5.3 Schematics of Schottky barrier (*left*), band offset (*middle*), and defect state (*right*). E_F, Φ_M, χ_S, CB, and VB are the Fermi level, work function, electron affinity, conduction band edge, and valence band edge, respectively. E_{vac} is the vacuum level. e^- and h^+ represent electron and hole, respectively

materials, as shown in Fig. 5.3 (middle). The conduction band offset (CBO) and the valence band offset (VBO) control injection of electrons and holes, respectively, from the insulator in the left to the one in the right in Fig. 5.3 (middle). In general, the SBH, VBO and CBO should be larger than 1 eV to prevent the injection of charge carriers from one material to the other. However, if point defects exist at the interface and in the insulator, they create defect energy levels, allowing for alternative or easier pathways for the transfer of charge carriers, as shown schematically in Fig. 5.3 (right). Furthermore, the presence of interface states can mediate conduction along the interface plane.

5.4.2 DFT Determination of Offsets

Robust DFT-based procedures are available to determine the SBH, VBO and CBO across interfaces. The standard approach is generally referred to as the "bulk plus band lineup" method (Van de Walle and Martin 1987; Tuttle et al. 2007). Following is the procedure for the determination of the VBO. Essentially, two sets of calculations are undertaken. First, calculations of the bulk systems making up the interface are performed, and the energy difference between the average effective potential (V_{eff} of (5.1)) and the VBM is noted for each of the two materials. Second, a separate calculation of the heterostructure containing the interface between the two materials is performed, and the energetic positions of V_{eff} in the interior parts of the two materials (i.e., sufficiently far away from the interface) are determined. Finally, the energy differences noted from the first step (bulk calculations) are used to locate the energetic positions of the VBM on either sides of the interface. This step-by-step procedure facilitates determination of the VBO.

The CBO can, in principle, be determined by replacing VBM by CBM in the above description. However, DFT underestimates band gaps of insulators, implying that the energetic location of the CBMs determined for the two materials may have arbitrary errors, leading to unknown errors in the calculated CBO. Hence, the ad hoc procedure adopted by the community is to use the energetic placement of VBM obtained by DFT, followed by determination of the energetic location of CBM using experimental band gap values for the two materials making up the interface. Thus while VBOs are computed without any experimental input, CBOs are computed using DFT VBOs and experimental band gaps.

If one of the materials making up the interface is a metal, then E_F plays the role of VBM for that material, and the same procedure is adopted to determine the offset between E_F for the metal and the VBM for the insulator. The SBH for the electrons is then determined using the experimental value of the band gap of the insulator. Work functions (WF) of metal surfaces, and electron affinities and ionization potentials of insulators can be determined by adopting the same procedure. In this case, we have an interface between a metal or an insulator, and vacuum.

Figure 5.4 shows the DFT predictions of SBH, CBO, VBO and WF, along with a comparison to experiments for a wide variety of technologically important systems

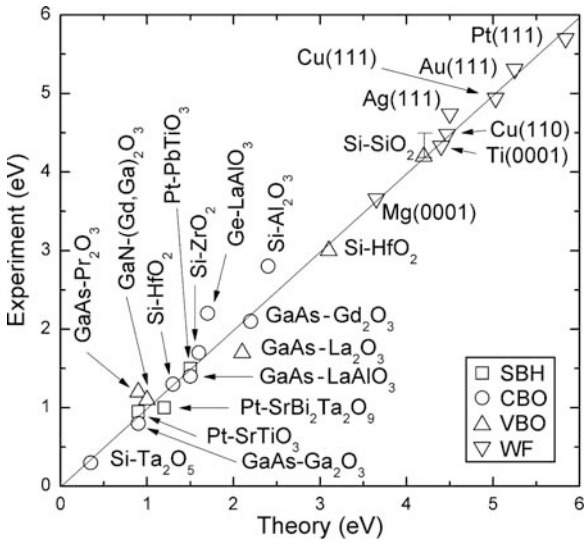

Fig. 5.4 DFT predictions of SBH, CBO, VBO and work functions (WF) versus experiment data. Data from various sources including (Peacock and Robertson 2002; Robertson and Falabretti 2006; Rusu and Brocks 2006; Marder 2000)

collected from various sources including (Peacock and Robertson 2002; Robertson and Falabretti 2006; Rusu and Brocks 2006; Tuttle et al. 2007). DFT does an excellent job of predicting these parameters.

5.4.3 The Layer-Decomposed Density of States

Having established the utility of DFT in characterizing the electronic structure of interfaces accurately (sometimes, after corrections based on experimental band gaps), other properties difficult to probe directly using experimental methods may be investigated. Examples include the specific role played by individual atoms, groups of atoms, or impurities in determining SBH, VBO and CBO. Compared with the conventional "bulk plus band lineup" method, the projected density of states (PDOS) or the layer-decomposed density of states (LaDOS) approach facilitates a more detailed analysis of the interfacial electronic structures (Shi 2008; Shi and Ramprasad 2008a, b), as described below.

The density of states (DOS) provides a quantitative description of the number of allowed electronic energy levels between energies ε and $\varepsilon + d\varepsilon$. Needless to say, the DOS is zero in the band gap region. The DOS of the entire system can be decomposed into contributions from individual atoms and individual atomic orbitals constituting the system. This sort of decomposition is possible as the wave function

of an electron belonging to the entire system can be decomposed in the following manner:

$$| \Psi_i \rangle = \sum_{al} \langle \phi_{al} | \Psi_i \rangle \, | \, \phi_{al} \rangle \tag{5.2}$$

where $|\Psi_i\rangle$ and $|\phi_{al}\rangle$ are the electronic wave function and the atomic orbitals, respectively, and *i, a*, and *l* are the indices for the electronic wave function, atom, and the atomic orbital, respectively. Note that we have adopted the Dirac notation for simplicity, and that $\langle \phi_{al} | \Psi_i \rangle$ is a projection of the electronic wave function on a specific atomic orbital, representing the contribution of that atomic orbital to the electronic wave function. The density of states $g_{al}(\varepsilon)$ arising from a specific atom *a* with atomic orbital *l* can be defined as:

$$g_{\mathrm{al}}(\varepsilon) = \sum_{i} |\langle \phi_{al} | \Psi_i \rangle|^2 \, \delta(\varepsilon - \varepsilon_i) \tag{5.3}$$

where δ represents the Dirac delta function.

If the interface under consideration is infinite along the interfacial plane (such as in the heterostructures under discussion here), grouping atoms into layers parallel to the interface plane, and combining the DOS contributions from all atoms within that layer, provides us with the LaDOS. The LaDOS contains the position dependence of the electronic structure normal to the interface plane, on the basis of which we can assess the contribution of differing parts of the system to the electronic structure.

Using the LaDOS method, Shi and Ramprasad studied the electronic structures of several Si-HfO_2 and SiO_2-polymer interfaces (Shi 2008; Shi and Ramprasad 2008a). SiO_2 has been a mainstay in Si-based electronic devices for last four decades (Green et al. 2001; Buchanan 1999), and its replacement by some other dielectric with a higher dielectric constant such as HfO_2 is imminent (Kingon et al. 2000; Wilk et al. 2001; Robertson et al. 2007). Several interface chemistry related issues, especially the role played by atomic level point defects, are critical in determining its electronic structure. Likewise, interfaces between polymeric and inorganic systems are important as such interfaces are frequently encountered in polymer nanocomposites in which the interfaces appear to play a particularly important role in determining conduction and dielectric properties (Nelson 2006; Roy et al. 2005).

Figure 5.5 (top) shows a coherent Si-HfO_2 heterostructure, in which HfO_2 was in the tetragonal phase, together with its LaDOS profile based on DFT calculations. The interface plane was chosen such that it is parallel to the (001) planes of both Si and HfO_2, and the atomic structure at the interface is constructed so that all relevant atoms have saturated bonds conforming to standard electron counting rules (Peacock and Robertson 2004). In the interior regions of Si and HfO_2, the LaDOS shows uniform band gaps of 0.45 and 4.5 eV for Si and HfO_2, respectively (shown by horizontal lines), both of which are underestimated relative to the experimental values of 1.1 and 6.0 eV, respectively.

Close to the interface, the Si band edges transform smoothly to those of HfO_2, leading to a VBO of 3.05 eV. Since the interfacial dangling bonds are well passi-

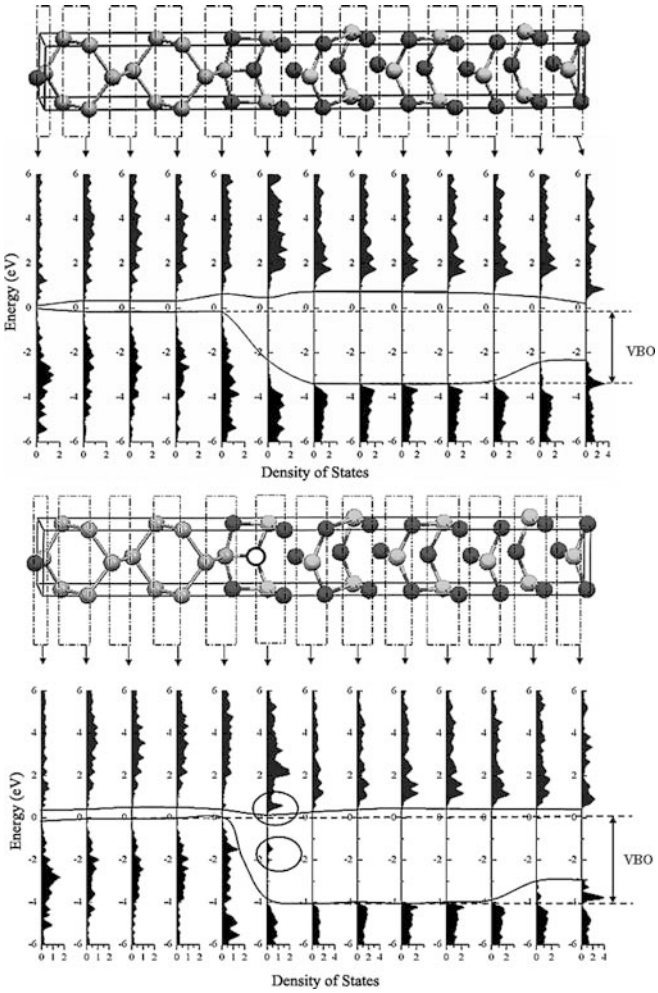

Fig. 5.5 Si-HfO_2 heterostructure model and its LaDOS profile for a defect free interface (*top*), and for the same interface with O vacancy defects close to the interface (*bottom*). Si: *light grey*, Hf: *grey*, O: *black*, O vacancy: *open circle*. Si is on the *left* and HfO_2 is on the *right*. The atomic models repeat periodically in the plane normal to the interface (*x*–*y*) plane. *Dashed rectangles* indicate atom groupings used to generate the LaDOS profiles. The zero of energy is Fermi energy. Defect states are highlighted by *circles*

vated, no defect states are detected in interface region in the LaDOS profile. Several types of such Si-HfO_2 heterojunctions were considered, differing in how the interfacial atoms are connected across the interface. The LaDOS method gives VBO values of 2.80–3.25 eV for the various Si-HfO_2 interfaces, in good agreement with experimental estimates of 2.95–3.24 eV (Sayan et al. 2004; Oshima et al. 2003; Renault et al. 2004).

Figure 5.5 (bottom) shows data for the same interface as at the top of the same figure, but for an array of O vacancies close to the interface. The presence of the O vacancies creates additional (defect) states in the band gap, shown using circles in the figure. For the configuration considered, both occupied and unoccupied defect states occur, and their energies depend on the distance of the defects from the interface (not shown in Fig. 5.5). For this class of defects, the VBO does not vary much as a result of the defects, but the presence of the defect states should impact device performance via charge trapping.

Figure 5.6 shows the atomic configuration and LaDOS profiles for a SiO_2-PVDF interface (Shi 2008; Shi and Ramprasad 2008a). An initiator species between SiO_2 and PVDF was included in an attempt to identify its role in determining the interface electronic structure. Two types of initiators were considered: a silane (SiH_4) species (Fig. 5.6 (top)) and a vinylsianediol ($SiH(OH)_2CHCH_2$) species (Fig. 5.6 (bottom)). For either choice of initiator, the LaDOS in the middle parts (bulk) of SiO_2 and polymer regions indicates large and uniform band gaps. However while the transition between the SiO_2 and polymer electronic structures is more or less smooth when silane is the initiator (with the prominent absence of defect states), the vinylsilane initiator results in occupied and unoccupied gap states that constrict somewhat the band gap in the interfacial region. Since these defect states are close to the band edges, they could serve as shallow traps or "hopping sites" for electrons or holes. Hence the appropriate choice of initiator is critical in determining charge transport along or perpendicular to the interface.

In summary, DFT based computations give reasonable descriptions of interfacial electronic structures such as barrier height and band offsets after some corrections. Particularly, the LaDOS approach is very useful for the study of electronic structure details at interfaces and can help identify trends in electronic structure which accompany physical or chemical modifications at the interface regions.

5.5 Dielectric Constant Across Interfaces

5.5.1 Background

The modern theory of polarization provides a rigorous quantum mechanical framework for the determination of the polarization (King-Smith and Vanderbilt 1993; Resta 1994) as well as the static and optical dielectric constant tensors of solids (Bernardini et al. 1997). This elegant technique has been used widely in the computation of the dielectric constant tensors for a wide variety of bulk solids (Wagmare and Rabe 2005; Detraux et al. 1998; French et al. 1994; Rignanese et al. 2001; Umari and Pasquarello 2002; Fu and Bellaiche 2003; Kunc and Resta 1983; King-Smith and Vanderbilt 1993; Zhao and Vanderbilt 2002a, b), some of which are shown in Fig. 5.2c. This method has also been used recently to explain anomalous dielectric constants in $Hf_xSi_{1-x}O_2$ (Pignedoli 2007) as well as to "design" high dielectric constant materials (Shevlin et al. 2005).

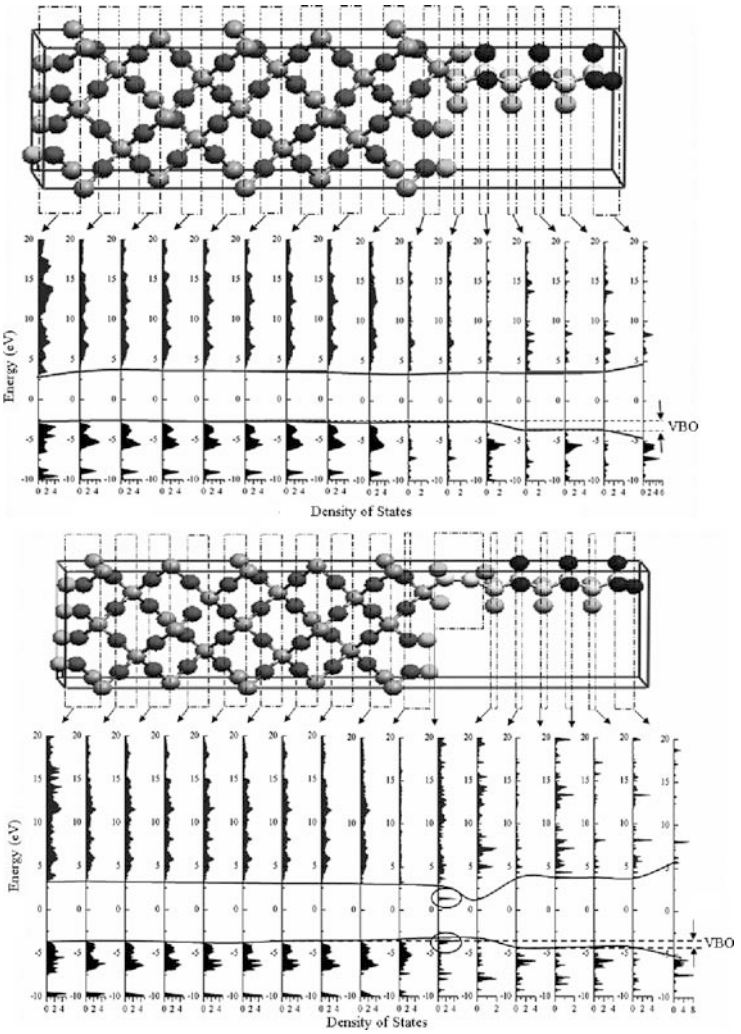

Fig. 5.6 SiO_2-PVDF heterojunction model and its LaDOS profile, in the presence of a silane (*top*) or a vinylsilane (*bottom*) initiator at the interface. Si: *light grey*, O: *black*, C: *light grey*, H: *grey*, F: *black*. The atomic models repeat periodically in the plane normal to the interface (*x*–*y*) plane. The zero of energy is Fermi energy. The defect states are highlighted by *circles*. Reprinted with permission from (Shi and Ramprasad 2008a)

In the case of multiple component systems, such as heterostructures between dissimilar materials containing interfaces, direct application of the standard approach presents difficulties. Firstly, the generally large number of atoms involved in heterostructures significantly increases the computational load to compute phonon frequencies; a necessary step in the determination of the dielectric tensor. Secondly, contributions to the dielectric constant from different parts of the heterostructure

(i.e., the *local* dielectric constant at the interface region, near-interface region, and at regions far from the interface) are inextricably combined. In order to circumvent these difficulties, recently, Giustino et al. (Giustino et al. 2003; Giustino and Pasquarello 2005) and Shi and Ramprasad (Shi and Ramprasad 2006) have introduced a practical method for the calculation of the *position-dependent*, or local, dielectric permittivity of multilayer systems in the presence of finite electric fields. These techniques go beyond the traditional ways of determining the dielectric permittivity of bulk materials (discussed above), and more recent ways of indirectly determining the surface or interface contributions to the total field-induced polarizations (Ramprasad and Shi 2005; Shi and Ramprasad 2005; Botti et al. 2002).

The simplicity of the new method to determine the position-dependent permittivity arises from the fact that most standard DFT implementations can be used without the need for additional code development. More importantly, this approach can treat finite systems such as slabs, with the bulk dielectric properties (optical and static) computed as a by-product. Within this new approach, a local permittivity function is introduced to describe variations of the dielectric response over length scales of the order of interatomic distances, which can be calculated from the local field-induced, self-consistent charge density profile, as described briefly below.

5.5.2 *Basics of the Theory of the Local Dielectric Permittivity*

The local microscopic dielectric polarization $\overrightarrow{\mathrm{p}}(\mathrm{r})$ can be obtained from the field induced charge density $\rho_{\mathrm{ind}}(\mathrm{r})$ through the in-medium Maxwell equation (Jackson 1998):

$$\nabla \cdot \overrightarrow{p}(\mathrm{r}) = -\rho_{ind}(\mathrm{r}) \tag{5.4}$$

In the case of multi-layered systems with the layers oriented along the x–y plane, such as those considered here, (5.4) reduces to:

$$\frac{d}{dz}\bar{\mathrm{p}}(\mathrm{z}) = -\bar{\rho}_{\mathrm{ind}}(\mathrm{z}) \tag{5.5}$$

where $\bar{\mathrm{p}}(\mathrm{z})$ and $\bar{\rho}_{\mathrm{ind}}(\mathrm{z})$ are the polarization and induced charge density along the z-axis, respectively, averaged along the x–y plane. The induced charge density $\bar{\rho}_{\mathrm{ind}}(\mathrm{z})$ can be evaluated as the difference of the total charge densities due to positive $(+\delta)$ and negative $(-\delta)$ external electric fields along the z-direction. The solution of (5.5) is the following:

$$\bar{\mathrm{p}}(\mathrm{z}) = \bar{\mathrm{p}}_{-\infty} - \int_{-\infty}^{z} \bar{\rho}_{ind}(\mathrm{z}')\mathrm{dz}' \tag{5.6}$$

For the case when the slab system is located about the $z = 0$ plane, the constant $\bar{\mathrm{p}}_{-\infty}$ can be set to zero as it corresponds to the polarization at $-\infty$, a region where charge density is zero.

Using the above procedure, both the optical (high frequency) and the static (low frequency) microscopic polarization can be calculated, by allowing only the electrons, or both the electrons and the atoms, to respond to the applied external electric field. The local permittivity profile can then be computed from the local polarization using:

$$\varepsilon(z) = \frac{\varepsilon_0 E_{ext}}{\varepsilon_0 E_{ext} - \bar{p}(z)} \tag{5.7}$$

where $E_{ext} = 2\delta$.

Further details of the theory of the local dielectric permittivity can be found elsewhere (Shi and Ramprasad 2006; Giustino and Pasquarello 2005; Giustino et al. 2003).

5.5.3 Applications

Next, applications of this theory are now presented to a few idealized, but technologically important, interface containing systems, including Si-SiO_2, Si-HfO_2 and polymer-SiO_2 heterostructures. As mentioned earlier, HfO_2 based electronic devices are expected to replace SiO_2 based devices in the near future. Although Hf-based oxides are thermodynamically stable on Si, they are not kinetically stable, and silicides, silicates and SiO_x can form at the interface, all of which have a much lower dielectric constant than HfO_2 (Fiorentini and Gulleri 2002; Peacock et al. 2006; Cockayne 2007; Nahar et al. 2007). An understanding of the factors that control the dielectric properties of the interface between the dielectric and other materials requires accurate determination of atomic-scale dielectric permittivity profiles across layered structures.

Figure 5.7 shows the static and optical permittivity profile across a Si-SiO_2 interface as a function of position along the direction normal to the interface (Shi and Ramprasad 2006; Shi and Ramprasad 2008a; Shi 2008). The dielectric constants in the interior of SiO_2 and Si regions are in excellent agreement with experimental values of the bulk systems (static and optical values of about 12 for Si (Balanis 1989), and 4.5 and 2.5 for SiO_2 (Ramos et al. 2004; Wolf et al. 1963), respectively). However, in the transition region between Si and SiO_2 and close to the outer surface planes, we find an enhancement of the dielectric constant compared to that of the bulk values. The deviation at the surface is due to the under-coordination of Si atoms, which renders these atoms more polarizable. The enhanced permittivity at the interface (on the SiO_2 side) is caused by the Si atoms in SiO_2 in multiple oxidation states (i.e., Si, Si^{+1}, Si^{+2} and Si^{+3}) and is in quantitative agreement with capacitance measurements performed on ultra-thin SiO_2 layers on Si (Chang et al. 2002).

Figure 5.8 shows similar dielectric constant profiles for a simple epitaxial model of the Si-HfO_2 interface. The model was created by placing an O-terminated (001) tetragonal HfO_2 slab on Si such that the HfO_2 slab was matched coherently on top of Si (Shi and Ramprasad 2007; Shi 2008). The thickness of Si and HfO_2 layers

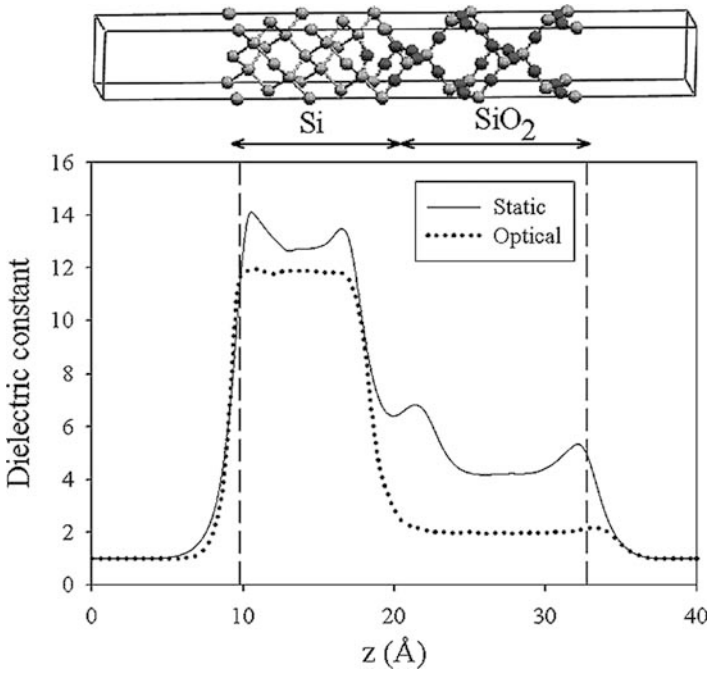

Fig. 5.7 *Above*: Atomic model of (001) Si-SiO_2 interface. Si: *light grey*, O: *black*. The atomic model repeats periodically in the plane normal to the interface (*x*–*y*) plane. *Below*: Static (*solid*) and optical (*dotted*) dielectric constant of Si-SiO_2 stack as a function of position z normal to the interface. Reprinted with permission from (Shi and Ramprasad 2006)

were 10.95 and 19.91 Å, respectively. The resulting relaxed structure shows that half the interface O atoms move downwards towards Si and the other half move upwards towards the Hf layer (Fig. 5.8), thereby forming Si-O-Si and Hf-O-Hf bonds which passivate all interfacial Si and Hf atoms. From the position-dependent dielectric constant along the normal to the Si-HfO_2 interface, the dielectric constants in the interior of the HfO_2 and Si regions again match well with the corresponding experimental bulk values. The static and optical permittivities of tetragonal HfO_2 are 16 and 5, respectively (Zhao and Vanderbilt 2002a, b; Rignanese et al. 2004). As in the Si-SiO_2 case, enhancement of the permittivities at the free surfaces compared to the bulk values can be seen, again due to under-coordination of surface atoms. However, in marked contrast with the Si-SiO_2 case, a decrease in the permittivity values results in the Si-HfO_2 interface region relative to the free surfaces. This important behavior, even in such an idealized interface, results from the interface Si and Hf atoms being passivated by the O atoms, which produces species in their nominal oxidation states (as indicated by a Mulliken charge analysis) and with lower polarizability than those at the free surfaces.

Nanocomposites made by blending oxide nanoparticles with polymers are known to display higher effective permittivities than expected from the permittivities of the

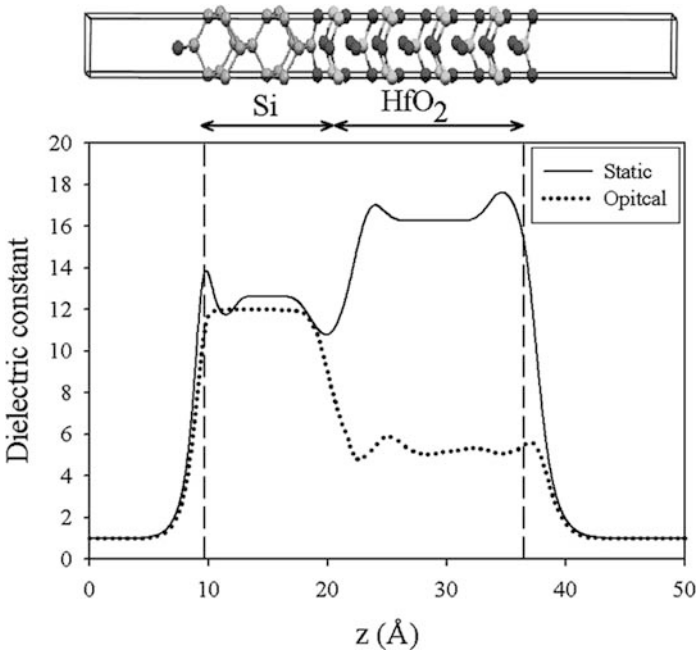

Fig. 5.8 *Above*: Atomic model of the (001) Si-HfO_2 interface with O termination. Si: *light grey*, O: *black*, Hf: *grey*. The atomic model repeats periodically in the plane normal to the interface (*x*–*y*) plane. *Below*: Static (*solid*) and optical (*dotted*) dielectric constant of the Si-HfO_2 interface as a function of position z normal to the interface

components, indicating the role played by enhanced interfacial polarization (Ray and Okamoto 2003; Rao and Wong 2004; O'Brian et al. 2001; Murugaraj et al. 2005). Here, we explore factors that could result in such permittivity enhancements in polymeric systems.

Shi and Ramprasad (Shi and Ramprasad 2006) have determined the position-dependent dielectric permittivity profile across a PE-SiO_2 interface, composed of SiO_2 in the α-quartz phase of thickness 15.96 Å; PE was approximated by a $C_{12}H_{26}$ molecule. Figure 5.9 shows the dielectric constant as a function of position along the normal SiO_2-polymer interface. Similar behavior of the dielectric constant is observed as with the Si-SiO_2 interface. The agreement is excellent for the dielectric constant in the interior region of SiO_2 and polymer ($C_{12}H_{26}$) with the corresponding experimental single component bulk values, and the dielectric constant on the SiO_2 side of the interface is enhanced. Analysis of the Mulliken charges of the atoms indicates that C atoms closest to the interface are in their nominal oxidation states (i.e., in oxidation states similar to that of C atoms in the interior of the polymer chain), whereas the Si and O atoms close to the interface are in varying oxidation states similar to that in the Si-SiO_2 case (Levien et al. 1980).

Permittivity enhancement at the interface is consistent with some prior experimental work (Murugaraj et al. 2005). Nevertheless, the SiO_2-polymer system

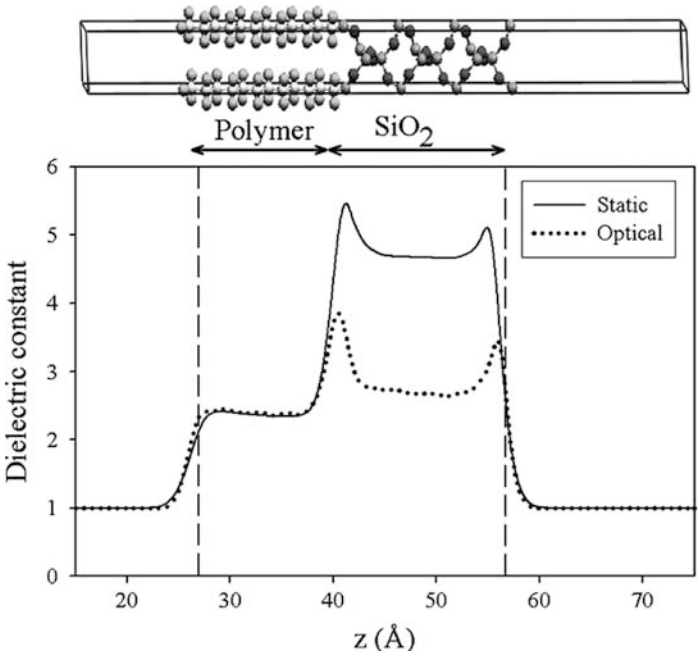

Fig. 5.9 *Above*: Atomic model of SiO_2-polymer. Si: *light grey*, O: *black*, C: *light grey*, H: *grey*. *Below*: Static (*solid*) and optical (*dotted*) dielectric constant of $C_{12}H_{25}$-SiO_2 stack as a function of position z normal to the interface. Reprinted with permission from (Shi and Ramprasad 2006)

modeled here corresponds to a situation in which the SiO_2 surface is "untreated" (which is the experimental situation involving "blends" as in (Murugaraj et al. 2005)). However, typical polymeric nanocomposites are made using silane-treated SiO_2 (Roy et al. 2005; Nelson 2006; Cao et al. 2004; Kaufhold et al. 2002). Silane treatment accomplishes the twin purposes of passivation of dangling bonds on silica surfaces by the silane-based initiator molecules and the creation of chemical bonds between the initiator and the polymer chains. Thus silane treatment is expected to *decrease* the polarizability and permittivity at the interface. In fact, recent experimental work indicates that the incorporation of silane-treated SiO_2 nanoparticles into polyethylene results in decreased effective permittivities (although the permittivity of SiO_2 is higher than that of the host polymer) (Roy et al. 2005). A more comprehensive analysis of SiO_2-polymer interfaces is necessary to understand the circumstances that would result in a permittivity increase or decrease at the interface.

Although to date, the method of the local dielectric permittivity has been applied to only coherent interfaces between dissimilar materials, this approach to computing the local polarization and permittivity can be used to explore systematically a variety of realistic situations, including atomic-level defects (e.g., vacancies), disorder, impurities and initiator species at the interface.

5.6 Electron-Phonon Interactions

Nanocomposites based on a polymer host matrix filled with inorganic dielectric nanoparticles show promise for high voltage applications (Nelson 2006; Roy et al. 2005). Recent work indicates that the incorporation of SiO_2 nanoparticles into polyethylene increases the breakdown strength, while incorporation of micron sized SiO_2 particles does not (Roy et al. 2005), which suggests that the interface between SiO_2 and polymer plays an important role in improving the dielectric strength (Roy et al. 2005).

As discussed in Sect. 5.4, the electronic structure at the interface between a polymer and SiO_2, in the presence of a typical initiator species such as vinyl silane, displays interface states. Such interface states could act as potential electron traps, thereby scavenging "hot" electrons. However, a possible dissipative mechanism for the energy released during the trapping process is required. Electron-phonon interactions could accomplish this dissipation, for instance, as a result of strong coupling between these interface states and phonons in SiO_2. Such a coupling, if present, could potentially increase the dielectric breakdown strength of the composite. In fact, the strong electron-phonon coupling mechanism has been instrumental in explaining the superior breakdown strength of SiO_2 by the microelectronics community (Arnold et al. 1994). A systematic investigation of various types of inorganic oxide-polymer interfaces, focusing on interface states, phonons, and interaction between these two will help to identify trends related to dielectric breakdown strength.

Phonons are collective, quantized vibrations of groups of atoms, which when excited, propagate through a material. DFT methods have been successful in determining vibration and phonon spectra, which involve computation of the second derivatives of the energy with respect to atomic positions (see, for instance, Fig. 5.2a, b; elastic moduli, shown in Fig. 5.2b, are also related to second derivatives of energy). One option to estimate the coupling between phonon modes and electronic states is the following two-step approach (Shi 2008; Shi and Ramprasad 2008b). First, the phonon band structure, or spectrum, is determined, resulting in all the phonon frequencies and eigenmodes (which is a computationally laborious process, and scales as N^3, where N in the number of atoms in the system). Second, for each phonon eigenmode, the atoms of the system are displaced by a "distance" $\delta\lambda$ from their equilibrium atomic configuration appropriate to that mode, and the associated shifts in each electronic level $\delta\varepsilon$ determined. With the knowledge of the phonon frequencies, modes and changes of the electronic eigenenergies caused by the phonon mode displacements, the electron-phonon coupling parameter can be estimated as $\delta\varepsilon/\delta\lambda$ (in units of energy per length).

Using this strategy, defect-free bulk SiO_2 and Al_2O_3 were investigated resulting in the electron-phonon coupling parameter as a function of electron energy and phonon frequency shown in Fig. 5.10. The coupling parameter is zero in the band gap for both systems, but at other energies, it is much greater in the case of SiO_2 than Al_2O_3.

Point defects such as O vacancies create defect states in the band gap of an otherwise perfect bulk system, similar to the trap states at interfaces. These are much

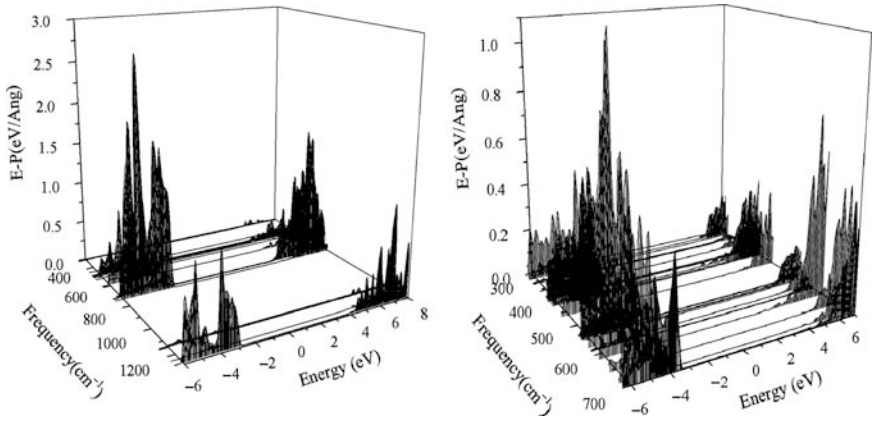

Fig. 5.10 The electron-phonon coupling for bulk SiO_2 (*left*) and bulk Al_2O_3 (*right*). Reprinted with permission from (Shi and Ramprasad 2008b)

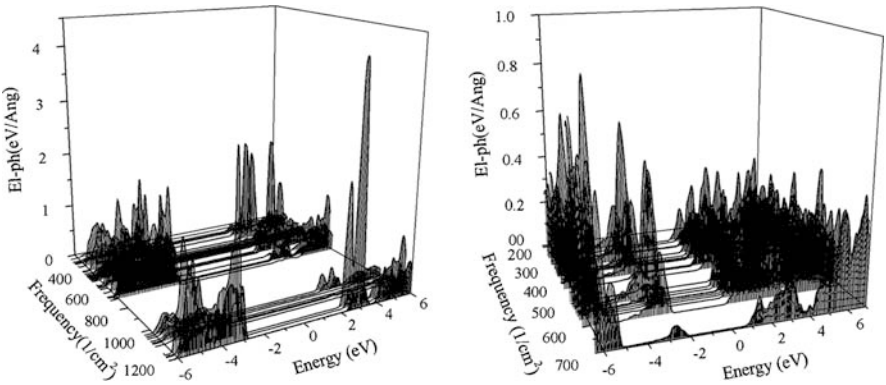

Fig. 5.11 Electron-phonon coupling in bulk SiO_2 (*left*) and bulk Al_2O_3 (*right*) with O vacancies. The *light grey* regions (energy ranges: 2–4 eV for SiO_2 and −5 to −1 eV for Al_2O_3) indicate the coupling of phonons with the electron at the defects states induced in the band gap region. Reprinted with permission from (Shi and Ramprasad 2008b)

easier systems to treat than heterostructures owing to the much smaller number of atoms, and hence were attempted first. The calculated electron-phonon coupling parameter results for SiO_2 and Al_2O_3 with O vacancy point defects are shown in Fig. 5.11. Significant electron-phonon coupling is observed for SiO_2 point defect states residing in the band gap (indicated in light grey) relative to the other "bulk" states. In the case of Al_2O_3, point defect states interact with phonons in the system but the extent of this interaction is weaker than in defect-free bulk Al_2O_3.

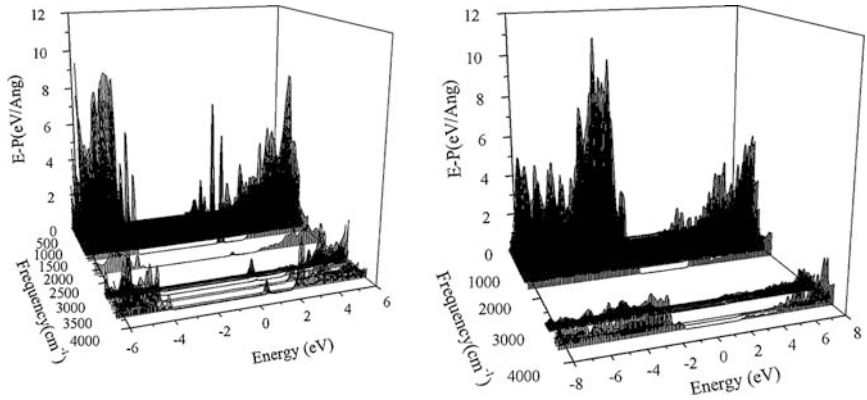

Fig. 5.12 Electron-phonon coupling for the SiO_2-vinysilanediol-PE interface (*left*) and the Al_2O_3-vinysilanediol-PE interface. Reprinted with permission from (Shi and Ramprasad 2008b)

Finally, the same procedure has been applied to SiO_2-PE and Al_2O_3-PE heterostructures, in which the polymer was modeled using a hydrocarbon chain as before, and the interface contained a vinyl silane initiator. In both cases, interfacial defect states were found in the band gap region, much as in Fig. 5.6 (bottom). The calculated electron-phonon coupling parameter for the SiO_2-polymer heterostructure is shown in Fig. 5.12 (left). As can be seen, the coupling of electrons at the interface state (shown in light grey) with phonons is high, similar to the behavior of bulk SiO_2 with O vacancies. On the other hand, from Fig. 5.12 (right) which applies to the Al_2O_3-PE heterostructure, the coupling parameter corresponding to the interface trap energy levels is relatively low. The rather large coupling parameter for the other states of both heterostructures is due to the contribution from the atoms close to the interface. The qualitatively differing levels of electron-phonon coupling displayed by the interface states in the two heterostructures is indicative of a more efficient energy loss mechanism in SiO_2 than in Al_2O_3, and correlate well with the observed superior breakdown strength of SiO_2. Further work spanning a wider range of oxides and initiators is necessary to establish a more comprehensive understanding of this complex subject.

5.7 Stability of Interfaces

As discussed so far, interfaces control many important electrical properties of materials. An important property which has been ignored so far is the bonding and stability of an interface itself, which can be studied using *ab initio* DFT techniques. Coverage of this topic here will be brief, and the reader is referred to other reviews on this subject (Finnis 1996; Munoz et al. 2006).

Microscopically, the strength of the chemical bonds among atoms making up an interface determines its mechanical strength (see Chap. 6) which is characterized by the work of adhesion or the energy required to separate the junctions at the interface. The accurate measurement of the work of adhesion is intricate. Also, the interfacial region, frequently a few atomic layers thick, poses challenges for experimental characterization, which makes atomic scale modeling a desirable technique for such investigations.

The most convenient theoretical bases for characterizing interface stability are the ideal work of separation, defined as the energy needed to cleave the interface into two free surfaces, or the interface free energy. In multiple component systems and non-stoichiometric interfaces this has to be determined in terms of the chemical potentials of the components. Motivated by situations encountered in electronic devices, interfaces between Si and various metal oxides have been studied extensively (Tang et al. 2007; Dong et al. 2005; Peacock and Robertson 2004; Puthenkovilakam and Chang 2004; Puthenkovilakam and Chang 2004; Fiorentini and Gulleri 2002), including the Si-SiO_2, Si-HfO_2, Si-ZrO_2, Si-Al_2O_3, Si-hafnium silicate interfaces. Electron counting rules that draw on "chemical intuition" have been developed based on these efforts and have been used to predict stable interface structures. Likewise, metal-metal oxide interfaces, including Pt-HfO_2, Re-HfO_2, Mo-HfO_2, WC-HfO_2, TiN-HfO_2, etc., have been studied extensively, and the stability of interfaces as a function of the interfacial oxygen content has been clarified (Gavrikov et al. 2007; Fonseca and Knizhnik 2006; Knizhnik et al. 2006a, b). A new development in this arena is the use of combined DFT-thermodynamic methods to determine the relationship between interfacial structure and the environment (i.e., temperature and partial pressure of the various gas phase species involved, e.g., oxygen) (Gavrikov et al. 2007).

Control of equilibrium shapes and surface facets in nanocrystals through proper choices of chemical environments and surface functionalization is also an active area of research (Manna et al. 2002). Recent DFT work in this area is also particularly notable (Pilania et al. 2009; Rempel et al. 2006; Manna et al. 2005).

5.8 Impurity Segregation at Interfaces

Migration of impurities in response to electric fields, temperature gradients, and chemical or thermodynamic driving forces can modify the physical structure, and, consequently, the electronic structure of the system. For instance, segregation of an ensemble of impurity species to an interface can mediate chemical reactions, resulting in the formation of a new phase at the interface. The properties of this interface phase (e.g., dielectric constant, CBM, VBM, etc.) may differ greatly from the parent phases, leading to unanticipated electrical characteristics. This type of strange behavior has plagued the Si-HfO_2 interface containing devices (Lee et al. 2004). One of the critical factors that has led to the choice of HfO_2 as a replacement of SiO_2 in electronics devices is the expected thermodynamic stability of HfO_2 in contact with

Si (Wallace and Wilk 2003). However, depending on the processing conditions, the formation of undesired silica, Hf silicides and silicates at the interfaces has been observed after the post-deposition annealing (Baik et al. 2004; Cho et al. 2005; Qiu et al. 2006). In general, annealing in oxygen ambient results in interfacial silica or Hf silicate, and annealing in oxygen deficient atmosphere causes interfacial Hf silicides. An understanding of the mechanisms controlling such behavior is gradually emerging based on point defect diffusion and segregation as described below.

The segregation of a single O interstitial (Tang and Ramprasad 2007) and vacancy (Tang et al. 2007) in Si-HfO_2 systems were studied using a coherent epitaxial interface model formed by Si and monoclinic HfO_2. For O interstitial segregation, as shown in Fig. 5.13 (top), an isolated O interstitial was created within the system at locations close to the numbered lattice O atoms. The formation energies of the interstitial at these locations, and the energy barriers for its hopping between these locations, are shown in Fig. 5.13 (bottom). Two important conclusions can be drawn from the energy profile. First, a strong thermodynamic driving force (about 1 eV) exists for an O interstitial to segregate from bulk HfO_2 to interfacial HfO_2

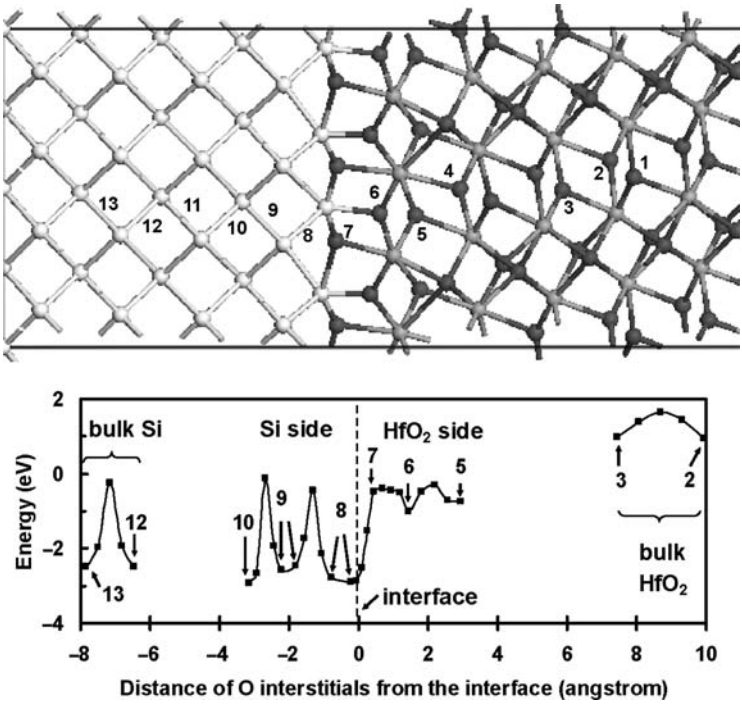

Fig. 5.13 (*top*) Si-HfO_2 heterojunction. Si: *white*, Hf: *grey*, O: *dark*. An O interstitial can sit close to the numbered sites. (*bottom*) Energy profile for O interstitial segregation. The energies of numbered points represent the formation energies at the corresponding locations, and the other points in between represent the relative energies of the system with intermediate geometry configurations during the hopping of O interstitial. Reprinted with permission from (Tang and Ramprasad 2007)

and then into Si (by a further 3 eV). Second, a strong kinetic driving force exists for the O interstitial to segregate from HfO_2 to Si layers close to the interface, as indicated by the almost-zero migration barrier between sites 7 and 8, while its further penetration into bulk Si is hampered by the large migration barriers. The calculated migration barrier of an O interstitial in bulk Si is 2.3 eV, in good agreement with the experimental value of 2.4 eV (Mikkelsen 1981). These results indicate the general tendency for interstitials to segregate to the Si side of the Si-HfO_2 interface and provide a mechanism for the formation of interfacial silica after annealing in an oxygen rich ambient.

Similarly, an O vacancy shows a tendency to segregate to the interface, which results in bonds between Si and Hf atoms, i.e., the formation of interfacial Hf silicide (Tang et al. 2007). The migration of Hf vacancies was also investigated (Tang and Ramprasad 2008a). After the favored segregation of a Hf vacancy to the interface, a neighboring Si atom tends to occupy the Hf vacancy site, aiding the formation of Hf silicates. Segregation of a collection of point defects simultaneously to the interface (Tang and Ramprasad 2008b) has provided a comprehensive understanding of the conditions that generate various types of interfaces.

DFT computations can thus be valuable in identifying driving forces for impurity segregation and/or formation of new phases at interfaces. The ability to treat segregation along with determination of interface stability discussed briefly in Sect. 5.7 will be particularly useful within the context of polymer nanocomposites, where the surface treatment of nanoparticles can be used to "tune" their dielectric properties.

5.9 Concluding Thoughts

Several recent developments in the area of atomic-level interface modeling made possible by modern ab initio DFT based methods were described in this chapter. The electronic structure and dielectric constant across interfaces, electron-phonon interactions, stability of interfaces and impurity segregation to interfaces were discussed. The DFT approach is complementary to experiments and more macroscopic modeling approaches, and can provide fundamental insights and systematic trends, enabling the optimization of the design of nanodielectrics.

Going into the future, a promising and exciting direction would be the development of unified charge transport, defect dynamics and electric field distribution models for nanodielectric devices, with the parameters of such models determined through DFT computations.

Acknowledgements The authors would like to thank Dr. Steve Boggs for stimulating and useful discussions, and for a critical reading of this chapter. The authors also acknowledge financial support of their nanodielectrics research by the Office of Naval Research, the National Science Foundation, the ACS Petroleum Research Fund and the Electric Power Research Institute.

References

Arnold D, Cartier E, DiMaria DJ (1994) Theory of high-field electron transport and impact ionization in silicon dioxide. Phys Rev B 49:10278–10297

Baik HS, Kim M, Park GS et al (2004) Interface structure and non-stoichiometry in HfO_2 dielectrics. Appl Phys Lett 85:672–674

Becke AD (1986) Completely numerical calculations on diatomic molecules in the local-density approximation. Phys Rev A 33:2786–2788

Bernardini F, Fiorentini V (1998) Electronic dielectric constants of insulators calculated by the polarization method. Phys Rev B 58:15292–15295

Bernardini F, Fiorentini V, Vanderbilt D (1997) Polarization-based calculation of the dielectric tensor of polar crystals. Phys Rev Lett 79:3958–3961

Bloor D (1976) Correlation of experimental and theoretical electron band energies of polyethylene. Chem Phys Lett 40:323–325

Boggs S (2005) Very high field phenomena in dielectrics. Trans IEEE DEI-12:929–938

Boggs S (2004) A rational consideration of space charge. IEEE Electr Insul Mag 20:22–27

Botti S, Vast N, Reining L et al (2002) Ab initio calculations of the anisotropic dielectric tensor of GaAs/AlAs superlattices. Phys Rev Lett 89:216803

Bottin F, Leroux S, Knyazev A et al (2008) Large-scale ab initio calculations based on three levels of parallelization. Comput Mater Sci 42:329–336

Buchanan DA (1999) Scaling the gate dielectric: materials, integration, and reliability. IBM J Res Dev 43:245–264

Cao Y, Irwin PC, Younsi K (2004) The future of nanodielectrics in the electrical power industry. Trans IEEE DEI-11:797–807

Chang HS, Yang HD, Hwang H (2002) Measurement of the physical and electrical thickness of ultrathin gate oxides. J Vac Sci Technol B 20:1836–1842

Cho DY, Park KS, Choi BH (2005) Control of silicidation in HfO_2/Si(100) interfaces. Appl Phys Lett 86:041913

Chu B, Zhou X, Ren K et al (2006) A dielectric polymer with high electric energy density and fast discharge speed. Science 313:334–336

Cockayne E (2007) Influence of oxygen vacancies on the dielectric properties of hafnia: first-principles calculations. Phys Rev B 75:094103

Detraux F, Ghosez Ph, Gonze X (1998) Long-range coulomb interaction in ZrO_2. Phys Rev Lett 81:3297–3297

Dong YF, Feng YP, Wang SJ et al (2005) First-principles study of ZrO_2/Si interfaces: energetics and band offsets. Phys Rev B 72:045327

Dudde R, Reihl B (1992) Complete electronic structure of oriented films of hexatriacontane. Chem Phys Lett 196:91–96

Finnis MW (1996) The theory of metal-ceramic interfaces. J Phys Condens Matter 8:5811–5836

Fiorentini V, Gulleri G (2002) Theoretical evaluation of zirconia and hafnia as gate oxides for Si microelectronics. Phys Rev Lett 89:266101

Fonseca LRC, Knizhnik AA (2006) First-principles calculation of the TiN effective work function on SiO_2 and on HfO_2. Phys Rev B 74:195304

French RH, Glass SJ, Ohuchi FS et al (1994) Experimental and theoretical determination of the electronic structure and optical properties of three phases of ZrO_2. Phys Rev B 49:5133–5142

Fu H, Bellaiche L (2003) First-principles determination of electromechanical responses of solids under finite electric fields. Phys Rev Lett 91:057601

Gavrikov AV, Knizhnik AA, Bagatur'yants AA et al (2007) Oxidation of the Pt/HfO_2 interface: the role of the oxygen chemical potential. J Appl Phys 101:014310

Giustino F, Pasquarello A (2005) Theory of atomic-scale dielectric permittivity at insulator interfaces. Phys Rev B 71:144104

Giustino F, Umari P, Pasquarello A (2003) Dielectric discontinuity at interfaces in the atomic-scale limit: permittivity of ultrathin oxide films on silicon. Phys Rev Lett 91:267601

Green ML, Gusev EP, Degreave R et al (2001) Ultrathin (< 4 nm) SiO_2 and Si-O-N gate dielectric layers for silicon microelectronics: understanding the processing, structure, and physical and electrical limits. J Appl Phys 90:2057–2121

Hafner J, Wolverton C, Ceder G (2006) Toward computational materials design: the impact of density functional theory on materials research. MRS Bull 31:659–665

Hohenberg P, Kohn W (1964) Inhomogeneous electron gas. Phys Rev 136:B864–B871

Ieda M (1984) Electrical conduction and carrier traps in polymeric materials. Trans IEEE EI-19:162–178

Jackson JD (1998) Classical electrodynamics. Wiley, New York

Kamran S, Chen K, Chen L (2009) Ab initio examination of ductility features of fcc metals. Phys Rev B 79:024106

Kaufhold M, Schafer K, Bauer K et al (2002) Interface phenomena in stator winding insulation – Challenges in design, diagnosis, and service experience. IEEE Electr Insul Mag 18:27–36

King-Smith RD, Vanderbilt D (1993) Theory of polarization of crystalline solids. Phys Rev B 47:1651–1654

Kingon AI, Maria JP, Streiffer SK (2000) Alternative dielectrics to silicon dioxide for memory and logic devices. Nature 406:1032–1038

Knizhnik AA, Gavrikov AV, Safonov AA et al (2006a) Segregation trends of the metal alloys Mo-Re and Mo-Pt on HfO_2: a first-principles study. J Appl Phys 100:013506

Knizhnik AA, Safonov AA, Iskandarova IM et al (2006b) First-principles investigation of the WC/HfO_2 interface properties. J Appl Phys 99:084104

Kobayashi K (2001) First-principles study of the electronic properties of transition metal nitride surfaces. Surf Sci 493:665–670

Kohn W, Sham LJ (1965) Self-consistent equations including exchange and correlation effects. Phys Rev 140:A1133–A1138

Kunc K, Resta R (1983) External fields in the self-consistent theory of electronic states: a new method for direct evaluation of macroscopic and microscopic dielectric response. Phys Rev Lett 51:686–689

Lee JC, Oh SJ, Cho MJ et al (2004) Chemical structure of the interface in ultrathin HfO_2/Si films. Appl Phys Lett 84:1305–1307

Levien L, Prewitt CT, Weidner DJ (1980) Structure and elastic properties of quartz at pressure. Am Miner 65:920–930

Lewis TJ (1994) Nanometric dielectrics. Trans IEEE DEI-1:812–825

Lewis TJ (2004) Interfaces are the dominant feature of dielectrics at the nanometric level. Trans IEEE DEI-11:739–753

Lombardo S, Stathis JH, Linder BP et al (2005) Dielectric breakdown mechanisms in gate oxides. J Appl Phys 98:121301

Manna L, Scher EC, Alivisatos AP (2002) Shape control of colloidal semiconductor nanocrystals. J Cluster Sci 13:521–532

Manna L, Wang LW, Cingolani R et al (2005) First-principles modeling of unpassivated and surfactant-passivated bulk facets of wurtzite CdSe: a model system for studying the anisotropic rowth of CdSe nanocrystals. J Phys Chem B 109:6183–6192

Marder MP (2000) Condensed matter physics. Wiley, New York

Martin R (2004) Electronic structure: basic theory and practical methods. Cambridge University Press, Cambridge

McPherson JW, Kim J, Shanware A et al (2003) Trends in the ultimate breakdown strength of high dielectric constant materials. Trans IEEE ED-50:1771–1778

Meunier M, Quirke N (2000) Molecular modeling of electron trapping in polymer insulators. J Chem Phys 113:369–376

Meunier M, Quirke N, Aslanides A (2001) Molecular modeling of electron traps in polymer insulators: chemical defects and impurities. J Chem Phys 115:2876–2881

Miao MS, Van Camp PE, Van Doren VE et al (1996) Conformation and electronic structure of polyethylene: a density-functional approach. Phys Rev B 54:10430–10435

Mikkelsen JC (1982) Diffusivity of oxygen in silicon during steam oxidation. Appl Phys Lett 40:336–337
Mitáš L, Martin RM (1994) Quantum monte carlo of nitrogen: atom, dimmer, atomic, and molecular solids. Phys Rev Lett 72:2438–2441
Montanari B, Jones RO (1997) Density functional study of crystalline polyethylene. Chem Phys Lett 272:347–352
Murugaraj P, Mainwaring D, Mora-Huertas N (2005) Dielectric enhancement in polymer-nanoparticle composites through interphase polarizability. J Appl Phys 98:054304
Munoz MC, Gallego S, Beltran JI et al (2006) Adhesion at metal-ZrO_2 interfaces. Surf Sci Rep 61:303–344
Nahar RK, Singh V, Sharma A (2007) Study of electrical and microstructure properties of high dielectric hafnium oxide thin film for MOS devices. J Mater Sci Mater Electron 18:615–619
Nelson JK (2006) The promise of dielectric nanocomposites. IEEE Int Symp Electr Insul (ISEI): 452–457
O'Brian S, Brus L, Murray CB (2001) Synthesis of monodisperse nanoparticles of barium titanate: toward a generalized strategy of oxide nanoparticle synthesis. J Am Chem Soc 123:12085–12086
O'Dwyer JJ (1973) Theory of electrical conduction and breakdown in solid dielectrics (Monographs on the physics and chemistry of materials). Oxford University Press, London
Oshima M, Toyoda S, Okumura T (2003) Chemistry and band offsets of HfO_2 thin films for gate insulators. Appl Phys Lett 83:2172–2174
Paulus B (2006) The method of increments – a wavefunction-based ab initio correlation method for solids. Phys Rep 428:1–52
Peacock PW, Robertson J (2002) Band offsets and Schottky barrier heights of high dielectric constant oxides. J Appl Phys 92:4712–4721
Peacock PW, Robertson J (2004) Bonding, energies, and band offsets of Si-ZrO_2 and HfO_2 gate oxide interfaces. Phys Rev Lett 92:057601
Peacock PW, Xiong K, Tse K et al (2006) Bonding and interface states of $Si:HfO_2$ and $Si:ZrO_2$ interfaces. Phys Rev B 73:075328
Pignedoli CA, Curioni A, Andreoni W (2007) Anomalous behavior of the dielectric constant of hafnium silicates: a first principles study. Phys Rev Lett 98:037602
Pilania G, Sadowski T, Ramprasad R (2009) Oxygen adsorption on CdSe surfaces: case study of asymmetric anisotropic growth through ab initio computations. J Phys Chem C 113:1863–1871
Puthenkovilakam R, Chang JP (2004) An accurate determination of barrier heights at the HfO_2/Si interfaces. J Appl Phys 96:2701–2707
Puthenkovilakam R, Carter EA, Chang JP (2004) First-principles exploration of alternative gate dielectrics: electronic structure of ZrO_2/Si and $ZrSiO_4$/Si interfaces. Phys Rev B 69:155329
Qiu XY, Liu HW, Fang F (2006) Phase separation and interfacial reaction of high-k $HfAlO_x$ films prepared by pulsed-laser deposition in oxygen-deficient ambient. Appl Phys Lett 88:072906
Ramos LE, Furthmuller J, Bechstedt F (2004) Quasiparticle band structures and optical spectra of β-cristobalite SiO_2. Phys Rev B 69:085102
Ramprasad R, Glassford KM, Adams JB et al (1996) CO on Pd(110): determination of the optimal adsorption site. Surf Sci 360:31–42
Ramprasad R, Shi N (2005) Dielectric properties of nanoscale HfO_2 slabs. Phys Rev B 72:052107
Ranjan V, Yu L, Nardelli MB et al (2007) Phase equilibria in high energy density PVDF-based polymers. Phys Rev Lett 99:047801
Rao Y, Wong CP (2004) Material characterization of a high-dielectric constant polymer-ceramic composite for embedded capacitor for RF applications. J Appl Polym Sci 92:2228–2231
Ray SS, Okamoto M (2003) Polymer/layered silicate nanocomposites: a review from preparation to processing. Prog Polym Sci 28:1539–1641
Rempel JY, Trout BL, Bawendi MG et al (2006) Density functional theory study of ligand binding on CdSe (0001), (000–1), and (11–20) single crystal relaxed and reconstructed surfaces: implications for nanocrystalline growth. J Phys Chem B 110:18007–18016

Renault O, Barrett NT, Samour D (2004) Electronics of SiO_2/HfO_2 interface by soft x-ray photoemission spectroscopy. Surf Sci 566:526–531
Resta R (1994) Macroscopic polarization in crystalline dielectrics: the geometric phase approach. Rev Mod Phys 66:899–915
Righi MC, Scandolo S, Serra S et al (2001) Surface states and negative electron affinity in polyethylene. Phys Rev Lett 87:076802
Rignanese GM, Detraux F, Gonze X et al (2001) First-principles study of dynamical and dielectric properties of tetragonal zirconia. Phys Rev B 64:134301
Rignanese GM, Gonze X, Jun G et al (2004) First-principles investigation of high-k dielectrics: comparison between the silicates and oxides of hafnium and zirconium. Phys Rev B 69:184301
Robertson J, Falabretti B (2006) Band offsets of high K gate oxides on III–V semiconductors. J Appl Phys 100:014111
Robertson J, Xiong K, Clark SJ (2006) Band gaps and defect levels in functional oxides. Thin Solid Films 496:1–7
Robertson J, Sharia O, Demkov AA (2007) Fermi level pinning by defects in HfO_2-metal gate stacks. Appl Phys Lett 91:132912
Roy M, Nelson JK, MacCrone RK et al (2005) Polymer nanocomposite dielectrics – the role of the interface. Trans IEEE DEI-12:629–643
Rusu PC, Brocks G (2006) Work functions of self-assembled monolayers on metal surfaces by first-principles calculations. Phys Rev B 74:073414
Sayan S, Emge T, Garfunkel E et al (2004) Band alignment issues related to HfO_2/SiO_2/p-Si gate stacks. J Appl Phys 96:7485–7491
Serra S, Tosatti E, Iarlori S et al (2000) Interchain electron states in polyethylene. Phys Rev B 62:4389–4393
Shevlin SA, Curioni A, Andreoni W (2005) Ab initio design of high-k dielectrics: $La_xY_{1-x}AlO_3$. Phys Rev Lett 94:146401
Shi N (2008) Properties of nanoscale dielectrics from first principles computations. PhD thesis, University of Connecticut, Storrs
Shi N, Ramprasad R (2005) Dielectric properties of ultrathin SiO_2 slabs. Appl Phys Lett 87:262102
Shi N, Ramprasad R (2006) Atomic-scale dielectric permittivity profiles in slabs and multilayers. Phys Rev B 74:045318
Shi N, Ramprasad R (2007) Local dielectric permittivity of HfO_2 based slabs and stacks: a first principles study. Appl Phys Lett 91:242906
Shi N, Ramprasad R (2008a) Local properties at interfaces in nanodielectrics: an ab initio computational study. Trans IEEE DEI-15:170–177
Shi N, Ramprasad R (2008b) Program on technology innovation: computational investigation of XLPE with SiO_2 nanofillers. EPRI Technical Update
Shishkin M, Marsman M, Kresse G (2007) Accurate quasiparticle spectra from self-consistent GW calculations with vertex corrections. Phys Rev Lett 99:246403
Smelyansky VI, Tse JS (1995) Theoretical study on the high-pressure phase transformation in ZnSe. Phys Rev B 52:4658–4661
Springborg M, Lev M (1989) Electronic structures of polyethylene and polytetrafluoroethylene. Phys Rev B 40:3333–3339
Sun G, Kürti J, Rajczy P et al (2003) Performance of the Vienna ab initio simulation package (VASP) in chemical applications. J Mol Struct (Theochem) 624:37–45
Tang C, Ramprasad R (2007) Ab initio study of oxygen interstitial diffusion near Si : HfO_2 interfaces. Phys Rev B 75:241302
Tang C, Ramprasad R (2008a) A study of Hf vacancies at Si : HfO_2 heterojunctions. Appl Phys Lett 92:152911
Tang C, Ramprasad R (2008b) Oxygen defect accumulation at Si : HfO_2 interfaces. Appl Phys Lett 92:182908
Tang C, Tuttle B, Ramprasad R (2007) Diffusion of O vacancies near Si : HfO_2 interfaces: an ab initio investigation. Phys Rev B 76:073306

Teyssedre G, Laurent C (2005) Charge transport modeling in insulating polymers: from molecular to macroscopic scale. Trans IEEE DEI-12:857–875

Tuttle BR, Tang C, Ramprasad R (2007) First-principles study of the valence band offset between silicon and hafnia. Phys Rev B 75:235324

Ueno N, Sugita K, Seki K et al (1986) Low-energy electron transmission and secondary-electron emission experiments on crystalline and molten long-chain alkanes. Phys Rev B 34:6386–6393

Umari P, Pasquarello A (2002) Ab initio molecular dynamics in a finite homogeneous electric field. Phys Rev Lett 89:157602

Van de Walle CG, Martin RM (1987) Theoretical study of band offsets at semiconductor interfaces. Phys Rev B 35:8154–8165

Wagmare UV, Rabe KM (2005) Dielectric properties of simple and complex oxides from first-principles. In: Demkov AA, Navrotsky A (eds) Materials fundamentals of gate dielectrics. Springer, New York

Wallace RM, Wilk GD (2003) High-kappa dielectric materials for microelectronics. Crit Rev Solid State Mater Sci 28:231–285

Wilk GD, Wallace RM, Anthony JM (2001) High-k gate dielectrics: current status and materials properties considerations. J Appl Phys 89:5243–5275

Williamson AJ, Hood RQ, Needs RJ et al (1998) Diffusion quantum Monte Carlo calculations of the excited states of silicon. Phys Rev B 57:12140–12144

Wolf WL, Stanley SB, McCarthy KA (1963) American institute of physics handbook. McGraw-Hill, New York

Zhao X, Vanderbilt D (2002a) First-principles study of structural, vibrational, and lattice dielectric properties of hafnium oxide. Phys Rev B 65:233106

Zhao X, Vanderbilt D (2002b) Phonons and lattice dielectric properties of zirconia. Phys Rev B 65:075105

Zheng Z, Boggs S (2005) Defect tolerance of solid dielectric transmission class cable. IEEE Electr Insul Mag 21:35–41

Chapter 6
Mechanical and Thermal Properties

Patricia Irwin, Wei Zhang, Yang Cao, Xiaomei Fang, and Daniel Qi Tan

6.1 Introduction

The reinforcement of polymers using fillers, whether inorganic or organic, is common in the production of modern polymeric dielectrics for improved discharge resistance, matching of the coefficient of thermal expansion, and higher thermal conductivity as well as mechanical reinforcement, abrasion and wear resistance and long term mechanical behavior (Cao et al. 2004). Nanodielectrics provide a unique opportunity to enhance microcomposite mechanical and thermal properties along with the improvement of dielectric aspects (Lewis 1994).

Polymer composite insulation often is subjected to constant vibration/abrasion by power frequency magnetic forces and high shear stress under rapid thermal loading conditions (Griffith et al. 2000). As a result, state-of-the-art composite insulation often undergoes void/crack initiation or delamination under these mechanical stresses with subsequent electrical discharge and catastrophic failure. Because of their high surface area-to-volume ratio, nanofillers have a high reinforcing efficiency even at very low concentrations. In general, the addition of inorganic filler particles to a polymer matrix produces an increase in stiffness, but sacrifices toughness, whereas addition of rubber particles increases toughness, but reduces stiffness. Recently, the introduction into a polymer matrix of nanofiller particles at a concentration of only a few weight percent has resulted in a remarkable combination of high stiffness and toughness. This synergy of properties is caused by changes in the morphology of the polymer matrix due to the combination of inorganic and organic components at the nanometer level. The enhanced modulus and potential rigid-phase toughening of nanocomposites open up new opportunities in applications of polymer matrix composites. The elastic modulus and the mechanical strength appear to be substantially enhanced for many nanocomposites, particularly with high aspect ratio nanofillers. Furthermore, the macroscopic mechanical properties of polymeric nanocomposite materials can be tailored over a range of lengths. The increase of fracture toughness through nanofillers is discussed on the basis of crack pinning,

P. Irwin (✉), W. Zhang, Y. Cao, X. Fang, and D. Qi Tan
GE Global Research Center, Niskayuna, NY, USA
e-mail: irwinpc@crd.ge.com

J.K. Nelson (ed.), *Dielectric Polymer Nanocomposites*,
DOI 10.1007/978-1-4419-1591-7_6,

crack deflection, de-bonding and plastic void growth, localized plastic deformation as well as micro-cracking and crack bridging. Long-term mechanical behaviors of nanocomposite such as wear and abrasion resistance, fatigue and creep are also found to be improved significantly. Such improvements are associated with good interfacial adhesion between the polymer matrix and nanoparticles, combined with restriction of molecular mobility of polymeric segments near the surface of nanoparticles (Shi et al. 1996; Messersmith et al. 1995).

However, the inverse thermo-mechanical behavior with reduction of both the viscoelastic response and the glass transition temperature is also reported for organoclay containing nanocomposites based on either high-functionality epoxy resin or polyester resin. These effects may be due to plasticization or lower crosslink density around the surface of nanofillers, and hence the lack of surrounding entanglement (Kotsilkova 2007). Hence, the glass-transition temperature of a polymer nanocomposite can be raised or lowered with the addition of nanoparticles with attractive or repulsive interaction with the matrix (Zou et al. 2008). Since glass transition temperature has been used in bulk nanocomposite systems as a measure of the particle/polymer interaction, further understanding of the interface between nanofiller and polymer, their interactions, as well as their effects on long chain dynamics and thermo-mechanical properties of the nanocomposites will enable thorough tailoring and control of the bulk properties. Enhancement of glass-temperature of polymeric insulation through proper nanocomposite engineering is essential to the development of new dielectric materials for high temperature, high-voltage and high-frequency applications.

Another important property enhancement for a polymer nanocomposite is the retardation of thermal degradation. The thermal stability and degradation are strongly affected by the amount of nanoparticles in the polymer matrix, as well as by the mesoscopic structures present (i.e., exfoliation vs. intercalation) (Kotsilkova 2007).

Lastly, the effect of nanofiller on the thermal conductivity of nanocomposites is discussed. Electrical insulation with high thermal conductivity is critical to the development of advanced electrical and electronic applications. More compact circuit and device designs necessitate higher energy density, thereby requiring more efficient heat dissipation. The nonmetallic materials used in these systems need to maintain excellent dielectric properties while limiting the thermal resistance they impart to the system. In addition, processing and manufacturing conditions must be adequate to prevent defects or imperfections, which would reduce the reliability of the final product. Initial study on nanocomposites revealed the possibility of overcoming the conventional thermal barrier as the size of filler inclusions becomes smaller than the phonon mean free path (10–100 nm at room temperature). Thermal conductivity can be further improved by altering the nanostructure of the composite so as to reduce the entropy of polymers, thereby restricting the free movement of molecular chains and enhancing the phonon velocity. The advance in nanotechnology has also expanded rapidly beyond the bulk thermal transport limits of natural materials. Wave-guiding and ballistic transport of phonons have been demonstrated in nanostructures such as nanotubes and rods. Single wall carbon nanotubes are

reported to have thermal conductivity of 3,500 W/mK, exceeding the 2,300 W/mK thermal conductivity of gem-quality diamond (Biercuka et al. 2002; Berber et al. 2000). Electrically insulating boron nitride nanorod has also shown unusually high thermal conductivity, making it particularly attractive for high performance thermal management for various energy conversion systems requiring high-voltage breakdown capability (Chen et al. 2006). However, some preliminary results have shown that the thermal conductivity of the nanocomposites follows the rule of mixtures for randomly dispersed nanotubes. This is due to the extremely small thermal conductance at the nanotube/rod-polymer interface. Recent work on surface modification of BN nanoparticles has shown significant improvement on thermal conductivity (Han et al. 2002; Wank et al. 2002).

The following sections outline some of the recent developments in the mechanical and thermal aspects of nanocomposites including stiffness, strength, toughness, micro cracking, long term behavior, abrasion, wear resistance, glass transition, and thermal conductivity.

6.2 The Effect on Elastic Modulus and Mechanical Strength

6.2.1 Nanofillers and Nanocomposites

Recent research shows promising new routes to synthesize advanced materials enabled by nanotechnology. Some of these nano-enabled composite materials have been utilized in commercial products for food packaging and automobile applications. The ultra small size and large specific surface area of nanoparticles, upon incorporation into a polymer matrix, result in a large interfacial area even with low filler loading as depicted in Fig. 1.1. The bulk properties of nanocomposites are highly dependent on the properties of the filler, the host matrix, and the interfacial properties. The interface can be tailored using techniques such as chemical functionalization and core-shell structuring to achieve desired properties. Given the materials properties of the different constituents in the matrix, the general mechanical properties of the overall composites can be predicted. The individual effects of filler/matrix volume ratio, filler aspect ratio, filler stiffness etc on the mechanical response of the overall composites have been predicted by several theories. Most of these theories were developed to model the traditional continuous fiber reinforced composite materials, however, they can also be applied to modeling and prediction of discontinuous particulate-filled composites/nanocomposites. Two most commonly used theories for micromechanics modeling of particulate filled composites are those of Halpin-Tsai and Mori-Tanaka.

Halpin and Tsai's theory for predicting the stiffness of unidirectional composites has been readily applied to analysis of nanocomposites (Halpin 1969, 1976) and a variety of reinforcement geometries (i.e. nano fiber, spherical nanoparticles) for both continuous and discontinuous composites. The longitudinal and

transverse engineering moduli, E_{11} and E_{22} are expressed in the general form (Halpin 1976):

$$\frac{E}{E_m} = \frac{1 + \xi\eta\phi_f}{1 - \eta\phi_f} \tag{6.1}$$

where: E and E_m represent the Young's modulus of the composite and matrix, respectively, ξ is a shape parameter that is dependent upon filler geometry and loading direction, ϕ_f is the volume fraction of filler, and η is given by:

$$\eta = \frac{E_f/E_m - 1}{E_f/E_m + \xi} \tag{6.2}$$

where: E_f represents the Young's modulus of the filler. By comparing model predictions with the two-dimensional finite element calculations by Foye for discontinuous oriented square fiber-reinforced composites (Foye 1966), Ashton et al. determined that $\xi = 2(a/b)$ provided good agreement for longitudinal modulus, E_{11}, where a and b are the length and thickness of the fiber (Ashton et al. 1969). The modulus perpendicular to the fiber direction (transverse), on the other hand, was found to be relatively insensitive to fiber aspect ratio, and could be approximated by $\xi = 2$ (Halpin 1976; Adams 1967). It should be noted that as $\xi \to 0$ the Halpin-Tsai theory converges to the inverse rule of mixtures (lower bound), i.e.

$$\frac{1}{E} = \frac{\phi_f}{E_f} + \frac{(1 - \phi_f)}{E_m} \tag{6.3}$$

When $\xi \to \infty$ the theory reduces to the rule of mixtures (upper bound), i.e.

$$E = \phi_f E_f + (1 - \phi_f) E_m \tag{6.4}$$

The Mori-Tanaka method was based on the principles of Eshelby's particle inclusion model for predicting an elastic stress distribution in and around an ellipsoidal particle in an infinite matrix (Eshelby 1957). To account for finite filler concentrations, Mori and Tanaka, however, considered a non-dilute composite consisting of many identical spherical particles that cause the matrix to experience an average stress different from that of the applied stress. To satisfy equilibrium conditions the volume average over the entire composite was forced to equal the applied stress (Mori 1973). Tandon and Weng used this assumption and Eshelby's solution to derive complete analytical solutions for the elastic moduli of an isotropic matrix filled with aligned spherical inclusions (Tandon 1984).

As the size of the filler shrinks to nanoscale, the fraction of interfacial region is significantly increased especially for fillers with large aspect ratio (i.e. carbon nanotubes). Liu and Brinson recently developed a numerical model based on Mori-Tanaka micro-mechanics for prediction of elastic properties of nanocomposites that takes the effects of interphase into account. They introduced the concept of influence range of fillers on the matrix in region near the interface. The region of the interphase

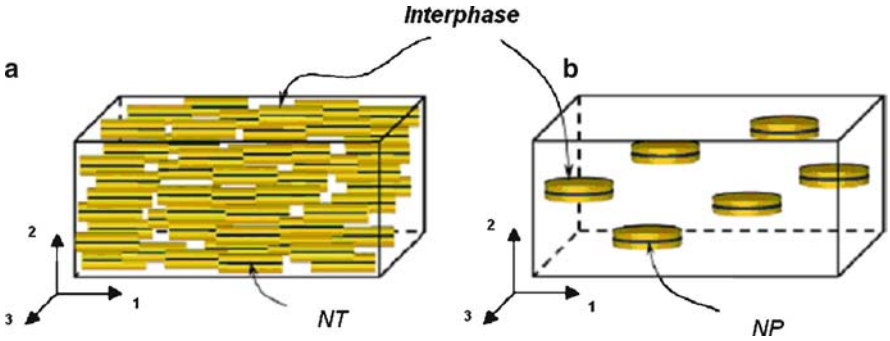

Fig. 6.1 Schematics of aligned (**a**) nanotube and (**b**) nano-platelet nanocomposites with interphase region (Liu and Brinson (2008), reprinted with permission from Elsevier)

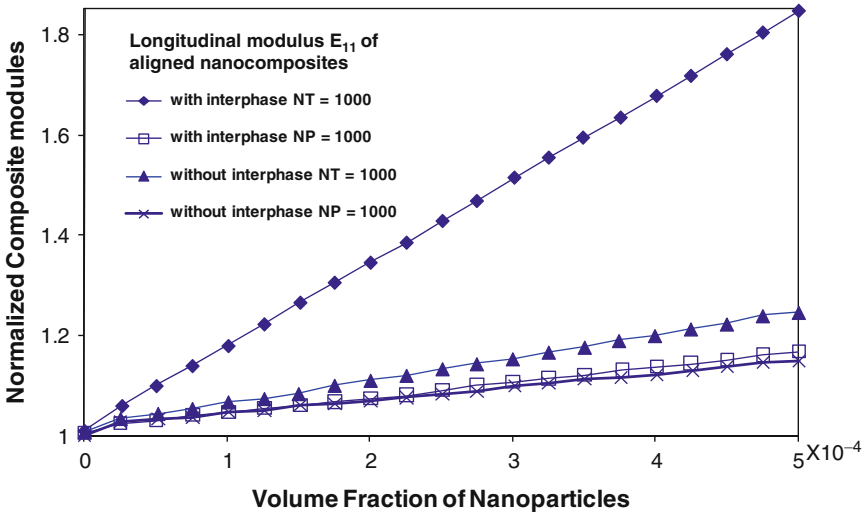

Fig. 6.2 Modeling results including the effects of interphase (Liu and Brinson (2008), reprinted with permission from Elsevier)

is schematically shown in Fig. 6.1 and this region is assumed to have gradient in property away from the filler. Figure 6.2 shows the modeling results for the nanotube and nanoplatelet reinforced nanocomposites with same filler loading level based on this new concept. It was shown that for large aspect ratio nano fillers, the effects of interphase on the elastic modulus are more profound than the nanoplatelet fillers due to its larger surface area (Liu and Brinson 2008).

6.2.2 Tensile Properties

Most bulk nano-filled polymer composites have mechanical properties that fall below the expected theoretical and experimentally determined values of the individual nano building blocks, except at low volume fractions of the reinforcement (Podsiadlo et al. 2007). The discrepancy between theory and experimental results of the composite is largely due to the difficulty of obtaining well-dispersed large volume fractions of the reinforcing nano fillers and improper interfacial bonding. The difficulty is also associated with realizing an effective load transfer from the polymeric matrix to the nanoscale components and the insufficiently understood mechanical interactions of the two constituents at the nanoscale. Recent progress in the processing and chemical functionalization of nano fillers has helped to narrow the gap between the theoretical limit of the nanocomposites and reality.

In a recent paper by Liu et al., mechanical properties of chemically functionalized single-nanotube PVA nanocomposites are studied. Figure 6.3 shows the comparison in mechanical behavior between the neat PVA and 0.8 wt% CNT Nanocomposites. Significant improvements in both the ultimate strength and Young's modulus are observed (Liu et al 2005). Surface hydroxyl group-functionalized carbon nanotubes are shown to improve the interaction between the nanotubes and the polymer matrix through hydrogen bonding to the host matrix as well as enhanced dispersion quality. The improved dispersion and interfacial bonding enhance load transfer from the weaker polymer to the stronger SWNT fillers. In addition, increased dispersion increases the available interfacial surface area for effective load transfer from the surrounding PVA matrix. Prediction of the modulus using the Halpin-Tsai equations shows very good agreement with experimental data assuming a filler aspect ratio.

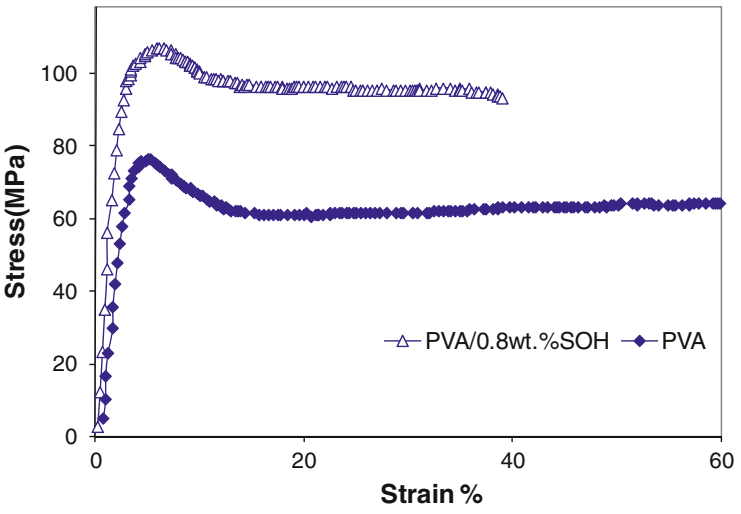

Fig. 6.3 Stress-strain curves for PVA and 0.8 wt% PVA nanocomposites (Liu et al. (2005), reprinted with permission from Wiley-VCH Verlag GmbH & Co.)

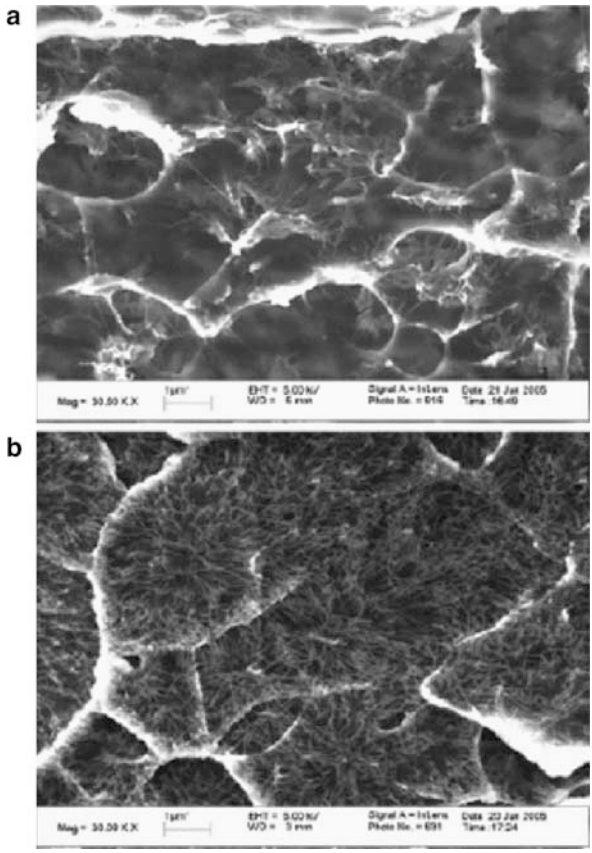

Fig. 6.4 SEM image of fracture surface of 1% SWNT nanocomposites (**a**) without functionalization and (**b**) with amide-functionalization (Ramanathan et al. (2005), reprinted with permission from Wiley)

Ramanathan et al. have reported dramatic improvement in mechanical properties with a small loading of amide-functionalized SWNT in a PMMA matrix. The SEM images in Fig. 6.4 show very uniform dispersion of filler for the functionalized CNTs and local clustering for the un-functionalized CNT. In comparison, unfunctionalized SWNT composites demonstrate a broadening of relaxation modes, but still retain the signature of bulk PMMA properties. Several mechanisms have been identified to explain the lower than predicted modulus increase: (1) insufficient dispersion of nanotubes, (2) weak interfacial bonding between filler and the matrix, which can result in interfacial slippage, and (3) poor interfacial contact (Ramanathan et al. 2005).

In another study by Guo et al., the mechanical properties of alumina nanocomposites were enhanced by functionalization of the alumina surface using (3-methacryloxypropyl) trimethoxysilane (MPS) through a neutral solvent method (Guo et al. 2006). MPS was found to be covalently bound with the nanoparticles and

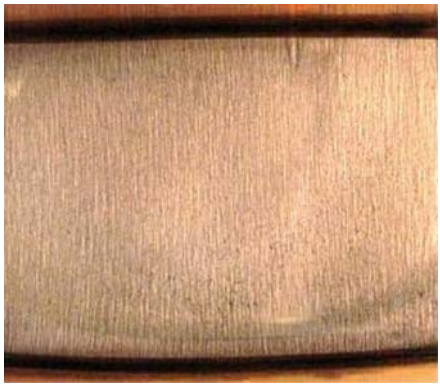

Fig. 6.5 Alignment of carbon nanotubes in PMMA using AC electric field ($f = 500\,\text{Hz},\ E = 120\,\text{V/cm}$) (Zhang et al. (2008), reprinted with permission from Elsevier)

to serve as a chemical bond linkage between the filler and the matrix. This linkage facilitates the nanocomposites behaving as a coherent unit, in which the tough nanoparticles make the resin stronger through chemical bonding. Micro-tensile test results revealed the Young's modulus and strength increasing with particle loading.

Podsiadlo et al. used a novel bottom-up layer-by-layer (LBL) assembly approach for fabrication of clay/polymer nanocomposites to produce essentially defect free nanocomposites with exceptional mechanical properties (Podsiadlo et al. 2007). A high level of ordering of the nanoscale building blocks, and interfacial covalent bonding are achieved, leading to highly effective load transfer between nano fillers and the matrix. Measurement of LBL assembled PVA/clay nanocomposites have shown over eight times improvement in ultimate strength for the cross-linked nanocomposites fabricated by the LBL process.

Alignment of high aspect ratio fillers such as nanotubes and nano fiber is expected to improve the mechanical properties of nanocomposites based on theoretical predictions. Methods such as electro-spinning, magnetic field, electrophoresis, high shear flow, mechanical stretching methods, etc. have been used to align SWNT in composites (Wang 2008). Under AC electric field ($f = 500\,\text{Hz},\ E = 120\,\text{V/cm}$), CNTs in a PMMA matrix were aligned and highly anisotropic mechanical and thermal properties were realized (Fig. 6.5) (Zhang 2008).

6.3 The Effect on Fracture and Impact Toughness

6.3.1 Fracture Toughness

In traditional physics, the fracture strength of a solid material is a function of the cohesive forces that exist between atoms, and the fracture energy will be simply equal to the energy to break all the bonds joining the two faces. However, the experimental fracture strengths of most engineering materials normally lie between 10 and 1000 times below the theoretical value. Fracture mechanics theory proposed

by Griffith in the 1920s and modified by Irwin and Orowan in the 1950s explained this discrepancy by introducing microscopic flaws or cracks that always exist under normal conditions at the surface and within the interior of a body of material. The critical stress required for crack propagation in a brittle material was described by (Griffith 1921):

$$\sigma_c = \left(\frac{2E\gamma_s}{\pi a}\right)^{1/2} \tag{6.5}$$

where E is the modulus of elasticity, γ_s is the specific surface energy, a is one half the length of an internal crack. The stresses in the vicinity of a crack tip can also be defined in terms of the stress intensity factor K. There is a critical value of K that may be used to specify the conditions for brittle fracture; this critical value is termed the *fracture toughness*, K_c and is defined by (Grellmann 2001)

$$K_c = Y\sigma_c\sqrt{\pi a} \tag{6.6}$$

Fracture toughness is a measure of a material's resistance to brittle fracture when a crack is present. Y is a dimensionless parameter and is a function of crack and specimen geometries, as well as local stress states. For planar specimens containing cracks that are much shorter than the specimen width, Y has a value of approximately unity (Anderson 1995). For ductile materials such as steel, the surface energy (γ_s) predicted by Griffith's theory is usually unrealistically high. It was later realized that plasticity plays a significant role in the fracture of ductile materials.

Dielectric materials are often an anisotropic material system designed for dielectric properties, providing physical and chemical protection for metal conductors, e.g., modern micaceous insulation for rotating machinery and glass fiber reinforced epoxy resin for MRI medical imaging equipment. Components of dielectrics include polymers, organic or inorganic fillers, and reinforcement fibers. Physical and chemical bonding between metal conductors and dielectric materials is usually required to secure the conductors in position within electrical devices.. The dielectric material also endures cyclic fatigue from vibrations and other periodic mechanical loadings, and thermal stress from thermal-humidity cycles in the environment. Such stresses can cause a variety of damage in dielectric materials, including resin micro cracking, resin/fiber delamination, and severe failures such as fiber breakage. Often micro cracking in the polymer matrix is the earliest damage mode observed in dielectric materials. Fracture resistance of dielectric polymers can be improved by incorporating toughening agents such as rubber particles (i.e. CTBN rubber) or other flexibilizers. However, these traditional fillers generally compromise important mechanical properties while improving the fracture toughness. Recent developments have shown that nanoparticles can overcome the drawbacks of traditional toughening agents by simultaneously improving the toughness and strength of epoxy, without sacrificing thermo-mechanical properties. Plastic deformation of the matrix, filler induced crazing, crack pinning, crack bridging, interfacial debonding/void growth by the rigid nanoparticles are the main toughening mechanisms attributed to nanoparticle-toughened matrices in the literature.

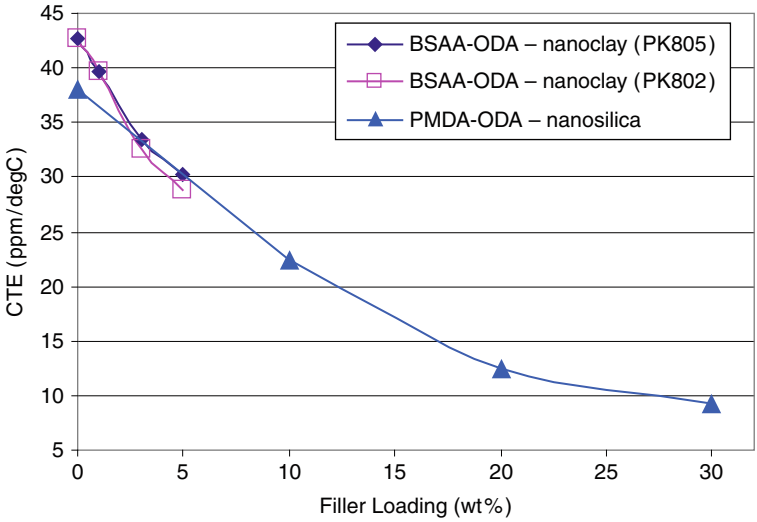

Fig. 6.6 CTE of polyimides with two smectic clays (Wang 2007) and nanosilica (Huang 2007)

In addition, external loading and/or residual stress can initiate cracks in a material system. A primary source of residual stress is the mismatch of the coefficients of thermal expansion (CTE) between the resin matrix and the fiber or metal conductor. Thermal stress-induced micro cracks become extremely significant when the material experiences thermal cycling between elevated and cryogenic temperatures. From micromechanics analysis, micro cracking in the resin matrix occurs when the residual stress becomes larger than the resin strength. In other words, micro cracks are generated when the strain induced by residual stress is greater than the strain at failure of resin matrix. A rigid nano filler with intrinsic dimensional stability can reduce the CTE mismatch between polymer matrix and fiber or metal conductor. Figure 6.6 shows that the CTE of nanocomposite matrix synthesized by the addition of nanosilica in a polyimde prepared from pyromellitic anhydride (PMDA) and ODA was much lower than that of the neat resin (Huang 2007). The same effect is observed with natural smectic nanoclays in Novolac cured epoxy resins (Tsai 2008) and a polyimide prepared from $4,4'$-$(4,4'$-isopropylidenediphenoxy) bis(phthalic anhydride) (BSAA) and 4,4-oxydianiline (ODA) (Wang 2007).

6.3.1.1 Crack Pinning

Crack pinning is a mechanism proposed by Lange for halting advancing cracks in composite materials (Lange 1970). Rigid particles can act as pinning and arresting points during crack propagation, as illustrated in Fig. 6.7. As a crack starts to propagate within a composite material, the crack front meets particle fillers and bows out between the rigid particles while still remaining pinned at all the positions where it

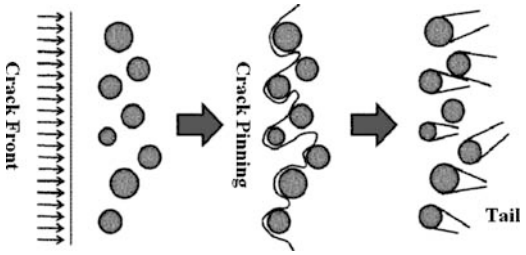

Fig. 6.7 Crack pinning process for toughening of composite materials

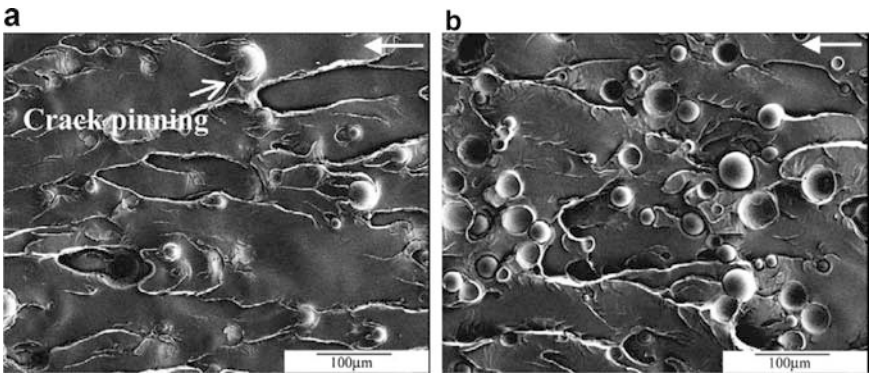

Fig. 6.8 SEM images of fatigue fracture surfaces of (**a**) the LGS-APS-A epoxy (good bonding) and (**b**) the LGS910)-nBS-A epoxy (weak bonding) (Kawaguchi (2004), reprinted with permission from Elsevier)

has encountered the filler particles. During this initial stage of crack propagation the length of the crack front is increased due to distortion of the front by the pinning particles. The pinning process can generate secondary cracks and new fracture surfaces which alleviate the stored strain energy. These secondary cracks then coalesce after passing the particles. As the strain energy increases, local step fracture occurs and the pinned points are released, leaving a "tail-like" feature on the fracture surface. Energy is absorbed and dissipated during the crack-pinning process, which leads to an increase in the fracture toughness of the material.

Crack pinning behavior has been observed in micron-scale rigid fillers (Kinloch 1985; Spanoudakis 1984; Kawaguchi 2004). One example is displayed in Fig. 6.8. Glass beads of 3.8–42 μm diameter functionalized with aminopropyltrimethoxysilane (APS) give greater interfacial bonding with the bisphenol-A epoxy resin than beads functionalized with n-butylrimethoxysilane (nBS). Crack pinning is observed only when filler/matrix bonding in a composite is strong. However, there have been few observations of crack pinning in nanoparticle filled resin systems. The effectiveness of nanofillers as pinning agents has been called into question (Johnsen 2007).

These workers believe that the displacement of a typical crack surface occurs on a length scale, which is larger than the nano-scale filler, so that the latter does not generate a crack pinning pattern on the fracture surface.

Ragosta et al. studied the fracture behavior of epoxy/silica nanocomposites. Chemical bonding between epoxy groups and silanol groups present on the surface of the silica phase was detected, leading to an increased interfacial adhesion (Ragosta et al. 2005). The fracture toughness of this epoxy/nano silica system is increased from $\sim 0.53\ MPa\sqrt{m}$ for the unfilled epoxy to $\sim 1.17\ MPa\sqrt{m}$ at 10 wt% of filler loading. In addition, the toughness enhancement using micron-size silica is not effective compared to that obtained with nano-size fillers. The fracture surfaces of the nanocomposites show extended river patterns suggesting increased ductility and degree of plastic deformation as compared to those of the neat resin. In a study by Naous et al., epoxy/Al_2O_3 nanocomposites show over 35% improvement in fracture toughness at a filler loading of only 2% by volume. The addition of nanoparticles changes local stress distribution at the polymer/particle interface, which facilitates ductile plastic deformation, and results in higher fracture toughness (Naous et al. 2006).

6.3.1.2 Crack Deflection

Crack deflection near or at particle/polymer interfaces is a source of energy dissipation during the crack propagation of particle filled polymer. As the crack front is approaching a polymer/particle interface, the crack can tilt and change direction when it encounters the rigid particles and passes around them. This process is illustrated in Fig. 6.9. Such deflection causes a continuous change in the local stress state from mode I to mixed-mode. To propagate a crack under mixed mode conditions requires a higher driving force than in pure mode I, which results in a higher fracture toughness of the material. Crack deflection leads to an increase in the total fracture surface area because the crack front follows a tortuous path around particles and therefore absorbs more energy compared to propagation in unfilled materials.

Wetzel et al. showed that the mechanical properties of the composites using nano-size filler are better than those using micron size fillers. The optimum filler loading level is 4 vol% TiO_2 nanoparticles (Wetzel et al. 2002). A nanocomposite exhibits more ductile fracture behavior than the corresponding neat resin, as indicated by a rougher and more textured fracture surface. This is due to the activation of additional energy dissipating fracture mechanisms such as crack deflection and crack pinning. Evidence of crack pinning is observed on the fracture surface where the characteristic "tails" are present. In addition, SEM images reveal many particles

Fig. 6.9 Crack deflection mechanism

pulled out of the matrix, leaving behind small holes, which are indications of poor matrix/particle adhesion. Zhao et al. also observed poor correlation between crack surface roughness and toughness in an alumina filled nanocomposite having weak particle/matrix bonding. (Zhao et al. 2008) When the alumina particles have been treated with 3-aminopropyltriethoxysilane (APTES), the resulting strong filler to matrix bonding produces greater crack surface area than that seen with no surface treatment.

6.3.1.3 De-bonding and Plastic Void Growth

De-bonding of rigid particles from the polymer matrix is another major toughening mechanism for particle filled composites. De-bonding can occur when the local tensile stress at the interface overcomes the thermal mismatch stress and the interfacial cohesive strength. The growth of plastic voids can be assessed with a model calculated from the area under a tensile stress-strain curve (ΔW_v) as follows:

$$\Delta W_v = 0.5\sigma_{yt}(V_v - V_f) \tag{6.7}$$

where σ_{yt} refers to the tensile yield stress of a neat epoxy resin, and V_v and V_f are the volume fraction of voids and volume fraction of fillers, respectively. The void growth toughening mechanism is frequently observed for rubber toughened polymer systems. For interface-dominated materials such as nanocomposites, there can be very significant energy dissipation if large-scale de-bonding occurs at the interfaces. In addition, the de-bonding of the particles allows subsequent plastic void growth within the polymer, another key energy dissipation mechanism (Fig. 6.10). The energy absorbed during this process depends on the adhesion and interfacial properties of the particle-matrix interface as well as far-field applied stress. Evans et al. observed that the onset of non-linearity in the stress-strain curve for some filled polymers coincides with the de-bonding initiation of the second phase (Evans et al. 1985). The advantage of nano-size particles is that these can create more cavitations and voids than micron sized fillers at the same filler weight percentage, resulting in more polymeric material being involved in the plastic deformation process. In addition, voids created by nano fillers are originally smaller and more stable than those created by a micro-filler, avoiding early brittle fracture. Johnsen et al. attributed the majority of the toughness increment seen in nanocomposites to the plastic void

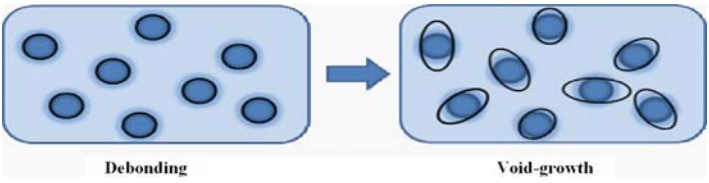

Fig. 6.10 De-bonding and void-growth mechanism

growth mechanism (Johnsen 2007) For a low T_g epoxy filled with core-shell nanorubber and clay, however, no obvious particle-generated voids were observed (Gam 2003). This observation suggests that rapid recovery of the matrix can occur if the molecular chain is close to its T_g.

In exfoliated clay-filled epoxy nanocomposites, micro cracks were observed extensively (Wang et al. 2005). The micro crack was probably formed within the clay due to the weak interlayer strength relative to that of the epoxy clay bond. The epoxy matrix near to the micro crack region then failed and was followed by the debonding of epoxy/clay.

6.3.1.4 Localized Plastic Deformation of Matrix (Shear Banding and Crazing)

The presence of rigid-particulate fillers may cause enhanced localized plastic deformation (i.e. shear banding and crazing) of the polymer matrix and enhanced fracture toughness. Shear banding is plastic flow in a glassy polymer that deforms by the formation and propagation of shear zones which initiate at stress levels below the tensile strength, and results in partial orientation of the polymer chains (Kausch 1972). Conditions for the shear banding formation are dependent on the temperature and the local stress states. Crazes are microscopic regions of highly localized plastic deformation similar to those developed on a macroscopic scale at large tensile strain in drawn glassy polymers. Crazing occurs in regions of high hydrostatic tension, or in regions of very localized yielding, which leads to the formation of microvoids and fibrils oriented parallel to the tensile direction. If an applied tensile load is sufficient, these crazed regions elongate and break, causing the microvoids to grow and coalesce and cracks begin to form. Inclusion of rigid particles induces stress concentrations and alters the local stress state, which favors local plastic deformation. Due to the large number of particles in nanocomposites, potentially more plastic deformation may exist in these systems than in the unfilled polymer, leading to higher fracture toughness.

Deng et al. evaluated the fracture toughness of epoxy/nano silica nanocomposites at low and high temperatures. The silica nanoparticles used in this study were synthesized using a sol–gel process (see Sect. 2.2.4) with a narrow size distribution centered around 20 nm. Elastic modulus, fracture toughness and flexural strength are all improved at both temperature extremes. Increase in the glass transition temperature in nanocomposites is an indication of strong interfacial interaction between the filler and the matrix (Deng et al. 2007). Crack deflection and crack pinning, as well as the increased plastic deformation, were the main toughening mechanisms observed on the fracture surfaces.

Shah et al. report significant improvement in both the stiffness and toughness of the nanoclay-PVDF composites. One order of magnitude improvement in fracture toughness was observed as compared to the neat PVDF as shown in Fig. 6.11 (Shah et al. 2004). The nano-structuring of the polymer induced by the nanoparticles, together with β-phase formation, are responsible for the toughness enhancement.

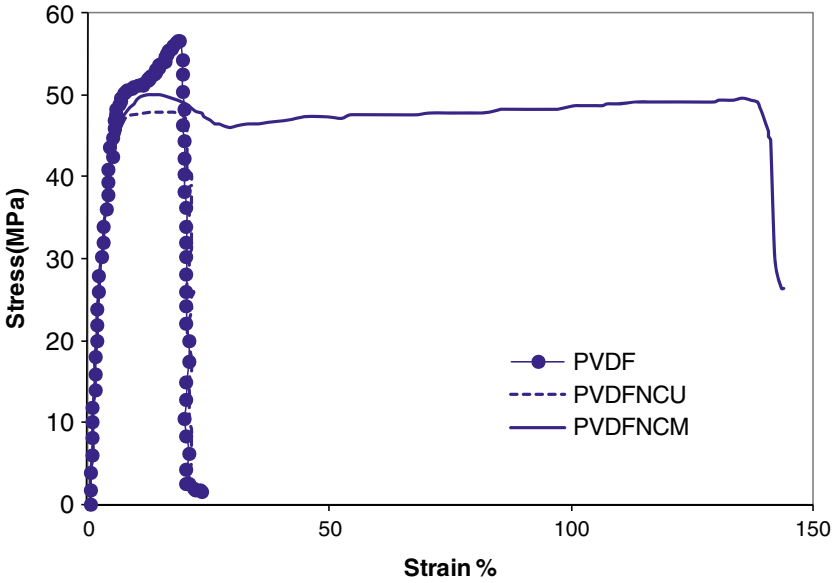

Fig. 6.11 Stress-strain curves for the PVDF/clay nanocomposites (Shah et al. (2004), reprinted with permission from Wiley-VCH Verlag GmbH & Co.)

They postulate that the nucleation of the fiber-like β-phase on the faces of individual clay filler leads to structure that is much more conducive to plastic deformation and large energy dissipation under applied stress.

6.3.1.5 Microcracking and Crack Bridging

Microcracking close to the crack tip can reduce the stress intensity and improve the fracture toughness. Zones of micro cracking essentially reduce the local modulus and lead to reduction of local stress. Micro cracking will also release some of the residual stress present in composites as a result of differential thermal shrinkage between polymer and fillers. Certain size and spatial distributions of micro-cracks in the vicinity of the main crack tip can effectively shield the crack and slow further crack advancement. Hutchinson et al. have determined that the maximum toughening achieved by a single micro-crack is roughly a factor of 2 in energy, assuming no contribution from the release of residual stress is taken into account (Hutchinson 1989).

Crack bridging is another key toughening mechanism for particle or fiber reinforced composite materials. Near the crack tip, the fibers/particles bridge the crack tip and slow down the crack growth. As the stress increases, fiber pullout or fiber breakage will occur and lead to partial dissipation of strain energy near the crack tip. The amount of toughness increase is highly dependent on the geometry (i.e., length and aspect ratio) as well as surface properties of the fillers (Bao et al. 1992).

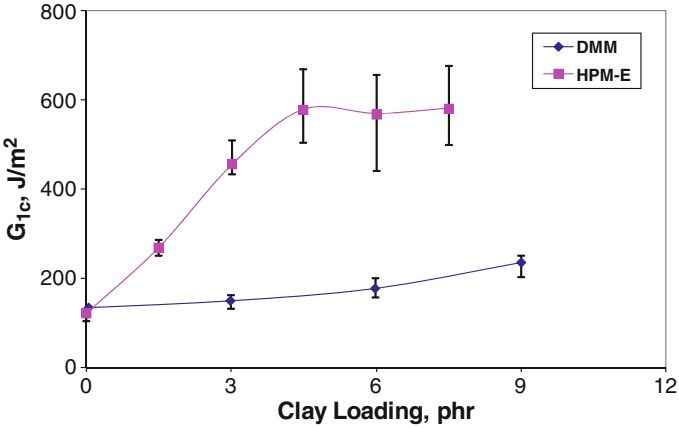

Fig. 6.12 Critical strain energy release rate (G_{IC}) of epoxy/clay nanocomposites high pressure mixing method and simple mixing method (Liu et al. (2005), reprinted with permission from Elsevier)

Liu et al. studied the fracture behavior of epoxy/clay nanocomposites synthesized using a high pressure mixing method (Liu et al. 2005). They found that the strain energy release rate (G_{IC}) of the 4.5 wt% epoxy/clay nanocomposites is 5.8 times that of the neat epoxy resin (Fig. 6.12). The key factor thought to be responsible for the increase is the degree of exfoliation (complete dispersion down to the individual sheets, or layers, at the nano-scale – see Sect 3.2) of the clay material in the epoxy matrix.

A ductile-brittle transition in carbon nanotube-loaded polycarbonate composites (Satapathy et al. 2005) has been observed when MWNT contents exceed 2%. Despite an efficient interaction between the nanotubes and the polymer, inhomogeneous distribution of the tubes may have caused high local strains Yu et al. studied the fracture behavior of epoxy/MWNT nanocomposites and saw over 60% improvement in fracture toughness for 3 wt% filler loading. The use of degassing agents during composite preparation leads to fewer air bubbles trapped inside the composites and reduces the number of initial flaws, which ultimately leads to higher fracture resistance. In addition to increased fracture toughness, the fatigue life is also improved by ~10 times (Yu et al. 2008).

6.3.2 Impact Toughness

Impact resistant polymeric materials are of great technological importance for such applications as aircraft windows required to withstand high speed impinging particles and car bumpers required to absorb a large amount of energy during collisions. Impact resistance is highly dependent on the presence and shape of stress concentrators and molecular properties (Kausch 1972). Polymers having high mechanical loss peaks such as PC, HDPE and PPO usually have very good impact strength.

If strength and plastic deformation can increase simultaneously, considerable toughening is to be expected. This can be realized by partial orientation of an un-oriented brittle polymer such as polystyrene. Molecular structure also plays a very significant role in the impact behavior. Due to their unique size and interfacial properties in nanocomposites, nanoparticles are expected to trigger various impact toughening mechanisms.

The impact mechanisms of nano calcium carbonate reinforced polypropylene nanocomposites have been studied using optical and electron microscopy. Charpy impact testing showed over two times improvement in impact strength for 9.3 vol% $CaCO_3$ nanocomposites as compared to the neat PP polymer (Weon et al. 2006). Change in molecular morphology induced by the nano filler is proposed to be the main reason for significant impact toughness enhancement. In a separate study by Zhang et al, non-ionic modification of the calcium carbonate nanoparticles using Polyoxyethylene Nonyphenol improves the impact strength of the polypropylene significantly via a different toughening mechanism. The PN modifier has a long alkyl chain with one hydroxyl end group. Enhanced compatibility of the $CaCO_3$ nanoparticles with the PP matrix is achieved through the polar long alkyl chains adsorbed on the surfaces of $CaCO_3$. The addition of PN modifier reduces the particle/particle interaction by lowering the surface free energy of $CaCO_3$, leading to better dispersion of $CaCO_3$ particles (Zhang et al. 2004).

Lin et al. studied the effects of thermal annealing on the impact toughness of PP/$CaCO_3$ nanocomposites (Lin et al. 2008). Injection molded impact and tensile bars were annealed at 150 °C for 2 h prior to testing. The annealed nanocomposite had much higher impact toughness than its un-annealed counterpart. A thin monolayer coating of stearic acid improved the dispersion quality of the nanoparticles in the matrix but also weakened interfacial adhesion.

Tanniru et al. studied the impact behavior of the nano clay reinforced high-density polyethylene where a reduction in impact strength was observed. They found that nano clay increased the crystallinity and stiffness, which reduced the degree of plastic deformation (Tanniru et al. 2006). The formation and fracture of dense fibrils in the PE copolymer is thought to be responsible for the significantly higher toughness seen in neat PP relative to that in the nanocomposite.

6.4 The Effect on Long-Term Behaviors

6.4.1 Wear and Abrasion Resistance

The working life of an engineering component is over when dimensional changes exceed its specified tolerance limits. Wear, along with other aging processes such as fatigue and creep, causes progressive dimensional change of parts, leading to premature failure. Wear is defined as the erosion of material from a solid surface by the action of another substance during contact. There are four typical wear processes: (1) adhesive wear; (2) abrasion; (3) surface fatigue; (4) fretting.

6.4.1.1 Adhesive Wear

Adhesive wear occurs when two solid surfaces slide over one another under pressure loading. Surface projections, or asperities, are plastically deformed and eventually welded together by the high local pressure. The three stages of adhesive wear process are illustrated in Fig. 6.13.

6.4.1.2 Abrasive Wear

Abrasive wear occurs when a rough, hard surface or a soft surface with hard particles embedded in its surface slides over a softer material. During abrasive wear, a "plowing" action takes place. Wear coefficients for abrasive wear are generally larger than for adhesive wear.

6.4.1.3 Surface Fatigue

Surface fatigue is a process by which the surface of a material is weakened by cyclic loading. Material is removed by cracking and pitting, due to cyclic elastic stress during rolling and sliding. The most common example is the action of a ball or roller bearing race. As the rolling element passes over a given spot on the raceway, it is stressed as the load is applied and released. With time, a relatively large piece of material will be released, leaving an uneven hole or pit.

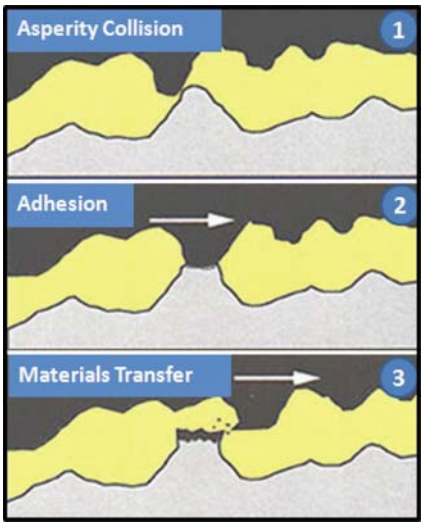

Fig. 6.13 Schematics of the adhesive wear process

6.4.1.4 Fretting Wear

Fretting wear is the repeated cyclical rubbing between two surfaces over a period of time, which will remove material from one or both surfaces in contact. Small wear particles are formed through the mechanism of adhesive wear. The particles produced then contribute to the wear through abrasive action. It occurs typically in bearings, although most bearings have their surfaces hardened to resist the problem. Schadler et al. extensively summarize the effects of various nanoscale fillers on the wear rate of PTFE nanocomposites (Fig. 6.14). PTFE is commonly used as dry lubricant due to its low friction coefficient properties. However, the disadvantage of homogenous PTFE is its high wear rate. The introduction of nanoscale fillers in the PTFE matrix reduce the wear rate up to 3–4 orders of magnitude with very small weight fraction of filler loading. It was hypothesized that the nano fillers stabilize the tougher phase within PTFE (phase I). The stabilization of this tougher phase promotes formation of a well-adhered transfer film on the contact surface and leads to significant reduction in the wear rate (Schadler et al. 2007).

Avella et al. studied the wear properties of PMMA/$CaCO_3$ nanocomposites prepared by an in situ polymerization technique (see Sect. 2.2.1). They have shown that with only 2 wt% $CaCO_3$ filler loading, the average weight loss is reduced by half as compared to that of neat PMMA (Fig. 6.15). For nanocomposites, the dominant wear process is the micro-cutting/micro plowing mechanism which occurs when the material is abraded by hard abrasive particles, while a neat PMMA sample suffers a larger amount of material removal by surface cracking and chipping. It is postulated that the finer dispersion of nanoparticles together with good interfacial adhesion between particle and matrix will lead to better abrasion resistance (Avella et al. 2001).

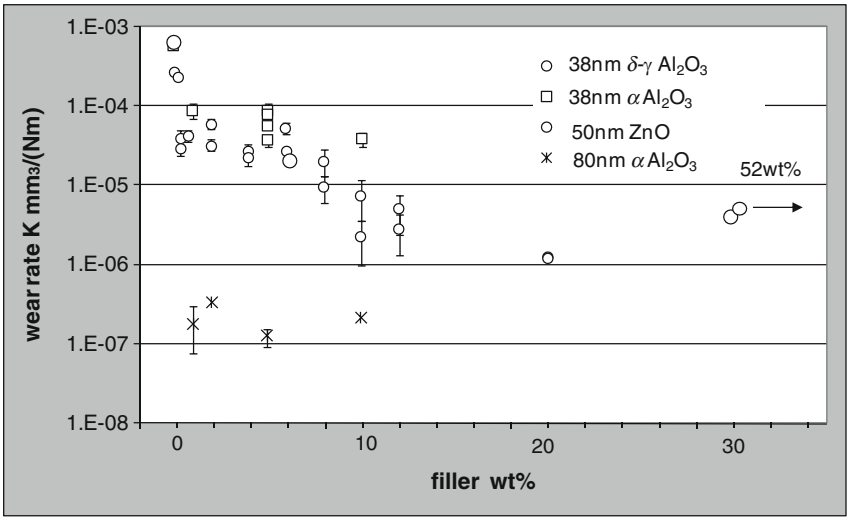

Fig. 6.14 Wear rate of PTFE as a function of nanoscale fillers (reprinted with permission from Springer) Schadler et al. 2007

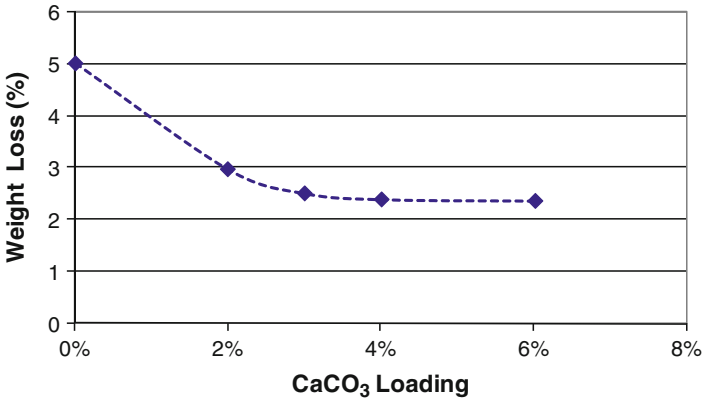

Fig. 6.15 Wear rate vs. $CaCO_3$ nanoparticles loading level (Data taken from Avella et al. (2001), with permission from American Chemical Society)

The wear characteristics of nanoclay filled polybutadiene nanocomposites produced using melt-compounding method have been investigated (Kim et al. 2006). Under high shear processing conditions, these nano-clays exhibit intercalated and exfoliated clay morphologies, which give rise to improvement in mechanical properties. For example, the abrasion resistance of clay-rubber composites is doubled. These improvements are the results of better dispersion quality as well as increased rubber/filler interfacial adhesion.

Wear behavior of carbon nano fiber (CNF) reinforced semi-crystalline PEEK nanocomposites was studied by Werner et al. PEEK/CNF nanocomposites were fabricated using injection-molding. The wear rate of this composite material is reduced by an order of magnitude as compared that of the neat PEEK polymer (Werner et al. 2004). The reduction in wear rate is likely due to the increase in shear strength of nanocomposites and the lubricating effects of the carbon nanofibers debris. The sliding surface appears to be smoother with the increase in CNF content. Friction and wear behavior of polyimide/CNT nanocomposites were investigated experimentally by Cai et al. Friction coefficient and wear rate are reduced significantly with CNT reinforcement and the improvement is most noticeable at higher force levels. The optimum CNT filler loading appears to be around 8%; the wear rate and friction coefficient are constant above this loading. The observed behavior can be explained by a large increase in micro-hardness due to the nanotube fillers, which reduces the abrasive wear by minimizing the "micro-plowing" action of abrasive particles (Cai et al. 2004).

Wang et al. demonstrated an improvement in scratch and abrasive resistance of alumina epoxy nanocomposites compared to the neat epoxy. Wear resistance of the 20 wt% alumina/epoxy composites is more than twice that of the neat epoxy (Fig. 6.16). They attribute these improvements in tribological properties to the dispersion hardening of alumina nanoparticles in nanocomposites. A strong correlation exists between the wear rate and micro-hardness of the nanocomposites (Wang et al. 2006).

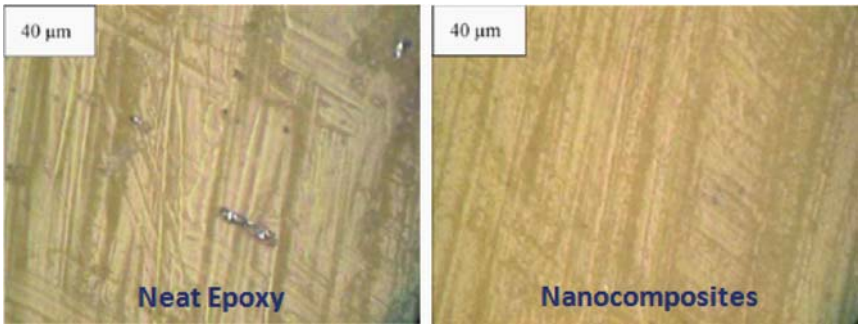

Fig. 6.16 Wear surface comparison between neat epoxy and Nanocomposites (Sawyer et al. (2003), reprinted with permission from Elsevier)

Sawyer et al. studied the tribological properties of PTFE alumina nanocomposites that were fabricated using injection-molding. The wear rate of the 20 wt% PTFE/alumina nanocomposites was reduced to about 1/600 that of the neat PTFE (Sawyer et al. 2003). The wear rate decreased monotonically with filler loading and no optimal loading level was observed. This behavior is attributed to the jet milling mixing process during which nanoparticles distribute around and encase the larger PTFE particles, thereby minimizing sub-surface cracking and removal of the PTFE.

6.4.2 Fatigue Behavior

Much work has been done on understanding the mechanisms of fatigue in both polymers and polymer composites. Fatigue resistance under cyclic loading has been widely studied on metallic materials and it is described either using stress versus number of cycles to failure curves (S-N curves) or analyzing fatigue crack propagation (FCP) following the fracture mechanics approach using crack speed versus applied stress intensity factor (i.e., da/dN-$\boldsymbol{\Delta K}$ curves). Some recent studies indicate that the mechanisms for fatigue suppression are quite different for CNTs as compared to nanoparticles.

Fractographic analysis was performed to identify the mechanisms responsible for reduction in fatigue crack growth rate (see Fig. 6.17) (Zhang 2007). Fiber pullout is considered a key mechanism for reduction of fatigue crack propagation rate since the stored strain energy is dissipated by both the pullout of the nanotube fibers and by the separation processes at the crack front. In the immediate wake of the crack tip, a fiber-bridging zone was observed; the nanotubes were pulled out of the matrix but were effectively bridging the crack faces. At a small distance behind the crack tip a combination of nanotubes was observed to bridge the crack. Far behind the crack tip, nanotubes were completely pulled out of the matrix with no evidence of crack bridging.

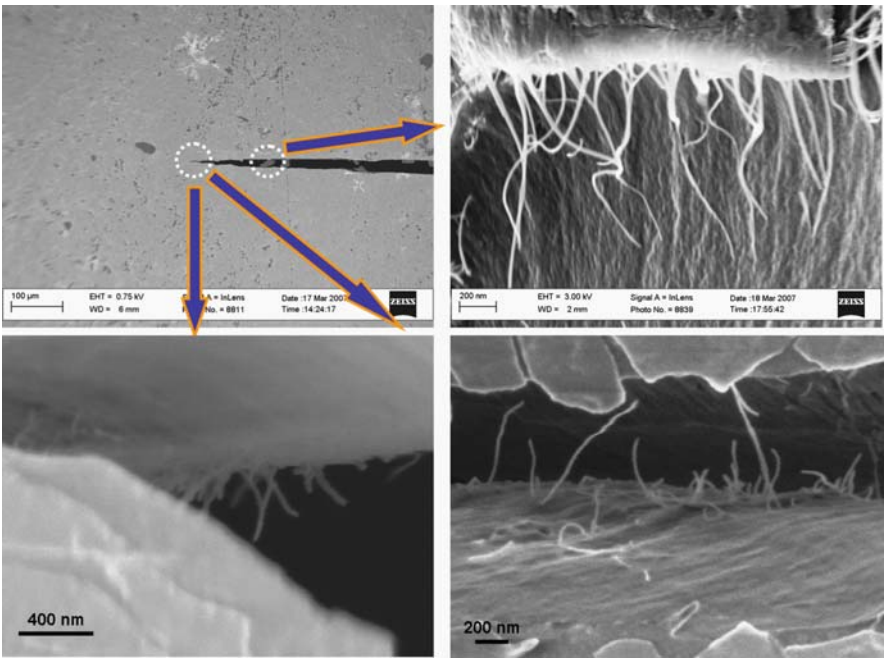

Fig. 6.17 Crack-bridging in CNT/epoxy nanocomposites (Zhang et al. (2007), reprinted with permission from American Institute of Physics)

One of the important variables affecting FCP behavior is the matrix/filler interfacial cohesive strength. When amine functionalized CNTs were introduced, dramatic improvements in FCP rate were obtained at both low and high stress intensity factors. Amine functional groups were attached to the sidewall of the CNTs to establish covalent bonding with epoxy chains. The size of the interfacial zone was expected to be considerable, making the epoxy chains in this region susceptible to crazing; the favored deformation mode in a, predominantly, tensile uniaxial stress state (Zhang et al. 2009). Recent experimental fatigue studies on alumina/epoxy nanocomposites by Zhao and Schadler et al. shows that surface chemical treatment has significant effects on the fatigue behavior of the nanocomposites. They measured the fatigue crack propagation rate of neat epoxy, untreated alumina/epoxy nanocomposites and silane treated alumina nanocomposites as a function of stress intensive factor ranges (Fig. 6.18). It was proposed that the dominant mechanisms for the improvement in fatigue were due to plastic void growth and a matrix/filler interfacial debonding process.

6.4.3 Creep Behavior

Creep is the time-dependent deformation of a structure under a persistent stress that is lower than the material's yield stress. Materials with high creep resistance

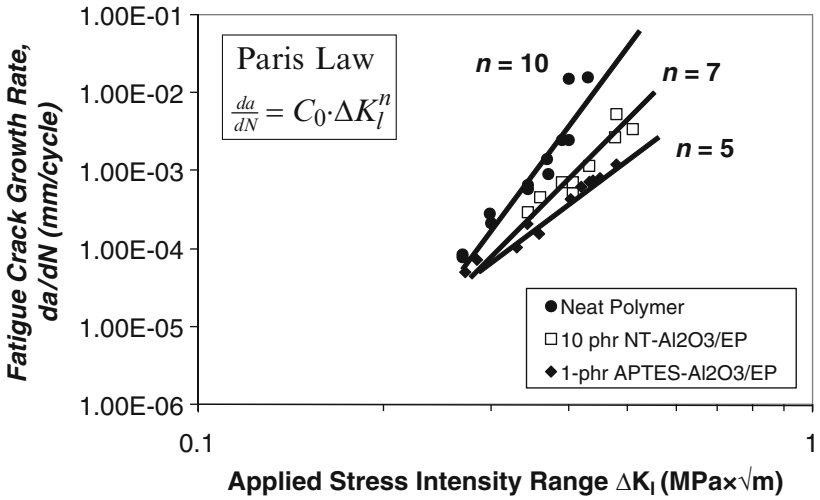

Fig. 6.18 Fatigue crack propagation rate of neat epoxy and surface treated alumina nanocomposites (Zhao et al. (2008), reprinted with permission from Elsevier)

are critical in long-term structural applications to ensure dimensional stability and maintain structural integrity. There are three stages of creep deformation: (1) primary creep, which proceeds at a relatively high rate, (2) the secondary creep, which proceeds at a constant rate, and (3) tertiary creep, which proceeds at an abruptly increased rate and leads to final failure of the material.

For polymeric materials, the creep behavior is affected by molecular weight, degree of crystallinity, and the chemical structure of the polymer (Ferry 1980). During creep deformation, the molecular chains are stretched and re-oriented. Recent studies (Zhang 2004; Yang 2006) have shown that addition of nanoparticles into a polymer matrix enhances its creep resistance at various stress and temperature levels. In another study (Vlasveld 2005), the creep behavior of nanocomposites that incorporate layered silicate in the matrix was investigated.

In the case of epoxy/CNT nanocomposites, the entangled high aspect ratio CNT's are expected to have strong interaction with the polymer chains and potentially act as physical barriers for chain re-orientation. This pseudo-physical barrier effectively reduces the creep deformation when the material is stressed (Fig. 6.19). At low stress levels this interfacial bonding holds and the CNT additives form an infiltrating network of cross-linking elements that interconnect the epoxy chains. This action increases the effective crosslink density of the network and reduces the mobility and re-orientation of the amorphous epoxy chains under mechanical stress. At higher stress levels the polymer/CNT interfaces are prone to failure and slippage, and, as a consequence, the ability of the nanotubes to limit polymer chain movement is negligible (Koratkar 2005; Suhr 2006).

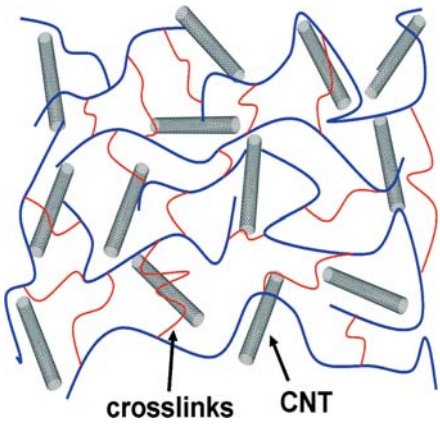

Fig. 6.19 Interactions of carbon nanotubes with epoxy polymer chains

6.5 The Effect of Particulate Inclusion on Glass Transition

The thermo-mechanical properties of polymer are dictated by the large scale, collective, segmental chain motion associated with the glass transition. Polymeric nanocomposites offer the potential to tailor thermo-mechanical properties via the interaction between nanoparticles and polymer chains. Over the past decade, significant research has been dedicated to the study of the interface between nanoparticles and polymer, which is the origin of improvements of the mechanical and thermal properties of the nanocomposites (Schadler et al. 2007).

The effect of nanoparticulate inclusion on the glass transition is profound and has been addressed previously in Sect. 4.3, but experimental results suggest that much further study is required. For instance, data suggest that the glass-transition temperatures of nanocomposites can either go up or go down relative to those of the neat polymer, depending on the nature of the nanoparticle-chain interaction. Very often T_g increases compared to that of the pure matrix, suggesting that the mobility of the entire volume of the polymer is restricted by the presence of the nanoparticles (Kang 2001; Shang 2002; Rittigstein 2006). However, reduction of T_g has also been reported in the case of weak interactions between filler and polymer (Ash et al. 2002; Preghenella et al. 2006), and, in many cases, the addition of nanoparticles causes no significant change in the glass transition. There are also cases where an initial increase in T_g is followed by a decrease with increasing nanofiller loading, and those where an initial reduction of T_g is followed by an increase at higher loading (Zou et al. 2008). While micron-sized filler inclusion generally has little impact on T_g of the polymer matrix, the sensitivity of T_g to nanoinclusions has aroused interest from both the fundamental standpoint and the practical engineering point of view (Sun et al. 2004). This behavior is believed to be closely related to the nature of the nanoparticle/polymer interface, which is not well characterized or understood. Two competing phenomena may be occurring. The presence of a high volume percentage

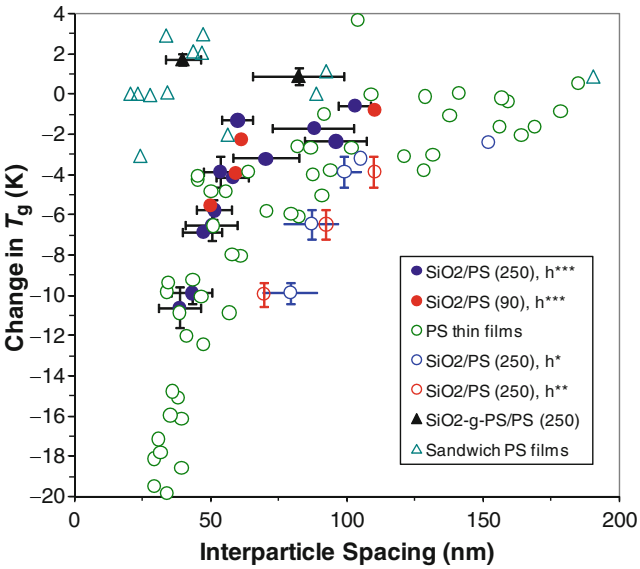

Fig. 6.20 Comparison between the glass-transition response of polystyrene nanocomposites and polystyrene thin films as a function of interparticle spacing, which represents the film thickness for thin films and an average interparticle spacing in the nanocomposites (Bansal et al. (2005), reprinted with permission from Nature Publishing)

interfacial region will generally restrict long chain motion. On the other hand, the interfacial region may also create extra free volume, which assists large scale segmental motion of the polymer chain. These two competing mechanisms may explain the widely divergent experimental observations of the effects of nanoparticles on the glass transition.

Careful comparison of the glass-transitions of PS nanocomposite and thin PS films indicates a good correlation between change in T_g and the average ligament thickness between non-wetting surfaces, as shown in Fig. 6.20 (Bansal et al. 2005). The underlying physics of the reduction of T_g relates to the entropy penalty associated with the non-wetting surface or interfaces, and the models predict the reduced T_g to be:

$$T_g(h) = T_g^{bulk} + \frac{2\xi(T_g(h))}{h}\left(T_g^{surg} - T_g^{bulk}\right) \tag{6.8}$$

where T_g^{bulk} is the bulk T_g and $\xi(T_g(h))$ is the thickness of the surface region with a glass-transition temperature of T_g^{surf} (Forrest et al. 2000).

A further study, which attempted enthalpic control of interfacial properties of nanocomposites, revealed the dependence of the glass transition on the difference of solubility parameters of the particle surface and polymer, and on the surface area (Schadler et al. 2007). As shown in Fig. 6.21, the glass transition temperatures for various nanocomposites correlate qualitatively to the product of the solubility difference between the surface and the polymer with the filler surface area. Tailoring

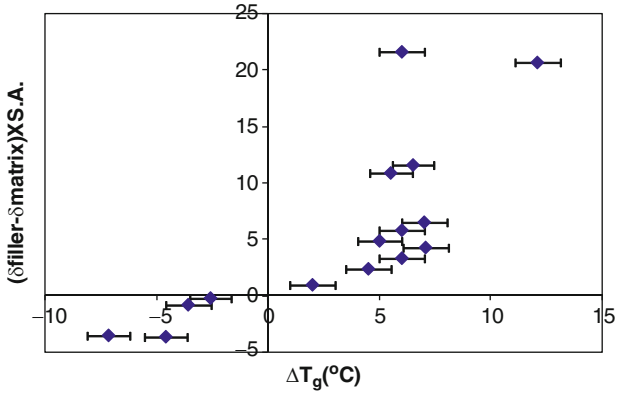

Fig. 6.21 Plot showing the effect of the difference in the solubility parameters multiplied by the surface area as a function of glass-transition temperature. The glass-transition data include melt-processed ZnO/polystyrene and calcium carbonate/poly(methyl methacrylate) composites with several surface modifications as well as data generated on solution-processed silica/polystyrene nanocomposites using both as-received and fluorinated 15-nm silica (Schadler et al. (2007), reprinted with permission from Materials Research Society)

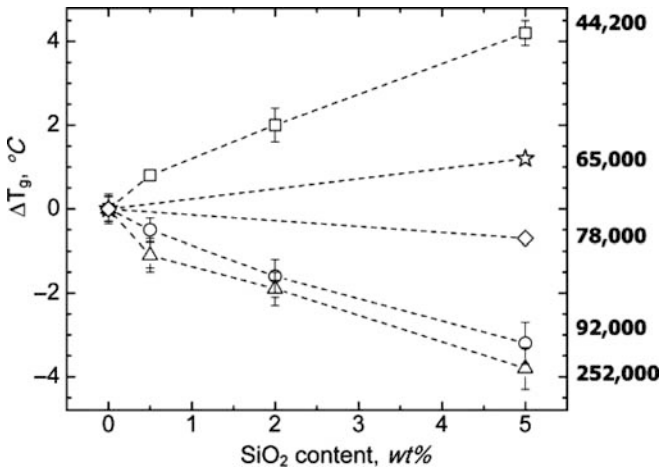

Fig. 6.22 Change in glass transition temperature (T_g) as a function of SiO_2 concentration for various MWs (in g/mol) of the matrix (Bansal et al. (2006), Reprinted with permission of John Wiley & Sons, Inc.)

nanoparticle interface via entropic control may also be effective. As shown in the Fig. 6.22, an increase in the molecular weight of the grafted PS on the silica surface may lead to a transition from wetting to partially-dewetting, and eventually to total dewetting (Bansal et al. 2006). This result implies that the glass transition temperature of the nanocomposite has a distinctive dependence on silica concentration stemming from entropic control.

The understanding of the interface between nanofiller and polymer, and interactions between these, as well as their effects on long chain dynamics and thermo-mechanical properties of the nanocomposites is continually advancing. The glass transition temperature of nanocomposites is an important probe for the particle/polymer interface and interaction. The full understanding of this interface will enable thorough tailoring and control of the bulk thermo-mechanical properties. The glass-transition temperature of polymeric dielectric also relates closely to their continuous use temperatures as their electrical properties deteriorate at temperatures approaching or above the glass transition. Enhancement of glass-temperature of polymeric insulation through proper nanocomposite engineering is essential to the development of new dielectric materials for high temperature, high voltage and high frequency applications. In addition, the underlying physics of such enhancement suggests the reduction of free volume of polymer chains surrounding the nanoparticles and hence the improved electrical breakdown strength, as is mentioned in other chapters.

Generally, the incorporation of inorganic nanoparticles, especially those with layered structures, into a polymer matrix leads to enhanced thermal stability. Varying the silicate content and the length of the intercalant will improve the thermal stability of nanocomposites. Filler content and the type of nanocomposite structure strongly impact the nanocomposite thermal decomposition temperature. This improvement is thought to be due to the formation of a superior isolation layer and mass transport barrier to volatiles generated during thermal decomposition. Study also suggests the thermal stabilities of organosmectite/epoxy nanocomposites can be improved through alkyl-ammonium pre-intercalation (Kotsilkova 2007). The onset of degradation depends strongly on the thermal stability of the organoclay modifier, while the thermal decomposition temperature is primarily affected by the silicate content and the type of nanocomposite structure. For polymeric dielectrics that may be subject to corona discharge during service, formation of such an isolation barrier via incorporation of layered nanostructures could be advantageous for corona resistance engineering.

Flame retardants make materials more difficult to ignite by slowing decomposition and increasing the ignition temperature, through a variety of mechanisms such as absorbing energy from the fire or preventing oxygen from reaching the fuel. The flammability behavior of a polymer may be defined, by measures such as burning rate, spread rate, and ignition characteristics. Limiting oxygen index and the cone calorimeter methods are often used to characterize the fire-retardant properties of polymeric materials by measuring the heat release rate, or heat peak release rate. Polymer nanocomposites are attractive for flame retardant applications, and the nanoscale silica particle is finding application for flame-retardant composites. The example in Fig. 6.23 shows that addition of nanosilica reduces the peak heat release rate of the PMMA sample to roughly 50% of the pure PMMA value (Kashiwagi et al. 2003). The flame-retardant mechanism in this case was inferred to be coagulation of the particles, and the accumulation of loose granular particles near the sample surface, which form a protective heat insulating layer and a barrier for evolved degradation products.

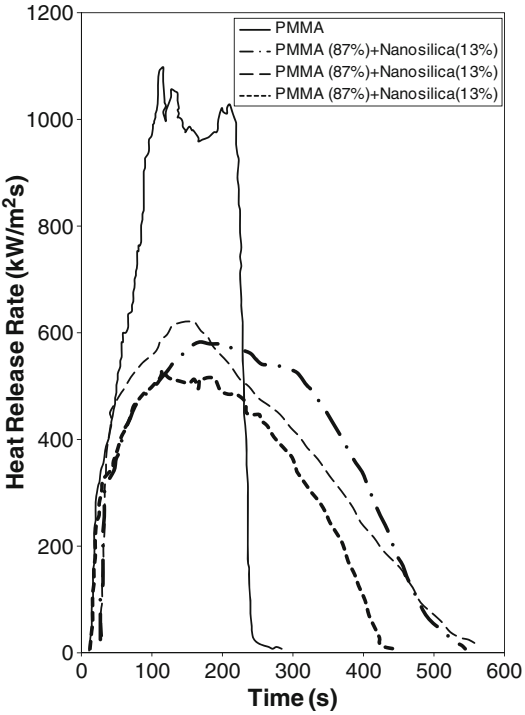

Fig. 6.23 The heat release rates of the PMMA and the PMMA/nanosilica sample prepared by in situ polymerization of MMA with colloidal silica (Kashiwagi et al. (2003), Reprinted with permission of John Wiley & Sons, Inc.)

6.6 Thermal Conductivity

Thermal conductivity is a critical property for high temperature, harsh environment, electrical applications where sensitive electrical and electronic devices must operate reliably and heat dissipation is required for long-term operation. A great deal of research is ongoing to develop highly thermally conductive composites using carbon nanotubes and nano-sized metallic particles. However, the electrical insulation properties of these are generally poor, due to the high electrical conductivity of the filler. Various ceramic and metallic nanofillers are also under study for improving thermal conduction of heat transfer fluids (Xie et al. 2002). Again, due to high electrical conductivity, these materials are generally not adequate for electrical applications. The focus of this section will therefore be limited to solid electrically insulating polymeric nanocomposites.

Modeling and development of improved thermal conductivity composites has been studied for many years. In general, the rule of mixtures summarizes the effects of filler and filler content on the thermal conductivity of a two-phase polymer composite. As filler level increases, thermal conductivity gradually rises due to increased

phonon transport. When the level of filler has reached the percolation threshold, thermal conductivity increases more dramatically. Other simple models include the inverse rule of mixture model and geometric models. Agari and colleagues have proposed a theory to estimate thermal conductivity using, electrical conductivity and volume content (Agari et al. 1993). They have suggested an analytical model (6.9) for calculating the thermal conductivity, λ, of the composite which incorporates (1) the thermal conductivity, λ_1, of the polymer, (2) the thermal conductivity, λ_2, of the fillers, (3) the volume V of the fillers, (4) a coefficient C_p which takes into account the changes in crystallinity and crystal size of the polymer due to the filler, and (5) the critical volume fraction (CVF) of the electrical conductivity, corresponding to the inflection point of the plot of log of electrical conductivity against filler volume content. In (6.9), the log of the quantity (1/*CVF*) has been substituted for C_f, a coefficient related to the ease of forming phonon conduction paths.

$$\log\left[\lambda/\left(C_p \cdot \lambda_1\right)\right] = V \cdot \log\left(1/C\,VF\right) \cdot \log\left[\lambda_2/\left(C_p \cdot \lambda_1\right)\right] \tag{6.9}$$

This equation has been verified experimentally for a variety of polymer filler combinations including spheres, fibers, ceramic oxides, graphite, with differing mixing methods, and at loadings up to 50 vol % of fillers. However these researchers (Agari et al. 1993) did not include the effects of particle size, but limited their analysis to filler particle sizes in the range ~5–10 μm. Very recently Kochetov and colleagues have prepared and evaluated BN and AlN filled epoxy nanocomposites. They have compared and contrasted the simple rule of mixture models, the geometric models and the model proposed by Agari et al. The Agari and Uno model showed the best correlation to their data (Kochetov et al. 2009).

Other researchers have studied the thermal conductivity of nanocomposites as a function of particle size and particle coating. The addition of nanometer-size alumina or silica to a polyamideimide thermoset showed an increase in thermal conductivity compared to that obtained with micron-sized alumina. Coating the particles with either a silane treatment or a thin coating of the cross-linked polyamideimide polymer enhanced the results. Figure 6.24 compares the thermal conductivity of coated and uncoated nanoparticles with micron-sized alumina.

The experimental data suggests that at low filler loadings, there is very little difference between the thermal conductivity of uncoated micron-sized composites and uncoated nanocomposites. However, when the nanoparticles are coated with either a silane treatment or a cured coating of the thermosetting polymer, the thermal conductivity is enhanced (Irwin et al. 2003).

Fan and colleagues (Fan et al. 2004) found that for a fixed filler loading of micron-sized alumina particles, 50 wt%, the thermal conductivity increases with increasing particle size, but if 50% of the micron or larger sized particles are replaced with nanoparticles, the thermal conductivity is reduced. They theorize that the reduction in conductivity is due to an increased number of interfaces along the phonon conduction paths with a corresponding increase in total thermal resistance due to resistance at the interfaces. Others theorize that higher interfacial thermal resistance

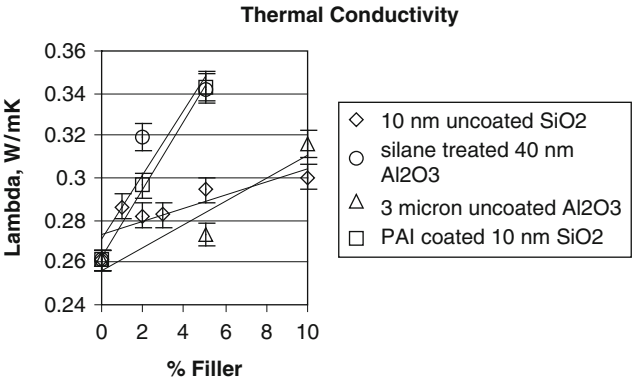

Fig. 6.24 Coated and uncoated nanoparticles vs. micron-sized particles (Data taken from Irwin et al. (2003) with permission from IEEE)

is due to phonon scattering. Furthermore, their modeling work suggests that phonon scattering is due to large differences in mechanical modulus between the filler and the resin (Han et al. 2005).

Han and colleagues also studied the effects of hexagonal BN and found, as expected, that the thermal conductivity increased with increasing levels of BN, but that the level of thermal conductivity was largely independent of BN particle size, be it nano, meso or micro. However, if the BN particles agglomerated into large spherical particles, an increase in thermal conductivity was measured, suggesting that isotropic particles are more effective in improving thermal conductivity. This could also be explained by the larger aggregates having fewer phonon-scattering interfaces.

The study of polymeric composites has matured over the years, permitting the development of conduction models for prediction of composite thermal conductivity. However, a deeper understanding of the fundamentals of nanocomposite conductivity, the role of the interface, and interfacial adhesion will be critical to successful application of nanocomposites for electrical applications.

Acknowledgements The authors wish to acknowledge Dr. Konrad Weeber, Dr. William Premerlani and Dr. Ryan Mills of GE Global Research for their advice and suggestions. Dr. Donald Buckley and Mr. Gerald Irwin offered technical editing comments on the chapter and their input is greatly appreciated.

References

Adams D, Doner D (1967) Transverse normal loading of a unidirectional composite. J Comp Mater 1:152–164

Agari Y, Ueda A, Nagai E, (1993) Thermal conductivity of a polymer nanocomposite. J Appl Polym Sci 49:1625–1631

Anderson TL (1995) Fracture mechanics: fundamentals and applications. CRC Press, Boca Raton
Ash B, Schadler LS, Siegel RW (2002) Glass transition behavior of alumina/polymethylmethacrylate nanocomposites, Mater Lett 55:83–87
Ashton JE, Halpin JC, Petit PH (1969) Primer on composite materials: analysis. Technomic Pub. Co., Stamford, CT
Avella M, Errico ME, Martuscelli E (2001) Novel PMMA/$CaCO_3$ Nanocomposites abrasion resistant prepared by an in situ polymerization process. Nano Lett 1:213–217
Bansal, A, Yang H, Li C et al (2005) Quantitative equivalence between polymer nanocomposites and thin polymer films, Nat Mater 4:693–698
Bansal A, Yang H, Li C et al (2006) Controlling the thermomechanical properties of polymer nanocomposites by tailoring the polymer-particle interface. J Polym Sci B Polym Phys 44:2944–2950
Bao G, Suo Z (1992) Remarks on crack bridging concepts. Appl Mech Rev 45:355–366
Berber S, Kwon Y-K, Tománek D et al (2000) Unusually high thermal conductivity of carbon nano-tubes. Phys Rev Lett 84:4613–4617
Biercuka MJ, Llaguno MC, Radosavljevic M et al (2002), Carbon nanotube composites for thermal management. Appl Phys Lett 80:2767–2769
Cai H, Yan F, Xue Q (2004) Investigation of tribological properties of polyimide/carbon nanotubes nanocomposites. Mat Sci Eng A 364:94–100
Cao Y, Irwin P, Younsi K, (2004) The future of nanodielectrics in the electrical power industry. Trans IEEE DEI-11:797–807
Chen YJ, Zhang HZ, Chen Y (2006), Pure boron nitride nanowires produced from boron triiodide. Nanotechnology 17:786–789
Deng S, Ye L, Friedrich K (2007) Fracture behaviours of epoxy nanocomposites with nano-silica at low and elevated temperatures. J Mater Sci 42:2766–2774
Eshelby JD (1957) The determination of the elastic field of an ellipsoidal inclusion, and related problems. Proc R Soc Lond A 241:376
Evans AG, Williams S, Beaumont PWR (1985) On the toughness of particulate filled polymers. J Mater Sci 20:3668–3674
Evans AG (1972), The strength of brittle materials containing second phase dispersions. Philos Mag 26:1327–1344
Fan L, Su B, Qu J, Wong C (2004) Electrical and thermal conductivities of polymer composites containing nano-sized particles. Proceedings – 2004 Electronic Components and Technology Conference, pp 148–154
Ferry JD (1980) Viscoelastic properties of polymers, 3rd edn. Wiley, New York
Forrest JA, Mattsson J (2000) Reduction of the glass transition temperature in thin polymer films: probing the length scale of cooperative dynamics. Phys Rev E 61:R53–R61
Foye RL (1966) An evaluation of various engineering estimates of the transverse properties of unidirectional composites. SAMPE 10:G-31
Gam KT, Miyamoto M, Nishuimura R, Sue HJ (2003) Fracture behavior of core-shell rubber-modified clay-epoxy nanocomposites. Polym Eng Sci 43:1635–1645
Griffith AA (1921) The phenomena of rupture and flow in solids. Philos Trans R Soc Lond A221:163–198
Griffith G, Tucker S, Milsom J, Stone, G. (2000) Problems with modern air-cooled generator stator winding insulation. IEEE Electr Insul Mag 16:6–10
Guo Z, Pereira T, Choi O et al (2006) Surface functionalized alumina nanoparticle filled polymeric nanocomposites with enhanced mechanical properties. J Mater Chem 16:2800–2808
Halpin JC, Pagano NJ (1969) The laminate approximation for randomly oriented fibrous composites. J Compos Mater 3:720–724
Halpin JC, Kardos JL (1976) The Halpin-Tsai equations: a review. Polym Eng Sci 16:344–352
Han WQ, Zettl A (2002) GaN nanorods coated with pure BN. Appl Phys Lett 81:5051–5053
Han Z, Wood J, Herman H et al (2008) Thermal properties of composites filled with different fillers. Conference Record of the 2008 IEEE International Symposium on Electrical Insulation, pp 497–501

Huang JW, Wen YL, Kang CC, Yeh MY (2007) Preparation of polyimide-silica nanocomposites from nanoscale colloidal silica. Polym J 39:654–658
Hutchinson JW (1989) Theoretical and applied mechanics. Elsevier, North Holland
Irwin P, Cao Y, Bansal A, Schadler L (2003) Thermal and mechanical properties of polyimide nanocomposites. 2003 Conf Elect Insul Dielectr Phen: 120–123
Johnsen BB, Kinloch AJ, Mohammed RD et al (2007) Toughening mechanisms of nanoparticle-modified epoxy polymers. Polymer 48:530–541
Kang S, Hong S, Choe C et al (2001) Preparation and characterization of epoxy composites filled with functionalized nanosilica particles obtained via sol–gel process. Polymer 42:879–887
Kashiwagi T, Morgan AB, Antonucci JM et al (2003) Thermal and flammability properties of a silica-poly(methylmethacrylate) nanocomposites. J Appl Polym Sci 89:2072–2078
Kausch HH, Hassell JA, Jaffee RI (1972) Deformation and fracture of high polymers. Plenum, New York
Kawaguchi T, Pearson RA (2004) The moisture effect on the fatigue crack growth of glass particle and fiber reinforced epoxies with strong and weak bonding condition: part 2. A microscopic study on toughening mechanism. Compos Sci Technol 64:1991–2007
Kim M-S, Kim D-W, Chowdhury SR et al (2006) Melt-compounded butadiene rubber nanocomposites with improved mechanical properties and abrasion resistance. J Appl Polym Sci 102:2062–2066
Kinloch AJ, Maxwell DL, Young RJ (1985) The fracture of hybrid-particulate composites. J Mater Sci 20:4169–4184
Kochetov R, Andritsch T, Lafont U et al (2009) Thermal behaviour of epoxy resin filled with high thermal conductivity nanopowders. IEEE Electrical Insulation Conference, pp 524–528
Koratkar N, Suhr J, Joshi A et al (2005) Characterizing energy dissipation in single-walled carbon nanotube polycarbonate composites. Appl Phys Lett 87:063102
Kotsilkova R (ed) (2007) Thermoset nanocomposites for engineering applications, Smithers Rapra. Chapter 6: performance of Thermoset Nanocomposites
Lange FF (1970) The interaction of a crack front with a second-phase dispersion. Philos Mag 22:983–992
Lewis TJ (1994) Nanometric dielectrics. Trans IEEE DEI-1:812–825
Liu H, Brinson LC (2006) A hybrid numerical-analytical method for modeling the viscoelastic properties of polymer nanocomposites. Trans ASME 73:758–768
Liu H, Brinson LC (2008) Reinforcing efficiency of nanoparticles: a simple comparison for polymer nanocomposites. Compos Sci Tech 68:1502–1512
Lin Y, Chen H, Chan C-M et al (2008) High impact toughness polypropylene/$CaCO_3$ nanocomposites and the toughening mechanism. Macromolecules 41:9204–9213
Liu L, Barber AH, Nuriel S et al (2005) Mechanical properties of functionalized single-walled carbon-nanotubes poly(vinyl alcohol) nanocomposites. Adv Funct Mater 15:975–980
Liu W, Hoa SV, Pugh M (2005) Fracture toughness and water uptake of high-performance epoxy/nanoclay nanocomposites. Compos Sci Tech 65:2364–2373
Messersmith PB, Giannelis EP (1995) Synthesis and barrier properties of poly(e-caprolactone)-layered silicate nanocomposites. J Polym Sci A Polym Chem 33:1047–1057
Mori T, Tanaka K (1973) Average stress in matrix and average elastic energy of materials with misfitting inclusions. Acta Metal 21:571–574
Naous W, Yu X-Y, Zhang Q-X et al (2006) Morphology, tensile properties, and fracture toughness of epoxy/Al_2O_3 nanocomposites. J. Polym Sci B Polym Phys 44:1466–1473
Podsiadlo P, Kaushik AK, Arruda EM et al (2007) Ultrastrong and stiff layered polymer nanocomposites. Science 318:80–83
Preghenella M, Pegoretti A, Migliaresi C (2005) Thermo-mechanical characterization of fumed silica-epoxy nanocomposites. Polymer 46:12065–12072
Ramanathan T, Liu H, Brinson LC (2005) Functionalized SWNT/polymer nanocomposites for dramatic property improvement. J Polym Sci B Polym Phys 43:2269–2279
Ragosta G, Abbate M, Musto P et al (2005) Epoxy-silica particulate nanocomposites: chemical interactions, reinforcement and fracture toughness. Polymer 46:10506–10516

Rittigstein P, Torkelson J (2006) Polymer-nanoparticle interfacial interactions in polymer nanocomposites: confinement effects on glass transition temperature and suppression of physical aging. J Polym Sci B Polym Phys 44:2935–2943

Satapathy BK, Weidisch R, Pötschke P et al (2005) Crack toughness behavior of multiwalled carbon nanotubes (MWNT)/polycarbonate nanocomposites. Macromol Rapid Commun 26:1246–1252

Sawyer WG, Freudenberg KD, Bhimaraj P et al (2003) A study on the friction and wear behavior of PTFE filled with alumina nanoparticles. Wear 254:573–580

Schadler LS, Brinson LC, Sawyer WG (2007) Polymer nanocomposites: a small part of the story. J Mater 59(3):53–60

Schadler LS, Kumar SK, Benicewicz BC et al (2007), Designed interfaces in polymer nanocomposites: a fundamental viewpoint. MRS Bull 32:335–340

Shah D, Maita P, Gunn E et al (2004) Dramatic enhancement in toughness of polyvinylidene fluoride Nanocomposites via nanoclay-directed crystal structure and morphology. Adv Mater 16:1173–1177

Shang XY, Zhu ZK, Yin J, Ma XD (2002). Compatibility of soluble polyimide/silica hybrids induced by a coupling agent. Chem Mater 14:71–77

Shi H, Lan T, Pinnavaia, TJ (1996) Interfacial effects on the reinforcement properties of polymer-organoclay nanocomposites. Chem Mater 8:1584–1587

Spanoudakis J, Young RJ (1984) Crack propagation in a glass particle-filled epoxy resin. Part 1: effect of particle volume fraction and size. J Mater Sci 19:473–486

Sun YY, Zhang Z, Moon KS, Wong CP (2004) Glass transition and relaxation behavior of epoxy nanocomposites. J Polym Sci B Polym Phys 42:3849–3858

Tandon GP, Weng GJ (1984) The effect of aspect ratio of inclusions on the elastic properties of unidirectionally aligned composites. Polym Compos 5:327–333

Tanniru M, Yuan Q, Misra RDK (2006) On significant retention of impact strength in clay-reinforced high-density polyethylene (HDPE) Nanocomposites. Polymer 47:2133–2146

Tsai TY, Lu ST, Hunag CJ et al (2008) The structure-property relationship of Novolac cured epoxy resin/clay nanocomposites. Polym Eng Sci 48:467–476

Vlasveld DPN, Bersee HEN, Picken SJ (2005) Creep and physical aging behavior of PA6 Nanocomposites. Polymer 46:12539–12545

Wang H, Dong R, Liu C, Chang H (2007) Effect of clay on properties of polyimide-clay nanocomposites. J Appl Polym Sci 104:318–324

Wang K, Chen L, Wu J et al (2005) Epoxy nanocomposites with highly exfoliated clay: mechanical properties and fracture mechanisms. Macromolecules 38:788–800

Wang Q, Dai J, Li W et al (2008) The effects of CNT alignment on electrical conductivity and mechanical properties of SWNT/epoxy Nanocomposites. Compos Sci Tech 68:1644–1648

Wang Y, Lim S, Luo JL et al (2006) Tribological and corrosion behavior of Al_2O_3/polymer nanocomposites coatings. Wear 260:976–983

Wank JS et al (2004). Nanocoating individual cohesive boron nitride particles in a fluidized bed by ALD. J Powder Technol 142:59–69

Wetzel B, Haupeiit F, Friedrich et al (2002) Impact and wear resistance of polymer nanocomposites at low filler content. Polym Eng Sci 42:1919–1927

Weon J-I, Sue H-J (2005) Effects of clay orientation and aspect ratio on mechanical behavior of nylon-6 nanocomposites. Polymer 46:6325–6334

Werner P, Volker A, Jaskulkac R et al (2004) Tribological behaviour of carbon nanofibre-reinforced poly(ether ether ketone). Wear 257:1006–1014

Wu YP, Jia QX, Yu DS et al (2004) Modeling Young's modulus of rubber-clay nanocomposites using composite theories. Polym Test 23:903–909

Xie H, Wang J, Xi T et al (2002) Thermal conductivity enhancements of suspensions containing nanosized alumina particles. J Appl Phys 91:4568–4572

Yang J-L, Zhang Z, Schlarb AK et al (2006) On the characterization of tensile creep resistance of polyamide 66 nanocomposites. Part I. Experimental results and general discussions. Polym 47:2791–2801

Yu N, Zhang ZH, He SY (2008) Fracture toughness and fatigue life of MWCNT/epoxy composites. Mater Sci Eng A 494:380–384

Zhang Q-X, Yu Z-Z, Xie X-L et al (2004) Crystallization and impact energy of polypropylene/$CaCO_3$ nanocomposites with nonionic modifier. Polymer 45:5985–5994

Zhang W, Picu C, Koratkar N (2007) Suppression of fatigue crack growth in carbon nanotubes composites. Appl Phys Lett 91:192109

Zhang W, Picu C, Koratkar N (2008) The effect of carbon nanotube dimensions and dispersion on the fatigue behavior of epoxy nanocomposites. Nanotechnology 19: 285709

Zhang W, Srivastava I, Zhu YF et al (2009) Heterogeneity in epoxy nanocomposites initiates crazing: significant improvements in fatigue resistance and toughening. Small 5:1403–1407

Zhang W, Joshi A, Wang Z et al (2007) Creep mitigation in composites using carbon nanotubes additives. Nanotechnology 18:185703–185707

Zhang Z, Yang J-L, Friedrich K (2004) Creep resistant polymeric nanocomposites. Polymer 45:3481–3485

Zhao S, Schadler LS, Duncan R et al (2008) Mechanisms leading to improved mechanical performance in nanoscale alumina filled epoxy. Compos Sci Technol 68:2965–2975

Zhao S, Schadler LS et al (2008) Improvements and mechanisms of fracture and fatigue properties of well-dispersed alumina/epoxy nanocomposites. Compos Sci Tech 68:2976–2982

Zou H, Wu S, Shen J (2008) Polymer/silica nanocomposites: preparation, characterization, properties, and applications. Chem Rev 108:3893–3957

Chapter 7
Electrical Properties

J.C. Fothergill

7.1 Charge Storage and Transport in Polymers and Nanocomposites

7.1.1 Introduction

Wintle (1983) points out that although there are plenty of theories regarding charge transport and storage in polymeric insulation, very little can actually be proved about what is occurring.

In metals, at least under current density conditions that are not too high, we observe "Ohmic" behavior; i.e., the current through the metal is proportional to the voltage across it. It obeys Ohm's law. In semiconductors, things can get more complicated, although it is usually still possible to explain what is going on. If "good" (i.e., non-blocking and non-rectifying) contacts are made to a crystalline semiconductor, then Ohmic behavior is observed. The charge carriers drift (i.e., "conduct") through the semiconductor under the influence of the electric field, E and result in a current density, J:

$$J = \sigma E \tag{7.1}$$

where σ is the conductivity and is given by:

$$\sigma = ne\mu_n + pe\mu_p \tag{7.2}$$

where n and p are the concentrations of electrons and holes, e is the elementary charge of a proton (1.602×10^{-19} C) and μ_n and μ_p are the mobilities of the electrons and holes. Generally either electrons or holes dominate, depending on whether the semiconductor is doped with donors or acceptors.

If a p-n junction exists, however, a non-linear relationship is observed between the current and the applied voltage; this gives rise to the use of such junctions as rectifiers. The higher concentration of electrons in the n-type material causes them

J.C. Fothergill (✉)
University of Leicester, Leicester, UK
e-mail: John.Fothergill@leicester.ac.uk

J.K. Nelson (ed.), *Dielectric Polymer Nanocomposites*,
DOI 10.1007/978-1-4419-1591-7_7,

to diffuse into the p-type material. Similarly, holes diffuse from the p-type to the n-type region. This causes a potential difference between the p and n sides, which causes the charge carriers to drift back to "their own" regions (electrons to the n-type and holes to the p-type). A dynamic equilibrium is achieved in which a contact potential exists between the two sides of the junction and at the junction there is a "depletion" layer in which the concentrations of free electrons and holes are very low. However, since the ionized donor and acceptor atoms cannot move out of the depletion region, they form a space charge, whose polarity and density is equal to that of the dopants. Since the charges either side of the junction must sum to zero, the space charge extends further into the more lightly doped side of the junction.

Under forward bias (i.e. when the p-type semiconductor is more positive than the n-type semiconductor), significant charge carrier movement takes place when the applied voltage approximately exceeds the contact potential. This is due to drift of carriers (i.e., conduction under the electric field) towards the junction where recombination occurs (leading to light emission in the case of an LED). The junction, acting as an interface, is allowing conduction to occur in the semiconductor regions and is controlling the current.

Under reverse bias, the depletion layer, which contains the regions of space charge, widens. Very few holes are available in the n-type region (they will mostly have recombined with the large number of electrons) and so very few holes are injected from the n-type into the p-type region for conduction. Similarly, there are very few electrons injected into the n-type region. The small reverse-bias current flow is mainly due to diffusion of minority carriers to the junction, where they recombine. In this case, the junction is acting to block conduction and the current may reach a saturation value that is not very dependent on the external voltage. Note that, under conditions of either forward or reverse bias, the current is *not* determined directly by the conductivity, as in (7.1). Whilst this is quite complicated, the processes are generally well understood.

7.1.2 Charge Transport in Insulating Systems

The situation in insulators is bound to be even more complicated. Perhaps the simplest scenario to consider would be where the insulator is, in fact, a lightly doped semiconductor (say p^--type) and the electrodes, rather than being metal, are heavily doped semiconductors (say n^+-type), which will behave very much like metals if sufficiently heavily doped. This is shown schematically in Fig. 7.1. In this case, the left p-n junction is forward biased. This could allow current flow and we would expect some electrons to be injected. However, these may recombine with the holes in the p^- type insulator. There is some negative space charge accumulation in the insulation next to the cathode which is known as "homocharge," and this causes a field reduction at this electrode. The right p-n junction is reverse-biased and it would block hole injection, although it may allow electrons to escape from the insulation into the n^+ electrode. A large negative space charge layer forms in the p^- insulator

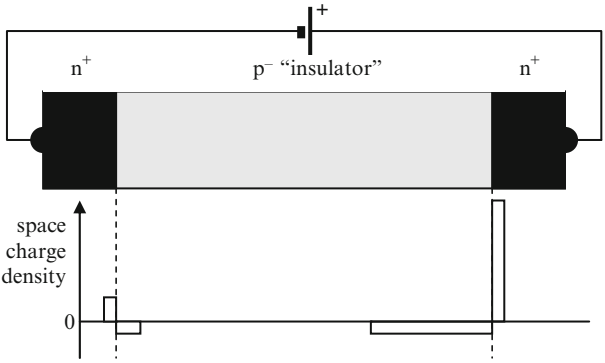

Fig. 7.1 A simple insulating system

adjacent to this positive electrode; which is known as "heterocharge" and this causes field enhancement at this electrode. It can be seen that this is rather like a MOSFET in which no gate voltage is applied and the device is turned off. The behavior of this device is well understood, but it does rely on materials and interfaces that are well characterized both chemically and physically. In particular, it is necessary to understand the nature of the interfaces and whether they will support injection, ejection and recombination under given bias conditions and to understand the nature and processes of transport of charge carriers through the material.

7.1.3 Charge Transport in Polymers

In polymeric insulation, the situation is much less well characterized and less well understood. Some polymeric materials are partially crystalline; perhaps the best known is polyethylene. With its repeating backbone of ethylene units, $-(CH_2) - (CH_2) - etc$, the unit cell is shown in Fig. 7.2, having a height of 255 pm.

These chains fold back and forth to form ribbon-like lamella which may be 50 unit cells thick and thousands of chains wide in the other two dimensions. A "corner" of one of these lamellar is shown schematically in Fig. 7.3. These lamellae are attached to each other by "cilia" – polymer chains that weave from one lamella to another. Further discussion of the physics and chemistry of polymers may be found in Chap. 4.

Within such crystalline parts of polymers, a reasonable electron energy band structure will exist and it would be possible for charges to move through delocalized bands. In polyethylene, the band gap is very wide, approximately 8 eV, and the conduction band edge is above the vacuum level which implies that electrons will be ejected from crystalline regions into the amorphous regions (or electrodes) adjacent to them. However, it may be possible for holes to move through such amorphous

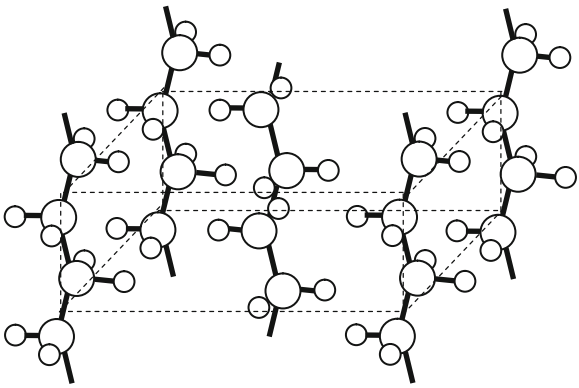

Fig. 7.2 The unit cell of polyethylene (Peacock (2000))

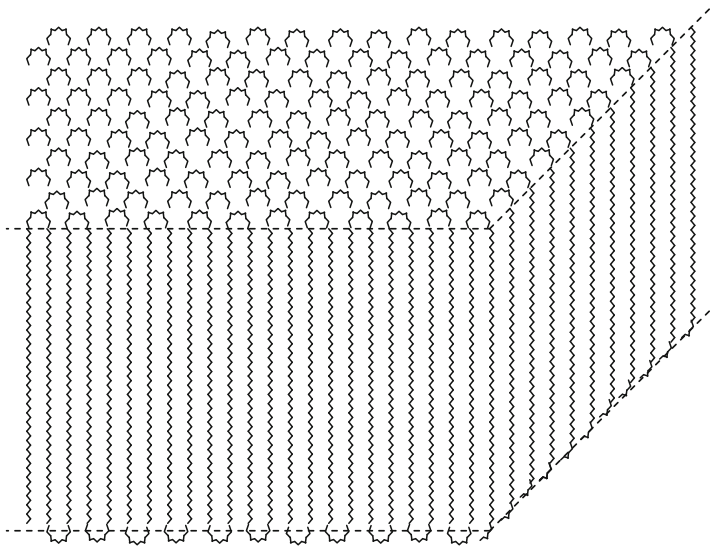

Fig. 7.3 Schematic of a "corner" of a somewhat idealized lamella

regions in polyethylene. Trapping would be likely since the crystalline regions are unlikely to be perfect and, in any case, the charge carrier would never be far from the surface of the lamella where trapping would be inevitable.

Surrounding these crystallites are amorphous regions. In polyethylene this is quite "liquid like" and ionic transport is more likely in these regions. These regions are also likely to contain impurities and additives, which may be polarizable and may even be able to move themselves through the amorphous regions. In these amorphous regions and in wholly amorphous materials (such as epoxy resin), there are likely to be high concentrations of traps.

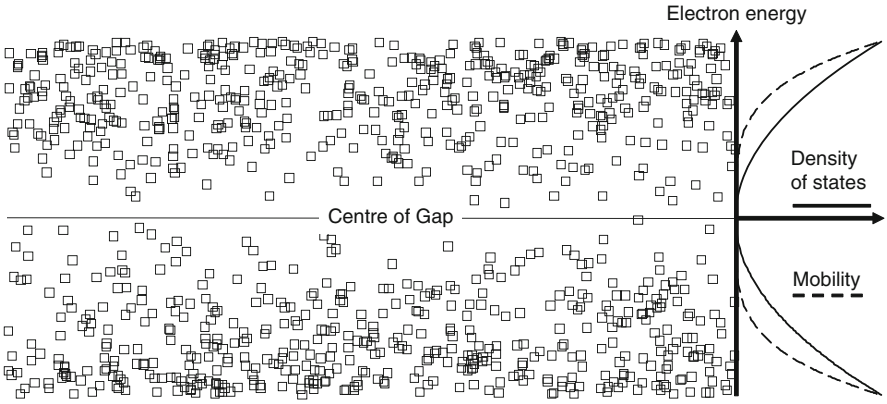

Fig. 7.4 Localized states in a non-crystalline material (indicated by *squares*) as a function of electron energy; the density of states and mobility are also shown (adapted from Dissado and Fothergill 1992)

As one moves from crystalline to amorphous, the well-defined delocalized band structure starts to become interrupted by traps. Eventually, one would expect the traps to dominate, as shown in Fig. 7.4. There is still some semblance of a band structure, but there are fewer traps at energies corresponding to the centre of the gap and there are high trap densities where there were bands. Carriers may be able to hop or tunnel between traps that are physically close to each other and so this results in a "mobility gap" (Mott 1967) near the centre of the band gap where there is a low concentration of states and it is unlikely that hopping or tunneling can take place between them. Conduction through the amorphous regions is therefore likely to be trap limited or ionic (for an overview of these processes see Dissado and Fothergill 1992, Chap. 9). In either case, carriers have to overcome energy barriers to move and so conduction is frequently found to follow an Arrhenius-type relationship:

$$\sigma\,(T) = \sigma_0 \exp\left\{-\frac{U}{kT}\right\} \tag{7.3}$$

where T is the absolute temperature, σ_0 is a constant of proportionality corresponding to a conductivity at 0 K, U is a barrier height and k is the Boltzmann constant (1.381×10^{-23} J K^{-1}). For example, Lampert and Mark (1970) derive the following formula for thermally-assisted ionic-hopping conduction current:

$$J = 2ndv \exp\left\{-\frac{U_B}{kT}\right\} \sinh\left\{\frac{eEd}{2kT}\right\} \tag{7.4}$$

where d is the hopping distance and v is the attempt to hop frequency.

7.1.4 Electrode Effects

Assuming that metal contacts are used, in which the only charge carriers are electrons, "good" contacts must either easily inject/accept electrons into/from the insulation. These electrons might flow through the insulation (perhaps attached to ionized species) or they may recombine with positive carriers (ions or holes).

In an ideal situation in which the metal electrode changes abruptly at a planar surface to become a perfect insulator, then electrons need to overcome a field-dependent Schottky barrier (Dissado and Fothergill 1992), an example is shown in Fig. 7.5. Schottky injection would result in a non-linear relation between current density and field of the form:

$$J \propto \exp\left(\sqrt{E}\right) \tag{7.5}$$

and although this is often observed, the constant of proportionality is usually several orders of magnitude smaller than would be expected. This is probably attributable to chemical and physical defects at the interface on the nanometer scale (e.g., a 2 nm metal oxide layer would result in a decrease of 6–7 orders of magnitude (Lewis 1954).

In practice, electrode – polymer interfaces are unlikely to be "good" even on the nanometer scale, let alone the atomic scale and so it is extremely difficult to predict, in practice, exactly what the effect of electrodes are likely to be – indeed it is thought that electrode effects often lead to irreproducibility in conductivity measurements in polymer insulators.

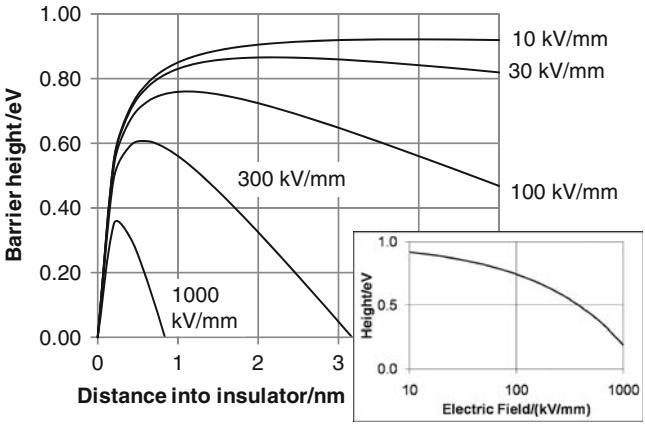

Fig. 7.5 Effective Schottky barrier for a metal with work function = 1 eV and an insulator with a relative permittivity of 2.2 as a function of distance into the insulator plotted for different electric fields. The *inset* shows how the maximum effective barrier height varies with field

7.1.5 Space Charge Effects

Figure 7.6 shows the main behaviors expected of charges in a solid insulator or at the electrodes. Given this variety, Wintle's comments that opened this chapter are not surprising. A further effect of these mechanisms is that charge is not necessarily entering and leaving a region at the same rates. In particular, charge may be injected at an electrode faster or slower than it is transported away in the insulation. Similarly charge may accumulate at an electrode if the coulombic barrier prevents it leaving the insulation as fast as it arrives there. The rate of accumulation will be governed by a continuity equation in which ρ is the total space charge density:

$$\frac{d\rho}{dt} = -\nabla.J \tag{7.6}$$

For example, Fig. 7.7 shows the space charge measurement in crosslinked polyethylene (XLPE) by Teyssedre et al. (2001). It can be seen that positive and negative charge built up on the electrodes as the voltage increased (as one would expect) but also that there was negative charge accumulation near the cathode. A possible reason for this is that electrons were being injected from the cathode corresponding to a current density that was out of balance (i.e., higher than) that due to conduction away from the electrode through the insulation.

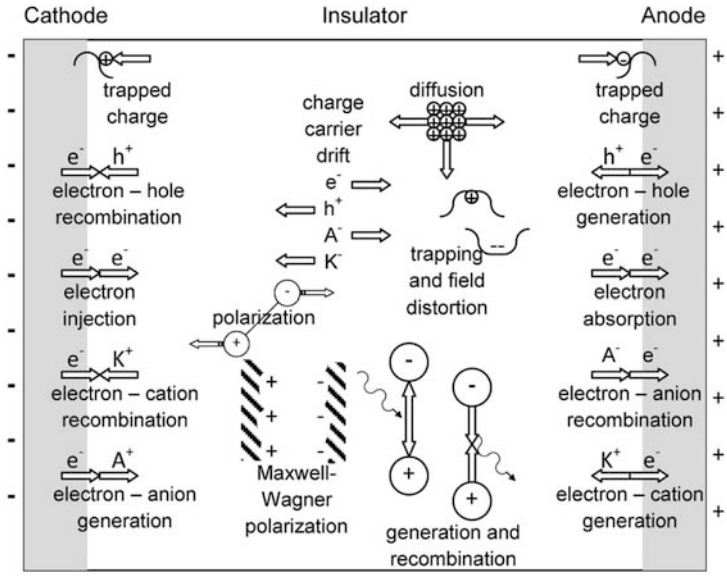

Fig. 7.6 A wide variety of charge behaviors in an insulator or at an insulator – electrode interface affect the external response

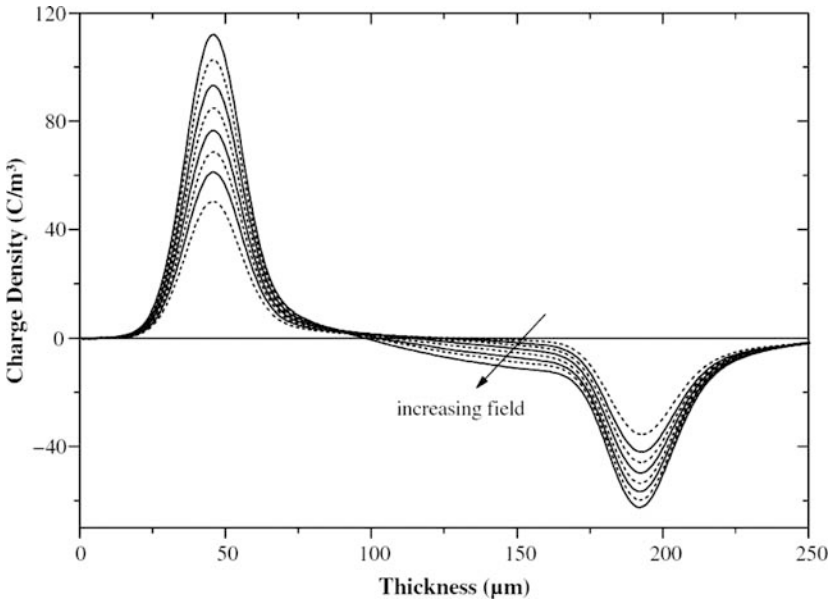

Fig. 7.7 Charge profiles at different fields for a progressive dc stress test on XLPE. The cathode is on the *right* and the anode is on the *left*. Profiles are shown at 60, 72, 80, 88, 96, 104, 112 and 120 kV mm^{-1} (Teyssedre et al. 2001)

The original theory of space charge limited current was developed by Mott and Gurney (1940), in the absence of experimental data from polymeric insulation. They considered an ideal dielectric (no thermal generation of carriers, no traps, ohmic contacts, only electrons, etc.) and showed that above a given voltage, the current would follow a square law. As the charge density builds up it may be expected to fill traps and, if a single trap level is assumed, then this will lead to a very rapid increase in current with voltage. Upon a further increase in voltage (i.e., after the traps are full), the relation of current to voltage would revert to a square law relationship. Given the assumptions in deriving this, it would seem unlikely that this is observed. However, it is commonly observed that, above a given voltage, the current does increase super-Ohmically; often following a square law. Below this voltage, it is often not clear that Ohm's law is obeyed and indeed, considering Fig. 7.1, we might not expect this to be the case. An unusually compliant example is that of Chutia and Barua (1980) shown in Fig. 7.8 for thin films of polyvinylacetate coated with aluminium electrodes.

It can be difficult however, to separate this behavior from the hyperbolic sinusoidal behavior predicted for space-charge limited current by (7.4). Assuming room temperature and a hopping distance of 5 nm, then the sinh term, $\left\{\frac{eEd}{2kT}\right\}$, is less than 1 for a value of $E < 10\,\mathrm{kV/mm}$ so that a slope of 1 on a $\log(J)$ versus $\log(E)$ (i.e., Ohmic behavior) would be predicted in this region (since $\sinh(x) \approx x$ for $x < 1$). Similarly, for fields of 10–30 kV/mm this would result in a plot that was close to

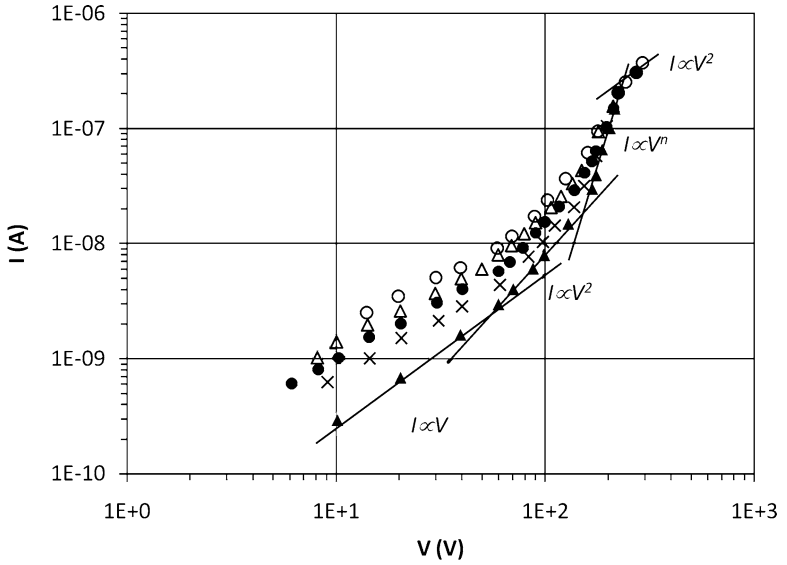

Fig. 7.8 Current–voltage characteristics for 1.2 μm PVAc films at different temperatures: *filled triangle* = −15° C, *times symbol* = 10° C, *filled circle* = 30° C, *open triangle* = 50° C, *open circle* = 80° C (Chutia and Barua 1980)

a straight line with a slope of around 2, perhaps being misconstrued as the onset of SCLC, and above this very high slopes would be observed. Clearly, there would not be a reversion to a slope of 2 at higher fields, but most dielectrics have reached breakdown by this field value.

7.1.6 Effect of Nanoparticles and Interaction Zone on Charge Transport

In considering the effect of the inclusion of nanoparticles (or other inclusions with nanoscopic dimensions) in an insulator there are perhaps two essential factors to take into account: (1) the effect of the nanoparticle on the physical and chemical structure of the material, and (2) how the particle changes the electrical properties of the material surrounding it. The properties of the material surrounding the particle are often substantially changed (certainly from an electrical point of view) and this changed material is said to fall within the "interaction zone" of the nanoparticle. Depending on the concentration and shape and size of the nanoparticles, these interaction zones may overlap giving rise to effects associated with percolation through the interaction zones. The first of these effects has been discussed in detail in Chap. 4. It is noted that surface functionalization of the nanoparticles has a profound effect on the morphology of the insulation and this will at least partly explain the effects on the breakdown voltage noted later in this chapter. Water, oxygen and other

species may also be adsorbed onto the surface of nanoparticles and form a physical layer of a new species between the particle and the host dielectric.

The second of these effects, the change of electrical properties, was explored in a seminal paper by Lewis (1994) entitled "Nanometric Dielectrics" following a theme by the same author that interfaces can dominate observed dielectric behavior. He expanded on this theme in 2004 (Lewis 2004). The "specific area," i.e., the surface area of nanoparticles per unit volume of nanocomposite, is extremely high (see Fig. 1.3) and so his comments are likely to be particularly apposite. Even for spherical nanoparticles, which have the smallest ratio of surface to volume equal to $3/r$, their radius, the specific area is high. In this case, it is equal to $3\psi/r$ where ψ is the volumetric fraction occupied by nanoparticles. So for $\psi = 0.05$ (say) and $r = 50$ nm, one cubic meter of nanocomposite would give rise to three square kilometers of surface area.

In order to remain within the main scope of this book, we will consider insulating particles in an insulating medium. However, it should be noted that there is a significant body of work on conducting nanoparticles (e.g., the carbon nanotubes considered in Chap. 9, or silver aerosol particles) in insulating media and vice versa. In his discussion, Lewis uses similar terminology to that of a charged particle in an electrolyte. For example, suppose that we have a material that has a positive surface charge. (This may arise as a chemical potential – rather like that existing across the p-n junction – or where there are dangling surface bonds, which we might expect in silica for example.)

Figure 7.9 shows a possible scenario. Let us assume that the surface of the particle is charged positively. This may result in a polarization of the host material in

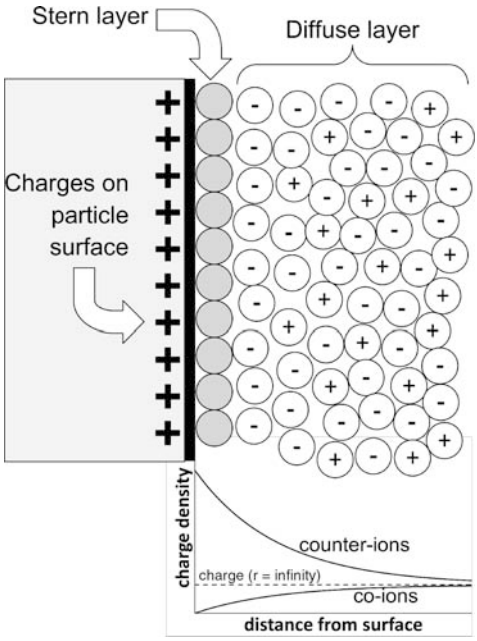

Fig. 7.9 Diffuse double layer produced by nanoparticle with charged surface within a dielectric (adapted from Lewis 2004). On the left is a cross-section through part of the particle showing charges on the surface. On the right is the host polymer

which the particle is located. This process (which is termed "reorganization" in electrochemistry) is dependent upon the permittivity of the medium. A second screening action occurs if the host contains mobile ions. Such ions may include atmospheric molecules that have become ionized by the electric field, for example. A first layer of ions, known as the "Stern" layer (shown as grey circles) may attach to the surface by forces that are stronger than the electrostatic forces attracting the diffusion layer in the interaction zone. In this diffusion layer "co-ions" (i.e., having the same charge as the particle's surface charge) are repelled and counter-ions are attracted towards the particle. Lewis (2004) shows that these may approximate to exponential functions (shown in Fig. 7.9).

The ions in the Stern layer are unlikely to be able to drift under the influence of an electric field. However, the diffuse layer may well be more conductive than the bulk insulation. The preponderance of one type of ion close to the particle implies that these will not be screened and will contribute to the conduction process. Grosse (2006) has considered a similar situation for suspensions of particles in a dielectric liquid. He concludes that, from the dielectric standpoint, a particle surrounded by a surface conductivity, G_S, behaves exactly as if it had no surface conductivity but its bulk (i.e., volume) conductivity were incremented by the $2G_S/a$, where a is the particle radius.

7.1.7 Percolation Effects

Nanoparticles will not be distributed completely uniformly through a nanocomposite. In the absence of forces that cause the particles to be attracted or repelled from one another, there will be a distribution of distances between particles. The implication of this is that interaction zones will overlap to form percolation networks.

Figure 1.2b shows a situation in which a host material is filled with spherical nanoparticles. There are interaction zones shown around each particle. If the widths are equal to the radius of the particle and the loading was 5 wt%, then approximately half the particles will have overlapping interaction zones. Although this is below the percolation level, there would still be significant sub-percolation paths. Furthermore, hopping and tunneling may be possible between zones. An approximation for calculating the probability of overlap (Fothergill 2007) may be undertaken as follows.

Let us assume that we have small spherical particles all of radius, r, that are surrounded by interaction zones of thickness, t. Two such particles will therefore interact if they are separated by a distance $2t$, i.e., if their centers are within a distance $2(r + t)$. This is equivalent to saying that there is more than one particle within a sphere of radius $2(r + t)$. The probability that there are x particles within such a sphere is given by the Poisson distribution:

$$P(x, \mu) = \frac{\exp\{-\mu\}\,\mu^x}{x!} \tag{7.7}$$

where μ is the average number of particles in such a sphere. The probability of two or more particles (the condition for overlap) is therefore[1]:

$$P(x,\mu) \approx 1-(1+\mu)\exp\{-\mu\} \text{ where } \mu = 8\psi\frac{(r+t)^3}{r^3} \tag{7.8}$$

The "approximately equal" sign is used as the radius of the particle becomes significant for small interaction zone thicknesses and the assumption that the particle is small becomes invalid. An example of this is shown in Fig. 7.10. It can be seen that, for a 5% v/v concentration of 50 nm diameter particles, an interaction zone thickness of 25 nm results in an 83% chance of overlap. This is in qualitative agreement with a 2-D simulation (>75% are interacting). Perhaps a more informative way of considering this is to consider percolation theory (Simulations on granular conductive-insulting composites, which may be useful to this area, have been published by He and Ekere (2004). Balberg (2009) has considered percolation allowing for tunneling between particles.)

The percolation limit for spheres, i.e., the concentration that is normally required to obtain a continuous pathway through touching spheres, p_c, is usually considered to be approximately 19%. An interesting question to ask then is, "What concentration of nanoparticles is required such that their interaction zones form a percolating network?" If there are n nanoparticles per unit volume, then their volumetric concentration, ψ, is obviously:

$$\psi = n \times \frac{4}{3}\pi r^3 \tag{7.9}$$

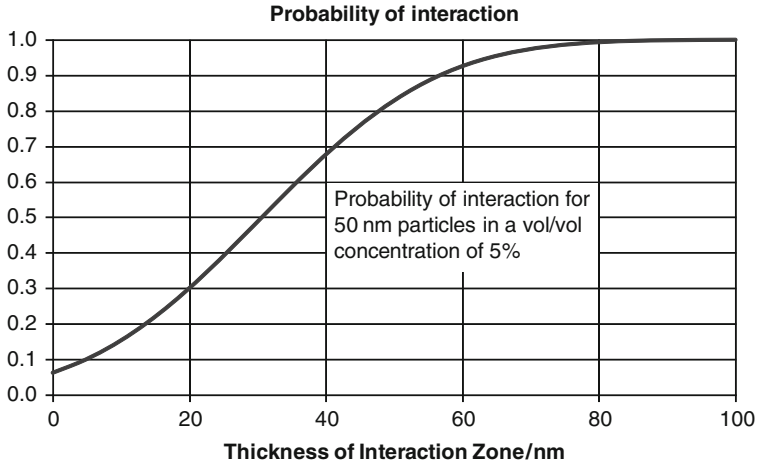

Fig. 7.10 Probability of interaction of the interaction zones of 50 nm spherical particles

[1] Assistance is acknowledged from Prof. Len Dissado with this derivation.

The interaction zones coat the spherical nanoparticles with a layer of thickness, t, so they form spheres of radius $(r + t)$. The volumetric concentration of the interaction zones containing the nanoparticles, ψ_Z, is therefore:

$$\psi_Z = n \times \frac{4}{3}\pi (r + t)^3 \tag{7.10}$$

For percolation to occur, ψ_Z must equal the percolation limit, p_c. The volumetric concentration of nanoparticles required to cause percolation between the interaction zones is therefore:

$$\psi = p_c \frac{r^3}{(r + t)^3} \tag{7.11}$$

Equation (7.11) is slightly oversimplified as it assumes that the interaction zones touch but do not overlap and that will necessarily result in a marked increase in conductivity. However, it should be useful for light loadings of particles. This is shown in Fig. 7.11.

For example, particles with a radius of 15 nm with a 15 nm thick interaction zone would only require a volumetric concentration of 2.4% to reach the percolation limit. *We therefore expect low concentrations of nanoparticles to have significant effects on the electrical properties.*

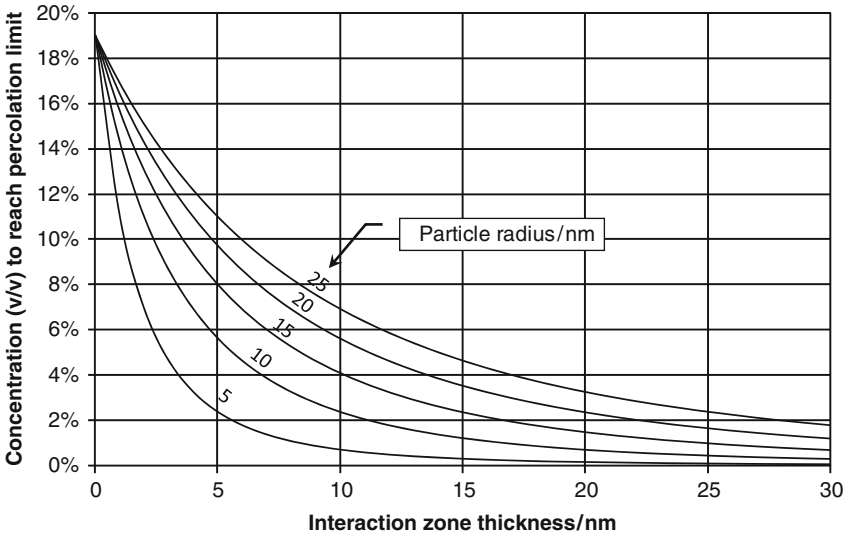

Fig. 7.11 Concentration of nanoparticles required to reach percolation limit from (7.11)

7.1.8 Examples of Charge Movement in Nanocomposites

Cao and Irwin (2003) have investigated the field and temperature dependence of the steady-state current density for a polyimide (PI) polymer with 10 wt% (approximately 6.5 vol%) 40 nm nanoparticles of silica. Their results (more clearly shown in Cao et al. 2004) are reproduced in Fig. 7.12.

Plotting this data on a $\log(J)$ versus $\log(E)$ plot instead would suggest a change from Ohmic to space charge limited current behavior at about 10–20 kV/mm. However, because the temperature dependence here is also found to fit the Lampert and Mark equation (7.4), this may be indicative of an ionic conduction process. The hopping distance is found to be 4.3 nm with activation energy of 0.68 eV. These parameters would not exclude an electronic conduction process, which may give rise to similar behavior. From Fig. 7.11, for percolation to be occurring, this would require an interaction zone thickness of approximately 10 nm. One could imagine a situation in which, for this composite, the interaction zone is less than this, perhaps 5 nm, and ions are required to hop the remaining 5 nm between interaction zones. The same authors reported that a 2 wt% ($\approx$1.6 vol%) addition of nanofiller reduced the conductivity by about half an order of magnitude (at 100°C) whereas an increase to 10 wt% ($\approx$6.5 vol%) increased it from this value by about an order of magnitude. The initial addition of nanofiller may therefore have been causing morphological changes which decreased the conductivity.

Zhang et al. (2006) have found similar results for PI filled with both nano SiO_2 and Al_2O_3. An example of this is shown in Fig. 7.13.

Zhang et al. attribute the change of slopes observed, at least at lower loadings, to the onset of space-charge limited current. This may be true but it would be difficult to be sure without making measurements as a function of temperature as well. For this nanocomposite the wt% and vol% loadings are similar and

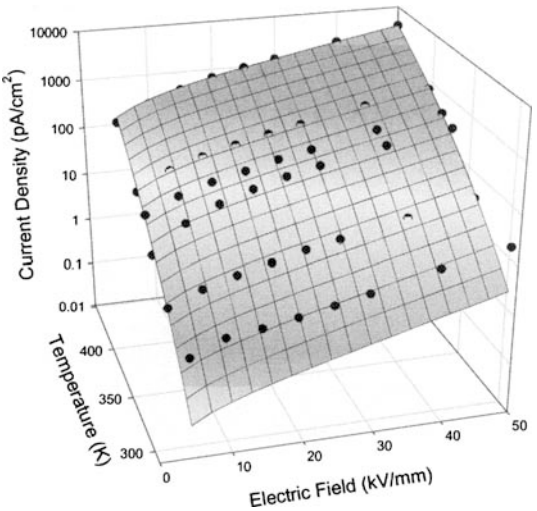

Fig. 7.12 Field and temperature dependence of current density for PI with 10 wt% nano-silica (Cao et al. 2004). © IEEE

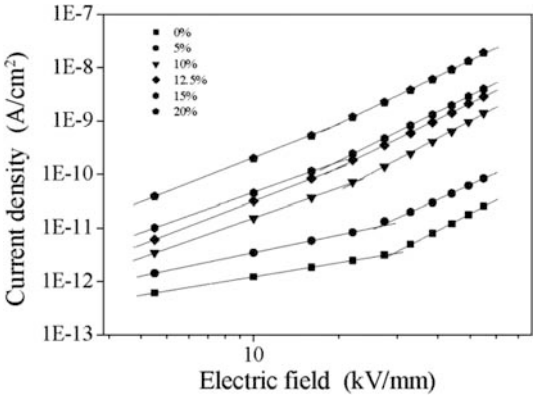

Fig. 7.13 The conduction current in PI filled with nano-Al_2O_3 (Zhang et al. 2006). © IEEE

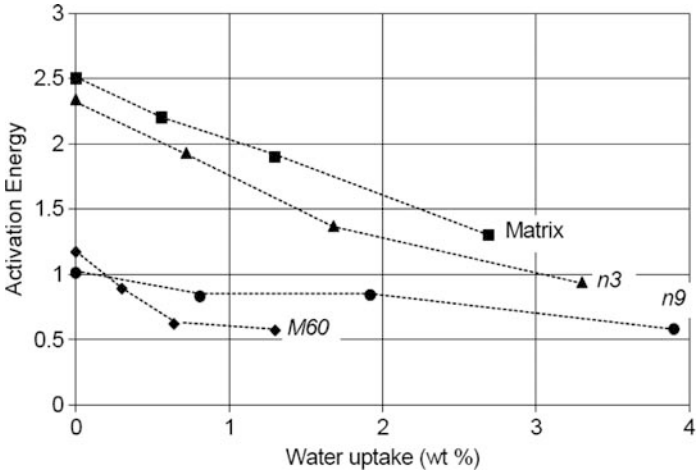

Fig. 7.14 Activation energy in electron-volts of low frequency charge transport process in nano-silica (50 nm diameter) filled epoxy (from Zou et al. 2008). Matrix = unfilled resin, n3 = 3 wt% nanofilled, n9 = 9 wt% nanofilled, M60 = 60 wt% filled with larger silica (tens of microns in diameter)

a substantial change is noted on increasing this from 5 to 10%. It may be that the latter corresponds to transport through substantially overlapping interaction zones. A selection of similar results has been reviewed by Tanaka et al. (2004).

Zou et al. (2008) introduced 50 nm silica particles, without any surface functionalisation, into epoxy resin. It was shown that this introduced a layer of water around the particles (under humid conditions), which we might consider acts as a well-defined interaction zone, whose thickness must be dependent upon humidity. This was also compared with an unfilled epoxy and an epoxy filled conventionally with larger silica particles of tens of microns in diameter. The activation energy of the low frequency charge transport process was found through dielectric spectroscopy at different temperatures. A summary of the results are shown in Fig. 7.14.

The results clearly show that the lightly (3 wt% ≈ 1.5 vol%) nano-filled material behaves very like the unfilled material. The "rate-determining step" in the charge transport is movement between interaction zones through the resin. The interaction zones must be reasonably well separated in this case. However for the more heavily nano-filled material (9 wt% ≈ 4.5 vol%) the activation energy is much lower – suggesting that charge movement is much easier and probably largely through overlapping interaction zones. This is similar to the heavily micro-filled material where we would expect this to be the case. This would suggest interaction zones of around 15–25 nm thick. Although the water layer was not this thick, it is clear from the unfilled material that the charge transport process is influenced by water in the resin itself. It is therefore likely that, although the nanoparticles may have been coated with a few monolayers of water (perhaps corresponding to the Stern layer), there was also a diffuse layer of water extending considerably further into the resin.

7.1.9 Internal Charge Distribution in Nanocomposites

Internal charge that is trapped in an insulating media is known as "space charge" (historically named after the charge that accumulates above the cathode in a thermionic valve). It is generally undesirable since it causes a distortion in the electric field in the insulator. Homocharge (charge near an electrode of the same polarity as the voltage on the electrode) decreases the field near the electrode (which may be desirable) but, because the same voltage is applied across the same thickness and the average field must be maintained, there must be a concomitant increase in electric field elsewhere in the insulation (which is undesirable). Heterocharge increases the field next to the electrode and is almost always undesirable. A reduction in space charge accumulation is therefore an important goal. There is a general increase in the proportion of high-voltage insulators required to support DC voltages as the requirement for long-distance electrical transmission increases. It is therefore particularly important to understand and reduce space charge accumulation in these cases.

Holé et al. (2006) have shown that it is very difficult to measure space charge distributions accurately in nano-filled composites. They analyzed the implications of filler particles on different space charge measurement techniques and showed that they produce perturbations to the space charge distribution signal irrespective of the measurement method. The problem is exacerbated by some particles, such as silica, that exhibit piezoelectricity; these induce a random like signal during the measurement owing to the random distribution and orientation of the particle in the host material. By reverse-engineering the signal they concluded that charge trapping around nanoparticles is likely to occur.

Nelson et al. (2002) were the first to report the reduction of space charge densities through nano-filling composites. Further work by these authors (Nelson and Fothergill 2004) reported how the maximum electric field (caused by the space charge distortion) is reduced by incorporating nanofillers, Fig. 7.15. A voltage of

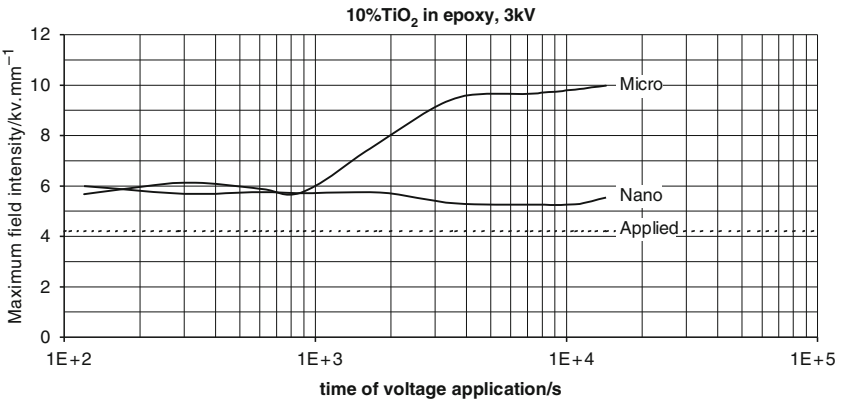

Fig. 7.15 Reduction in field distortion through the incorporation of nanofillers (Nelson and Fothergill 2004)

3 kV was applied to epoxy resin specimens approximately 0.7 mm thick, resulting in an average (or "applied") field of 4.2 kV/mm. The specimens were filled with 10 wt% TiO_2 of either nanometric or micron-sized dimensions. Due to space charge accumulation, the maximum measured field initially was around 6 kV/mm. After about 15 min, the maximum field in the micro-composite increased significantly, as might be expected, as space charge was injected. However, this was not the case in the nanocomposite. In this case, no further space charge injection was observed.

At very high fields, "charge packets" may be observed in some insulators. This is an unstable, chaotic phenomenon in which waves of charge, typically of a magnitude that would double the local field intensity, travel slowly across the insulator. They may take minutes or even an hour to travel a millimeter. Whilst these may not be of particular interest from an engineering point of view – they only happen at very high fields – they may give clues as to the mechanisms of charge transport in such insulators. These charge packets are generally found to be reduced by the addition of nanoparticles. For example, Murata et al. (2008) and Hayase et al. (2007) added nano sized MgO filler to crosslinked polyethylene (XLPE) and reported on the volume resistivity and space charge behavior. The results indicate the suitability of XLPE(S)/MgO nanocomposite material for HVDC insulation; the "S" referring to a "special" XLPE with reduced crosslinking byproducts (This would include acetophenone which is highly mobile and ionizable.) Figure 7.16 shows the charge packet behavior they observed: packets are observed in the XLPE(S) material crossing the specimen in about 20 min. However the nanoparticles appear to quench this behavior completely.

Zilg et al. (2003) have measured space charge accumulation in polypropylene (PP) and ethylene vinyl acetate (EVA) doped with fluorohectorite surface modified with protonated octadecylamin (ODA) in 2, 3 and 6 wt% concentrations. Again they see a general reduction in space charge (Fig. 7.17).

Their conclusions are fairly typical. The magnitude of the space charge decreased at high fields, although this is not necessarily observed at low fields. The space

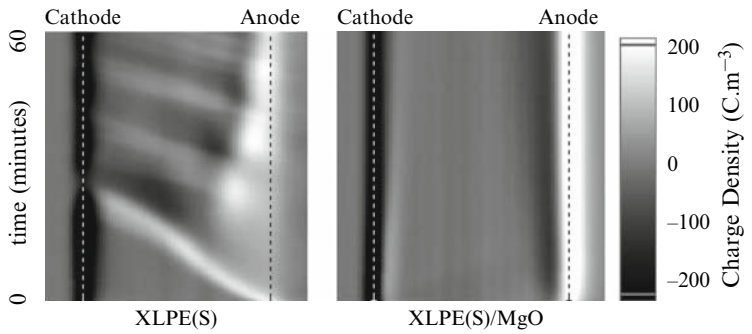

Fig. 7.16 Time dependent space charge distribution in XLPE(S) and XLPE(S)/MgO under electric field of 150 kV/mm (Murata et al. 2008). © IEEE

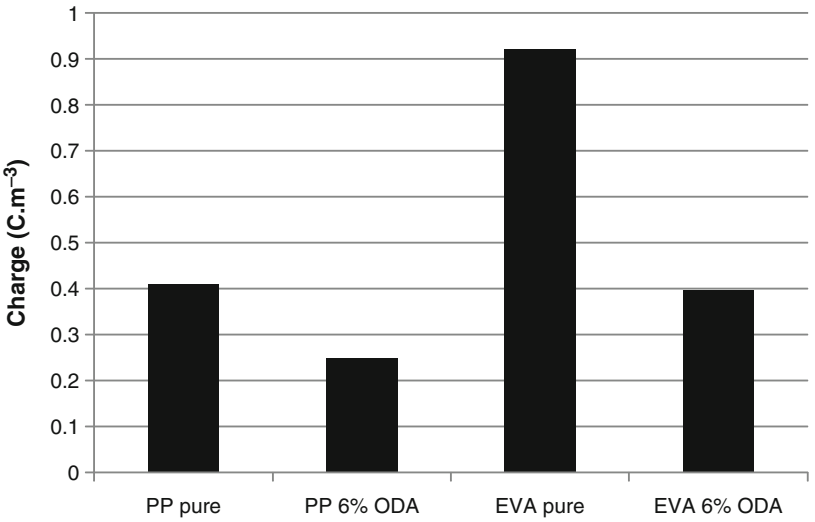

Fig. 7.17 Reduction in space charge observed by Zilg et al. (2003) for PP and EVA doped with fluorohectorite nanoparticles surface modified with protonated octadecylamin (ODA)

charge inception voltage decreased (from 14 to 5 kV/mm for PP) upon the addition of nanofillers – and further decreased if the nanofiller content increased. The decay of charge in the material was faster for the nanofilled materials. The review paper of Tanaka et al. (2004) made similar conclusions. "Nanomization" causes the following effects

- Space charge increases at low fields and decreases at high fields (e.g., Zilg et al. 2003, Ma et al. 2005)
- Space charge inception field decreases (Zilg et al. 2003)
- Space charge is generated internally (Nelson et al. 2002)
- Charge decay time decreases (Zilg et al. 2003; Nelson et al. 2002)

7.1.10 Concluding Remarks on Charges in Nanocomposites

It seems likely that ionic conductivity is enhanced by the addition of nanoparticles to insulating polymers. Small concentrations of particles, surrounded by interaction zones, allow percolation of such ions to be enhanced. Ionic conduction is greatly enhanced by increased electric fields. Space charges can give rise to local increases in electric fields. The increased conduction at these fields by the addition of nanoparticles causes these space charges to disperse. Charges will naturally occur around nanoparticles, increasing the space charge at low fields, however this is at a sufficiently small level that it is unlikely to be a problem at technologically important fields. The space charge inception voltage – i.e., the voltage at which super-Ohmic behavior occurs, may be due to ionic charges. Indeed, it is possible that this onset field is more to do with ionic charge transport than a significant increase in charge accumulation.

7.2 Dielectric Response

7.2.1 Dielectric Spectroscopy

Dielectric spectroscopy is frequently used by engineers to evaluate the effect of using a dielectric in a circuit (be that an electronic circuit or a high voltage transmission system) and by chemists to improve understanding of dipolar processes. Processes include: very low frequency ("sub-Hertz") processes which provide information about charge transport processes; Maxwell-Wagner polarization processes, which provide information about charge trapping associated with internal surfaces (such as those found on nanoparticles and electrodes); and relaxation processes associated with dipoles reorientation.

Dielectric spectroscopy usually involves the application of a sinusoidal voltage and the measurement of the resulting sinusoidal current. The relative amplitudes and phases of the voltage and current allow the complex impedance of the sample to be evaluated. Time domain techniques may also be used and the frequency domain behavior calculated through deconvolution using a Fourier transform. The electrical impedance may be considered as $\mathbf{Z}(\omega) = R(\omega) + \mathbf{j}X(\omega)$ where R is the resistance and X is the reactance of the specimen under test and ω is the angular frequency, i.e., $\omega = 2\pi f$. In order to analyze the loss mechanisms, it is often more convenient to express this impedance as a complex capacitance $\mathbf{C}(\omega) = C'(\omega) - \mathbf{j}C''(\omega) = 1/\mathbf{j}\omega\mathbf{Z}(\omega)$. Measurements are usually made over a range of frequencies and temperatures.

In the case of a capacitive specimen, such as a power cable, the real part of the capacitance, $C'(\omega)$, simply represents the capacitance of the cable, which would normally only change slightly with frequencies around the power frequency. Since this component is reactive, this gives rise to charging ("displacement") currents that are out of phase with voltage under AC conditions but no power loss.

The imaginary part of the capacitance, $C''(\omega)$, is resistive in nature, and therefore does lead to power dissipation. In the case of an XLPE power cable, one would normally expect this to be small and highly frequency dependent. The imaginary part of the capacitance is normally attributed to two types of physical mechanism. Firstly, if there is some sort of DC conduction mechanism that has a conductance, G_{DC}, (i.e., a parallel resistance equal to $1/G_{DC}$), then this will lead to a component of $C''(\omega)$ that is equal to G_{DC}/ω. This is likely to dominate at low frequencies and is easily observable since, on a Bode plot of $\log\{C\}$ versus $\log\{f\}$, C' is flat (slope $= 0$) whereas C'' has a slope of -1. Secondly, there may be power loss due to the movement of dipoles within the dielectric. This is frequency dependent. At sufficiently high frequencies, a given type of dipole will not be able to align quickly enough with the alternating field and so will not dissipate power. At sufficiently low frequencies, the dipole moves so slowly that any power dissipation becomes negligible. There is, therefore, a dispersion or "loss peak" at a frequency at which the maximum power is dissipated. From an engineering point of view, this is equivalent to a frequency dependent conductance, $G_{AC}(\omega)$ so that $C''(\omega) = (G_{DC} + G_{AC}(\omega))/\omega$.

7.2.2 Dielectric Response of Nanocomposites

The addition of nanoparticles causes major changes in the dielectric response consistent with the formation of interaction zones as described earlier. An example, which illustrates these mechanisms, is shown in Fig. 7.18, taken from Nelson and Fothergill (2004).

At high frequencies the micro-composite has a higher relative permittivity, presumably because the filler has a high permittivity ($\approx$99). For example at 1 kHz, the measured real permittivities are: 9.99 (base resin), 13.8 (micro-composite), and 8.49 (nanocomposite). It is interesting that the nanocomposite has a lower permittivity than the base resin. This may be in part due to the very small size of the particles giving rise to limited cooperative movements of dipolar reorientation within them, but it is probably also due to the restriction by the nanoparticles of movement of end-chains or side-chains of the epoxy molecules.

In the mid range of 0.1–100 Hz, the base resin and nanocomposite behave in similar ways; there is some evidence of a small dielectric relaxation possibly due to bound water. The activation energy of this process drops from 1.7 eV for the micro-composite to 1.4 eV for the nanocomposite perhaps indicating that the water is "less bound" – possibly in the diffuse layer around the nanoparticles.

The real permittivity of the micro-composite shows a significant increase with decreasing frequency associated with Maxwell-Wagner interfacial polarization. (Although the frequency for such a mechanism might be considered rather high, the polarization is probably between the micro-particles rather than the electrodes and, as these are quite close together – about 1.5 μm – the time required for polarization to occur is correspondingly small.) The base resin exhibits the classic indicator of Maxwell-Wagner polarization below 0.1 Hz – slopes of -2 and -1 respectively for

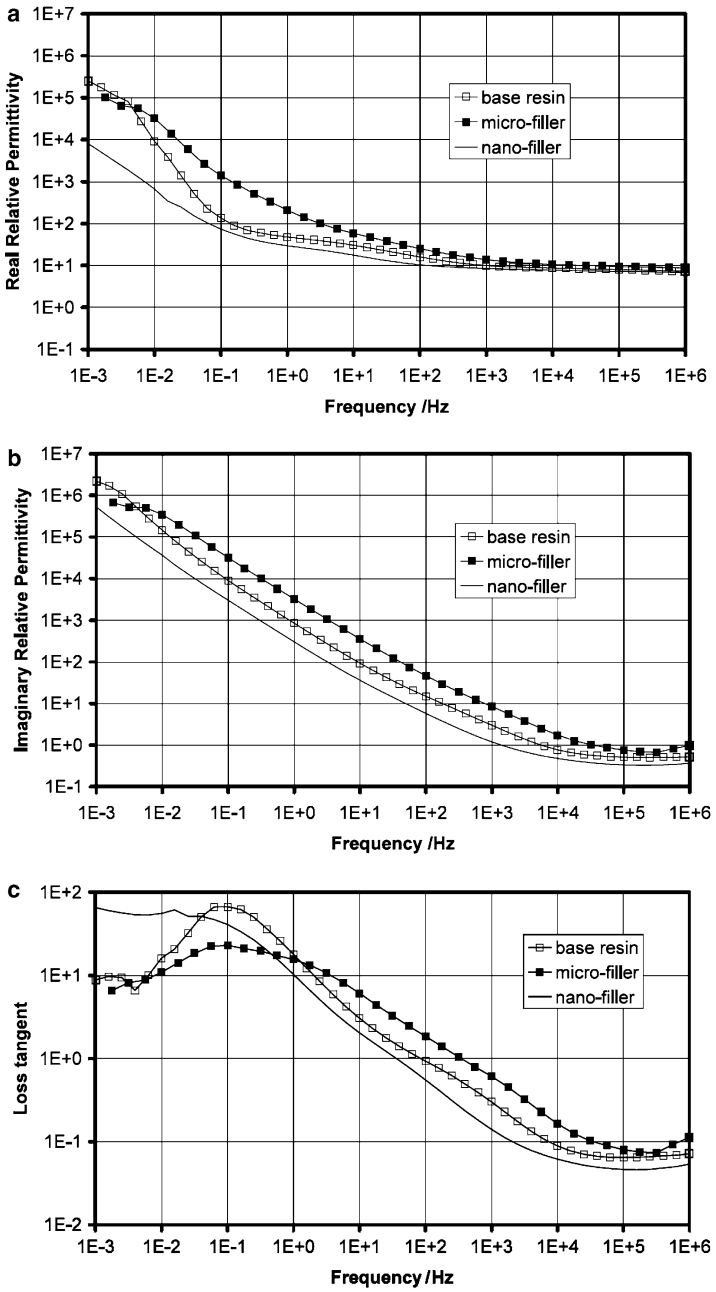

Fig. 7.18 Dielectric response of TiO_2 – epoxy composite (**a**) Real and (**b**) Imaginary parts of permittivity and (**c**) loss tangent (Nelson and Fothergill 2004)

the real and imaginary parts of the permittivity on these Bode plots. This results in a peak in the loss tangent, also observed for the micro-composite – in this case due to Maxwell-Wagner polarization at the electrodes.

The nanocomposite shows quite different behavior at low frequencies. Instead of the real part having a slope of −2, it is parallel to the imaginary part with a slope of −1 and the loss tangent is flat and independent of frequency. This is symptomatic of what Jonscher (1983) refers to as a "low-frequency dispersion" and Dissado and Hill (1984) refer to as "quasi-DC" or QDC. This is characteristic of charge carriers having limited freedom of movement within a material; they may follow tortuous paths that do not allow transport completely through the material. Dissado and Hill (1988) later modeled this in terms of fractal circuits. It seems quite reasonable to assume that such behavior would occur if the paths formed by overlapping interaction zones were at the sub-percolation level for this composite (Although the wt% concentration is 10%, for this combination of particle and host, the vol% concentration is only about 2.8%. So for 38 nm particles, from Fig. 7.11, we might expect to have interaction zones 20 nm thick for percolation to occur.) This transport mechanism is likely to lead to the mitigation of space charge accumulation.

Figure 7.19 shows the dielectric spectroscopy of polyimide measured by Cao and Irwin (2003). The micro-composite has a loss peak at ∼1 kHz, which does not exist for the unfilled material. This corresponds to Maxwell-Wagner interfacial polarization. In the nanocomposite, this interfacial polarization peak is largely reduced by the field mitigation with the shrinking of filler dimension.

Mixing polymers with layered silicates leads to three different types of structures (Elmahdy et al. 2006): phase separated micro-composites; intercalated and exfoliated nanocomposites as discussed in Chap. 3. The dielectric properties of intercalated nanocomposites are markedly different from the base resins. For example Elmahdy et al. (2006) studied the hydrophilic polymer, polyethylene

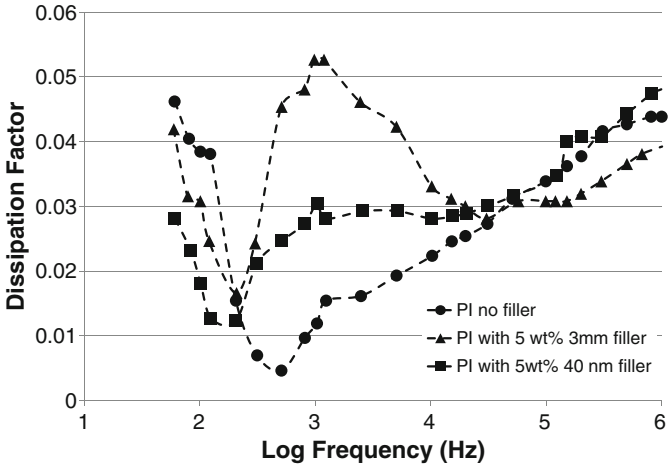

Fig. 7.19 Dielectric dissipation factor for PI nanocomposites (Cao and Irwin 2003)

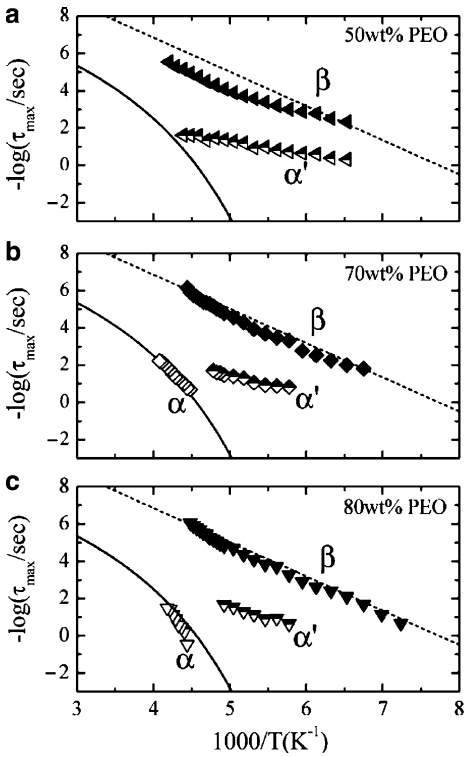

Fig. 7.20 Arrhenius relaxation plots for PEO – Na^+MMT nanocomposites (**a**) 50 wt%, (**b**) 70 wt% and (**c**) 80 wt% PEO (Elmahdy et al. 2006)

oxide (PEO) intercalated within the hydrophilic silicate, sodium montmorillonite, Na^+MMT. These may have applications in electro-active devices and solid-state batteries. The confinement of the PEO films within the MMT galleries causes an increase in the speed of the PEO segmental relaxation (displaying Arrhenius temperature dependence) and also an increased ionic conduction.

Figure 7.20 illustrates this effect, the solid and dashed lines indicating the α and β processes for the pure PEO. The relaxation times of the α-process follow the Vogel-Fulcher-Tamman equation:

$$\tau = \tau_0 \exp\left\{\frac{B}{T - T_0}\right\} \tag{7.12}$$

with $\tau_0 = 1.0 \times 10^{-11}$ s, $B = 2,700 \pm 300$ K and T_0 (the glass transition temperature) $= 112 \pm 10$ K. The relaxation times for the fast local β process of pure PEO correspond to an Arrhenius type process (7.3) with the activation energy $U = 0.36$ eV and $\tau_0 = 6 \times 10^{-15}$ s. For the 50 wt% PEO system (and less), the PEO α process is not observed at all since all the PEO segments are confined within the galleries and relax at a faster rate, shown as an α′ process. In contrast, for the 70 and 80 wt% cases, the α process is seen and is due to the segmental motion of the amorphous regions of the PEO chains that reside outside the galleries and crystallize

in a similar way to that of bulk PEO. The main finding from the dielectric relaxation point of view, is that of a new α' process due to the confinement of polymer mobility. The activation energy of this process is dependent on the PEO concentration: 0.29 eV (80%), 0.18 eV (70%), 0.13 eV (50%) and 0.12 eV (30%). The fast local β-process is observed with a rate comparable to that of bulk PEO due to its local character.

7.3 Electrical Breakdown

7.3.1 Introduction

The increase in reliability of high-voltage products such as power cables (e.g., Bertini 2009) has been largely due to incremental improvements that have reduced contaminants, protrusions (from electrodes) and voids. The effect of new technologies on the electrical breakdown characteristics are therefore difficult to assess. In the case of nanocomposites, one has to compare a mature technology in which virtually perfect electrical insulation systems are compared with insulators that potentially contain agglomerations of particles and impurities and imperfections that are difficult to avoid in a laboratory process. It is therefore unsurprising that there are contradictory results. However, recent results, in which the production processes of nanocomposites have improved, are showing encouraging results.

Electrical breakdown results are frequently analyzed using Weibull statistics and presented on Weibull plots (e.g. IEEE Standard 930 2004) in which the cumulative probability of breakdown (which would equate to the proportion of specimens failed for a large sample size) is plotted on appropriate axes as a function of the breakdown voltage. This is further discussed in Sect. A.9.1 and the probability described by variants of (A.12).

Just as we might expect the charge transport processes to be affected by both changes of morphology and changes to carriers densities and mobilities induced by including nanoparticles, so we would expect these two factors to influence the breakdown characteristics.

7.3.2 Polyethylene Nanocomposites

The effect of morphology is well illustrated by the work of Vaughan et al. (2006) who prepared a range of nanocomposites containing polyethylene and montmorillonite (MMT) clay using different procedures, such that the extent of MMT dispersion varied. They found that when the MMT is poorly dispersed, the short-term breakdown strength is reduced but the situation is much improved when efforts are made to maximize the dispersion.

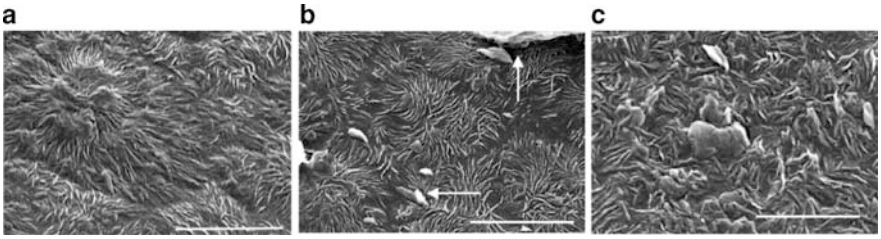

Fig. 7.21 Morphological structures of polyethylene – MMT composites (Vaughan et al. 2006):
(**a**) normal spherulitic structure for unfilled PE (scale bar = 10 μm).
(**b**) Poor dispersal – bright inclusions are aggregates of MMT (scale bar = 10 μm).
(**c**) Well dispersed MMT – morphology is highly perturbed by MMT (scale bar = 5 μm)

Figure 7.21a shows a SEM image of an etched surface of unfilled PE in which the banded spherulites can be clearly seen. Figure 7.21b shows a 5% addition of MMT in which there is poor dispersion. There is no evidence of the polyethylene interacting with the MMT: the spherulitic structure is very similar to Fig. 7.21a and aggregates of MMT are clearly seen to exist. In Fig. 7.21c, in which the workers had set out to disperse the MMT maximally, although aggregates can still be seen, it is generally difficult to distinguish the MMT platelets from the polymer lamellae. The morphology has been grossly disturbed and there is now little evidence of spherulitic structure. This has made a huge difference to the breakdown voltage. Figure 7.22 shows Weibull plots for the poorly dispersed and well dispersed materials corresponding to Fig. 7.21b, c. The better dispersed material, with the much more irregular lamella structure, results in a higher breakdown strength (an increase in the α value from ∼120 to ∼180 kV/mm) and an increase in β from ∼10 to ∼20.

Figure 7.23 depicts the results of Hoyos et al. (2008), who found similar results using a variety of MMT formulations with LDPE. The reader is referred to the original paper for details. They were able to achieve extremely high β values of >70 (i.e., extremely reproducible results) indicating that the effect of the nano-additive had produced a material that was highly uniform and homogeneous. The characteristic breakdown voltage (α), defined by (A.12), increased slightly but the increase in β is highly significant if high reliability systems are to be produced. They considered that a laminar geometry "is a must" if an increase in dielectric strength is required. They also note that adequate processing conditions are required for increasing the value of the shape parameter.

7.3.3 Epoxy Nanocomposites

Montanari et al. (2005) using nanostructured epoxy-silicate insulating materials found similar results. They concluded that the characteristic breakdown voltage was not changed by nanostructuring the material (it remained at 31.1 kV/mm) but that

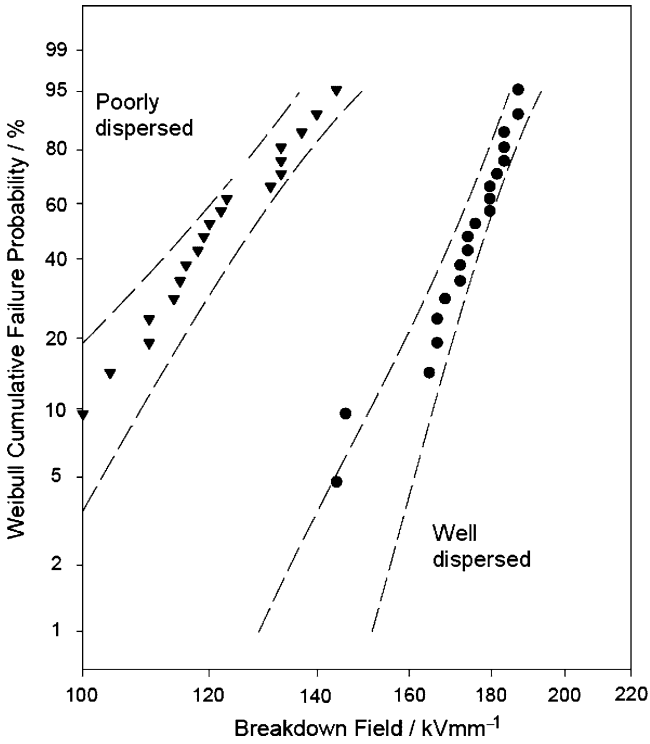

Fig. 7.22 Breakdown voltage of polyethylene – MMT composites (Vaughan et al. 2006)

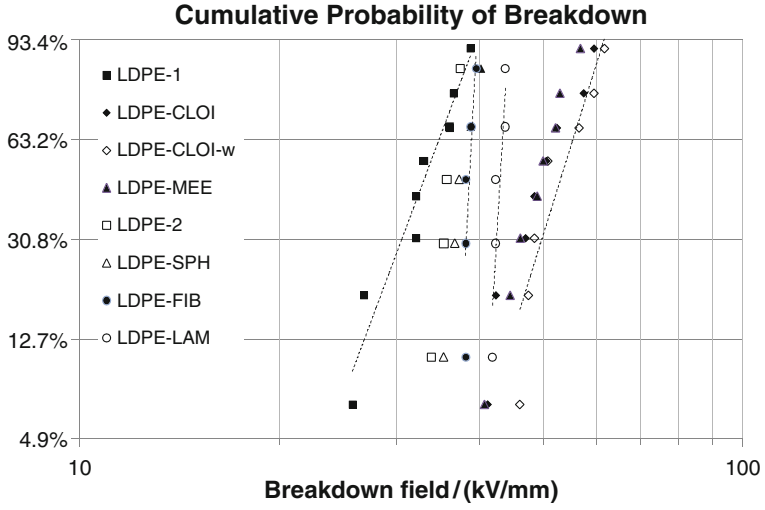

Fig. 7.23 LDPE-MMT nanocomposites formulated by Hoyos et al. (2008). The LDPE-LAM curve has a β value >70

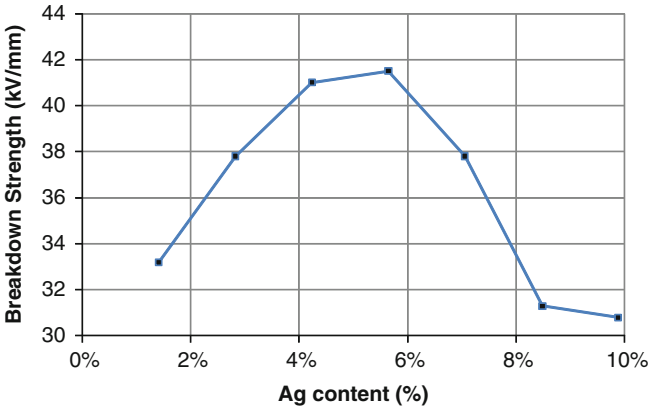

Fig. 7.24 AC breakdown strength of nano-Ag – epoxy resin composites

the shape parameter increased from 60 to 112. This was attributed to a more homogeneous material and, they speculate, that the nanocomposite may have fewer microcavities.

It is interesting that even conducting nanoparticles may lead to an increase in breakdown strength. Wang et al. (2006) have measured the AC breakdown strength of nano-silver – epoxy resins and find an increase in breakdown strength as shown in Fig. 7.24. They invoke a "coulomb blockade" mechanism to explain this phenomenon. The results also show another common effect: if the loadings of nanoparticles exceed a certain amount, the dielectric breakdown strength starts to reduce again. This has been reported by Nelson et al. (2003) who found a loading of about 5% to be optimum for some epoxy–ceramic nanocomposites.

7.3.4 PVA Nanocomposite

Tuncer et al. (2007) investigated the dielectric properties (as a function of frequency and temperature), and the conduction and breakdown properties of a nanocomposite comprising poly-vinyl-acetate (PVA) with barium titanate. The breakdown results obtained from a short-term ramp test are shown in Fig. 7.25. Again the Weibull shape parameter appears to have increased more than the value of characteristic breakdown strength.

7.3.5 Surface Functionalization of Nanoparticles

The results of the above suggest that "nanomization" would tend to improve the reliability of dielectrics by increasing the shape parameter rather than increasing the characteristic breakdown strength. Increases in the shape parameter suggest an

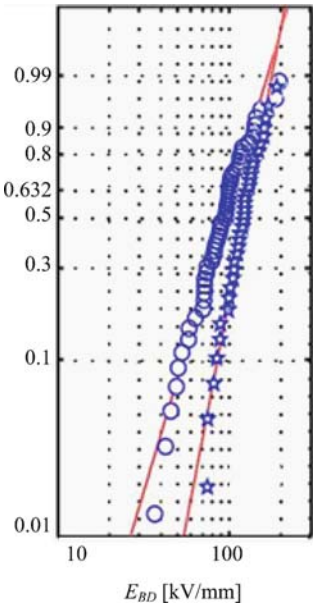

Fig. 7.25 Short-term breakdown test on a PVA – barium titanate nanocomposite. *Circles* = unfilled PVA, *stars* = 6.9 wt% filled PVA (Tuncer et al. 2007)

increased homogeneity on the scale that is important to breakdown – this may be the result of decreasing the concentration or size of micro-cavities that are likely to precipitate breakdown.

However, Roy et al. (2008) (as well as others) have shown that appropriate surface functionalisation may also increase the breakdown strength – without adversely affecting the shape parameter. In this work, the DC breakdown strength was measured using recessed specimens with gold electrodes with specimens ranging in thickness from 0.15 to 0.015 mm. The recessed samples were created using a mold that allowed 25 samples to be prepared on a single wafer thereby allowing multiple specimens to be created simultaneously to permit the large number of breakdown measurements needed to obtain reliable estimates of stochastic parameters. Their results have been shown earlier in Fig. 1.8 and certainly appear to show that surface functionalization is capable of increasing the characteristic breakdown strength, α. The results of this work were obtained for several temperatures. For example, at 25°C, the vinylsilane ("TES") treated nanosilica composites had α (kV/mm) and (β) values of 446 and (1.73) compared with 269 and (2.49) for unfilled XLPE.

7.3.6 Voltage Endurance

Roy et al. (2008) have also reviewed work on *voltage endurance*, i.e., the time-to-breakdown upon the application of a given field. Their results, Fig. 7.26, are relating to the highly divergent fields that occur from electrode pin tips. The fields are therefore much higher than those found in most engineering applications. Their results may relate to electrical tree growth rather than long term aging mechanisms. The re-

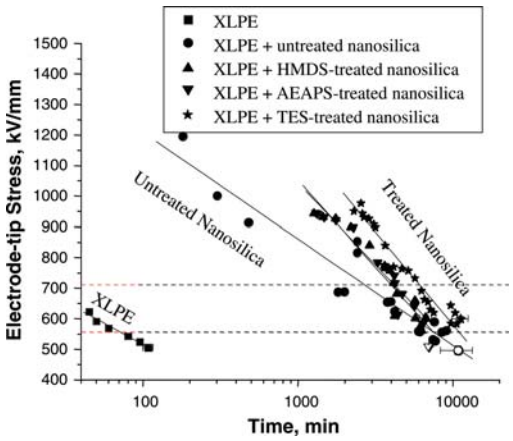

Fig. 7.26 Voltage endurance of XLPE and untreated and functionalized nanocomposites (Roy et al. 2007)

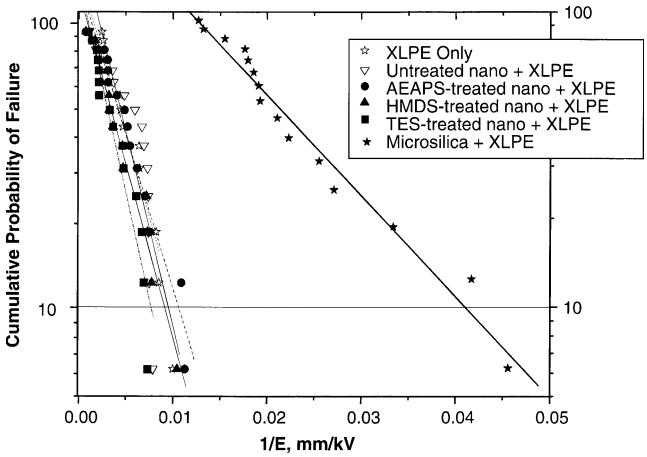

Fig. 7.27 Failure probability as a function of reciprocal field (Roy et al. 2007)

sults indicate the massive improvements that show how important this work is. Gone are the days of incremental improvements in this area; this is a major step forward.

Comparing nanocomposites with micro-composites, it is obvious that nanocomposites are more likely to be uniform than micro-composites. Generally micro-composites contain much higher levels of fillers and it would not be surprising if there were voids surrounding the crevices in such materials. In nanocomposites, although there could conceivably be voids and crevices, these would be on much smaller scales and unlikely to lead to breakdown. If one assumes that the size of defects is exponentially distributed and that the breakdown strength is inversely proportional to the size of the defect then Roy et al. (2007) point out that it is possible to plot the cumulative probability of failure as a function of 1/E to test this hypothesis. Figure 7.27 shows the results represented previously in Fig. 1.8 in this way. This suggests that the micro-composite must have a much larger defect size distribution that the nanocomposites and the base polymer.

7.4 Concluding Comments

Including nanoparticles in insulating polymers has significant effects on the electrical charge transport, dielectric breakdown and endurance properties of materials. To understand these, it is necessary to consider both how the particles change the morphology and local chemistry and physical structure of the polymer. It is also necessary to consider how electrostatic forces around the particle surfaces, resulting in an interaction zone, change the electrical properties.

Nanocomposites appear to increase the DC dielectric breakdown strength and voltage endurance in comparison to unfilled and micron filled materials. The increase in the shape parameter for layered composites suggests that the materials are more homogeneous at the scales relevant for causing breakdown. If one assumes that this may be due to discharges, then this scale may be of the 100s of nm. It has been shown that nanoparticles certainly interfere with the morphology of polyethylene, for example. The particles may also act as "scattering centers" preventing gaseous discharges from taking place but also preventing solid-state avalanches. In either case, the nanoparticles would prevent the carrier multiplication normally recognized as being necessary for breakdown to occur.

Surface functionalisation, whilst important, does not lead to such significant effects as the inclusion of nanoparticles. It is also unclear how such functionalization would affect the interaction zones and hence the electrical transport properties and the mitigation of space charge. However, it is important in controlling the morphological structure of the surrounding polymer. Lewis stated in his 1994 paper, "It has been shown that the dielectric and conductive properties of interfaces will be important if, as seems inevitable, dielectric materials are to be incorporated in nanometric scale devices. ... Equally important will be applications of these interfacial ideas to the technical problem of the electrical breakdown of solid and liquid insulants." How right he was!

References

Balberg I (2009) Tunnelling and percolation in lattices and the continuum. J Phys D Appl Phys 42:1848–1852

Bertini GJ (2009) Diagnostic testing of stochastic cables. IEEE Electr Insul Mag 25(2):6–12

Cao Y, Irwin PC (2003) The electrical conduction in polyimide nanocomposites. IEEE Conf Electr Insul Dielectr Phenom: 116–119

Cao Y, Irwin PC, Younsi K (2004) The future of nanodielectrics in the electrical power industry. Trans IEEE DEI-11(5):797–807

Chutia J, Barua K (1980) DC conduction phenomenon in polyvinylacetate films. J Phys D Appl Phys 13:L9–L13

Dissado L A, Hill R M (1984) Anomalous low frequency dispersion. A near DC conductivity in disordered low dimensional materials. J Chem Soc Faraday Trans II 80:291–319

Dissado LA, Hill RM (1988) Constant-phase-angle and power-law regimes in the frequency response of a general determinate fractal circuit. Phys Rev B 37:3434–3439

Dissado LA and Fothergill JC (1992) Electrical degradation and breakdown in polymers. Peter Peregrinus Ltd. for the IEE, London

Elmahdy MM, Chrissopoulou K, Afratis A et al (2006) Effect of confinement on polymer segmental motion and ion mobility in PEO/layered silicate nanocomposites. Macromolecules 39(16):5170–5173

Fothergill JC (2007) Ageing, space charge and nanodielectrics: ten things we don't know about dielectrics, IEEE Int Conf Solid Dielectr: 1–10

Grosse C (2006) Dielectric properties of suspensions of solid particles. In: Encyclopedia of surface and colloid science. Taylor and Francis, 1688–1705

Hayase Y, Aoyama H, Tanaka Y et al (2007) Space charge formation in LDPE/MgO nanocomposite thin film under ultra-high DC electric stress. Proc IEEE Int Conf Prop Appl Dielectr Mater: 159–162

He D, Ekere NN (2004) Effect of particle size ratio on the conducting percolation threshold of granular conductive – insulating composites. J Phys D Appl Phys 37:1848–1852

Holé S, Sylvestre A, Gallot Lavellée O et al (2006) Space charge distribution measurement methods and particle loaded insulating materials. J Phys D Appl Phys 39:950–956

Hoyos M, Garcia N, Navarro R et al (2008) Electrical strength in ramp voltage AC tests of LDPE and its nanocomposites with silica and fibrous and laminar silicates. J Polym Sci B 46(13):1301–1311

IEEE Standard 930-2004 (2004) IEEE guide for the statistical analysis of electrical insulation breakdown data, ISBN 0-7381-4468-1 SH95269

Jonscher AK (1983) Dielectric relaxation in solids. Chelsea Dielectric Press, London, Section 5.6

Lampert MA, Mark P (eds) (1970) Current injection in solids, Academic, New York p 24

Lewis TJ (1954) The work function of irregular metal surfaces. Proc Phys Soc B 67(3):187–200

Lewis TJ (1994) Nanometric dielectrics. Trans IEEE DEI-1(5):812–825

Lewis TJ (2004) Interfaces are the dominant feature of dielectrics at the nanometric level. Trans IEEE DEI-11(5):739–753

Ma D, Hugener TA, Siegel RW et al (2005) Influence of nanoparticle surface modification on the electrical behavior of polyethylene nanocomposites. Nanotechnology 16(6):724–731

Montanani GC, Ciani F, Testa L et al (2005) Electric strength, space charge and surface discharge characterization of nanostructured epoxy-silicate insulating materials. Int Symp Electr Insul Mater 206–209

Mott MF and Gurney RW (1940) Electronic processes in ionic crystals. Oxford University Press, London

Mott MF (1967) Electrons in disordered structures. Adv Phys 16(61):49–144

Murata Y, Goshowaki M, Reddy CC (2008) Investigation of space charge distribution and volume resistivity of XLPE/MgO nanocomposite material under DC voltage application. IEEE Int Symp Electr Insul Mater: 502–505

Nelson JK, Fothergill JC, Dissado LA, Peasgood W (2002) Towards an understanding of nanometric dielectrics. IEEE Conf Electr Insul Dielectr Phenom: 295–298

Nelson JK, Hu Y, Thiticharoenpong J (2003) Electrical properties of TiO_2 nanocomposites. IEEE Conf Electr Insul Dielectr Phenom: 295–298

Nelson JK, Fothergill JC (2004) Internal charge behavior of nanocomposites. Nanotechnology 15:1–10

Peacock A (2000) Handbook of polyethylene structures, properties and applications. CRC, Boca Raton, FL

Roy M, Nelson JK, MacCrone RK, Schadler LS (2007) Candidate mechanisms controlling the electrical characteristics of silica/XLPE nanodielectrics. J Mater Sci 42:3789–3799

Teyssedre G, Laurent C, Montanari GC et al (2001) Charge distribution and electroluminescence in cross-linked polyethylene under dc field. J Phys D 34(18):2830–2844

Tanaka T, Montanari GC, Mülhaupt RM (2004) Polymer Nanocomposites as dielectrics and electrical insulation – Perspectives for processing technologies, material characterization and future applications. Trans IEEE DEI-11(5):763–784

Tuncer E, Duckworth RC, Sauers I (2007) Dielectric properties of polyvinyl alcohol filled with nanometer size barium titanate particles. IEEE Conf Electr Insul Dielectr Phenom: 225–227

Vaughan AS, Swingler SG, Zhang Y (2006) Polyethylene nanodielectrics: the influence of nanoclays on structure formation and dielectric breakdown. IEEJ Trans Fundam Mater 126(11):1057–1063

Wang L, Xu M, Feng J, Cao X (2006) Study on AC breakdown property of nanoAg/epoxy resin composite. IEEE Int Conf Prop Appl Dielectr Mater 163–166

Wintle HJ (1983) Conduction processes in polymers. In: Bartnikas R, Eichorn RM (eds). Engineering dielectrics. Vol IIA, Electrical properties of solid insulating materials: molecular structure and electrical behaviour. ASTM Special Technical Publication 783, Philadelphia, PA 239–354

Zilg C, Kaempfer D, Thotnann R (2003) Electrical properties of polymer nanocomposites based upon organophilic layered silicates. IEEE Conf Electr Insul Dielectr Phenom: 546–550

Zhang P, Li G, Gai L, Lei Q (2006) Conduction current characteristics of nanoinorganic composite polyimide films. Proc IEEE Int Conf Prop Appl Dielectr Mater: 755–758

Zou C, Fothergill JC, Rowe SW (2008) The effect of water absorption on the dielectric properties of epoxy nanocomposites. Trans IEEE DEI-15(1):106–117

Chapter 8
Interface Properties and Surface Erosion Resistance

Toshikatsu Tanaka

8.1 Introduction

Polymer nanocomposites are composite materials with nanostructure formulated in such a way that inorganic particles of nanometric size are homogeneously dispersed in polymers by several wt %. This new type of nanostructured composite material has recently received much attention (Chujo 2001; Toray 2002; Ray et al. 2003; Ajayan et al. 2004; Lewis 1994, 2004, 2006; Fréchette et al. 2004, 2006; Tanaka et al. 2004; Tanaka 2005), because such nanostructure can bring about significant improvements in various properties cited earlier. Polymer nanocomposites are especially distinctive because they are endowed with enormously large internal surface area of interfaces when compared to their conventional polymer composite counterparts. Polymers such as polyamide (PA), polyethylene (PE), polypropylene (PP), ethylene vinyl acetate (EVA), epoxy resins and silicone rubbers are combined with nano-fillers such as layered silicate (LS), silica (SiO_2), titania (TiO_2), alumina (Al_2O_3), and magnesia (MgO). Polyamide/layered silicate nanocomposite was commercialized as an engineering plastic in the 1990s. It has good mechanical strength, thermal endurance and gas barrier performance. Layered silicate is especially interesting as one of the nano-fillers, because it has not only a large surface area but also a large aspect ratio. The stacked layers are about 1 nm in thickness and 100 nm in length. Layered silicates are also interesting from the standpoint of electrical insulating materials. Epoxy is one of the typical dielectric materials and, thus, composites of epoxy resins with layered silicates have been targeted as advanced high performance insulating materials. It is necessary to exfoliate and disperse silicate layers down to their single mono-layers as has been explained in Chaps. 2 and 3, and so there is plenty of room for improvement in material formulation.

The internal interfaces are represented by local interaction zones that are comprised of (1) a bonded layer, (2) a bound layer (bound polymer), and (3) a loose coupling layer. However, interactions originating from polymer morphology will have long range effects up to several hundred nm. A multi-core model has been

T. Tanaka (✉)
Waseda University, Japan
e-mail: t-tanaka@waseda.jp

J.K. Nelson (ed.), *Dielectric Polymer Nanocomposites*,
DOI 10.1007/978-1-4419-1591-7_8,

proposed to include the above picture (Tanaka et al. 2005). By means of such models, some of the mechanisms underlying the enhanced performance have been partially clarified. On the basis of their excellent properties, it is now expected that nanodielectrics will emerge as high-voltage insulation for AC and DC power cables, molded transformers, dry type switchgears, capacitors, outdoor insulation and the like (Tanaka 2006).

This chapter mainly deals with interface properties as they relate to erosion processes in the external and internal surfaces (tree channels) of polymer nanocomposites.

8.2 Interface Properties of Nanocomposites

8.2.1 Silane Couplings

Silane coupling is a form of rather strong binding of organic polymers with inorganic substances (nano fillers in this case) and has been treated in depth in Chap. 4, but is depicted in Fig. 8.1. This represents a hydrogen bonding force to bind two kinds of immiscible substances.

8.2.2 Wilkes' Model

Interfaces with finite mesoscopic thickness are different from either the fillers or the matrix in character. The morphology in the mesoscopic region is postulated from the

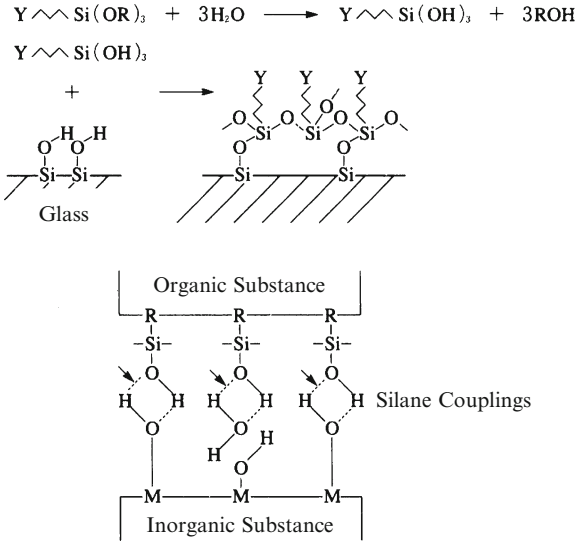

Fig. 8.1 Chemical structure of silane couplings (Tanaka et al. 2005)

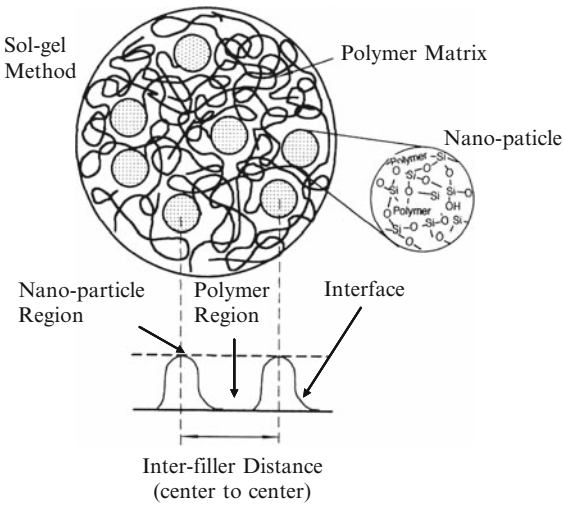

Fig. 8.2 Wilkes's model for an interface (Tanaka et al. 2005)

small angle X-ray scattering experiments (SAXS) and depicted in Fig. 8.2 (Tanaka et al. 2005; Huang et al. 1987). As an example, when a polymer-silica nanocomposite is formulated by the sol–gel method, there is a definite silica rich layer with polymer partially or totally compatibilized. This is considered to be an interaction zone as introduced in previous Chapters. However, two types of morphology may prevail depending on the formulation method:

(a) Silica is partially distributed in the outer polymer region in the covalent bonding system that is produced in the end cap method.
(b) Silica and polymer are interposed mutually to form a network structure in the hydrogen bonding system that is produced in the direct mixing method.

A broad peak appears in SAXS in the case of (a). This indicates that silica clusters (namely nanoparticles) are homogeneously dispersed in a certain correlation distance (inter nanoparticle distance). Silica domains (nanoparticles) are rich in inorganic substance but are compatibilized in part with the polymer phase. A distinct interface exists between the matrix and the silica region, giving rise to a peak in SAXS spectrum. Peaks are also observed in a PPG (polypropylene glycol)/SiO_2 system, a PEG (polyethylene glycol)/TiO_2 system, and a PTMO (polytetra-methylene oxide)/SiO_2 system.

In the case of (b), no peak appears in SAXS. Scattering intensity is characterized by the formula that it is proportional to q^{-D}, where q and D are the wave number and the fractal dimension, respectively. From investigation of various kinds of colloids, it is ascertained that colloid particles have the smooth surface for $D = 4$, the rough surface for $D = 3$, and have branches to form three dimensional network structures for $1.9 > D > 2.5$. PVA (polyvinyl alcohol) nanocomposites prepared by the blend method have hydrogen bonds, and, in that case, D is equal to 1.97. It is presumed that SiO_2 chains and PVA chains are mutually penetrated to form a network structure. The same is true for a PTMO/WO_3 system.

8.2.3 *Interface Models*

8.2.3.1 Conceptual Illustration of Interfaces

An interface can have a thickness of less than 1 nm or greater than 10 nm depending on chemical or physical bonds. At the interface, the polymer chains are chemically and/or physically bonded to the particle surface. Therefore the polymer chains can have an ordered structure, i.e., they can be arranged radially to the filler particle or in parallel to the filler surface. In either case the polymer structure differs highly from the structure of the remaining randomly arranged matrix structure, as shown in Fig. 8.3 (Rätzke et al. 2006).

The interface structure depends on the matrix materials as well as the filler type and the surface treatment where appropriate. Similar to polymers with semi-crystallinity, the structure of the interface can have an influence on the properties of the polymer. Due to the different interfacial structure and/or the bonding to the filler particle, the properties of the interface differ from the properties of the remaining matrix material. The side chains of the polymer and the surface groups of the filler particles determine whether chemical bonds between polymer and filler exist or not. Polymer can be bonded chemically to the filler surface only if both are polar or not polar. Therefore, surface treatment of fillers and coupling agents can have a major influence on the interface, because nonpolar surface groups can become polar and vice versa. Spherulites are considered to be formed around nano fillers in polyamide nanocomposites. This situation corresponds to the case (c) in Fig. 8.3.

8.2.3.2 Bound Polymer*s*

A concept of bound polymers was introduced to explain mechanical interaction, as shown in Fig. 8.4. In this model, matrix molecules near the interface with nano fillers are constrained in their free movement to form immobile layers, i.e., bound polymers, at the surface of the fillers. As the interactions become stronger, the bound

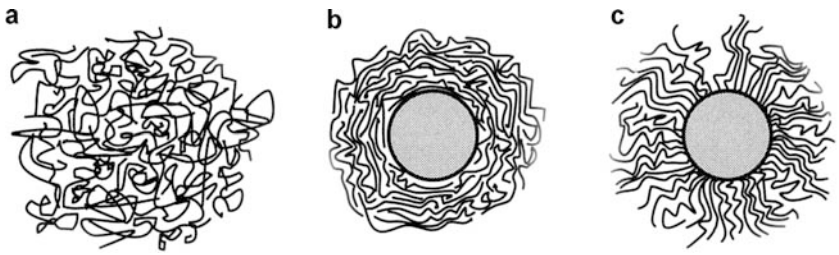

Fig. 8.3 Schematic illustration of the interface (**a**) randomly arranged polymer matrices, (**b**) polymer chains arranged in parallel to the nanoparticle surface, and (**c**) polymer chains radially bonded to the nanoparticle surface (Rätzke et al. 2006)

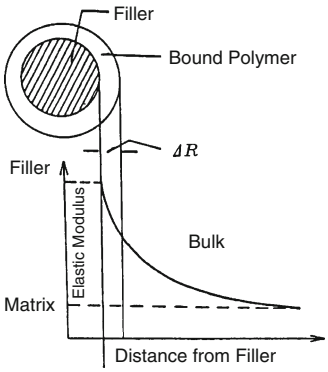

Fig. 8.4 Conceptual image of bound polymer

Table 8.1 Thickness of bound polymers in nm

	Tg method	Direct method	Dynamic viscoelasticity
PX	7.1	9.2	110–130
PX(SC)	14.2	14.7	140–220
PM	–	23.0	150–

Unit: nm
PX: PVC-non-processed zeolite
PX(SC): PVC-amino-silane-processed zeolite (1 wt%)
PM: non-processed mica

polymers become thicker. Some examples are shown in Table 8.1 (Nakao 2004). The thickness is estimated as several tens nm for rubber-carbon black systems according to the measurement by glass transition temperature (T_g) and direct methods. By the dynamic viscoelasticity method, it can be extended up to about 100 nm. This difference may be caused by the sensitivity of the method used for measurement.

8.2.3.3 Evidence for Far-Distance Interaction

Two kinds of specimens, i.e., a real nanocomposite and a sandwiched thin film as thick as 10–500 nm were used to measure glass transition temperatures (T_g) (Rittingstein et al. 2007). P2VP (poly(2-vinyl pyridine)), PMMA, and polystyrene with nano silica were evaluated as representative materials. One of the results is shown in Fig. 8.5 which indicates a large increase in T_g (as large as 5–10 K) in about 100 nm thickness or inter-particle distance. PMMA and P2VP interact by hydrogen bonding with silica containing hydroxyl groups. Polystyrene does not interact with silica surfaces. It is considered that the increase in T_g for a PMMA-silica system can be attributed to the attractive interaction in interfaces between the polymer matrices and the nano fillers so as to suppress cooperative segmental motion. The same mechanism can also be postulated for a P2VP-silica system. Interaction distance, depending on the kind of interaction force, can be 300 nm, when the hydrogen bond force is effective.

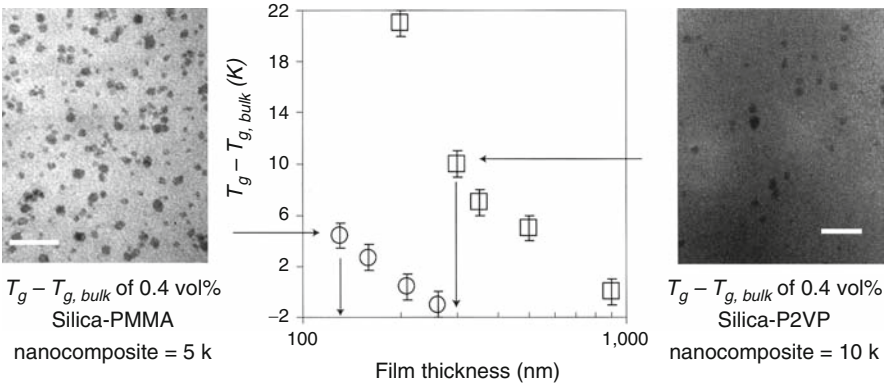

Fig. 8.5 Interlayer spacing (film thickness) in "Model" nanocomposites that yield the same T_g deviation as 0.4 vol% silica-PMMA and silica-P2VP nanocomposites (Rüttingstein et al. 2007) *Note:* T_g deviations of P2VP nanocomposites (*open squares*) and PMMA "model" nanocomposites (*open circles*). *Right* and *left*: Transmission electron microscopy images of 0.4 vol% silica (*right*) and 0.4 vol% silica-PMMA (*left*) nanocomposites (scale bars = 100 nm). The error bars (±1 K) represent the inherent error due to the fitting of the data required to obtain T_g. P2VP represents poly (2-vinyl pyridine)

Table 8.2 Triboelectricity series of various kinds of materials

Rank in order from positive to negative tendency as
quartz (+) > **silicone elastomer** (+) > glass (+) > polyformaldehyde (+) > polymethyl methacylate (+) > human hair (+) > ethyl cellulose (+) > **polyamide** (+) > salt (NaCl) (+) > melamine (+) > wool (+) > fur (+) > silk (+) > aluminum (+) > cellulose acetate (+) > cotton (+) >
steel (−) > wood (−) > amber (−) > copper (−) > zinc (−) > gold (−) > polyester (−) > polyurethane elastomer (−) > polystylene (−) > natural rubber (−) > **polypropylene** (−) > polyvinyl chloride (−) > polytetrafluoroethylene (−) >
Other data indicate somewhat different series as
dry human skin (+) > leather (+) > rabbit fur (+) > glass (+) > human hair (+) > **nylon** (+) > wool (+) > lead (+) > cat fur (+) > silk (+) > aluminum (+) > paper (+) > cotton (±0), steel (±0) >
amber (−) >, hard rubber (−) > nickel & copper (−) > brass & silver (−) > polyester (−) > polystylene (styrofoam) (−) > saran wrap (−) > polyurethane (−) > **polypropylene** (−) > polyvinylchloride (−) > silicon (−) > polytetrafluoroethylene (Teflon) (−)

Forces can be active for a very long distance for the case of hydrogen bonds. Furthermore, forces other than chemical bonds are also available. For instance, an electrostatic force can be generated due the formation of the electric double layers. This force is effective for a long distance because it is coulombic, as was shown previously in Fig. 7.8 (Lewis 2006). This kind of force is generated due to charge transfer between two kinds of materials, when they are brought in contact with each other, so as to equalize the electro-chemical potential. This is closely related to the degree of triboelectricity of materials used, as shown in Table 8.2 (Tanaka et al. 2004). Polyamide and polypropylene must show opposite polarity characteristics, for instance.

8.2.3.4 Multi-core Model

A multi-core model has been proposed (Tanaka et al. 2005) as shown in Fig. 8.6 and consists of:

1. A bonded layer (the first layer)
2. A bound layer (the second layer)
3. A loose layer (the third layer)
4. An electric double layer overlapping the above three layers

Spherical nanoparticles of several tens of nm in diameter are homogeneously dispersed in a distance similar to the diameter. Inter-particle distance and diameter are of the order of 1–10 nm. Inter-particle interaction such as a percolation process will possibly take place when the inter-particle distance is reduced to about 1 nm. It is already clarified that interfacial layers are formed, which are different from both matrices and nano fillers. A three layered structure is postulated in this multi-core model. The first layer corresponds to a region of chemical bonding between inorganic fillers and organic polymer matrices. The second layer is attributed to a

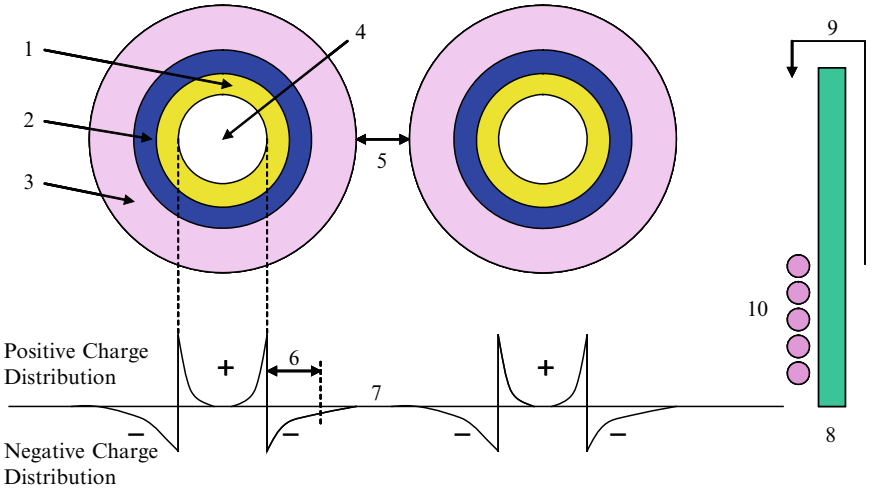

1: The first layer with mutual tight binding: several nm
2: The second layer with deep traps: about 10 nm
3: The third layer with large local free volume
as ion traps and shallow electronic traps: several tens nm
4: Nano-particles: 20 to 50 nm in diameter
5: Interparticle distance (surface to surface): 40 to 100 nm
6: Debye shielding distance: up to about 100 nm
7: Possible overlapping of the third layers and charge tails of nano-particles
8: Electrode facing accumulated charge tails of nano-fillers
9: Charge carrier injection via Schottky emission at high electric field
10: Collective charge tail effect will modify carrier injection.

Fig. 8.6 Multi-core model for nanocomposites

region of special morphology such as spherulites formed due to the influence of the first layer, or a stoichiometrically cross-linked region. The third layer is a region of morphology (still different from the matrix) which is considered to be formed due to the creation of the second layer. This is a region of less stoichiometrical cross-linking, for example.

1. Bonded layer (the first layer)

The first layer corresponds to a transition layer tightly bonded to both inorganic and organic substances by coupling agents such as silane. The thickness is postulated to be of the order of 1 nm. The sol–gel method consists of the end-cap method, the blend method, and the copolymerization method and the implications of the preparation method from SAXS have been discussed in Sect. 8.2.2.

In general, the first layer (the bonded layer) is bound by ionic, covalent, hydrogen, and van der Waals bondings, and the strength is in this order.

2. Bound layer (the second layer)

The second layer is an interfacial region consisting of a layer of polymer chains strongly bound to the first layer and the surface of the inorganic particle. Morphological structure is rather orderly in this region. The layer thickness cited is in the range of 2–9 nm. These values, of course, depend on the strength of the polymer-particle interaction and, the stronger the interaction, the larger the bound polymer fraction.

Chain mobility and crystallinity are intimately involved. The former is directly related to the glass transition temperature. In addition, the average chain conformation can be altered and/or the type and degree of crystallinity can change with the addition of filler. The chain conformation includes the orientation of constituent radical groups and polymer chains stacked to the surface of nano fillers, the local density of interfaces, the folded structure of polymer chains, and other conformational structures. Crystallinity is also sensitive to interfacial interaction. When curing agents are adsorbed selectively to nano fillers, the region around them consists of a layer of stoichiometrically crosslinked thermoset region with excess curing agent. In the case of polyamide/layered silicate nanocomposites, the spherulite region around the nanoparticles is considered to correspond to this second layer.

3. Loose layer (the third layer)

The third layer is a region loosely coupled to the second layer. It is generally considered that the loose layer has different chain conformation, chain mobility, and even free volume or crystallinity from the polymer matrix. This layer may be as large as several tens of nm. When the preferential adsorption of a curing agent at the interface occurs, the third layer will be somewhat depleted of curing agent and thus less-than-stoichiometric cross-linking will result. This phenomenon has been observed in fiber-filled polymers and epoxy/titania nanocomposites. More subtle changes could also occur, such as preferential adsorption of low molecular weight material at the surface.

4. Electric double layer

In addition to the above general speculation for interfacial structures obtained from the chemistry, a coulombic interaction is superimposed. When a polymer has mobile charge carriers, they are distributed at the interface in such a way that the counter charge carriers (with the opposite polarity) are diffused outward from the contact surface to the Debye shielding length. This corresponds to the Gouy-Chapman diffuse layer in which charge decays exponentially with distance according to the Born approximation. The Debye shielding length is calculated as about 30 nm.

The electric double layer forms a long distance dipole. It is important to detect this dipole moment that may have slow time response. This will affect electrical conduction and dielectric properties in the low frequency region. From the triboelectric series, it is postulated that polyethylene (PE), polypropylene (PP) and ethylene vinyl acetate (EVA) tend to become positively charged, while silicone elastomer, polyamide and epoxy tend to become negatively charged. Polyolefin and condensed polymers have negative and positive charge tendencies, respectively.

In summary, the thickness for the above layers is considered to be 1 nm, several nm and several tens nm for the first, second and third layers, respectively. It is questionable whether or not the thickness of the loose layer is the same as that of the Gouy-Chapman diffuse layer (Lewis 2004, 2006). The latter might extend over the former. A far-field effect must be involved in mesoscopic interactions in the third layer and/or the diffuse Gouy-Chapman layer, and must cause some collaborative effect among neighboring nanoparticles. Macroscopic phenomena and parameters can be expected to be different from one material to another due to the relative difference in thickness and interaction strengths with the far-field effect.

8.2.3.5 Water Shell Model

A water shell model has been advanced, as shown in Fig. 8.7 (Zou et al. 2008), where water absorption is taken into consideration in the interfaces between nanoparticles and surrounding polymer matrix. Interfaces are likely to be thermodynamically unstable in the presence of water, especially when they are not surface-treated. Water is considered to exist mainly in the second layer of the multi-core model introduced in Sect. 8.2.3.4. This model is applied to explain some dielectric relaxation processes at low frequency in epoxy nanocomposites.

8.3 Partial Discharge Resistance of Polymer Nanocomposites

8.3.1 Evaluation Methods for PD Resistance

Partial discharge (PD) resistance of polymer insulation is evaluated by using several kinds of electrode systems such as IEC (b) electrode and rod-to-plane electrode

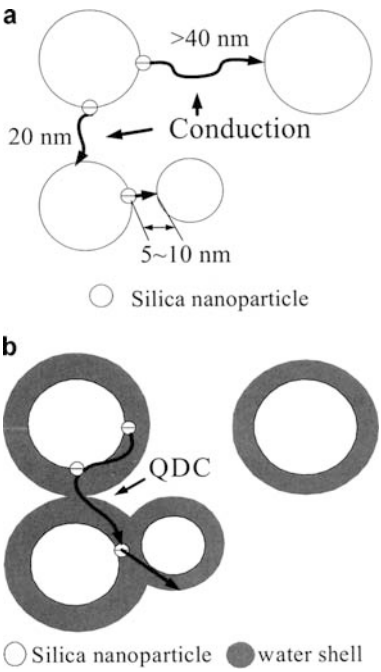

Fig. 8.7 Water shell model (**a**) non-overlapping water shells, (**b**) overlapping water layers (Zou et al. 2008) (*Note:* "QDC" stands for Quasi DC conduction)

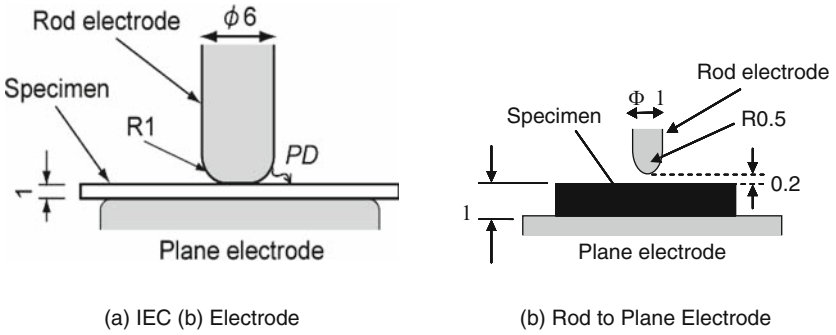

Fig. 8.8 Evaluation methods for PD resistance

systems, as shown in Fig. 8.8. In the case of nanocomposites, these two electrode systems are usually utilized. The former gives surface roughness, while the latter allows evaluation of erosion depth.

Examples of erosion profiles in cross section are shown in Fig. 8.9, which depend on the kind of electrode systems. In the case of IEC (b) electrode system, the surface roughness can be estimated in the region of relatively flat areas, as well as the maximum erosion depth. Atomic Force Microscope (AFM) images are obtained in

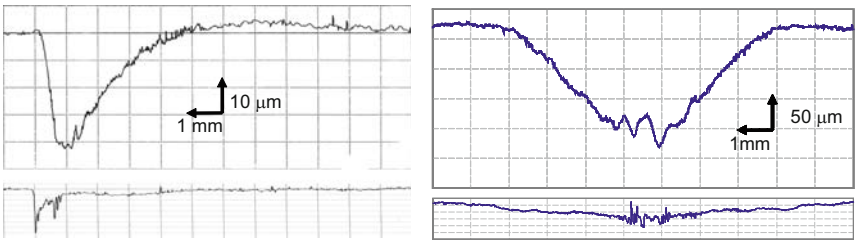

Fig. 8.9 Cross sectional erosion profiles

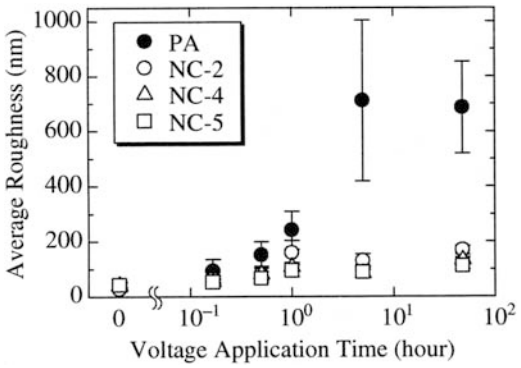

Fig. 8.10 Surface roughness change with time for base polyamide and nano-filled polyamide subjected to partial discharges (Tanaka 2005): NC-2, NC-4 and NC-5: layered silicate content 2, 4 and 5 wt%, respectively

some cases. In the case of the rod-to-plane electrode system, the maximum erosion depth is usually measured. In both cases, the extent of PD erosion can be estimated.

8.3.2 Polyamide/Layered Silicate Nanocomposites

It was first found that partial discharge resistance is enhanced by using a base polyamide (PA) to formulate a polyamide layered silicate nanocomposite (Tanaka 2005). The surface of polyamide sheets is exposed to partial discharges using an energized IEC (b) electrode system, and evaluated by the surface roughness measured by an AFM. Typical data is shown in Fig. 8.10 (Tanaka 2005) for the average surface roughness for base PA, PA nanocomposite specimens with nano-filler content 2, 4, and 5 wt% as a function of time under 6 kV AC voltage application. This clearly demonstrates that PD resistance is enormously enhanced by nanostructuration.

For an explanation of how PA layered silicate nanocomposite is resistant to PD erosion, the following four points are considered as influencing factors.

(i) Bonding strength between fillers and matrices
(ii) Inter-filler space or matrix volume surrounded by neighboring fillers

(iii) Morphology in the inter-filler space
(iv) Mesoscopic interaction

In the context of the multi-core model introduced in Sect. 8.2.3.4, the first layer can be ascribed to the above item (i). Ionic bonding is suggested in this case, where the surface of the organically-modified layered silicate is bound to the surrounding PA matrix. Items (ii) and (iii) can be identified with the second and third layers of the multi-core model. The second layer or some ordered structure such as spherulites and crystallites are created around the first layer, which is evident from the wide angle X-ray analysis (WAXA). The third layer is predominantly amorphous, and makes contact with the third layer of the nearest neighbor fillers. A diffuse layer must overlap the three layers, and therefore, these structures might be formed electrochemically by the mesoscopic interaction.

The second layer of the multi-core model is considered to be almost adjacent to that of its nearest neighbor filler, and then will occupy almost the whole volume of PA layered silicate nanocomposite. If spherulites formed around the filler, the second layers are strong against PDs compared to the original PA matrix. PD degradation must start in the amorphous regions between the neighboring third layers or the less PD resistant third layer and proceed into the more PD resistant second layer. The same process will occur in the next filler environment, as PDs encounter the next amorphous region, third layer, and second layer. An erosion process is illustrated in Fig. 8.11 (Tanaka et al. 2005).

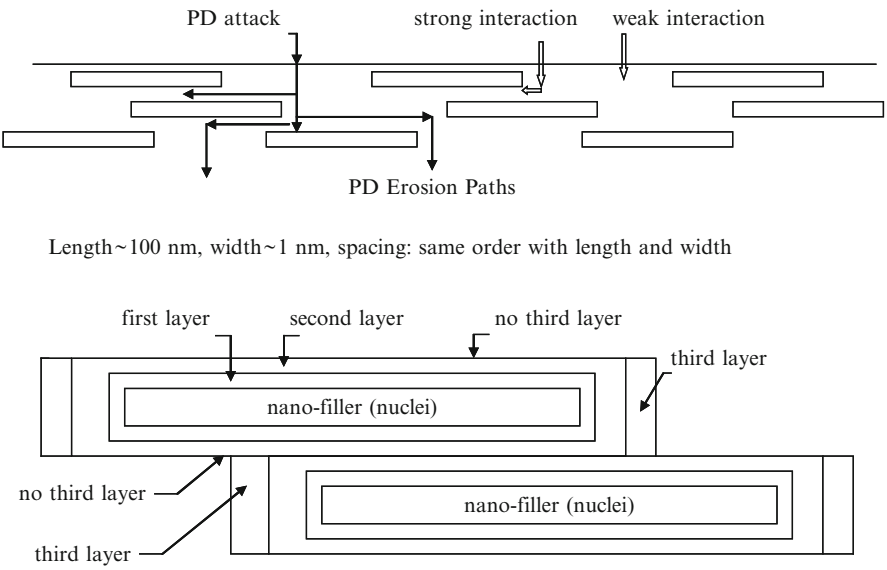

Fig. 8.11 PD erosion process for polyamide/layered silicate nanocomposite (Tanaka et al. 2005)

8.3.3 *Epoxy Nanocomposites*

PD resistance characteristics of epoxy/titania nanocomposites are shown in Fig. 8.12 (Tanaka et al. 2006b). A rod-to-plane electrode system was used instead of the IEC (b) electrode system. It was confirmed for different materials and electrodes that there is a similar positive effect of nano fillers on PD resistance. PD resistance is strengthened about three times at ageing time 90 h. Figure 8.13 shows the dependence of PD erosion depth on filler size and the effects of silane coupling on

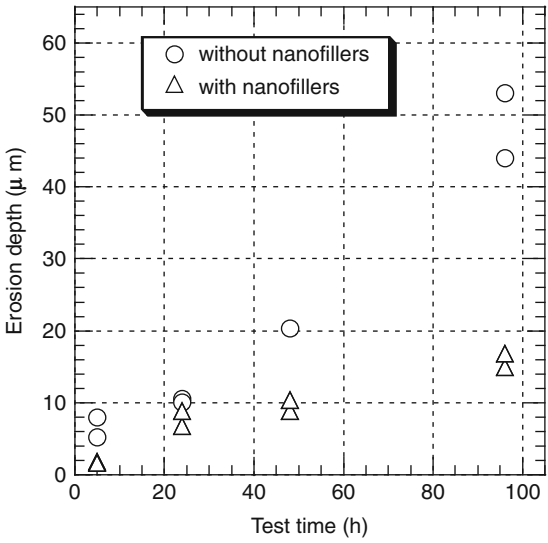

Fig. 8.12 Erosion depth vs. PD time for epoxy/titania nanocomposites: 60 Hz, 6 kV(Tanaka et al. 2006b)

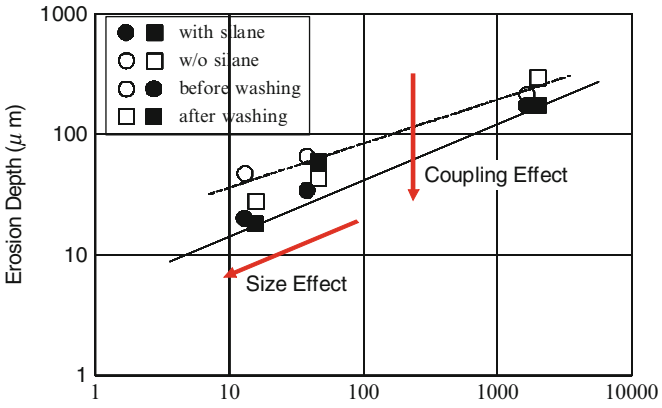

Fig. 8.13 Dependence of PD erosion depth on the size of silica fillers at aging time 1,440 h (Tanaka et al. 2008a)

erosion depth (Tanaka et al. 2008a). It is clear that PD resistance tends to increase with the decrease of filler size between 1.2 nm and 1.6 μm.

Therefore the following conclusions can be drawn.

1. There is a positive effect of nano fillers on PD resistance. Both particle-like fillers such as silica and titania and belt-like fillers such as layered silicate have a similar effect.
2. Tight interfaces and well ordered morphology will increase PD resistance. Silane couplings and grown spherulites are some examples.
3. Two- and three-dimensional segmentation of organic polymers by inorganic fillers seems to work well against material attack by partial discharges.

Similar results were obtained in epoxy/alumina nanocomposites (Kozako et al. 2004), epoxy/alumina and titania nanocomposites (Maity et al. 2008a, b), and epoxy/silica and alumina (Preetha et al. 2008). It was found (Maity et al. 2008b) that heating of nano fillers in vacuum before mixing and silane coupling treatment are essential to obtain nanocomposites with excellent properties. Heating must free up the hydroxyl groups on the surface of nanoparticles to make them available for hydrogen bonding with the polymer matrix. It is further believed that functionalization by silane will help form covalent bonding such as Si-O-Al bonds. An epoxy/nano SiC system has also been investigated (Tanaka et al. 2008b), which shows almost the same results as epoxy/silica nanocomposites.

8.3.4 Polyethylene and Polypropylene Nanocomposites

Depth of erosion caused by PD depends on the content of nano-fillers as shown in Fig. 8.14 (Tanaka et al. 2006c). It decreases with the increase of nano-fillers. In addition, it is worthwhile to mention that a big improvement is observed, when only 1 phr of nano-fillers is added. Investigation has also been made on polypropylene nanocomposite in use for capacitors (Takala et al. 2008).

8.3.5 Possible Mechanism for PD Erosion

A possible mechanism for erosion of nanocomposites subjected to partial discharges is illustrated in Fig. 8.15. A nanocomposite substance is eroded mainly in its polymer regions. Inorganic filler materials are far more PD resistive than organic polymers. Therefore, PDs will attack organic polymer regions preferentially. Segmentation of organic substances into many small areas and/or volumes is considered to be effective against PD attack.

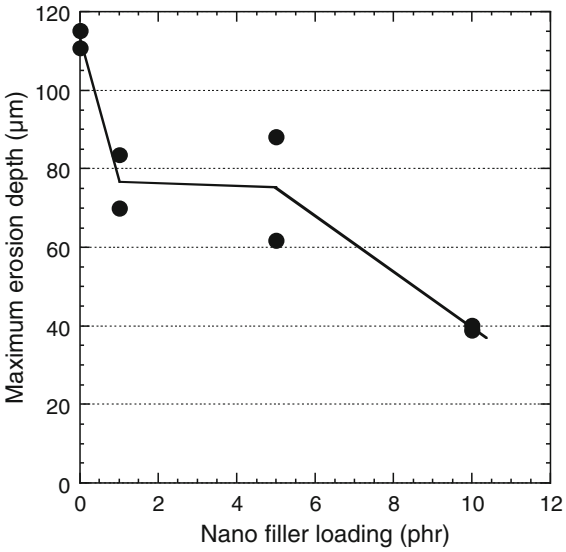

Fig. 8.14 PD resistance of LDPE/MgO nanocomposite (Tanaka et al. 2006b)

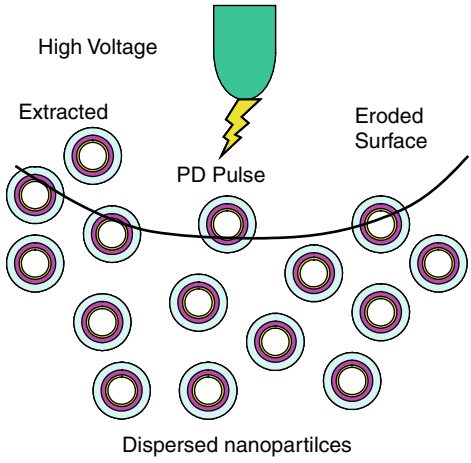

Fig. 8.15 Possible mechanism for PD erosion

How can the multi-core model describe the resistance to PD attack? Nano segmentation or mesoscopic segmentation is a major factor to PD ageing. The first layer corresponds to the silane coupling region for both polyamide and epoxy. The second layer is related to the spherulites in polyamide and the stoichiometrically crosslinked region in epoxy. The first and second layers will help increase PD resistance. Both of them will resist extraction of nano fillers from the nanocomposite, as indicated in Fig. 8.15. Polyethylene is probably protected against PDs by the nano segmentation only.

8.4 Laser and Plasma Ablation Resistance of Polymer Nanocomposites

Laser ablation has been widely used for processing such as ultra-precision micro-machining, synthesis and surface treatment, micro-component fabrication and the like (Njuguna et al. 2004; Zeng et al. 2002). This method is applicable to evaluate the erosion resistance of silicone rubber composites, which is based on the following understanding (Meyer et al. 2005). Silicone rubber for outdoor applications is subjected to dry band arcing and aged due to heat, oxidation and ultra-violet (UV) light. Aging is primarily caused by the heat generated by the arcing, and then by the secondary effects of ozone reactions and UV light. Laser ablation is considered to represent the major contribution from heat to evaluate thermal aging under dry band arcing, and to give reliable data due to the constant energy that the laser will produce. A near-infrared semiconductor laser source operating at a wavelength 808 nm is selected and might provide a basis for validating the correlation in ranking of silicone rubber composite specimens between the laser ablation method and the conventional inclined plane test. This method was applied to silicone nanocomposites to evaluate erosion resistance. Based on this method, the effects of nano fillers and associated surfactants on erosion mass were clarified, as discussed in the next section.

Plasma ablation is utilized to simulate the erosion of polyamide and polyamide/layered silicate nanocomposite caused by partial discharges (Fuse et al. 2008). A reactive etching system (Samco FA-1) is used to produce the glow discharge oxygen plasma by excitation with radio frequency waves (13.56 MHz) having a power of 50 W in oxygen atmosphere of several 10 Pa. There are two findings. Firstly, restriction of molecular motion around nano fillers is evidenced by finding the decrease in permittivity due to inclusion of nano fillers. Secondly, observation of aged surfaces by the scanning electron microscope, the energy dispersive X-ray spectroscopy and X-ray diffraction shows that nano fillers are piled up to form a layered structure on specimen surfaces. This structure is considered to act as barrier against impact of charged particles and diffusion of gases such as oxygen. The first function is intrinsic and would enhance degradation. The second function is extrinsic, but would contribute to the effectiveness of plasma resistance.

Erosion by oxygen plasma is restricted by the inclusion of layered silicate into polyamide as shown in Fig. 8.16 (Fuse et al. 2008). Five possible mechanisms are proposed, as follows. The first mechanism is a gas barrier property. A zigzag structure formed by the dispersed nano fillers will restrict gas diffusion thereby retarding resin oxidation. The second mechanism is crystal formation indicated by XRD analysis. Crystalline regions are more resistant to particle impact. Moreover, molecular motion is restricted in crystalline regions, which delays the diffusion of gases such as oxygen and thus again slows down oxidation. The third mechanism is a strong interaction between the resin and nano fillers indicated by permittivity analysis, which also restricts the molecular motion since the total area of such resin/nano filler interfaces is so large in nanocomposites. The fourth mechanism is the formation layered

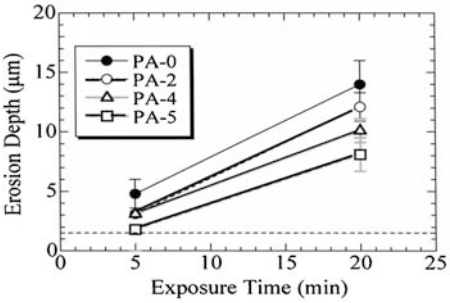

Fig. 8.16 Depth of erosion caused by oxygen plasma ablation in the case of polyamide and polyamide/layered silicate nanocomposite specimens of 1 mm thick (Fuse et al. 2008). The designation PA-0, PA-2, PA-4 and PA-5 represents the filler content in wt% in each polyamide specimen

structures of nano fillers on the specimen surface, which is indicated from SEM, EDX and XRD. This structure created in an early stage of degradation will improve the resistance against further degradation. Furthermore, growth of degradation cavities on the surface by partial discharges is significantly restricted by the presence of nano fillers. This is the fifth mechanism. It is to be noted that there are mechanisms specific to polyamide/layered silicate nanocomposite included in the above.

8.5 Surface Erosion Resistance of Silicone Nanocomposites for Outdoor Use

Silicone elastomers to be used for outdoor insulators are expected to have better performance by including nanoparticles (Lan et al. 2003, 2004; Yang et al. 2006; Rätzke et al. 2005; Cai et al. 2004a, b; El-Hag et al. 2004; Meyer et al. 2006; Ramirez et al. 2008, 2009). Flame retardancy improves in silicone elastomers embodying layered silicates (Lan et al. 2003; Yang et al. 2006). PD resistance (Lan et al. 2004), high voltage arcing resistance (Ajayan 2004), mechanical properties (Cai et al. 2004a, b), and material preparation methods (Cai et al. 2004b) have all been investigated.

Insufficient data are available at present for tracking performance and dry band arcing, but some data have been obtained to indicate a positive effect of nano fillers on tracking (Meyer et al. 2006). Tracking is a carbonaceous process that can take place in polymers such as epoxy, but erosion is the main phenomenon for silicone rubber without carbon in the polymer backbone. Silica with median particle sizes of about 15 nm and 43 μm are added to a two-part room temperature (RTV) silicone rubber consisting of 60–80% vinyl polydimethyl siloxane and 10–30% vinyl resin, where no fumed silica reinforcing fillers are added. Such nanocomposite specimens are subjected to the Inclined Plane Test (IP Test). The resulting eroded volume is clearly reduced due to filler inclusion, as shown in Fig. 8.17 (Meyer et al. 2006). This also demonstrates that RTV SR specimens filled with nano silica particles have

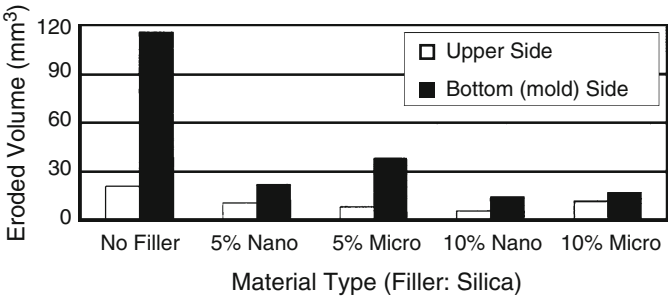

Fig. 8.17 Effect of nano silica addition on eroded mass of silicone rubber when subjected to the Inclined Plane (IP) Test (ASTM D 2303, IEC60587 and IEC61621) (Meyer et al. 2006) *Note:* Erosion was evaluated on both the upper and bottom parts of the specimens arranged for the IP test

higher tracking and erosion resistance than the specimens with micro silica particles. Roughness and hydrophobicity are also evaluated. The analysis of the results indicates that the RTV silicone rubber with nano silica has lower roughness and slightly lower hydrophobicity than that with micro silica.

As in all cases, uniform mixing and particle dispersion are critical in preparing these nanocomposites, since nanoparticles tend to agglomerate easily for cases where a hydrophobic polymer is incompatible with hydrophilic nanoparticles, resulting in poor interfacial interaction (Ramirez et al. 2008). In addition to mixing techniques, surface modification by using surfactants is a promising solution. A common surfactant such as Triton^{TM} X-100 promotes dispersion of nano silica and alumina in silicone rubber through its amphiphilic character. This surfactant embodies a hydrophilic poly(ethylene oxide) group and a hydrocarbon lipophilic or hydrophilic group (C_8H_{17}-C_6H_4-$(OCH_2CH_2)_nOH$). The main advantage of such surfactants is the lowered surface energy and interfacial tension of the nano fillers used. This will reduce agglomeration and facilitate the separation of nanoparticles during mixing, resulting in improved dispersion. Silicone nanocomposites have been prepared by dispersing fumed silica, natural silica and alumina nanoparticles in a two-part addition cure silicone rubber (SiR).

The laser ablation method is applicable to simulate the thermal effects of dry band arcing in place of the IP Test. There are some results available by using infrared laser light with wavelength 802 nm. It was found that the eroded mass decreases with the increase of the content of surfactant at a given content of nano fillers, as shown in Fig. 8.18 (Ramirez et al. 2008) for fumed nano silica, as a typical example. Fumed silica seems to impart greater heat ablation resistance than either nano natural silica or nano alumina. There is no big difference in erosion resistance between silicone/natural silica nanocomposites and silicone/alumina nanocomposites. The ablation observed on nano silica-filled specimens suggests that the silica accumulated at the surface forms a heat-resistant barrier preventing further erosion. This phenomenon is not observed in nano alumina specimens.

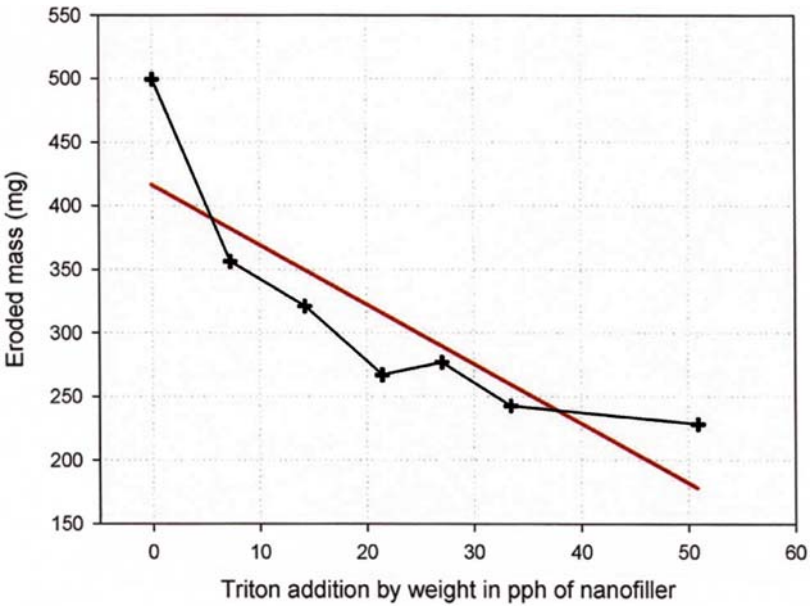

Fig. 8.18 Effect of Triton™ X-100 surfactant addition on eroded mass of silicone specimens with 2.5 wt% nano fumed silica when they are subjected to an infrared laser light ablation test (Ramirez et al. 2008) *Note:* The first order linear regression line is drawn as a straight line

It is worthwhile to state that the addition of nano fillers to micro filled silicone rubber specimens is still effective as an inhibitor for laser ablation (Tanaka et al. 2004). It is an encouraging result. Admixture of both micro filers and nano fillers might be an engineering solution, but it is necessary to take other characteristics such as mechanical properties, thermal properties and weathering properties into consideration. One trial in this field has been made.

In summary, nano fillers certainly act against erosion and/or thermal degradation, when dispersed homogeneously and furthermore they are particularly effective when tightly bound with the surrounded polymer at their interfaces. Surfactants are considered to play a positive role for erosion resistance, but too much addition will cause an adverse effect. The multi-core model introduced requires much more information to characterize the multiple interfacial layers. Consequently, it is difficult to identify which of the three layers is instrumental in mitigating surface erosion and tracking. This discussion has concerned the intrinsic effect of nano fillers and their dispersion. However, the extrinsic effect is also recognizable. Silica is accumulated at the surfaces to form a heat resistant barrier preventing further erosion of the silicon rubber (Ramirez et al. 2008, 2009).

8.6 Treeing Resistance of Polymer Nanocomposites

8.6.1 Electrode Systems for Treeing Experiments

Electrical (as opposed to electrochemical) treeing experiments are usually carried out by using an electrode system as shown in Fig. 8.19 (Iizuka et al. 2009), for example. An steel needle of 1 mm in diameter whose tip radius is typically 3–5 μm is inserted or molded into the polymer sample. Semiconducting carbon loaded polymers are also good candidates as electrode materials. Typical tree shapes are shown in Fig. 8.20. Some difference is seen between the two kinds of materials (Tanaka et al. 2006a). Mechanisms for treeing in polymers in relation to charge transport and injection have been documented elsewhere (Tanaka 2001).

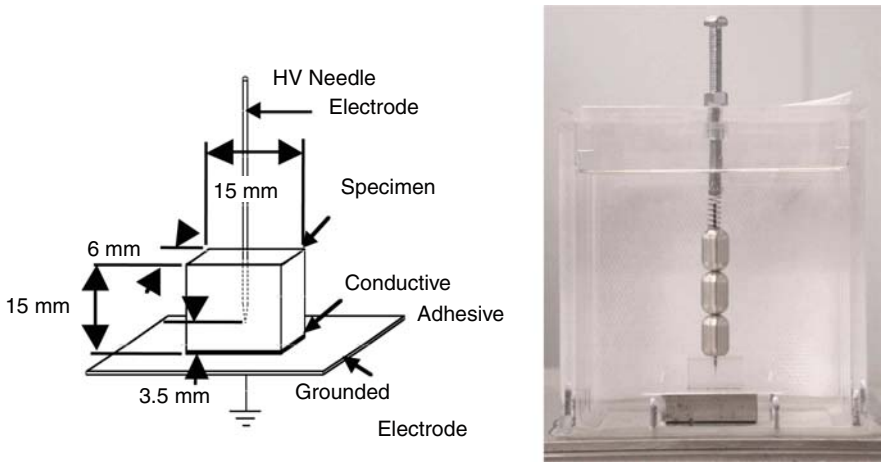

Fig. 8.19 Electrode system for treeing experiments

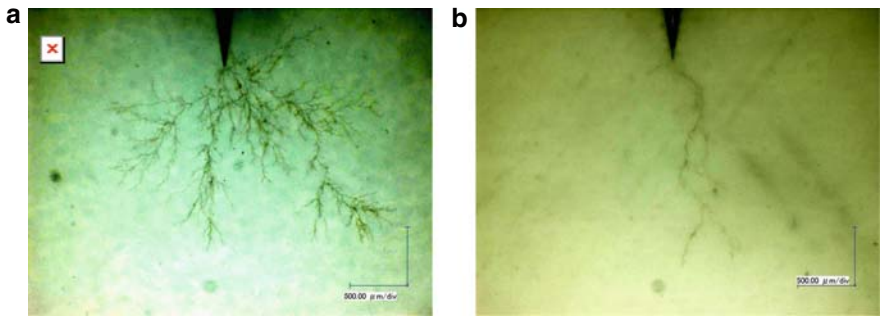

Fig. 8.20 Examples of tree shapes for neat epoxy and epoxy nanocomposite

8.6.2 Treeing Lifetime

Figure 1.9 in Chap. 1 shows classical representative data to demonstrate that treeing lifetime can be dramatically extended (Nelson and Hu 2004), when polymers such as epoxy are nanostructured by the addition of small amounts of nano fillers such as titania especially under relatively low electric stress. Similar data has been obtained for PE/MgO, epoxy/silica, and epoxy/boehmite alumina nanocomposites. Silane couplings will work to increase treeing lifetime.

Tree growth characteristics are represented by Fig. 8.21 (Vogelsang 2004). There are three stages or periods depicted, i.e., an incubation period, a growth period, and a tree channel widening period. In general, no breakdown takes place, even if a thin tree channel reaches the opposite electrode. There is some time needed for breakdown. This phenomenon can be observed in many insulating materials such as pure epoxy, polyethylene, and nanocomposites.

A crossover phenomenon is observed under a certain conditions as shown in Fig. 8.22 (Tanaka et al. 2006a). Tree growth speed is different between base epoxy and its nanocomposite under different voltage condition. At low voltage (10 kV in Fig. 8.22), the tree growth speed for nanocomposite is slower than that for base epoxy. In contrast, at high voltage, the former is faster than the latter. It is concluded that an erosion type of degradation takes place under low voltage conditions, while a progressive type of degradation occurs under high stress conditions.

Microscopic images of internal surfaces of trees formed in epoxy and an epoxy/boehmite alumina nanocomposite are shown in Fig. 8.23 (Tanaka et al. 2006a). The internal surface of a tree channel is smooth for base epoxy, while it is rough for nanocomposite. The latter has agglomerated filler particles on its inner surface. These particles are considered to be formed during the period in which an incipient thin channel is widened from inside by PD attack.

A narrow tree channel grows rather rapidly up to the opposite electrode, but does not directly cause material breakdown. Following that, partial discharges will erode the inside of the tree. This corresponds to the stage 3 in Fig. 8.21. Narrow channels are formed due to solid dielectric breakdown, while wide channels are generated

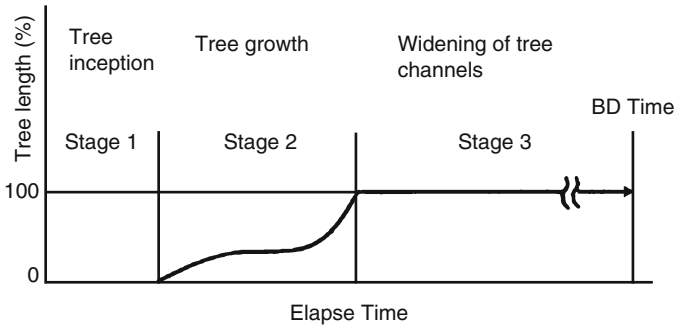

Fig. 8.21 Tree growth characteristic (Vogelsang 2004)

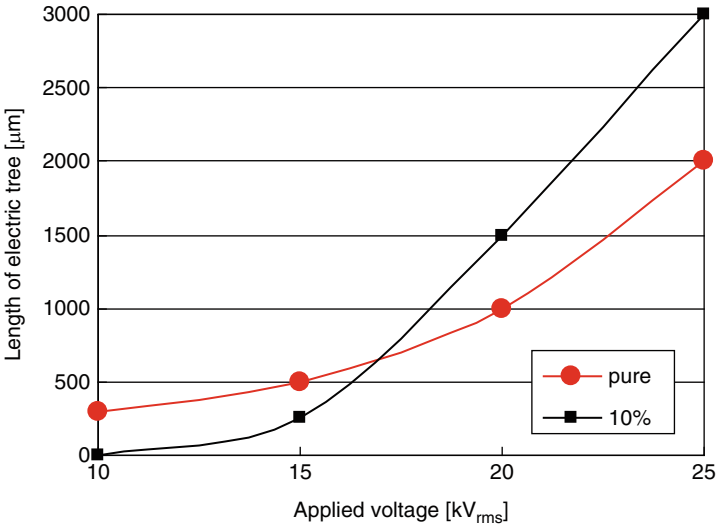

Fig. 8.22 Crossover phenomenon in tree length vs. voltage for epoxy/boehmite alumina nanocomposite (Tanaka et al. 2006a)

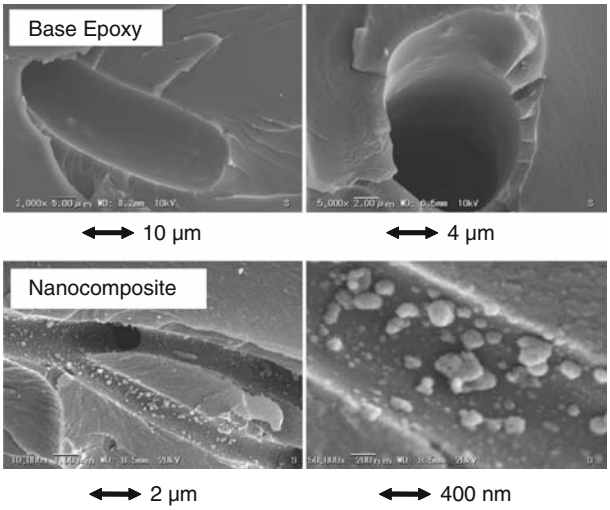

Fig. 8.23 Internal surfaces of trees formed in epoxy and epoxy/boehmite alumina nanocomposite (Tanaka et al. 2006a)

by PD attack subsequently. Dramatic treeing lifetime extension is considered to be related to the PD degradation process inside a tree under moderate applied voltage conditions. Similar results were obtained in PE/MgO nanocomposite (Kurnianto et al. 2007), where three kinds of characteristic time, i.e., time to reach the opposite electrode, time to breakdown and time lag to breakdown are separately obtained.

8.6.3 Possible Effects of Nano-fillers on Treeing

A progressive type of tree growth process is illustrated in Fig. 8.24 in the case of high-voltage application. Tree channels are formed by successive solid breakdown at the tree tip location. It should be noted that this process is totally different from an erosion process caused by gaseous partial discharges inside tree channels. Trees are formed in either of the two following processes.

1. Electrons are accelerated by the electric field, but decelerated by the nanoparticles.
2. Electrons are accelerated by the electric field, and further accelerated by the nanoparticles.

Deceleration and acceleration take place due to attractive and repulsive forces generated around the nanoparticles, respectively. Electric field is induced around the Debye shielding distance due to the formation of the electric double layers.

An anomalous phenomenon is sometimes observed that solid state breakdown (thin channel formation) occurs more easily in the nanocomposite than in base epoxy. To understand this phenomenon, it is hypothesized that the repulsive force generated in epoxy nanocomposite will work against accelerated electrons. Such high energy electrons migrate only in the epoxy spaces between neighboring nanoparticles, being influenced by the repulsive force. In the case of LDPE/MgO nanocomposite, a thin tree formation (solid state breakdown) is retarded by the addition of nano fillers. This may correspond to the deceleration case.

Such two different processes can be understood by the difference of the tendency of the triboelectricity to cause the far-distance interactive force. It is closely related to the electric double layers.

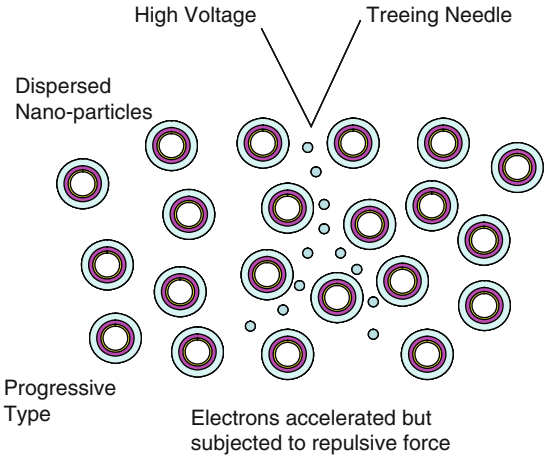

Fig. 8.24 Possible mechanism for high voltage tree formation

8.6.4 Tree Initiation

No pure tree initiation data are available for nanocomposites. Tree initiation is governed by an electron injection and extraction process. The way in which the potential barrier at the electrodes is influenced by the inclusion of nano fillers becomes a pivotal question. It is shown diagrammatically in Fig. 8.6 that negative charge may be formed near the electrodes in the case of negative triboelectricity. This suppresses electron injection and thereby tree initiation. This model will also apply to the threshold for space charge formation and electroluminescence (see Sects. A.2 and A.6 for measurement techniques).

V-t characteristics for quasi-initiation for treeing in epoxy/layered silicate nanocomposite specimens is shown in Fig. 8.25 (Rätzke et al. 2008), which are similar to the treeing breakdown (voltage endurance) V-t characteristics previously shown in Fig. 1.9. The advantage of nanocomposites is clearly confirmed, but the tree length required to recognize initiation is about 100 μm. This means that initiation has not correctly been measured since it includes some early growth process in which the inner surfaces must be subjected to internal partial discharges.

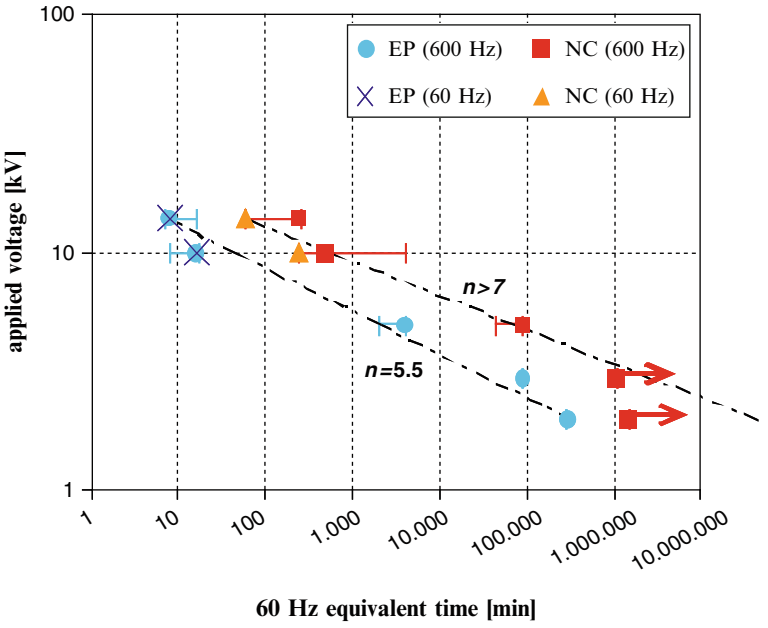

Fig. 8.25 Treeing lifetime vs. applied voltage for neat epoxy and epoxy/layered silicate nanocomposite (Rätzke et al. 2008). *Note:* Data taken under 600 Hz voltage instead of 60 Hz for acceleration

8.7 Mechanisms of Surface Erosion and Tree Propagation in Polymer Nanocomposites

8.7.1 Summary for Experimental Verification

There are several major characteristics for which a favorable change is desired when polymers are nanostructured. Among them, partial discharge resistance, space charge reduction, and treeing lifetime are clearly important. These effects of nanofillers can be summarized, as shown in Table 8.3.

This chapter mainly describes characteristics of resistance against partial discharges and tracking represented by laser and plasma ablation, and treeing phenomena including treeing breakdown and lifetime. Other dielectric properties such as permittivity, dielectric loss, DC conductivity, high field conduction, space charge, etc. are covered in Chap. 7.

8.7.2 Consideration of Mechanisms of Erosion due to Partial Discharge and Treeing

Suppression of PD-caused surface erosion by nano filler inclusion in polymers originates from three major processes, i.e., tight coupling at the internal interfaces (if any), the nanometer segmentation of the polymer matrix by nano fillers as the intrinsic process, and the piling-up of nano fillers on the surface of the material under test as the extrinsic process. Treeing lifetime is greatly extended under moderate electric field conditions. Short-time breakdown voltage may also increase modestly. There is no clear finding for a dramatic increase in short-time breakdown voltage by nano filler addition. A phenomenon is observed that tree length is smaller in

Table 8.3 Summary of the characteristics of polymer nanocomposites

Possible change in characteristics from base polymers	Remarks
Big enhancement in **PD resistance**	Nano-segmentation
Big prolongation in **treeing lifetime**	Especially under moderate field
Big reduction in **space charge**	Elevated threshold for charge injection and EL inception
Improved tracking resistance	Similar to PD resistance
Improved BD strength	No reduction at least
Peculiar change in permittivity	Decrease in some case. Reduction in Maxwell–Wagner type polarization
Complicated change in dielectric loss vs. temperature and frequency	Represents complicated structures of interfaces
Decrease or increase in dc conductivity	Nanofillers might act as ion traps, accidental introduction of ionic impurities

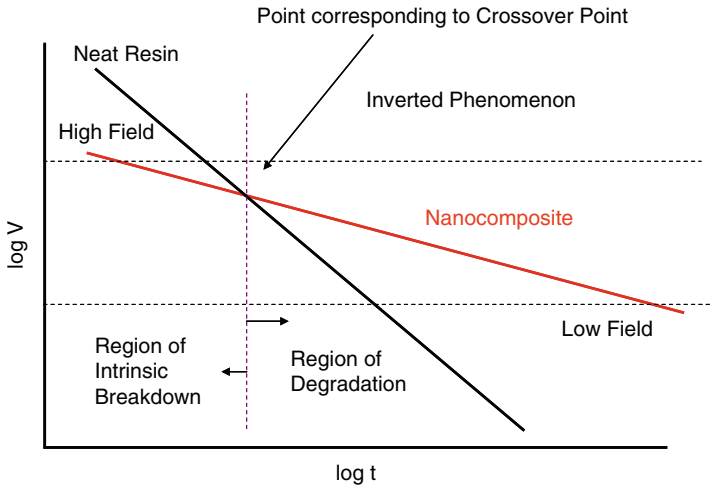

Fig. 8.26 Generalized treeing V-t characteristics

a nanocomposite than in its neat resin at a medium voltage, but this tendency is reversed at high electric field. Therefore, a cross point of tree length appears at a certain voltage. It is recognized that a thin treeing path reaches the opposite electrode in the nanocomposite more quickly than in the neat resin at high fields above the crossover point.

Those phenomena can be represented by the generalized treeing V-t characteristics as shown in Fig. 8.26. The slope of the V-t curve is less steep for a nanocomposite than for its base resin so that a cross point appears at a certain elapsed time, which can be called the characteristic time. Short-time breakdown or quasi intrinsic breakdown takes place below the characteristic time, while long-time breakdown, including some degradation processes, occurs beyond the characteristic time. It is not suggested by this figure that nanocomposites always have lower short-time breakdown strength than their neat resins below the characteristic time. In reality the slope might tend to flatten. However, this figure means that it would not be strange even if lower breakdown values are obtained for nanocomposites. It is evidenced by the experimental fact that tree initiation time is more or less insensitive to whether or not nano fillers are added.

Treeing phenomena at medium electric field beyond the characteristic time are considered to be similar to the PD-caused erosion process. SEM observation indicates that many agglomerates are created inside tree channels. Such agglomerates are considered to be formed due to inner surface erosion inside tree channels which can be enlarged in inner diameter due to PD attacks. A block area as shown in the bottom of Fig. 8.27 is one of the examples showing such a phenomenon. Many nano filler agglomerates are created inside a part of a tree channel.

It is interesting to note that a single thin tree grows in a selective path avoiding regions of nano fillers to form a small zig-zag path. It is not clear whether or not a tip

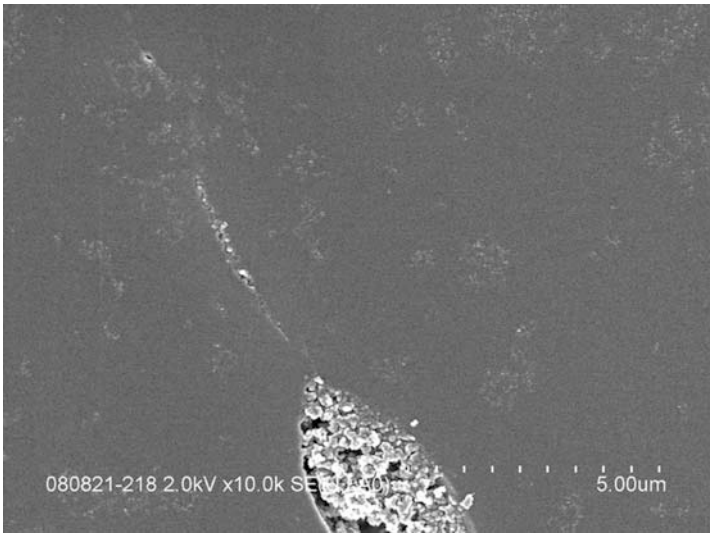

Fig. 8.27 Treeing path in epoxy/silica nanocomposite

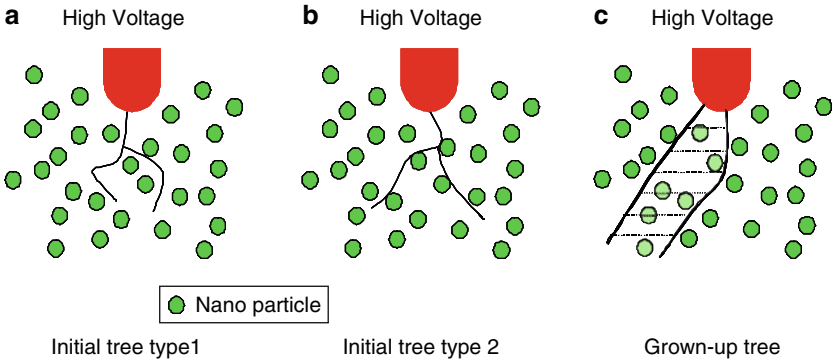

Fig. 8.28 Possible processes for tree initiation and growth in nanocomposites representing initial tree type 1, initial tree type 2, and grown-up tree

of the tree touches the surface of a nano filler particle. It might depend on whether a nanoparticle is charged or not, as described in the explanation of the multi-core model.

Possible processes are shown for tree initiation and growth in Fig. 8.28. There are two kinds of processes in the tree initiation stage. Firstly a tree proceeds without interacting with the nanoparticulates, or, secondly, it extends by colliding with nanoparticles. In the tree growth stage, it grows in length and width inside which partial discharges are taking place to form nano filler agglomerates by evaporating part of the resin.

8.8 Conclusions

Nano fillers are considered to play a significant role in improving the dielectric performance of polymers, when even a small amount is homogeneously dispersed. It is certainly effective in the sense that inorganic nano fillers with tremendously large specific surface interact with polymer matrices surrounding themselves to form "an interaction zone." Wilkes' model, the multi-core model and the water shell model have been advanced to explain how polymers and nano fillers would interact with each other. It has been experimentally confirmed that coupling agents are significantly effective. This fact also indicates the importance of "the interaction zone."

Partial discharge (PD) resistance is one of the characteristics that could be most improved due to nano filler inclusion. One of the mechanisms is considered to be the fact that polymer matrices are segmented three-dimensionally at the nanometer scale. Wetness or couplings between the two kinds of materials are effective in improving PD resistance. Other factors include the accumulation of nano fillers on the surface of nanocomposites and the electric field concentration on nano fillers due to the difference in permittivity. Tracking resistance is complicated due to the fact that there are many factors that will damage polymers. Similar effects of nanofillers can be assumed but the thermal stability of the material must also be a potential factor to improve tracking resistance.

Treeing has a delicate character. Nano fillers can act negatively as well as positively. Nano filler agglomeration causes a reduction in both treeing and breakdown performance. Treeing breakdown time is drastically increased due to homogeneous dispersion of nano fillers. This is considered to be due to the same mechanisms working for PD resistance. Nano fillers would suppress PDs occurring inside tree channels to retard tree propagation. As for tree initiation, the electric field and the charge distribution around nano fillers must be important factors. Some correlation between surface erosion and tree propagation in polymer nanocomposites exists.

Polymer nanocomposites are promising as engineering materials, but much remains to be solved in the fundamental understanding of performance and mechanisms, and material preparation methods. Homogeneous dispersion of nano fillers in polymers is a prerequisite to make nanocomposites a reality as engineering materials.

References

Ajayan PM, Schadler LS, Braun PV (2004) Nanocomposite science and technology. Wiley-VCH, Weinheim

Cai D, Yu J, Wen X, Lan L (2004a) Research on characterization of RTV silicone rubber/LS(layered silicate) electrical insulation nanocomposites. Proc IEEE-ICSD 7 P-1:796–799

Cai D, Wen X, Lan L, Yu J (2004b) Study on RTV silicone rubber/SiO2 electrical insulating nanocomposites. Proc IEEE-ICSD 7 P-2:800–803

Chujo K (2001) Advanced technology and application of polymer nanocomposites, CMC Press, Tokyo

El-Hag AH, Jayaram SH, Cherney EA (2004) Comparison between silicone rubber containing micro- and nano-size silica fillers. Annu Rep IEEE CEIDP 5A-12:381–384
Fréchette MF, Trudeau ML, Alamdari HD, Boily S (2004) Introductory remarks on nanodielectrics. Trans IEEE DEI-11:808–818
Fréchette MF, Reed CW, Sedding H (2006) Progress, understanding and challenges in the field of nanodielectrics, IEEJ Trans FM 126-11:1031–1043
Fuse N, Ohki Y, Kozako M, Tanaka T (2008) Possible mechanisms of superior resistance of polyamide nanocomposite to partial discharges and plasmas. Trans IEEE DEI-15-1:161–169
Huang HH, Wilkes GL (1987) Structure-property behavior of new hybrid materials incorporating oigmeric poly(tetramethylene oxide) with inorganic silicates by a sol–gel processes. Polym Bull 18:455–462
Iizuka T, Uchida K, Tanaka T (2009) Voltage endurance characteristics of epoxy/silica nanocomposites. IEEJ Trans FM 129-3:123–129
Imai T, Sawa F, Ozaki T et al (2006) Approach by nano- micro-filler mixture toward epoxy-based nanocomposites as industrial insulating materials, IEEJ Trans FM 126-11:1136–1143
Kozako M, Fuse N, Ohki Y et al (2004) Surface degradation of polyamide nanocomposites caused by partial discharges using IEC (b) electrodes. Trans IEEE DEI-11-5:833–839
Kozako M, Ohki Y, Kohtoh M et al (2006) Preparation and various characteristics of epoxy/alumina nanocomposites. IEEJ Trans FM 126-11:1121–1127
Kurnianto R, Murakami Y, Nagao M et al (2007) Treeing breakdown in inorganic-filler/LDPE nanocomposite material. IEEJ Trans FM 127-1:29–34
Lan L, Wen X, Cai D, Liu H (2003) Study of the properties of RTV nanocomposite coatings. Proc 8th ISH:4
Lan L, Wen X, Cai D (2004) Corona ageing tests of RTV nanocomposite materials. Proc IEEE-ICSD 7P-3:804–807
Lewis TJ (1994) Nanometric dielectrics. Trans IEEE DEI-1-5:812–825
Lewis TJ (2004) Interfaces are the dominant feature of dielectrics at the nanometric level. Trans IEEE DEI-11-5:739–753
Lewis TJ (2006) Nanocomposite dielectrics: the dielectric nature of the nanoparticle environment. IEEJ Trans FM 126-11:1020–1030
Maity P, Basu S, Parameswaran V, Gupta N (2008a) Degradation of polymer dielectric with nanometric metal-oxide fillers due to surface discharges, Trans IEEE DEI-15-1:52–62
Maity P, Kasisomayajula SV, Parameswaran V et al (2008b) Improvement in surface degradation properties of polymer composites due to pre-processes nanometric alumina fillers. Trans IEEE DEI-15-1:63–72
Meyer LH, Jayaram SH, Cherney EA (2005) A novel technique to evaluate the erosion resistance of silicone rubber composites for high voltage outdoor insulation using infrared laser erosion. Trans IEEE DEI-12-6:1201–1208
Meyer LH, Cabral SHL, Araujo E et al (2006) Use of nano-silica in silicone rubber for ceramic insulators coatings in coastal areas. Conf Rec IEEE ISEI 2006:474–477
Nakao K (ed) (2004) Composite materials and fillers. CMC Press, Tokyo (in Japanese)
Nelson JK, Hu Y (2004) The impact of nanocomposite formulations on electrical voltage endurance. Proc IEEE-ICSD 7 P-10:832–835
Njuguna J, Pielichowski K (2004) Polymer nanocomposites for aerospace applications: fabrication. Adv Eng Mater 6–4:193–203
Preetha P, Alapati S, Singha S et al(2008) Electrical discharge resistant characteristics of epoxy nanocomposites. 2008 Annu Rep CEIDP 8-4:718–721
Rätzke S, Kindersberger J (2005) Erosion behavior of nano filled silicone elastomer. Proc XIVth Int Symp High Voltage Eng C-09:4
Rätzke S, Kindersberger J (2006) The effects of interphase structures in nanodielectrics. IEEJ Trans FM 126-11:1044–1049
Rätzke S, Ohki Y, Imai T et al (2008) Enhanced performance of tree initiation V-t characteristics of epoxy/clay nanocomposite in comparison with neat epoxy resin. Annu Rep IEEE CEIDP 6-2:528–531

Rittingstein P, Priestley RD, Broadbelt LJ, Torkelson JM (2007) Model polymer nanocomposites provide an understanding of confinement effects in real nanocomposites. Nat Mater 6-4: 278–282

Ramirez I, Cherney EA, Jararam S, Gauthier M (2008) Nanofilled silicone dielectric prepared with surfactant for outdoor insulation applications. Trans IEEE DEI-15-1:228–235

Ramirez I, Jararam S, Cherney EA, Gauthier M, Simon L (2009) Erosion resistance and mechanical properties of silicone nanocomposite insulation. Trans IEEE DEI-16-1:52–59

Ray SS, Okamoto M (2003) Polymer/layered silicate nanocomposites: a review from preparation to processing. Prog Polym Sci 28:1539–1641

Takala T, Sallinen T, Nevalainen P et al (2008) Surface degradation of nanostructured polypropylene compounds caused by partial discharges. Proc IEEE Int Symp Electr Insul No. S3:205–209

Tanaka T (2001) Space charge injected via interfaces and tree initiation in polymers. Trans IEEE DEI-8-5:733–743

Tanaka T, Montanari GC, Mülhaupt R (2004) Polymer nanocomposites as dielectrics and electrical insulation – perspectives for processing technologies, material characterization and future applications. Trans IEEE DEI-11-5:763–784

Tanaka T, Kozako M, Fuse N, Ohki Y (2005) Proposal of a multi-core model for polymer nanocomposite dielectrics. Trans IEEE DEI-12-4:669–681

Tanaka T (2005) Dielectrics nanocomposites with insulating properties. Trans IEEE DEI-12-5:914–928

Tanaka T, Matsunawa A, Ohki Y et al (2006a) Treeing phenomena in epoxy/alumina nanocomposite and interpretation by a multi-core model. IEEJ Trans FM 126-11:1128–1135

Tanaka T (2006) Emerging nanocomposite dielectrics. CIGRE Electra 226:24–32

Tanaka T, Ohki Y, Shimizu T, Okabe S (2006b) Superiority in partial discharge resistance of several polymer nanocomposites. CIGRE 2006 Paper D1-303:8

Tanaka T, Nose A, Ohki Y, Murata Y (2006c) PD resistance evaluation of LDPE/MgO nanocomposite by a rod-to-plane electrode system. Proc ICPADM:319–322

Tanaka T, Kuge S, Kozako M (2008a) Nano effects on PD endurance of epoxy nanocomposites. Proc ICEE ME1-01:4

Tanaka T, Matsuo Y, Uchida K (2008b) Partial discharge endurance of epoxy/SiC nanocomposite. Annu Rep CEIDP 1-1:13–16

Toray R (2002) Technological trend in nano-controlled composite materials. Toray Research Center Library:1–471 (in Japanese)

Vogelsang R (2004) Time to breakdown of high voltage winding insulations with respect to microscopic properties and manufacturing qualities. PhD Dissertation ETH No. 15656

Yang L, Hu Y, Lu H, Song L (2006) Morphology, thermal, and mechanical properties of flame-retardant silicone rubber/montmorillonite nanocomposites. J Appl Polym Sci 99-6:3275–3280

Zeng R., Rong MZ, Zhang MQ et al (2002) Laser ablation of polymer-based silver nanocomposites. App Surf Sci 187:239–247

Zou C, Fothergill JC, Rowe SW (2008) The effect of water absorption on the dielectric properties of epoxy nanocomposites. Trans IEEE DEI-15-1:106–117

Chapter 9
Non-linear Field Grading Materials and Carbon Nanotube Nanocomposites with Controlled Conductivity

L.S. Schadler, X. Wang, J.K. Nelson, and H. Hillborg

9.1 Introduction

While the emphasis of this book is on highly insulating materials, there are applications where tailored conductivity and non-linear conductivity are critical. For example, field grading applications require careful control of the conductivity as a function of field and EMI shielding applications or anti-static applications require relatively high conductivity. There is a recent set of literature in which semiconducting nanofillers are added to polymers to create non-linear electrical properties, and a set of literature in which carbon nanotubes are used to tailor polymer conductivity. In both these cases, percolation is a critical concept in controlling dielectric properties. To start, therefore, the chapter introduces examples of applications where more conductive dielectrics are required including applications of field grading materials and shielding applications. Percolation is then briefly introduced with an emphasis on the impact of filler geometry and dispersion on percolation. Recent materials tested for use in field grading applications are introduced. The proposed mechanisms leading to non-linear behavior are discussed with an emphasis on the implications for controlling the properties of composites. Finally, the important parameters for tailoring the conductivity of nanotube filled polymers are reviewed.

9.2 Application of Electric Field Grading Materials for High-Voltage Cable Terminations

In a number of high-voltage (HV) and medium-voltage (MV) applications such as cable accessories (Nikolajeic et al. 1997; Rivenc and Leby 1999), generator or motor end windings (Roberts 1995) or bushings (Hesamzadeh et al. 2008); problems with

L.S. Schadler (✉), X. Wang, J.K. Nelson
Rensselaer Polytechnic Institute, Troy, NY, USA
e-mail: schadl@rpi.edu

H. Hillborg
ABB AB, Corporate Research, Västerås, Sweden

J.K. Nelson (ed.), *Dielectric Polymer Nanocomposites*,
DOI 10.1007/978-1-4419-1591-7_9,

electrical stress concentrations may occur. In all these situations it is necessary to control the field in order to avoid breakdown or flashover. The purpose of a field grading material is to reduce this local surface stress so it does not exceed the breakdown strength in any location. Traditionally field grading materials have been restricted to AC (Alternating Current) terminations for MV applications since the comparatively large dielectric loss of these materials gives rise to thermal problems when used in HVAC applications. Today, as the voltage requirements steadily increase and the size of the components is decreasing, field grading is needed for MV and HV applications, under both AC and DC (Direct Current) conditions. Thus, the electrical properties of the field grading material are often a limitation in the design of prefabricated AC and DC cable accessories. The situation becomes particularly complex in some HVDC-components, where the field grading material must work under DC as well as AC and impulse conditions. This means that for each design, a field grading material with specific electrical properties is desired, to avoid electrical breakdown as well as thermal problems.

When reduced to their essential components, cables consist of a conductor, insulation and a grounded shield (Fig. 9.1). The entire potential difference between the conductor and the shield occurs across the insulation. Along the cable, the radial stress is non-linear, but well behaved and leads to a satisfactory design as long as the insulation sustains the voltage, but problems may occur in joints or at the end of the cable. To terminate the cable, the shield has to be removed, and at this discontinuity, the concentrated field in the insulation has to be spread out in a controlled

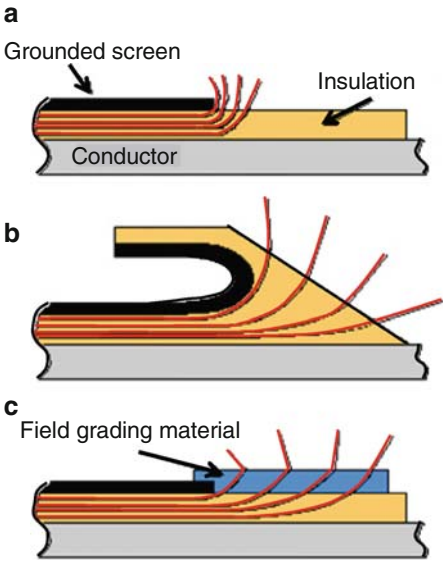

Fig. 9.1 A schematic of the of equipotential lines in AC cable terminations (in cross section): (**a**) An example when no action is taken to control the field, which will lead to field concentrations next to the grounded screen, (**b**) an example of geometric control, and (**c**) an illustration of the use of a field grading material (Mårtensson 2003)

manner. If no such action is taken, the field stresses may cause flashover problems or breakdown. In Fig. 9.1, a cable termination is illustrated with its electrical equipotential lines. The situation when no action to control the field is taken is shown in Fig. 9.1a and demonstrates the risk of flashover at the surface of the terminated cable, next to the end of the grounded screen. One solution to solve this problem is to bend the shield and increase the thickness of the insulation. In this manner the shape of the bent shield, together with the increased thickness of the insulation, provide the stress control. This is called geometrical stress control and is illustrated in Fig. 9.1b. The major drawback of this solution is the size and cost of this component, especially in HV applications.

A more advantageous solution is to have a material that has the ability to distribute the field by itself, i.e., a field grading material. Usually this material is a composite of an insulating material and a semi-conducting material. The use of such a composite is illustrated in Fig. 9.1c. In order to accomplish this function, the electrical properties of the field grading material must be field dependent. For AC applications, the field grading material can provide field grading in two ways, either by non-linear resistivity, which is discussed further in following sections, or by capacitive field grading (Roberts 1995). Capacitive field grading means that the dielectric constant becomes high enough to redistribute the field. In many AC applications, a combination of field dependent resistivity and a capacitive field grading is also an alternative. Moreover, in many cases a combination of a field grading material and geometric control is necessary, which is true even for DC applications.

In High-Voltage DC (HVDC) applications, on the other hand, field grading can be controlled by having a material with field dependent resistivity. This means that the material should become conductive at high fields and stay (more or less completely) insulating at low fields. It is important to remember in this context that, even in the DC case, the dielectric properties of the field grading material are still important. In some HVDC equipment, voltage spikes and other time-varying stresses of various kinds exist. Therefore, a field grading material for DC applications must also have the right dielectric properties. Figure 9.2a shows a DC cable joint where a field grading material is used. The potential field lines are drawn in Fig. 9.2b illustrating the effect of the field grading material.

9.3 Shielding Applications for Highly Conductive Composites

Although materials such as doped poly-acetylenes have been introduced to create highly conducting polymers (particularly for battery technology) with resistivities below $10^{-5}\ \Omega$m (Ku and Liepins 1987), there are numerous applications in which HV designs require a conducting layer in order to define an equipotential surface. This could be a ground plane surrounding an insulated high-voltage component, or, at the other extreme, a conducting layer of large radius tied to the potential of a high-voltage termination to afford some protection from unwanted corona. Such

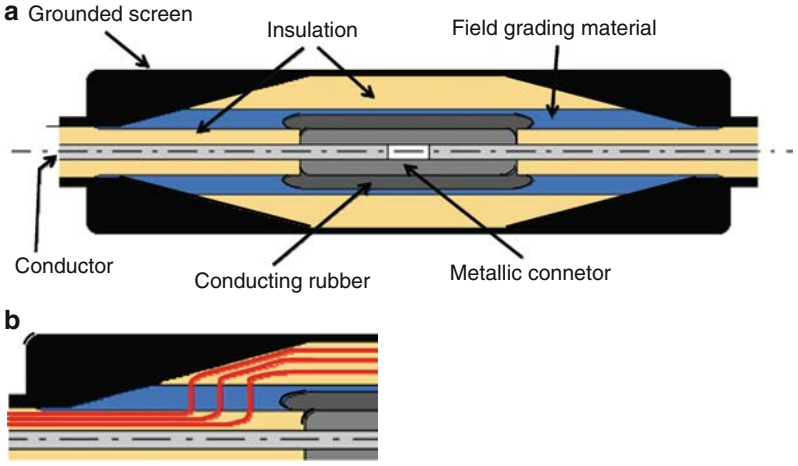

Fig. 9.2 (**a**) A schematic of a DC cable joint. Notice that the field grading material is in contact with the conductor and the grounded screen. The equipotential field lines are shown in (**b**) illustrating that the field grading material has distributed the field and avoided concentrations (Mårtensson 2003)

conducting layers usually do not have to carry currents (other than small displacement currents due to parasitic capacitance) and so the resistivity does not need to be as low as a metal for it to be effective. Indeed, since the resistivity of most insulation is between 10^{11} and 10^{16} Ωcm (Shugg 1995) even a modest conductivity imparted to a polymer can be effective. A good example of this may be found in the use of graphite ink for rendering cellulose layers conductive as a substitute for metallic foils in the internal stress grading of HV bushings. Similarly, semiconducting layers have been used for cables to screen conductor asperities for many years, through the use of carbon black, which can yield an extruded layer with a resistivity as low as 10^2 Ωcm (Tanaka and Greenwood 1983). The light weight and moldability of polymers make them very attractive for EMI shielding and as an answer to electromagnetic pollution.

In the context of this book, carbon nanotubes and nanofibers offer an alternative way to impart some conductivity (and also enhanced relative permittivity) to conventional polymers while still maintaining some of the multifunctional advantages introduced in Chap. 1. In a recent example (Liang and Tjong 2008) were able to generate a polystyrene with a resistivity reduced to 10^6 Ωcm with less than 2 vol% of carbon nanotubes. If the nanotubes are aligned, then resistivity can be further lowered dramatically to values approaching 10^{-1} Ωcm at room temperature for sulphonated polyetheretherketone (PEEK) (Peng and Sun 2009).

9.4 Background on Percolation

Percolation is a critical concept in understanding transport properties in disordered systems and, for purposes of this chapter, in understanding the conductivity of composites comprising an insulating matrix and conducting or semiconducting nanoparticles (Sahimi 1994). For example, it is well known that there is a critical volume fraction of conducting filler in an insulating matrix, above which the electrical or thermal conductivity increases dramatically due to the development of a continuous path of electron transport. This critical volume fraction, which is the minimum concentration required to create an infinitely connected network, is called the percolation threshold. In classical percolation theory applied to composites, the theory assumes a physical connection between the filler particles. The resistivity or conductivity near the percolation threshold can then be described by (9.1)

$$\sigma \propto (\phi - \phi_c)^t \tag{9.1}$$

where ϕ is the volume fraction of filler, ϕ_c is the percolation threshold, and t is a power law constant that depends on the geometry of the system. ϕ_c is also a function of the filler geometry, dispersion, and the type of connectivity between particles (e.g., tunneling, vs. Schottky barrier) (Balberg et al. 2004; Grimaldi and Balberg 2006). Typical values for three dimensional systems of interest here are, $t = 2.0$ and $\phi_c = 0.17$ for spherical particles.

In addition to the changes in ϕ_c and t that occur due to filler geometry and dispersion, the conduction in nanoparticle filled polymers has some added complications that require modifications to the model. First, particularly for nanofilled polymers, there can be a thin polymer layer completely encasing the nanofillers within the nanocomposite, preventing direct particle-particle contact. Therefore, electrical percolation does not always occur due to particle-particle contact but can occur when the particles are close enough for tunneling conduction through the interstitial layer. This has been well documented in carbon black nanofilled polymers, and it has been shown that ϕ_c and t differ significantly from that predicted by universal percolation theory (Reboul and Moussalli 1976; Carmona 1989; Donnet et al. 1993; Balberg 2002). This has implications for the effect of particle size on percolation. As the particle size decreases, the interparticle spacing decreases. Therefore, smaller particles will reach an interparticle distance equal to the tunnelling distance at lower percolation thresholds (Hong et al. 2003).

Second, many spherical nanofillers are not perfectly dispersed in the matrix. Typically they are fractally agglomerated during synthesis or agglomerate during processing. The resulting agglomerate is not necessarily spherical. This shifts the percolation threshold because the fillers have an aspect ratio greater than 1 or they effectively fill a larger volume because of the fractal shape. Balberg et al. (1984a, b) showed that ϕ_c could be predicted by using the concept of an excluded volume, defined as the volume around the filler that cannot be occupied by the center of

another object. When the volume fraction of a high aspect ratio filler is equal to the ratio of the actual volume of the filler over the excluded volume, V_{exc}, percolation is reached.

In general, for a random dispersion of spherocylinders (cylinders with spherical caps), V_{exc} is defined as shown in (9.2) (Berhan and Sastry 2007).

$$V_{exc} = \frac{32\pi}{3} R^3 \left[1 + \frac{3}{4}\left(\frac{L}{R}\right) + \frac{3}{8\pi} \langle \sin(\theta) \rangle \left(\frac{L}{R}\right)^2 \right] \tag{9.2}$$

where L is the filler length, R its radius, and $< \sin(\theta) >$, the average $\sin(\theta)$ between the fillers. The effects of orientation can be predicted based on the average angle, θ, between the two fillers. For a random distribution, (9.2) reduces to (Berhan and Sastry 2007):

$$V_{exc} = \frac{32\pi}{3} R^3 \left[1 + \frac{3}{4}\left(\frac{L}{R}\right) + \frac{3}{32}\left(\frac{L}{R}\right)^2 \right] \tag{9.3}$$

ϕ_c can be shown to be proportional to the ratio of the hard volume of the filler divided by the excluded volume. Therefore, as the aspect ratio increases, and V_{exc} increases, ϕ_c decreases. If there is alignment, then ϕ_c will change and has been found experimentally to first increase and decrease as alignment increases (Du et al. 2005). Implicit in this calculation is a uniform distribution of fillers. If the distribution is non-uniform, then the local volume fraction of the filler changes, and the apparent percolation threshold will decrease (Hong et al. 2006; Mu et al. 2008).

In addition, Balberg has published a series of papers in which he considers the impact of tunneling distance on t, the power law parameter (Balberg et al. 1984a, b, 2004; Balberg 2002, 2008). The reader is referred to a recent review for more depth (Balberg et al. 2004). These papers conclude that when the average interparticle spacing has a narrow distribution, then the values for t are similar to that for universal percolation theory, while, when it is broad, t increases. For practical application, however, while percolation theory can be used to guide the processing approach, the percolation threshold is best measured experimentally and then understood using percolation theory.

Carbon nanotubes are a special case of nanofillers. If processed properly, the aspect ratio can be in the range 100–10,000. In addition, while they tend to bundle, their overall shape remains cylindrical. This leads to an improved ability to predict ϕ_c. There have been several recent papers in this area (Berhan and Sastry 2007; Kyrylyuk and van der Schoot 2008) that conclude that a hard core model is the most appropriate. In this case, the inclusion is modeled as a hard conducting core of the nanotube, and a soft layer related to the tunneling distance. The soft layers of the two inclusions can overlap, while the hard conducting cores cannot. Behran and Sastry (2007) have considered a nanotube or a bundle of tubes with a soft layer surrounding the tubes. A parameter t, is defined as the ratio of the hard radius, r, to the radius of the outer shell, R. The excluded volume of the filler is larger than that predicted for just the filler alone. It is equal to the difference between the

excluded volume of an outer shell of radius R and the core volume or actual volume of the nanotubes. This leads to the following prediction (9.4–9.6) for the percolation threshold where s depends on t, but becomes a constant for high aspect ratio fillers.

$$V_{core} = \pi r^2 L + \frac{4}{3}\pi r^3 \tag{9.4}$$

$$V_{exc} = \frac{32\pi}{3} R^3 \left[\left(1 - t^3\right) + \frac{3}{4}\left(\frac{L}{R}\right)\left(1 - t^2\right) + \frac{3}{32}\left(\frac{L}{R}\right)^2 (1 - t) \right] \tag{9.5}$$

$$\phi_c = \frac{(1 + s)\, V_{core}}{V_{exc}} \tag{9.6}$$

Further application of this work shows that fiber waviness has a significant impact on the percolation threshold, but that the use of the excluded volume concept still holds. Kyrylyuk and van der Schoot (2008) also used a hard core approach and showed that the distribution of aspect ratios had a strong impact on ϕ_c, with larger aspect ratios contributing more to ϕ_c than short ones. In addition, they found that as the "degree of connectedness" which is related to the tunneling distance, increases, ϕ_c decreases. In contrast to Behran and Sastry, however, they found a weak dependence on waviness.

From these models, several experimental approaches to controlling percolation emerge.

1. Increasing aspect ratio decreases ϕ_c
2. Increasing the tunneling distance with higher dielectric constant matrices or layers, decreases ϕ_c
3. Inhomogeneous dispersion will decrease ϕ_c. This is implied in the models as they assume that the volume fraction of filler is distributed evenly on the mesoscale
4. Orientation of high aspect ratio fillers will increase the ϕ_c up to a certain level of orientation and then will begin to decrease it

There is one further complication that is relevant. There are cases, where two percolation thresholds have been observed and predicted even for composites with one type of particle due to two populations of contacts (Sheng and Kohn 1982; Berlyand and Golden 1994; Nettelblad et al. 2003). The work by Nettelblad et al. (2003) showed that for angular silicon carbide (SiC) grains, two percolation thresholds were observed, and this was modeled using cubic grains and found to agree well with the concept of two types of contacts: point contacts and edge contacts. For the same SiC that had been rounded through processing, there was only one percolation threshold. Thus, not only are particle size, aspect ratio, and dispersion critical to controlling ϕ_c, so is the angularity of the shape of the particles.

9.5 Non-linear Electrical Nanocomposites for Field Grading Applications

9.5.1 Introduction

As previously discussed, the common characteristics for field-grading materials used in DC-applications are their non-linear I–V (current to voltage) properties, also referred to as non-Ohmic behavior. In order to compare these materials, measurements of their electrical properties are often fitted to a varistor characteristic (Bernasconi et al. 1977). The non-linear relation of a varistor is given by

$$I = I_0(V/V_0)^{\alpha} \tag{9.7}$$

where I_0 and V_0 are material constants and α is the non-linearity exponent of the material. The value of α is obtained from the inverse of the slope of the *log I-log V* curve at any value of voltage, V (Bhushan et al. 1981). However, this relationship may only be valid in a specified intermediate field-region. At lower fields, the electrical behavior could be ohmic, and at higher fields if ohmic heating or dielectric losses become too high, thermal runaway and subsequent breakdown may occur.

The value of α (3 as depicted in Fig. 9.3) is not the only parameter that is important for the function of a field grading material. The level of the resistivity in the insulating region (1 as depicted in Fig. 9.3) and E-field strength where the material starts to become non-linear (2 as depicted in Fig. 9.3) are also important. The desired values of these parameters are dependent on the geometry of the component and the voltage of the conductor. Having a material with tuneable resistivity in a wide range of electric field, and with robust properties is desirable.

There are two primary types of materials used to make resistive field grading materials. The first is a conducting filler (e.g., carbon black)/polymer matrix (typically polyolefins or ethylene-propylene-diene monomer). In this case, the non-

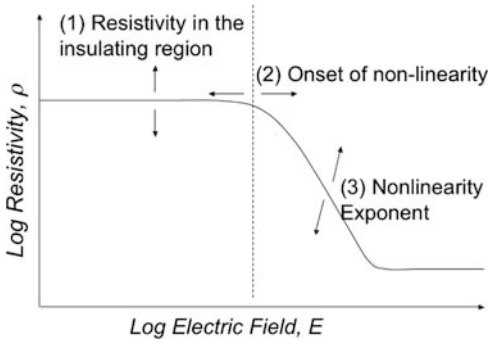

Fig. 9.3 Principle of resistivity vs. E-field for a field grading material. The level of the resistivity (1), the onset of non-linearity (2) and the non-linear exponent α (3) are shown

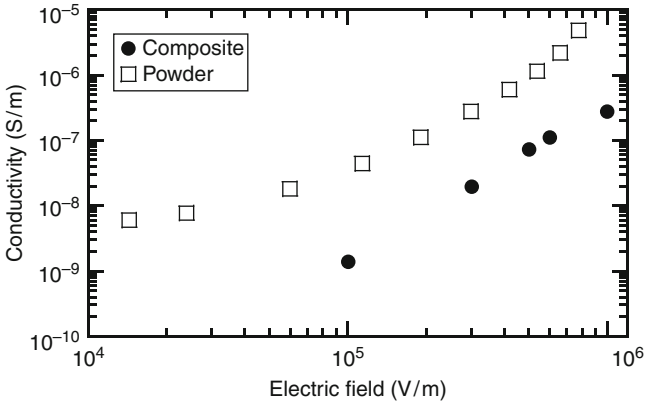

Fig. 9.4 Electric field dependence of the conductivity measured for EPDM mixed with 50 vol% SiC particles compared to that of SiC powder alone (Mårtensson 2003)

linearity is observed at loadings close to the percolation level and is due to tunnelling through a thin polymer layer between the fillers (Nakamura et al. 1997; Mårtensson et al. 1998; Tucci and Vitelli 2000; Önneby et al. 2001). This non-linearity, however, often leads to early breakdown and irreversible behavior. In addition, the resistivity of such materials is sensitive to small fluctuations of the parameters influencing particle dispersion.

An alternative field grading material is based on ZnO microvaristors or other semiconducting fillers such as SiC in a silicone rubber or other polymer matrix (Tavernier et al. 1998; Donzel et al. 2004). The electrical properties of such formulations are reproducible, since the resistivity of the composite depends on the intrinsic (bulk) properties of the filler particles. Figure 9.4 shows an example of this. The powder properties and the composite properties show the same field dependence, but the conductivity of the composite is lower than that of the powder due to interface resistance between powders caused by the polymer. With microvaristor particles, the volume content of the filler can be chosen to be higher than the percolation limit, and the properties of the compound show little sensitivity to the processing conditions. One advantage of the microvaristor materials (such as ZnO) over micron scale SiC, is that ZnO particles are less abrasive resulting in less wear of the production tools.

9.5.2 Effect of Particle Size on Composite Resistivity and Onset of Non-linearity

A hypothesis put forward by Önneby et al. (2001) suggests that the composite volume resistivity will scale with the number of contacts through the thickness of the sample and the resistance of that contact. The volts per contact were determined by

assuming that percolation had been reached and that a conductive path was achieved by the shortest path through the sample.

$$V_c = \frac{Applied\ voltage}{Number\ of\ contacts} = E_A g \tag{9.8}$$

where E_A is the applied field and g is the particle size. They supported this hypothesis in a SiC/EPDM composite system by systematically varying the particle size from micron scale to submicron scale. Figure 9.5a shows typical results. A plot of resistivity *vs.* volts per contact collapsed the data from all particle sizes onto one plot, Fig. 9.5b, thus proving the hypothesis that the number of contacts is important in controlling the resistivity and the onset of non-linearity.

In attempting to push this hypothesis further, Fig. 9.6 shows the composite resistivity for SiC in silicone rubber (SiR) and ZnO and doped ZnO in SiR nanocomposites at about 25 vol% loading as a function of volt/contact. The data does not collapse on a universal curve. The most obvious effect is that the volt/contact at which non-linearity begins is shifted. It is similar for the two SiC powders, but is shifted to the left for the ZnO. Interestingly, the degree to which the onset of non-linearity is shifted increases as the powder resistivity decreases compared to the SiC and Cu doped ZnO nanoparticle composites. Thus, the intrinsic conductivity of the powder must also be important in controlling the non-linear behavior and onset. If, however, we normalize by the powder conductivity, the data still does not collapse onto one curve.

This raises an additional complication. If the conduction occurs via tunnelling through a thin polymer layer as suggested (Hong et al. 2003; Grimaldi and Balberg 2006), then the tunnelling distance will affect the volume fraction at which percolation occurs (see Sect. 9.4). In addition, the tunnelling behavior will control, to a large extent, the onset voltage/contact, and lead to a shift in the resistivity versus voltage/contact curves. The tunnelling behavior will be a function of the polymer resistivity as well as the field concentration between the particles.

A second observation is that the low field composite resistivities are not all the same. This is to be expected because the powder resistivities vary. While it is again tempting to normalize the resistivity by the resistivity of the powder, this is not straightforward because of the field dependence. Thus, for each powder size and conductivity, a separate curve would need to be generated, which is not beneficial. The effect of particle conductivity is perhaps appropriately illustrated with a plot from work by Mårtensson et al. (1998) in which SiC was mixed with carbon black. The greater the percentage of carbon black, the higher the conductivity of the composite, and the lower the onset voltage and the lower the non-linearity exponent.

While the original hypothesis assumes a straight connection through the sample, in order to calculate volts per contact, as recognized by Önneby et al. (2001) the distribution and volume fraction difference from the percolation threshold, will affect this number. This is difficult to quantify and include in a universal curve. Thus, it is clear that more complex models are needed to predict the non-linear response.

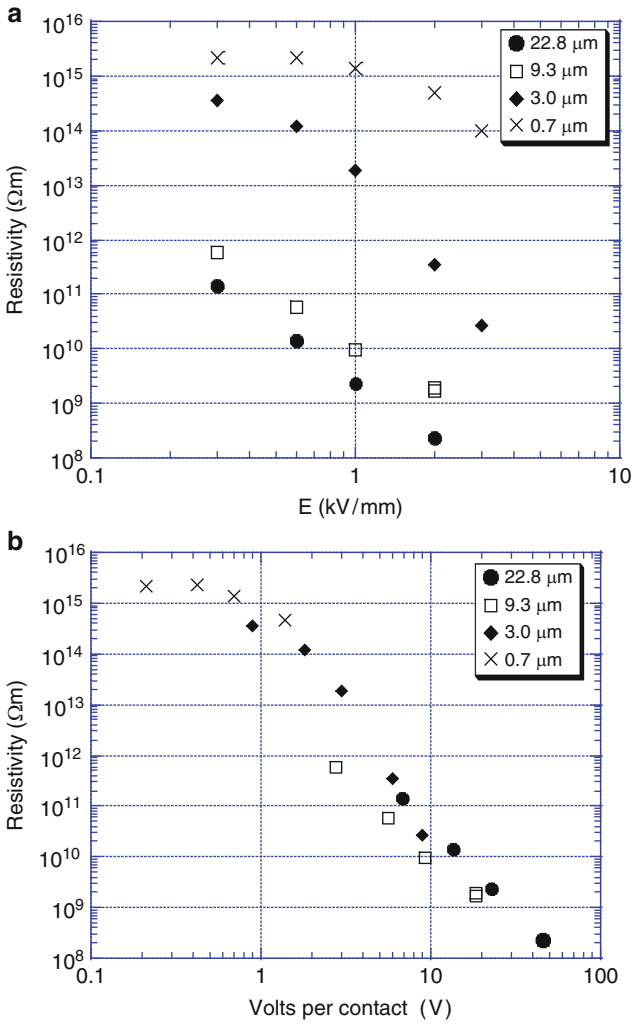

Fig. 9.5 (**a**) Resistivity as a function of electric field for ethylene-propylene rubber (EPDM) mixtures with SiC particles of various sizes, (**b**) Resistivity as in (**a**) for different particle sizes versus volts per contact. Reproduced from (Önneby et al. 2001). ©2001 IEEE

9.5.3 Network Model for Non-linear Behavior

As recognized by Mårtensson and Gäfvert (2004), a 3D model that includes the dispersion of the fillers, the character of the particle/particle conductivity, as well as the intrinsic properties of the constituents is required to predict the non-linear response. To that end, they developed a 3D network model to predict the field dependent behavior of semiconducting particle filled polymer composites. For the case

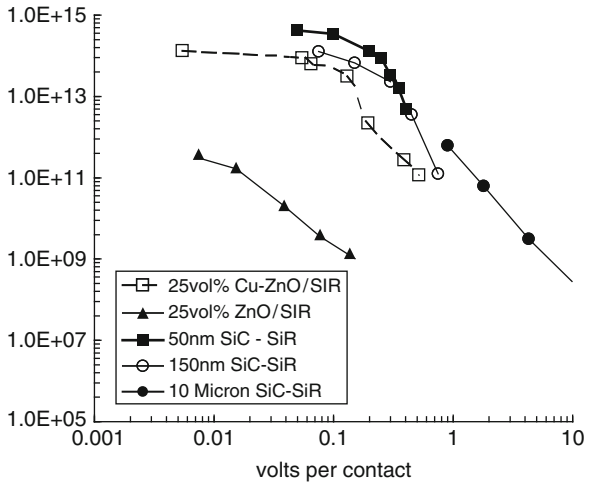

Fig. 9.6 Resistivity (in Ωcm) vs. volt/contact for several nanoparticles in a silicone rubber matrix

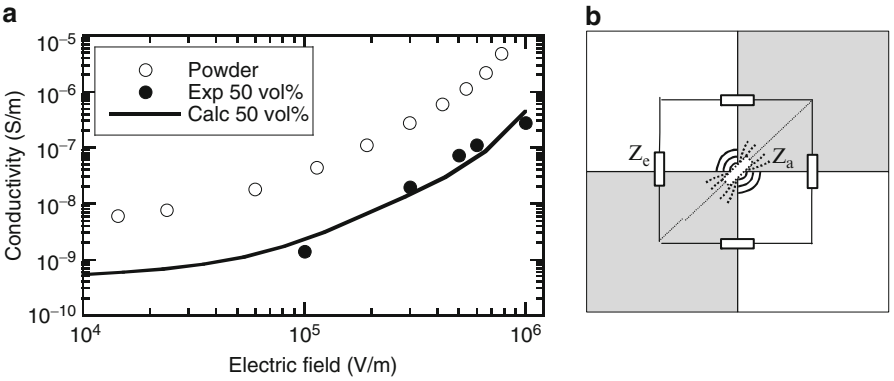

Fig. 9.7 (**a**) A plot of conductivity vs electric field showing the correlation between prediction and experiment for SiC/EPDM composites. (**b**) A two-dimensional cut of a choke point where the current must be transported between the conducting (*grey*) particles. The edge connection is modelled as four equivalent impedances, Z_e when the contact area is small. Reproduced from (Mårtensson and Gäfvert 2004), IOP Publishing Limited

of a highly percolated system in which the particle/particle contact is controlled by a double Schottky barrier, they were able to predict the composite behavior well (Fig. 9.7a). The particle/particle contact was modelled as an RC network link with a non-linear resistor and a capacitor with zero loss. While the published results are for random particle dispersion, this is a variable in the model. In addition, they allowed for two types of contacts: face-to-face contacts for faceted particles, which represent the double Schottky barrier, and edge contacts (Fig. 9.7b). Edge contacts are indirect contacts and for small contact areas will require current conduction through the matrix. In addition, there will be a local field enhancement, which can be quite large.

To avoid this complication, the edge contacts were assigned a complex conductivity shown in (9.9) and is a geometric mean of the complex conductivities of the constituents (Berlyand and Golden 1994).

$$\tilde{\sigma}_e = \sqrt{\tilde{\sigma}_i \tilde{\sigma}_c} \tag{9.9}$$

In concert with this, is the description of an edge contact as a "choke point" (Fig. 9.7b) where the conduction is described through four impedances at each matrix/particle contact area. The impedance, Z_e is the inverse of the equivalent conductivity shown in (9.9). Thus, the model provides the ability to represent both particle/particle direct contacts, and, as observed more commonly in nanocomposites, particles with a polymer layer in between. Using this approach, the linear behavior could be modelled as a function of filler concentration, and the percolation points observed in the composites predicted. The challenge for using this model for nanocomposites is that the model did not predict the non-linear behavior for the case where the matrix had significant influence (as modelled by edge/edge contacts). It does, however, provide a framework for including such behavior and is ripe for exploitation to do so. To do that, however, requires the appropriate understanding of the mechanism leading to transport in the matrix. The following section reviews such mechanisms.

9.5.4 Character of the Particle/Particle Conductivity

The non-linear behavior is a strong function of the powder non-linearity if there is particle/particle contact as described earlier. The commonly accepted model for charge transport through semiconducting particle contacts is still the one proposed by Hagen in 1971 (Hagen 1971), where back-to-back double Schottky-like potential barriers (Fig. 9.8) are assumed to form at the each contact, which gives rise to its well known nonlinear I-V behavior. Here, V_c stands for the voltage applied on a single SiC/SiC contact, which raises the Fermi level of the left SiC to the amount eV_c.

Unlike the ordinary Schottky barrier formed between a metal and a semiconductor due to the difference in Fermi level, however, this double Schottky-like SiC/SiC contact barrier is essentially a space charge barrier. It is formed due to either acceptor- or donor-like SiC surface states, which may arise from dangling bonds where outside impurity atoms have been adsorbed, or due to the possible SiO_2/SiC interface states (assuming silica less than 3 nm thick is formed on top of SiC particles).

The typical conduction pathway for charge carriers passing through this double Schottky barrier is therefore: electrons in the left SiC grain flow upstream under the forward bias, going through surface states, then exit into the conduction band of the other SiC grain under reverse bias. The overall conduction is apparently controlled by the reverse bias, where electrons can either jump over the barrier via field-assisted thermionic emission (Richardson-Schottky effect), or tunnel (field

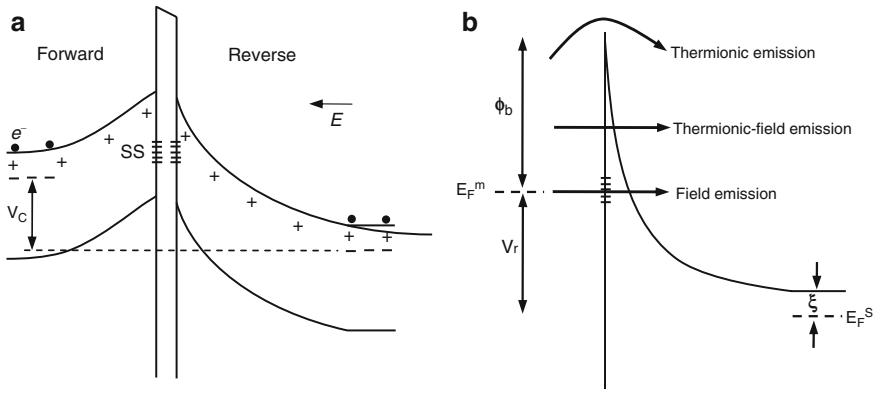

Fig. 9.8 (**a**) A Model of (n-type) SiC space charge barrier at particle contact and (**b**) possible charge transport mechanisms (SS are the surface/interface states and V_c the applied contact voltage) Reproduced from (Hagen 1971)

emission) through the barrier if the reverse bias is large enough (causing surface states on the left to move upward towards the more narrow regime). Thermally-assisted tunneling is illustrated in Fig. 9.8b. For Schottky emission over the barrier, the overall current density is given by:

$$J = AT^2 \cdot \exp(\frac{-\phi_B}{kT}) \cdot [1 - \exp(-\frac{eV_c}{kT})] \tag{9.10}$$

where Φ_B is the effective field dependent barrier height, V is applied voltage across the contact, A is the Richardson constant.

If, however, there is conduction through the matrix either via edge/edge contacts as described by Mårtensson and Gäfvert (2004), or due to a thin coating of polymer surrounding each particle, the double Schottky barrier concept is no longer valid. Evidence for this is the higher non-linearity exponents observed for some composites than for the powders (Hong et al. 2005; Wang et al. 2006). This change in charge transport mechanism will also affect the onset voltage in the composite.

One such model from transport through the polymer is a tunnelling mechanism (Celzard et al. 1997). In this case, the conduction path is interrupted by barriers thin enough to allow tunnelling between the nanoparticles through a polymer layer. This occurs at very high fields and is called Fowler-Nordheim tunneling. The field (E) dependence on the current density can be described by (9.11).

$$J = \frac{e^2E^2}{8\pi h\phi_{eff}} \exp\left[-\frac{8\pi}{3heE}(2m)^{1/2}\phi_{eff}^{3/2}\right] \tag{9.11}$$

where ϕ_{eff} is the effective barrier height after Schottky barrier lowering (i.e., $\phi - \Delta\phi$), h is Planck's constant and m is the electron mass. The polymer layer can also

transport charge via a hopping mechanism. In this case, the band structure is not a typical valence band, conduction band structure (Blythe 1986). Instead there are weakly localized states concentrated at the narrow conduction band tail. They are spatially distributed (not continuous) and their density is on the order of 10^{22} cm^{-3} with an energy range of up to 1 eV below the conduction band. The residence time of a carrier in these states is between $\sim 10^{-13}$ s for a level at 0.1 eV to about 500 s for a level at $\sim$ 1 eV. In addition, localized donor or acceptor sites at deeper energy levels and at lower density can be present as a result of impurities or chemical disorder.

Hopping conduction is a second mechanism and can occur through occupied Anderson or impurity states to nearby empty ones, if the spatial density of these states is large enough (Fig. 9.9) (Blaise 2001). This allows each localized state to overlap numerous others (for the highly localized impurity states, the organic dielectric generally has to be doped intentionally). The consequence is that the conduction is by thermally activated hopping (phonon-assisted hopping) from one localized state to another, with an activation energy well below 1 eV, or direct tunnelling between overlapped states of equal energy (tunnel hopping). For this reason, the mobility of electrons injected into these hopping sites can be sufficient to produce conduction at room temperature and above, even for a large band gap insulators. The equation governing the field dependence in this case is shown in (9.12).

$$J = eRkTN(E_F)\nu_{Ph}\exp(-2\alpha R)\cdot\exp\left(-\frac{\Delta E}{kT}\right)\cdot\sinh\left(\frac{eRE}{kT}\right) \tag{9.12}$$

Here R is the hopping distance, $N(E_F)$ is the carrier population, V_{Ph} is the phonon frequency, α is the wave overlap parameter, and ΔE is the average hopping activation energy. The field dependence of these equations is very similar, making it

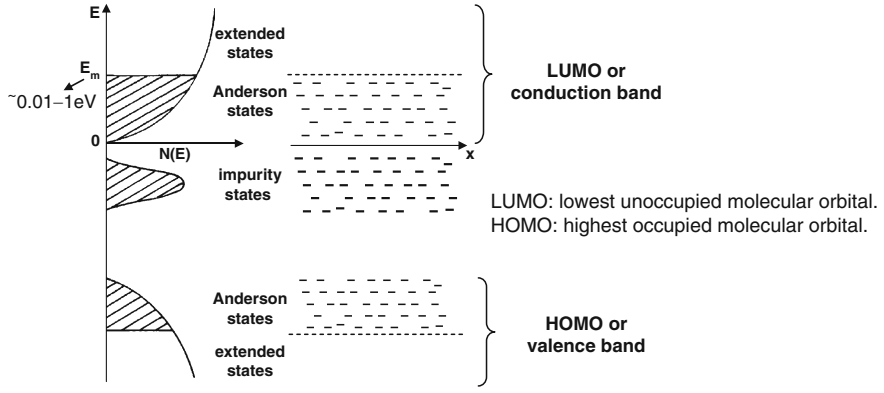

Fig. 9.9 Typical band structure of an organic dielectric containing impurities (Blaise 2001). Reprinted from Blaise G Charge localization and transport in disordered dielectric materials. J Electrostat 50(2):69–89, Copyright (2001), with permission from Elsevier

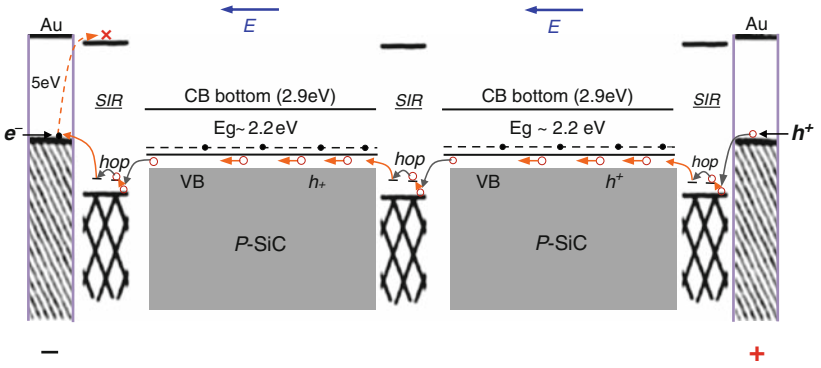

Fig. 9.10 A schematic of the proposed band diagram for a p-type SiC nanoparticle/silicone rubber composite. The electrode bands are not shifted for clarity of presentation

difficult to distinguish these mechanisms and there is no common understanding in the literature of the mechanism leading to non-linear behavior in nanofilled polymers.

Recent work by Wang et al. (2009) suggests that a hopping mechanism leads to a non-linear behavior. Figure 9.10 shows a schematic of the proposed band diagram for a p-type 25 vol% nano-SiC/silicone rubber (SIR) composite, where 2.3 eV is the band gap for SiC. The hypothesis for the high field nonlinear I-V behavior is based on two fundamental assumptions: (1) the composite is below geometric percolation, or there are thin SIR layers sandwiched between p-SiC particles; (2) holes are the main charge carrier. Experimentally, no significant electron injection from the cathode occurred. It should be noted, however, that electron hopping could be observed in other systems. The hypothesis is that composite nonlinearity is mainly due to thermally-activated hole hopping transport through the sandwiched SIR layers, either directly from particle to particle or across multiple steps at hopping sites near the SIR valence band. This mechanism basically gives an exponential nonlinear J-E dependence as:

$$\sinh\left(\frac{eR}{kT}\cdot E\right)\approx\frac{1}{2}\cdot e^{\left(\frac{eR}{kT}\cdot E\right)} \tag{9.13}$$

The non-linearity then arises from the much larger forward hopping probability due to the field, than backward hopping probability.

Based on Wang et al. J-E data on the 25 vol% nano-SiC/SIR at temperatures ranging between 25 and 120° C, it was found that all J-E data at different temperatures mentioned previously in the sentence could be fitted well by the two parameter hyperbolic hopping equation, as shown for example in Fig. 9.11a. Moreover, by replacing the term $kTN(E_F)$ denoting carrier population in the impurity band with the p-SiC hole density, which is proportional to $\exp(-E_A/2kT)$ and assuming $v_{Ph}=kT/h$, (9.12) can be modified as:

$$J=eR\frac{kT}{h}\cdot\exp(-2\alpha R)\cdot\exp(-(\Delta E+\frac{E_A}{2})/kT)\cdot\sinh(eRE/kT) \tag{9.14a}$$

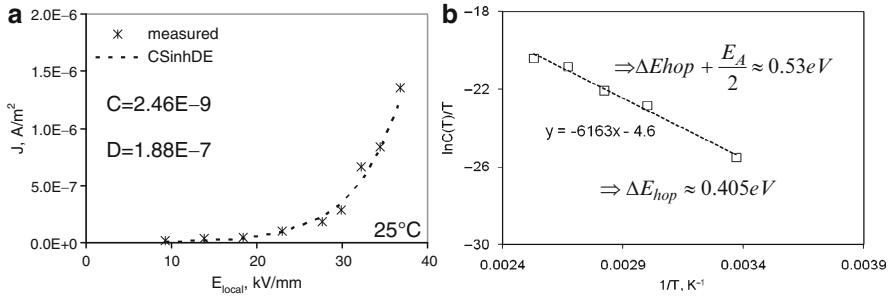

Fig. 9.11 A representative J-E two parameter sine hyperbolic hopping fitting for the 25 vol% nano-SiC/SIR (**a**) at 25° C and (**b**) further ln(C/T) vs. 1/T hopping fitting based on a modified hopping equation, the linear slope of which is used to derive the average hopping activation energy, ΔE

which can be simplified as

$$J = C(T) \cdot \sinh(D(T) \cdot E) \tag{9.14b}$$

where $C(T) \propto T \cdot \exp(-(\Delta E + \frac{E_A}{2})/kT)$. A plot of ln(C(T)/T) vs. 1/T for all temperatures, should result in a linear curve with a negative slope, the magnitude of which can give rise to the hopping activation energy ΔE, which agrees with Fig. 9.11b.

While the hopping mechanism may not apply to other nanocomposite systems, and Fowler-Nordheim tunnelling may be more applicable, the point remains, that any model predicting behavior in nanocomposite systems will have to address the charge transport through the matrix. The Mårtensson model suggests that if an equivalent circuit can be used to describe such behavior, then this too can be incorporated into the network model (Mårtensson and Gäfvert 2004).

9.5.5 Capacitive Field Grading Materials

An alternative field grading strategy (for time varying voltages only) is to adjust capacitance. A material with a high permittivity is positioned in the region of unacceptable stress enhancement which serves to redistribute the electric field to the insulation in series, resulting in a spreading of the equipotential lines. In this case, the challenge is increasing the permittivity without increasing the dielectric loss significantly or decreasing the breakdown strength. Early work using carbon black nanofillers showed that as the size decreased, the dielectric constant increased (Nelson and Hervig 1984), but the dielectric strength also decreased for all fillers (Fig. 9.12). The limitation of these materials is that they become too conductive at the loadings required to achieve a high dielectric constant. Barium titanate has also been used to create high dielectric constant composites. The advantage of

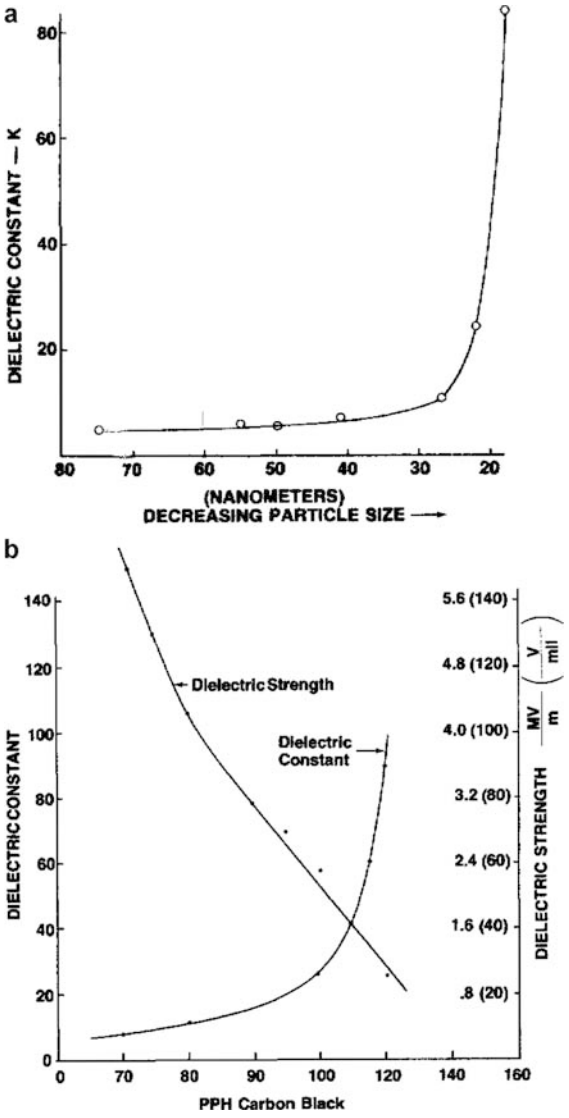

Fig. 9.12 (**a**) A plot showing the change in dielectric constant as a function of particles size at a loading of 25 phr, (**b**) a plot of dielectric constant and dielectric strength as a function of loading for carbon black. Reproduced from (Nelson and Hervig 1984). ©2001 IEEE

barium titanate is that the dielectric constant increases with temperature, providing an added level of control (Strumpler et al. 1995). A relatively new approach has been to coat conducting nanofillers with an insulating layer. This prevents conducting particle/conducting particle contact, but still creates a large interface region with high capacitance (Xu and Wong 2005; Shen et al. 2007). It has been shown that the smaller the particle size, the larger the increase in dielectric constant due to the large interfacial area introduced. Recently Yang et al. (2009), showed that by coating Multi-walled carbon nanotubes (MWNT) with an insulating layer

and dispersing them in polystyrene, they could increase the dielectric constant to more than 40 while maintaining the loss tangent below 0.06 from the Hz to MHz frequency range at room temperature. The covalently attached polymer layer prevented MWNT/MWNT contact. Composites with as received MWNT also exhibited high dielectric constants, but the loss tangent was more than 10. In addition, the coated MWNT/polystyrene nanocomposites maintained a breakdown strength of 200 MV/m.

9.6 Carbon Nanotube/Insulating Polymer Composites for High Conductivity Applications

Carbon nanotubes are a unique filler because of their high aspect ratio, conductivity ranging from semiconducting to conducting, and their potential to mechanically reinforce while improving the electrical conductivity. Nanotubes can also lead to highly conductive transparent polymer films (Gu and Swager 2008) which is not attainable for traditional graphite fibers. The focus in this section, however, will be on the morphology and processing that controls the conductivity of single walled nanotube (SWNT) and multi-walled carbon nanotube (MWNT)/insulating polymer composites. There are several reviews on this subject (Moniruzzaman and Winey 2006; Bokobza 2007; Winey et al. 2007). One early observation was that the electrical conductivities were not as high as expected given the conductivity of the nanotubes. This is in part due to the population of semiconducting nanotubes in SWNT mixtures, but is also due to the strong attraction of many polymers to the nanotube surface. This leads to a coating of MWNT or bundles of SWNT with polymer, and a high contact resistance creating primarily a tunnelling conduction mechanism between the MWNTs. To complicate matters further, the papers reporting the conductivity of nanotube filled insulating polymers used SWNT that were a mixture of metallic and semiconducting nanotubes. In addition, the distribution in aspect ratio of the tubes is large for most systems and the degree of dispersion varies. Thus a consistent picture is only just beginning to emerge.

First, as the tunnelling distance increases, the percolation threshold also decreases. This has been shown theoretically (Kyrylyuk and van der Schoot 2008), and can perhaps be seen experimentally for composites with similar dispersion but different matrices that show different percolation thresholds (Ramasubramaniam et al. 2003). In addition, the conductivity achieved at percolation will depend on the interface resistance and thus be matrix dependent (Winey et al. 2007).

Second, the aspect ratio and distribution of aspect ratios strongly affects the percolation threshold as shown using an excluded volume approach calculation in Fig. 9.13a (Balberg et al. 1984a). Gojny et al. (2006) undertook an elegant study showing the effect of aspect ratio on percolation threshold. While the aspect ratio was not measured explicitly, Fig. 9.13b shows that carbon black has the highest percolation threshold and MWNTs, that maintained their length, the lowest. The data for MWNT that were functionalized shows a lower percolation threshold because,

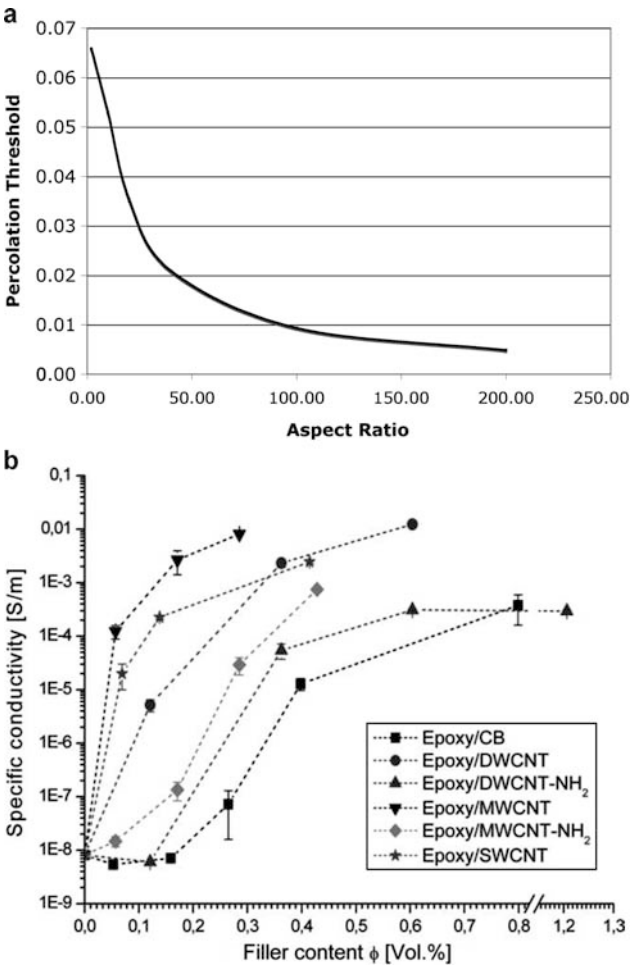

Fig. 9.13 (**a**) A plot of the percolation threshold as a function of aspect ratio based on an excluded volume approach (Balberg et al. 1984a) (**b**) electrical conductivity of the nanocomposites as function of filler content in weight percent (Gojny et al. 2006) Reprinted from Gojny FH. Evaluation and identification of electrical and thermal conduction mechanisms in carbon nanotube/epoxy composites. Polymer 47(6):2036–2045, Copyright (2006), with permission from Elsevier

despite better dispersion, the functionalization reduced the aspect ratio. Similar arguments were made for all the data and essentially, as the percolation threshold transitions from high to low, the aspect ratio increases.

Third, nanotube alignment strongly affects the conductivity (Choi et al. 2003). This was shown very thoroughly by Du et al. (2005) and White et al. (2009) in SWNT/PMMA composites (Fig. 9.14) using both experiment and theory. Holding the SWNT loading constant, but varying the method of processing to create either anisotropic or isotropic composites with several degrees of alignment, the effect of

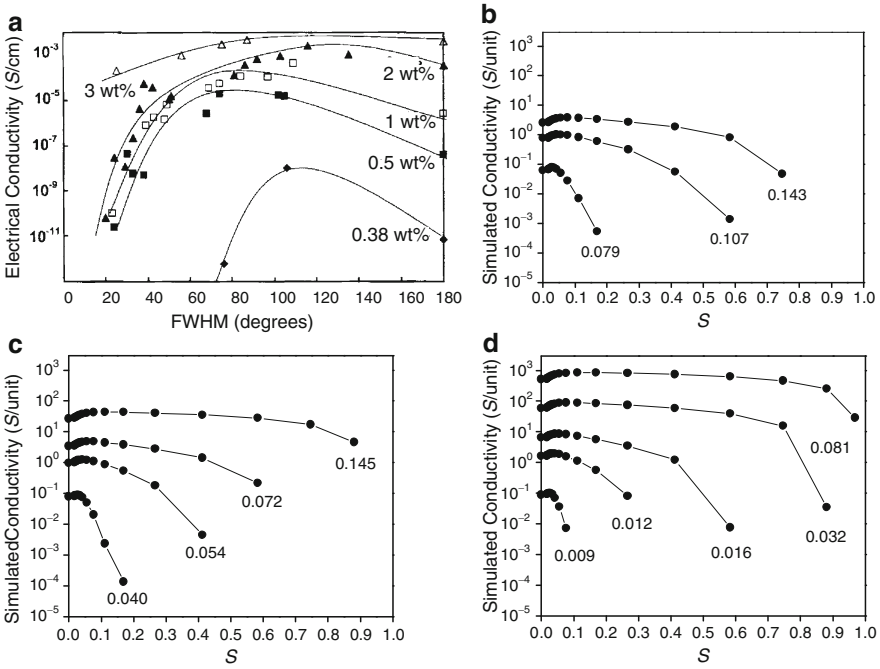

Fig. 9.14 (**a**) Experimental results showing the effect of alignment and loading and the conductivity of MWNT filled polymer composites, Reprinted figure with permission from Du F, Fischer JE, Winey KL (2005) Phys Rev B 72:121404, Copyright (2005) by the American Physical Society. (**b–d**) Simulation results showing the effect of loading and orientation on the conductivity of MWNT filled polymer composites at an aspect ratio of 10 (**b**), 20 (**c**) and 80 (**d**) Reprinted figure with permission from White SI, DiDonna BA, Mu, M, Lubensky TC, Winey KI Phys Rev B 79(2):024301–024306. Copyright (2009) by the American Physical Society

alignment was quantified and the results were found to agree closely with a Monte Carlo method that follows the methods of Balberg and Binenbaum (Balberg et al. 1984b). As quantified using small-angle X-ray (SAXS) (Du et al. 2005), the degree of anisotropy was varied from isotropic (Full Width Half Max – FWHM of 180° in the figures shown) to highly aligned or anisotropic (FWHM of 20° and below). The results are shown in Fig. 9.14a noting that a large FWHM implies a more isotropic sample. As the degree of anisotropy is increased (FWHM decreases from 180°), the conductivity increases by a factor of 10–1,000. Larger increases due to alignment are observed at lower loadings. At a critical anisotropy (FWHM), however, the conductivity decreases dramatically because the probability of two nanotubes being in close enough contact for tunneling decreases. Thus careful processing is required to optimize the conductivity and, for injection molded parts, the local conductivity will vary with the flow fields generated during molding. White et al. (2009) built on the work of Du et al. (2005) and created a network model simulation method of soft-core rod-shaped nanotubes in a 3D network where the aspect ratio loading and orientation could be varied independently (Fig. 9.14b–d. The strength of this

approach over an analytical approach is the ability to predict behavior for small aspect ratio fillers and handle inhomogeneous dispersion.

The degree of dispersion is critically important as has been emphasized in previous chapters. There are two components to this. First, as the fillers agglomerate, their aspect ratio changes and this can lead to either decreases in percolation threshold for spherical fillers that form oblong aggregates or an increase in percolation threshold for high aspect ratio fillers that bundle into lower aspect ratio fillers. An example of this more subtle effect of heterogeneity is seen due to changes in the percolation threshold for carbon black materials (Balberg 2002).

As interesting, are results applying an old concept to new materials: creating a cell like structure with the conductive filler as the cell wall and the insulating polymer as the cell interior (Grunlan et al. 2004, 2006; Grossiord et al. 2005, 2008). This has been achieved using polymer latex particles with surfactants and nanotubes, or using an aqueous particle coating process (Mu et al. 2008) that does not require surfactants. Figure 9.15b shows the resulting SWNT/Polystyrene (PS)

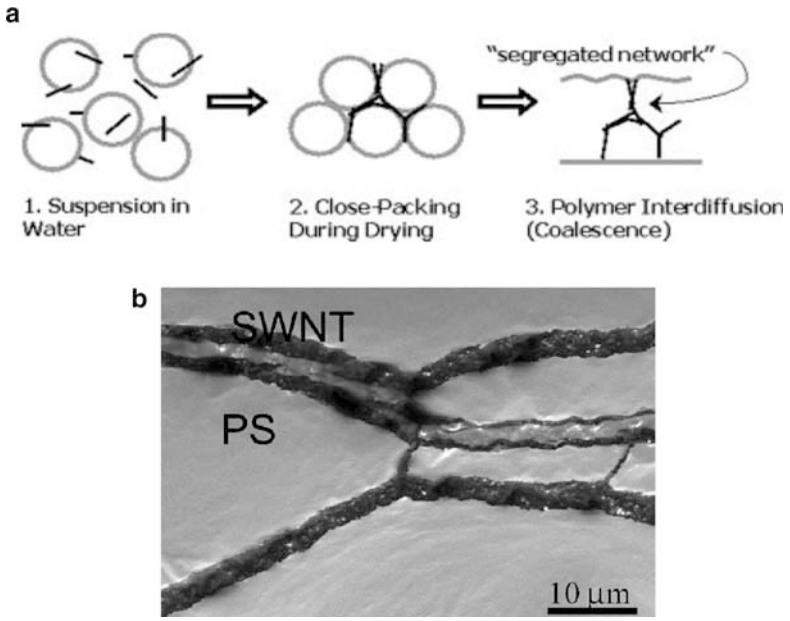

Fig. 9.15 (**a**) A schematic showing a process for making a heterogeneous nanotube/polymer composite by suspending the nanotubes and polymer particles in water, drying the mixture, and then consolidating the composite. Reprinted from Grunlan JC, Mehrabi AR, Bannon MV, Bahr JL (2004) Water-based single-walled-nanotube-filled polymer composite with an exceptionally low percolation threshold. Adv Mater 16(2):150–153. Copyright Wiley-VCH Verlag GmbH & Co. KGaA. Reproduced with permission. (**b**) An SEM micrograph of a SWNT/polystyrene composites made by coating polystyrene pellets with SWNT and then compression molding sample to create a cell like network of SWNT. Reprinted from Mu M et al Cellular structures of carbon nanotubes in a polymer matrix improve properties relative to composites with dispersed nanotubes. Polymer 49(5):1332–1337, Copyright (2008), with permission from Elsevier

structure created by Mu et al. using the particle coating process (Mu et al. 2008). There are several advantages to this approach. First, the high viscosity created when nanotubes are melt mixed with a polymer is avoided. Second, the potential exists for more nanotube/nanotube contacts and thus a lower contact resistance. Since dispersion is not critical, exfoliation is also not necessary reducing the number of processing steps and chemicals used in processing substantially. What these papers have found is that, as the size of the particle increases, the percolation threshold decreases.

9.7 Summary

In summary, nanofillers offer the ability to tailor and optimize the dielectric and conducting properties of polymers. The primary challenges that remain in making commercial use of such materials is in controlling the dispersion during large scale processing, and understanding the underlying conduction mechanisms. There is a need for robust models such as those proposed by White et al. (2009) for nanotubes, and Mårtensson and Gäfvert (2004) for field grading materials to aid in that understanding and in the design of new combinations of composites. There is also the need for fundamental studies that provide the opportunity to further explore the interface between the nanofillers and the polymer and its role in modifying behavior (Önneby et al. 2001).

References

Balberg I (2002) A comprehensive picture of the electrical phenomena in carbon black-polymer composites. Carbon 40(2):139–143

Balberg I (2008) Electrical transport phenomena in systems of semiconductor quantum dots. J Nanosci Nanotechnol 8(2):745–758

Balberg I, Anderson CH, Alexander S et al (1984a) Excluded volume and its relation to the onset of percolation. Phys Rev B 30:3933–3943

Balberg I, Azula D, Toker D et al (2004) Percolation and tunneling in composite materials. Int J Mod Phys B 18(15):1091–2121

Balberg I, Binenbaum N, Wagner N (1984b) Percolation thresholds in the three-dimensional sticks system. Phys Rev Lett 52:1465–1468

Berhan L, Sastry AM (2007) Modeling percolation in high-aspect-ratio fiber systems. I. Soft-core versus hard-core models. Phys Rev E Stat Nonlin Soft Matter Phys 75(4):041120

Berlyand L, Golden K (1994) Exact result for the effective conductivity of a continuum percolation model. Phys Rev B 50(4):2114

Bernasconi J, Stresler S, Knecht B (1977) Zinc oxide based varistors: a possible mechanism. Solid State Commun 21:867–870

Bhushan B, Kashyap SC, Chopra KL (1981) Electrical and dielectric behavior of zinc oxide composite. J Appl Phys 52(4):2932–2936

Blaise G (2001) Charge localization and transport in disordered dielectric materials. J Electrostat 50(2):69–89

Blythe AR (1986) Electrical properties of polymers. Cambridge University Press, Cambridge, UK

Bokobza L (2007) Multiwall carbon nanotube elastomeric composites: a review. Polymer 48(17):4907–4920

Carmona F (1989) Conducting filled polymers. Phys A Stat Theor Phys 157(1):461–461

Celzard A, McRae E, Furdin G et al (1997) Conduction mechanisms in some graphite-polymer composites: the effect of a direct-current electric field. J Phys Condens Matter 9(10):2225–2237

Choi ES, Brooks JS, Eaton DL et al (2003) Enhancement of thermal and electrical properties of carbon nanotube polymer composites by magnetic field processing. J Appl Phys 94(9):6034–6039

Donnet JB, Bansal RL, Wang M-J (1993) Carbon black. Marcel Dekker, New York

Donzel L, Christen T, Kessler R et al (2004) Silicone composites for HV applications based on microvaristors. Int Conf Solid Dielectr. Toulouse, France, 403–406

Du F, Fischer JE, Winey KL (2005) Effect of nanotube alignment on percolation conductivity in carbon nanotube/polymer composites. Phys Rev B 72:121404

Gojny FH, Wichmann MHG, Fiedler B et al (2006) Evaluation and identification of electrical and thermal conduction mechanisms in carbon nanotube/epoxy composites. Polymer 47(6):2036–2045

Grimaldi C, Balberg I (2006) Tunneling and nonuniversality in continuum percolation systems. Phys Rev Lett 96(6):066602

Grossiord N, Loos J, Coning CE (2005) Strategies for dispersing carbon nanotubes in highly viscous polymers. J Mater Chem 15(24):2349–2352

Grossiord N, Loos J, Van Laake L et al (2008) High-conductivity polymer nanocomposites obtained by tailoring the characteristics of carbon nanotube fillers. Adv Funct Mater 18(20):3226–3234

Grunlan JC, Kim YS, Ziaee S et al (2006) Thermal and mechanical behavior of carbon-nanotube-filled latex. Macromol Mater Eng 291(9):1035–1043

Grunlan JC, Mehrabi AR, Bannon MV et al (2004) Water-based single-walled-nanotube-filled polymer composite with an exceptionally low percolation threshold. Adv Mater 16(2): 150–153

Gu H, Swager TM (2008) Fabrication of free-standing, conductive, and transparent carbon nanotube films. Adv Mater 20(23):4433–4437

Hagen SH (1971) Conduction mechanism in silicon carbide voltage-dependent resistors. Philips Res Rep 26(6):486–518

Hesamzadeh MR, Hosseinzadeh N, Wolf P (2008) An advanced optimal approach for high voltage AC bushing design. Trans IEEE DEI-15(2):461–466

Hong JI, Schadler LS et al (2003) Rescaled electrical properties of ZnO/low density polyethylene nanocomposites. Appl Phys Lett 82(12):1956–1958

Hong JI, Schadler LS, Siegel RW et al (2006) Electrical behavior of low density polyethylene containing an inhomogeneous distribution of ZnO nanoparticles. J Mater Sci 41(18):5810–5814

Hong JI, Winberg P, Schadler LS et al (2005) Dielectric properties of zinc oxide/low density polyethylene nanocomposites. Mater Lett 59(4):473–476

Ku CC, Liepins R (1987) Electrical properties of polymers. Hanser, Munich

Kyrylyuk AV, van der Schoot P (2008) Continuum percolation of carbon nanotubes in polymeric and colloidal media. Proc Natl Acad Sci USA 105(24):8221–8226

Liang GD, Tjong SC (2008) Electrical properties of percolative polystyrene/carbon nanofiber composites. Trans IEEE DEI-15(1):214–220

Mårtensson E (2003) Modeling electrical properties of composite materials. Royal Institute of Technology. Department of Electrial Engineering. Stockholm, Sweden, Swedish for Royal Institute of Technology, Ph.D. Thesis

Mårtensson E, Gäfvert U (2004) A three-dimensional network model describing a non-linear composite material. J Phys D Appl Phys 37(1):112–119
Mårtensson E, Nettelblad B, Gäfvert U et al (1998). Electrical properties of field grading materials with silicon carbide and carbon black. Int Conf Cond Breakdown in Solid Dielectrics. Västerås, Sweden, 548–552
Moniruzzaman M, Winey KI (2006) Polymer nanocomposites containing carbon nanotubes. Macromolecules 39(16):5194–5205
Mu M, Walker AM, Torkelson JM (2008) Cellular structures of carbon nanotubes in a polymer matrix improve properties relative to composites with dispersed nanotubes. Polymer 49(5):1332–1337
Nakamura S, Saito K, Sawa G et al (1997) Percolation threshold of carbon black – Polyethylene composites. Jpn J Appl Phys 36:5163
Nelson PN, Hervig HC (1984) High dielectric constant materials for primary voltage cable terminations. Trans IEEE PAS-103(11):3211–3216
Nettelblad B, Mårtensson E, Önneby C et al (2003) Two percolation thresholds due to geometrical effects: experimental and simulated results. J Phys D Appl Phys 36(4):399–405
Nikolajeic S, Pekaric-Nad N, Dimitrijevic RM (1997) Optimization of cable terminations. Trans IEEE PD-12(2):527–532
Önneby C, Mårtensson E, Gäfvert U et al (2001) Electrical properties of field grading materials influenced by the silicon carbide grain size. Int Conf Solid Dielectrics. Eindhoven, the Netherlands, 43–45
Peng H, Sun X (2009) Highly aligned carbon nanotube/polymer composites with much improved electrical conductivities. Chem Phys Lett 471(1–3):103–105
Ramasubramaniam R, Chen J, Liu H (2003) Homogeneous carbon nanotube/polymer composites for electrical applications. Appl Phys Lett 83(14):2928–2930
Reboul JP, Moussalli G (1976) About some DC conduction processes in carbon black filled polymers. Int J Polym Mater 5(2):133–146
Rivenc J, Leby T (1999) An overview of electrical properties for stress grading optimization. Trans IEEE DEI-6(3):309–318
Roberts A (1995) Stress grading for high voltage motor and generator coils. IEEE Electr Insul Mag 11(4):26–31
Sahimi M (1994) Applications of percolation theory. Taylor and Francis, London
Shen Y, Lin Y, Nan C-W (2007) Interfacial effect on dielectric properties of polymer nanocomposites filled with core/shell-structured particles. Adv Funct Mater 17(14):2405–2410
Sheng P, Kohn RV (1982) Geometric effects in continuous-media percolation. Phys Rev B 26(3):1331
Shugg WT (1995) Handbook of electrical and electronic insulating materials. IEEE Press, New York
Strumpler R, Rhyner J, Greuter F et al (1995) Nonlinear dielectric composites. Smart Mater Struct 4(3):215–222
Tanaka T, Greenwood AN (1983) Advanced power cable technology, vol 1. CRC, Boca Raton, FL
Tavernier K, Auckland DW, Varlow BR (1998) Improvement in the electrical performance of electrical insulation by non-linear fillers. Int Conf Cond Breakdown in Solid Dielectrics. Västerås, Sweden, pp 533–538
Tucci V, Vitelli M (2000) On the effect of anisotropy in nonlinear composite materials for stress grading applications. Trans IEEE DEI-7(3):387–393
Wang X, Herth S, Hugener T et al (2006) Nonlinear electrical behavior of treated ZnO-EPDM nanocomposites. Annual Report Conference on Electrical Insulation and Dielectric Phenomena (CEIDP), pp 421–424
Wang X, Nelson JK, Schadler LS et al (2009) Hopping conduction based high field nonlinear I-V mechanism for field grading nano-SiC/silicone rubber composite. J Appl Phys In Preparation

White SI, DiDonna BA, Mu M et al (2009) Simulations and electrical conductivity of percolated networks of finite rods with various degrees of axial alignment. Phys Rev B 79(2):024301–024306

Winey KI, Kashiwagi T, Mu M (2007) Improving electrical conductivity and thermal properties of polymers by the addition of carbon nanotubes as fillers. MRS Bull 32(4): 348–353

Xu J, Wong CP (2005) Low-loss percolative dielectric composite. Appl Phys Lett 87(8):1–3

Yang C, Lin Y, Nan CW (2009) Modified carbon nanotube composites with high dielectric constant, low dielectric loss and large energy density. Carbon 47(4):1096–1101

Chapter 10
The Emerging Mechanistic Picture

R.J. Fleming

10.1 Introduction

A nanodielectric may be defined as a solid composite material consisting of a dielectric matrix (frequently a polymer) in which are embedded filler particles measuring less than 100 nm in at least one dimension (Smith et al. 2008). A typical filler loading is 5% by weight. Some nanodielectrics show significant improvements in dielectric strength and voltage endurance relative to the relevant unfilled matrix as was highlighted in Chap. 7, and are therefore attractive, both commercially and from the point of view of basic science, since understanding the mechanisms leading to the improved characteristics would be expected to lead to even greater improvements. Research work on nanodielectrics was greatly stimulated by the publication of an influential paper (Lewis 1994). He predicted that, in response to the demand for ever-smaller electronic devices, much future dielectric research would be concerned with the properties of dielectrics in contexts where relatively few molecules are involved, e.g., in molecular monolayers, interfaces and macromolecules.

This chapter is concerned with the mechanisms of DC conductivity and space charge accumulation in polymer-based nanodielectrics. Currently these mechanisms are far from being completely understood, despite the huge amount of work which has been done. In part, this situation is due to the extensive range of systems which have been investigated, as researchers attempt to synthesize a nanodielectric which will satisfy a very specific application. Many authors, having described the properties of the particular nanodielectric which they have studied, and feeling obliged to attempt some explanation of their results, understandably prefer to err on the side of caution and therefore restrict themselves to very tentative conclusions. Nevertheless, some useful general conclusions may be drawn.

R.J. Fleming (✉)
Monash University, Melbourne, VIC, Australia
e-mail: Robert.Fleming@sci.monash.edu.au

J.K. Nelson (ed.), *Dielectric Polymer Nanocomposites*,
DOI 10.1007/978-1-4419-1591-7_10,

10.2 Charge Transport in Insulating Polymers

In order to put the mechanisms of conduction in nanodielectrics in context, the "tutorial" material introduced in Chaps. 7 and 8 is augmented here to specifically include the physics perspective. This is done in the same way that the chemistry was covered in Chap. 4.

10.2.1 Electronic or Ionic Charge Carriers?

The transport of charge through polymers has been extensively investigated over the last 50–60 years (Wintle 1983, 2003; Ieda 1987; Das-Gupta 1997; Mizutani 2006). Wintle (2003) states that "Technical insulators, whether gas, liquid or solid, are largely characterized by unipolar ionic flow." However, electronic charge injection at the electrodes and transport through the sample bulk must play a major role in their DC conductivity, except perhaps at very short times after voltage application. In many cases the current flowing under an applied DC voltage (absorption current) is given initially by

$$I(t) = A\, t^{-n} \tag{10.1}$$

where the voltage is applied at $t = 0$, $n \sim 1$ and A is a constant (Baird 1968; Guo and Guo 1983; Jonscher 1983). After a few hours it reaches (ideally) a constant value. In practice a very slowly decaying current is observed (Lowell 1990; Zaengl 2003). This nearly constant current, which can be as large as 10^{-8} A in planar polyethylene samples 150 μm thick with electrode diameter 45 mm, under an applied field of 20 kV/mm (Fleming et al. 2005, 2008), implies an inexhaustible supply of charge carriers, inconsistent with a limited number of positive ions moving through the sample bulk towards the cathode and being neutralized there. A nearly constant current in the same direction and with much the same magnitude is recovered if the sample is short-circuited, allowed to stand until the discharge current has fallen to a very small fraction of the nearly constant current, and the voltage is then re-applied. Again, this seems inconsistent with a limited number of ionic charge carriers. We will therefore assume that the steady-state DC conductivity of an insulating polymer is dominated by electronic transport.

10.2.2 Electronic Energy Bands

The electronic energy band structure of crystalline polyethylene was first calculated in the late 1960s, and the calculations on this and other organic polymers have been considerably refined since then (McCubbin and Manne 1968; Falk and Fleming 1973; Hoffmann et al. 1991; Sulston et al. 2003). However, many polymers

are semi-crystalline as was discussed in Chap. 7, so that electronic charge transport through them involves a combination of intrachain transport through the crystalline regions and interchain transport through the amorphous regions.

In crystalline polyethylene the picture is further complicated by the fact that it has a negative electron affinity, i.e., the bottom of the conduction band lies *above* the vacuum level. The energy difference between the two has been calculated (Righi et al. 2001; Cubero et al. 2003a) and experimentally estimated (Ueno et al. 1986) to be in the range 0.2–0.6 eV. On the other hand, the bottom of the conduction band in the amorphous regions lies approximately 0.3 eV *below* the vacuum level (Cubero et al. 2003b). It follows that electrons, seeking the lowest energy states, will move through the amorphous rather than through the crystalline regions. However, it should be remembered that the amorphous regions include the volume between adjacent lamellae within a spherulite (containing chain loops depicted in Fig. 7.3, tie chains running between adjacent lamellae, chain entanglements and chain ends or cilia) as well as the volume between spherulites. Thus electron transport need not be confined to the volume between spherulites. A positive hole is of course an unfilled electron energy level within the valence band, and hole transport within the valence band in the direction of the local electric field arises from electron "hops" between adjacent covalent bonds in the opposite direction. Thus electron-hole recombination would be unlikely within lamellae, but more probable at crystalline-amorphous interfaces, where impurities might act as recombination centers (Lewis 2002).

Finally it should be noted that the energy gap between the valence and conduction band edges is large in polymers, e.g., approximately 8.8 eV in polyethylene (Lewis 2002). It follows that the concentration of electrons in the conduction band will be negligible, except perhaps for very short periods following injection of very high energy electrons or holes from the electrodes.

10.2.3 Electron Injection, Transport and Trapping

Electron and hole injection or extraction across the interface between a dielectric and metallic electrodes has been studied extensively for many years. There are two main models applicable at applied field strengths less than approximately 10^9 V/m:

(a) The Schottky model (Dissado and Fothergill 1992) treats injection as field-assisted thermal excitation of an electron from the Fermi level in the electrode to the bottom of the conduction band in the dielectric. The electron leaving the electrode is subject to its image force in the electrode, drawing it back towards the electrode, and the force due to the electric field in the dielectric, drawing it into the dielectric. Both forces are functions of the electron's position. The potential barrier which the electron has to surmount peaks at a distance from the interface which varies as $E^{-0.5}$ and $\varepsilon_r^{-0.5}$, where E and ε_r are respectively the applied field and the relative permittivity of the dielectric. It should be pointed out that the applicability of the Schottky model has been questioned on the

grounds that the thermally excited electron may be thermalized by collisions before reaching the peak of the potential barrier (Wintle 2003).

(b) The surface state tunneling model (Lewis 1986) envisages charge transfer between the electrode and the dielectric as a tunneling process between two sets of surface states, which occurs in order to equate the Fermi levels. The electrode will possess a high density of donor and acceptor states centered around its Fermi level, and the dielectric will also possess surface states associated with dangling bonds and adsorbed impurities. If $E_D > E_F$, or $E_A < E_F$, where E_D and E_A are donor and acceptor levels respectively in the dielectric, and E_F is the electrode Fermi level, charge transfer may occur provided the tunneling distances are not too large. It is unlikely to occur uniformly over the interface surface, since the intimacy of the contact will not be uniform on a molecular scale.

Electrons and holes in polymers would be expected to move rapidly through the extended intrachain states in the conduction and valence bands respectively. The *minimum* mobility arising from band transport is given by

$$\mu_{min} = \pi e a^2 / 4h \tag{10.2}$$

where e is the electronic charge, a is the lattice spacing and h is Planck's constant (Ritsko 1982). Substituting $a = 0.254\,\text{nm}$ for polyethylene yields $\mu_{\min} = 1.2 \times 10^{-5}\,\text{m}^2\,\text{V}^{-1}\,\text{s}^{-1}$. A value of $2.5 \times 10^{-3}\,\text{m}^2\,\text{V}^{-1}\,\text{s}^{-1}$ has been deduced from the band structure of polyethylene (Andre and Leroy 1970). However, the values obtained experimentally are very much smaller, mostly in the range 10^{-13}–$10^{-15}\,\text{m}^2\,\text{V}^{-1}\,\text{s}^{-1}$ for several insulating polymers at room or slightly higher temperatures (Martin and Hirsch 1970; Gross et al. 1979; Bambery and Fleming 1998; Mazzanti et al. 2003). This difference strongly suggests that electronic transport is effectively controlled by trapping, i.e., an electron may travel rapidly through the conduction band for a short time, but its effective or average mobility is greatly reduced as a result of being immobilized for much longer periods in localized states (traps). Some workers report that the mobility shows a negative exponential dependence on inverse temperature, suggesting that the carriers escape from the traps via a thermally activated process.

A trap is a region in which an electron occupies a localized state, i.e., a state which does not extend throughout the material. Such a state will exist at points where the periodicity of the crystalline lattice is disturbed, say by chain folding defects along the polymer backbone, or chain termination within a lamella. The electron energies of these states will lie in the energy gap below the conduction band edge. The amorphous regions between adjacent lamellae and between adjacent spherulites are largely disordered, and thus electrons moving through these regions can occupy only localized states, again with energies lying in the band gap. These states are formed by the configurations of the polymer chains themselves (Fleming 1990), and by chemical "defects," e.g., cross-linking sites, by-products of cross-linking reactions, additives, chain branches and double bonds along the backbone. The traps formed by the configurations of the polymer chains themselves

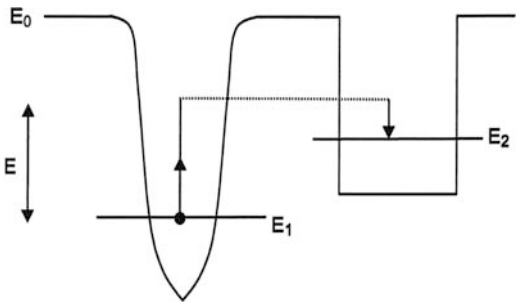

Fig. 10.1 Schematic of an electron undergoing thermally assisted resonance tunneling between two traps

are not permanent, in the sense that they may be destroyed by the onset of particular forms of chain segment motion when the temperature exceeds a particular value, e.g., crankshaft motion in the amorphous regions of polyethylene beginning around 150 K. In that case the trapped electron escapes simply because the trap disintegrates.

If the trap structure is "permanent" the electron may escape by gaining sufficient thermal energy from its surroundings, or less likely from the local electric field, to surmount the top of the potential well presented by the trap. It may then move freely through the conduction band until it is captured by another trap. However, this process would be possible only for traps lying about 0.1 eV below the bottom of the conduction band, i.e., a few times kT where $T < 400$ K for most polymers. More likely is electron transfer between two adjacent traps via thermally assisted resonance tunneling through the potential barrier separating the traps. This is shown in very simplified form in Fig. 10.1, where it is assumed that the trap is neutral when empty and charged when occupied. Thus the shape of the potential well associated with the occupied trap is shown as approximately Coulombic. The electron gains a certain amount of energy E, where $E_2{-}E_1 < E < E_0{-}E_1$, tunnels through the barrier at constant energy and then relaxes to the ground state of the new trap. Expressions for the transfer rate between the two traps, and for the drift velocity characterizing long-range transport resulting from multiple transfers under an applied electric field, are given in Lewis (2002).

10.3 Nanodielectric Models

Any model of a polymer-based nanocomposite must be compatible with established theory of polymer chain configurations adjacent to an impenetrable solid surface. It is therefore pertinent to discuss briefly some important aspects of this subject before turning to specific models. A more detailed discussion will be found in Picu and Keblinski 2005.

Near a solid surface the configurational entropy of the chain decreases because the number of accessible chain configurations decreases. This creates an entropic force which causes the chain to recoil from the surface, the force increasing linearly

with temperature. In this way a layer in which the polymer density is reduced forms close to the surface, and within this layer the chain mobility is expected to increase. The decreased density close to the surface is balanced by an increase in the more distant volume. On the other hand, given a strong attractive chain-surface interaction, adsorption may occur. For weaker attractive interactions surface chain segments will be preferentially aligned parallel to the surface, and may adopt a "docking" configuration at high temperatures.

An increased concentration of chain ends is expected close to the surface, because the decrease in entropy (due to the reduced number of accessible configurations) will be smaller if one end of a chain contacts the surface. Consequently chains whose centers of mass lie within twice their radii of gyration from the surface will tend to contact the surface at one end rather than nearer the middle.

10.3.1 The Interface Model

At present one model of polymer-based nanodielectrics has been generally accepted. Two formulations of this model have been proposed (Tanaka et al. 2005; Lewis 2005). They are based on the assumption that, due to the interaction with the particle surface, the properties of the polymer chains immediately adjacent to each nanoparticle differ considerably from the properties of the more distant chains. Thus the interface zone between the particle and the polymer exerts a significant influence on the properties of the nanodielectric as a whole. The physical properties of the interface material near the particle would be expected to be very similar to those of the particle and, close to the polymer matrix, to approach those of the matrix. The form of the variation between these two limits will depend on the property being considered.

It is of interest to note that, 20 years ago, a similar explanation was advanced for the observation that Young's modulus for each of four polymers filled with silane-treated glass beads was independent of bead size, whereas it varied significantly with the size of untreated glass beads (Vollenberg and Heikens 1989). The bead diameters were in the range 0.035–100 μm. The authors suggested that the difference between silane-treated and untreated beads indicated that the surface properties of the beads were important, altering the morphology of the surrounding polymer. They also suggested that large particles were surrounded by two thin polymer layers, the inner with high modulus and the outer with low modulus. In the case of small particles the total polymer volume is of high modulus.

10.3.1.1 Interface Dimensions

Figure 10.2 shows two adjacent spherical nanosized particles of radius r, each surrounded by an interface zone of thickness t. The distance between the centres of the two particles is D. Simple one-dimensional calculations show that, if V_f is the

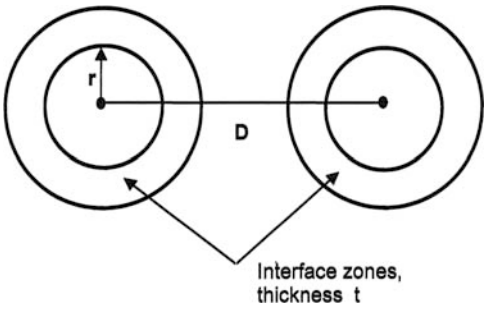

Fig. 10.2 Two adjacent spherical particles of radius r, each surrounded by an interface zone of thickness t. The distance between the centres of the particles is D

volume fraction of ideally dispersed nanoparticles in the nanocomposite, and S is the nanoparticle surface area per unit volume of the nanocomposite, then

$$D \approx 2r(V_f^{-1/3}) \tag{10.3}$$

$$S = 3\,V_f/r \tag{10.4}$$

If $r = 25$ nm and $V_f = 5\%$, typical experimental values, then D $\approx$ 135 nm and $S = 6\,\mathrm{km}^2/\mathrm{m}^3$. The latter value emphasizes the enormous surface area of the nanoparticles depicted in Fig. 1.3. The fraction f of the total volume (particle + interface) taken up by the interface is given by

$$f = 1/(1 + r/(3t)) \tag{10.5}$$

Estimates of t vary, but it is unlikely to be less than $0.5\,r$, corresponding to $f = 0.6$. If $t = 5\,r$, $f = 0.94$. Therefore, insofar as volume is a controlling factor, the influence of the interfaces on the properties of the nanodielectric would be expected to dominate that of the nanoparticles themselves.

A strong electrical interaction may occur between adjacent nanoparticles, since their surfaces are separated by a distance comparable to their diameters. It is therefore of interest to calculate the probability that the interface regions of two adjacent nanoparticles will overlap. More precisely, we want to calculate the probability that, if D, r and t are respectively the average distance between the centres of adjacent particles, the particle radius and the interface thickness, then the distance between the centres of two adjacent particles chosen at random will be $2(r+t)$ or less (it cannot be smaller than $2r$). Fothergill (2007) has assumed that the distances between the centres of adjacent particles will follow a Poisson distribution. In that case the probability of overlap P will be $1-\exp(-2t/D)$, or $P = 0.5$ when $t/D = 0.347$. A particle radius of 25 nm would then imply $t = 17.3$ nm. This is not an unreasonable number. However, one of the conditions for a Poisson distribution is that the probability of the event, in this case overlap of adjacent interaction zones, be very small. Since $P = 0.5$ can hardly be considered a small probability, it might be better to assume a normal distribution of the distance between centres. Clearly this is also related to the percolation phenomenon covered in Sects. 7.1.7 and 9.4.

10.3.1.2 The Tanaka et al. Formulation

According to this formulation (Tanaka et al. 2005), the interface zone surrounding each nanoparticle consists of at most three polymer layers, with total thickness comparable to the diameter of the nanoparticle itself, i.e., several tens of nm. These layers are illustrated in Fig. 8.6 and a detailed explanation may be found in Chap. 8. According to the model, the bonded layer of the interface will not be formed unless the polymer and the nanoparticle surfaces have an affinity with each other, i.e., their surface tensions are comparable, or have been made so by the introduction of a functionalization (or coupling) agent such as methoxysilane or ethoxysilane. Charge transfer between the polymer and the nanoparticle occurs in order to equalize the Fermi levels, but may take considerable time to reach equilibrium. The polarity of the polymer will depend on its identity, and ions from the polymer may also be adsorbed on the polymer surface. If the polymer does not contain mobile charges the electric field resulting from the charge transfer will generate electronic polarization and possibly dipole orientation within the polymer. If it does contain mobile charges they will tend to form one side of an electrical double layer. The second (bound) and third (loose) layers are described in detail in Sect. 8.2.3.4.

The diffuse electrical double layer, when formed in polymers containing significant concentrations of mobile ionic charge, consists of the charge on the nanoparticle surface and a diffuse assembly of positive and negative ions. If the charge on the nanoparticle is positive, the negative ion concentration exceeds the positive ion concentration close to the particle surface, and the opposite is true at the other edge of the layer, beyond the loose layer.

It is envisaged that, in some cases, only the bonded layer will be formed. It is also possible that, if adjacent interfacial zones overlap, as discussed above, co-operative phenomena between neighboring particles will occur.

10.3.1.3 The Lewis Formulation

This formulation (Lewis 2005) is based on the electrochemistry of the interface between a metallic electrode and a liquid electrolyte. The latter has been studied for more than a century, and is now well established (Brett and Brett 1994; Bockris et al. 2000). An illustration of this model has been provided in Fig. 7.9 although other variations have been proposed in the liquid context (Grahame 1947).

The Lewis (2005) formulation of the interface model distinguishes three layers and was introduced in Sect. 7.1.6. The first layer is a double layer formed *within* the nanoparticle, consisting of charged surface states and counter-charges supplied by mobile electrons and holes, immobile charged impurities and trapped carriers. The second layer, called the Stern or Helmholtz double layer, consists of ions and dipoles from the polymer adsorbed on the nanoparticle surface, and, further away, other ions from the polymer attracted to the charge on the nanoparticle surface. (Presumably it is assumed that the mobile electronic charge concentration is negligible in the polymer in the absence of injection from the electrodes). The thickness of

this second layer will be around 1 nm. The third layer (the diffuse Gouy-Chapman double layer) consists of mobile positive and negative ionic charge attracted to any unscreened charge at the outer edge of the second layer. Its thickness would be around 100 nm in a weakly ionically conductive polymer, but could shrink to almost zero in more conductive polymers. Since this layer contains mobile charges it may greatly influence the dispersion of the nanoparticles in the polymer matrix.

It is important to realize that, if the nanoparticles and the polymer matrix have low conductivities, equilibrium across the interface may not be established for some considerable time, except possibly at high temperatures.

10.3.2 Conductivity, Space Charge and the Interface Model

In what ways would one expect the polymer-nanoparticle interface to influence DC conductivity and space charge accumulation in a sample?

Assuming that the steady state conductivity is dominated by electronic charge transport, the influence of the interface on electron injection from the electrodes must first be considered. The injection process is probably more realistically modeled as electron tunneling between two sets of surface states rather than electron passage over the Schottky potential barrier (Sect. 10.2.3). The interface would have little effect on the surface states of the metal electrode, but would probably present a very different spectrum of electron acceptor states, and tunneling barriers, compared to the unfilled polymer. A different dependence of the injection rate on the applied field strength would also be expected; the double layer component of the interface is a highly polarizable region, so that the charge distribution within it is sensitive to the applied field (Lewis 2004), and this distribution will influence the height and shape of the tunneling barriers. Thus one would certainly expect the injection rate to be affected by the interface, but quantitative predictions, which would probably require bold simplifying assumptions, have not yet been reported.

Turning to electron transport through the nanocomposite bulk, the electron path will be a combination of sectors through interface and polymer matrix regions, unless sufficient adjacent interface overlap occurs. Transport through the polymer matrix will be dominated by the lower electron mobility in the amorphous volume, and will proceed via thermally assisted resonance tunneling through the potential barriers separating the traps (Sect. 10.2.3). Transport through an interface, specifically the electron mobility, will be influenced by the polarization and ionic charge separation within it (Lewis 2004). The nanoparticles with their large surface areas may act as additional electron traps, but conversely they may decrease the average hopping distance relative to that of the polymer matrix and thus increase the mobility. Clearly a change in conductivity would be expected as a result of nanoparticle loading, but its magnitude and sign would be difficult to calculate, even assuming an unchanged injection rate.

Increasing the nanoparticle loading would lead eventually to sufficient interface overlap that electrons could cross the sample from cathode to anode travelling

exclusively through interface volume. Provided the conductivity was volume controlled, it would probably not change significantly with further increase in nanoparticle loading, at constant applied field. The constant conductivity would be a maximum (minimum) if the electron mobility in the interface was larger (smaller) than that in the matrix. If the conductivity were controlled by the steady-state electron injection rate at the cathode, its variation with increasing nanoparticle loading would depend on the factors discussed above.

Space charge accumulation immediately adjacent to the electrodes, i.e., homocharge and heterocharge, will depend on the injection rate, the concentration and mobility of the ions in the interfaces close to the electrodes, and, to a lesser extent, ionization and transport of impurities in the polymer matrix. Clearly, a quantitative description of the interface structure is a prerequisite for a confident explanation of space charge profiles near the electrodes. Unfortunately, the limited spatial resolution of most space charge measurements (typically 10 μm) is incompatible with explanation at the nanometric level. Space charge accumulation in the bulk will depend mainly on the electron mobility, which will certainly be affected by the particle loading level.

A reasonable conclusion is that while conductivity and space charge accumulation will certainly be affected by the structure and fractional volume of the particle/polymer interfaces, quantitative prediction for a specific particle/polymer combination is very limited at present.

10.4 Conductivity and Space Charge in Selected Nanodielectrics

Much work has been done on the DC conductivity of polymer-based nanocomposites, and the related space charge and electric field profiles. Before describing some of this work in detail, it is appropriate to comment briefly on space charge and electric field profile measurements.

Such measurements in solid dielectrics are now commonplace. There are four main techniques, namely:

1. Pressure wave propagation (PWP), also known as laser-induced-pressure-pulse (LIPP)
2. Pulsed-electro-acoustic (PEA)
3. Thermal step method (TSM)
4. Laser-intensity-modulated method (LIMM).

Of these, the PEA method is the most widely-used at present and has been described in Sect. A.2. Recent developments in the PWP and PEA methods have been described by Holé (2009) and by Fukunaga (2008) respectively. The TSM is particularly suited to thick ($>$ 2 mm) samples. It was not held in high regard initially, mainly because of the physically implausible space charge distributions published by some authors, but improved experimental procedures and data analysis have largely restored its reputation. A paper presenting some results for XLPE

has been published recently (Castellon et al. 2009). LIMM is particularly suited to thin (<100 μm) samples; the achievable spatial resolution (in the thickness direction) is 1–2 μm close to the irradiated electrode, but deteriorates (increases) rapidly with increasing depth, due to the spreading of the heat wave in transit. A description of the technique and the most common methods of data analysis will be found in Lang (2004).

Homocharge is positive charge accumulating near the anode, or negative charge accumulating near the cathode. Heterocharge is negative charge accumulating near the anode, or positive charge accumulating near the cathode. (In classical Greek, "homos" means the same and "heteros" means other or different). Clearly these words cannot be used to describe charge near the mid-point of the sample.

If electrons injected into the dielectric from the cathode are deeply or permanently trapped near the cathode, homocharge (negative) is generated. If the field near the cathode is sufficiently strong to ionize impurity molecules, and the resulting free electrons drift towards the anode while the low mobility positive ions remain close to the cathode, heterocharge (positive) is generated. If electrons injected form the cathode drift close to the anode but do not all exit from the dielectric, because the contact is partially blocking, heterocharge (negative) is generated. Several of these processes may occur simultaneously, so space charge profiles need to be interpreted with care.

The papers discussed in some detail below were chosen in order to cover several different polymer/nanoparticle combinations, with an emphasis on recently-published work (after 2002). Of necessity they represent a very small fraction of the relevant literature, and no doubt reflect this author's prejudices and preferences! However, the objective is to examine the evidence available to support mechanistic explanations of nanodielectric phenomena. It will be seen that the conclusions reached for each polymer/nanoparticle combination are qualitatively compatible with the interface model, but cannot be considered quantitative support for it, because it has not yet been developed in sufficiently quantitative detail.

10.4.1 XLPE/Silica

Roy et al (2007) investigated micro- and nanocomposites of XLPE with SiO_2 filler particles. Some of the nanoparticles were surface-treated with triethoxyvinylsilane (TES), aminoethyl-aminopropyl-trimethoxysilane (AEAPS), or hexamethyldisilazane (HMDS). Of these three agents the first is non-polar and promotes covalent particle-polymer bonding, while the other two are polar and render the particle surface incompatible with the polymer. The nanoparticles (5% weight loading) and the base polyethylene were melt-mixed to an aggregate size less than 100 nm. After mixing, the base polyethylene was cross-linked using dicumyl peroxide, and the samples were subsequently held in vacuum to remove the cross-linking byproducts.

Thermally stimulated current (TSC) measurements (van Turnhout 1980) were made on planar samples approximately 100 μm thick, with sputtered platinum electrodes on both surfaces. The polarizing voltage was applied at 60°C, the sample was cooled to 40°C with the voltage still applied, and the current was then measured in short circuit as the temperature was raised to 100°C at 2°C/ min. All samples showed a current peak in the approximate range 55–60°C, the current magnitude at the peak in the microcomposite being two to three times that in the other samples. A peak in the same temperature range in polyethylene (Mizutani 2006) has been ascribed to charge carrier release from traps located at the amorphous/crystalline interfaces. In the microcomposite the current increased markedly over the range 85–100°C. The AEAPS- and HMDS-treated nanocomposites showed a strong current peak around 90°C. The current in the untreated and TES-treated nanocomposites varied very slowly between 75 and 100°C, with a very poorly defined peak in the range 80–90°C and a magnitude only about one-fifth of that in the AEAPS- and HMDS-treated nanocomposites. The authors suggested that the higher temperature peak may originate in charge release from traps associated with the polar groups on the surfaces of the SiO_2 particles.

In order to investigate these traps further, the trap depths were evaluated over a narrow temperature range just below the maximum of each peak, rather than the more common choice of the range in which the peak begins to rise (Maeta and Sakaguchi 1980). The trap depth for the 55–60°C peak in all samples was 1.1 ± 0.1 eV. The trap depth for the 90°C peak was around 0.4 eV for the untreated and TES-treated nanocomposites, and the microcomposites, and 2.0 ± 0.1 and 2.4 ± 0.1 eV for the HMDS- and AEAPS-treated nanocomposites respectively. It is surprising that, in the untreated and TES-treated nanocomposites and in the microcomposite, the trap depth for the lower temperature peak is greater than that for the higher temperature peak. It seems likely that different escape mechanisms are associated with the two peaks in these samples.

A field of 2 kV/mm was applied across each composite at room temperature, and the resulting absorption current recorded for 10^4 s. The current is expected to follow (10.1) initially, before reaching an almost steady value. Figure 10.3 is a double log plot of the current similar to that shown in Fig. 1.14, and is generally consistent with expectation. Of note is the reduction in slope in the unfilled XLPE and microcomposite samples at times between 200 and 300 s. Similar slope reductions were observed, but only in these two types, at various fields up to 10 kV/mm; the authors attributed them to interfacial polarization.

A few other workers studying absorption currents in polymers have observed the current to increase for some time after voltage application, and then decay towards a nearly constant value (Fischer and Rohl 1977; Malec et al. 1998). The initial increase is attributed to an increasing number of carriers in transit through the sample bulk, having been injected from one of the electrodes. These carriers will be trapped and released many times in transit across the sample, some becoming permanently trapped in deep traps and thereby creating space charge. Clearly the average drift speed of a given carrier in transit, defined as the distance travelled through the sample (normal to the electrodes) divided by the time since it was injected, will vary

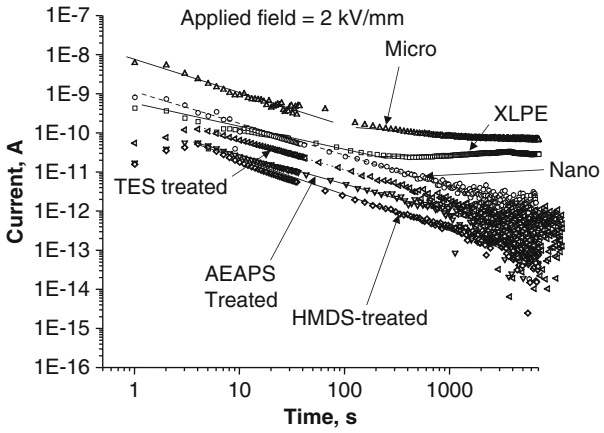

Fig. 10.3 Absorption current for unfilled XLPE and composites at an applied field of 2 kV/mm (Roy et al. 2007)

depending on its trapping history, but would be expected to decrease with increasing time and approach an equilibrium value. The peak in the measured current is interpreted as signaling the arrival at the distant electrode of the leading edge of the charge carrier "sheet" injected from the other electrode, and the loss of carriers from the sample.

Current maxima can be seen around $t = 4$–5 s in Fig. 10.3 for some sample types. According to the theory of space-charge limited currents (Many and Rakavy 1962), the carrier mobility μ, may be estimated from (A.10) in the Appendix. The resulting mobility values were very nearly the same (around 10^{-9} m^2 V^{-1} s^{-1}) for all types of composite at an applied field strength of 0.1 kV/mm. In the unfilled XLPE and the microcomposite they increased to around 10^{-8} m^2 V^{-1} s^{-1} at 9 kV/mm, but in the other types they decreased to 10^{-10} m^2 V^{-1} s^{-1} or less. However, even the latter value is about three orders of magnitude greater than the largest experimental values reported by other authors for a variety of polymers not incorporating nanoparticles (Martin and Hirsch 1970; Gross et al. 1979; Bambery and Fleming 1998; Mazzanti et al. 2003). Since the carrier mobilities decreased with increased nanoparticle loading, it was suggested that the nanoparticles scatter the carriers.

In order to investigate the influence of the surface treatment (functionalization) of the nanoparticles on the generation of charge in the bulk of the samples, the charge induced on one of the electrodes was noted as the applied voltage was increased by 1 kV/h. The charge on each electrode would be expected to increase linearly with applied voltage, since the sample behaves essentially as a capacitor ($q = CV$). However, if uncompensated charge accumulates in the sample bulk, it will induce charge of the opposite sign on the electrodes, with a fractional magnitude dependent on the distance of the charge from the electrode in question. In that case a departure from linearity should be observed, provided the net internal charge is sufficiently large. The arrows in Fig. 10.4 show such a departure in the case of untreated nanoparticles in the base XLPE, for both applied voltage polarities.

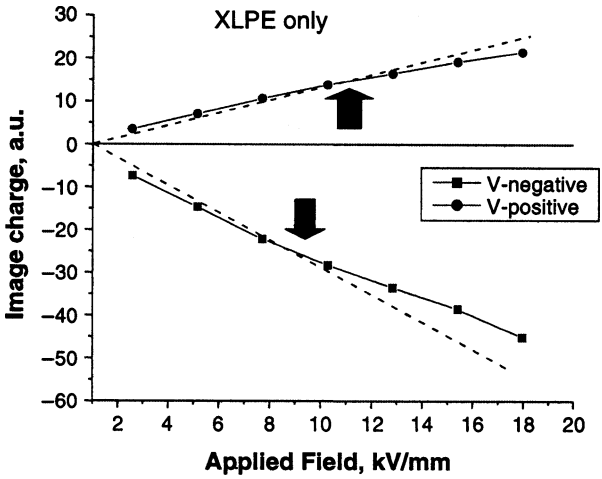

Fig. 10.4 Image charge accumulation for unfilled XLPE, showing departure from linearity (Roy et al. 2007)

The field strengths at which the departures appeared were little affected by the addition of micro- or untreated nanoparticles, but were approximately twice as large for HMDS- and TES-treated nanoparticles. (Departure from linearity had not been observed in the AEAPS-treated samples when breakdown occurred). These data give no indication of the sign or location of the charge in the sample bulk. Detailed study of the space charge profiles showed that

1. In composites containing functionalized nanoparticles, less internal charge was generated at the same applied field strength, and therefore less distortion of the internal field occurred. The distortion was greatest in the microcomposites.
2. All samples showed homocharge accumulation in front of the electrodes, suggesting charge injection from the electrodes and rapid trapping.
3. The AEAPS composites showed anomalous behavior in that the internal charge decreased with increasing poling time.

Another group made absorption current measurements at room temperature on XLPE samples containing 12.5 wt% silica particles of nominal size 12 nm or 6 μm (Smith et al. 2008). Some of the nanoparticles had been surface treated with triethoxyvinylsilane (TES) vapour. The sample thickness was approximately 100 μm, and the applied field strength was 30 kV/mm. TSC measurements were also made, the samples being poled at 30 kV/mm and 25°C, cooled to −160°C with the field still applied, and then heated to 90°C at 3°C/ min.

Figure 10.5 shows an absorption current plot for the unfilled base XLPE and a nanocomposite in which the silica particle surfaces had been treated with vinyl silane. The changes in slope indicated by the arrows were again interpreted as marking the arrival of the leading edge of the carrier sheet at the distant electrode, from which the average mobility of the carriers was calculated by the method of Many and

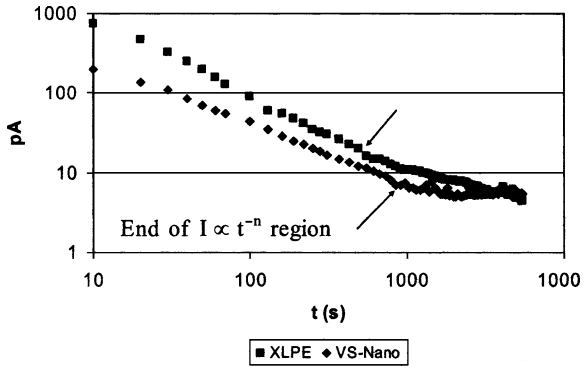

Fig. 10.5 Absorption current plots for unfilled XLPE and a nanocomposite in which the silica particle surfaces had been treated with vinyl silane. The applied field strength was 30 kV/mm. The *arrows* indicate changes in slope which signal the arrival of injected charge carriers at the opposite electrode. The XLPE data are offset by a factor of two between the two plots (Smith et al. 2008)

Rakavy (1962) as described earlier. The arrival time for the surface-treated sample is almost twice that of the base polymer, but the current magnitude is approximately half. The authors suggested that the particles present additional trapping sites for charge carriers and thus reduce the absorption current magnitude, while additional scattering of the carriers on the particles reduces the carrier mobility. The exponent n in (10.1) was evaluated from the short-circuit current flowing after poling for 90 min (usually called the resorption current). The values obtained were 1.34, 1.49, 1.04 and 1.05 for unfilled XLPE, microsilica/XLPE, untreated nanosilica/XLPE and surface-treated nanosilica/XLPE respectively.

The authors comment that the ordering of the magnitude of n, i.e., microsilica > unfilled > nanosilica is consistent with the idea that scattering of charge carriers by the nanoparticles leads to reduced mobility, and thus a slower decay of the current because the carriers take longer to reach the electrodes. However no explanation for the apparent increase in mobility in the microcomposite is suggested. It should be noted that $0 \leq n \leq 2$ is consistent with dipole orientation, carrier tunnelling and carrier hopping, while $0 \leq n \leq 1$ is consistent with charge injection forming trapped space charge (Wintle 1983).

Figure 10.6 shows TSC plots for unfilled XLPE and XLPE/untreated nanosilica (Smith et al. 2008). The curves are of similar shape, the current being larger in the composite than in the unfilled polymer. The α-peaks are usually attributed to the onset of motion of segments of the polymer backbone at the glass transition (van Turnhout 1980). The α-peak current maximum in the nanocomposite is about three times that in the unfilled XLPE, and appears about 20°C lower. The greater magnitude is attributed by the authors to an increase in the number of trapping sites, and so a greater number of trapped carriers will be released from the traps. The lower temperature is consistent with a decrease in the glass transition temperature, due to addition of the nanoparticles.

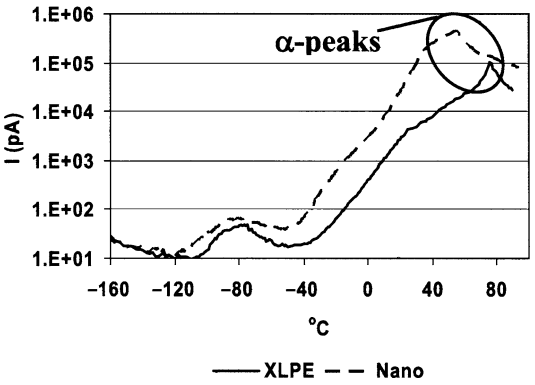

Fig. 10.6 TSC plots for unfilled XLPE and a 12.5 wt% XLPE/untreated nanosilicate composite. The poling field strength was 30 kV/mm (Smith et al. 2008)

The main conclusions from this work on XLPE/silica are:

1. Silica nanoparticles act as additional trapping centres for electrons, reducing their mobility
2. Surface treatment (or functionalization) of the nanoparticles tends to reduce space charge accumulation in the sample bulk
3. The space charge is generated mainly by injection of charge from the electrodes (homocharge) and rapid trapping.

10.4.2 LDPE/TiO$_2$

Uncoated TiO_2 (anatase) particles with average size 21 nm, and micron size (300 nm) TiO_2 particles, were incorporated in additive-free low density polyethylene using a commercially supplied dispersant thought to be poly(hydroxy stearic acid) (Fleming et al. 2005). The particle loadings were 2 and 10% by weight, and the dispersant loading was 4% of the particle loading.

DC conductivity measurements were made on hot-pressed planar samples 150–200 μm thick, carrying sputtered aluminum electrodes and a guard ring. Applied field strengths were 10 and 20 kV/mm. Measurements were made over the temperature range 30–70°C in vacuum (pressure approximately 1.3×10^{-3} Pa or 10^{-5} Torr), in order to avoid oxidation of the LDPE, and at atmospheric pressure at 30°C. Before measurements were commenced each sample was held between grounded electrodes at 70°C in vacuum for at least 24 h so that excess charge might dissipate.

The current flowing after at least 21 h following voltage application was used to calculate the "steady-state" conductivity. Assuming that the conductivity σ(T) is a thermally activated process, we have

$$\sigma(T) = \sigma_0 \, exp\,(-E_a/kT) \tag{10.6}$$

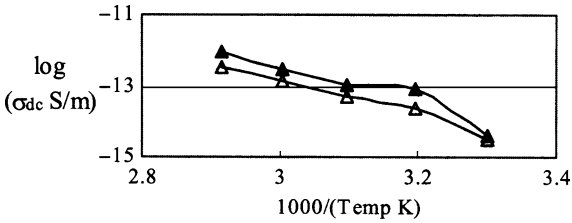

Fig. 10.7 DC conductivity versus 1,000/T for LDPE in vacuum, at 20 kV/mm. *Open triangle* – without additive, *filled triangle* – with 0.4 wt% dispersant (Fleming et al. 2008)

where σ_0 is a constant, E_a is the activation energy of the conductivity, k is Boltzmann's constant and T is the absolute temperature. E_a values in the range 0.4–1.1 eV were obtained, but no consistent variation with temperature, applied field or additive content was observed. Similarly, no consistent variation of the exponent n in (10.1) was observed.

The principal findings for measurements in vacuum were as follows:

1. The addition of 0.4 wt% dispersant to the LDPE increased the steady-state current, at all temperatures and fields, by factors mainly in the range 1.5–5. See Fig. 10.7.
2. A marked decrease in steady-state current was observed in the samples containing nanosized TiO_2, relative to samples containing only the dispersant. At 10 wt% nanoparticle loading the difference was one to two orders of magnitude at 30°C, increasing to more than three orders at 70°C.
3. In samples containing 10 wt% microsized TiO_2 and 0.4 wt% dispersant the steady-state current *increased* relative to a sample with the same dispersant concentration, but only by a factor of 2–3.

The same effects were observed in measurements at 30°C in air, but the magnitude of the changes was much smaller.

The molecular packing within the crystalline regions of polyethylene is sufficiently dense to exclude gases, and presumably micro-sized and nano-sized TiO_2 particles as well. As discussed earlier, the negative electron affinity of polyethylene restricts electron transport to the amorphous regions and over the surfaces of the crystalline regions, while holes will travel through the crystalline volume. Assuming negligible ionic contribution to the conductivity, consistent with the low activation energies calculated, the large changes to the conductivity resulting from incorporation of the TiO_2 particles seem to indicate that the majority charge carriers are electrons, not holes (This was not discussed by the authors). However, it is unclear why microparticles should increase the conductivity, while nanoparticles decrease it.

The vacuum conductivity at 30°C of a sample in which the dispersant was the only additive was 1.4×10^{-15} and 7.5×10^{-15} Sm^{-1} at 10 and 20 kV/mm respectively. The vacuum conductivity of nanosized anatase TiO_2 at 30°C is approximately eight orders of magnitude higher, and one might therefore expect that samples containing the dispersant and 10 wt% of nanosized anatase TiO_2, homogeneously distributed through the sample volume, would have considerably higher conductivity. Since the nanocomposite had lower conductivities at all temperatures and fields,

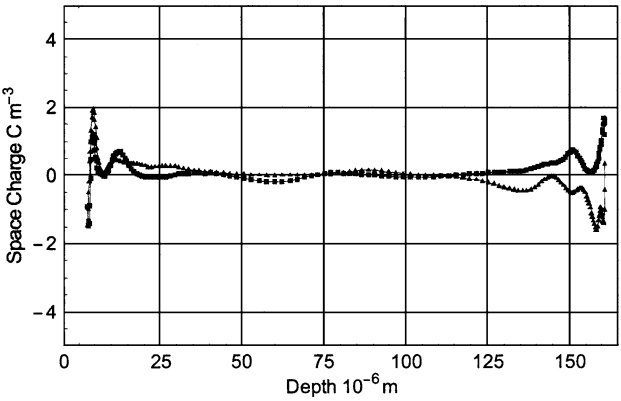

Fig. 10.8 LIMM space charge profile for LDPE with 0.4 wt% dispersant recorded in short-circuit, after poling for 6 h at 20 kV/mm, with opposite polarities. Darker curve – anode at depth zero, lighter curve – cathode at depth zero (Fleming et al. 2005)

the authors suggested that the nanoparticles strongly depress the steady-state charge injection rate at the electrodes. It may be that they also decrease the carrier mobility in the sample bulk, as was found in XLPE/silica.

Incorporation of microsized TiO_2 increased the vacuum conductivity at all temperatures and fields. Vacuum conductivity data for microsized TiO_2 are not available, but figures in the range 10^{-10}–10^{-16} Sm^{-1} in air at 25°C have been published. Since the conductivity of a sample containing 10 wt% of microsized TiO_2 was a factor 2–3 greater, in vacuum and in air, than a sample with dispersant as the only additive, it would seem that the conductivity of the microsized particles used in this work had conductivities near the higher end of the range quoted above.

Figure 10.8 shows two LIMM space charge profiles for a sample containing 0.4 wt% dispersant, recorded in short-circuit after poling for 6 h at 20 kV/mm. The two curves are for opposite poling polarities. In both cases the laser irradiated electrode was at zero depth. The scale transformation method (Lang 2004) was used to analyze the data. Most of the charge was concentrated near the electrodes. Homocharge accumulated near the unirradiated electrode, but the profile near the irradiated electrode was largely independent of polarity. Figure 10.9 shows corresponding profiles for a sample containing 0.4 wt% dispersant and 10 wt% micro-TiO_2 particles. There is much more charge remote from the electrodes than in the sample with dispersant only (Fig. 10.8). Since the DC conductivity was much greater in the microcomposites, the increased charge, remote from the electrodes, could be due to increased injection from the electrodes. Figure 10.10 shows corresponding profiles for a sample containing 0.4 wt% dispersant and 10 wt% nano-TiO_2 particles. There is little charge remote from the electrodes. Homocharge accumulates close to both electrodes, with a much smaller heterocharge peak more distant from the unirradiated (right side) electrode. The homocharge is probably due to electron/hole injection from the cathode/anode, but the origin of the heterocharge peak is unknown.

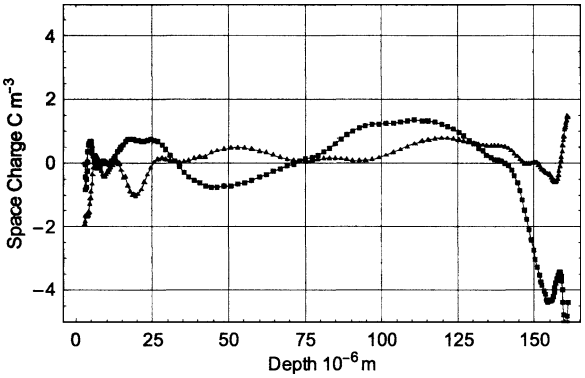

Fig. 10.9 LIMM space charge profile for LDPE with 0.4 wt% dispersant and 10 wt% micro-TiO_2, recorded in short circuit after poling for 6 h at 20 kV/mm, with opposite polarities. *Filled square* – anode at depth zero, *filled triangle* – cathode at depth zero (Fleming et al 2005)

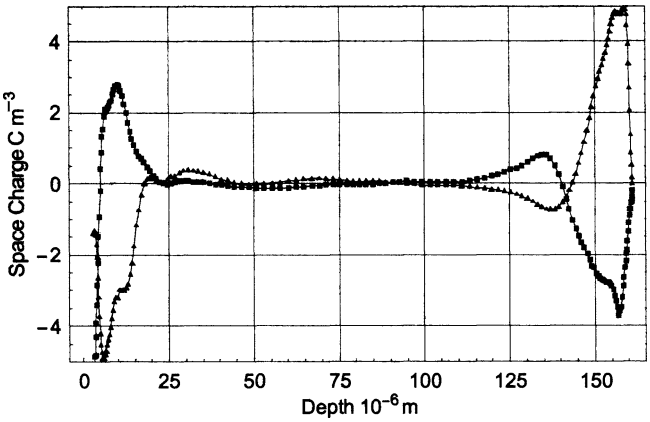

Fig. 10.10 LIMM space charge profile for LDPE with 0.4 wt% dispersant and 10 wt% nano-TiO_2, recorded in short-circuit after poling at 20 kV/mm. *Filled square* – for 6 h with anode at depth zero, *filled triangle* – for 18 h with cathode at depth zero (Fleming et al. 2005)

The main conclusions from this work are:

1. TiO_2 nanoparticles decrease the conductivity at atmospheric pressure and in vacuum, by reducing the charge injection rate from the electrodes and/or the carrier mobility in the sample bulk
2. The nanoparticles cause homocharge accumulation near both electrodes, probably as a result of charge injection from the electrodes and rapid trapping

10.4.3 LDPE/ZnO

In this work (Fleming et al. 2008) the samples were prepared as described above for TiO_2 particles, and the conductivity measurements were carried out in the same manner. Figure 10.11 shows log conductivity versus 1,000/T in vacuum at 20 kV/mm for a sample without additive, a sample containing microsized ZnO particles and dispersant, and one with dispersant and nanosized ZnO particles.

The microsized particles increased the conductivity at higher temperatures, but decreased it at lower temperatures. The nanosized particles decreased the conductivity at all temperatures, but not as much as the nanosized TiO_2 particles.

Approximate values for the activation energies, E_a, and the constant σ_o in (10.6) were calculated using linear least-squares regression fitting. The associated coefficients of determination R^2 were around 0.97 in most cases, suggesting that the steady state conductivity is dominated by a single thermally-activated process. The activation energy reflects the energy required to inject an electron into the sample from the cathode, plus the energy required to transport it through the sample bulk. It has been suggested that, in undoped LDPE, the injection component dominates the transport component (Bambery et al. 2001). If this suggestion is correct, the fact that the activation energies for samples containing nanosized particles were very similar to those for samples without additive implies that the reduction in conductivity in the former is due to a reduction in electronic mobility in the sample bulk, even at concentrations as low as 2 wt%.

The E_a and σ_o values obtained for samples containing microsized particles were much larger than those with nanosized particles, typically 1.4 compared with 1.0 eV, and 10^5–10^8 compared to 10^{-1}–10^4 Sm^{-1}. This suggests that the microparticles increase the electron energy injection barrier at the cathode, but increase the effective mobility in the bulk so that the overall conductivity is largely unaffected.

It has been suggested that the conductivity σ_C of a composite of two homogeneously mixed weakly-conducting components 1 and 2 is given by

$$\log \sigma_C = w_1 \log \sigma_1 + w_2 \log \sigma_2 \tag{10.7}$$

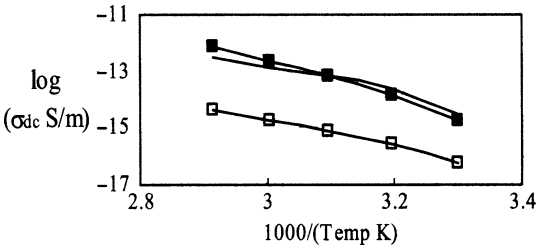

Fig. 10.11 DC conductivity versus 1,000/T for LDPE in vacuum at 20 kV/mm. Without additive, *filled square* – with 0.4 wt% dispersant and 10 wt% microsized ZnO particles, *open square* – with 0.4 wt% dispersant and 10 wt nanosized ZnO particles (Fleming et al. 2008)

where w_1 and w_2 are the *weight* fractions of components 1 and 2 respectively (Baryshev and Yares'ko 1980). This equation strongly resembles the well-known Lichtenecker-Rother equation for the relative permittivity ε_C of a composite material

$$\log \varepsilon_C = v_1 \log \varepsilon_1 + v_2 \log \varepsilon_2 \tag{10.8}$$

where v_1 and v_2 are the *volume* fractions (Reynold and Hough 1957). The authors (Fleming et al. 2008) selected component 1 as LDPE without additive, and component 2 as undoped ZnO nanoparticles spin-coated on a glass substrate, and applied (10.7) to calculate the conductivity of the nanocomposite. The result was roughly three orders of magnitude larger than the measured value! Two possible explanations come to mind. Equation (10.7) is only one of several "classical" mixing formulae (Sihvola 1999). However, the other formulae involve the conductivity, rather than its logarithm. Since the conductivity of the nanoparticles was thought to be roughly 13 orders of magnitude greater than that of LDPE, the other formulae would probably lead to even greater discrepancies between calculated and measured conductivity. Another possibility is that (10.7) applies to a two-component mixture, while the experimental samples were, strictly speaking, three-component mixtures (LDPE, dispersant and nanoparticles). However this seems an unlikely explanation, since the dispersant concentration was small and it generated relatively small changes in conductivity when it was the sole additive. It would therefore seem reasonable to regard the dispersant as additional LDPE and use (10.7).

It was concluded above that the reduced conductivity in the nanocomposites was probably due to reduced electron mobility in the sample bulk. This reduction may be the result of very strong electron scattering by the nanoparticles, due to their enormous surface area, a mechanism not included in the analysis on which (10.7) is based.

Hong et al. (2003) measured the conductivity, at room temperature and 1 kV/mm, of composites of a commercial grade LDPE with ZnO particles 49 nm or several hundred nm in diameter. In the nanoparticle case the conductivity began to *increase* at 14 vol % and continued increasing up to 40 vol %. In the microcomposite case an increase commenced around 30 vol % and then increased much more rapidly than in the nanocomposite case. A rapid increase above some threshold volume fraction would be expected from percolation theory. The authors suggested that the conductivity mechanism involved tunneling between adjacent ZnO particles. This increase in conductivity contrasts starkly with the decrease reported by Fleming et al. (2008). The difference may be due to the very different applied field strengths.

The main conclusion from this work is that ZnO nanoparticles reduce the conductivity, probably by strongly scattering the carriers in transit through the sample bulk and thereby decreasing their mobility.

10.4.4 LDPE/MgO

Murakami et al. (2008) fabricated LDPE/MgO composites. The MgO particles, with diameters several tens of nm, had undergone surface treatment using silane and jet grinding. The filler loading was 0.2–10 wt%. TEM photographs and energy-dispersive X-ray fluorescence spectra indicated that MgO agglomerates not more than 200 nm in diameter were dispersed homogeneously through the LDPE matrix.

DC conductivity measurements were made on 0.1 mm thick samples carrying vacuum-evaporated gold electrodes and a guard ring. Measurements were made at 30°C under an applied field of 40 or 80 kV/mm. In all samples the current reached a steady value within 600 s. Figure 10.12 shows the volume resistivity as a function of filler content. Each point is the average over three samples with a given filler content. Close examination shows that addition of the fillers decreased the conductivity at both applied fields, and that the conductivity reached a steady value at a filler loading around 2 wt%. However no explanation of the saturation is offered.

Figure 10.13 shows space charge and electric field profiles recorded using the PEA method under an applied field of approximately 80 kV/mm at 30°C, 1 and 600 s after field application. (The profiles had stabilized at 600 s). In the sample without nanoparticles the 1 and 600 s plots are almost indistinguishable, while significant homocharge developed beside both electrodes in the 1 wt% sample at 600 s. Figure 10.14 shows the corresponding plots for an applied field around 120 kV/mm. In this case a very large positive (heterocharge) density accumulated beside the cathode at 600 s in the sample without nanoparticles. Observation of the profiles at earlier times showed that this charge was injected from the anode and gradually moved across the sample. Such charge packet injection under very high field has been observed experimentally in XLPE (Hozumi et al. 1998) and predicted from computer simulation (Kaneko and Mizutani 1999). On the other hand the traces for the sample with 1 wt% nanoparticles are largely indistinguishable.

Figure 10.15 shows the maximum field in the LDPE at 600 s, as a function of the applied field. If there were zero net space charge everywhere the plot would

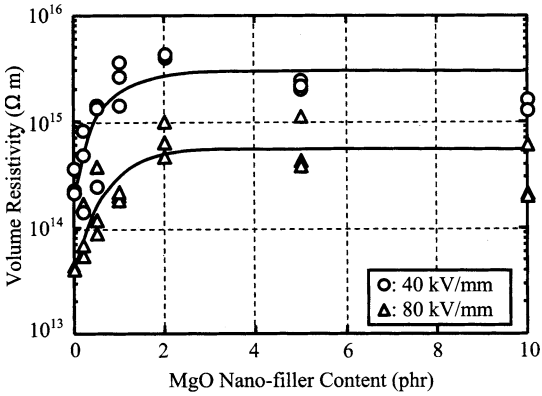

Fig. 10.12 Resistance of LDPE/MgO nanocomposite as a function of MgO loading. 1 phr = 1 wt% (Murakami et al. 2008)

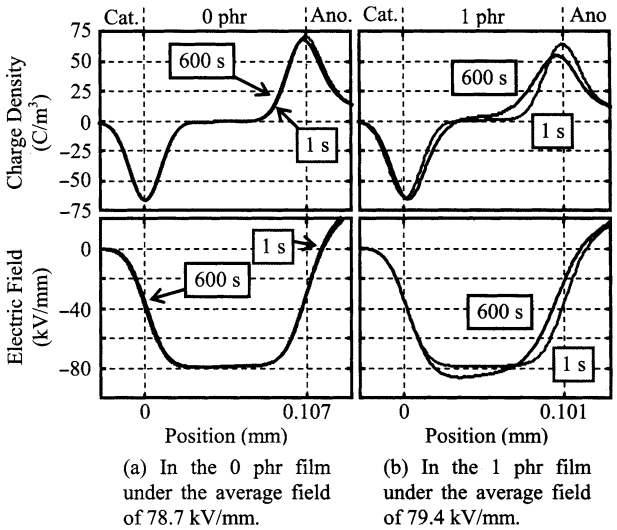

Fig. 10.13 Electric field and space charge profiles for unfilled LDPE and LDPE/MgO nanocomposite with 1 wt% MgO loading, recorded under voltage at 30°C, 1 and 600 s after application of approximately 80 kV(Murakami et al. 2008)

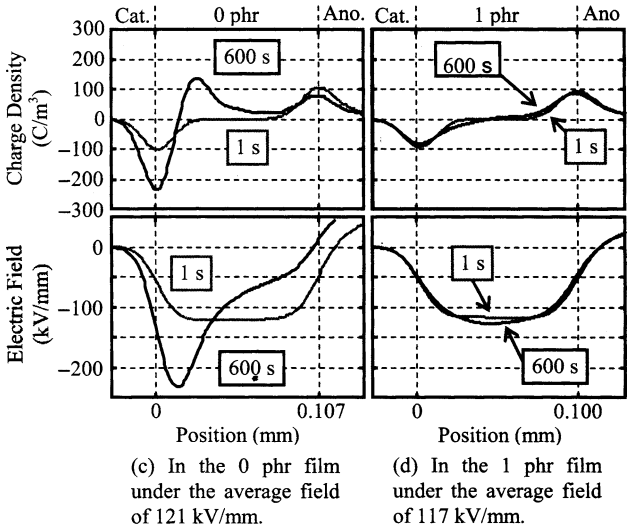

Fig. 10.14 Electric field and space charge profiles for unfilled LDPE and LDPE/MgO nanocomposite with 1 wt% MgO loading, recorded under voltage at 30°C, 1 and 600 s after application of approximately 120 kV(Murakami et al. 2008)

pass through the origin and have slope unity, as shown by the diagonal dotted line; any departure from unity indicates space charge accumulation. Marked departures will be seen at zero and 0.2 phr (equal to 0.2 wt% nanoparticles) at field strengths

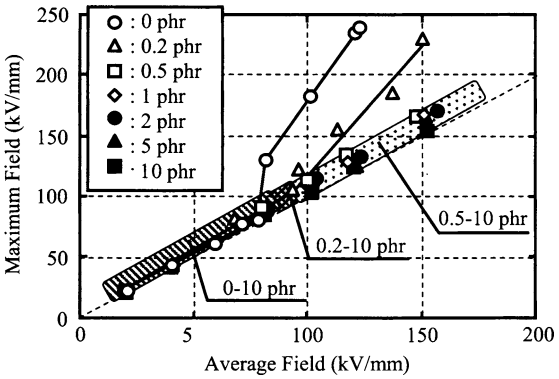

Fig. 10.15 Maximum electric field strength in various LDPE/MgO nanocomposites as a function of applied field. The *diagonal dotted line* has unity slope, corresponding to zero net space charge (Murakami et al. 2008)

exceeding 75 kV/mm. However there are no departures at higher concentrations. It was suggested that increased charge trapping at higher concentrations inhibits charge injection at the electrodes. This suggestion is confirmed by plots showing that the amount of injected charge expressed in C/m^3, and the charge mobility, decrease monotonically with increasing nanofiller content. However, the procedure followed to obtain the data presented in these plots is unclear.

The main conclusions from this work are:

1. MgO nanoparticles reduce the conductivity, which reaches a steady value around 2 wt % MgO
2. The nanoparticles cause homocharge accumulation near both electrodes at moderate applied fields, but appear to suppress charge packet formation and transport at higher fields
3. Higher nanoparticle concentration appears to inhibit charge injection from the electrodes.

10.4.5 Poly(Ethylene-Ethyl Acrylate)/Carbon Nanotubes

In this study (Lee et al. 2008) pellets of a commercially supplied mixture of ethylene and ethyl acrylate (EEA) containing 15 wt% ethyl acrylate were milled and compression molded with powdered carbon nanotubes (CNT) of diameter 30–60 nm and length 20–30 μm. Antioxidant, cross-linking promoter, stabilizer, flame retardant and cross-linking agent (dicumyl peroxide) were added to the EEA before milling. The nanotube concentration was 1, 5 and 10 wt%. Sheets roughly 1 mm thick, with silver paint electrodes, were used for volume resistivity measurements at 25°C and 50% relative humidity. Other conditions and measurement procedures were in accordance with ASTM Standards D991 (1998).

The results are shown in Fig. 10.16. Addition of 1 wt % CNT filler increased the conductivity by more than five orders of magnitude, but further addition had little effect. The expected increase to semiconductor-like values at higher CNT loadings

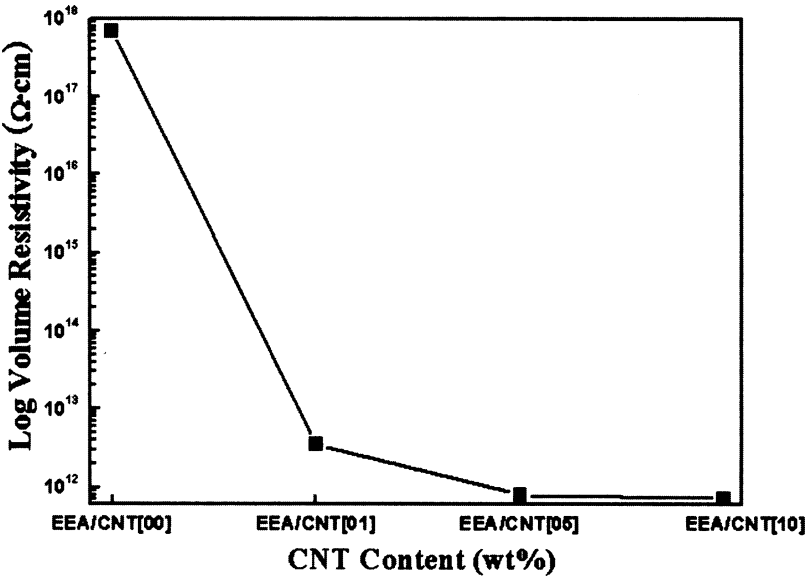

Fig. 10.16 Volume resistivity of poly(ethylene-co-ethyl acrylate)/carbon nanotube composites, at 25°C and 50% relative humidity, as a function of nanotube loading (Lee et al 2008)

may have been prevented by (a) poor dispersion of the CNT through the polymer, (b) scission of the CNT during mixing, or (c) blocking of electron transport by the "dynamic structure" of the CNT.

The main conclusion from this work is that CNTs *increase* the conductivity enormously at concentrations as low as 1 wt%, presumably because the percolation threshold is approached at these levels. This is qualitatively consistent with the interface volume increasing as a fraction of the total sample volume, and the interface volume being more conductive than the unfilled polymer. However, a very large increase at 1 wt% loading is surprising. The use of CNT in controlling conductivity is covered in more detail in Sect. 9.6

10.4.6 Polystyrene/Carbon Nanofiber Composites

In this work (Liang and Tjong 2008) polystyrene/carbon nanofibre (CNF) composites were prepared by melt-blending commercial polystyrene pellets with CNF powder in a Brabender mixer. The maximum CNF loading was 1.7 vol %. The outer diameter of the CNFs was 80–200 nm, and their length was 0.5–20 μm. The blended mixtures were hot-pressed into 1 mm thick plates at 250°C and 10 MPa. Samples 12 mm in diameter were coated with silver paint, and metallic electrodes attached. The conductivity and dielectric constant were measured over the range 40–10^7 Hz.

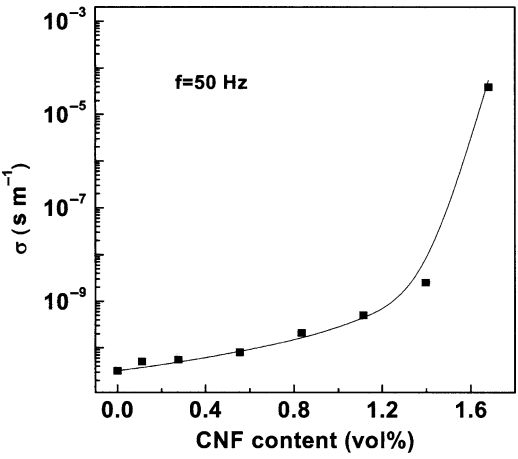

Fig. 10.17 Volume resistivity of polystyrene/carbon nanofibre (CNF) composites at room temperature, measured at 50 Hz, as a function of nanofibre loading (Liang and Tjong 2008)

Figure 10.17 shows the variation of room temperature conductivity at 50 Hz as a function of CNF content. It increases slowly up to about 1.2 vol %, and then rapidly up to the maximum loading. This variation suggests the onset of percolation around 1.2 vol %. The authors fitted the conductivity data below the percolation threshold to the expression

$$\sigma(\varphi) = \sigma_0(1 - \varphi/\varphi_c)^{-s} \tag{10.9}$$

where $\sigma(\varphi)$ is the conductivity of the composite with CNF concentration φ, σ_0 is the conductivity of the polystyrene matrix, φ_c is the percolation threshold and s is a critical exponent (Wu and McLachlan 1997). They found $\varphi_c = 1.71$ vol % and $s = 1.3$. They fitted an equation of the same form to their relative permittivity data at 1 kHz, and again found $\varphi_c = 1.71$ vol % but $s = 0.9$. SEM micrographs of cryogenic fractured surfaces showed that the CNFs began to link up with each other at 0.5 vol % loading, and formed a network covering the fracture surface at 1.7 vol %. $\varphi_c = 1.71$ vol % lies between the minimum and maximum values predicted by Balberg's percolation theory based on the excluded volume concept (Balberg et al. 1984). The excluded volume of an object is defined as the volume surrounding the object into which the centre of another similar object must not enter if overlapping of the two objects is to be avoided.

Figure 10.18 shows the variation of the conductivity of the CNFs and the 1.7 vol % composite, relative to their values at 25°C, measured when the samples were heated at 10°C/min. In the CNFs it varied little between −150 and 0°C, decreased up to about 60°C and then was constant to 150°C. Such variation is unusual. In the composite the conductivity increased slightly between −150 and 0°C, decreased rapidly up to 100°C and then increased up to 150°C. When the sample was cooled at 10°C/min, the conductivity showed much the same variation with temperature although the minimum occurred around 70°C. The glass transition occurs in polystyrene around 100°C (Bower 2002). The authors suggested that, in the range 0–90°C, the gradual increase in movement of segments of the polystyrene

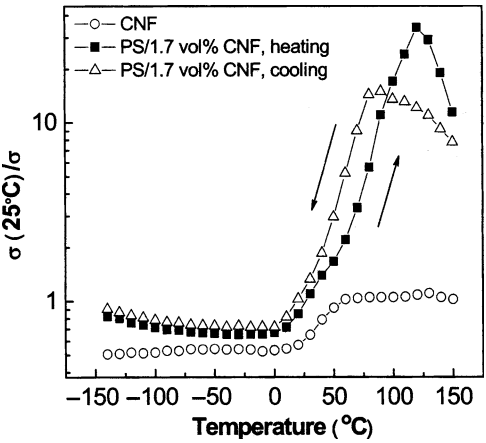

Fig. 10.18 Variation of the conductivity of carbon nanofibres (CNF) and 1.7 vol % polystyrene/CNF nanocomposite, relative to their values at 25°C, measured when the samples were heated at 10°C/min (Liang and Tjong 2008)

backbone impedes charge transfer through the conductive CNF network and so lowers the conductivity. However, the network conductivity is restored when the temperature falls. Although some aspects of these data remain unexplained, it seems that percolation through this nanocomposite can be explained satisfactorily using well-established models of polymer chain dynamics.

Very recent work on a similar nanocomposite system has produced very striking results (Grossiord et al. 2008). Industrially-produced carbon *nanotube* powders (IPCNTs), and in-house fabricated vertically-aligned arrays (VACNTs) were used as fillers. Before incorporation in the polystyrene matrix the IPCNTs were highly entangled and agglomerated, with an average diameter of 20 nm, corresponding to 15 walls. The VACNTs showed uniform alignment normal to the Si substrate on which they were grown, with average diameter of 9 nm, corresponding to five to seven walls. SEM pictures showed that the dispersion of the CNTs in the polystyrene matrix was comparable for all the nanocomposites prepared.

The conductivity was measured using the four-probe technique (Harrop 1972). At low CNT loading the conductivity in both types remained close to that of the polystyrene matrix, around 10^{-10} S/m. The percolation threshold, at which the filler particles form a conductive path through the matrix, was reached in the VACNT composites at a filler loading of 0.15–0.20 wt %, when the conductivity increased by roughly ten orders of magnitude. This is a remarkably large increase at such a low CNT loading level; it saturated around 10^3 S/m at a loading of 1.5–2 wt %. The percolation threshold in the IPCNTs was around 0.85 wt %, when the conductivity was about 50 S/m.

The difference in percolation thresholds is consistent with the difference in aspect ratio, i.e., the ratio length/diameter of the filler tubes. The aspect ratio of the IPCNTs is smaller than that of the VACNTs by a factor of about six (one-third of the length and twice the diameter). Assuming isotropic tubes in three dimensions, in the slender rod limit, the percolation threshold is expected to vary inversely with the excluded volume associated with the tubes (Bug et al. 1985). Calculation of the

excluded volume associated with randomly oriented tubes with a given aspect ratio is complex (Balberg et al. 1984). The fact that the measured percolation thresholds were roughly an order of magnitude higher than the predicted values was attributed to the CNTs embedded in the matrix being curved, rather than straight as assumed in the theory.

The difference in percolation conductivity between the two types must originate in transport between adjacent filler particles, and/or transport through the filler itself. The authors discuss this topic at length, but do not reach any firm conclusions.

The main conclusion from this work is that the increase in conductivity with CNT loading is consistent with established theories of percolation and polymer chain dynamics. Again this is in qualitative agreement with the interface model.

10.4.7 Polypropylene/Layered Silicate

Montanari and his co-workers (Zilg et al. 2003; Montanari et al. 2004) prepared nanocomposites of isotactic polypropylene (iPP) with an organophilic layered silicate, specifically a synthetic fluorohectorite which had been surface-modified by protonated octodecylamine (ODA) so that it became organophilic. This choice of filler, rather than the more common montmorillonite, offered the advantage of working with an extra clean material. The modified fluorohectorite consists of two-dimensional laminas approximately 1 nm thick with lateral dimensions up to several μm. Exfoliation was achieved by grafting a compatibilizer (iPP + 3.5% maleic anhydride) to the iPP backbone. A typical filler concentration was 5 wt %.

Absorption currents were measured at 20° C in nitrogen at a pressure of 300 kPa, on samples approximately 0.5 mm thick carrying sputtered gold electrodes. The samples were held at 50° C for 120 h before measurements were commenced. Field strengths up to 60 kV/mm were applied, for poling times up to 12 h. Figure 10.19 is a double-log plot of the quasi steady-state current in unfilled and 6 wt % filled samples as a function of poling field strength. According to space-charge-limited-current (SCLC) theory (Many and Rakavy 1962), the slope of such a plot should be unity at low field, increasing to 2 when the space charge limited conduction regime is established. The arrows in the plot indicate the transition field, which is considerably lower in the filled sample. The authors comment that such a plot reflects the influence of the shallower traps on the conductivity, since carriers trapped in the deeper traps (perhaps permanently) will contribute little to the current.

Figure 10.20 is a double log plot of the trap-controlled time-dependent mobilities $\mu(t)$, deduced from space charge profiles recorded using the PEA method at various times during depolarization. The $\mu(t)$ values were calculated from

$$\mu(t) = (2\varepsilon/\rho(t)^2)(d\rho(t)/dt) \tag{10.10}$$

where ε is the permittivity of the composite and $\rho(t)$ was calculated by integrating the *absolute value* of the charge density over the sample volume at time t during

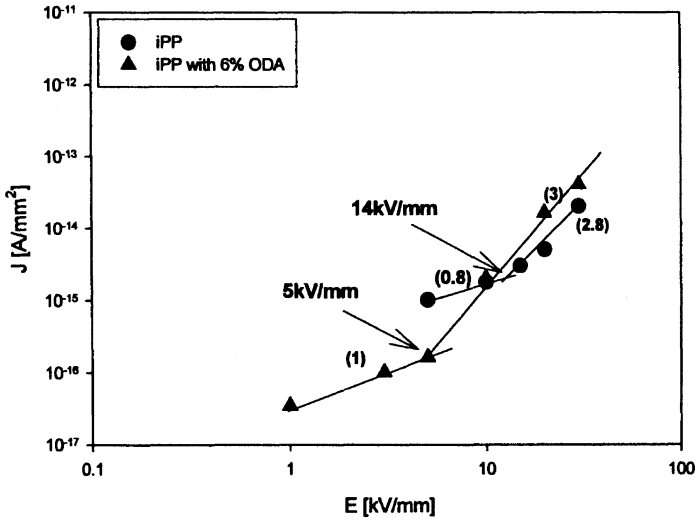

Fig. 10.19 Quasi-steady state current density as a function of applied field strength, in unfilled isotactic polypropylene (iPP), and in a iPP/fluorohectorite nanocomposite containing 6 wt% of synthetic fluorohectorite (a layered silicate) which had been surface-modified by protonated octodecylamine (ODA). Measurements were made at 20° C in nitrogen at 300 kPa. The *arrows* indicate a change in slope, which marks the onset of a space-charge-limited-current regime (Montanari et al 2004)

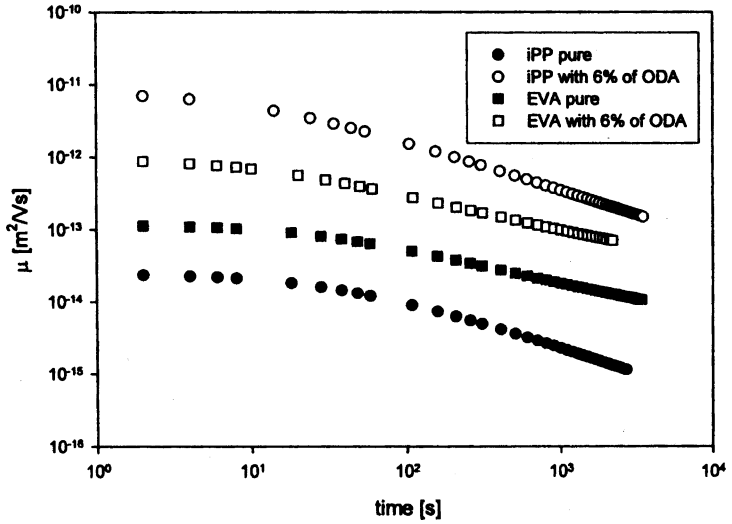

Fig. 10.20 Trap controlled mobilities in unfilled isotactic polypropylene (iPP), and in a iPP/fluorohectorite nanocomposite containing 6 wt % of synthetic fluorohectorite (a layered silicate) which had been surface-modified by protonated octodecylamine (ODA). The mobilities were calculated from space charge profiles recorded at various times (shown on the horizontal axis) during depolarizing current measurements. The poling field strength was 60 kV/mm (Montanari et al. 2004)

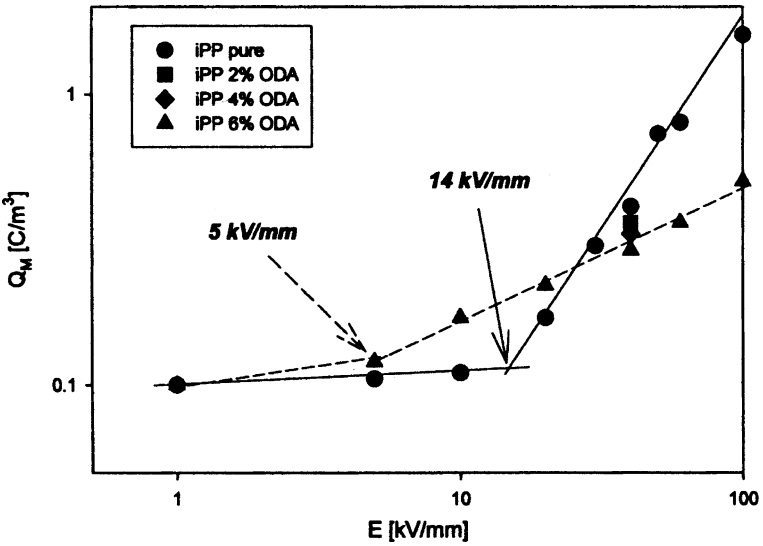

Fig. 10.21 Maximum stored charge Q_M against poling field, as a function of applied field, for unfilled iPP and three iPP/fluorohectorite nanocomposites with various loadings of synthetic fluorohectorite (a layered silicate) which had been surface-modified by protonated octodecylamine (ODA). The *arrows* indicate a change in slope, marking the onset of a space-charge-limited-current regime (after Montanari et al. 2004, Fig. 7)

depolarization and dividing by the sample thickness (Mazzanti et al. 2003). The resulting mobilities are certainly of the expected order of magnitude, although the derivation of (10.10) involves several questionable assumptions. It envisages an effective mobility decreasing with time as an electron travels through the sample, the decrease depending on its trapping/detrapping history. The authors (Montanari et al. 2004) comment that the greatly increased trap-controlled mobility in the composite over the complete measurement time reflects a range of trap depths in the nanocomposite which partially overlaps that in the iPP but extends to lower values. They do not comment on the location or structure of the traps.

Figure 10.21 is a double log plot of the maximum stored charge Q_M in the sample against the poling field, for unfilled iPP and three nanocomposites with varying filler content. Q_M corresponds to the quantity $\rho(t)$ defined above, except that it was obtained from a space charge distribution measurement made after short-circuiting the sample for a short time during poling, rather than during a protracted depolarization current measurement (Montanari 2000). The poling field was 40 kV/mm, but the times at which the space charge measurements were made are not given. The changes of slope indicated by the arrows were again interpreted as indicating the field strength at which a space charge limited current (SCLC) regime was established. These field strengths agree well with those deduced from steady-state conduction currents (Fig. 10.19). It is interesting that they are considerably lower in the composites than in the unfilled iPP.

The main conclusions from this work are:

1. incorporation of the layered silicates *increases* the electron mobilities, due to a lowering of the effective range of trap depths
2. space charge begins to accumulate at much lower applied fields in the nanocomposites.

10.5 Tailoring Charge Transport Properties

The data discussed above are drawn from a very limited range of polymer-based nanocomposites, and therefore any conclusions based on these data must be treated with caution. The following summary may be useful as a guide when attempting to fabricate nanocomposites with specific charge transport properties.

1. *Steady state conductivity*
   (a) "Compact" nanoparticles such as TiO_2, ZnO and MgO decrease the conductivity relative to the unfilled polymer. Since the classical mixing formulae predict an increase, it seems likely that the nanoparticles influence the conductivity by lowering the steady-state charge injection rate at the electrodes
   (b) CNTs and CNFs increase the conductivity by several orders of magnitude at filler loadings as small as 1–2 wt %, probably because of the approach to the percolation threshold (see Chap. 9)
   (c) Layered silicate fillers increase the conductivity by introducing shallower trapping centres, which increases the electron mobility.
2. *Space charge accumulation*
   (a) Compact nanoparticle fillers promote the formation of homocharge near both electrodes, due to charge injection from the electrodes and rapid trapping
   (b) Layered silicate promotes the accumulation of space charge at much lower fields than in the unfilled polymer.
3. *Functionalization*
   Surface treatment of the nanoparticle surfaces, e.g., by using silane compounds, can significantly influence charge transport and charge accumulation in the nanocomposite. However, more data are required before specific outcomes can be confidently predicted.

10.6 Emerging Charge Transport Mechanisms

The conductivity and space charge data presented in Sect. 10.4 are qualitatively consistent with the interface model described in Sect. 10.3, in that the nanoparticles significantly affect the charge transport properties of the composites. On the other

hand the data do not specifically endorse the proposed multi-layer structure of the interface. The interpretations are based on the accepted models of charge injection, transport and trapping in unfilled polymers described briefly in Sect. 10.2, or on standard percolation theory advanced in Chaps. 7 and 9. However, many unanswered questions remain, e.g., why do nanoparticles reduce the rate of charge injection in some polymers, while others cause a reduction in the applied field strength at which a space-charge-limited-current regime is established, and why do TiO_2 and ZnO nanoparticles decrease the conductivity in LDPE while the corresponding microparticles increase it?

It should be noted that the claimed lack of quantitative support for the interface model applies only to the conductivity and space charge accumulation data presently available. The same is not necessarily true of other electrical properties. Thus it has been reported that polyamide layered silicate nanocomposites are more resistive to partial discharge than the host polyamide, or the corresponding microcomposites (Fuse et al. 2004), and an explanation based on the interface model has been proposed (Tanaka et al. 2005).

References

Andre JM, Leroy G (1970) All-electrons band structure of polyethylene in the nearest cell approximation. Chem Phys Lett 5:71–74

Baird ME (1968) Determination of dielectric behaviour at low frequencies from measurements of anomalous charging and discharging currents. Rev Mod Phys 40:219–227

Balberg I, Anderson CH, Alexander S et al (1984) Excluded volume and its relation to the onset of percolation. Phys Rev B 30:3933–3943

Bambery KR, Fleming RJ (1998) Space charge accumulation in two power cable grades of XLPE. Trans IEEE DEI-5:103–109

Bambery KR, Fleming RJ, Holbøll JT (2001) Space charge profiles in low density polyethylene samples containing a permittivity/conductivity gradient. J Phys D Appl Phys 34:3071–3077

Baryshev VA, Yares'ko TD (1980) Specific bulk electrical resistance of two-component mixtures of dispersed materials. Pharm Chem 14:341–343

Bockris JO'M, Reddy AKN, Gamboa-Aldeco M (2000) Modern electrochemistry 2A fundamentals of electrodics. Kluwer/Plenum, New York

Bower DI (2002) An introduction to polymer physics. Cambridge University Press, Cambridge

Brett CMA, Brett AMO (1994) Electrochemistry principles, methods, and applications. Oxford University Press, New York

Bug ALR, Safran SA, Webman I (1985) Continuum percolation of rods. Phys Rev Lett 54:1412–1415

Castellon J, Notingher P Jr, Agnel S et al (2009) Electric field and space charge measurements in thick power cable insulation using the thermal step method. IEEE Electr Insul Mag 25:30–42

Cubero D, Quirke N, Coker DF (2003a) Electronic states for excess electrons in polyethylene compared to long-chain alkanes. Chem Phys Lett 370:21–25

Cubero D, Quirke N, Coker DF (2003b) Electronic transport in disordered n-alkanes: from fluid methane to amorphous polyethylene. J Chem Phys 119:2669–2679

Das-Gupta DK (1997) Conduction mechanisms and high-field effects in synthetic insulating polymers. Trans IEEE DEI-4:149–156

Dissado LA, Fothergill JC (1992) Electrical degradation and breakdown in polymers. Peter Peregrinus Ltd, London
Falk JE, Fleming RJ (1973) Calculation of the electronic energy band structure of polyethylene. J Phys C Solid State Phys 6:2954–2966
Fischer P, Rohl P (1977) Transient currents in oxidized low-density polyethylene. Prog Colloid Polym Sci 62:149–153
Fleming RJ (1990) Charge carrier trapping in organic polymers. Int J Radiat Phys Chem 36:59–68
Fleming RJ, Ammala A, Casey PS et al (2008) Conductivity and space charge in LDPE containing nano- and micro-sized ZnO particles. Trans IEEE DEI-15:118–126
Fleming RJ, Pawlowski T, Ammala A et al (2005) Electrical conductivity and space charge in LDPE containing TiO_2 nanoparticles. Trans IEEE DEI-12:745–753
Fothergill JC (2007) Ageing, space charge and nanodielectrics: ten things we don't know about dielectrics. Proc IEEE Conf Solid Dielectr, 1–10
Fukunaga K (2008) Progress and prospects in PEA space charge measurement techniques. IEEE Electr Insul Mag 24:26–37
Fuse N, Kozako M, Tanaka T et al (2004) Possible mechanism of superior partial-discharge resistance of polyamide nanocomposites. Annual Report IEEE Conference on Dielectrics and Electrical Insulation, pp 322–325
Grahame DC (1947) The electrical double layer and the theory of electrocapillarity. Chem Rev 41:441–501
Gross B, Sessler GM, von Seggern H et al (1979) Hole transit in Teflon films. Appl Phys Lett 34:555–557
Grossiord N, Loos J, van Laake L et al (2008) High-conductivity polymer nanocomposites obtained by tailoring the characteristics of carbon nanotube fillers. Adv Funct Mater 18:3226–3234
Guo TC, Guo WW (1983) A transient state theory of dielectric relaxation and the Curie-von Schweidler law. J Phys C Solid State Phys 16:1955–1960
Harrop PJ (1972) Dielectrics. Butterworth & Co, London 114–116
Hoffmann R, Janiak C, Kollmar C (1991) A chemical approach to the orbitals of organic polymers. Macromolecules 24:3725–3746
Holé S (2009) Recent developments in the pressure wave propagation method. IEEE Electr Insul Mag 25:7–20
Hong JI, Schadler LS, Siegel RW, Mårtensson E (2003) Rescaled electrical properties of ZnO/low density polyethylene nanocomposites. Appl Phys Lett 12:1956–1958
Hozumi N, Takeda T, Suzuki H, Okamoto T (1998) Space charge behavior in XLPE cable insulation under 0.2–1.2 MV/cm DC fields. Trans IEEE DEI-5:82–90
Ieda M (1987) Carrier injection, space charge and electrical breakdown in insulating polymers. Trans IEEE EI-22:261–267
Jonscher AK (1983) Dielectric relaxation in solids. Chelsea Dielectrics Press, London
Kaneko K, Mizutani T (1999) Computer simulation on formation of space charge packets in XLPE films. Trans IEEE DEI-6:152–158
Lang SB (2004) Laser intensity modulation method (LIMM): review of the fundamentals and a new method for data analysis. Trans IEEE DEI-11:3–12
Lee KY, Kim KY, Han WY et al (2008) Thermal, electrical characteristics and morphology of Poly(ethylene-co-ethyl acrylate)/CNT nanocomposites. Trans IEEE 15:205–213
Lewis TJ (1986) Electrical effects at interfaces and surfaces. Trans IEEE EI-21:289–295
Lewis TJ (1994) Nanometric dielectrics. Trans IEEE DEI-1:812–825
Lewis TJ (2002) Polyethylene under electrical stress. Trans IEEE DEI-9:717–729
Lewis TJ (2004) Interfaces are the dominant feature of dielectrics at the nanometric level. Trans IEEE DEI-11:739–753
Lewis TJ (2005) Interfaces: nanometric dielectrics. J Phys D Appl Phys 38:202–212
Liang GD, Tjong SC (2008) Electrical properties of percolative polystyrene/carbon nanofiber composites. Trans IEEE DEI-15:214–220
Lowell J (1990) Absorption and conduction currents in polymers: a unified model. J Phys D Appl Phys 23:205–210

Maeta S, Sakaguchi K (1980) On the determination of trap depths from thermally stimulated currents. Jpn J Appl Phys 19:519–526
Malec D, Truong VH, Essolbi R et al (1998) Carrier mobility in LDPE at high temperature and pressure. Trans IEEE DEI-5:301–303
Many A, Rakavy G (1962) Theory of transient-space-charge-limited currents in solids in the presence of trapping. Phys Rev 126:1980–1988
Martin EH, Hirsch J (1970) Charge transport and carrier mobilities in insulating polymers. J Non-Cryst Solids 4:133–137
Mazzanti G, Montanari GC, Alison JM (2003) A space-charge based method for the estimation of apparent mobility and trap depth as markers for insulation degradation. Theoretical basis and experimental validation. Trans IEEE DEI-10:187–197
Mazzanti G, Montanari GC, Palmieri F et al (2003) Apparent trap-controlled mobility evaluation in insulating polymers through depolarization characteristics derived by space charge measurements. J Appl Phys 94:5997–6004
McCubbin WL, Manne R (1968) LCAO band calculation for the ideal polyethylene chain. Chem Phys Lett 2:230–232
Mizutani T (2006) Behavior of charge carriers in organic insulating materials. Annu Rep Conf Electr Insul Dielectr Phenomena (CEIDP): 1–10
Montanari GC, Fabiani D, Palmieri F et al (2004) Modification of electrical properties and performance of EVA and PP insulation through nanostructure by organophilic silicates. Trans IEEE DEI-11:754–762
Montanari GC (2000) The electrical degradation threshold of polyethylene investigated by space charge and conduction current measurements. Trans IEEE DEI-7:309–315
Murakami Y, Nemoto M, Okuzumi S et al (2008) DC conduction and electrical breakdown of MgO/LDPE nanocomposite. Trans IEEE DEI-15:33–39
Picu C, Keblinski P (2005) Modeling of nanocomposites. In: Ajayan PM, Schadler LS, Braun PV (eds) Nanocomposite science and technology, Chapter 4. Wiley-VCH, Weinheim
Reynold JA, Hough JM (1957) Formulae for dielectric constant of mixtures. Proc Phys Soc 70:769–775
Righi MC, Scandolo S, Serra S et al (2001) Surface states and negative electron affinity in polyethylene. Phys Rev Lett 87:076802-1–076802-4
Ritsko JJ (1982) Electronic states and triboelectricity. In: Mort J, Pfister G (eds) Electronic properties of polymers. Wiley, New York, pp 13–57
Roy M, Nelson JK, MacCrone RK et al (2007) Candidate mechanisms controlling the electrical characteristics of silica/XLPE nanodielectrics. J Mater Sci 42:3789–3799
Sihvola A (1999) Electromagnetic mixing formulas and applications. IEE Electromagnetic Waves Series 47, Institution of Electrical Engineers, London, UK
Smith RC, Liang C, Landry M et al (2008) The mechanisms leading to the useful electrical properties of polymer nanodielectrics. Trans IEEE DEI-15:187–196
Sulston KW, Davison SG, Burrows BL (2003) Properties, dynamics and electronic structure of condensed systems and clusters. Int J Quantum Chem 4:341–346
Tanaka T, Kozako M, Fuse N et al (2005) Proposal of a multi-core model for polymer nanocomposite dielectrics. Trans IEEE DEI-12:669–681
Ueno N, Sugita K, Seki K et al (1986) Low-energy electron transmission and secondary-electron emission experiments on crystalline and molten long-chain alkanes. Phys Rev B 34:6386–6393
van Turnhout J (1980) Thermally stimulated discharge of electrets. In: Sessler GM (ed) Electrets. Topics in applied physics, vol 33. Springer, Heidelberg, pp 81–215
Vollenberg PHT, Heikens D (1989) Particle size dependence of the Young's modulus of filled polymers: 1. Preliminary experiments. Polymer 30:1656–1662
Wintle HJ (1983) Conduction processes in polymers. In: Bartnikas R, Eichhorn RM (eds) Engineering dielectrics, vol IIA. ASTM, Philadelphia, pp 239–354
Wintle HJ (2003) Charge motion in technical insulators: facts, fancies and simulations. Trans IEEE DEI-10:826–841

Wu J, McLachlan DS (1997) Percolation exponents and thresholds obtained from the nearly ideal continuum percolation system graphite – boron nitride. Phys Rev B 56:1236–1248

Zaengl WS (2003) Dielectric spectroscopy in time and frequency domain for HV power equipment, Part I: theoretical considerations. IEEE Electr Insul Mag 19:5–19

Zilg C, Kampfer D, Thomann R et al (2003) Electrical properties of polymer nanocomposites based upon organophilic silicates. Annual Report IEEE Conference on Electrical Insulation and Dielectric Phenomena (CEIDP), pp 546–550

Chapter 11
Industrial Applications Perspective of Nanodielectrics*

Enis Tuncer and Isidor Sauers

11.1 Introduction

One should not forget that power technology (high-voltage apparatus, transmission, and most electrical components) could not exist without satisfactory electrical insulation. It is a challenging task to design and optimize an electrical insulation system while energy demand, voltage levels, and operating temperatures are either increasing in conventional applications or decreasing to cryogenic temperatures in superconducting applications. In addition, these electrical components and equipment sizes are becoming smaller and more compact than conventional devices, placing greater demands on the insulation. New insulation materials are expected to have better endurance and to have better reliability than their conventional counterparts. Recent developments in composite materials filled with nanometer-size particles (defined here as particles in which at least one dimension is in the range 1–100 nm) have shown some interesting results, creating a new research field in electrical insulation being referred to as nanodielectrics (Lewis 1994, 2006; Nelson and Fothergill 2004; Cao et al. 2004).

A detailed description of dielectrics for high-voltage applications was provided in earlier work by Dakin (1978). In this chapter, our discussion will focus on recent developments in the field of nanodielectrics. Only solid insulation materials composed of nanoparticle-loaded polymers will be considered here. The chapter is organized as follows. Different aspects of the nanodielectrics will be considered starting with the background and challenges faced in synthesizing nanocomposites. Some of the significant advantages of the nanodielectrics and their impact

E. Tuncer (✉) and I. Sauers
Oak Ridge National Laboratory, Oak Ridge, TN, USA
e-mail: Enis.Tuncer@physics.org

*This submission was sponsored by a contractor of the United States Government under contract DE-AC05-00OR22725 with the United States Department of Energy.

J.K. Nelson (ed.), *Dielectric Polymer Nanocomposites*,
DOI 10.1007/978-1-4419-1591-7_11,

on the electrical insulation industry are then discussed in the context of dielectric breakdown and voltage endurance. Nanodielectric applications at high- and low-temperatures together with specific device/component applications are discussed as well.

11.2 Background

Solid electrical insulation materials, or dielectrics, in high-voltage applications were historically made of natural materials, such as silk, glass, and ceramic materials in the early days of electrical power applications. However, improvements in materials science and the introduction of plastics have changed the perception that electrical insulation for different power components could benefit from new materials that were initially developed for or used in other technologies. Amazingly, there remain two areas where few advances have been observed. Cellulose-based paper is still the main insulation material used in power transformers, and, in some sub-water cable applications, paper has been used for decades. Outdoor electrical insulation materials for high-voltage lines and bushings have been almost exclusively based on ceramic and glass technology. However, for the last several decades composite materials and polymeric materials with better surface performance and lighter than their earlier counterparts have been utilized.

The introduction of artificial rubbers followed by novel polymeric materials opened a new horizon in materials science and manufacturability after the World War II. Most of the hard-to-manufacture or shape materials used in different industrial applications were replaced by new plastics. In electrical applications, these plastics have been easier to shape and process compared to glass and ceramics. Many polymers without any filler particle inclusions do not possess sufficient mechanical strength. Consequently, fillers have been introduced to improve the mechanical, and other, properties of polymers. Fillers like silica, asbestos fibers, alumina, titania, etc., have been extensively employed for property enhancement, and some of these fillers have also been used to improve the electrical properties of polymers.

It is still not completely understood how dielectric breakdown in insulating materials occurs. However, it is known that degradation in materials, by heat or electric field, impurities, and/or defects, leads to undesired insulation failure. It is therefore critical that new methods of manufacturing defect-free or defect-tolerant materials be developed. It appears that nanoparticles in a composite dielectric help to create defect-tolerant regions. Improving properties of an existing material or synthesizing a new material has often been based on an Edisonian approach that requires testing many samples to build reliable statistics for a candidate material. Recent research results have illustrated that various nanodielectric systems have a promising future in electric insulation science.

11.3 Polymer Nanocomposites

Polymeric materials have been used by mankind for centuries in the form of natural materials (e.g., tar, shellac, etc.). Nowadays synthetic materials are produced in different forms for engineering applications. Although these synthetic polymeric materials can be employed without any fillers, they are often loaded with inorganic fillers either to reduce cost or to produce a product with unique properties that is suitable for multifunctional applications (Winey and Vaia 2007). The multifunctional features can be attributed to properties such as improved thermal/flame resistance (Xiong et al. 2004, 2007; Xie et al. 2002), moisture resistance, decreased permittivity (Nelson and Fothergill 2004; Tuncer et al. 2007a), space-charge tolerance, increased mechanical strength, chemical resistance, and increased toughness (Koo 2006).

An example of improved thermal/flame resistance is hydrated alumina (aluminum trihydrate)-filled silicone rubber (Tuncer and Gubanski 2000), which is utilized in high-voltage outdoor insulation in transmission lines and bushings. The hydrated alumina used as a fire retardant in packaging applications and in high-voltage applications improves the arcing resistance of insulation. Another example is pure silicone rubber (polydimethylsiloxane(PDMS)), which is brittle without any fillers, and is filled with either micrometer- or nanometer-size silica particles to improve the mechanical properties of the silicone (Koo 2006).

The nanocomposites concept started to appear in the late 1980s (Winey and Vaia 2007). These early works mainly focused on montmorillonite clays, material synthesis, and mechanical properties of the composites (Fukushima and Inagaki 1987; Usuki et al. 1993a, b, 1995; Kojima et al. 1993a, b). Other metal oxides and metal fillers in the nanometer-size range in polymeric composites have also been investigated (Ciebien et al. 1998; Shi et al. 2004; Ma et al. 2005a, b). The latter materials are used for electromagnetic shielding and flexible electrode structures (Kruisa et al. 1998; Althues et al. 2007).

Although the initial studies of nanocomposites focused on the improvements in the mechanical properties of the unfilled polymers, the benefit of using these new materials for thermal and electrical applications cannot be disregarded. The main advantage of using nanometer fillers is the large surface area they provide compared to the same volume fraction of micrometer fillers. The surface area highlights the importance of the inherent interfacial regions. For example, there are many locations for the base polymer coils to form strong bonds to particle surfaces (Koo 2006). The increased surface area leads to an increase in the mechanical strength of base polymer. The effect of the increased interface area on electrical and optical properties was not clear due to the paucity of early investigations in this area. However, recent studies have shown that polarization in nanocomposites was complicated because the measured dielectric permittivities of the base nanocomposite materials were lower than the permittivity value of the base polymer (Tuncer 2007a; Nelson and Fothergill 2004).

In addition the measured space charge densities for nanocomposites, which are also related to the polarization, were less than those of the base polymers

(Nelson and Fothergill 2004). These unexpected observations reveal some of the unique application possibilities for polymer nanocomposites. While understanding the conduction and polarization mechanisms in dielectrics has been a major challenge for the dielectric community since the beginning of the electrical era in the late nineteenth century, nanocomposite dielectrics have introduced new phenomena that need to be further understood for the informed application of these new materials. Major areas of polymer nanocomposite applications are described in the following sections.

11.4 The Commercial Impact of Enhanced Electric Strength and Endurance

Solid dielectric insulation materials used in power applications mainly sustain the system voltage when used as a structural support. Any improvement in the dielectric strength of this spacer material would lead to thinner insulation for the same voltage level, leading to less electrical insulation material. According to Dakin (1978), "the minimum insulation is often the least costly overall and provides the most compact equipment, but should not be achieved without assurance of adequate reliability". In cases where the transportation cost and real estate values are important, less insulation would result in lighter systems and a smaller footprint than the conventional systems. Improvement in the dielectric strength would then lead to significant savings for manufacturers and utilities. Some specific examples of electrical components that can benefit from improved breakdown and endurance are power cables, transformers, and power capacitors.

In highly congested areas such as in large metropolitan cities, less insulation in power cables would result in more power delivery from the same conduit used for conventional cable applications. The space savings from the insulation cross section could be spent on conductor thickness, so larger currents could be carried on the same cable cross section. For short lengths (less than 2 km) a competing technology already exists, a cryogenic high-temperature superconductor power cable, which can carry approximately ten times the power in the same cross section. There are system-level issues for long cable lengths due to the current cryo-cooling technology. Polymeric nanocomposites have currently been studied as electrical insulation materials (Tuncer et al. 2007a). This topic will be discussed later.

A similar argument on insulation thickness is true for the power transformers, such that less insulation would result in lighter and smaller power equipment. Once a better insulation material is found for transformers, a compact transformer can be installed on trailers for mobile applications in cases of emergency power recovery (Schwenterly et al. 1999, 2002; Weber et al. 2005). In addition a compact transformer would be preferable in substation locations with high real estate values.

One should consider insulation design for power equipment and systems from the point of view of utility companies. For example, maintenance of the power grid and its components is an important part of the utility companies' costs, improvements

to which would provide significant financial benefits. Improvements in the insulation endurance would lead to less maintenance and longer component lifetime compared to the conventional equipment built with conventional materials. It has been shown by Nelson and collaborators that polymeric composites with nano-size particles would have improved electrical properties (Roy et al. 2005; Nelson and Fothergill 2004). Although not such significant enhancement in the dielectric breakdown strengths was observed, the studied materials indicated voltage endurance that was orders of magnitude longer than for the unfilled polymers or for composites filled with micron-size particles. These aspects have been addressed in more detail in Chap. 7.

The voltage endurance, which is defined as the time to breakdown under electrical stress at a field lower than the field for immediate failure, would be clearly observed in electrical tree propagation. In nanocomposites that were studied, it was shown that a base epoxy suffered breakdowns after 1 h of tree initiation, while an epoxy nanocomposite survived for more than 5 h (Alapati and Thomas 2008). The addition of nano-filler slowed down the electrical tree initiation and propagation. Similar studies on electrical and thermal properties of three component resin-based composites have also been reported by Imai et al. (2005). These systems contained nano- and micro-fillers in which the samples were made with nanometer-scale layered silicates and micrometer-scale silica fillers in an epoxy resin. The nanocomposites had a thermal expansion coefficient similar to that of the conventional filled epoxy. In voltage ramp tests, the nanocomposite had 7% higher insulation breakdown strength than the conventional filled epoxy. In endurance tests under constant AC voltage (10 kV at 1 kHz), the nanocomposite had an insulation breakdown time of more than 20,000 min, whereas the conventional filled epoxy had a breakdown time of 830 min. Composite samples synthesized with epoxy resin and zinc oxide microparticles and nanoparticles had improved electrical treeing breakdown resistance (Ding and Varlow 2004). A small amount (< 1 wt%) of nonlinear zinc oxide particles, which show non-ohmic conductivity as a function of electric field, was enough to increase the electrical tree resistance. Nano-structural differences created with the nanoparticles (also nonlinear particles) show a clear indication of improvement in the insulation breakdown strength and endurance.

Indications of improved endurance can be attributed, in part, to less space charge buildup in insulation materials. Fothergill et al. (2004) reported results of dielectric spectroscopy and space charge measurements on epoxy resin filled with micro- and nano-sized particles. The particles in their study were titania (TiO_2), alumina (Al_3O_2), and zinc oxide (ZnO). They concluded that the results did not indicate any significant effect of particle types and that the dielectric properties of such nano-filled composites are controlled by Stern-Gouy-Chapman layers ("interaction zones") around the particles (Lewis 1994, 2006).

The important implications regarding electrical insulation properties of metal oxide-filled nanocomposites were presented in a recent paper by Smith et al. (2008). It is now clear that polymer nanocomposites with nanoparticle fillers can exhibit improved dielectric breakdown strength and voltage endurance when compared to their neat resin or micrometer particle-filled counterparts. It has been stated that

the inclusion of nanoparticles provides multiple scattering obstacles and trapping sites in the charge carriers' paths, effectively reducing carrier mobility and thus carrier energy. One can visualize the particles as holes and bumps on a landscape where a rolling ball would be deflected by bumps and trapped by holes and argue that the structure of a disordered material (i.e., polymer or amorphous ceramics) would be similar. However, the landscape of a metal oxide nanocomposite is very different since the bumps and holes have the additional functionality of increased height and depth. This argument very well explains the experimental observation of high-electric-field properties of nanodielectrics. Such arguments were also mentioned in view of homo-charge buildup at the electrodes, as determined by electroluminescence, pulsed electro acoustic analysis, and thermally stimulated current measurements in Smith et al. (2008).

Voltage endurance tests in the form of partial discharge (PD) experiments were carried out in epoxy nanocomposites where two different particles were employed, nanoparticles of silicon carbide (SiC) and silicon dioxide (SiO_2) (Tanaka et al. 2008a). It was observed that erosion caused by PD, as evidenced by the depth and eroded cross-sectional area, was much less in nanodielectric resin, where an increase in PD resistance was observed. This is the subject of Chap. 8. In another study (Nakamura et al. 2008), enamel insulation materials on wires were investigated by also employing PD tests. Similar results, as reported by Tanaka et al. (2008a), were presented where a reduction of deterioration depth and of the surface condition of nanocomposite enamel wires were observed after repetitive surge voltage application with successive PD events/tests (Ul Haq et al. 2007a, b). It was clearly indicated that the erosion of nanocomposite enamel layers was suppressed in the depth of erosion caused by decomposition byproducts and dispersed in the longitudinal direction along the enamel surface, which contributed to the longer time-to-breakdown than for conventional wires (Nakamura et al. 2008). Resistance to PD was illustrated in epoxy nanocomposites and compared to neat epoxy resin and an epoxy resin with SiO_2 micro-filler (Kozako et al. 2005). In this work it was shown that the size of the particles is important and that smaller nanoparticles led to a more PD-resistant material compared to unfilled composites or those containing large particles. Partial discharge resistance of nanocomposite resin with clays has also been reported to be better than just with neat resin (Tanaka et al. 2008b). When samples with nano-micro clays were compared to the nanocomposite, they were found to be superior. A detailed study of PD degradation of polyamide both with and without nanoparticles was investigated by Kozako et al. (2004). Surface structure analysis showed that the roughness was considerably less in nanocomposites. The PD resistance of polyamide nanocomposites was significantly better than that of unfilled polyamide.

Huang et al. (2007) presented a general review of polymer nanocomposites in which recent advances on polymer nanocomposites and investigations concerning the electrical conduction, dielectric strength, space charge, dielectric permittivity, dielectric loss, and PD were discussed. Recent research indicates that engineered materials like polyhedral oligomeric silsesquioxane (POSS) would be useful in insulation applications. These materials contain extremely small silica particles (< 5 nm) and are designed to be compatible with many thermosets and

thermoplastics. A paper by Takala et al. (2008a) presents thermal, mechanical, and dielectric measurements conducted on polymer nanocomposites consisting of epoxy and POSS. Glass transition temperatures and tensile strength of the nanocomposites were lower than those of the neat resin. However AC and impulse breakdown strengths showed slight improvements with the addition of POSS. A similar investigation by the same group using polypropylene as the matrix also showed slight improvements in AC and impulse breakdown strength in nanocomposites with POSS (Takala et al. 2008b). In most of the nanocomposite systems, particles are mixed in a matrix using an ex situ technique. Recent work by Tuncer (2007b) has focused on synthesizing particles in situ in the matrix. Fabricated polyvinyl alcohol/titania nanodielectrics had breakdown strengths, measured in liquid nitrogen, that were significantly higher than those of unfilled polyvinyl alcohol. One can consider nanometer-sized particles as voltage stabilization additives.

Discussions related to particle-size-dependent properties were presented by Roy et al. (2005, 2007). In relation to the development of HV cable dielectrics, samples of polyethylene (Roy et al. 2005) and cross-linked polyethylene (Roy et al. 2007) with silica nanoparticles increased breakdown and voltage endurance. The endurance results were impressive, which indicated an increase in time scales of two orders of magnitude. This observation was attributed to the large interfacial region in the nanocomposites. These regions could be responsible for a reduction in charge mobility and a change in the defect size (Roy et al. 2007). In another polyethylene study (Huang et al. 2008), improvements in the physical properties of linear, low-density polyethylene/aluminum nanocomposites were reported with morphological properties. The frequency-dependent properties of the nanocomposites illustrated an increase in the dielectric constant of nanocomposites. It was found that highly filled nanocomposites had good mechanical properties and breakdown strength.

Direct-current transmission systems based on cables could benefit from the implementation of nanodielectrics. Reedy and Ramu (2008) reported on not only the electrical but also the thermal properties of nanocomposites. Previous investigations showed improvements in volume resistivity and the DC breakdown strength of nanocomposites. Nanocomposites of low-density polyethylene with magnesium oxide (MgO) nanoparticles showed a considerable improvement in their thermal properties as related to breakdown properties.

Other types of engineering polymers, polyarylene ether nitriles (PEN) and their corresponding nanocomposites, have been studied with titania loading using sol–gel synthesis (Li et al. 2005a). The dielectric and thermal properties of the films were characterized, and it was reported that mechanical and thermal properties were improved without dielectric breakdown degradation.

Outdoor insulation applications have also benefitted from nanocomposite dielectrics. For example, improved erosion resistance (electrical arcing tolerance), tensile strength, elongation at break, hardness, low dielectric permittivity, weather resistance, superhydrophobicity, and thermal stability are some of the material physical properties desired for outdoor insulation applications. Silicone rubber samples with nanometer and micrometer fillers have been studied and have shown that the fillers used were able to improve the erosion resistance of the rubber (Ramirez

et al. 2009). The effect of surfactant on mechanical and erosion resistance was also observed, indicating that excess surfactant had a negative effect on the properties considered.

Clays are nano-structured minerals with a huge potential for use as nanodielectric fillers due to their lower cost compared to other engineered nano-powder. Clays can be used in various resins to improve the physical properties of the base materials; however, once nanoparticles are put in the base material, the curing procedure of the resin might change. Therefore, significant effort should be spent on the curing and mixing techniques. Tagami et al. (2008) presented the effects of curing agents and filler dispersion method on the dielectric properties of epoxy nanocomposites. They observed that, independent of the mixing methods, electrical properties (permittivity and conductivity) were more affected by the curing agents and less by the clay particles and the mixing method.

Increasing power electronics circuitry demands, due to inverters and converters, require that improvements in the packaging and electrical insulation materials be made. Okubo et al. (2007a, b) and Hayakawa and Okubo (2008) investigated the breakdown lifetime characteristics under repetitive surge voltage application for nanocomposite-enameled wires. It was observed that the nanocomposite-enameled wires had a breakdown lifetime 1,000 times longer than conventional enameled wires under surge voltage application.

11.5 Opportunities for Enhanced High-Temperature Dielectrics

High-temperature dielectrics are needed in generators (motors and drives), compact transformers, and specialty capacitors. In addition, the performance of insulation and its lifetime at various temperatures yields valuable information regarding its deterioration and the rate of deterioration (Berberich and Dakin 1956). Thermal integrity chemical effects such as oxidation, depolymerization, hydrolysis, undesired chemical reactions, etc., and physical effects such as melting, softening, volatilization, hardening, cracking, and change in mechanical, thermal, and electrical properties should be considered (Berberich and Dakin 1956). These effects might be either postponed (slowed down) or avoided with the addition of nanoparticles.

Electrical insulation materials with better thermal properties can be used in electrical devices where improvements in heat dissipation are needed. An epoxy resin with high thermal conduction can be attained by reduced scattering of phonons, which affect the thermal properties, by controlling the nanoscale structure (Takezawa et al. 2003). Thermal properties and improvements were reported for two resins that were designed with liquid-crystalline molecules (mesogens), which act as inclusions at the nanoscale. It was shown that thermal conductivities would become greater when the amounts of mesogens were increased (Takezawa et al. 2003); for example, a thermal conductivity increase of a factor of 5 could be attained compared to conventional resin.

Improvements in the thermal properties of a material can also be achieved by addition of carbon nanofibers or nanotubes (Frormann et al. 2008). When high shear mixing was used to disperse and distribute the nanofibers, a good dispersion of the fibers within the polypropylene matrix was observed. Thermal property analysis showed thermal stability enhancements and an increase in the melting temperature of polypropylene. The fibers also increased the storage modulus and decreased the mechanical loss factor (tan δ). The main advantage of using fibers was the improvement in the thermal conductivity.

Polyimides are high-performance polymers with good electrical insulation properties (Zhou et al 2006). Polyimide samples prepared with silica nanoparticles showed that the thermal stability via thermogravimetric analysis (TGA) was improved with nanoparticles (Zhang et al. 2007). Aluminum nitride-filled nanocomposite polyimide was characterized as a dielectric material for microelectronic packaging (Saeed et al. 2006). The mechanical properties, elastic modulus and strength, were improved with an increase in filler content. Studies of the electrical properties of polyimide, characterized by the thermally stimulated depolarization method, have concluded that the nature of conductivity of this material is ionic (Cao and Irwin 2003). Nanometer-size particle inclusions altered the main thermally stimulated current peak to higher temperatures, which indicated that nano-fillers changed the trap density and depth. Cao and Irwin (2003) concluded that the electrical breakdown strength of nanocomposite polyimide would not degrade.

A different approach to investigating polyimide nanocomposites was performed by Jiaqi et al. (2006). Electroluminescence experiments on unfilled and nanoparticle-filled polyimide films were conducted under DC field. Pre-breakdown fields for filled polyimide were higher than those for the unfilled material, which also indicated improvements in the dielectric breakdown characteristics of polymers with nanoparticle addition. A polyimide mixture with varied amounts of alumina has shown improved thermal stability from TGA and electrical aging performance as compared with pure polyimide film (Hong et al. 2003).

A detailed analysis of electrical properties of polyimide nanocomposites as insulation for enameled wires and investigations of surface erosion under stress and partial discharge resistance showed that nano-filled polyimide has improved insulating properties (Saeed et al. 2006). Anisotropic silicates were proposed to enhance the physical properties of polyimides (An et al. 2008). Rod-shaped silicates were mixed into polyimide, which resulted in significant improvements in strength and toughness as well as increases in the thermal decomposition temperature.

Various insulating varnish nanocomposite systems composed of polyester and low loading of nanoparticles of fumed silica, silica and titanium dioxide, zinc oxide, or clays (montmorillonite) were processed, and their mechanical, electrical, barrier, and thermal properties were investigated (Gornicka et al. 2007). The polyester varnishes are utilized in high temperature insulation applications. Therefore, improvements in their dielectric properties (electrical strength, resistance to pulse voltage) would be possible by incorporation of various nanoparticles. The inclusion of nanofillers has also exhibited an increase in thermal endurance (Gornicka et al. 2007).

11.6 Cryogenic Applications and Other Extreme Environments

Electrical insulation material requirements for technologies such as cryogenic (high-temperature superconductive) power applications (Schneider 1991; Dale et al. 1990a, b), novel energy applications such as fusion (Moreschi et al. 2003), and space devices (Masayuki 2004) are clearly more demanding and of recent interest. However, improvements in superconducting materials and industrial processing techniques have now made it possible to manufacture devices with superconductors. Early applications were low-voltage superconducting magnets, which could tolerate imperfections in the insulation (Forsyth 1993) since the voltage stresses were low. In cryogenic applications, insulation failure could be caused by mechanical stress as well as a mismatch of thermal properties of components or the intrinsic thermal properties of materials. In addition, the entire insulation system needs to be designed to be PD free due to the likelihood of electrical degradation (Gerhold 1998, 2002; Gerhold 1998; James and Sauers 2004; Sauers et al. 2004), leading to insulation failure. Many micro-filler composite materials have been characterized for cryogenic insulation applications (Sauers et al. 2004; Tuncer et al. 2007a). However the addition of micrometer-size particles has generally lowered the dielectric breakdown strength of base polymers.

Several nanocomposite systems characterized by the authors of this chapter have demonstrated the potential of nanodielectrics in cryogenic applications. The materials selected for cryogenics applications were either based on thermoplastics – polyvinyl alcohol (Tuncer et al. 2007a, 2008) or polymethyl methacrylate (Tuncer et al. 2009); or a thermoset – epoxy (Araldite® 5808) (Tuncer et al. 2007a). It was shown that nanometer-size particles could serve as a voltage stabilizing additive (Tuncer et al. 2008).

As has been addressed in Chap. 9, field grading and tailoring the permittivity are important in cryogenic applications, with possibilities of adjusting permittivity using barium titanate nanoparticles. These materials have been demonstrated to be potential candidates for cryogenic capacitors or for field grading applications (Tuncer et al. 2008). Monodispersed cobalt ferrite nanoparticles have improved the dielectric characteristics of polymethyl methacrylate (Tuncer et al. 2009). The structural and dielectric properties of nanocomposite dielectrics were presented with plausible explanations for the observed low effective dielectric permittivity values in nanodielectric systems. Nanoparticle composites with large permittivity particles can exhibit a low dielectric permittivity regardless of what the permittivities of the nanoparticles are when the particles are coordinated with a low dielectric permittivity surfactant (Tuncer et al. 2009). Systems with low permittivity surfactants demonstrate better electric potential distribution in material that improves the electric stress distribution and breakdown strength (Tuncer et al. 2009).

Glass fiber composites, such as those with designations FR4, G10 or G11, are often used as structural support in fusion, space, or power applications. Recent studies on the dielectric and mechanical properties of nanowire-alumina-filled polybutylene terephthalate/glass-fiber composites have been investigated (Yu et al. 2006). A crack bridging toughening mechanism was observed in which nanowires reduced

the crystallinity. It was concluded that alumina wires may have reduced the number of micro-defects and thus improved the electrical strength of the nanocomposite system.

11.7 High-Voltage Stress Grading Materials and Conducting Nanocomposites

The design of stress-grading materials is the subject of a specialist chapter in this book (Chap. 9) and will not be reviewed again here in detail. However, designing the conductivity of materials is of importance for DC power and resistive field grading applications. An increase in permittivity could be expected in nanotube-filled polymers due to Maxwell-Wagner-Sillars polarization below the percolation threshold. However, the percolation threshold is highly dependent on the shape and dimension of the tubes. Experimental and numerical simulation results on nanotube-polymer-composite systems have been presented by various researchers who took into account percolation and charge transport aspects of the systems (Simoes et al. 2009; Jiang et al. 2007).

Anisotropic composites could be used to design improved electrical response. In a recent study employing dielectrophoresis, anisotropic barium titanate silicone composites were created (Tomer and Randall 2008). The electrical properties of these composites were found to be dependent on the anisotropy present in the system. Materials with tailored structure/anisotropy could be employed to control dielectric breakdown strengths and nonlinear conduction.

A power law behavior in electrical properties as a function of filler content was observed near the percolation threshold for styrene-acrylonitrile graphite sheet composites (Panwar and Mehra 2008). A similar study with polystyrene/foliated graphite has illustrated that a nonlinear-to-linear dependence in current-voltage characteristics of the composites was observed as the volume faction of graphite was increased over the percolation threshold (insulator-conductor transition) (Srivastava and Mehra 2008).

Contact resistance lowering applications require easy-to-apply conducting grease. Benedetto et al. (2007) have designed a nanocomposite material with lubricant and improved electrical properties. The material was based on carbon nanotubes and different electrochemically grafted organic matrices.

11.8 Applications in the Capacitor Industry

Insulating materials with high permittivity and high breakdown strength would yield large electrical energy density (Tan et al. 2006). The stored energy, W, is expressed as a function of the dielectric permittivity, ε, and the square of the applied electric field, E:

$$W = \frac{1}{2}\varepsilon E^2 \tag{11.1}$$

It would be beneficial to improve the design field, where, for example, an improvement in twice the design field would quadruple the stored energy. However this is not an easy task. It is usually more straightforward to increase the dielectric permittivity of a composite just by increasing the content of the high permittivity component. Recent results and developments in nanocomposite polymers have illustrated that an increase in permittivity has also yielded either improvement or no significant change in the dielectric breakdown strength (which is related to the design field). Li et al. (2007) have discussed several issues in nanocomposite dielectrics by analyzing the effective permittivity, breakdown strength, and electric energy density of systems with an effective medium approach. They have concluded that the structure of nanocomposites would play an important role, and special attention should be given to control it.

The synthesis and properties of ferroelectric nanometer-sized powders play an important role in the fabrication of nanocomposite materials for capacitor applications. Lu et al. (2004) discussed the structural and physical properties of inorganic materials in the context of their particle size. A detailed description was given on the characteristic parameters of capacitors with enhanced dielectric permittivity, breakdown voltage, ageing, resistivity, mechanical strength, etc. When these particles are introduced into polymers, the physical properties of composite systems could be tailored to achieve the best performance (Tan et al. 2006). Porous materials composed of carbon nanotubes and doped polypyrrole showed high specific capacitance of 131 F/g when the mixture is 50–50 (Oh et al. 2008). These new nanocomposite materials could be used in capacitors and electrodes for batteries and electromechanical actuators.

Poly(vinylidene fluoride) (PVDF) is a high-permittivity polymer proposed for use in capacitor applications. A nanocomposite based on PVDF and poly(p-chloromethyl styrene) coated copper phthalocyanine (CuPc) oligomer has been shown to have a dielectric constant of 325 at 100 Hz for the composite with 15 wt % filler particles (this value is approximately seven times larger than PVDF with CuPc particles, and about 40-fold higher than unfilled PVDF) (Wang et al. 2009).

High-performance polymers and high-permittivity ceramics have been studied for capacitor applications. One such composite system is barium titanate-filled polyimide nanocomposites. Dang et al. (2008) have reported a thermally stable nanocomposite system with high dielectric permittivity (20), and a breakdown strength of 67 kV/mm. Surface-modified barium titanate nanoparticles in poly(vinylidenefluoride-co-hexafluoropropylene) have also been shown to possess large relative permittivities and unusually high dielectric breakdown strengths (Kim et al. 2007a). Nickel and barium titanate nanoparticle-filled polyamide systems have been studied by Li et al. (2005b), where both systems yielded high relative permittivity for embedded capacitor applications.

Cryogenic capacitors would be needed if cryogenic power applications were built with the same coolant system or in space applications. Tuncer et al. (2008) reported electrical properties of a nanocomposite system composed of polyvinyl alcohol and barium titanate nanoparticles that could be used in a cryogenic capacitor. The

sample with the highest filler concentration had a relative permittivity of approximately 9 and 1% breakdown probability breakdown strength of 20 kV/mm.

A nanocomposite system with conductive polyaniline nanofibers dispersed in polyvinylidene fluoride–trifluoroethylene copolymers exhibited a dielectric constant 50 times higher than that of the ferroelectric polymer matrix (Wang et al. 2008). The drastic reduction in electric field strength that was required to switch spontaneous polarization of the matrix was attributed to the nanofibers.

11.9 Multi-functional Opportunities

Actuator materials capable of converting mechanical energy to electrical energy or vice versa are needed for many industrial applications, such as robotics, micro air vehicles, flat loudspeakers, micro-electromechanical systems, and microfluidic devices. In actuator applications large displacement with high precision and speed are required with durability and reliability. The elastic energy related to the mechanical properties of the actuator is proportional to the product of half of its Young's modulus, Y, and the strain, S:

$$W_a = \frac{1}{2} Y \ S^2 \tag{11.2}$$

This energy is supplied by the electrical input (Maxwell stress tensor), which is $1/2(\varepsilon E^2)$. Hence, for the highest strain (displacement), a material with low stiffness (low Young's modulus), high breakdown strength, and high permittivity is desired. With recent developments in nanocomposites, novel materials for actuators can be tailored because of the potential to increase permittivity and keep dielectric strength appreciably high. In actuator applications, the electrode materials are considered to have low stiffness. Polyurethane with a conductive filler nanocomposite system was proposed, and, among the fillers that were considered (carbon black, vapor grown carbon fiber, and silver powder), a carbon nanocomposite electrode had the largest displacement (Kim et al. 2007b).

An ionic polymer/metal composite and a nanoclay-filled polymer nanocomposite were studied for actuator applications (Paquette et al. 2003). It was shown that the current/voltage (I/V) curves could be used to create an optimized effective polymer actuator. An approach similar to that of Paquette et al. (2003) was proposed by employing Nafion™ and carbon nanotubes (Lee et al. 2006). It was concluded that nanocomposites produced a significantly larger elastic modulus and improved electromechanical coupling compared to those of the unfilled Nafion™. Uniform distribution of nanotubes is needed for improved performance (Lee et al. 2004).

Another example may be found in the work of Huang et al. (2005) who used a polyurethane polymer with small volume fraction of copper phthalocyanine oligomer. The nanocomposite exhibited a colossal dielectric relative permittivity (about 10,000) and electromechanical response. A piezoelectric paint has also been

investigated with nanowires (instead of nanoparticles) of barium titanate (Feenstra and Sodano 2008). The nanowires employed improved the electromechanical coupling threefold compared to the nanocomposite.

11.10 Conclusions

An overview of polymeric nanocomposites and their potential use in industrial applications is provided in this chapter. It is clear that continued developments in chemistry and materials sciences are critical to electrical insulation research in the field of nanodielectrics.

Acknowledgment The valuable assistance of Mrs. Julia Wignall is highly appreciated in preparation of this manuscript.

References

Alapati S, Thomas MJ (2008) Electrical treeing in polymer nanocomposites. Fifteenth National Power Systems Conference (NPSC), IIT Bombay, pp 351–355

Althues H, Henle J, Kaskel S (2007) Functional inorganic nanofillers for transparent polymers. Chem Soc Rev 36:1454–1465

An L, Pan YZ, Shen XW et al (2008) Rod-like attapulgite/polyimide nanocomposites with simultaneously improved strength, toughness, thermal stability and related mechanisms. J Mater Chem 18(41):4928–4941

Benedetto A, Viel P, Noel S et al (2007) Carbon nanotubes/fluorinated polymers nanocomposite thin films for electrical contacts lubrication. Surf Sci 601(18):3687–3692

Berberich LJ, Dakin TW (1956) Guiding principles in the thermal evaluation of electrical insulation, power apparatus and systems, Part III. Trans Am Inst Electr Eng 75(3):752–761

Cao Y, Irwin PC (2003) The electrical conduction in polyimide nanocomposites. Conf on Elect Ins and Diel Phen, 116–119

Cao Y, Irwin PC, Younsi KY (2004) The future of nanodielectrics in the electrical power industry. Trans IEEE DEI-11(5):797–807

Ciebien JF, Clay RT, Sohn BH et al (1998) Brief review of metal nanoclusters in block copolymer films. New J Chem 22:685–691

Dakin TW (1978) High voltage insulation applications. Trans IEEE E1-13(4):318–326

Dale SJ, Wolf SM, Schneider TR (eds) (1990a) Energy applications on high-temperature superconductivity, vol 1. US Dept Energy and EPRI

Dale SJ, Wolf SM, Schneider TR (eds) (1990b) Energy applications on high-temperature superconductivity, vol 2. US Dept Energy and EPRI

Dang ZM, Lin YQ, Xu HP et al (2008) Fabrication and dielectric characterization of advanced BaTiO3/polyimide nanocomposite films with high thermal stability. Adv Funct Mater 18(10):1509–1517

Ding H-Z, Varlow BR (2004) Effect of nano-fillers on electrical treeing in epoxy resin subjected to AC voltage. Conf on Electr Insul and Dielectr Phen: 332–335

Feenstra J, Sodano HA (2008) Enhanced active piezoelectric 0-3 nanocomposites fabricated through electrospun nanowires. J Appl Phys 103(12):124108

Forsyth EB (1993) The aging of electrical insulation at cryogenic temperatures. Trans IEEE EI-28(5):845–854

Fothergill JC, Nelson JK, Fu M (2004) Dielectric properties of epoxy nanocomposites containing TiO_2, Al_2O_3 and ZnO fillers. Conf on Elect Ins and Diel Phen: 406–409

Frormann L, Iqbal A, Abdullah SA (2008) Thermo-viscoelastic behavior of PCNF-filled polypropylene nanocomposites. J Appl Polym Sci 107(4):2695–2703

Fukushima Y, Inagaki S J (1987) Synthesis of an intercalated compound of montmorillonite and 6-polyamide. J Inclusion Phenom 5:473–482

Gerhold J (1998) Properties of cryogenic insulants. Cryogenics 38:1063–1081

Gerhold J (2002) Cryogenic liquids – A prospective insulation basis for future power equipment. Trans IEEE DEI-9(1):68–75

Gerhold J, Tanaka T (1998) Cryogenic electrical insulation of superconducting power transmission lines: transfer of experience learned from metal superconductors to high critical temperature superconductors. Cryogenics 38:1173–1188

Gornicka B, Czolowska B, Mazurek B et al (2007) Varnishes modified with nanoparticles for use in electrical insulation. Polimery 52(5):367–370

Hayakawa N, Okubo H (2008) Lifetime characteristics of nanocomposite enameled wire under surge voltage application. IEEE Electr Insul Mag 24(2):22–27

Hong JI, Schadler LS, Siegel RW et al (2003) Rescaled electrical properties of ZnO/low density polyethylene nanocomposites. Appl Phys Lett 82(12):1956–1958

Huang XY, Jiang PK, Kim CN, Ke QQ (2007) Polymer nanocomposite dielectrics. Prog Chem 19(11):1776–1782

Huang XY, Jiang PK, Kim CN et al (2008) Preparation, microstructure and properties of polyethylene aluminum nanocomposite dielectrics. Compos Sci Technol 68(9):2134–2140

Huang C, Zhang QM, Li JY et al (2005) Colossal dielectric and electromechanical responses in self-assembled polymeric nanocomposites. Appl Phys Lett 87(18):182901

Imai T, Sawa F, Nakano T et al (2006) Effects of nano- and micro-filler mixture on electrical insulation properties of epoxy based composites. Trans IEEE DEI-13(2):319–326

Imai T, Sawa F, Nakano T et al (2005) Insulation properties of nano- and micro-filler mixture composite. Conf on Elect Ins and Diel Phen: 171–174

James DR, Sauers I (2004) Electrical insulation materials for superconducting coil applications. IEEE Power Engineering Society General Meeting, vol 2, pp 2062–2064

Jiang MJ, Dang ZM, Xu HP (2007) Enhanced electrical conductivity in chemically modified carbon nanotube/methylvinyl silicone rubber nanocomposite. Eur Polym J 43(12):4924–4930

Jiaqi L, Caixia L, Zhiba Z et al (2006) Electroluminescence in both original and nanoparticle doped polyimide films. 8th International Conference on Properties and Applications of Dielectric Materials, pp 175–178

Kim P, Jones SC, Hotchkiss PJ et al (2007a) Phosphonic acid-modified barium titanate polymer nanocomposites with high permittivity and dielectric strength. Adv Mater 19(7):1001–1005

Kim CH, Lim HO, Chung I et al (2007b) Actuation behavior of waterborne polyurethane/conductive filler nanocomposite electrode. Compos Interfaces 14(5–6):477–491

Kojima Y, Usuki A, Kawasumi M et al (1993) Mechanical-properties of nylon-6 clay hybrid. J Mater Res 8:1185–1189

Kojima Y, Usuki A, Kawasumi M et al (1993) Synthesis of nylon 6-clay hybrid by montmorillonite intercalated with caprolactam. J Polym Sci A Polym Chem 31(4):983–986

Koo JH (2006) Polymer nanocomposites: processing, characterization and applications. McGraw-Hill, New York

Kozako M, Fuse N, Ohki Y et al (2004) Surface degradation of polyamide nanocomposites caused by partial discharges using IEC(b) electrodes. Trans IEEE DEI-11(5):833–839

Kozako M, Kuge S, Imai T et al (2005) Surface erosion due to partial discharges on several kinds of epoxy nanocomposites. Conf on Elect Insul and Diel Phen: 162–165

Kruisa FE, Fissana H, Peleda A (1998) Synthesis of nanoparticles in the gas phase for electronic, optical and magnetic applications – A review. J Aerosol Sci 29(5–6):511–535

Lee DY, Kim KJ, Heo S et al (2006), Nakamura T, Yamashita K, Neo M (eds) Application of an equivalent circuit model for ionic polymer-metal composite (IPMC) bending actuator loaded with multiwalled carbon nanotube (M-CNT). Key Eng Mater Bioceramics 309–311:593–596

Lewis TJ (1994) Nanometric dielectrics. Trans IEEE DEI-1:812–825

Lewis TJ (2006) Nano-composite dielectrics: the dielectric nature of the nanoparticle environment. IEEJ Trans Fundam Mater 126(11):1020–1030

Li C, Tang AB, Zou YB et al (2005a) Preparation and dielectric properties of polyarylene ether nitriles/TiO2 nanocomposite film. Mater Lett 59(1):59–63

Li L, Takahashi A, Hao JJ et al (2005b) Novel polymer-ceramic nanocomposite based on new concepts for embedded capacitor application (I). Trans IEEE CPT-28(4):754–759

Li JY, Zhang L, Ducharme S (2007) Electric energy density of dielectric nanocomposites. Appl Phys Lett 90(13):132901

Lu SG, Li BR, Mak CL et al (2004) Preparation, properties and application prospects of ferroelectric nanomaterials. J Inorg Mater 19(6):1231–1239

Ma D, Hugener T, Siegel RW et al (2005a) Influence of nanoparticle surface modification on the electrical behavior of polyethylene nanocomposites. Nanotechnology 16:724–731

Ma D, Akpalu YA, Li Y et al (2005b) Effect of titania nanoparticles on the morphology of low density polyethylene. J Polym Sci B Polym Phys 43(5):463–533

Masayuki N (2004) Cryogenic electrical insulation and its advantage. IEEJ Trans Fundam Mater 124(9):759–762

Moreschi LF, Rossi P, Agostini M et al (2003) Full scale electrical insulation coating development. 22nd symposium on fusion technology fusion engineering and design, vol 69, no 1–4, pp 303–307

Nakamura Y, Inano H, Hiroshima S et al (2008) Partial discharge resistant aging mechanism of nanocomposite enamel wires under repetitive surge voltage condition. Conf on Elect Insul and Diel Phen: 375–378

Nelson JK, Fothergill JC (2004) Internal charge behaviour of nanocomposites. Nanotechnology 15:586–595

Oh J, Kozlov ME, Kim BG et al (2008) Preparation and electrochemical characterization of porous SWNT-PPy nanocomposite sheets for supercapacitor applications. Synth Met 158(15):638–64

Okubo H, Hayakawa N, Montanari GC (2007a) Technical development on partial discharge measurement and electrical insulation techniques for low voltage motors driven by voltage inverters. Trans IEEE DEI-14(6):1516–1530

Okubo H, Nakamura Y, Inano H et al (2007b) Lifetime characteristics of nanocomposite enameled wire under surge voltage application. Conf on Elect Ins and Diel Phen: 13–16

Panwar V, Mehra RM (2008) Study of electrical and dielectric properties of styrene-acrylonitrile/graphite sheets composites. Eur Polym J 44(7):2367–2375

Ramirez I, Jayaram S, Cherney EA et al (2009) Erosion resistance and mechanical properties of silicone nanocomposite insulation. Trans IEEE DEI-16(1):52–59

Paquette JW, Kim KJ, Nam JD et al (2003) An equivalent circuit model for ionic polymer-metal composites and their performance improvement by a clay-based polymer nanocomposite technique. J Intell Mater Syst Struct 14(10):633–642

Reddy CC, Ramu TS (2008) Polymer nanocomposites as insulation for HVDC cables – Investigations on the thermal breakdown. Trans IEEE DEI-15(1):221–227

Roy M, Nelson JK, MacCrone RK et al (2007) Candidate mechanisms controlling the electrical characteristics of silica/XLPE nanodielectrics. J Mater Sci 42(11):3789–3799

Roy M, Nelson JK, MacCrone RK et al (2005) Polymer nanocomposite dielectrics – The role of the interface. Trans IEEE DEI-12(4):629–643

Saeed MB, Zhan MS (2006) Adhesive and mechanical properties of nanoparticle filled thermoplastic polyimide dielectric films for microelectronics packaging. Int Conf Emerging Techn ICET '06: 342–347

Sauers I, James DR, Ellis AR et al (2004) High voltage studies of dielectric materials for HTS power equipment. Trans IEEE DEI-9(6):922–931

Schneider TR (1991) Energy applications of superconductivity. Annu Rev Energy Environ 16:533–555

Schwenterly SW, McConnell BW, Demko JA et al (1999) Performance of a 1-MVA HTS demonstration transformer. Trans IEEE AS-9(2):680–684

Schwenterly SW, Mehta SP, Walker MS et al (2002) Development of HTS power transformers for the 21st century: Waukesha Electric Systems/IGC-SuperPower/RG&E/ORNL SPI collaboration. Physica C 382(1):1–6

Simoes R, Silva J, Vaia R et al (2009) Low percolation transitions in carbon nanotube networks dispersed in a polymer matrix: dielectric properties, simulations and experiments. Nanotechnology 20(3):035703

Shi JL, Hua ZL, Zhang LX (2004) Nanocomposites from ordered mesoporous materials. J Mater Chem 14:795–806

Smith RC, Liang C, Landry M et al (2008) The mechanisms leading to the useful electrical properties of polymer nanodielectrics. Trans IEEE DEI-15(1):187–196

Srivastava NK, Mehra RM (2008) Study of structural, electrical, and dielectric properties of polystyrene/foliated graphite nanocomposite developed via in situ polymerization. J Appl Polym Sci 109(6):3991–3999

Tagami N, Okada M, Hirai N et al (2008) Dielectric properties of epoxy/clay nanocomposites – Effects of curing agent and cay dispersion method. Trans IEEE DEI-15(1):24–32

Takala M, Karttunen M, Pelto J et al (2008a) Thermal, mechanical and dielectric properties of nanostructured epoxy-polyhedral oli-gomeric silsesquioxane composites. Trans IEEE DEI-15(5):1224–1235

Takala M, Karttunen M, Salovaara, P et al (2008b) Dielectric properties of nanostructured polypropylene-polyhedral oligomeric silsesqui-oxane compounds. Trans IEEE DEI-15(1):40–51

Takezawa Y, Akatsuka M, Farren C (2003) High thermal conductive epoxy resins with controlled high order structure. Proceedings of the 7th international conference on properties and applications of dielectric materials, vol 3, pp 1146–1149

Tan Q, Irwin P, Cao Y (2006) Advanced dielectrics for capacitors. IEEJ Trans Fundam Mater 126(11):1153–1159

Tanaka T, Matsuo Y, Uchida K (2008a) Partial discharge endurance of Epoxy/SiC nanocomposite. Conf on Elect Ins and Diel Phen, pp 13–16

Tanaka T, Ohki Y, Ochi M et al (2008b) Enhanced partial discharge resistance of epoxy/clay nanocomposite prepared by newly developed organic modification and solubilization methods. Trans IEEE DEI-15(1):81–89

Tomer V, Randall CA (2008) High field dielectric properties of anisotropic polymer-ceramic composites. J Appl Phys 104(7):074106

Tuncer E, Gubanski SM (2000) Electrical properties of silicone rubber. J Phys Condens Matter 12(8):1873–1897

Tuncer E, Sauers I, James DR et al (2007a) Electrical properties of epoxy resin based nanocomposites. Nanotechnology 18(2):025703

Tuncer E, Rondinone AJ, Woodward J et al (2009) Cobalt iron-oxide nanoparticle modified poly(methyl methacrylate) nanodielectrics. Appl Phys A 94(4):843–852

Tuncer E, Sauers I, James DR et al (2007b) Enhancement of dielectric strength in nanocomposites. Nanotechnology 18(32):325704

Tuncer E, Sauers I, James DR et al (2008) Nanodielectric system for cryogenic applications: barium titanate filled polyvinyl alcohol. Trans IEEE DEI-15(1):236–242

Ul Haq S, Jayaram SH, Cherney EA (2007a) Evaluation of medium voltage enameled wire exposed to fast repetitive voltage pulses. Trans IEEE DEI-14(1):194–203

Ul Haq S, Jayaram SH, Cherney EA (2007b) Performance of nanofillers in medium voltage magnet wire insulation under high frequency applications. Trans IEEE DEI-14(2):417–426

Usuki A, Koiwai A, Kojima Y et al (1995) Interaction of nylon-6 clay surface and mechanical-properties of nylon-6 clay hybrid. J Appl Polym Sci 55:119–123

Usuki A, Kojima Y, Kawasumi M et al (1993a) Synthesis of nylon-6 clay hybrid. J Mater Res 8:1179–1184

Usuki A, Kawasumi M, Kojima Y et al (1993b) Swelling behavior of montmorillonite cation exchanged for ω-amino acids by ε-caprolactam. J Mater Res 8(5):1174–1178

Wang JW, Wang Y, Wang F et al (2009) A large enhancement in dielectric properties of poly(vinylidene fluoride) based all-organic nanocomposite. Polymer 50(2):679–684

Wang CC, Song JF, Bao HM et al (2008) Enhancement of electrical properties of ferroelectric polymers by polyaniline nanofibers with controllable conductivities. Adv Funct Mater 18(8):1299–1306

Weber CS, Reis CT, Hazelton DW et al (2005) Design and operational testing of a 5/10-MVA HTS utility power transformer. Trans IEEE AS-15(2):2210–2213

Winey KI, Vaia RA (2007) Polymer nanocomposites. MRS Bull 32:315–319

Xie W, Xie R, Pan WP et al (2002) Thermal stability of quaternary phosphonium modified montmorillonite. Chem Mater 14(11):4837–4845

Xiong J, Liu Y, Yang X et al (2004) Thermal and mechanical properties of polyurethane/ montmorillonite nanocomposites based on a novel reactive modifier. Polym Degrad Stab 86(3):549–555

Xiong J, Zheng Z, Jiang H et al (2007) Reinforcement of polyurethane composites with an organically modified montmorillonite. Compos A Appl Sci Manuf 38(1):132–137

Zhang MY, Zeng SJ, Dong TQ et al (2007) Synthesis and characterization of polyimide/silica nanocomposite films. IEEE International Conference on Solid Dielectrics ICSD'07, pp 357–359

Zhou H, Fan Y, Lei Q (2006) Synthesis and characterization of corona-resistant polyimide/alumina hybrid films. 8th international conference on properties and applications of dielectric materials, pp 736–738

Appendix A
Diagnostic Methods for Mechanistic Studies in Polymer Nanocomposites

A.1 Dielectric Spectroscopy

The representation of a dielectric material in its simplest case by a capacitor and resistor in parallel immediately implies that the current through such a medium must have both an in-phase (real) and a quadrature (imaginary) component. This can conveniently be taken into account by defining the relative permittivity, ε_r^*, as having real and imaginary terms:

$$\varepsilon_r^* = \varepsilon' - j\varepsilon'' \tag{A.1}$$

where ε' represents the "conventional" permittivity and ε'' represents the loss component. Power factor measurements made on both equipment and materials samples used to be undertaken using a power frequency bridge, such as a Schering bridge which could be operated, if necessary, at high voltage, providing the loss tangent of the object given by:

$$\tan\delta = \frac{\varepsilon''}{\varepsilon'} \tag{A.2}$$

However, modern instrumentation now allows the real and imaginary parts of the permittivity to be obtained continuously and automatically over a very wide frequency band (typically from 10^{-5} to 10^{7} Hz). Since many of the physical processes in polymers are also temperature activated, it is also usual to undertake such measurements as a function of an appropriate temperature range. Indeed, one can often obtain the activation energy for such processes from dielectric spectroscopy taken at a number of different temperatures.

When a sinusoidal electric field is imposed across a dielectric, a series of frequency and temperature dependent polarization processes occur which result in decreases in dielectric permittivity until, at the very highest (optical) frequencies the material displays a permittivity which is related approximately to the optical refractive index, n.

$$\varepsilon' \approx n^2 \tag{A.3}$$

Detailed treatments are available elsewhere (Bartnikas 1983; Jonscher 1983; McCrum 1967; Raju 2003), but the frequency dependent dispersions which can

be observed are related to a number of different polarization process (optical, ionic, dipolar, etc.) and usually mirrored with loss peaks in the ε'' spectrum associated with the viscous processes required to move or orientate the species involved. In particular, the classical Debye process for a single relaxation of dipolar segments in the molecular structure yields a dispersion which is given by:

$$\begin{aligned} \varepsilon' &= \varepsilon_\infty + \frac{\varepsilon_s - \varepsilon_\infty}{1 + \omega^2 \tau^2} \\ \varepsilon'' &= \frac{\omega \tau \left(\varepsilon_s - \varepsilon_\infty\right)}{1 + \omega^2 \tau^2} \end{aligned} \tag{A.4}$$

where τ is the time constant associated with the relaxation process and ε_s and ε_∞ are the static and infinite frequency permittivities.

A wealth of processes may be discerned through this technique. For example, movement of short chain segments (of perhaps 1 or 2 nm) becomes evident above the amorphous glass transition temperature in semi-crystalline polymers (Many and Rakavi 1962), while a well-defined low-frequency peak in the loss permittivity ε'' can indicate that dipolar impurities (e.g., water, especially significant in a nominally non-polar polymers like polyolefins (Schonahls 1998)) have found their way into the material during processing.

For composites, in particular, the surface area introduced by the particles can lead to interfacial polarization which is seen by dielectric spectroscopy at low frequencies as a Maxwell-Wagner-Sillars process due to the accumulation of carriers between the regions of different conductivity and/or permittivity, resulting in an increase in the apparent real electric permittivity ε', as well as an increase in the imaginary ε'' in the low frequency regime, in which conduction toward these interfaces is taking place. Analysis of interfacial polarization yields equations which are of the same form as the Debye equations introduced above, except that an additional term is seen in the imaginary permittivity which dominates at low frequencies and for which ε'' characteristically decays as ω^{-1} as shown schematically in Fig. A.1. The issue of sub-Hertz spectroscopy is important in the context of polymer composites and has recently been reviewed (Fothergill et al. 2005).

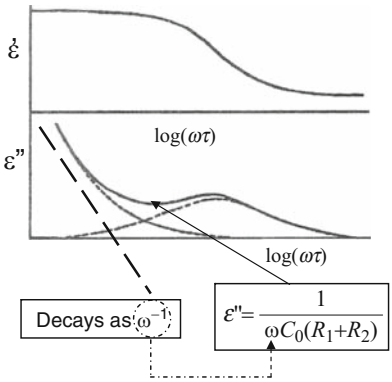

Fig. A.1 Idealized variation of a resonant dispersion process in a dielectric, including the effects of interfacial polarization seen at low frequencies

When considering the dielectric spectroscopy of real polymers, it becomes clear that the above illustrations are both idealized and greatly simplified. First, the various phenomena that do occur are not always well decoupled (i.e. separated in frequency), so it can be difficult to discern the individual constituents that create the overall shape of a ε' or ε'' vs. frequency plot. As a result, response curves can appear to have characteristics of both charge migration and dipole alignment happening at approximately the same frequency. In addition, as the frequency of the applied electric field is decreased, there is the possibility of *low frequency dispersion*, where, along with the imaginary permittivity increase dictated by conduction, there is also an increase in the real permittivity as a result of the interfacial buildup of charge in the form of polarization layers near the electrodes, or at bulk heterogeneities (such as particles) and there may also be percolative charge migration at low frequencies. It is important to note, however, that the dielectric spectroscopy experiment is usually conducted at very low applied fields ($\sim$10 V mm^{-1}), and, consequently, any space charge that does build up within the material is almost surely there before the experiment is started, or is generated via dissociation, since the threshold for significant charge injection for most polymers is several kV mm^{-1}.

While systematic and mathematics-intensive methods for the deconstruction of permittivity data plots into constituent relaxations do exist, a purely empirical expression, proposed by Havriliak and Negami, is often used (Raju 2003):

$$\frac{\varepsilon_\omega - \varepsilon_\infty}{\varepsilon_0 - \varepsilon_\infty} = \frac{1}{(1 + (j\omega\tau)^\alpha)^\beta} \tag{A.5}$$

α and β are values between zero and unity, and describe the amount of symmetric and asymmetric broadening from the Debye response ($\alpha = \beta = 1$).

While the emphasis here is clearly on the processes occurring at the composite internal interfaces, it is appropriate to indicate that the technique has also been used to good effect to monitor polymer curing (Jonscher 1983), aging processes, crystallization, etc.

A.2 Pulsed Electroacoustic Analysis

The pulsed electroacoustic (PEA) method is one of a family of techniques (identified in Sect. 10.4) that may be used to examine the magnitude, distribution and dynamics of charges in the bulk of a stressed dielectric. This is covered here at some length since it is clear that modifications to the internal charge distribution occasioned by the use of nanoparticles is a fundamental result and thus can provide valuable mechanistic insight and data on charge carrier dynamics (Mazzanti et al. 2003). The topic is also the subject of a specialized text (Fothergill and Dissado 1998), and the results have to be interpreted with care. The PEA method (Alison 1998) provides an evaluation of the space charge density in polymeric materials by measuring the sound wave initiated from the charge when perturbed by an electric pulse.

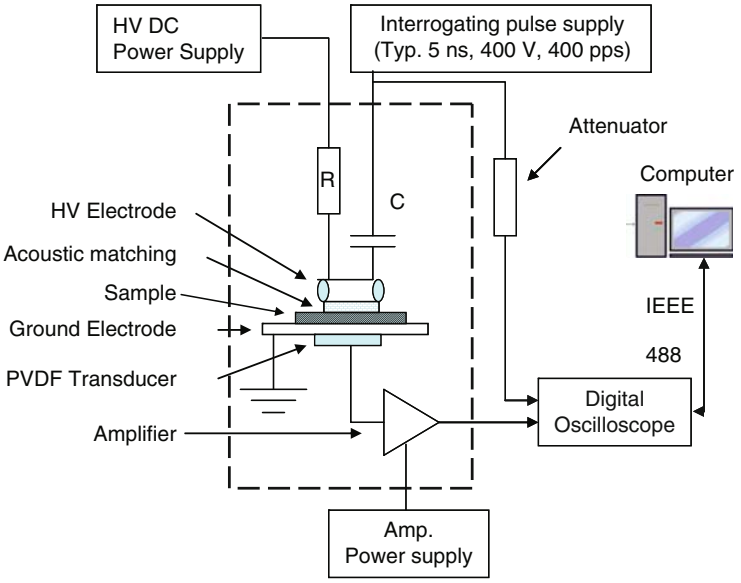

Fig. A.2 Block diagram of a typical basic PEA System (diagrammatic only)

Figure A.2 presents a PEA system in block diagram form. A thin laminar sample of the material under test is placed in a special test cell (shown by the broken line in Fig. A.2) and an electric field established, from a high-voltage supplied through a limiting resistor, R, to build up space charge. A fast interrogating pulse is coupled to the sample through a capacitor, C, and the resulting acoustic oscillations are measured with a PVDF transducer and amplifier as shown in Fig. A.2. An oscilloscope records these measurements, improves the sensitivity through signal averaging, and passes the information to a computer program for processing.

The propagation speed of sound in the material, along with its electric permittivity ε_r, are both needed to translate the raw signals into a one-dimensional charge density profile, $\rho(x)$ using a spatial deconvolution algorithm. Since the Laplacian (i.e. applied) electric field (V/d) is known, one can also calculate an electric field profile along the thickness based on Poisson's equation:

$$E(x) = \int \frac{\rho(x)dx}{\varepsilon_0 \varepsilon_r} \tag{A.6}$$

The charge density and/or electric field profile can be determined for any time of interest after the application of the field, or after its removal.

When an electric field is applied to a laminar dielectric sample, the material will polarize resulting in a large image charge appearing at the electrodes. However, if the field is sufficiently high that injection occurs from the electrodes, then charges can be accumulated in the bulk which can be seen, in both magnitude and distribution, from the PEA signal. Such injected charge will both change the magnitude of

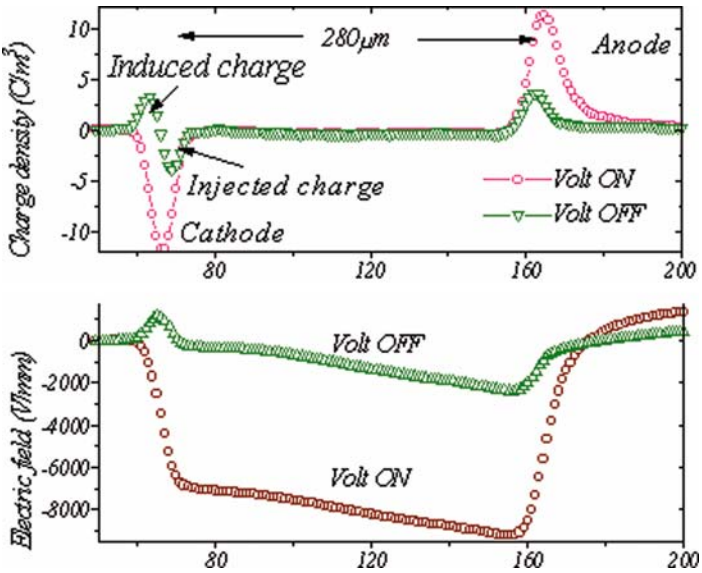

Fig. A.3 Example of charge and field profiles from PEA measurements with the voltage applied and removed (Griseri 2000)

the image charge on the electrodes and distort the bulk $\underline{E}$-field. These features are shown in Fig. A.3 which also shows the plot obtained after the voltage is removed. In this instance, the polarization charge quickly decays and renders any trapped charge (and its image on the electrodes) more visible. In the example given here, negative charge (homocharge) has been injected from the cathode and has depressed the $\underline{E}$-field in front of the cathode by shielding action.

While the PEA method provides a basis for examining the injection of charge into polymers, if the image charges are examined as a function of the applied stress, the injection threshold and the magnitude and sign of the charge can readily be quantified by examining departures from linearity. Prior to significant injection a linear characteristic would be expected with departures occurring at the injection threshold as have been depicted in Fig. 10.4 in the process of considering the mechanism of charge injection and transport in nanodielectrics.

A.2.1 Experimental Details

There are some requirements for the electric pulse characteristics if useful measurements are to be obtained. First of all, the width of the pulse voltage must be shorter than the transit time across the sample in order to be able to detect the internal charge distribution. The transit time is the ratio of the distance to the speed of the acoustic wave (d/s), and is an intrinsic property of the sample. The magnitude

of the interrogating pulse must be limited to a few percent of the DC field applied to the specimen. Typically a 5 ns pulse of a few hundred volts with a repetition frequency of about 300 s^{-1} would be appropriate. A general feature of the measurement method is that the acoustic wave generated and detected has the same shape as the HV electric pulse applied. It is then important to apply a narrow electric pulse in order to create a narrow acoustic pulse to propagate through the bulk. In other words, to improve the spatial resolution of the charge distribution it is necessary to reduce the width of the acoustic signal detected. This can be achieved by reducing the length of the applied electric pulse. Usually the resolution is measured in terms of "half width" for the signal detected from the electrodes, but, because it is difficult to distinguish the charges in the "width", the resolution is, in practice, limited within the range of several microns.

The acoustic impedance of the sample and the HV electrode must also match in order to retain the narrow shape of the pulse that is transmitted in the bulk of the polymer under investigation. This is achieved by inserting a piece of semiconducting impedance matching material, usually PVC, between the top electrode and the polymeric film. This procedure prevents any reflection and loss of the signal at the sample-electrode interface.

The detection system in the PEA technique is a piezoelectric transducer, coupled to a reflection absorber. Typically, the transducer is often a highly polar Poly-Vinylidene Fluoride (PVDF) film that is located in the bottom electrode. PVDF offers a wide frequency range of dynamic response and low acoustic impedance compared to conventional ceramic transducers. The voltage generated by the transducer is amplified by a low noise, wideband amplifier and recorded by a digital storage oscilloscope connected to a computer. The voltage trace observed on the screen is the representation of the pressure wave profile and is not directly proportional to the charge distribution in the sample. To reach the correct profile a signal processing calculation step is required.

Because of a high pulse repetition rate, it is possible to make a running average over many measurements sufficient to give an accurate update of the signal over intervals of a few seconds. Thus it is possible to measure the space charge density as a function of time during voltage application and the decay after its removal. The minimum charge density that can be detected is about 0.1 C/m^3, although it depends somewhat on the noise level. This value corresponds to one electric charge per 10^{11} atoms, and such a charge would be able to distort the electric field by 5 kV/mm over a thickness of 1 mm. The typical resolution is about 10 μm.

The method may also be used for alternating current stresses through a phase-resolved embodiment of the technique (Bamji et al. 2006).

A.2.2 Signal Processing and Calibration

If a high direct voltage is applied to a sample containing no space charges, the sample capacitance causes surface charges to be built up on both sides of the sample.

This surface charge density, σ, would be expected to be a delta-function (δ) of the volume space charge density, but, due to the limit in the resolution of the detection apparatus and the finite width of the interrogating electric pulse, the induced surface charge signals appear as broadened peaks - positive at the anode and negative at the cathode. Molecular dipoles can be regarded as possessing a zero net charge within the spatial limits of resolution of the PEA technique. They, therefore, do not contribute to the bulk signal as long as they are uniformly distributed in space.

In order to reach a resolution of a few μm, signal processing is necessary. It is performed by means of a computer that introduces a measured reference to correct the response. In the case of the signal originating on the top electrode the modification of the pulse during propagation of the acoustic wave through the sample should be taken into account. Once this is done the integration of the area below the peak gives correct results for the surface charge density. The electric field, $\underline{E}(x)$, and the voltage, $V(x)$, are calculated by integration of the charge density. The electric field should be zero on the electrodes. When a dielectric material is inserted between two plane electrodes with a DC voltage V_0 applied, the internal electric field is initially constant and defined as $E_0 = V_0/d$ in the absence of space charge; where d is the thickness of the sample. Molecular dipoles will be oriented by the applied field but not give a field distortion as long as they are uniformly distributed in space. They do, however, induce a corresponding charge on the electrodes, with the same polarities as that which would be produced by a heterocharge region built-up close to the electrodes. Experimentally, it has been observed that, due to a mismatch of acoustic impedance between the sample and the electrode, the values of $\underline{E}(x)$ can be slightly different from zero and then some corrections are necessary for the calculation.

In the presence of net internal charges, a Coulomb force appears when the pulse voltage is applied. This induces a perturbation force proportional to the local net charge that is transmitted to the system instantaneously. The pressure wave propagates through the insulator as two components traveling in opposite directions. The component that reaches the lower electrode is transmitted to the detection system. The pressure of the acoustic wave thus detected is proportional to $\rho(x)$ the one dimensional charge density distribution in the material. The signal reaching the side in contact with the top electrode is time delayed due to the necessary propagation across the sample before it reaches the bottom electrode of the apparatus where the detector is located.

In this way, if charge is present in front of the electrodes or is injected into the bulk, then its location and sign becomes visible, and the image charges on the electrodes will become modified appropriately (the closer the space charge to a given electrode the larger the charge it induces on that electrode). However, it often happens that small amounts of injected charge are masked by the polarization of the dielectric. It is thus often efficacious to examine the charge distribution after the applied stress has been removed and the short-lived polarization has decayed as depicted in Fig. A.3. In the case shown in Fig. A.3, the negative charge in front of the cathode (homocharge) is clearly visible and has resulted in a depression of the cathode field. The only way to obtain an accurate charge distribution profile in the sample is by using a calibration technique, and, consequently, a reference sample

is used which is often different from the one studied. The calibration consists in the determination of the interface charge due to the application of a DC voltage, V_0, which does not produce injected charge. In reality, the output signal recorded is likely to be independent of the material because it is caused by the electrostatic force generated at the interface (electrode/sample). The only parameters used are the sample thickness and sound velocity, but it is assumed that the system has a linear response. As a practical matter, polymethyl methacrylate (PMMA) is often used for calibration since it does not significantly attenuate or distort the acoustic wave during the propagation and, more importantly, the accumulation of internal charge is not observed in the condition used for the calibration. Once the voltage calibration has been undertaken, $\rho(x)$ can be calculated by one of several integration and Fourier transformations. The reader is referred to Alison (1998) for further details on the method and the theory of the associated deconvolution.

A.3 Thermally Stimulated Currents

The non-isothermal dielectric relaxation behavior of polymers may be used to study both the nature of permanent dipoles and also charges trapped in the material. Since dielectric relaxation is inherently characterized by the hindrance of the motion of charges by frictional forces that are a strong function of temperature, it follows that the response time of dipoles and charges will also be temperature dependent. This is the basis for the thermally stimulated currents (TSC) method which seeks to obtain a fingerprint of these processes through the thermal activation of bound and free charges. The method is the subject of a comprehensive treatise by Van Turnhout (1975) and much of the experimental work to establish the technique was carried out in Japan (Ieda et al. 1980). Since there is increasing evidence that the internal interface regions in nanodielectrics provide sites for carrier traps, this technique can be used to probe the interaction zone by examining the temperature-activated movement of stored charge in the interfacial regions surrounding the particles.

A.3.1 Methodology

In the simplest form of the measurement, a poling field is applied to a dielectric thin film for some period of time. The material is then cooled with the poling field in place. The temperature to which the sample is cooled is dependent on the objectives of the measurement, but, if the molecular motions associated with glass transition are being studied, then, clearly, the temperature needs to be low enough to put the material into its glassy state. The poling stress is then removed and the material short circuited through a sensitive electrometer while the temperature is slowly and uniformly ramped (typically at $\approx 2^{\circ}$C per minute). This protocol is depicted diagrammatically in Fig. A.4.

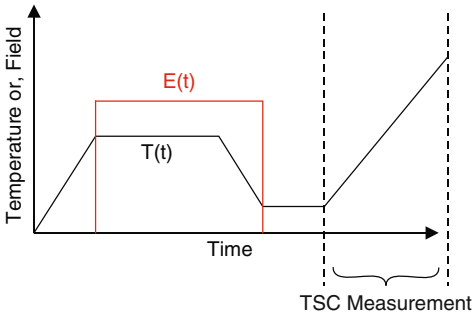

Fig. A.4 Temperature and applied electric field profile over time utilized for the TSC method. The range over which TSC spectra (current versus temperature) are determined is demarcated

Since the dielectric current I_δ for some relaxation process δ tends to be temperature activated with an energy E_δ, TSC current peaks can be fitted to an Arrhenius curve $I_\delta = I_{0,\delta} \frac{E_\delta}{kT}$ (k is the Boltzmann constant, T the temperature, $I_{0,\delta}$ a constant) to determine that energy. Oriented dipole relaxation, carrier release from traps, and ionic migration can all contribute to the relaxations. During poling, both polarization and true charges are "frozen" in place, and the external current reflects the change in compensating charge on the electrodes as the material is warmed and the charges relax or move about.

While there is some correspondence between TSC peaks and relaxations measured via dielectric spectroscopy, the experimental principles are different, and thus the spectroscopy experiment must be conducted at low frequencies to observe this correspondence. According to the equivalent frequency method, the required dielectric spectroscopy experimental frequency is given by (Suh et al. 1992)

$$\omega_{DS} = \frac{R_h E_\delta}{k T_m^2} \tag{A.7}$$

where R_h is the TSC heating rate (°K/s) and T_m is the temperature at which the peak occurs. For an activation energy of 1 eV, a heating rate of 3°C/ min, and a TSC peak temperature of 70°C, the equivalent dielectric spectroscopy frequency is of the order of 1 mHz. Since the collection of spectroscopic data at that frequency and at several temperatures requires considerable time, the TSC experiment may be considered a higher-resolution alternative to spectroscopy for the determination of the activation energy. A number of methods are available for estimating the carrier trap depth from TSC data (Maeta and Sakaguchi 1980).

Variations of the basic technique have also been employed. These include poling the material with a corona source, an e-beam or by the application of X-rays. Similarly, detrapping can also be accomplished using a monochromatic light source to bring about photoexcitation and the resulting current monitored (Ieda et al. 1980). Procedures for "thermal cleaning" or fractional polarization (Neagu and Neagu 2004) have also been successfully used to separate peaks in cases where the energies of several traps are close together.

A.4 Electron Paramagnetic Resonance

Electron transport in undoped polymer dielectrics takes place by electrons moving between traps or localized states. The term impurity conduction, used here, denotes the tunneling or hopping of electrons from filled donors to empty acceptors without thermal ionization into the conduction band. Despite the recognition that impurity conduction is important in polymeric insulators, and extensive literature discussion of the trapping of charge in localized traps, the actual donor and acceptor trap sites have eluded direct spectral and structural identification. For example, in the case of thermally stimulated currents, the estimation of the trap site activation energy is deduced from the results, but the actual nature of the trap site is not. One method for probing these electrically active sites is Electron Paramagnetic Resonance (EPR). In this technique, a magnetic field on the sample, placed in an X-band microwave cavity, is increased until the energy difference between the spin-up and spin-down orientations, which are also affected by the local environment, match the microwave frequency of the instrument. Strong absorption is then detected.

A.4.1 Experimental Method

The principle of the EPR technique has been previously described (Wolter et al. 1987) and a representative configuration is depicted in Fig. A.5. The application of

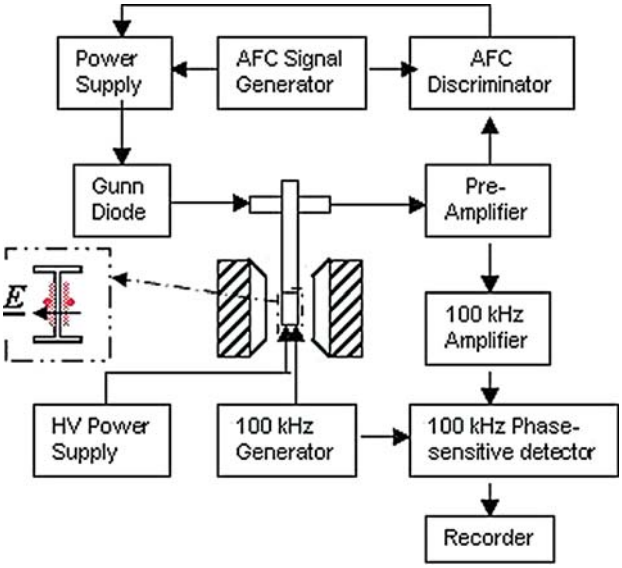

Fig. A.5 A schematic of the EPR arrangement – sample configuration shown in the *insert* allows simultaneous application of electric field

electric fields to a polymer specimen while being scanned in the microwave cavity of the EPR spectrometer requires a special "I"-shaped sample to achieve large creep surfaces to accommodate the high-voltage (see *insert* of Fig. A.4). Note that the polymer chains will likely be oriented vertically in the web due to flow during molding. Thus when the magnetic field is parallel to the electric field, it will be across the chain direction and when the magnetic field is perpendicular to the electric field, it will be along the chain direction. EPR provides information on the concentration and structure of free radicals. The unpaired electrons in a sample create a magnetic field, and one can thus apply a magnetic field and measure the energy, ΔE, required to flip states (parallel or anti-parallel)

$$\boldsymbol{\Delta} E = \boldsymbol{g}\boldsymbol{\beta}\underline{\boldsymbol{H}} \tag{A.8}$$

(β is the magnetic moment and $2.002 < g < 2.004$).
The energy is supplied by orthogonal microwave radiation at a critical frequency to meet the resonance condition:

$$\boldsymbol{h}\boldsymbol{\nu} = \boldsymbol{g}\boldsymbol{\beta}\underline{\boldsymbol{H}} \tag{A.9}$$

However, as a practical matter, the microwave (X-band) frequency, $\boldsymbol{\nu}$, is kept constant and the magnetic field intensity, $\underline{\boldsymbol{H}}$, is swept over the range of interest to meet this condition At particular values of magnetic field (depending on the radicals present) absorption of energy occurs and is detected in the intensity of the reflected microwave beam.

A.4.2 Interpretation

In the simplest case of spin only, a very sharp peak and trough line would be observed. On the scale of the signals here, the peak and trough (only a few mT wide) would not be resolved. Fortunately, in the cases involved with dielectrics, the signal arises from oxygen radicals in a tetragonal orthorhombic environment. The EPR parameters depend on the details of the chemical bonding. A random orientation of such a set of moieties gives rise rather to a very broad (25–50 mT) asymmetrical peak. For this, such a set is identified by the location of the low field maximum on the magnetic field axis.

Polymer nanocomposites based on silicon dioxide have previously (Roy et al. 2005) been shown to be rich in oxygen radicals. It is important to note that:

- There can be several different structural types of oxygen radical species present,
- Each type of oxygen radical species is associated with a unique donor or acceptor energy, and
- There were few organic radicals, or defects, that could be detected that are associated with the carbon atoms of the organic polymer itself.

Identifying qualitatively and quantitatively the acceptor and donor traps around the nanoparticles may involve not only ions, but also states responsible for impurity con-

duction. To prove this conclusively requires that the filled donor and empty acceptor concentration changes induced by an electric field be monitored. This implies in situ measurements. Consider a simple model shown below of five oxygen radicals.

$$\mathbf{O}(.)\text{–}\mathbf{O}(.)\text{–}\mathbf{O}(.)\text{–}\mathbf{O}(.)\text{–}\mathbf{O}(.)$$

Here the (.) represents an unpaired (EPR active) electron spin on the oxygen. The EPR spectrum of this structure would have a relative amplitude of 5. On polarization the electron arrangement might be:

$$\mathbf{O}()\text{–}\mathbf{O}(.)\text{–}\mathbf{O}(.)\text{–}\mathbf{O}(.)\text{–}\mathbf{O}(..)$$

now having a relative amplitude of 3. This predicted decrease in EPR intensity is considerably more general than the very specific model used above might imply. The instrument plots the derivative of the imaginary part of the magnetic susceptibility as a function of field, and the resulting spectra can be interpreted since:

(a) The intensity of absorbance depends on the radial concentration, and
(b) The structure of the radial is determined by energy level splitting which can be extracted from the spectra.

A.5 Dielectric Absorption

If a step voltage is applied to a dielectric there will be a charging transient corresponding to the sample capacitance followed by a slowly decreasing current transient until a steady-state dc value is attained. This process is referred to as dielectric absorption. For a linear dipolar material, this transient current is related to the dielectric constant, $\varepsilon'(\omega)$, in the frequency domain through the Kramers-Kronig relations (Raju 2003) and so such absorption current measurements may be used to supplement dielectric loss determinations described in Sect. A.1 in the sub Hertz region. The slow decrease of current towards its conduction value generally follows a shape given by the Curie-von Schweidler Law $I(t) = At^{-n}$, where $A = A(T)$ and $n(\sim 1)$ are constants under isothermal conditions (Guo and Guo 1983). Factors which are believed to influence the absorption current response are the buildup of space charge, slow polarization (i.e., from dipolar species rotating in the applied electric field), the migration and accumulation of charges at heterogeneities, and the hopping of charges between localized states (Das-Gupta and Brockley 1978). Changes in slope of the discharging current at longer times can be illuminating. An increase in the value of n is usually attributed to a dipolar mechanism, whereas a reduction is indicative of interfacial polarization and is common with conventional (micro)composites. Subsequent removal of the poling voltage and shorting of the sample terminals results in a similar current decay, except of the opposite sign, although the presence of space charge can disrupt the symmetry between the charging and discharging (desorption) tests (Wintle 1974).

The experimental arrangement required is very simple. The sample is usually placed between plane-parallel guarded electrodes to which the high direct-voltage source is applied. The current flowing in the dielectric is then measured using a sensitive electrometer and data logger. Such absorption measurements can often be used to good effect when combined with space charge determinations (see Sect. A.2) and as a relative measure of dielectric aging (Neagu and Marat-Mendes 2001). Furthermore, frequency dependent loss can be estimated from desorption data through Hamon's approximation (Raju 2003). Unlike dielectric spectroscopy which is typically conducted under low-field conditions, the desorption curves can contribute loss vs. frequency information at electric field intensities that are more realistic when considering real electrical equipment and systems.

If care is taken in measuring the absorption current at short times, it is also possible to use transit time methods to estimate the carrier mobility (Many and Rakavy 1962) although the accuracy has been questioned (Wintle 1983). The method relies on a slope change in the J vs. t curve at some time t_{p} which is taken to reflect the arrival, at the measuring electrode, of a *front* of charge. The charge mobility μ in a sample of thickness d, across which a voltage V is impressed is given by

$$\mu = \frac{0.786 d^2}{t_p V} \tag{A.10}$$

Charge mobility is an important parameter in describing the particle interfacial zones; particularly as percolation of these regions is approached.

A.6 Spectrally-Resolved Electroluminescence

Polymers can undergo electroluminescence when highly stressed. However, it is important to distinguish light emitted by this process from that due to partial discharge taking place in the structure. Electroluminescence is a solid state process in which photons are generated in two general ways:

- The recombination of charge of opposite polarities in the same region, or
- The emission of light from luminescence centers subjected to hot carrier process (impact excitation or ionization).

The excitation is provided by supplying either potential (recombination) or kinetic (hot carrier) energy, or both. In the context of polymers under an electric field, carriers can be generated by injection from the electrodes, by electro-dissociation or by internal detrapping. Typically an excited species can be formed through a "hot" electron interaction represented in a molecular approach as:

$$AB + e^-_{hot} \rightarrow AB^* + e^-_{th} \tag{A.11}$$

yielding the excited species, AB^*, and a thermalized electron, $e_{th}{}^-$. Excited carriers can lose energy by many different pathways during which light can be emitted and electroluminescence can be detected. The reader is referred to the substantial

body of literature which provides guidance on the likely pathways and luminescent centers in a range of polymers (Laurent et al. 1997; Teyssèdre et al. 1999; Griseri et al. 2001). Detailed interpretation can be difficult if the luminescent centers are not known a priori, and because of the multiple pathways available. However, if the spectral quality of the light can also be determined, then the value of the technique is much enhanced.

A.6.1 Experimental Details

The technique, although straightforward, is complicated by the fact that fields required for emission are often close to those required for breakdown, and because the level of light emission in polymers is very low indeed. The situation is further complicated for those materials which are opaque at the wavelengths emitted. The paucity of the emission will often not permit the use of a monochrometer, but dictates that a sensitive multi-dynode photomultiplier tube (PMT) is used as a detector, and spectral resolution obtained, coarsely, through the use of calibrated interference filters. A block diagram of a basic system is shown in Fig. A.6. The output of the PMT (which is sometimes cooled to reduce the dark currents) is recorded by a scintillation counter or multi-channel analyzer. The gating circuit is required to prevent the photocathode being damaged by light emission from partial discharges accidentally occurring during the conduct of the experiment. The arrangement in Fig. A.6 shows a specimen in which the electrodes form a point-plane gap as depicted in Fig. A.7a. The needle may be fabricated by electrolytically etching tungsten to form a radius of curvature in the range 5–20 μm. In this way, the light emission can be localized to the high-field region surrounding the point electrode and collimating quartz optics (not shown) used to focus the light onto the

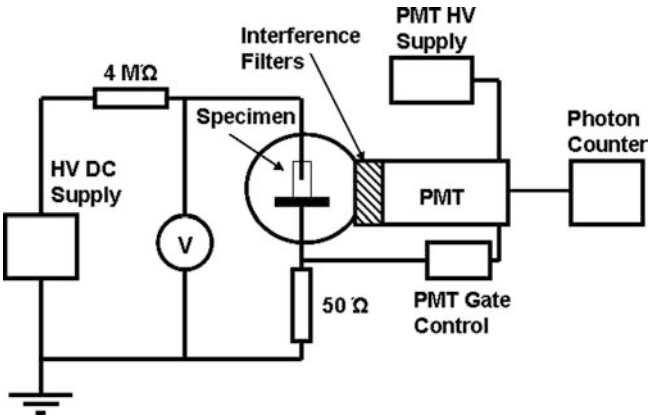

Fig. A.6 A block diagram depicting the elements of a typical basic electroluminescence experiment

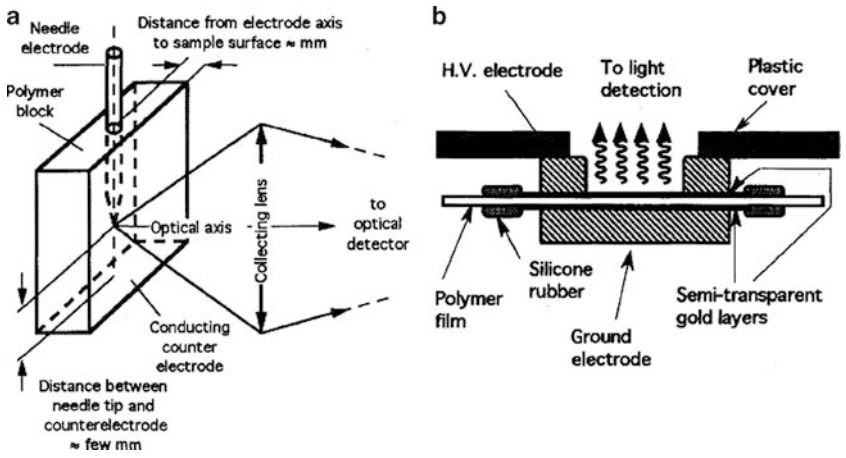

Fig. A.7 Arrangement for capturing electroluminescence in (**a**) divergent and (**b**) uniform electric fields (Laurent et al. 1997)

photocathode after passing through the optical filter. This arrangement solves the problem of the low light emission and the generation of high electric fields without breakdown, but the highly divergent field complicates the sample preparation and subsequent interpretation. Techniques developed by the group at the Université Paul Sabatier in France (Laurent et al. 1997) have permitted these measurements also to be undertaken in uniform fields using an annular arrangement with semi-transparent layers as shown in Fig. A.7b. This arrangement also allows the use of the PEA technique (see Sect. A.2) to track the internal charge accumulation but differentiation between bulk and electrode processes is problematical.

Spectrally-resolved results do need to be corrected for any wavelength dependent sensitivity for the photocathode being used. The technique can be applied for either direct or alternating voltage, but the mechanisms are not necessarily the same (Teyssèdre et al. 2001).

A.7 Infrared Spectroscopy

Infrared spectroscopy seeks to use the absorption of energy in the mid-infrared part of the electromagnetic spectrum (4,000–400 cm^{-1}) to identify compounds or investigate structure. This is achieved by exploiting the behavior of molecules which have very specific frequencies at which they rotate or vibrate. The resonant frequencies for these vibrational modes are determined by the energy levels involved, the masses of the atoms participating in the process and the associated coupling. In this way, the wavelength of a particular vibration can be associated with a particular bond type. Although a simple diatomic molecule may only have one bond capable of stretching, a complex molecule will have multiple bonds and modes of vibration

that will give rise to several infrared absorptions at characteristic wavelengths which can be used to pinpoint the structure. In studying spectral features, one can obtain information about functional groups, interatomic distances, bond-force constants, and molecular charge distributions. Generally, the frequencies for stretching are higher than those for bending since it is easier to distort a molecule by bending. A symmetrical stretching vibration which does not cause a changing dipole moment will be inactive in the infrared, but may be active in the Raman spectrum. Wavelengths are usually depicted as wavenumbers which are the reciprocal (with a unit of cm^{-1}).

A.7.1 Sample Preparation and Measurement

There are a number of ways that a sample may be prepared. However, for polymers specimens are usually prepared by casting into a film or by using a microtome to cut a thin film. The film must be sufficiently thin (20–100 μm) to allow the propagation of the light beam.

Conventionally, the beam of infrared light from a monochromator is split into two. One is passed through the sample to be investigated and the other through a reference. The two beams are then alternately fed to a detector and the signals compared and processed. However, most modern instruments use a Fourier Transform Infrared (FTIR) technique which is radically different from the conventional double beam refraction spectrometer. In the FTIR instrument the light is taken through a Michelson interferometer before passing through the sample. This is achieved by splitting the IR beam (derived from a heated ceramic source) and using a fixed and a continuously moveable mirror to form an interference pattern when the signals from the two phase-shifted arms are recombined. The measured signal is then an interferogram from which the spectrum can be extracted mathematically through Fourier transformation. Since all frequencies are collected simultaneously, the FTIR method is inherently faster.

A.7.2 Interpretation

Infrared spectroscopy is a well established analytical technique and tables of characteristic absorption peaks are tabulated in the literature. Some instruments have such databases of reference spectra built into the associated software to permit automated identification of spectral features.

The use of this technique for nanocomposites stems from the need to identify the nature of the coupling which is characteristic of the interface zones surrounding the particulates. An example is provided in Fig. A.8 depicting composites derived from both micro- and nano-epoxy composted utilizing TiO_2 (Nelson and Hu 2005).

The spectra show two major differences (arrowed in Fig. A.8) between the two composites at 600–700 cm^{-1} and 1,050–1,150 cm^{-1}. Around 1,070 cm^{-1}, the

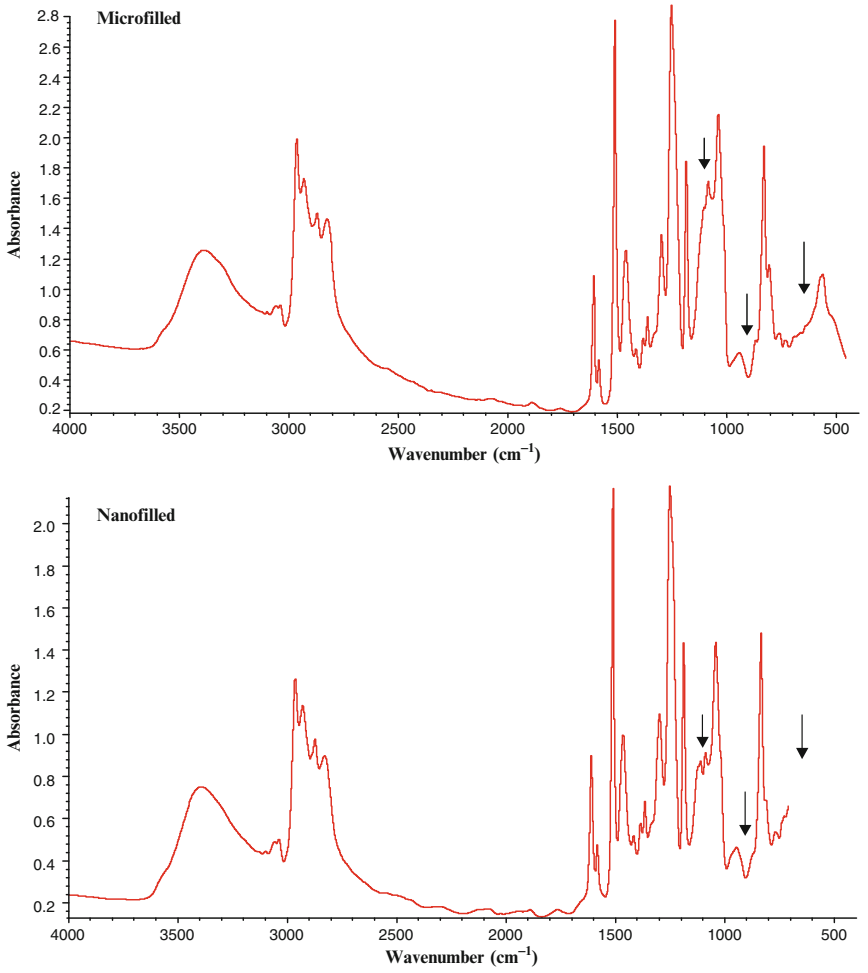

Fig. A.8 FTIR spectra of micro- and nanocomposites based on Epoxy-TiO_2 (Nelson and Hu 2005)

nanocomposite shows two low split peaks in contrast to the single high peak in the microcomposite. These two split peaks are also observed in the uncured resin in the same band. This shows that in the nanocomposite, fewer C–N bonds were produced in the curing process, which implies that the cross-link density in nanocomposites is less than in the equivalent micromaterial. The FTIR spectrum shows that both microparticles and nanoparticles have –OH groups on the surface. By adding particles to the polymer, the number of surface hydroxyl groups in the material is increased. If the concentration of hydroxyl groups is high enough, the epoxide rings will open up and react with the hydroxyl groups instead of with the amine groups. Due to the much larger surface area of nanometric particles, the –OH groups at the surface of the particles in the nanocomposite will be more than that in the microcomposite.

A.8 Differential Scanning Calorimetry

This is another standard technique which has become a useful tool for quantifying some of the physical and morphological aspects of nanocomposites. In particular the technique may be applied to the study of phase transitions, such as melting, glass transitions, or exothermic decompositions (Dean 1995). These transitions involve energy changes or heat capacity changes that can be sensitively detected by differential scanning calorimetry (DSC). Many of these attributes are affected by the addition of nanoparticles and by functionalization which makes the technique attractive in the study of nanodielectrics.

DSC is a thermoanalytical technique in which the difference in the amount of heat required to increase the temperature of a sample and reference (having a well-defined heat capacity over the range of temperatures to be scanned and often utilizing air) are measured as the temperature is increased linearly as a function of time. The differential heat flow to maintain both the sample and the reference at the same temperature can be endothermic, as might occur during a phase transition from solid to liquid, or exothermic which might, for example, be representative of crystallization (Purgor 1995). A schematic representation of the arrangement is shown in Fig. A.9.

It has been found that the addition of particulates to semi-crystalline polymers can have an effect on the crystalline lamellar. In addition some coupling agents also act as crystalline nucleation centers. Integration of the endothermic peak on a DSC thermogram yields the heat of fusion associated with the crystalline regions of the polymer from which the percent crystallinity can be estimated by compared with the heat of fusion of a 100% amorphous sample ($295\,\mathrm{Jg}^{-1}$, for example, for polyethylene) after establishing the baseline for the process (Peacock 2000).

A sister technique is also sometimes used in which the heat flux is maintained constant and differences in temperature are detected. This is usually known as Differential Thermal Analysis (DTA).

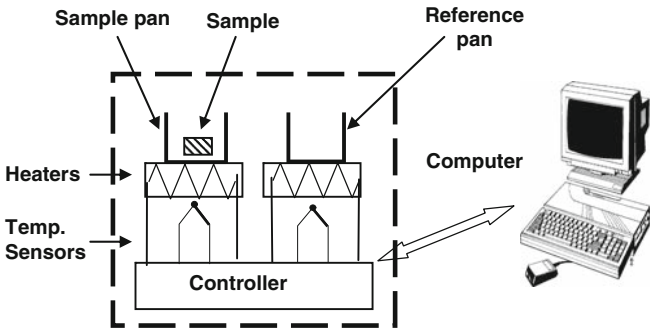

Fig. A.9 A schematic representation of a DSC apparatus

A.9 Electric Strength, Voltage Endurance, and Partial Discharge Measurements

The motivation for the development of nanodielectrics is often to elevate the dielectric strength or improve the aging properties of a material in comparison with the equivalent measures exhibited by the base polymer. In some instances there have been standards developed for the measurement of these properties. Examples for the electric strength of solids may be found in IEC 243 or ASTM D149 (Nelson 1983), but these are often difficult to apply during the development stages of nanocomposites since they require specific sample size and/or dimensions which is often inconvenient. All the tests described in this section involve the use of high, and thus lethal, voltages. Consequently it is imperative that they be carried out by trained individuals in a properly screened and interlocked area with appropriate safeguards and grounding.

There is often a great deal of confusion between the meaning of dielectric strength and voltage endurance. Electric strength involves the application of increasing voltage to a sample or piece of equipment until it fails. The instantaneous voltage (or equivalent voltage gradient) at the point of failure is then recorded as a measure of the electric strength. In contrast, the voltage endurance involves the application of a fixed voltage and the measurement of the time until failure (i.e. the longevity). For voltages at the high end of the range, failure may occur in minutes (or even shorter). This is illustrated in Fig. A.10 introduced later where the first data point is taken less than 1 min after voltage application. In such circumstances the electric strength and voltage endurances tests are really synonymous. However, at lower stresses, failure may take months, or even years so that the voltage endurance test is measuring the aging properties of the material (or device).

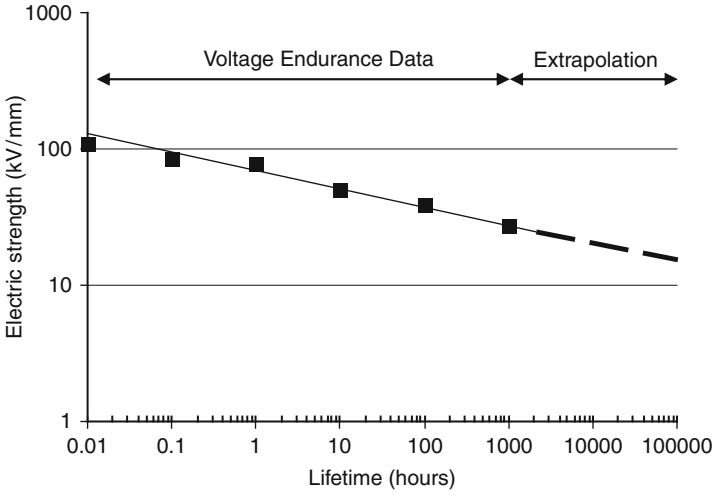

Fig. A.10 Example of a voltage endurance curve for an epoxy resin in a mildly divergent field

A.9.1 The Stochastic Nature of Electrical Failure

Electric breakdown is a stochastic process, and both the electric strength and voltage endurance are distributed parameters. Unlike gaseous dielectrics, electric strength measurements in solids exhibit a substantial scatter which dictates that a large number of breakdown measurements are required in order to establish a reliable mean (characteristic value) and standard deviation. Typically, the probability density distribution often has a long lower tail which dictates that designers build in large margins of safety. Although it is beyond the scope of this book to examine the background, it is sufficient to recognize that the "weak link" nature of electric breakdown often favors the statistical description of breakdown by one of the asymptotic extreme value distributions (Gumbel 1967). Most commonly used is the 1st or 3rd (Weibull) distribution of smallest values (Dissado and Fothergill 1992). This cumulative Weibull distribution is defined by the relationship:

$$\begin{aligned} P(x) &= 1 - \exp\left[- \left\{ \frac{(x-\gamma}{\alpha} \right\}^{\beta} \right] \quad x \geq \gamma \\ &= 0 \quad x < \gamma \end{aligned} \tag{A.12}$$

where x is the stochastic failure variable (stress or time for a strength or endurance test respectively), α is the characteristic value (scale parameter), β is the shape parameter, and γ is the location parameter. It is common to simplify this relationship into a 2-parameter distribution by assuming $\gamma = 0$ which allows an unreal finite probability of failure at zero stress in an electric strength test. Unlike a Gaussian distribution where the mean corresponds to a 50% probability, the characteristic value of a Weibull distribution corresponds to $P = 0.632$. The shape parameter, β, is a measure of the spread of the distribution (in the same way as the standard deviation in a Normal distribution) - the smaller the value of β, the greater the scatter. The treatment of dielectric data in this way, the use of confidence bounds and life prediction may be found elsewhere (Wilkens 1987; Montanari and Fothergill 2005).

A.9.2 Electric Strength

The electric strength of a solid dielectric may be determined under direct, alternating (usually power frequency) or impulse voltages. In general they will produce widely different results (even if the DC case is compared with the peak AC voltage). The reasons for this involve both the well-known volt-time relationship for breakdown and also the build up of space charge to modify the internal field.

Breakdown tests are usually conducted with laminar samples between plane parallel electrodes with contoured edges to create a uniform field. However, there is often a problem of breakdown around the edges for thin samples. In such cases recessed samples with deposited metallic electrodes (Nelson 1983) are to be pre-

ferred, but a liquid, or high-pressure electronegative gas, ambient can also be used to circumvent unwanted "creep" failure. Tests at elevated temperatures are often needed and can be accommodated by placing the test electrodes in a thermostatically controlled oven equipped with a high-voltage bushing. It is usual to place a limiting resistor between the high-voltage power supply and the test cell to limit the current which flows on breakdown to safe levels. In the case of impulse voltages, such resistors will also be needed to provide the desired waveshape. However, it is important to insure that the voltage measurement is made directly across the test cell and not on the power supply side of the limiting resistor. A resistive voltage divider is suitable for measuring the breakdown voltage under DC conditions, but time-varying voltages often necessitate the use of dividers which compensate for the effects of stray capacitance (Kuffel and Zaengl 1984).

The inherent non self-healing nature of breakdown dictates that a virgin specimen is used for each test. The number of tests required to establish a reliable mean value depends on the level of confidence required, but results using less than about ten samples will not be reliable – see Sect. A.9.1.

A.9.3 Voltage Endurance

The measurement of the life of a dielectric material or system at a given voltage is used either when the system tested is characterized by non-uniform field or internal imperfections such as gaseous voids. Under these circumstances, the mechanism of breakdown involves partial discharge deterioration or discharge channeling which are time consuming processes. Attempts to undertake voltage endurance tests on materials without imperfections under uniform fields usually results in the initiation of breakdown propagating immediately to failure. Endurance measurements are, however, important for nanodielectrics since the proliferation of internal interfaces have been shown to act as barriers to hinder channel propagation and, consequently, substantially enhance the lifetime of the material. An example of a voltage endurance plot is shown in Fig. A.10, scaled in term of stress. It is usually found that the data is approximately linear on a log-log plot implying a power law relationship relating the endurance, t, to the applied voltage, V:

$$t = AV^{-n} \tag{A.13}$$

For polymers the exponent, n, is in the range 3–8 but can be as high as 12 for materials such as those used in machine stator bars containing mica to resist partial discharge degradation. In some circumstances failure in the lower stresses can take many months making this test very time consuming. Consequently, it is common practice to populate the high stress region of the plot first and then extrapolate the curve into the lower stress region. However the usual caveats apply when extrapolating through several orders of magnitude, and attempts to estimate the lifetime at working voltage levels usually fall into this situation.

A.9.4 Partial Discharge Measurements

The practice of making partial discharge (PD) measurements has become commonplace over the last 25 years for high-voltage equipment, but it may also be used to assess materials. The book by Kreuger (1989) is dedicated to the subject but most books of high-voltage engineering include a chapter on PD measurements to which the reader is referred for detail (Kuffel and Zaengl 1984; Bartnikas and McMahon 1984) and commercial detectors are widely available. When a solid material is either subjected to a highly divergent electric field, or contains gas-filled voids/delaminations, then it is likely that small discharges will occur within the structure without immediately prejudicing the dielectric integrity. However, over a period of time, such internal discharge activity will erode the material through ion bombardment, soft-X rays, and electrochemical processes so that the lifetime is truncated and failure occurs prematurely.

The PD technique is usually undertaken with AC energization (see later) and essentially detects the high frequency components generated by the internal discharges that can be made to circulate in an external circuit. By appropriate calibration, one can assess the discharge inception voltage and the magnitude and number of the partial discharges. In some circumstances, the technique is combined with advanced signal processing techniques to generate phase-resolved data, fractal dimensions, statistical information, time series analysis, etc. which can provide indices correlated with condition. The simplified schematic in Fig. A.11 illustrates the basic principle.

The test object is energized through a high-voltage transformer provided with filters on the primary and secondary sides to eliminate high-frequency signals originating from the mains or within the test transformer itself. All the components in the high-voltage circuit must be discharge-free, the conductors of sufficient radius to

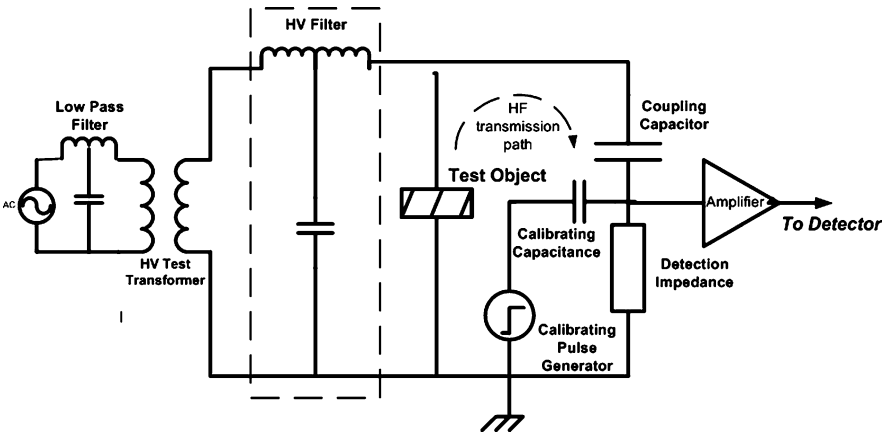

Fig. A.11 Schematic of basic PD detection arrangement

eliminate discharges, and connections shielded with large radius shields. PD occurring within the test object circulate high-frequency pulses around the loop formed by the coupling capacitor on the right hand side of the circuit (see Fig. A.11). These pulses drop a voltage across the detection impedance, which is amplified and fed to some form of detector. In the most basic arrangement, the detector could be an oscilloscope (perhaps with an elliptical timebase to facilitate phase resolution of the PD pulses), but modern detectors usually involve fast A-D converters and the storage of the digitized signal for further processing. The detection impedance can take various forms depending on the frequency response and sensitivity desired. The system can be calibrated by injecting a pulse of known amplitude through a specified coupling capacitance (as shown in Fig. A.11) so that the output pulses can be expressed in terms of the apparent charge (usually in pC).

PD often arise due to the presence of voids since the permittivity ratio between the gaseous void and the dielectric in series (in the range of 2.5–6 for most nonpolar polymers) creates a field enhancement, by capacitive divider action, in the void which contains the weaker dielectric (air). By this means, copious discharge activity may be present for every half cycle of a power frequency waveform. In contrast, although PD does also occur for direct voltages, the cavity must now be charged through the volume resistivity in series. This corresponds to a large time constant and results in far fewer discharges than in the AC situation. As a result, the DC duty is much less onerous.

References

Alison JM (1998) The pulsed electro-acoustic method for the measurement of the dynamic space charge profile within insulators. In: Fothergill JC, Dissado (eds) Space charge in solid dielectrics. Dielectrics Society, UK

Bamji SS, Abou Dakka M, and Bulinski A (2006) Phase-resolved PEA technique to measure space charge distribution in polymeric insulation. Proc IEEE Int Symp on Electr Insul: 350–353

Bartnikas R (1983) Dielectric loss in solids. In: Bartnikas R, Eichhorn RM (eds) Engineering dielectrics, IIA. ASTM STP783, Philadelphia, pp 3–117

Bartnikas R, McMahon EJ (1984) Engineering dielectrics, I. ASTM STP669, Philadelphia

Das-Gupta DK, Brockley RS (1978) A study of 'absorption currents' in low-density polyethylene. J Phys D 11:955–962

Dean JA (1995) The analytical chemistry handbook. McGraw Hill, New York

Dissado LA, Fothergill JC (1992) Electrical degradation and breakdown in polymers. Peter Peregrinus, London

Fothergill JC, Dissado LA (1998) Space charge in solid dielectrics. The Dielectrics Society, UK

Fothergill JC, See KBA, Ajour MN et al. (2005) "Sub-Hertz" dielectric spectroscopy. Proc Int Symp Electr Insul Mater: 821–824

Griseri V (2000) The effects of high electric fields on an epoxy resin, Ph.D. Thesis, University of Leicester, UK

Griseri V, Dissado LA, Fothergill JC et al. (2001) Photoluminescence, recombination induced luminescence and electroluminescence in epoxy resin. J Phys D 34:2534–2540

Gumbel EJ (1967) Statistics of extremes. Columbia Univ Press, New York

Guo TC, Guo WW (1983) A transient-state theory of dielectric relaxation and the Curie-von Schweidler law. J Phys C 16:1955–1960

Ieda M, Mizutani T, Suzuoki Y (1980) TSC and TL studies of carrier trapping in insulating polymers, vol 32. Memoirs of the Faculty of Engineering, Nagoya University, Nagoya, pp 173–219
Jonscher AK (1983) Dielectric relaxation in solids. Chelsea Dielectrics Press, London, pp 161–253
Kreuger FH (1989) Discharge detection in high-voltage equipment. Butterworths, London
Kuffel E, Zaengl WS (1984) High voltage engineering. Pergamon, Oxford
Laurent C, Massines F, Mayoux C (1997) Optical emission due to space charge effects in electrically stressed polymers. Trans IEEE DEI 4:585–603
Maeta S, Sakaguchi K (1980) A new method for determining the trap depth from thermally stimulated current. Jpn J App Phys 19:597–606
Many A, Rakavi G (1962) Theory of transient space-charge-limited currents in solids in the presence of trapping. Phys Rev 126:1980–1988
Mazzanti G, Montanari GC, Palmieri F et al. (2003) Apparent trap-controlled mobility evaluation in insulating polymers through depolarization characteristics derived by space charge measurements. J App Phys 94:5997–6004
McCrum NG, Read BE, Williams G (1967) Anelastic and dielectric effects in polymeric solids. Dover, New York
Montanari GC, Fothergill JC (2005) IEEE Guide for the statistical analysis of electrical insulation breakdown data. IEEE Std 930-2005 IEEE New York
Neagu ER, Marat-Mendes JN (2001) Anomalous transient currents in low-density polyethylene. Jpn J Appl Phys 40: L810–L812
Neagu R, Neagu ER (2004) Analysis of relaxation parameters and their distributions using fractional polarization thermally stimulated discharge currents. Trans IEEE DEI 11:242–248
Nelson JK (1983) Breakdown strength of solids. In: Bartnikas R, Eichhorn RM (eds) Engineering dielectrics, vol 2A. ASTM 783, Philadelphia
Nelson JK, Hu Y (2005) Nanocomposite dielectrics – properties and implications. J Phys D 38:213–222
Peacock AJ (2000) Handbook of polyethylene: structures, properties and applications. Marcel Dekker, New York
Pungor E (1995). A practical guide to instrumental analysis. CRC, Boca Raton
Raju GG (2003) Dielectrics in electric fields. Marcel Dekker, New York
Roy M, Nelson JK, MacCrone RK et al. (2005) Polymer nanocomposite dielectrics – the role of the interface. Trans IEEE DEI-12:629–643 &1273
Roy M, Nelson JK, MacCrone RK et al. (2007) Candidate mechanisms controlling the electrical characteristics of silica/XLPE nanodielectrics. J Mater Sci 42:3789–3799
Schonahls A (1998) Dielectric spectroscopy on the dynamics of amorphous polymeric systems. Novocontrol Appl Note Dielectr 1:1–16
Suh K-S, Tanaka J, Damon D (1992) What is TSC? IEEE Electr Insul Mag 8:13–20
Teyssèdre G, Cissé L, Mary D et al. (1999) Identification of the components of the electroluminescence spectrum of PE excited in uniform fields. Trans IEEE DEI-6:11–19
Teyssèdre G, Tardieu G, Mary D et al. (2001) AC and DC electroluminescence in insulating polymers and implication for electrical ageing. J Phys D 34:2220–2229
Van Turnhout (1975) Thermally stimulated discharge of polymer electrets. Elsevier, Amsterdam
Wilkens WD (1987) Statistical methods for the evaluation of electrical insulating systems. In: Bartnikas (ed) Engineering dielectrics, vol 2B. ASTM 926, Philadelphia
Wintle HJ (1974) Absorption currents and steady currents in polymer dielectrics. J Non-Cryst Solids 15:471–486
Wintle HJ (1983) Conduction processes in polymers. In: Bartnikas R, Eichhorn RM (eds) Engineering dielectrics, IIA ASTM, Philadelphia
Wolter KD, Johnson JF, Tanaka J (1987) Polymer degradation and its measurement. In: Bartnikas (ed) Engineering dielectrics, vol 2B. ASTM 926, Philadelphia

Index

A

Ab initio computations, 134–137, 153, 156
Abrasion, Abrasive wear, 163–165, 179–183
Absorption current, 286, 296–299, 312, 350, 351
Acoustic wave, 343–346
Activation energy, 20, 121, 210–212, 216, 219, 220, 273, 275, 301, 304, 339, 347, 348
Actuator, 332, 333
Adhesion, Adhesive wear, 39, 44, 154, 164, 174, 175, 179–182, 192
Agglomerates, 7, 36, 46, 246, 254, 255, 263, 280, 306
Aggregates, 7–11, 32, 36, 42, 43, 53, 59, 125, 192, 221, 280, 295
Alkyl-ammonium, 68, 71, 74, 76–78, 80–83, 189
Alkyl-ammonium chloride, 48
Alkyl-chlorosilanes, 36
Alkyl groups, 36
Alkyl-phosphonium, 37
Alkyl-silazanes, 36
Alumina (Al_2O_3). *See* Aluminum oxide
Aluminum oxide (Al_2O_3), 7, 33, 102, 114, 119–121, 151–153, 174, 210, 229
Aminoethyl-aminopropyl-trimethoxysilane (AEAPS), 24, 25, 112, 295
3-Aminopropyltrimethoxysilane (APS), 173
Amorphous, 13, 25, 47, 97, 98, 101, 114, 138, 185, 199–201, 219, 240, 287–289, 293, 301, 326, 340, 356
Anionic exchange capacity (AEC), 39
Arc resistance, 2
Arrhenius relationship, 201
Aspect ratio, 31–33, 35, 53, 54, 56, 57, 59, 127, 165–168, 170, 177, 185, 229, 263–265, 277–280, 311, 312

B

Band gap, 135–138, 140–142, 144, 151–153, 199, 201, 273, 274, 288
Band offset, 134, 135, 139, 140, 144
Basal spacing, 74, 75, 78, 80, 82, 85, 86, 91
Boehmite, 32, 37, 47, 48, 53–57, 249, 250
Bonding, 6, 11–13, 20, 95–97, 100, 108–114, 116–126, 137, 153, 164, 168–171, 173–175, 184, 185, 230–233, 235, 239, 240, 242, 295, 349
Breakdown strength. *See* Electric strength
Bulk moduli, 135, 137
By-products, 48–52, 146, 288

C

Cable terminations, 259–261
Capacitive field grading, 261, 275–277
Capacitor applications, 4, 98, 102, 332
Carbon nanofiber (CNF), 182, 309–312, 315, 329
Carbon nanotube (CNT), 7, 32, 35, 36, 39, 40, 44, 45, 60, 164, 168–170, 178, 182–186, 206, 259, 262, 264, 276–281, 308–309, 311, 312, 315, 332, 333
Carbon number, 82, 83
Cationic exchange capacity (CEC), 41, 105
Ceramics, 33, 47, 73, 223, 322, 326, 332, 344, 354, 190191
Charge distribution, 212–214, 255, 256, 293, 294, 314, 341, 343–345, 354
Charge injection, 21, 55, 109–110, 133, 213, 286, 298, 299, 303, 308, 315, 316, 341, 343
Charge mobility. *See* Mobility
Charge recombination, 26, 351
Charge storage and transport, 11, 16, 18, 197–215
Chemical bonding. *See* Bonding
Chemical defect, 138, 202, 288

Chemical functionalization. *See* Functionalization
Chemical structure of nanoparticles, 34, 102–104, 107–108
Clay, 2, 7, 8, 16–18, 34, 35, 40–44, 47, 58–60, 65–92, 104, 108, 113, 114, 116, 121, 123, 124, 170, 176–179, 182, 220, 328
Clay slurry, 88
Clustering, 9, 11, 43, 46, 169
Coarse-grained molecular dynamics, 86, 87
Colloidal nanoparticles, 101, 103–104, 108
Compatibilization process, 32, 36, 48–52
Compounding, 6–14, 36, 41, 43, 45, 46, 82–88, 95, 111, 182
Conduction band minimum (CBM), 138–140, 154
Conduction band offset (CBO), 140, 141
Conduction current, 53, 54, 201, 211, 314
Conductivity, 4, 6, 17, 26, 27, 33, 36, 53, 102, 121, 138, 163–165, 190–192, 197, 198, 201, 202, 207, 209, 210, 215, 253, 259–281, 285, 286, 293–316, 325, 328, 329, 331, 340
Conformational disorder, 138
Contaminants, 48–57, 220
Corona resistance, 2, 189
Coupling agent, 6, 20, 24, 36, 39, 76, 95, 96, 102, 103, 108, 110–114, 116, 125–127, 232, 236, 256, 292, 356
Crack bridging, 164, 171, 177–178, 183, 184, 330
Crack deflection, 164, 174–176
Crack pinning, 163, 171–174, 176
Creep behavior, 184–186
Cryogenic, 172, 321, 324, 330–332
Crystallites, Crystallinity, 17, 25–27, 98, 100, 111, 113, 124, 126, 179, 185, 191, 200, 232, 236, 240, 331, 356
Curie von Schweidler law, 350
Curing, 42–44, 75, 85, 90, 121, 236, 328, 341, 355

D
De-bonding, 164, 175–176
Debye process, 340
Deconvolution algorithm, 342
Defect state, 133, 139, 143–145, 151–153
Degradation, 13, 17, 133, 164, 189, 244, 245, 249, 250, 254, 322, 326, 327, 330, 359
Delamination, 8, 37, 41, 59, 60, 163, 171, 360
Density functional theory (DFT), 134–142, 144, 146, 151, 153, 154, 156
Density of states (DOS), 141, 142, 201
Dicumyl peroxide, 15, 99, 111, 113, 295, 308
Dielectric absorption, 21–24, 350–351
Dielectric constant, 134–137, 142, 144–150, 154, 156, 261, 265, 275–277, 309, 327, 332, 333, 350. *See also* Relative permittivity
Dielectric loss, 1, 7, 19, 50, 100, 121, 127, 253, 260, 326, 350
Dielectric response, 121, 133, 135, 146, 215–220
Dielectric spectroscopy, 13, 19–20, 51, 56, 57, 127, 211, 215–216, 218, 339–341, 347, 351
Differential scanning calorimetry (DSC), 124, 356
Dipole relaxation, 119, 121, 347
Dispersion, 3, 7–11, 20, 36, 37, 39, 41, 43–48, 58–60, 67–74, 76, 77, 85–88, 103, 105, 113, 114, 120, 121, 168, 169, 178, 179, 181, 182, 216, 218, 220, 221, 246, 247, 256, 259, 263–265, 267, 269, 270, 277, 278, 280, 281, 293, 309, 311, 328, 329, 339–341
Distribution, 1, 3, 4, 6–9, 11, 21, 43, 45, 46, 49, 54, 58, 102, 139, 156, 166, 174, 176–178, 207, 212–214, 225, 256, 264, 265, 277, 291, 293, 294, 314, 330, 333, 341, 343–345, 354, 358
Dynamic mechanical analysis (DMA), 68

E
Edisonian approach, 322
Elastic constant, Elastic modulus, 135, 163, 165–170, 176, 329, 333
Electrical breakdown. *See* Electric strength
Electrical insulation, 1–7, 18, 50, 67, 69–70, 164, 190, 220, 321, 322, 324, 325, 328–330, 334
Electrical mobility, 138, 273, 293–295, 304, 305, 315
Electrical treeing, 16, 20, 71, 224, 325
Electric strength, 1, 4, 7, 14, 26, 27, 35, 49, 53–55, 151, 221, 275, 276, 285, 324–328, 333, 357–361
Electrochemical treeing, 20, 248
Electrode effects, 202
Electroluminescence, 25–26, 125, 252, 329, 351–353
Electromagnetic shielding, 323
Electron affinity, 138, 139, 287, 301
Electronic structure, 12, 27, 133, 137–144, 151, 154, 156
Electron Mobility. *See* Electrical mobility

Electron paramagnetic resonance (EPR), 12, 100, 107, 109, 117, 122–124, 127, 348–350
Electron transport, 263, 293, 301, 309, 348
Entanglement, 6, 17, 113, 116–126, 164, 287
Entropic control, 188
Epoxy resin, 14, 32, 33, 43, 44, 65, 68, 70, 71, 75, 77, 82, 84–87, 90, 91, 99, 120, 164, 171–173, 175, 178, 200, 211, 213, 223, 229, 325, 326, 357
Epoxy-TiO_2 formulation, 16
Erosion, 4, 17, 18, 35, 46, 69, 179, 229–256, 326–329
Ethylene-vinylacetate (EVA), 32, 42, 48–52, 54, 106, 124, 127, 213, 214, 229, 237
Excluded volume, 263–265, 277, 278, 310–312
Exfoliation, 33, 37, 41–43, 59, 60, 73–76, 78, 83–86, 88–90, 95, 104, 106, 108, 114, 164, 178, 281, 312
Extensional flow mixer (EFM), 46
Extrusion, 26, 41, 45, 98, 107

F
Fatigue crack propagation (FCP), 183–185
Fermi energy, 139, 143, 145
Field grading, 259–281, 330
First principles methods, 135
Flame resistance, Flame retardants, 67, 71–73, 104, 189, 245, 308, 323
Flammability, 4, 189
Flexural modulus, 74
Fluorohectorite, 48, 53–57, 106, 127, 213, 214, 312–314
Formation energy, 155
Fourier transform infrared spectroscopy (FTIR), 12, 13, 80, 108, 112, 116–118, 120, 127, 354, 355
Fowler-Nordheim tunneling, 272, 275
Fracture energy, 46, 90, 91, 170
Fracture toughness, 163, 170–178
Free volume, 27, 100–101, 113–116, 122, 127, 187, 189, 235, 236
Fretting wear, 179, 181–183
Friction, 181, 182, 346
FTIR spectra, 12, 13, 118, 355
Fumed nanoparticles, 36, 102, 108, 111, 113, 245, 246, 329
Functionalization, 6, 11–14, 17, 20, 23, 33, 36, 39, 40, 47, 76, 95–127, 154, 168, 169, 205, 223–224, 226, 242, 278, 292, 297, 300, 315, 356
Functional properties, 67, 91
Fundamental properties, 67, 91

G
Gas barrier, 67, 71, 72, 104, 229, 244
Glass, 17, 19, 24, 26, 27, 32, 33, 36, 43, 47, 65, 66, 92, 96, 98–101, 104, 112–117, 122–124, 127, 164, 165, 171, 173, 176, 186–190, 219, 233, 236, 290, 299, 305, 310, 322, 327, 330, 340, 346, 356
Glass fiber, 65, 66, 92, 171, 330
Glass transition, 17, 19, 24, 26, 43, 96, 98–101, 113–117, 123, 124, 127, 164, 165, 176, 186–190, 219, 233, 236, 299, 310, 327, 340, 346, 356
3-Glycidoxypropyltrimethoxysilane, 17
Gouy-Chapman-Stern layer, 5, 27, 96, 113, 116, 124–125, 237, 293, 325
Grahame model, 292

H
Hafnia (HfO_2), 142, 143, 147, 148, 154–156
Halpin-Tsai theory, 165, 166, 168
Hamon's approximation, 351
Hardener, 43, 68, 75, 82, 84, 85, 90, 110, 117, 119
Heat distortion temperature (HDT), 74
Hectorite, 32, 33, 89, 90, 105
Helmholtz double layer, 96, 116, 292
Heterocharge, 21, 199, 212, 294, 295, 302, 306, 345
Heterostructure, 140, 142, 143, 145, 147, 152, 153
Hexamethyldisilazane (HMDS), 15, 24, 25, 295, 296, 298
Hopping conduction, 201, 273
Hot electron processes, 26, 151
Humid environment, 52, 53, 56
Hydrogen bonding, 13, 36, 108, 117, 168, 230, 231, 233, 234
Hydrotalcites, 32, 37, 38

I
Image charge, 298, 342, 343, 345
ImageJ®, 9, 11
Impact excitation, 351
Impact toughness, 178–179
Impurity conduction, 117, 348, 349
Infrared spectroscopy, 353–355
In-situ polymerization, 7, 36, 40–45, 88–91, 104, 105, 107, 113, 181, 190
Interaction zone, 6, 27, 205–212, 216, 218, 226, 229, 256, 291, 346
Intercalation, 33, 37, 39, 41, 44, 59, 73–76, 82, 83, 85, 86, 88, 104, 123, 124, 164, 189

Interface chemistry, 27, 110, 116–126, 142
Interface model, 155, 156, 232–237, 290–295, 312, 315, 316
Interface properties, 229–256
Interface region, 11–13, 17, 95–127
Interfacial bonding, 168, 169, 173, 185
Interfacial layer. *See* Interaction zone
Interfacial phonon scattering, 192
Interfacial polarization, 6, 19, 23, 50, 51, 117, 120–122, 149, 216, 218, 296, 340, 350
Interstitial, 155, 156, 263
Inverter, 4, 254, 328
Ionization potential, 135, 139, 140

J
Jet grinding, 306

K
Kramers-Kronig relationship, 350

L
Lamella, 35, 40–43, 53, 199, 200, 221, 287, 288
Layer-decomposed density of states (LaDOS), 141–145
Layered double hydroxides (LDH), 38, 39
Layered silicates, 7, 33–35, 40, 41, 44, 48, 56, 58, 82–88, 104, 105, 107, 119, 185, 218, 229, 236, 239–240, 242, 244, 245, 252, 312–316, 325
LDPE/MgO nanocomposite, 21, 243, 251, 306–308
LDPE/TiO_2 nanocomposite, 300–302
LDPE/ZnO nanocomposite, 304–305, 315, 316
Lichtenecker-Rother formula, 17, 305
Low frequency dispersion, 20, 218, 341

M
Magnesium oxide (MgO), 21, 22, 32, 33, 213, 214, 229, 243, 249–251, 306–308, 315, 327
Maxwell-Wagner effect, 6, 19
Mechanical properties, 4, 33, 35, 66, 68, 69, 74, 82, 92, 100, 108, 163–165, 168–171, 174, 186, 189, 245, 247, 323, 327, 329, 330
Melt blending, 40, 42, 45–47, 74, 75, 124, 309
Metal alkoxide, 47, 104
Metallic oxides, 32, 41
3-Methacryloxypropyltrimethoxysilane, 169
Michelson interferometer, 354
Micro-mechanics, 166
Migration barrier, 156
Mobility, 20, 23, 24, 101, 116, 119, 121, 124, 125, 138, 164, 185, 186, 201, 236, 273, 288, 290, 293–295, 297–300, 302–305, 308, 314, 315, 326, 327, 351. *See also* Electrical mobility
Moisture absorption and migration, 20, 52, 53, 56
Molecular mobility, 164
Montmorillonite, 7, 32, 33, 37, 41, 53, 65–67, 72, 80, 86, 89, 90, 219, 220, 312, 323, 329
Mori-Tanaka method, 166
Morphology, 8, 17, 29, 43, 45, 59, 100–101, 111, 113–117, 163, 179, 205, 220, 221, 226, 229–231, 236, 240, 242, 277, 290
Multifunctionality, 3–4, 14
Multilayer model, 146

N
Nanoclays, 32, 33, 107, 114, 127, 172
Nanofiller, 6, 12, 26, 31–33, 36, 41–43, 45–47, 51, 53–56, 58, 59, 106, 107, 119, 120, 124, 125, 163–167, 173, 186, 189, 190, 210, 212–214, 253, 256, 259, 263, 264, 275, 276, 281, 308, 329
Nanostructured materials, 36
Nanotube composites, 309
Nearest neighbor distance, 9
Newtonian flow, 86
Non-linear conductivity, 26, 259
Nucleation effects, 126

O
Organic modification, 36, 37, 73, 76–83, 88
Oxidation state, 133, 147–149
Oxygen radicals, 109, 349, 350

P
Packaging, 165, 323, 328, 329
Partial discharge, 17, 18, 69–70, 237–245, 249–251, 253–256, 316, 326, 329, 330, 351, 359–361
Particle functionality, 117, 126
Percolation, 6, 13, 26, 53–55, 57, 114, 127, 191, 205, 207–210, 215, 218, 235, 259, 263–265, 267, 268, 271, 274, 278, 280, 281, 291, 305, 310–312, 315, 316, 331, 351
Percolation threshold, 6, 191, 263–265, 268, 277, 278, 280, 281, 310–312, 315, 331
Phonon, 4, 134, 135, 145, 151–153, 156, 164, 191, 192, 273, 328

Photoluminescence, 26
Phyllosilicates, 33, 34, 38, 65, 104, 108
Piezoelectric transducer, 344
Plasma ablation, 244–245, 253
Plastic void growth, 164, 175–176, 184
Platelet, 31, 37, 58, 59, 116, 221
p-n junction, 197, 198, 206
Point defect, 134, 139, 140, 142, 151, 152, 155, 156
Polarization processes, 57, 339, 340
Poling, 50, 53, 298–300, 302, 303, 312–314, 346, 347, 350
Polyamide (PA), 18, 40, 41, 59, 66, 69, 74, 75, 77, 88–90, 98, 114, 116, 229, 232, 234, 236, 237, 239–240, 243–245, 316, 326, 332
Poly(ethylene-ethyl acrylate)/carbon nanotubes, 308–309
Polycrystals, 47
Polyethylene (PE), 12, 13, 15, 20, 21, 23–25, 33, 34, 42, 98–101, 103, 105, 107, 111, 113, 114, 120, 121, 124, 137, 138, 149–151, 153, 199, 200, 203, 213, 218, 220–222, 226, 229, 237, 242, 243, 249, 250, 286–289, 295, 296, 301, 327, 356
Polyethylene oxide (PEO), 34, 219, 220
Polyethylene–silica nanocomposite, 12
Polyimide, 17, 71, 72, 98, 172, 182, 210, 218, 329, 332
Polymerization filling technique (PFT), 42
Polymethylmethacrylate, 42, 45, 67, 98, 169, 170, 181, 189, 190, 233, 234, 278, 346
Polyolefins, 33, 42, 77, 266, 340
Polypropylene, 17, 33, 67, 68, 98, 106, 179, 213, 229, 231, 234, 237, 242, 312–315, 327, 329
Polypropylene/layered silicates, 312–315
Polystyrene, 42, 45, 66, 71–73, 98, 101, 116, 179, 187, 188, 233, 262, 277, 280, 309–312, 331
Polystyrene/carbon nanofibers, 309–312
Polytetrafluoroethylene (PTFE), 181, 183
Polyvinyl alcohol (PVA), 34, 98, 231, 327, 330, 332
Polyvinylidene fluoride (PVDF), 98, 125, 126, 137, 138, 144, 145, 176, 177, 332, 333, 342, 344
Projected density of states (PDOS), 141
Protonated octadecylamine, 48, 106, 213, 214, 312–314
Pulsed electroacoustic analysis (PEA), 21, 48, 49, 54, 294, 306, 312, 341–346, 353
Purification procedure, 48

Q
Quadrat method, 8, 11
Quantum-mechanical effects, 6

R
Relative permittivity, 1, 17, 19, 202, 216, 262, 287, 305, 310, 333, 339
Relaxation, 17, 24, 27, 51, 59, 100, 117–122, 125–127, 169, 216, 219, 237, 340, 341, 346, 347
Rheology, 26, 88

S
Scanning electron microscopy (SEM), 8, 59, 105, 106, 109, 169, 173, 174, 221, 245, 254, 280, 310, 311
Scattering effects, 16
Schottky barrier, 133, 139, 202, 263, 270–272
Segregation, 134, 154–156
Semiconducting nanoparticles, 263
Shear banding and crazing, 176–177
Shear moduli, 135, 137
Silane, 9, 10, 32, 36, 39, 76, 110–112, 126, 144, 145, 150, 151, 153, 184, 191, 230, 236, 241–243, 249, 290, 298, 299, 306, 315
Silanization, 36, 37, 39
Silanol groups, 12, 13, 36, 174
Silica. *See* Silicon dioxide (SiO_2)
Silicon, 32, 47, 59, 102, 104, 247, 265, 326, 349
Silicon carbide (SiC), 242, 265–272, 274, 275, 326
Silicon dioxide (SiO_2), 7, 12–14, 19, 20, 23–32, 102, 103, 108–111, 113, 125–127, 142, 144, 147–154, 188, 210, 229, 231, 271, 295, 296, 326, 349
Skewness, 8, 11
Sodium chloride, 48
Sol-gel process, 32, 47–48, 102, 104, 176
Solvent method, 40, 44, 45, 169
Space charge, 4, 16, 21, 22, 48–50, 54, 56, 96, 109, 125, 126, 198, 203–205, 210, 212–215, 218, 226, 252, 253, 271, 272, 293–316, 323, 325, 326, 341, 342, 344, 345, 350, 351, 358
Space charge limited current, 204, 210, 297, 313, 314, 316
Spherical particles, 31, 33, 102–104, 109, 111, 126, 166, 192, 207, 208, 263, 291
Statistical distribution, 1
Stern layer, 207, 212

Stoichiometry of nanoparticles, 95
Sub-hertz spectroscopy, 215, 340
Superconducting power cables, 324
Superhydrophobicity, 327
Surface erosion, 17, 229–256, 329
Surface fatigue, 179, 180
Surface functionalization. *See* Functionalization
Surface state tunneling, 288
Swelling, 33, 41, 75, 77, 90
Synthetic clays and micas, 95, 105, 107, 127

T
Tensile strength, 68, 83, 99, 176, 327
Tethered entanglement, 6, 17, 116
Thermal conductivity, 4, 17, 33, 102, 164, 165, 190–192, 263, 328, 329
Thermal degradation, 164
Thermal endurance, 229, 329
Thermal expansion, 2, 43, 163, 172, 325
Thermally stimulated currents (TSC), 24–25, 296, 298–300, 326, 346–348
Thermal stability, 112, 164, 189, 256, 327, 329
Thermo-mechanical properties, 164, 171, 186, 189
Thermoplastic, 7, 32, 40–42, 44, 48, 60, 74, 97, 98, 100, 111, 327, 330
Thermosetting, 32, 40–44, 191
Time-to-breakdown, 326
Titanium dioxide (TiO_2), 7, 16, 17, 25, 26, 33, 102, 103, 114, 115, 117, 119, 120, 122, 174, 213, 217, 229, 231, 300–304, 315, 316, 325, 329, 354, 355
Toughening mechanism, 171, 175–177, 179, 330
Transformer, 230, 322, 324, 328, 360
Transmission electron microscopy (TEM), 8–11, 58–60, 106, 124, 234, 306
Trap, 12, 13, 24, 25, 109–110, 121, 133, 135, 138, 144, 151, 153, 178, 200, 201, 204, 212, 215, 235, 287–289, 292, 293, 295–300, 303, 308, 312–316, 326, 329, 343, 346–349
Treeing lifetime, 249–250, 252, 253
Treeing resistance, 248–252
Tree propagation, 20, 71, 253–256, 325
Trialkoxysilanes, 36, 47
Triethoxyvinylsilane, 12, 15, 24, 25, 224, 295, 296, 298
Tunneling, 201, 207, 208, 263–265, 272, 279, 288, 289, 293, 305, 348

U
Ultrasonic methods, 7
Unpaired electrons, 349

V
Vacancy, 108, 143, 152, 156
Valence band maximum (VBM), 139, 140, 154
Valence band offset (VBO), 140–144
Varnish, 329
Vibrational frequency, 134, 135, 137, 353
Vinylsilane. *See* Triethoxyvinylsilane
Vinylsilane-treated particles, 12
Viscoelastic response, 164
Voltage endurance, 2, 4, 16, 17, 26, 224–226, 252, 285, 322, 325–327, 357, 358

W
Washing treatment, 48–50, 52
Water, 13, 14, 19, 20, 33, 42, 44, 47, 48, 52–56, 71, 72, 88, 95, 102, 105, 107, 108, 111, 112, 117, 120, 121, 125–127, 205, 211, 212, 216, 237, 238, 256, 280, 322, 340
Water shell model, 237, 238, 256
Water treeing. *See* Electrochemical treeing
Wave functions, 134, 135, 141, 142
Weak link, 1, 358
Wear and abrasion resistance, 164, 179–183
Weibull statistics, 14, 220
Whiskers, 31, 33
Wilkes model, 230–231, 256
Work function, 135, 139–141, 202
Work of adhesion, 154
Work of separation, 154

X
X-band microwave absorption, 348
XLPE/silica nanocomposite, 295–300, 302
X-ray diffraction (XRD), 58, 59, 82, 85, 244, 245

Y
Young's modulus, 17, 68, 166, 168, 170, 290, 333

Z
Zinc oxide (ZnO), 33, 37, 102, 114, 115, 117, 119, 120, 188, 267, 268, 304–305, 315, 316, 325, 329